Convection and Dynamo Action in Massive Stars

by

K. C. Augustson

B.S., Oregon State University, 2006

M.S., University of Colorado Boulder, 2009

A thesis submitted to the

Faculty of the Graduate School of the

University of Colorado in partial fulfillment

of the requirements for the degree of

Doctor of Philosophy

Department of Astrophysical and Planetary Sciences

2013

This thesis entitled:
Convection and Dynamo Action in Massive Stars
written by K. C. Augustson
has been approved for the Department of Astrophysical and Planetary Sciences

Juri Toomre

Prof. Bradley W. Hindman

Prof. Mark S. Miesch

Prof. Mark P. Rast

Prof. Jeffrey B. Weiss

Date

The final copy of this thesis has been examined by the signatories, and we find that both the content and the form meet acceptable presentation standards of scholarly work in the above mentioned discipline.

Augustson, K. C. (Ph.D., Astrophysical and Planetary Sciences)

Convection and Dynamo Action in Massive Stars

Thesis directed by Professor Juri Toomre

Contact between numerical simulations and observations of stellar magnetism is sought, with an emphasis on those stars that are the most readily observed and those that may have magnetic activity cycles: the Sun, F-type, and B-type stars. Two approaches are taken in studying stellar dynamos and dynamics, utilizing three-dimensional MHD simulations run on massively parallel supercomputers with the full spherical geometry and employing a new compressible code in the spherical wedge geometry. A 3D MHD simulation of the solar dynamo that utilizes the Anelastic Spherical Harmonic (ASH) code is presented. This simulation self-consistently exhibits four prominent aspects of solar magnetism: activity cycles, polarity cycles, the equatorward field migration, and grand minima. The ASH framework and this simulation's ability to capture many aspects of the solar dynamo represent a first step toward a more complete model of the Sun's global-scale magnetic activity and its cycles. The dynamics and dynamos of F-type stars are studied through global-scale ASH simulations, with significant contact made between the observed differential rotation and magnetic cycle periods of these stars and those achieved in the simulations. Separately, ASH simulations of core convection in the massive B-type stars show that generation of superequipartition magnetic fields with peak strengths above 1 MG is possible within their cores, which has implications for the evolution of these stars as well as for the properties of their remnants. The internal waves excited by overshooting convection and rotation in these stars radiative exteriors are assessed for their asteroseismic signatures. The results of 3D compressive MHD simulations of the solar near-surface shear layer with the Compressible Spherical Segment (CSS) code are shown, with such layers arising in the coupled dynamics of ASH and CSS as well as in a more rapidly rotating, thin convective envelope of an F-type star.

Dedication

To the RK4:

time cruelly marches on.

To RK45:

error tolerance, smooths

over the rough spots.

Acknowledgements

I would foremost like to thank Brad Hindman, Mark Miesch, Mark Rast, Juri Toomre, and Jeff Weiss for agreeing to serve on my thesis committee. Hopefully, it was not too daunting a task and the wide range of topics covered not too disparate.

Through his kindness and steady support, Juri Toomre has provided phenomenal opportunities throughout my tenure as a graduate student: from the influential months at the Les Houches summer school on dynamo theory to appreciating the idea-crystallizing opportunities that proposal writing can create. He has particularly been a kind guide and a patient friend during difficult times, allowing me the time to rekindle my passion for mathematical physics and turbulence theory. I am deeply appreciative the many lunches Juri and I have shared while discussing a plethora of topics we each enjoy. Moreover, the frequent dinners and after-dinner conversations he graciously invited me to share in were always delightful. To that end, Linda Toomre also deserves a hearty thank you.

Sacha Brun has been a mentor from afar, kindly offering several opportunities to work in France and to gain further exposure to the astrophysics community of Europe. During his extended stays in Boulder, I have always enjoyed his company, energy, and enthusiasm, whether it be the long hours spent slaving away in LCD or fine dining at Closerie de Lilas. Even though it has not yet happened, someday we will have our jam session!

I also have enjoyed conversations with Mark Rast, whose interest in the depths of turbulence theory has spurred my interest in alternative approaches to mean-field dynamics. Furthermore, his exuberance, openness, and philosophical approach to theoretical fluid mechanics encouraged my curiousity about the mathematical side of turbulence theory.

Similarly, Ben Brown's contagious enthusiasm for many aspects of fluid dynamics and applied mathematics kept me engaged in my first few years of graduate school, and has continued to yield interesting new avenues of research. For the untold hours of amusing conversation when we shared an office and for trying to coax me out of LCD during the four months of thesis writing, Nick Featherstone merits a thank you. Regner Trampedach has been a fount of knowledge and patient in answering my sometimes esoteric questions, but he also read portions of the thesis and his comments helped clarify them for which I am grateful. Gwen Dickinson certainly also deserves my gratitude for our wide-ranging conversations that almost always conclude with something depressingly political, and for being the wizard behind the curtain that keeps the group organized.

Finally, I wish to acknowledge my parents. Despite the anxiety and chaos of an early life in poverty, they formed a united front and insulated my siblings and me from the worst of it, and emerged from it through dedication and education. Though the hardest of those times have long since passed, they have left their lingering imprints. They nevertheless managed to foster in us a curiosity about the workings of the world and encouraged us to explore it through our imaginations and creativity. Had it not been for my mother's dedication to the family and my father's courage to be the first in his family to attend college, all done while working several jobs, I certainly would not have been able to wander down this long road.

Contents

Chapter

Tables

Table

Figures

Figure

Chapter 1

A Perspective on Solar Magnetism

"Stars... they are like living entities in a way, quite unpredictable." – Timicin

Magnetic fields and phenomena associated with them pervade the observable universe. The study of these phenomena has taken on a broad and necessary role in modern astrophysics. Indeed, magnetism impacts a wide variety of processes across the known progression of spatial and temporal scales of the universe: from its microscopic imprint in synchrotron emission emerging from supernova remnants to its macroscopic manifestations in collimating jets from supermassive blackholes in galactic centers. It also impacts processes from small-scale phenomenon such as the pair production of electron and positrons in the hypermagnetized atmospheres of young neutron stars to large-scale processes such as Faraday rotation of light traversing the vast gulfs between galaxies.

Magnetism may have even had a role in our universe's cosmogenesis, either through battery effects or through phase changes in the quantum fields dominant during early inflation (e.g., Grasso & Rubinstein, 2001; Brandenburg & Subramanian, 2005). Thus magnetic fields likely existed prior to the formation of the first stars. Those stars could amplify the primordial field through concerted dynamo action during their formation and evolution. Through their often explosive demise, they may have quickly injected strong magnetic fields into the nascent universe. It was through numerous recyclings of this first field that permitted the Sun to form from strongly magnetized plasma.

Yet the discovery of magnetic fields of stars is a relatively recent event, with the first

observations of solar magnetism by George Hale in 1908. This discovery inspired a search for magnetism on other stars, giving rise to the field of the solar-stellar connection and to stellar dynamo theory. It has turned out that magnetic fields impact processes in nearly all stars at some point during their lifetimes. Indeed, magnetic fields likely are a crucial ingredient in the accretion processes of star formation as they can easily modify pressure balances and angular momentum transport. They also may lead to the acceleration and collimation of polar jets observed in young stellar objects.

Most lower mass stars on the main sequence, namely those possessing a convective outer envelope like the Sun, are affected by magnetic processes. These stars exhibit a rich variety of magnetic behavior that influence the properties of stars and their environment, including any planets and circumstellar disks that they may host. Higher mass main-sequence stars too possess magnetic fields that lead to both enhanced angular momentum and mass loss, partly arising from dynamos in their convective cores. These fields are likely to have profound impacts on the lifetimes of such massive stars and on the resulting magnetism of any stellar remnants such as black holes, neutron stars, and white dwarfs.

Magnetic activity is now believed to be the primary driver for many of the properties of these stellar remnants. These include the X-ray spectrum and dramatic variability of accreting black holes and neutron stars, and the powerful relativistic jets that they produce. Magnetic fields are also invoked as the main ingredient that focuses the most energetic explosions in the universe: cosmic gamma-ray bursts. Yet despite the disparate regimes in which these stellar magnetic phenomenon exist, much of the physics that is applied in these areas of astrophysics is based directly on our understanding of the Sun's magnetic field.

To link these fields of study, a brief historical sketch provides an overview of some of the progress over the last century in the field of solar and stellar magnetism. This is then followed by a summary of current observational and theoretical efforts to understand the dynamics of magnetic fields in stars. Given that this field has largely observational origins and that these observations provide key constraints on stellar dynamo theory, they will be

expounded upon first.

1.1 Spatial Scales of Solar Magnetism

The dynamics proceeding within the Sun and its sphere of influence exhibit a vast range of spatial and temporal scales. A wide swath of our current understanding of physics must be simultaneously invoked to understand these dynamics, from the detailed atomic and molecular physics occurring at small-scales, which are linked across astrophysical scales to the dynamics captured by kinetic theory and radiation-magnetohydrodynamics. The influence of the Sun and its magnetism extends from the planets it hosts to the heliopause, where it melds with the interstellar medium. Some of this range of scales is apparent in Figures 1.1 to 1.6: from some of the smaller scales of magnetic bright points in the roughly 100 km wide intergranular lanes and to sunspots with 20 Mm scales (Figure 1.1), to supergranular scales (about 30 Mm) and networks of field on the solar disk (Figure 1.2), to the activity over its surface and in the transition region which occurs on scales of about 50 Mm as in Figure 1.3, to the broad behavior of the Sun's corona that exhibits scales of motion on the order of several solar radii (Figure 1.4), to the interplanetary magnetic field with scales of astronomical units (AU) (Figure 1.5), and finally to the outer boundary of the Sun's influence shown in Figure 1.6.

A small patch of the Sun's surface is shown in Figure 1.1a, from a modern ground-based telescope with adaptive optics. This exceptional image of the solar photosphere shows in great detail what was but "corrugations" to Herschel (William 1801). The patterns seen in the image are representative of the ubiquitous granular pattern of convection that covers the solar surface. Solar granulation occurs on a scale of about 1 Mm, with individual granules lasting about 10 minutes. In Figure 1.1a, the granules are imaged in photometric intensity, reflecting the temperature characteristics of the flow. Namely, a granule consists of a warm broad upflow rising from the deeper interior and cool narrow downflows. Rapid radiative cooling brakes these buoyantly driven upflows as photons can escape from the photosphere.

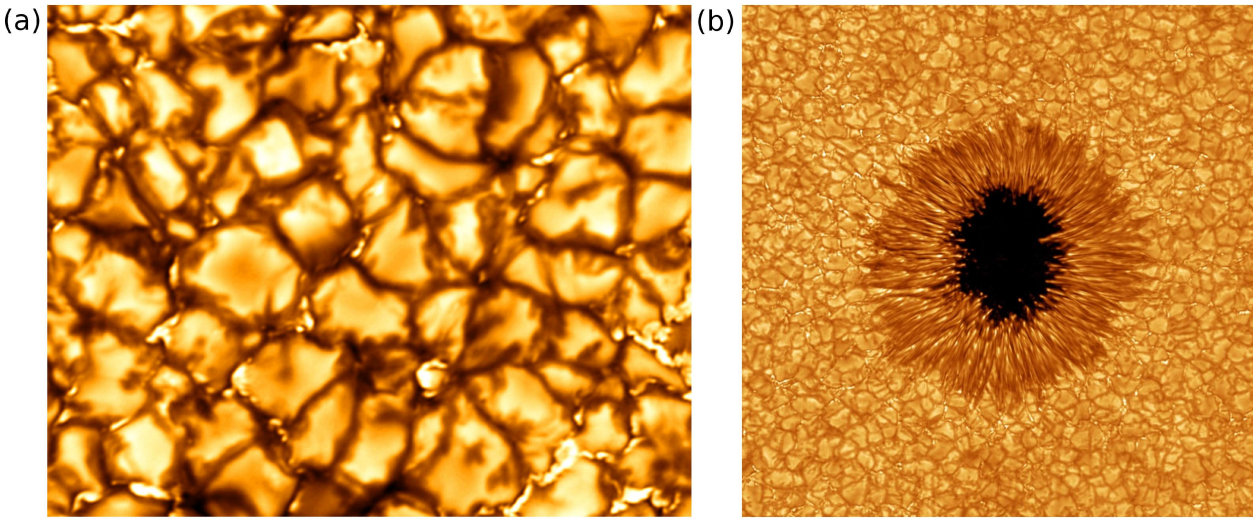

Figure 1.1: (a) High resolution solar granulation in wide-band 3964 Å Ca II emission, illustrating granulation with its 1 Mm scale, mesogranulation, bright points, and intergranular magnetism (23 May 2010, Swedish Solar Telescope). (b) Photospheric emission near 7060 Å passed through a TiO filter with a 10 Å bandpass, showing a sunspot with strong magnetic fields in its dark umbra and filamentary penumbra (active region NOAA 1084) and the surrounding granulation (2 July 2010, Big Bear Solar Observatory/NJIT).

The nearly sonic horizontal flows of these cells whisk this now cool fluid into the narrow downflow lanes that define a granule's boundary, where additional cooling further accelerates them inward. These flows also sweep fibrils of magnetic field into the intergranular lanes. These field fibrils form the bright points and networks seen in Figure 1.1a and represent the smallest currently resolvable magnetic feature on the Sun. Magnetic structures likely exist below this scale. Many of these smaller scales may be influenced by small-scale local dynamo action occurring both in the regions of strong shear between upflows and downflows and within the helical turbulence of the downflow itself (Vögler & Schüssler, 2007; Stein, 2012).

Magnetism has a substantial influence on the processes occurring below the solar surface. Figure 1.1b shows the omnipresent pattern of granulation, but punctuated with the dark umbra and penumbra of a single sunspot and lightened by emission from magnetic

structures in the intergranular lanes. Sunspots are regions where a fluted loop of strong magnetic field perforates the photosphere and can persist for just a few hours or up to several months. The magnetic field associated with the spot is typically several kG in strength, which largely suppresses convection in the region. In this image it appears dark since the blackbody emission from the region has a much lower temperature, about 1000 K cooler, than the surrounding photosphere. In this region, the magnetic pressure is a large fraction of the gas pressure. Since the spots exist very much longer than the sound crossing time across it. The sunspot is roughly in pressure equilibrium with the surrounding plasma, which requires that the gas pressure (and correspondingly the temperature) be lower in the spot. This leads to less emission in the observed bandpass, and to diminished emission at many other wavelengths as well. Recently, there have been major advances in understanding not only the surface dynamics but also the deeper dynamics within the upper 20 Mm of the Sun in regions around a sunspot, arising from both helioseismology and numerical simulations (Rempel & Schlichenmaier, 2011).

Supergranulation is a distinct convective scale seen at the solar surface, particularly in Doppler images, which exhibit spatial scales of about 30 Mm and persist for about a day (Leighton et al., 1962; Simon & Leighton, 1964; Rieutord & Rincon, 2010). This larger convective pattern is shown in Figure 1.2a in a Dopplergram from the Helioseismic and Magnetic Imager instrument (HMI) on the Solar Dynamics Observatory (SDO). Supergranulation is one of three distinct scales of convective patterns seen on the solar surface, along with granulation and the less well defined mesogranulation (which in turn has scales of about 5 Mm and lifetimes of a few hours, November et al. (1981); Rast (2003)). The mesogranular scale is somewhat evident as the smaller scale corrugations within the dominant supergranular signal. As with granulation, the supergranular signal is complicated as the line-of-sight (LOS) velocity changes across the disk: near disk center the LOS velocity of the plasma is predominantly radial, while near the limb it is mostly horizontal. So what is imaged across most of the disk are the fast $500\,\mathrm{m\,s^{-1}}$ diverging horizontal flows, giving rise to the alternating

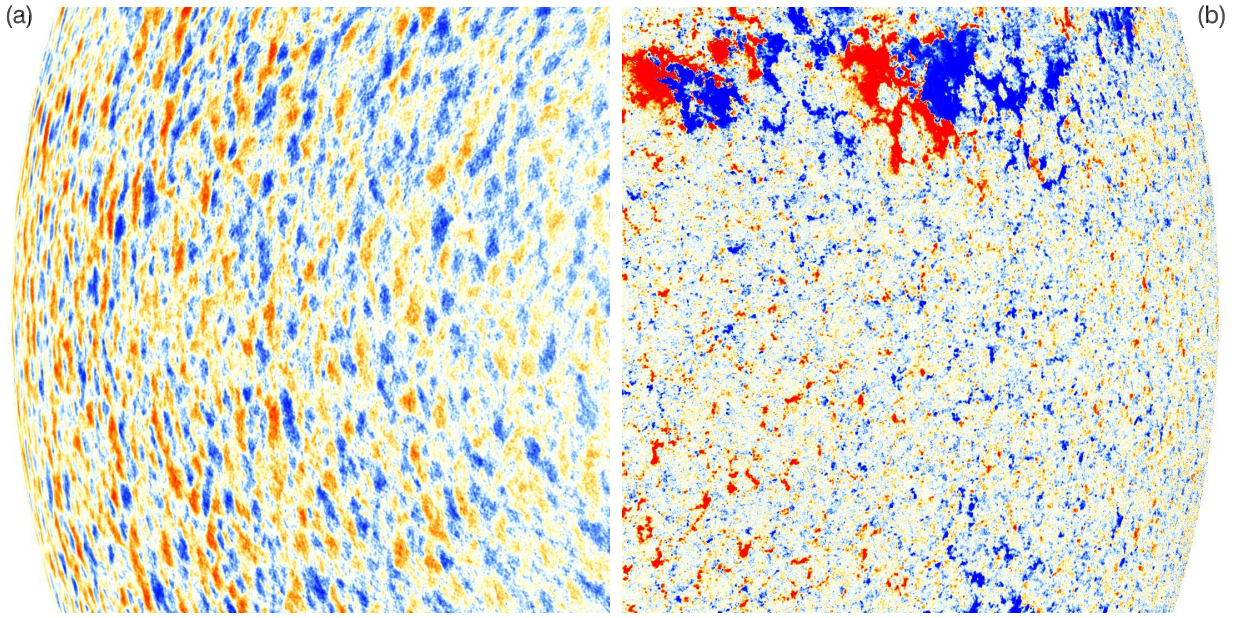

Figure 1.2: (a) The supergranular scale becomes apparent in time-averaged line-of-sight Dopplergrams of the surface convection from 21 July 2013. Blue tones indicate material moving toward the observer, and red tones the opposite. (b) An HMI magnetogram also from 21 July 2013, showing the line-of-sight magnetic field. The magnetogram is derived from spectropolarimetric measurements of the solar surface and serves to illustrate the supergranular magnetic networks in less active regions and the strong magnetic field linking sunspots in active regions. The field shown in red (blue) is directed toward (away from) the observer.

pattern of red and blue shifts seen in Figure 1.2a, with the front of a supergranule moving toward the observer and the back away. Figure 1.2b shows that the small-scale magnetic field horizontally advected by granulation and swept into the intergranular lanes organizes into larger-scale networks. This serves to demarcate the supergranules as magnetic field collects in their narrow downflow lanes. This figure also displays active regions that bristle with strong magnetic field that link sunspots of opposite polarity in arcades that soar above the photosphere as seen in Figure 1.3a.

Figure 1.3 shows emission in the Fe IX resonance line at 171 Å, which samples temperatures of about 0.6 MK. These temperatures occur in the transition region between the chromosphere and the corona. A single snapshot of this region is seen in Figure 1.3a, with a

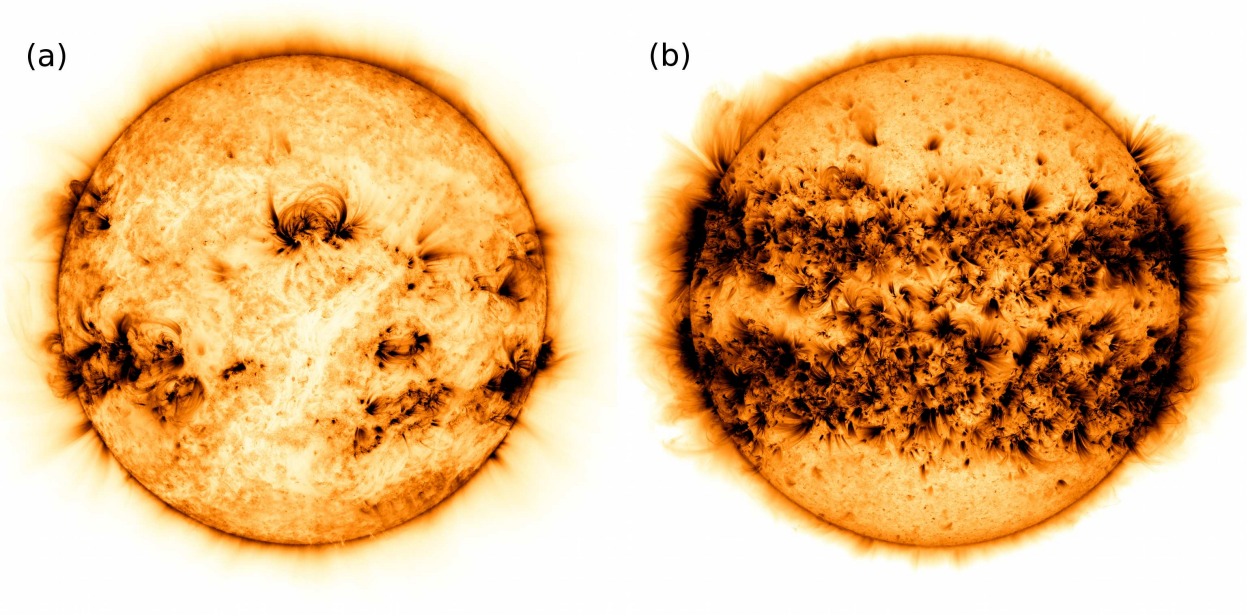

Figure 1.3: (a) The solar transition region imaged in the 171 Å channel with AIA on SDO from 20 July 2013, dark tones indicate areas of high emission and light tones low emission. (b) A composite of 25 images from the period between 16 March 2012 to 15 March 2013 in the same Fe IX resonance line, illustrating latitudinal bands of magnetic activity (NASA/SDO/AIA & S. Wiessinger).

prominent Ω loop of magnetic field linking two sunspot groups visible near the prime meridian in the northern hemisphere. Indeed, the magnetic field associated with sunspots can rise high into the solar atmosphere leading to inhomogeneity and local structural changes in the chromosphere and transition regions due to the loss of hydrostatic balance. This is evident in the composite image in Figure 1.3b, where the presence of active regions and strong magnetic fields at low heliographic latitudes are associated with a more extensive chromosphere. This is partially due to the low plasma β (ratio of gas pressure to magnetic pressure) in these regions, which causes the dynamics do be dominated by changes in the magnetic field. It is also a result of hot plasma being guided along the field lines and lifted higher into the atmosphere. Thus, over this year-long sampling, the base of the corona is further from the solar photosphere at low latitudes than at the poles, with the transition to the corona occurring at a height two to three times greater. More to the point, however,

Figure 1.4: Solar corona imaged during the 22 July 2009 total eclipse, showing the structure of the coronal magnetic field to about 5 solar radii (M. Druckmüller). A STEREO Helium 304 Å image from the time of the eclipse is lain over what would otherwise be the moon illuminated by earthshine (NASA/STEREO).

the emergence of active regions in latitudinal bands is a property of the global nature of the magnetic field and hints at the deeper mechanisms behind solar magnetic activity and its variability.

In the corona, plasma is largely frozen into the magnetic field and accelerated away from the Sun in its wind, with its density dropping quickly with increasing distance from the photosphere whereas the temperature remains nearly constant to nearly $10\,R_\odot$. These fields are normally difficult to image without something to mask the intense barrage of photons coming from the solar disk, so eclipses present an excellent opportunity for both enthusiasts and professionals to capture great images such as the one in Figure 1.4. This image shows

the structure of the fields lines in visible light near a minimum in the solar activity cycle. The field lines can be seen out to roughly 5 solar radii, with nearly open field lines stretching from the polar regions. Such open magnetic fields occur in coronal holes, which allows plasma to be rapidly evacuated along the field lines and so form the fast solar wind. On the other hand, the field is much more structured at low latitudes with some closed loops, often with the cusped field lines called helmet streamers. It is more difficult for the plasma to escape these regions, where the wind must do work against magnetic tension in order to escape and consequently loses some of its kinetic energy to the magnetic field. Hence, it is thought that these lower-latitude structures are responsible for the slow component of the solar wind. Yet once this plasma has escaped the Sun's surface, it can impact the planets and speed toward the boundary of the Sun's magnetic influence, where it eventually merges with magnetic fields and flows of interstellar space.

As the Sun rotates, the magnetic fields emanating radially from its surface are slowly wound, approximately producing an Archimedean spiral, which has been dubbed the Parker spiral after Parker (1958). Examples of this field can be seen in Figure 1.5, where three field lines are traced from the inner solar system to the heliopause. This figure also shows how the magnetic field becomes more tightly wound outside the termination shock. This shock forms when the pressure of the solar wind, which decreases as the square of the distance from the Sun, becomes equal to the ambient pressure in the interstellar medium (ISM). It forces the solar wind to slow to become submagnetosonic, heating and compressing the plasma and causing the streamlines of the solar plasma to slowly bend toward streamlines of the plasma flow in the ISM. This means that it is a dynamical, asymmetric surface that is modulated by the solar cycle, which has associated increases in particle fluxes, magnetic field strength, and wind speeds (Stone et al., 2008). The termination shock is believed to vary between 75 to 90 AU from the Sun, as measured by the two Voyager spacecraft (Stone et al., 2005). This shock also causes the magnetic field to be compressed, which sets the stage for its connection to the external magnetic field of the ISM.

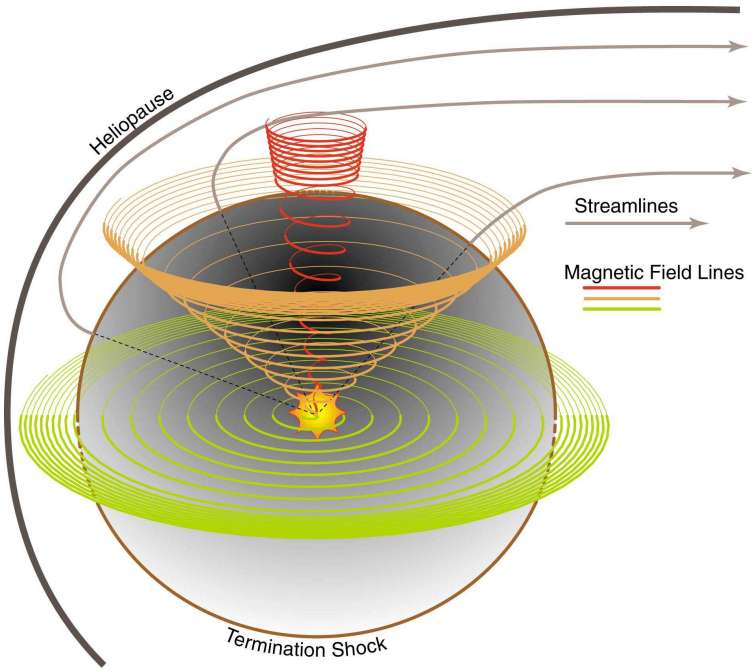

Figure 1.5: A sketch of the Sun's magnetic field, showing magnetic field lines spiraling outward from the photosphere, crossing the termination shock, and merging with the ISM at the heliopause. Three field lines are shown, one from the solar equator, and two from increasingly higher heliographic latitudes (S. Suess/NASA).

In order to probe the outer limits of the Sun's magnetic influence, two recent advances must be considered. The first is that the long-running Voyager mission has revealed a much stronger magnetic field outside of the termination shock than previously expected. It is on the order of 5 μG oriented about 30° above the galactic plane (Opher et al., 2009), whereas previous estimates had placed this value closer to 2 μG and at higher inclinations. Thus the local ISM is dominated by magnetic pressure with $\beta \sim 1/2$. This has several implications for the heliosheath, which is the region where the solar wind and the Sun's magnetism merge with that of the local ISM. It has recently been postulated that Voyager has already crossed the boundary into interstellar space and that the transition was just not as abrupt as expected (Swisdak et al., 2013). The second observational advancement comes from the surprising observations of the Interstellar Boundary Explorer (IBEX).

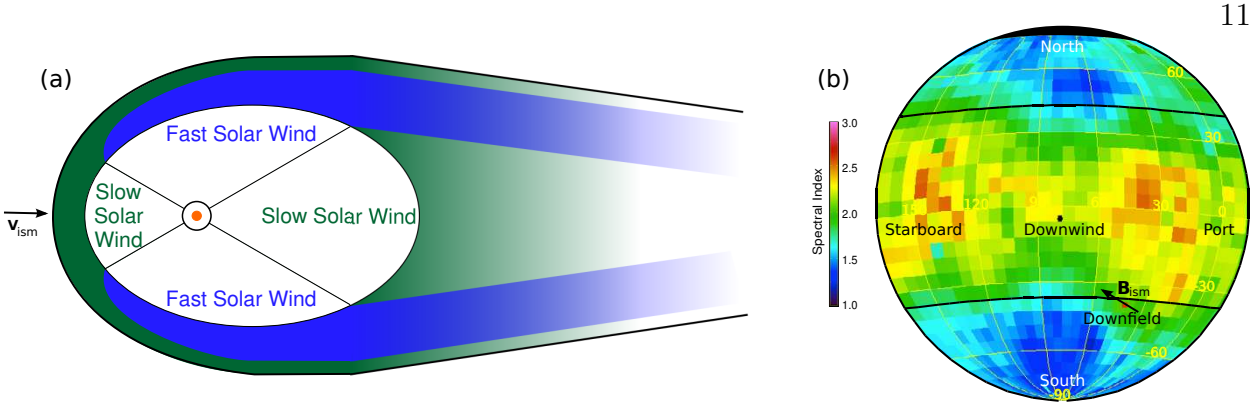

Figure 1.6: Schematic diagram showing (a) a cut parallel to the ISM velocity ($\mathbf{v}_{\rm ism}$) through the heliotail. (b) A Mollweide projection of the downwind hemisphere of the all-sky integrated IBEX spectral index observations, with the downwind direction at the origin showing the full latitude but only the longitudes between $-15°$ and $175°$. This shows the twisting of the solar wind plasma sheet in the direction of the external magnetic field ($\mathbf{B}_{\rm ism}$). Fast solar wind regions in (a) are indicated in blue and slow solar wind regions in green. The tail structure in (a) fades with distance as charge exchange losses deplete the heliospheric ions, and is tapered as external magnetic tension flattens it and the ions thermalize with the ISM (Adapted from McComas et al. (2013)).

Figure 1.6a presents a diagram of a potential heliosheath configuration, showing its cylindrical structure parallel to the direction of the mean flow of the interstellar medium (ISM). In Figure 1.6b the heliosheath is viewed as if looking down the tail, where observations from IBEX are displayed. IBEX detects back scattered solar wind ions that have been converted to energized neutral atoms through charge exchange interactions with the ISM plasma in the inner heliosheath. The intrinsically very low brightness of the heliosheath means that it cannot currently be observed by other means. Some of these scattered atoms are aimed at Earth, and since they are virtually unaffected by magnetic fields they travel in straight lines.

Moreover, these observations show that the kinetic energy spectra of weakly energized neutral atoms have slopes that vary spatially, being dominated by its quadrupolar component. Figure 1.6b shows that the slow-wind structure is tilted by roughly 10°, which is likely due to an interaction with the external ISM magnetic field. The direction of this field,

projected onto the observing plane, is indicated in the lower right of Figure 1.6b. The slow wind coming from the upwind side of the Sun is initially headed in the upwind direction. So it fills a thin layer just inside of the heliopause; the latter is shown with a thin black line. Given that there is a spectrum of wind velocities, the charge exchange interaction produces a heliotail with an extinction distance that roughly varies with the angular distance from the downwind flow direction. Homogenization through the exchange interaction also means that the tail is effectively evaporated within about 1000 AU. The heliosheath and heliotail should be squeezed along the ISM flow direction as the external magnetic and particle pressures increasingly push in from the sides. These processes are sketched in Figure 1.6a, where the heliospheric tail fades out and is tapered. It is here that the Sun's influence finally wanes, defining the largest spatial scale of its magnetism.

With the spatial extents of the Sun's observable magnetic field mapped out, the next question to ask is how does it vary with time? Thus the following sections detail the time scales exhibited by the Sun's observed magnetic fields. This ranges from indirect measurements utilizing our current knowledge of the solar-terrestrial connection and paleogeologic records to the most reliable and complete record of the Sun's magnetic activity: direct observations of sunspots. The modern era of sunspot observations provides a reasonable point to launch this retrospective look at the Sun's temporal variability.

1.2 Modern Sunspot Record

The modern record of sunspots begins in May 1874, with subsequent observations taking place across the world. The powerhouse behind the meticulous collection of sunspot areas and positions was the Royal Greenwich Observatory (RGO). Between this observatory and its sister sites in Cape Town, Kodaikanal, and Mauritius, photographic plates were used to collect sunspot data continuously between 1 May 1874 and 31 December 1976. These data included both overall sunspot area and just the umbral area, which were corrected for foreshortening effects and were given in micro-Hemispheres (μHem or $2\pi \times 10^{-6}$ steradians) as

in Figure 1.7b. In 1977 these measurements became the domain of the U. S. Air Force (USAF) and the National Oceanic and Atmospheric Administration (NOAA), with data being taken at five USAF Solar Observing Optical Network (SOON) sites. The techniques between the two observing campaigns differ in that sunspot areas are measured differently and that umbral areas are not measured. Other observatories have contributed to the overall effort with sunspot data available from Catania (1978-1999), Debrecen (1986-1998), Kodaikanal (1907-1987), Mt. Wilson (1917-1985), Rome (1958-2000), and Yunnan (1981-1992). This is useful when constructing a contiguous record, filling in any gaps in either the NOAA or RGO records (Hathaway, 2010).

The Wolf sunspot number R has enjoyed long-term use since its inception in 1848 by Rudolf Wolf (e.g. Wolf, 1850, 1861). It is defined as a linear function of the number of sunspot groups g and the total number of distinct spots s, with $R = K_O(10g+s)$, where K_O is constant that is intended to compensate for different observational methods. The later is particularly relevant when attempting to extend the modern record back to the first Western observations in 1610. An alternative measure is the Group sunspot number, which was introduced by Hoyt & Schatten (1998). The Group number is defined as $R_G = 12.08/N \sum_i^N k_i G_i$, with N the number of observers, k_i the i-th observer's correction factor, and G_i the number of sunspot groups observed by observer i. The factor of 12.08 normalizes R_G to R.

Though they have a shorter record than either the Wolf or Group sunspot numbers, sunspot areas are thought to be a more physical measure of solar activity since their area correlates with the flux of the magnetic field. Furthermore, as opposed to earlier observations, the modern record also provides accurate positional information. This allows the time dependent joint distribution of sunspot area and latitude (see Figure 1.7a), and/or longitude, to be easily examined without having to infer the coordinate system from dates and drawings as in earlier observations. Such figures are called Maunder or "butterfly" diagrams, following Edward Maunder's work at the turn of the last century (Maunder, 1904).

Such diagrams show some of the fundamental temporal and spatial features of the

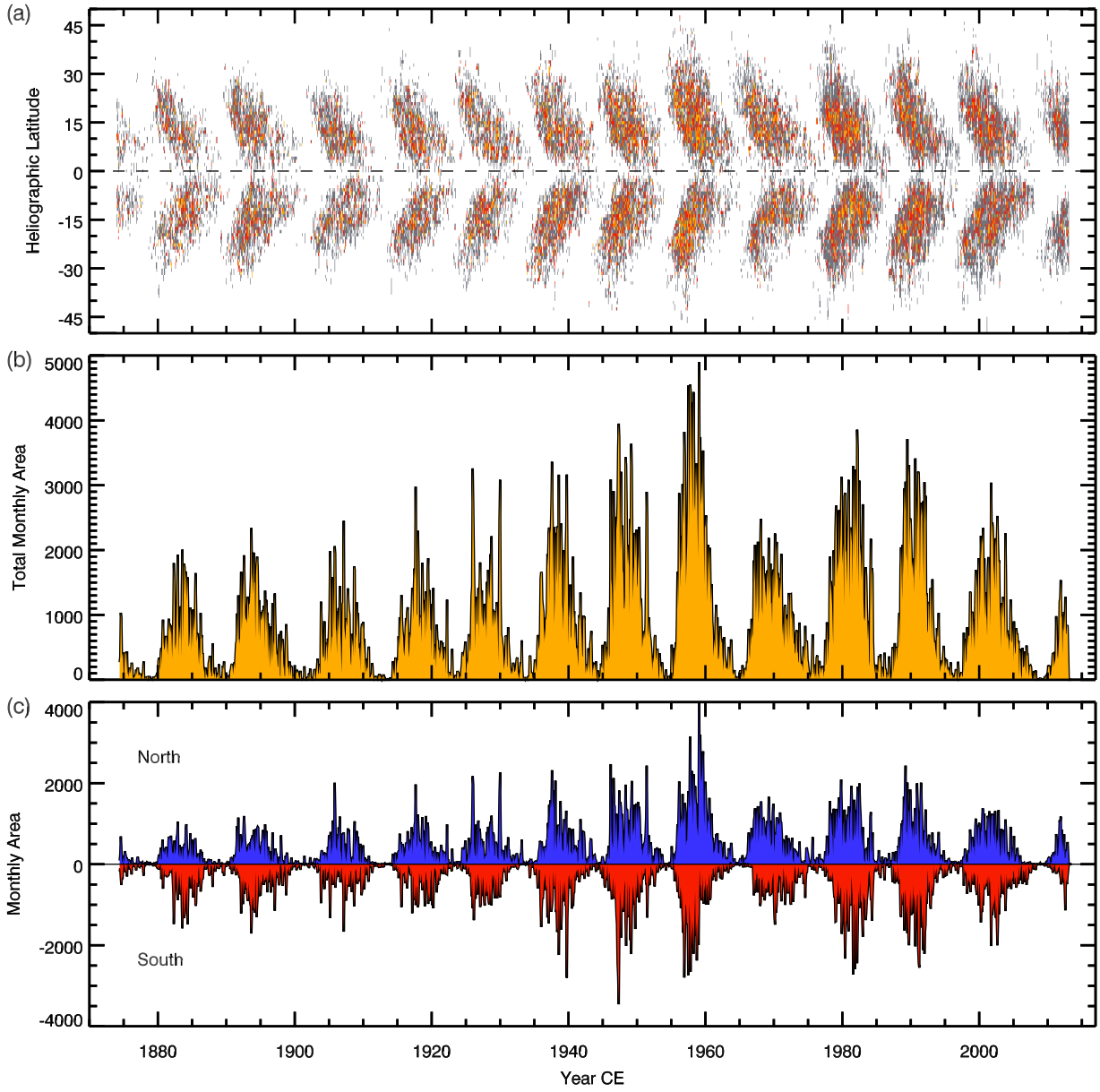

Figure 1.7: (a) A Maunder diagram that shows sunspot areal coverage in heliographic latitude and time, illustrating the equatorward propagation of spot emergence over the course of the many 11 year Schwabe cycles. Colors indicate sunspots with areas in the lower (gray), middle (red), and upper (blue) tertiles of their distribution. (b) Average monthly sunspot area in μHem, displaying the variability and longer-term modulation in sunspot area over the modern sequence of Schwabe cycles. (c) Average monthly sunspot area in each hemisphere (units as in panel b), indicating the phase differences between the northern (blue) and southern (red) hemispheres. (Here constructed from data provided by D. Hathaway/NASA)

solar dynamo, with the foremost such time scale being the roughly 11 year Schwabe cycle in sunspot area (Schwabe, 1844). During these magnetic activity cycles the total sunspot area and emergence frequency increases as the cycle progresses toward maximum and declines in its tail end. Each of these cycles is quite self-similar, with the migration of the magnetically active latitudes from mid-latitudes at the beginning of a cycle to low latitudes near its end. The quantification of this behavior is one of Gustav Spörer's contributions from the late nineteenth century, and has been dubbed Spörer's law of zones (Maunder, 1903). There is no mathematical rigor to this law, and it was first hypothesized by Richard Carrington in 1863 (Carrington, 1863). Yet the law of zones is qualitatively accurate for most known Schwabe cycles (11 year magnetic activity cycle) and was formulated and demonstrated by Spörer (1889): "Un peu avant le minimum, il n'y a de taches que près de l'equateur solaire, entre $+5°$ et $-5°$. A partir du minimum, les taches, qui avaient depuis longtemps déserté les hautes latitudes, s'y montrent brusquement vers $+30°$. Puis elles se multiplient, un peu partout, à peu prés entre ces limites, jusqu'au maximum, mais leur latitude moyenne diminue constamment jusqu'à l'époque du nouveau minimum."

As Spörer describes, this migratory pattern of sunspot emergence from mid-heliographic latitudes near the minima in magnetic activity to low-heliographic latitudes near maxima is consistent between cycles. In particular, for the records available since the mid-eighteenth century, even as the Sun entered the Dalton Minimum (1798-1825, see Figure 1.12), the cycles in magnetic activity are remarkably self-similar (Figure 1.7a). However, the precise origins of this particular behavior remain somewhat mysterious. Though, as will be shown in Chapter 3, there are theoretical clues that may lead to a better understanding of the solar cycle.

As evident in Figure 1.7a, it is notable that the cycles overlap by about a year with spots of the former cycle still emerging near the equator while spots of the succeeding cycle begin to appear at higher latitudes. The area of sunspots also builds towards a maximum (Figure 1.7b), which indicates that the mechanism producing them may be rising closer to the

surface or is increasing in intensity. The latitudinal extent of the activity bands widen during the rise to the maximum and narrow during the decline. Furthermore, the stronger cycles, namely those with greater monthly area, tend to have sunspots emerging at higher latitudes at the beginning of the cycle than the weaker cycles. The cycles are highly symmetric about the equator which is likely reflecting the strong dipole linking the hemispheres and a possible underlying toroidal magnetic field structure in the deeper interior.

If the cycles are considered independently, it is also clear that the Schwabe cycle is only approximate as cycles can vary in length by several years, although, the standard deviation of the cycle length is only 14 months. Appealing to Figure 1.7b, it is clear that cycles exhibit a positive skew, with a rapid rise toward maximum and a longer decay toward minimum. There is additionally a great deal of shorter time scale variability within a given cycle, particularly in the daily sunspot data, though, it is also evident in the monthly data displayed here. The multi-peaked nature of some of the cycles occurs when the two hemispheres become slightly out of phase so that they peak at slightly different times, as can be seen in Figure 1.7c. This phasing difference is most apparent as the cycle winds down with one hemisphere tending to have a greater number of spots.

Sunspots tend to erupt successively in groups that are more extended in longitude than in latitude. These groups often have one magnetic polarity associated with the westerly spots and the opposite polarity associated with the trailing spots (Figure 1.8b), reflecting the symmetry arising from the Sun's rotation. This feature of the Sun's magnetism was first described by Hale et al. (1919): "We already know that the preceding and following spots of binary groups, with few exceptions, are of opposite polarity, and that the corresponding spots of such groups in the Northern and Southern hemispheres are also of opposite sign. Furthermore, the spots of the present cycle are opposite in polarity to those of the last cycle." This is now codified as Hale's law.

The spots can form large groups, with the leading spots positioned at lower latitudes than the trailing spots, as in Figure 1.8a, and is called Joy's law after Hale et al. (1919): "It

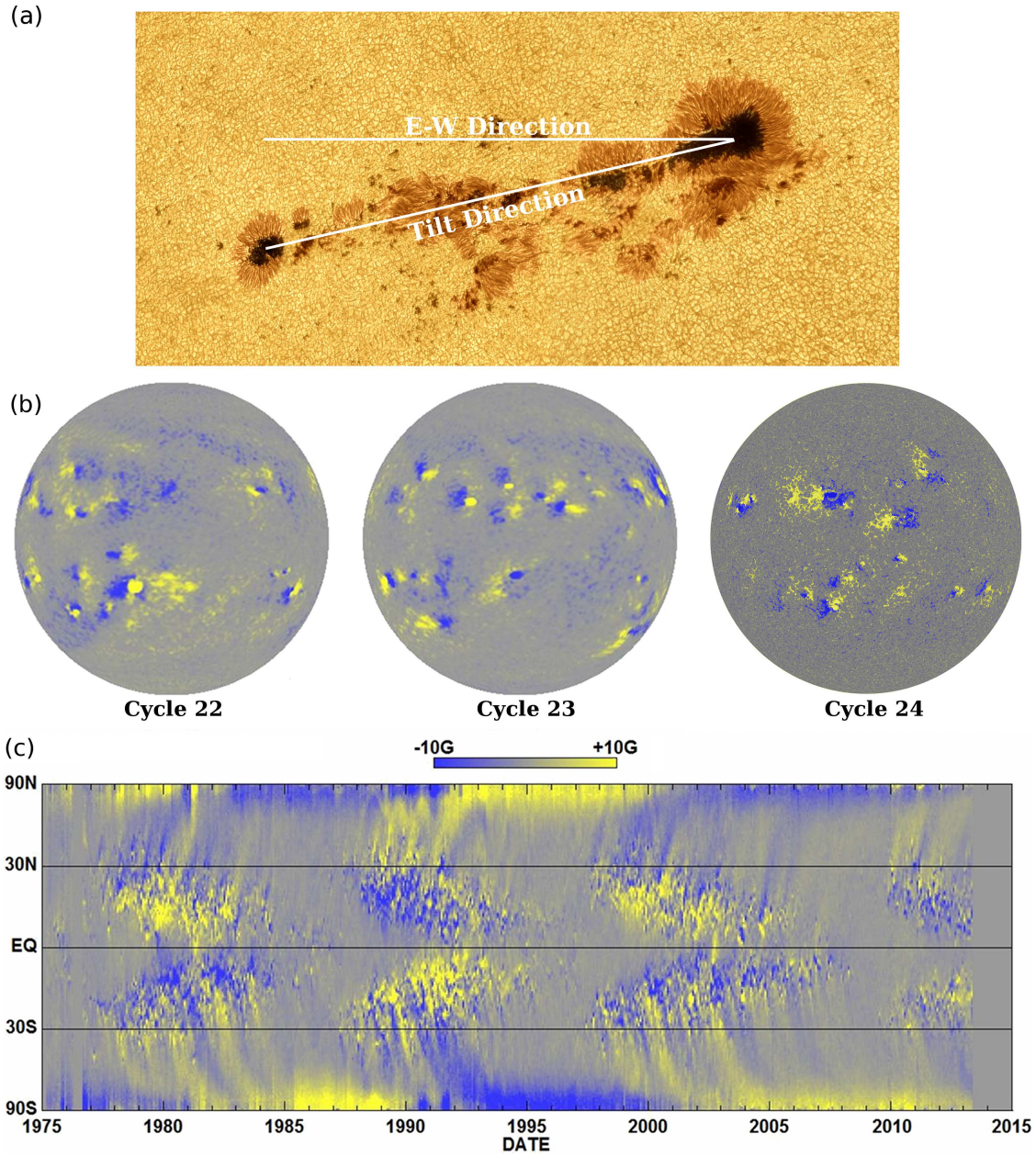

Figure 1.8: (a) A sunspot group in the southern hemisphere exhibiting Joy's law, with the smaller trailing spot (lower left) tilted away from the E-W line. (b) Magnetograms from sunspot cycles 22 (left), 23 (middle), and the current cycle 24 (right) displaying the line-of-sight magnetic field, with negative field in blue and positive field in yellow. This shows Hale's polarity law. (c) A magnetic Maunder diagram built from longitudinally averaged Carrington maps of the line-of-sight magnetic field, which were obtained from Kitt Peak and SOHO. This serves to illustrate the polar field reversals, and the poleward advection or slip of magnetic field (July 2013, D. Hathaway/NASA).

is probably a significant fact that the axis of the group usually makes only a small angle with the equator. A study by Joy [...] shows that there is little change in this angle during the life of the group, but that in the mean the angle bears a definite relation to the latitude of the group. [...] The following spot of the pair tends to appear farther from the equator than the preceding spot, and the higher the latitude, the greater is the inclination of the axis to the equator." This is thought to represent the twisting of the underlying magnetic field by convection as the flux tube of the sunspot rises toward the Sun's surface layers (Fan, 2009). This hypothesis has recently been challenged in an extensive and systematic statistical study of bipolar regions from the Michelson Doppler Imager (MDI) instrument on the Solar and Heliospheric Observatory (SoHO) (Stenflo & Kosovichev, 2012). They find that about 4% of all large bipolar magnetic regions violate both Joy's and Hale's laws, with a larger fraction for the smaller-scale bipoles.

Figure 1.8c displays the actual magnetic properties of sunspots during a Schwabe cycle. Primarily, the magnetic polarity of the sunspots reverse between cycles, with the reversal beginning as the cycle nears and enters a minimum in activity. This simple fact was a tremendous surprise when first uncovered during the solar minimum of 1912 (Hale, 1915), with a great deal of effort going into confirming this unexpected behavior. The polar magnetic fields, on the other hand, reverse polarity earlier at about the time of maximum activity, a consequence of a large amount of magnetic flux having been transported to the pole as first described in Babcock (1959).

1.3 Origins of Modern Sunspot Observations

The modern methods of solar observations were largely pioneered in the nineteenth century, being a product of those vigorous times early in the industrial revolution. There were several important discoveries that would bear fruit more immediately, and a few that would have to wait nearly a century for our theoretical understanding to catch up to the observations.

Though it did not immediately lead to multiple breakthroughs in astronomy, given Joseph von Fraunhofer's predilection for optical physics, his invention of the spectrograph in 1819 and improvements in the production of quality of optical glass were critical to later observations. It did, however, lead to his rediscovery of the "dark lines" in the solar spectrum, which had been noticed 15 years earlier (Wollaston, 1802), that piqued the interest of many astronomers. Yet Fraunhofer pursued these observations primarily as a means to produce standards by which the quality of optical glasses could be quantitatively compared (Fraunhofer, 1817). Yet with the spectroscope in the hands of the famous duo of a chemist Robert Bunsen and a physicist Gustav Kirchoff, it was realized that elements could be identified through their spectral lines by passing white light through heated gases (Kirchhoff & Bunsen, 1860). It was quickly understood then that the Fraunhofer lines could be used to infer properties of the solar atmosphere (Kirchhoff, 1860). This was a major breakthrough in astrophysics leading to the discovery of many new objects and providing new ways of understanding and classifying stars, and eventually to Hale's discovery of the magnetic character of sunspots.

While the direct study of the Sun's magnetism was not yet available, several dedicated observers throughout the nineteenth century provided nearly continuous, reliable, and independent observations of the Sun between November 1825 and the beginning of the modern record in 1874. There were four significant contributors to solar astronomy during this period: Richard Carrington, Samuel Schwabe, Gustav Spörer (mentioned above), and Rudolf Wolf. They each became engaged in work regarding the primary solar research focus of the time, which was the nature of sunspots and the solar atmosphere.

By virtue of birth, Samuel Schwabe was the first of these three to begin observing. He fastidiously recorded the solar disk nearly every day from 5 November 1825 to 29 December 1867, producing 8,486 drawings thereof. Initially, this apothecary turned astronomer was hunting for a planet inside of Mercury's orbit and not for sunspots. Yet his meticulous observations amounted to a total of 135,000 sunspot measurements. Overall his drawings

are accurate to around 5% of the solar radius or to about 3° in heliographic coordinates. Most of these drawings provide a coordinate grid aligned with the celestial coordinate system, though a subset of 1168 drawings have no indication of their orientation. Despite not finding the hypothesized planet Vulcan after 17 years of dedicated observation, Schwabe described the fundamental frequency exhibited by the Sun in Schwabe (1844): "Vergleicht man nun die Zahl der Gruppen und der fleckenfreien Tage mit einander, so findet man, dass die Sonnenflecken eine Periode von ungefähr zehn Jahren hatten und daß dieselben fünf Jahre hindurch so häufig erschienen, daß in dieser Zeit wenig oder keine fleckenfreie Tage statt fanden."

Given its import, it bears repeating that by "comparing the number of days with sunspot groups and those without, we find that the sunspots have a period of about ten years and that within this period, five years are so heavily spotted that hardly any days were spot-free." This hint at a periodicity in solar maculation prompted a great deal of interest, though only after being popularized by Alexander Humboldt in his famous treatise "Kosmos" (Humboldt & Bromme, 1850). This is not to say that Schwabe slackened his observational ardor after publishing 1844, rather he continued apace until 1868.

The entire data set collected by Schwabe has recently been digitized and collected in a data base (Arlt et al., 2013), and are shown in Figure 1.9. The properties of the solar cycles here are quite similar to those of the modern record, with the equatorial propagation of sunspot emergence locations as the cycle progresses (Figure 1.9a). Yet there does appear to be a greater difference in phase between the hemispheres than in later cycles, which is more clearly illustrated in 1.9c. This may be related to a recovery in magnetic activity following the Dalton Minimum that began in April 1798 (Usoskin et al., 2009), though detailed observations from 1796 to 1825 seem to be lacking. Figure 1.9b shows the Group sunspot number (R_G) as the orange filled curve with the data provided by D. Hathaway. The overlain blue curve shows the sunspot area as derived from Schwabe's data. Overall there is good agreement between these two activity measures, though, there is a curious discrepancy

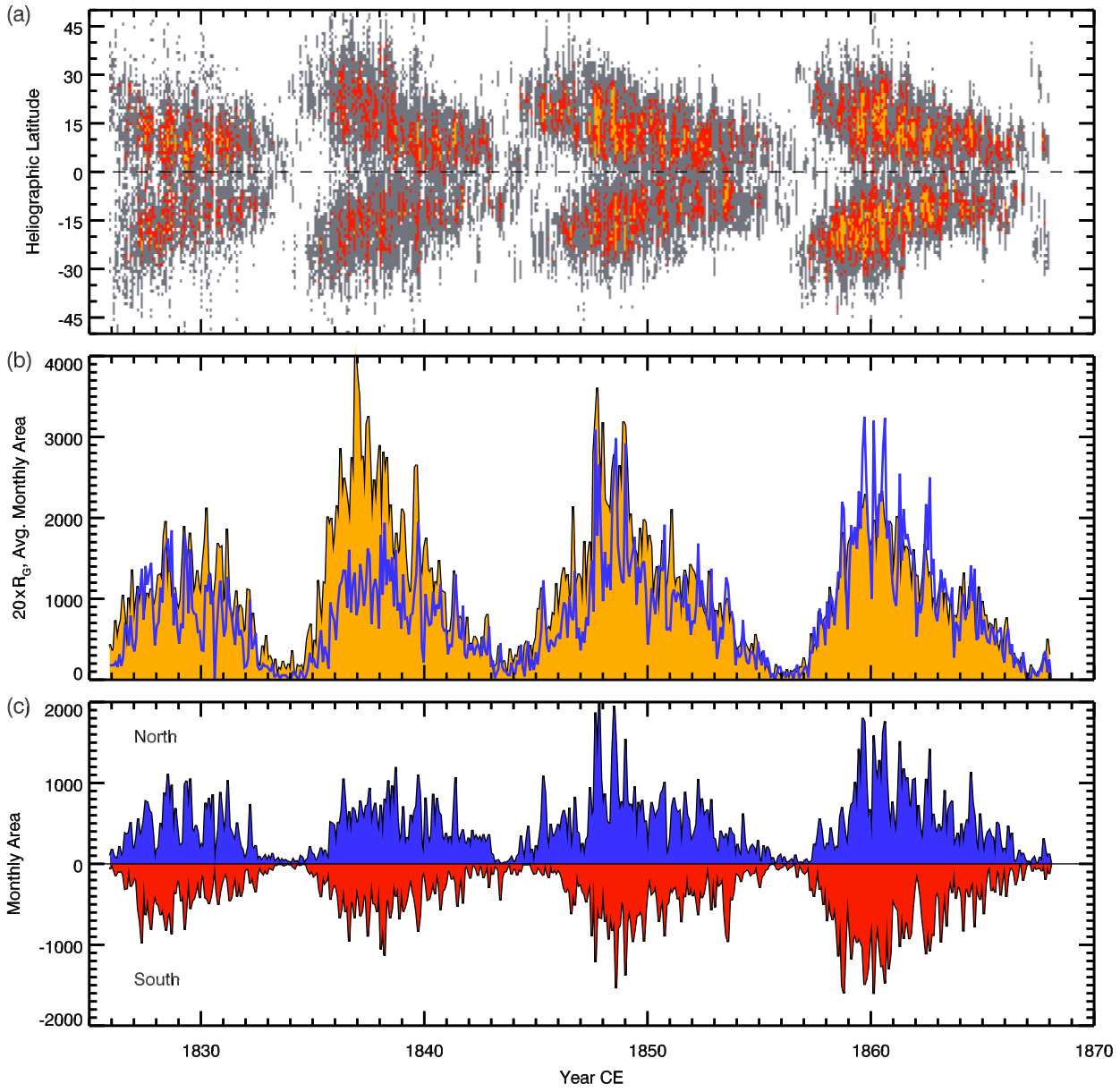

Figure 1.9: (a) A Maunder diagram showing sunspot areal coverage in latitude and time between 1825 and 1868. Sunspot area is broken into 12 bins determined from Schwabe's drawings (Arlt et al., 2013). Colors indicate sunspots with areas in the bottom four of these classes (gray), medium sized spots of the middle four classes (red), and larger spots and groups in the upper four classes (orange). (b) Group sunspot number multiplied by 20 approximates the area and is the filled orange curve, while the area integrated over all the classes is shown in blue, displaying the monthly variability in sunspot area over these four Schwabe cycles. (Constructed from data provided by NOAA). (c) Average monthly sunspot area in each hemisphere (units as in panel b), indicating the phase differences between the northern (blue) and southern (red) hemispheres (Realized with data provided by R. Arlt/AIP).

between them in the cycle beginning in roughly 1834.

The period between November 1853 and April 1861 is one that can be cross-correlated with Richard Carrington's observations (Carrington, 1863). Largely inspired by Schwabe's observations of possible solar cycles and also by his distaste for the lack of systematic observations, Carrington became one of Schwabe's contemporaries, embarking on a crusade to systematically observe an entire solar cycle. Ultimately, after seven years of devising new observing techniques and proper coordinate systems, he divested himself of these pursuits after he was excluded from the directorship of the Cambridge observatory by the university's syndicate. Nonetheless he continued his solar observations for two additional years and in yet two more years time published his tome on sunspots "Observations of the Spots on the Sun from 9 November 1853 to 24 March 1861, Made at Redhill" in 1863. This work contained major contributions to solar physics: the accurate quantification of the solar differential rotation (though his was not its initial discovery), the co-discovery of equatorward migration of sunspot emergence with Gustav Spörer, the hitherto most precise measurement of the solar rotation axis relative to the ecliptic, and a happenstance observation of a white light solar flare. The last discovery was a furtherance of the growing evidence for the linking of geomagnetic and solar magnetic activity. This connection between the 11-year solar activity cycle and terrestrial magnetic phenomenon was a notion devised independently by four scientists in 1852, though Edward Sabine was the first (Sabine, 1852), and will be discussed further in §1.5.

Rudolf Wolf was one of these four scientists, and another inspired by Schwabe's findings. He too undertook a multi-decade observing campaign beginning in 1848 and continued until shortly before his death in 1893. To better understand the Sun's cycles, Wolf aimed to construct as complete a record of observations as possible, assembling a large trove of verbal and pictorial sunspot observations from the previous two centuries. Having begun this pursuit in 1850 (Wolf, 1850), he had largely finished reconstructing this record by 1866 (Wolf, 1866). He was able, in addition to his own observations, to produce a fairly complete

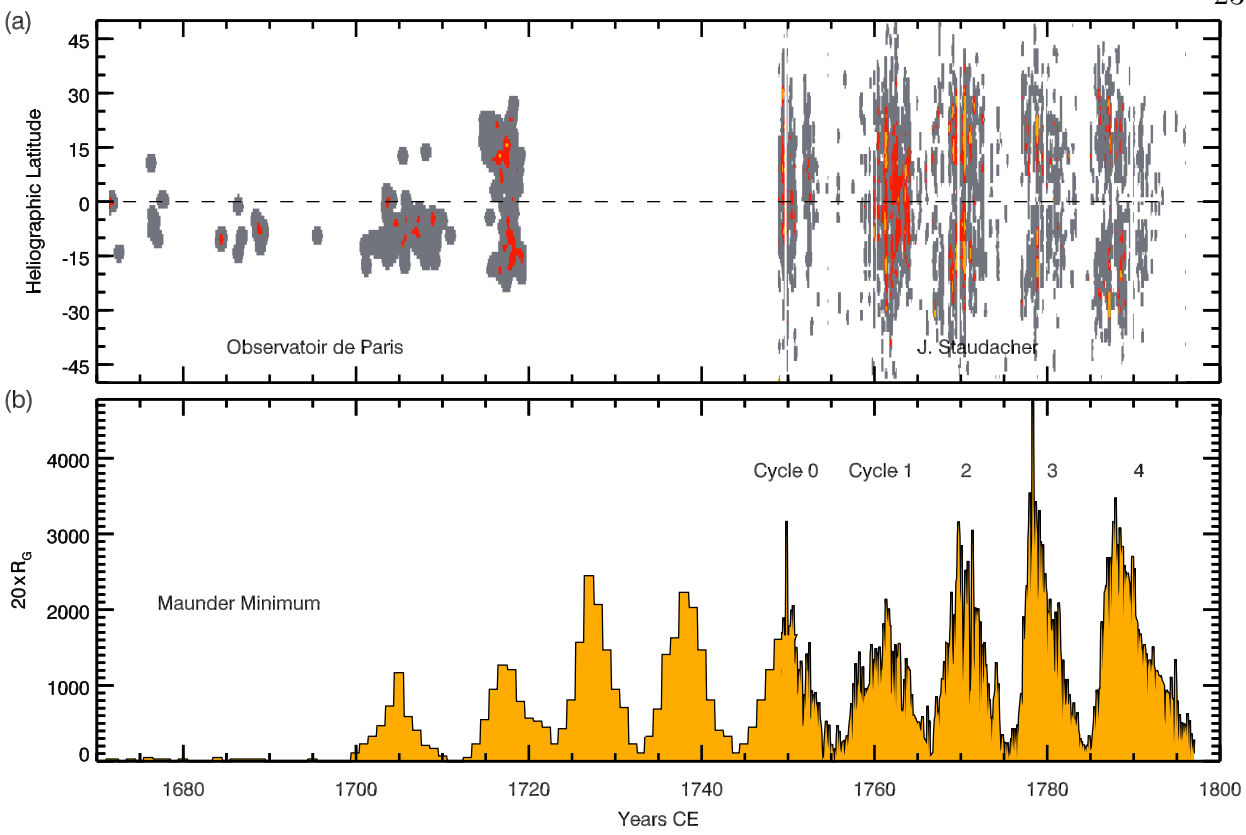

Figure 1.10: (a) A Maunder diagram showing sunspot areal coverage in latitude and time between 1670 and 1796, as determined from multiple sources in Ribes & Nesme-Ribes (1993) and from Staudacher's drawings (Arlt, 2009). Colors indicate sunspots with areas in the smaller areas (gray), medium-sized spots (red), and larger spots and groups (orange). (b) Group sunspot number multiplied by 20 as it approximates the area (filled orange curve), constructed from data provided by NOAA.

observational record dating back to 1610. Yet he suffered from the problem of calibration that often appears when comparing disparate data. To accommodate the varying data sets Wolf established a consistent measure now called the Wolf, Zürich, or international sunspot number, which is still in prominent use today. In particular, it provides a significant portion of the information used to construct the Group sunspot number (Hathaway, 2010). This Group number is what has been shown here and in Figures 1.7, 1.9, and 1.10.

The observations of Galileo and others in the seventeenth century provided the impetus for subsequent observations throughout much of the Maunder Minimum (a long period with

very few sunspots between 1645-1715, see Figure 1.12) and into the eighteenth century, including those of a contingent of French observers at the Observatoire de Paris such as Jean Picard (Ribes & Nesme-Ribes, 1993). The set of daily measurements from the Observatoire accumulated to about 8,000 between 1671 and 1719. These drawings cover the later half of the Maunder Minimum, showing sunspot positions and area which are displayed as a Maunder diagram in Figure 1.10. These observations had been previously known, but not fully quantified as they were in Ribes & Nesme-Ribes (1993). Indeed, in two papers shortly before his death, Spörer described the period later dubbed the Maunder Minimum. He, and subsequently Edward Maunder, presented evidence that for much of this period there were no sunspots, and that for about half its 70 year duration spots were only sporadically observed in the southern hemisphere (e.g., Spörer, 1890; Eddy, 1976). These states with single hemispheres of dynamo action have also been seen in some simulations and models (e.g., Tobias, 1997; Gallet & Pétrélis, 2009; Augustson et al., 2011). What is also of some interest, following from the work of Eddy and Ribes, is that these early sunspot observations indicated that the Sun's differential rotation was markedly different during the Maunder Minimum. Sunspot tracking suggests that the solar differential rotation was actually stronger and had a much steeper latitudinal decline rate between the equator and poles, supporting the notion of an equatorially confined jet (Eddy et al., 1976).

Also shown in Figure 1.10 are another large set of sunspot drawings that encompass several cycles, though it was not until 1749 that these regular measurements began. This was largely the work of Johann Staudacher, who spent nearly 47 years drawing observations of the solar disk. His drawings over this period, unlike Samuel Schwabe's, did not possess an accurate coordinate system and often lacked the orientation information for the solar disk. Nonetheless digitized Staudacher's drawings have been used to determine sunspot positions for the interval 1749 to 1796. Several techniques have been employed to reconstruct the sunspot positions, the choice of which depends on the quality and accuracy of a given drawing. These methodologies permitted the determination of the heliographic latitudes and

longitudes for 6,285 sunspots over 999 days of this 47 year interval (Arlt, 2009).

The results of this reconstruction are shown in Figure 1.10, where the resulting Maunder diagram exhibits a dense population at or near the equator during the first two cycles (cycles 0 and 1 in the current parlance). They seem to occur even near the beginning of the cycle, where they would normally be at much higher latitudes. Cycle 2 shows an intermediate behavior with two prominent bands at higher latitudes, but still with a great deal of equatorial activity. However, cycles 3 and 4 show a typical butterfly shape. This could be the result of Staudacher's improving skill, but that does not seem particularly likely given that he had already been observing for many years when cycle 1 began. A tentative explanation may be the transient dominance of a quadrupolar magnetic field during the first two cycles, as can occur in the chaos of deterministic systems (e.g., Weiss & Tobias, 2000; Brandenburg & Spiegel, 2008) and as can be seen in some dynamo models (Dikpati & Gilman, 2001).

1.4 Beginning of the Western Sunspot Record

In this retrospective look at solar magnetism, the clock has ticked back 350 years to the midpoint of the Maunder Minimum. How far back does this record go and is it still reliable and sufficiently accurate to characterize the longer term variability? At this point, the direct documentation of solar activity becomes increasingly sparse. However, there is evidence that solar observations were pursued in China some 2,900 years ago, with the first sunspots being recorded during the Xi Han dynasty about 165 BCE. Looking across multiple cultures and through 1,500 years of historical records, there at least 235 drawings and verbal accounts of naked eye sunspot sightings spanning the interval between 165 BCE and 1684 CE (Wittmann & Xu, 1987). Yet the world had to wait until the seventeenth century for the advent of optics and telescopes before they could be more routinely observed.

More systematic study and observation of sunspots began following Galileo Galilei and Thomas Harriot's solar observations in 1610, with examples of such early observations shown in Figure 1.11. However, the first published work was that of Johannes (Goldsmid) Fabricius

in 1611 entitled *"De Maculis in Sole observatis, et apparente earum cum Sole conversione narratio,"* or *"Of spots observed in the Sun, and a narrative on their apparent rotation with the Sun."* When translating the title, it is easy to overlook the latter clause. Yet it is equally profound that in the short few months between Galileo's observations, published in his poetry inspiring "Sidereus Nuncius" and his subsequent formal letters to Markus Wesler from the Accademia dei Lincei, Fabricius found that the spots also indicated the Sun's rotation. However due to Galileo's prominence, his telescopic and heliocentric revelations about the universe, such as the phases of Venus, Jupiter's moons, and of course sunspots, greatly disturbed many in the Ptolemaic school of thought. This included Christoph Scheiner who, given that he was a Jesuit priest, was deeply entrenched in Ptolemaic dogma. The academic rivalry and personal animosity that grew between these two scholars drove the initially skeptical Scheiner to several major discoveries. Particularly, Scheiner's stubborn adherence to the perfection of the Sun drew Galileo's wrath. Though it probably did not help that Scheiner was a Jesuit given the near constant threat of inquisition raised by the Catholic church. Moreover, despite many years of observations, Scheiner continued to believe for some time that the spots were satellites in a very close orbit. Galileo did eventually disabuse him of this notion after several vibrant exchanges with one of Scheiner's benefactors.

Scheiner's greatest contributions were the determination of both the inclination angle of the solar rotation axis relative to the ecliptic and the magnitude of the Sun's surface differential rotation. These discoveries were both detailed in Scheiner's blandiloquently titled four-volume magnum opus published in 1630: *"Rosa Ursina, sive sol ex admirando facularum et macularum suarum phoenomeno varius: necnon circa centrum suum et axem fixum ab occasu in ortum annua, circaque alium axem mobilem ab ortu in occasu conversione quasi menstrua, super polos proprios, libris quatuor mobilis ostensus."*

This translates to *"The Bear's Rose, that is the Sun and on the admiration of flares and sunspots and their various phenomenon: as well as on its center of rotation and its annually fixed rotation axis, and on another rotation axis leading to a separate monthly rotation of*

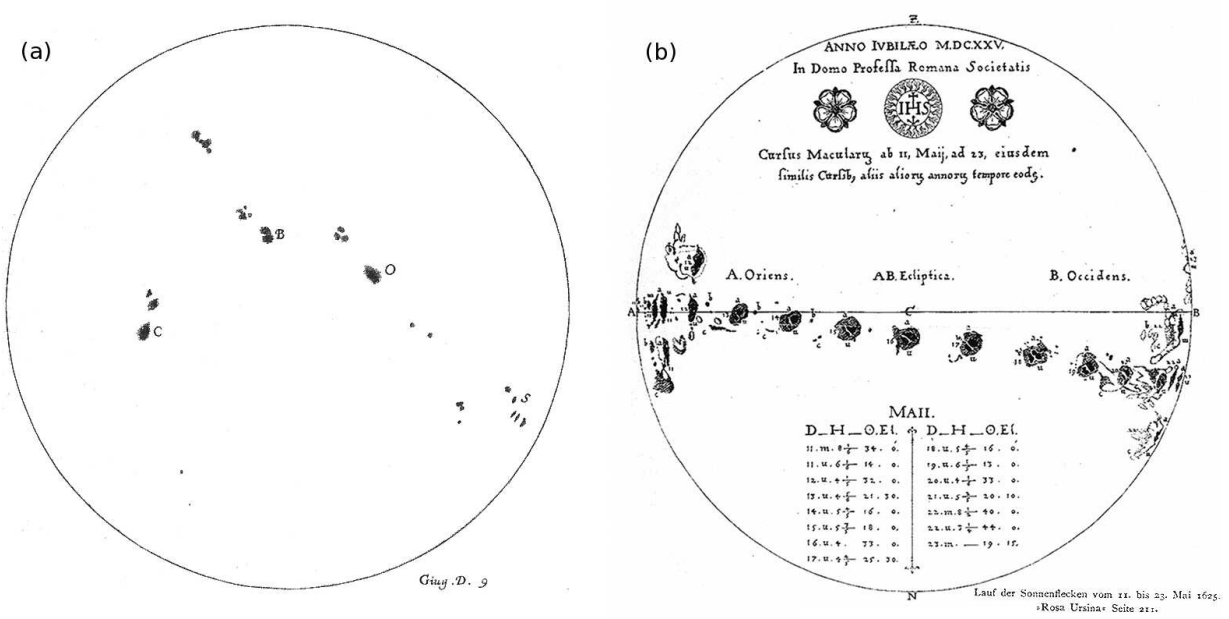

Figure 1.11: Drawings of sunspots from (a) G. Galilei in 1612 and from (b) the 1625 edition of the Rosa Ursina by C. Scheiner.

the poles, in a four volume set." In deference to his patron, "Ursina" is a play upon the family name of the Duke of Bracciano Paolo Giordano Orsini II. Thus, an ursine theme is ubiquitous in the book's many illustrations. Despite this excessive flattery and Scheiner's difficulty in selling the book, it became the seminal text in the field of solar astronomy for nearly a century. Though, as Jack Eddy remarks in his 1976 paper, perhaps both of these circumstances may be due to its excessive and pedantic detail (Eddy, 1976).

This rapid pace of innovation spurred on by multiple scientists in the early part of the seventeenth century quickly came to a halt as the number of sunspots dwindled during the Maunder Minimum between 1645 and 1715. However, there is one nagging question and that is why were sunspots discovered only late in the Renaissance, especially given that many other observations had occurred centuries earlier. Part of the answer to this is that there had been a prolonged solar grand minimum for much of the preceding 300 years, a period that had followed the so called Medieval Maximum that ended around 1350. Despite this paucity of spots during the birth of modern science, sunspots have enjoyed more or less continuous

observation in the succeeding 400 years, as is illustrated in Figure 1.12, with even sufficient fidelity to be able to reconstruct the Maunder diagram for a substantial portion of this time. Here the extent of the post-Renaissance sunspot number record is evident in Figure 1.12b, with yearly data between 1610 and 1749, monthly data between 1749 and 1874, and daily sunspot counts afterward (Hoyt & Schatten, 1998). The three most prominent features are the Maunder Minimum (1645-1715), the Dalton Minimum (1798-1835), and the Modern Maximum in the 1960s.

1.5 Terrestrial Record of Solar Variability

As with most of the longer time scales of the Sun, including the Schwabe cycle, their regularity and even existence is difficult to ascertain. For instance if we wished to ask how long the 11-year cycle has been active, we can only directly assess this for the last 400 years. Yet the Sun and its magnetism have existed for billions of years. What might its cycles, if it had them at all, have been like 1,000, 10,000, or millions of years ago? Do larger scale ISM or galactic phenomenon have any impact on these longest of time scales? Furthermore, do any internal structural or rotational changes that the Sun has undergone over the eons influence the timing of the dynamo? Indeed, deciphering its longer-term variability is an uncertain business, but there are a few techniques that allow solar activity on these millennial or even longer time scales to be measured. But before moving on to the solar-terrestrial connection, it should be noted that there are a few longer term periodicities visible in the direct observations. As evident in the full data set shown in Figure 1.12, there is a modulation of about 88 years known as the Gleissberg cycle (Gleissberg, 1939). Its cousin, the 209 year Suess cycle may also be present in this data (Suess, 1980), but it would be seen at most twice. Since we have but snapshot of the Sun's magnetism on geological time scales, this latter cycle's behavior may be muddied by even longer time scale processes.

As mentioned in §1.4, the link between geomagnetic activity and solar activity was made as early as 1852. Once the theoretical connection was made, it was inevitable that

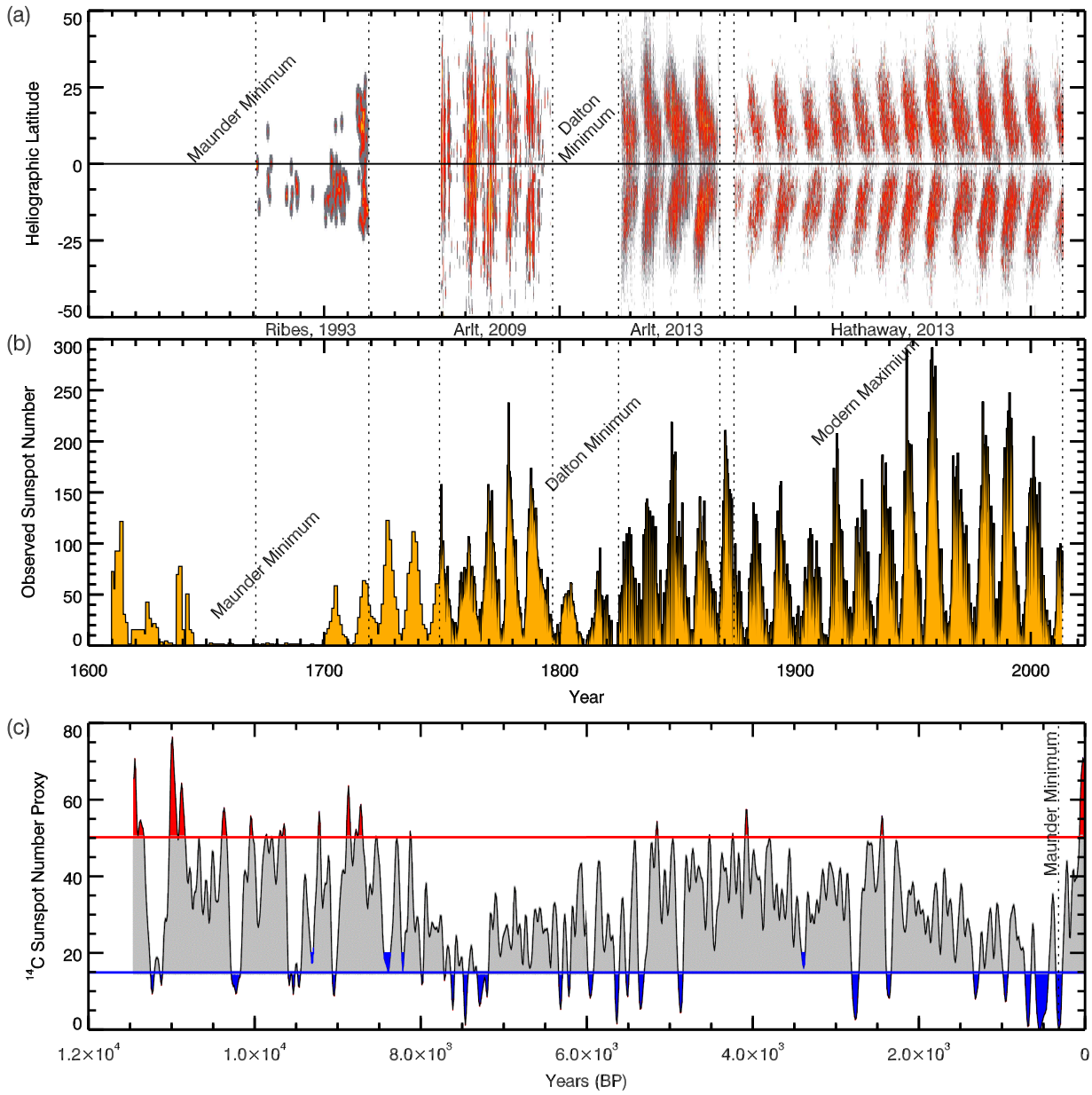

Figure 1.12: (a) A Maunder diagram covering the period between 1670 to 2013. Colors indicate proxies for sunspot areas, or in the case of the modern data the actual areas, in the lower (gray), middle (red), and upper (blue) tertiles of the respective distributions of the data. (b) Average monthly Group sunspot number, displaying the variability and longer-term modulation in sunspot area over the many Schwabe cycles. (c) Solar cycle variability over the last 12,000 years as derived from ^{14}C sunspot number proxies (Usoskin, 2008). Grand minima in activity fall below the blue line and grand maxima above the red. The Maunder Minimum is indicated for reference, so modern telescopic observations occupy only the last 3% of panel (c).

someone would go looking for it. Indeed, the two cycles just mentioned, and perhaps even the Schwabe cycle, are seen in many proxies for solar activity throughout a large portion of Earth's geological history. Both of these periodicities, and many others, seen in magnetic activity indicators could simply be harmonics of the 11-year Schwabe cycle. However, these longer term cycles led to my inclusion of Figure 1.12c, wherein a robust proxy for solar paleomaculations is shown. This sunspot proxy is a normalized concentration of radioactive ^{14}C in dendrochronological samples or polar ice cores (e.g., Usoskin, 2013). These data elucidate the multi-periodic and chaotic nature of the solar dynamo, though not without caveats. Those involve two major influences on the radiocarbon proxy method that must be accounted for: seasonal weather changes that heavily influence short term variation (less than decadal time scales) and the secular changes in the Earth's magnetic field that impact millennial time scales. These shortcomings can be partly ameliorated by smoothing and detrending the data, after which several periodicities and extrema become apparent.

An analysis of the extrema seen in Figure 1.12c indicate that the distributions of both grand minima and maxima deviate from exponential characteristics, and so are likely not purely random. Moreover, the minima show a bimodal distribution with most minima being like the Maunder Minimum, lasting an average 60 years, and a secondary peak at longer Spörer-like minima that last about 150 years (Usoskin et al., 2007). The periodicities present in this radiocarbon data are the centennial Gleissberg, duocentennial Suess, and duomillenial Hallstadtzeit cycles. There have been explanations of these time scales in this ^{14}C proxy record that invoke a mechanical forcing due to planetary orbits the most recent being Abreu et al. (2012), with the idea originating with the sunspot pioneer Rudolf Wolf in the mid-nineteenth century (Charbonneau, 2013).

This sunspot narrative does not end lost in a thicket of tree rings or frozen below the ice. In fact, there has been evidence of the Schwabe, Hale (the 22-year polarity cycle), Gleissberg, Suess, and longer potentially solar related periodicities in the fossilized sediments of Jurassic, upper-Permian and upper pre-Cambrian lake beds. The sedimentary varve records in the

170 Myr old Jurassic Todilto formation in New Mexico form an unbroken 900 yr record of climatic variability associated with solar forcing (Anderson & Kirkland, 1966). The 240 Myr old Castile formation, also in New Mexico, has a 250,000 year record and high laminar resolution. This means that intermediate time-scales can be identified between the 22-year Hale cycle and the decamillenial Milankovitch cycles, which are periodicities associated with orbital forcings such as changes in eccentricity, axial title, and precession (Anderson, 1982; Anderson & Dean, 1995; Kirkland, 2003).

Finally, the most compelling geological record can be found in the 650 Myr old pre-Cambrian sandstone formations of the Southern Australian Elatina formation (Williams & Sonett, 1985; Bracewell, 1988). This formation has the Schwabe, Hale, Gleissberg, and Suess cycles prominently etched in a record untouched by biological processes and unharmed by oxidation due to the anoxic atmospheric chemistry during its sedimentation. This is a most fascinating record. If this result is robust, it shows that the temporal characteristics of the solar cycle have remained essentially unchanged since the late Proterozoic eon. What is compelling is that the solar magnetic cycle may have continued unabated even as the underlying solar structure evolved, which is a given as this period represents about 14% of the Sun's current age, during which the solar luminosity has increased by 2%.

1.6 Short Time Scale Solar Variability

The most obvious short term variability arises from the rotation of the Sun, occurring on a 27 day time scale, which gives more information about the spatial organization of the solar activity than its temporal organization. However, there exist mid-range time scales of variability between 27 days and 11 years. The most prominent of these mid-range time scales is the 153 day Rieger oscillation, which primarily occurs near solar maximum. This period actually varies between 140 and 170 days, and is detected in a variety of observations. It was first seen in gamma-ray flares (Rieger et al., 1984), but has been found in active region parameters and in the 10.7 cm solar radio signal (Lean & Brueckner, 1989), as well as in

variations of the interplanetary magnetic field (Cane et al., 1998). Additionally, there are time scales of 51, 128, and 257 days that are slightly less statistically robust, with false alarm probabilities of about 10% (Bai, 2003). These periodicities are again associated with solar maxima. The origins of these quasi-periodic time scales have been variously attributed to magnetic Rossby waves operating either in the tachocline (Zaqarashvili et al., 2010) or near the solar surface (Lou, 2000), among several other mechanisms. Furthermore, there is also evidence for oscillations of the solar neutrino flux, with a period of about 38.7 days (Sturrock et al., 2013). This would be quite interesting as it would imply that the nuclear energy generation rate in the core is varying with time.

For completeness, the briefest time scales observed on the Sun occur on the order of milliseconds, such as the reconnection events that lead to flares, CMEs, and the waves associated with them. There is of course the granular convective overturning time scale of about 10 minutes, which sets the pace for many of the time scales in the chromosphere as well as the photosphere. One such impact is on the magnetic fields responsible for photospheric bright points, which dance about each other in the intergranular lanes. This dance continues as individual magnetic flux bundles repel or annihilate depending upon their relative helicity, with this process taking about 20 minutes. There are indeed a very large number of processes taking place in the solar atmosphere that possess a very diverse set of short time scales. However, these processes are largely beyond the scope of the dynamo and convection simulations that make up the bulk of this thesis and will not be covered in depth.

The multitude of spatial scales of the Sun (§1.1) are thus accompanied by an equally diverse set of time scales that stretch across billions of years as the Sun evolves to the 10 minute time-scales of granulation and to the even shorter time-scales of reconnection that launch flares and CMEs. Yet explaining and understanding how all these processes occurring in the Sun give rise to a magnetic activity cycle that seems to persist for nearly a billion years is largely a mystery. Indeed, one of the oldest problems in physics lies cloaked below the tumult of the solar atmosphere: what drives this rhythmic heartbeat of the Sun?

Chapter 2

Observations of Stellar Magnetic Activity

"Thousands of stars, in the same stage of evolution as the Sun, doubtless exhibit similar phenomena, which are hidden from us by distance... The simplest and most obvious step would be to make just such a study of the physical phenomena of selected stars, representing different phases of evolution, as we are now making of the Sun." – George Ellory Hale (1915)

One path to attempt to solve the mystery of the persistent magnetic activity cycles of the Sun is to appeal to observations of other stars. This, as most things in stellar astronomy and astrophysics, has a substantial history behind it. Indeed stellar observations had been ongoing for at least two centuries before it was realized that other stars might behave like the Sun, with many displaying magnetic activity and a distinguished few that also have observed activity cycles. There were several pieces that had to fall into place before even solar magnetism was considered plausible. The first being the invention of the spectroscope, which spurred many astronomers to take spectra of ever fainter objects and stars throughout the nineteenth century. It took the additional development of electromagnetic theory and atomic physics before the connections between electromagnetic phenomena and solar activity were made in the early twentieth century.

During the spring of 1896, three years after his doctoral thesis work on the Kerr effect, Pieter Zeeman rebelliously repurposed his supervisor's laboratory equipment in order to measure the splitting of spectral lines by magnetic fields. This pioneering work in early

quantum phenomenology led to his 1902 Nobel prize and to many other profound discoveries in physics, such as Lorentz's theoretical considerations of the electron. Its implications were just as great for stellar astrophysics. Indeed, a short decade later and enabled by the discovery of the Zeeman effect, George Hale ushered in a century of astronomical study of magnetic phenomenon with his observations of the magnetic field strength in sunspots (Hale, 1908). At this point it was not a huge leap to ask if other stars might be like the Sun.

After such detection of magnetic fields on the Sun, the field of stellar magnetism began to unfold. Indeed, in a "minor contribution" to the Astrophysical Journal (Eberhard & Schwarzschild, 1913), the first detection of variable Ca H and K emission from another star was published just five years after the discovery of magnetic field in sunspots. In this paper it was stated that the "reversal of lines in spectra are not rare [...]," and also presciently speculated that "[... though] it remains to be shown whether the emission lines of the star have a possible variation in intensity analogous to the sun-spot period." The H and K lines of singly ionized calcium is a robust indicator of chromospheric structure. Indeed, their utility in constraining the spatial character and temporal variability of structures in the high solar atmosphere has been recognized since Hale's initial investigations. A stream of papers followed this early work based on the premise that other stars may also exhibit variability in the Ca H and K lines. This literature typically presented individual stars with either a fairly short or undetectable time variability in the calcium lines over a broad range of stellar spectral types. These early searches for stellar magnetic variability were cataloged in Joy & Wilson (1949) and Bidelman (1954), which provided the basis for Olin Wilson's later work.

In the early 1950s, Wilson began laying the groundwork for the Calcium H & K Project at the serendipitously named Mount Wilson Observatory (MWO) (Wilson, 1978; Hall et al., 2007). This long-term monitoring project now covers 99 stars including the Sun. Of these 99 stars, 72 show variability, 14 are not variable but have activity, and the remaining 13 show no activity within the measurement uncertainty. The full MWO archive holds just over 6000 stars that have been less systematically observed in these Ca H and K lines and

possess calibrated measures of their magnetic activity (Mittag et al., 2013).

Despite there having long been this indirect evidence and theoretical motivation for the existence of magnetism in lower mass stars, nearly forty years passed between the first recognition of magnetic fields on the Sun and the direct detection of the magnetic field on another star. In 1947, Horace Babcock uncovered the presence of 1500 G magnetic fields on the chemically peculiar A-type star 78 Virginis (Babcock, 1947). There were many subsequent detections of magnetic fields among this class of higher-mass, chemically-peculiar stars, which was primarily due to their relatively strong mean magnetic fields. This leads to widely Zeeman-split spectral lines and thus to easier detection with the limited spectral resolution of the instruments of the time.

The next set of stars with directly detected magnetic fields were compact objects. In 1970, following his theoretical and laboratory work on gray-body magneto-emission, James Kemp pursued an astronomical detection of this phenomenon. To first order, this spectrum of emission arises from a thermal source in a magnetic field and is characterized by a spectrally diffuse circular polarization directed along the line-of-sight component of the magnetic field. The circularly polarized visible light signature of this kind of emission was indeed found on a white dwarf (Kemp et al., 1970), utilizing the relatively modest telescopes at the Pine Mountain Observatory in Oregon. This gray-body magneto-emission betrayed the presence of a very strong magnetic field of about 10^6 G, which is roughly 1,000 times greater than that of the Sun.

Using a phased-array radio telescope, composed of simple dipoles in a wire frame, Jocelyn Bell and Antony Hewish serendipitously discovered one of the most magnetized objects in the known universe: the pulsar. These stellar remnants have magnetic field strengths at least 10 billion times that of the roughly 1 kG fields on stars like the Sun. The direct detection of the enormous magnetic fields of these stars came a decade later with the measurement of cyclotron absorption lines seen in the X-ray spectra of Hercules X-1 (Trümper et al., 1977).

After the polarimetric detection of magnetic fields on compact objects, it took just a few more years of innovation in both observing technology and data analysis techniques, particularly in spectropolarimetry, before it was possible to directly detect the magnetic fields on distant lower mass stars similar to the Sun. If we may draw upon the magnetic phenomena observed on the Sun as proxies for other such stars, the difficulty in observing fields on these stars largely arises from the local cancellation of bipolar magnetic flux structures during the averaging processes undertaken when observing a point source in polarization measurements (e.g., Schrijver & Zwaan, 2000). However, a new method was invented that can partially overcome this difficulty. The essence of it was to perform a Fourier deconvolution of a non-magnetically sensitive line profile from a magnetically sensitive one. It goes a bit further in that there is a very rudimentary model of the stellar surface magnetism accompanying the line deconvolution. Indeed, there is a least-squares minimization of the deconvolution where the model function parameterizes the supposition that some fraction of the stellar surface is covered in magnetic field of some strength in the Zeeman splitting parameter Δ (Robinson, 1979). Thus it was finally possible to assess these averaged signals to produce a single measurement of the magnetic field strength, though it still lacked directional and spatial information about the field. This technique was first successfully applied in measurements of the surface magnetic field of two lower mass stars, namely ξ Bootis (a G8V-type star) and 70 Ophiuchi A (a K0V-type star) (Robinson et al., 1980).

Before delving into the plethora of recent observations of stellar magnetism, it is useful to provide an outline of the techniques that are currently being employed to make assessments of the long-term behavior and morphology of stellar magnetic fields. To understand the various aspects of the photospheric, chromospheric, and coronal magnetic fields and their variability, ongoing observations utilize primarily four techniques: photospheric photometric variability and spot modeling, long-term chromospheric Ca H and K line monitoring, spectropolarimetry and Zeemann-Doppler imaging, and coronal X-ray observations.

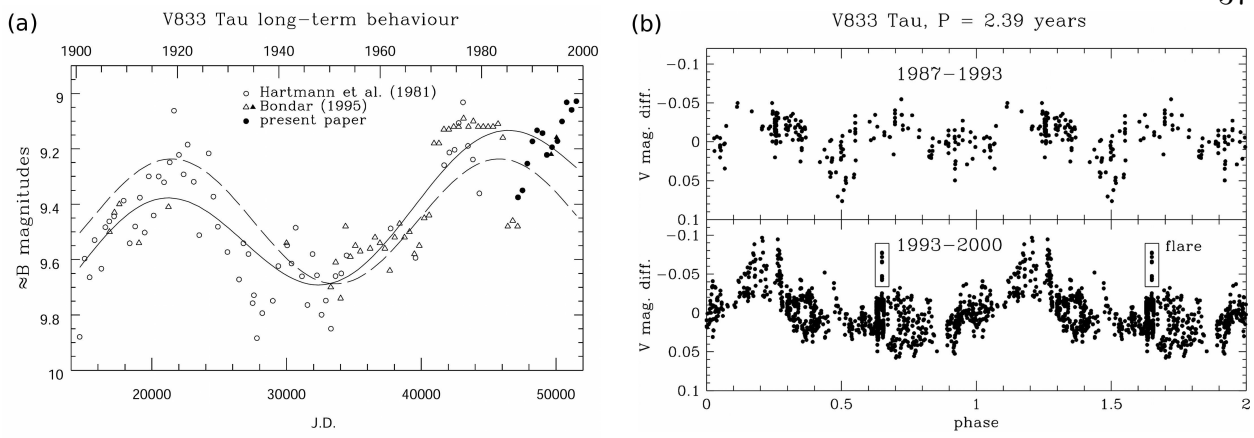

Figure 2.1: (a) Slightly more than 100 years (see upper abscissa) of photometric data from photographic and photoelectric measurements of the K7V star V833 Tau, showing a long-term Gleissberg-like modulation. (b) Short-term variability of V833 Tau, showing its shorter 2.4-year periodicity and a bright white-light flare occurring during the peak of one of these cycles (Adapted from Oláh et al. (2001)).

2.1 Photometric Variability

The simplest of observational technique is to measure the relative photometric brightness variations of a star. However, beneath this simplicity lies a great deal of complexity and information as the signal is the integrated intensity over some bandpass of the star's spectrum, usually in the visible. This means that anything in the line of sight, say a planet, or phenomenon on the stellar surface such as starspots can cause intensity variations. Furthermore, pulsational modes, either acoustic or buoyancy driven gravitational waves, cause minute deviations in the brightness of the star. These qualities are those that motivated recent planet-finding and photometric-monitoring missions such as MOST, CoRoT, and Kepler.

One interpretation of these photometric variations is that a portion of the signal arises from a changing number of starspots on the stellar surface that is caused either by the star's rotation or through the shorter lifetime of the spots. With the Sun as a reference point, this is taken to mean that the star may be undergoing magnetic cycles or at least possess some

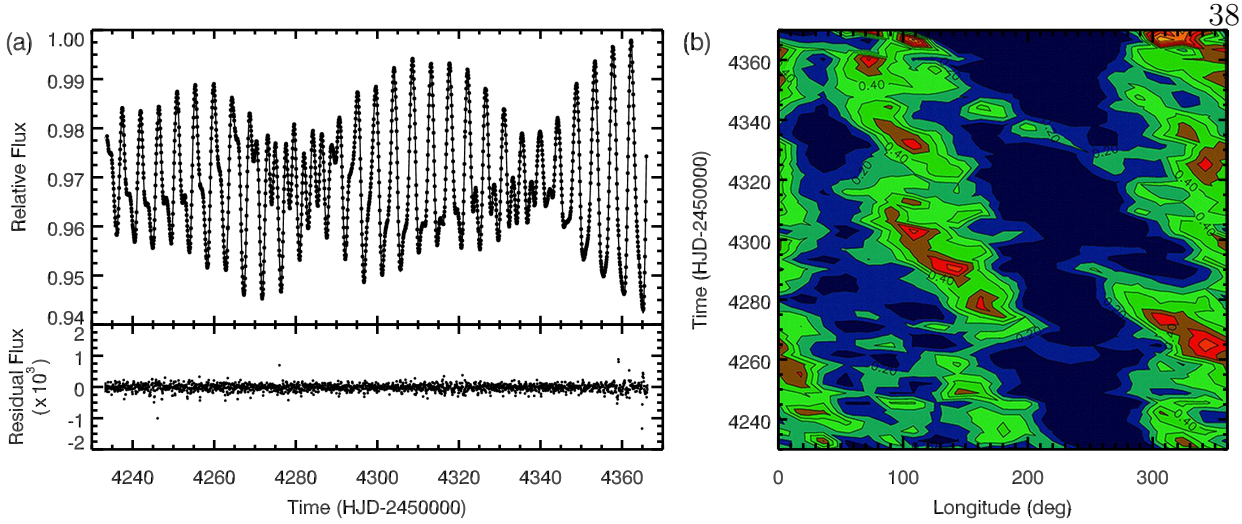

Figure 2.2: (a) Photometry from the CoRoT satellite showing the variability of the main-sequence wide binary star system CoRoT-2a, with the primary component being a G7V type star and its companion being a K9V type star, with 140 days of data shown. (b) Star-spot modeling of the primary component of this binary system, illustrating active longitudes and spot migration (Adapted from Lanza et al. (2009)).

magnetic variability (e.g., Strassmeier, 2005). This is the case in Figure 2.1, where 100 years of photometric data are shown for a main sequence K-type star. This star, much like the Sun, shows multiple periodicities with an approximately 60-year cycle long-term cycle that appears to be like the Gleissberg cycle of the Sun and two short-term periodicities of 6 and 2.4 years. The latter period is taken to be this star's Schwabe cycle, while the 6 year period is likely its Hale cycle (Oláh et al., 2001).

Given that photometry simply counts photons to measure this kind of variability, one can measure such activity on a very large sample of stars. This provides detailed statistics about possible magnetic phenomenon across the Hertzsprung-Russell diagram, enabling nearly anyone with a telescope and a method to accurately monitor photometric variability to make measurements of potential stellar magnetic activity. However, there are a few drawbacks. For instance, the brightness variations of main-sequence stars do not always correlate with other measures of their activity such as the chromospheric Ca H and K observations or measurements of X-ray luminosities (e.g., Pallavicini et al., 1981; Radick et al., 1998). These

correlations also depend upon the nature of the target being observed, as binary or multiple star systems can behave quite differently from single stars (e.g., Berdyugina, 2005). Thus it is essential to follow up with spectroscopic measurements to better characterize the target.

The second approach utilizing photometric data attempts to extract maps of cool starspots from the stellar photometric variations (e.g., Berdyugina, 2005; Lanza et al., 2007, 2009). One of these methods is direct light-curve modeling. This is a trial-and-error method wherein a number of spots with a predetermined shape are varied in area, latitudinal and longitudinal position, and in spot temperature relative to the effective temperature. These spots are rotationally modulated in an attempt to reconstruct the light curve. These models obviously have a large number of free parameters and the solutions are not unique, and they are best reserved for peculiar higher mass stars that tend to have only one or two large spots. The second technique fits for a fractional spot coverage with a two temperature model against which the observed light curve can be inverted to give information about the time-dependent longitudinal distribution of spots. Both of these starspot modeling techniques can be improved to yield information about the latitudinal dependence by incorporating temporal information from Doppler-shifted spectral lines (e.g., Strassmeier, 2009).

Differential rotation is certainly one of the primary components of a polarity-reversing dynamo. Although internal differential rotation is crucial, it is often difficult to observe. However, photometric measurements of spotted stars can provide access to information about the surface differential rotation. This is typically possible in stars with a sufficiently large differential rotation that it can be distinguished as a secondary rotational signal in a Lomb-Scargle periodogram (effectively a Fourier transform for irregularly sampled data). The Kepler mission has allowed the long-term photometric observation of a large sample of stars, for the main-sequence stars in this sample a recent effort has been made to identify the rates of rotation and differential rotation (Reinhold et al., 2013). The author has amassed differential rotation measurements for roughly 20,000 Kepler stars and has attempted to correlate them with stellar effective temperatures and with a photometric proxy for magnetic

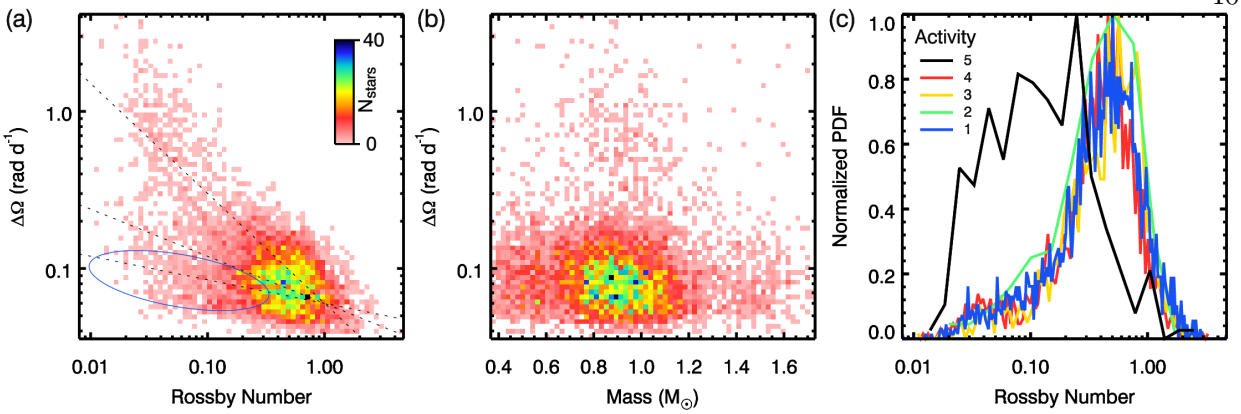

Figure 2.3: Differential rotation scaling with Rossby number and stellar mass in 20,000 Kepler stars. (a) Joint PDF of absolute differential rotation $\Delta\Omega$ and Rossby number, with color indicating the number of stars in each pixel. The three dashed lines indicate possible Rossby number scalings in the normal regime, the fast rotator branch and in a super-saturated branch. The blue circled area indicates those stars that may be running super-saturated dynamos (see text). (b) Joint PDF of $\Delta\Omega$ and stellar mass, showing little variation outside of a fairly narrow band. Colors as in (a). (c) Marginal distributions of Rossby number, integrating over $\Delta\Omega$ for five classes of activity levels, with five being the highest activity as measured by a photometric proxy. The most active stars represent those that may possess super-saturated dynamos. (Constructed with data from Reinhold et al. (2013)).

activity. Indeed, they find a correlation between rotation period and relative differential rotation (α, shearing rate over rotation rate) that decreases roughly as $\alpha \propto P^{-1}$. They also find that α varies little with effective temperature (T_{eff}) for stars with $T_{eff} < 6000$ K, with a fairly rapid increase in α above this temperature as also found in Barnes et al. (2005); Reiners (2006), and Ammler-von Eiff & Reiners (2012).

Some additional insight could be gained if Reinhold and coauthors also use previously defined empirical conversions between T_{eff} and Rossby number as in Noyes et al. (1984). The Rossby number Ro is a measure of the relative strengths of the nonlinear convective force to the Coriolis force, which here is defined as the ratio of the rotation period to an empirically determined convective overturning time (e.g., Kiraga & Stepien, 2007). Such an approach helps to lift the mass dependency as the definition of rapid rotation becomes one of low Rossby number rather than absolute rotation rate. This approach is attempted here,

using the data from Reinhold et al. (2013) to construct the Rossby number correlations of $\Delta\Omega$. The Rossby number is derived from an empirical fit to T_{eff} as in Wright et al. (2011). Figure 2.3a shows that there may be several regimes of Rossby number dependence, which have been fitted as follows. The bulk of the stars, where the colors are darker tones, seem to have $\Delta\Omega \propto Ro^{-0.3}$ as indicated by the middle dashed line. The upper branch of stars have $\Delta\Omega \propto Ro^{-0.7}$. One might suspect that these stars would be more massive, but this turns out not to be the case as there are stars of every mass within the sample in this branch. Stars in the lower branch, with $\Delta\Omega \propto Ro^{-0.15}$, have an anomalously low differential rotation for the given Rossby number. These stars are also the most active and have a markedly different marginal distribution in Rossby number from the other stars in the sample (Figure 2.3c). It could be suggested that they are pulsating stars, however they tend to be lower mass stars of spectral type G and K and thus this scenario is less likely. Another possibility is that they are running saturated dynamos with strong Lorentz-force feedbacks that modulate the amplitude of the differential rotation. Nonetheless, it is curious that there appear to be two classes of rapidly rotating stars, which causes one to ponder what might be structurally different between stars of the same mass and Rossby number that allows such a state. Finally, as mentioned in the caption of Figure 2.3b, it is evident that $\Delta\Omega$ is nearly independent of mass, with only a small sample of stars having more differential rotation than about 0.2 $\mathrm{rad\,d^{-1}}$. This does not contradict the findings in Reinhold et al. (2013), as it is being shown as a distribution, which tends to hide the scatter in $\Delta\Omega$ at higher masses due to there being fewer of such stars. This is in contrast to plotting all the data points as is done in their paper for T_{eff}.

2.2 Chromospheric Activity

It is helpful to first define the chromosphere, which literally means "colored sphere" and refers to its red hue in visual observations during eclipses. This is a rather difficult task in itself as the chromospheric region is heterogeneous due in part to magnetic structures and

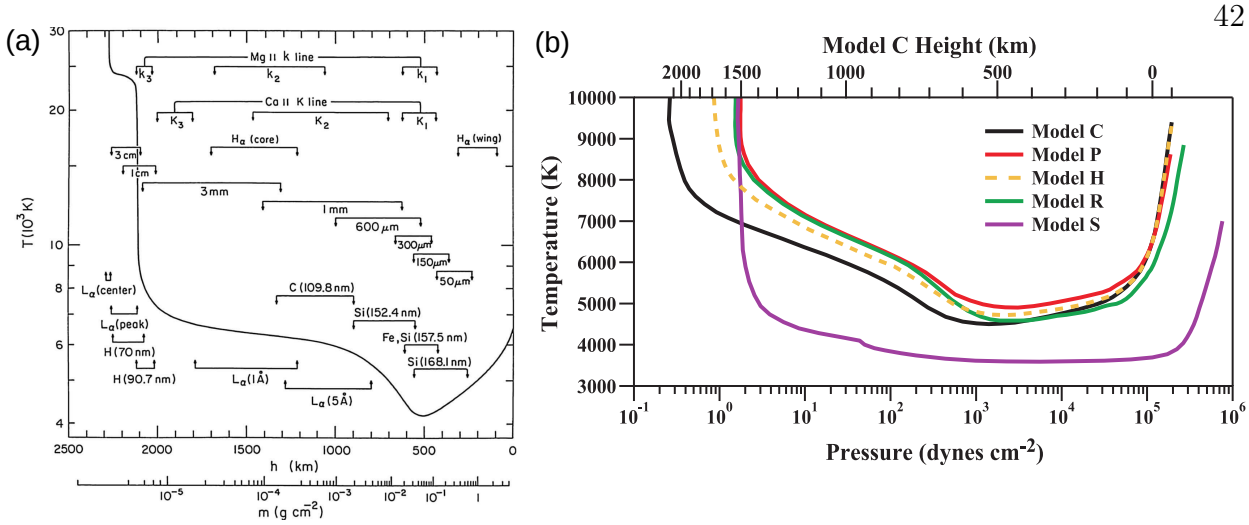

Figure 2.4: (a) The mean solar chromosphere, showing the temperature structure with height in kilometers above the photosphere as well as with column density 'm' (the second set of abscissa). The temperature reaches a minimum about 500 km above the photosphere and has a very steep rise into the transition region. The heights of line formation regions for a wide variety of lines are indicated, such as the six regions of Mg II and Ca II H and K emission (From Vernazza et al. (1981)). (b) Temperature as a function of pressure (height in km with the upper abscissa) above several classical solar features: Model C (quiet-Sun), Model P (faculae), Model H (plage), Model R (penumbrae), Model S (umbrae), with image from Fontenla et al. (2006).

a low plasma β and also in part to non-LTE radiative processes. A working definition is given in Hall (2008), in which the chromosphere is taken to be "[...] the regions of a stellar atmosphere (a) where we observe emission in excess of that expected in radiative equilibrium and (b) where cooling occurs mainly by radiation in strong resonance lines [...] of abundant species such as Mg II and Ca II H and K."

Figure 2.4 illustrates the mean chromospheric temperature structure of the Sun as well as the range of heights over which certain emission and absorption features arise. The Ca II H and K lines form throughout much of the chromosphere between 500 km and 2000 km above the photosphere, which is due to the relative insensitivity of these line to the plasma density in this region. This behavior is manifest given that the region is nearly isothermal whereas the density drops exponentially. The structure of the solar chromosphere may be taken as an approximate homomorphism for the chromospheres of other lower mass stars.

However, it is a Goldilocks homology, wherein the structure of the atmospheres of other stars must not be too cool so that a dusty plasma forms and not so hot that the atmosphere is severely out of local thermodynamic equilibrium (LTE). Regardless, Figure 2.4 illustrates the homological structure of the atmospheres above other lower mass stars with respect to the Sun. This picture has recently been bolstered with the detection of a temperature minimum and chromospheric temperature variations in the atmosphere of our nearest stellar neighbor α Centaurus A, mimicking the Sun's chromospheric structure (Liseau et al., 2013). Thus for the majority of lower mass stars it is likely that, if they have surface magnetic features and emission in the Ca H and K lines, this kind of emission can be used as a reasonable proxy for their magnetic activity.

Although the corona and transition region are coupled to the photosphere through the chromosphere by magnetic fields and waves, the properties of the plasma in these two regions differ significantly. Chromospheric plasma is much less dense than the photosphere, which has a number of implications for observations and also for modeling it. Primarily, the low density of the plasma results in the plasma β becoming less than unity and a much smaller optical depth, with line emission and non-LTE effects, such as scattering, becoming more important than continuum emission. The need to account for non-LTE effects complicates the interpretation of most of these diagnostics. Yet recent advances in ground- and space-borne instrumentation, such as the Sunrise balloon mission and the IRIS mission, have provided a route to observe the small spatial scales of the dynamic and intermittent structures seen in current simulations of the chromosphere (e.g., Wedemeyer-Böhm et al., 2009; Leenaarts et al., 2013). The coexistence and interaction of magnetic fields and large amplitude magnetosonic waves makes modeling the chromosphere a challenging task. Although observations have exhibited the inhomogeneous structure of the chromosphere for many years, only recently has modeling been able to show that its structure is not as simple as in 1-D models (Figures 2.4b). Instead, both the magnetic and thermodynamic fields can vary horizontally and radially in the presence of magnetism as demonstrated in Figure 2.5

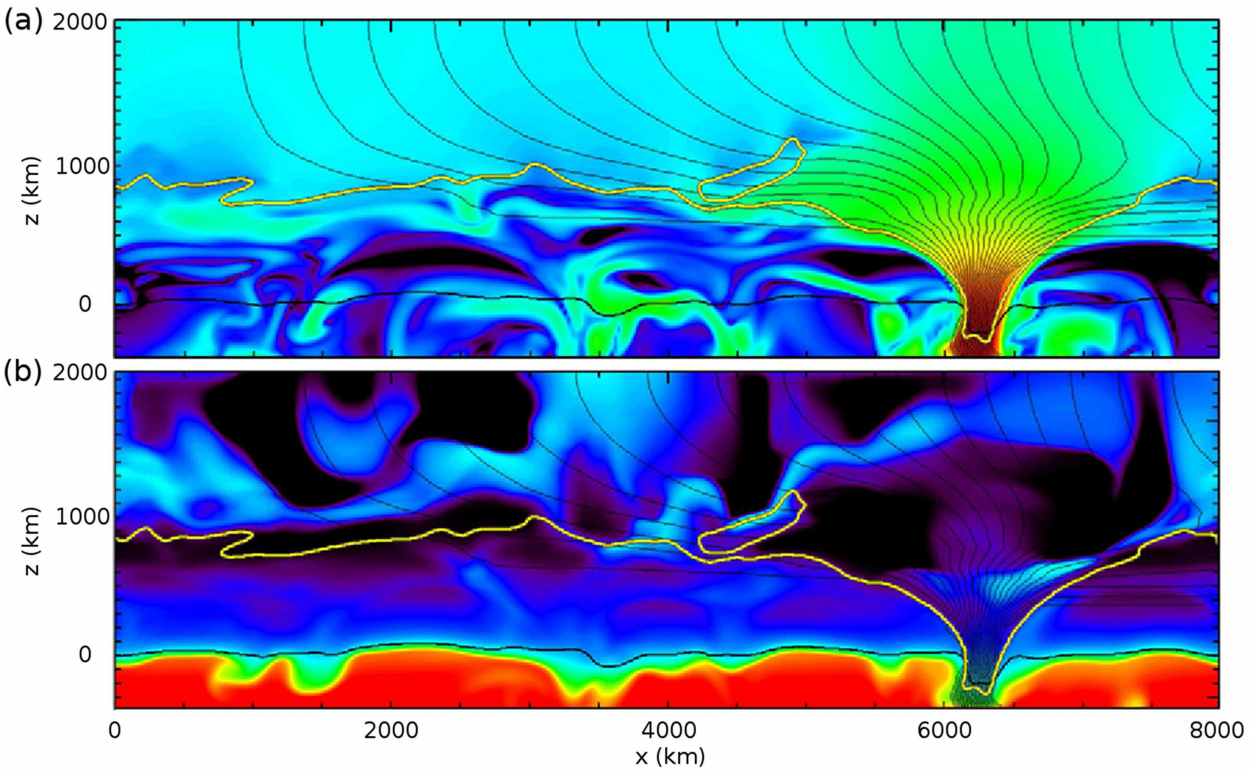

Figure 2.5: (a) A vertical cut through a 3D simulation of the solar chromosphere, showing logarithmic magnetic field strength between 1 G (deep blue) and 3 kG (dark red) and its horizontal expansion with height. The photosphere is indicated with the corrugated black line near zero height or optical depth with $\tau = 1$. A pore is evident with field lines expanding into the chromosphere. (b) Temperature in the same slice ranging between 2,500 and 12,000 K. The yellow line indicates the height at which the plasma $\beta = 1$ (Adapted from Freytag et al. (2012)).

as well as in Freytag et al. (2012). This variability in temperature and density gives rise to greater emission from regions where magnetic field threads through the chromosphere, as seen in the synthetic Stokes inversions of de la Cruz Rodríguez et al. (2012). Indeed, the temperature sensitivities of Ca H and K line formation causes the emergent intensity variations. The intensity variations can be inverted to produce maps of density and temperature, and of the line-of-sight magnetic field much like those in Figure 1.2b.

Having assessed the photometric measures of stellar variability, it is now useful to compare it against other methods of measuring magnetic activity. It is also worth building a

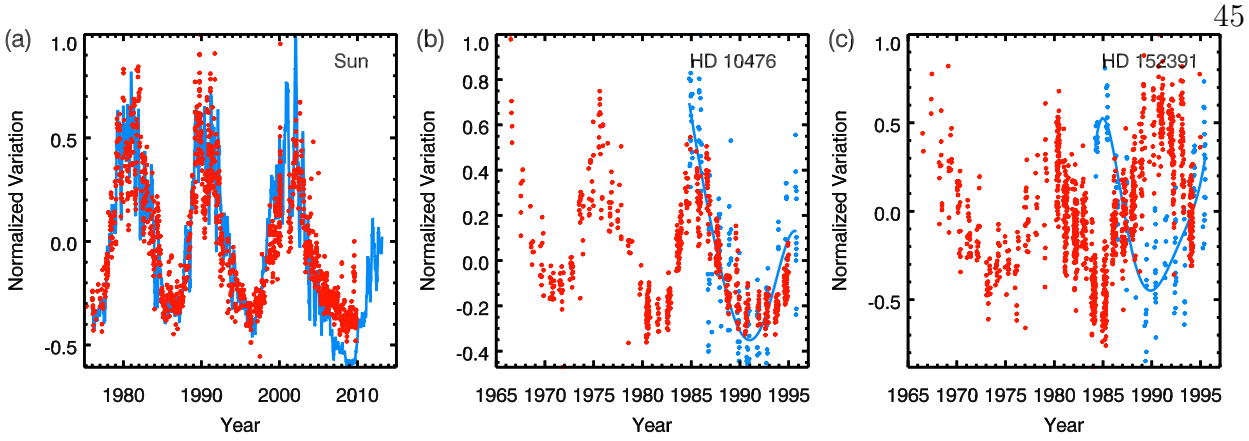

Figure 2.6: (a) Comparison over 30 years of total solar irradiance (TSI) changes (Fröhlich, 2013) and Mt. Wilson Ca H and K emission variations (Livingston et al., 2007), illustrating the Schwabe cycle and the close correlation between these two measurements of variability. The red dots are Ca measurements and the blue line is an 81 day smoothing of the TSI. (b) Photometric brightness and Ca H and K measurements from Mt. Wilson for the K1V star HD 10476, showing its equivalent Schwabe cycles as well as its brightness and S-index (chromospheric variation) correlations. Brightness variations in blue dots with a blue line showing a polynomial fit and red dots showing the longer-term Ca H and K observations. (c) Photometric brightness and Ca H and K measurements from Mt. Wilson for the spot-dominated G8.5V star HD 152391, showing its equivalent Schwabe cycles as well as its brightness and S-index anti-correlations [b and c constructed from data in Radick et al. (1998)].

framework to understand how chromospheric activity is described. Indeed, one method of characterizing the observed chromospheric activity called the "S" activity index was developed during the long running MWO Calcium H & K Project. This index was introduced by Vaughan et al. (1978) as a dimensionless proxy for chromospheric activity in the Ca H and K lines as measured with MWO spectrometers. More generally, the flux is measured in two narrow bands centered on the Ca H and K and is normalized by the flux in two wide-band continuum filters, referred to as Johnson visible (V) and red (R). Thus the S-index values can be constructed as

$$\mathrm{S} = \alpha \frac{H + K}{R + V}. \tag{2.1}$$

where H, K, R, and V are the values for the flux measured in the various bandpasses and α is an instrumental calibration factor. This calibration is necessary to adjust the measured

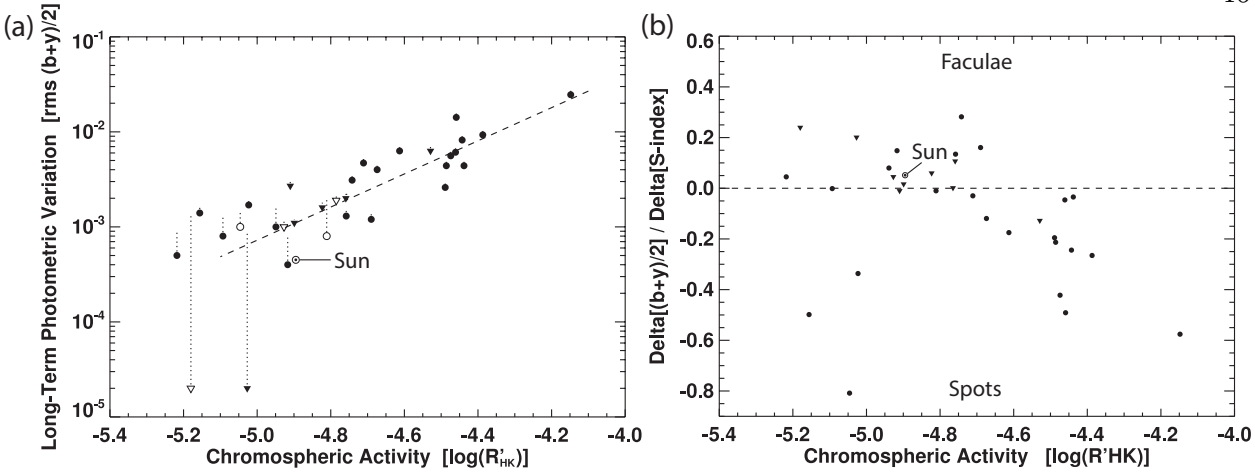

Figure 2.7: (a) Correlation between average photometric amplitude and and average chromospheric activity (under the $\log R'_{HK}$ measure) for 32 stars in the Mt. Wilson catalog, with the Sun labeled for reference. (b) Correlation between the photometric variation and S-index as a function of chromospheric activity, indicating that some stars show a correlation in Ca H and K emission and in brightness variations whereas others show an anti-correlation (Figures adapted from Lockwood et al. (2007)).

activity indices from the two instruments at Mount Wilson. Values for α range from 1.3 (Cincunegui et al., 2007) to 5 (Gray et al., 2003). However, the S index is a measurement of the total Ca H and K flux from a star and not the amount due only to the chromosphere. It takes a bit more work to isolate the chromospheric contribution, which is a better measure of magnetic activity.

The first step is to introduce the $B-V$ color (the difference between the flux in the blue B and visible bandpasses) and the second is to remove the photospheric component. As such there is an empirical affine map between the S-index and the chromospheric activity measure R'_{HK} (Middelkoop, 1982). This mapping is defined as $R'_{HK} = 1.34 \times 10^{-4} C_{\rm cf} \mathrm{S} - R_{\rm phot}$, where C_{cf} is the conversion factor for main-sequence stars with $0.3 \leq B - V \leq 1.6$ and $R_{\rm phot}$ is the photospheric contribution. Both of these factors have been empirically determined by correlating the S-index with other means of gathering magnetic activity and are found from a fit with a cubic polynomial in $B - V$ Noyes et al. (1984).

With this definition in hand, some of the results from the multi-decadal stellar activity

can now be explored. Figure 2.6 shows a comparison between the brightness variations and the variations in the Ca H and K lines as measured by the S-index. These temporal changes in the Sun's output are characterized by the 11-year Schwabe cycle and a close correlation between Ca H and K emission and total irradiance (Figure 2.6a). This is also true of HD 10476, whose brightness and Ca emission are shown in Figure 2.6b. Such cycles are evident across the range of low mass stars that populate the lower end of the HR diagram, and there is now enough data collected to begin to build statistics about the nature of cycle periods and their relation to rotation rate and stellar mass (Baliunas et al., 1995). Yet, like the Sun, these stars exhibit a multitude of timescales, with Maunder Minimum-like grand minima as well as many other short and long-term periodicities.

In contrast to the Sun and HD 10476, the much younger BY Draconis-type variable star HD 152391 shows an anti-correlation between these two measures of activity induced variability (Figure 2.6c). This divergence is but one example of one of the broader behaviors of stellar activity found using measurements of variations in the Ca H and K lines. Indeed, examining the entire Mount Wilson sample reveals a division in the brightness and chromospheric variation between young and old stars (e.g., Radick et al., 1998; Lockwood et al., 2007). If one assumes that old stars have activity cycles like the Sun, their photometric behavior is then dominated by faculae and so have a positive correlation with chromospheric variations (Figure 2.7a). Conversely, it appears that young stars are spot-dominated and exhibit a negative correlation between photometric and chromospheric variations. This is illustrated in Figure 2.7b, where the dividing line between such behavior is near $\log R'_{\rm HK} = -4.7$. The degree of correlation between the $\log R'_{\rm HK}$ measure of stellar activity and the amplitude of photometric variation for a set of stars with long-term measurements is shown in Figure 2.7a. The agreement between the rms value of the photometric variations and $R'_{\rm HK}$ is reasonably robust over about a decade in activity. This correlation does not change between the spot and faculae dominated regimes until systematic errors arising from a lack of photons creep in at low levels of activity.

The Sun has afforded us the opportunity to study a magnetic cycle in great detail. Yet to begin to parameterize how a dynamo evolves and varies, we must turn to other solar-like stars. The Ca H & K project target stars are effectively the only source of long-term observations of active stars. Indeed, this project provided the first results regarding long-term magnetic activity (e.g., Baliunas et al., 1985, 1996; Saar & Brandenburg, 1999), with many of the stars in their sample appearing to have magnetic activity cycles akin to the solar cycle in length and character. However, the results were a bit puzzling. There was little, if any, relationship found between cycle periods and other properties thought relevant to dynamos such as rotation rate. Later work did find various, but often contradictory, correlations with rotation (e.g., Saar & Brandenburg, 2001; Saar, 2009). As it stands, there is still a great deal of uncertainty regarding the correlation between cycle period and the rate of rotation due to a paucity of data. Recent work has attempted to reanalyze the Ca H & K data with a more careful sampling of the data. When such a sampling is carried out, as in Saar (2009), several branches in the behavior of cycle frequency ω_{cyc} seem to emerge, where each branch can be correlated with the inverse Rossby number ($\mathrm{Ro}^{-1} = \tau_C \Omega$, with τ_C is an empirical convective overturning time and Ω the bulk rotation rate). Figure 2.8 shows two possible interpretations of the Ca H & K data, with either a fairly linear scaling with Coriolis number (the ratio between the overturning time and the rotation period) or a fit that is nearly independent of Coriolis number. The latter is favored because of its lower uncertainty in the fit. Such a result, if robust, is quite surprising as it would indicate that it is not the rotation rate itself that sets the cycle period. Rather, another processes must be at work that, given the regularity of the cycles, must be fairly linear.

2.3 Spectropolarimetry and Zeeman-Doppler Imaging

The direct detection of magnetic fields relies upon the lifting of the degeneracy of quantum states in ions, atoms, and molecules when they are in the presence of a magnetic field. Moreover, it is the interactions of photons with this split set of states that imprints

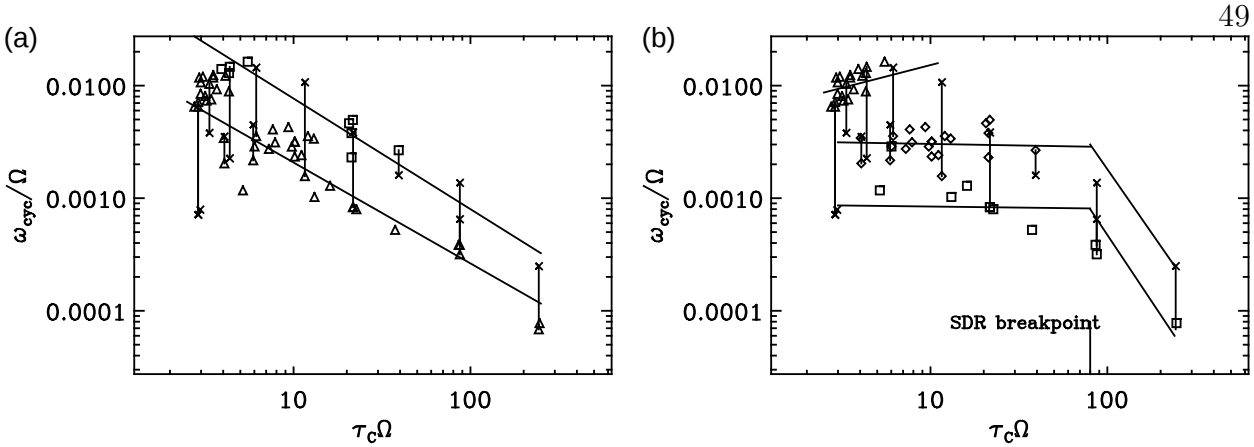

Figure 2.8: Relationship between cycle frequency and inverse Rossby number. (a) Primary cycle frequency normalized by the bulk rotation rate (ω_{cyc}/Ω) versus inverse Rossby number $Ro^{-1} = \tau_C\Omega$, with fits to two branches: $\omega_{cyc}/\Omega \propto (\tau_C\Omega)^{-0.98}$ or $(\tau_C\Omega)^{-0.90}$. (b) A different interpretation of the same data with three potential branches, utilizing the secondary cycle periods for the data shown as squares. The secondary cycle periods are the lower bound of the vertical dashed lines, with a change in behavior as surface differential rotation begins to disappear (labeled as SDR breakpoint). This figure is adapted from Saar (2009).

the signature of the magnetic field on the polarization of the photons that are eventually detected here on Earth. The description of this effect is attributed to Zeeman (§2). The Zeeman effect splits spectral lines and so allows many types of magnetic fields to be detected, from the μG fields in the ISM and molecular clouds to the very strong MG fields on white dwarfs. A large fraction of the measurements of magnetic fields reported in the literature have been obtained through Zeeman spectroscopy, with few other options available outside of the Hanle effect or Faraday rotation.

The well-known result from early quantum mechanics is that in the presence of a magnetic field each degenerate energy level splits into $2J + 1$ sublevels $j = -J \ldots J$, with J the total angular momentum quantum. This in turn is due to the force that the external magnetic field exerts on the different magnetic moments associated with each angular momentum state of the bound system of charged particles. This picture remains valid provided the energy difference between sublevels is below the spin-orbit coupling energy, after which the angular and spin momenta decouple due to the stronger interaction of the magnetic field

with a particle's spin. The energy difference δE between each of these angular momentum sublevels is linear in the magnetic field $\mathbf{B}$ and is given by

$$\delta E = \mu_0 \hat{\mu}_J \cdot \mathbf{B} g_J j, \tag{2.2}$$

where μ_0 is the vacuum permeability, $\hat{\mu}_J$ is the unit vector in the direction of the magnetic moment of the base state J, and g_J is the dimensionless Landé factor with values of order unity that depends on the total angular momentum of the unsplit state and upon relativistic quantum electrodynamical effects. The relevant energy difference ΔE is between the unsplit energy of the base level J and the split level, which is

$$\Delta E = \mu_0 \hat{\mu}_{\mathrm{j_i}} \cdot \mathbf{B} \left(j_{\mathrm{f}} \Delta g + g_{\mathrm{j_i}} \Delta j \right), \tag{2.3}$$

where $\Delta g = g_{\mathrm{j_f}} - g_{\mathrm{j_i}}$ and $\Delta j = j_{\mathrm{f}} - j_{\mathrm{i}}$, with i being the initial state and f the final state. Dipolar transitions between the levels obey the selection rule $\Delta j = -1$, 0 or $+1$ and the resulting spectral lines form three corresponding groups. The lines due to transitions with $\Delta j = 0$, though with possible changes in orbital or spin states that subsequently change g but not j, are the π components. Such components are distributed symmetrically around the unsplit line, with no signal at the line core. The two groups of lines formed by transitions with $\Delta j = \pm 1$ are the σ components and are shifted symmetrically about the unsplit line, with transitions of $\Delta j = 1$ on one side and transitions of $\Delta j = 1$ on the other side. Though, they still have a signal at the line core.

However, the Zeeman effect is not without its limitations. For weaker fields less than about 1 kG, other effects tend to erase the splitting signature as the lines are broadened due to thermal effects, rotation, and turbulent velocity fields. This problem can largely be circumvented when one uses polarizing filters to select out portions of the signal, wherein much weaker fields can be detected by taking differences between components with different polarizations. This process is called spectropolarimetry and can be utilized to detect fields with simple topologies that are as weak as a few Gauss. The photon polarization can

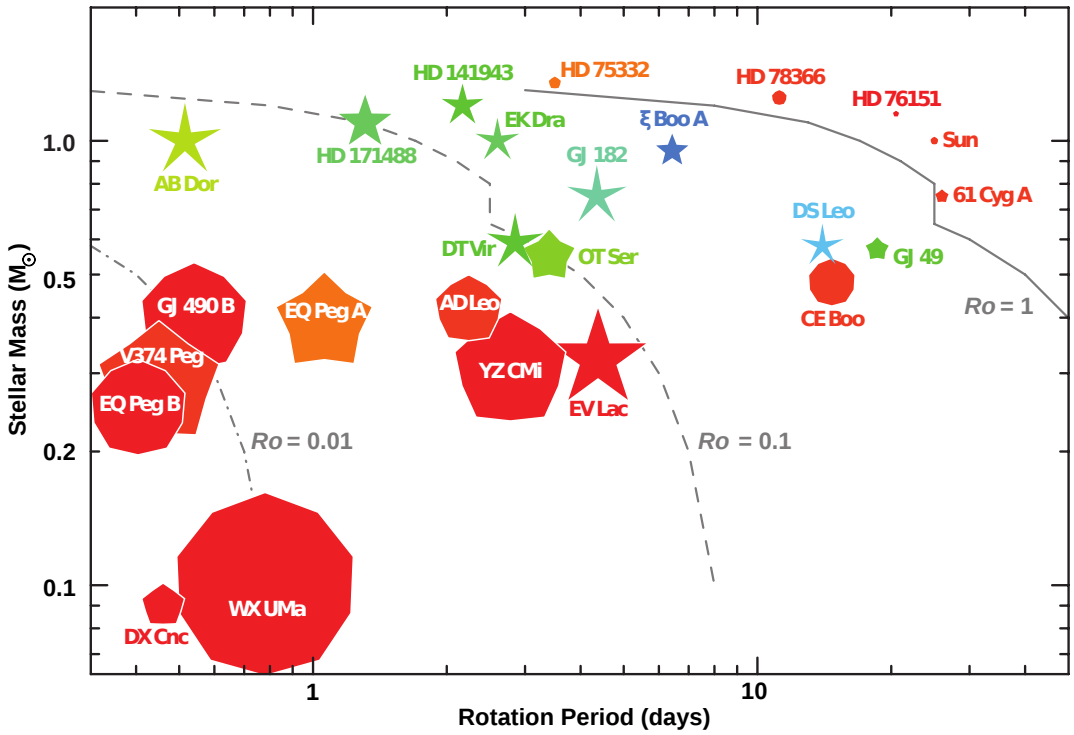

Figure 2.9: Global-scale morphology of spectropolarimetrically reconstructed magnetic fields on low-mass stars, as a function of stellar mass and rotation rate. Symbol size indicates rms magnetic field strength and symbol color illustrates field configurations, with blue for purely toroidal fields and red for purely poloidal fields. The symbol geometry is meant to depict the degree of axisymmetry of the poloidal field component, where the fully convex decagon indicates purely axisymmetric fields and the most concave star represents purely non-axisymmetric poloidal fields. The curves trace contours of constant Rossby number ($Ro = P/\tau_c$), with solid at $Ro = 1$, dashed at $Ro = 0.1$, and dash-dot at $Ro = 0.01$ (using convective turnover times τ_c from Kiraga & Stepien (2007)). The smallest and largest symbols correspond to mean large-scale field strengths of 3 G and 1.5 kG on a logarithmic scale. (Adapted from Donati & Landstreet (2009)).

probe these weaker fields because there are differences in the polarization states of emitted photons that depend upon the energy of the photon. Namely, this energy selects one of the π or σ states. Both states can emit linearly polarized photons due to angular momentum transitions, but only the σ states emit circularly polarized photons due to spin transitions. Thus passing a magnetically sensitive emission line through a polarizing filter allows the split lines to be detected in the line core even in the presence of significant broadening. Moreover, given the variable alignment of the magnetic moment of the electronic state of the bound

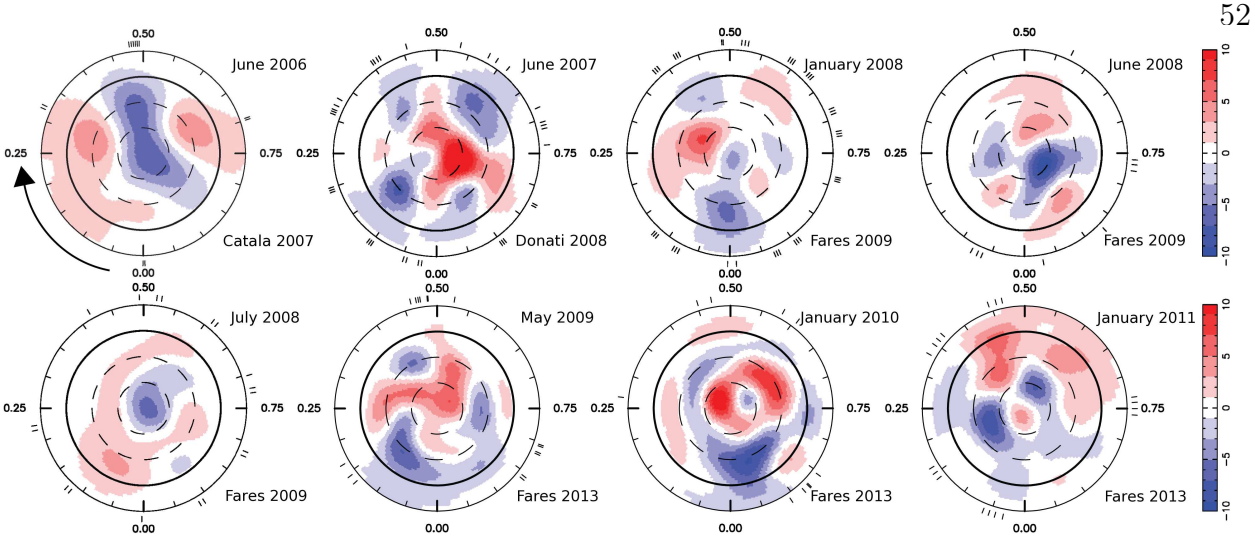

Figure 2.10: Radial magnetic field on the surface of τ Boötis reconstructed using the tomographic techniques of Zeeman-Doppler imaging. The view is aligned with the rotation axis. Red denotes positive field pointing away from the star, blue the opposite, as indicated with the color bar. Each sub-panel shows the reconstruction from multiple observations during the month and year given in the upper right, whereas the source for the image is given in the lower right. The arrow indicates the direction of rotation and the small tick marks denote the rotational phase of the star during observing nights (Images from Catala et al. (2007); Fares et al. (2009, 2013)).

system with vector components of the magnetic field, this effect can be used to determine the orientation of the magnetic field as the circularly polarized states gives the magnitude of the line-of-sight magnetic field and the linear polarization gives information about the magnitude of the transverse field.

This is only the magnetic portion of the Zeeman-Doppler mapping technique, and on its own is a robust way to detect magnetic fields. Yet it can also be taken a step further by including multiple observations of many magnetically sensitive lines over many distinct rotational phases of the star and Doppler information from the circularly polarized subset of the lines. This is essential as there is a degeneracy between the line-of-sight velocity Doppler shifts and magnetic field Zeeman shifts, as well as an alignment or anti-alignment ambiguity. However, this degeneracy can be partially lifted by incorporating information from the linear polarization filters and thus the transverse field components. Finally, maximum entropy

modeling of the differential rotation of the star allows the morphology of the large-scale field to be reconstructed through tomographic mapping.

Such reconstructions have been performed on a growing number of stars, slowly building a comprehensive picture of stellar magnetic field morphologies as function of mass and rotation rate (Figure 2.9). Stars must be observed during multiple phases of their rotational periods in order to accurately reconstruct the star's rotation profile and the surface magnetic fields, so measuring this for many stars is a significant observing campaign. Nonetheless, the basic stellar properties that have bearing on the structure of the surface magnetism of stars is being mapped out, where the total surface magnetic energy density seem to be largely determined by mass and rotation rate. The ratio of the toroidal and poloidal field magnitudes also seems to depend upon those values. Indeed, Figure 2.9 suggests that stars with masses above about $0.5\,\mathrm{M}_\odot$ and Rossby numbers less than unity build larger toroidal fields and non-axisymmetric poloidal fields. In contrast, those stars with masses below about $0.5\,\mathrm{M}_\odot$ predominantly build strong axisymmetric poloidal fields. Furthermore, there seems to be a close relationship between magnetic field strength and rotation rate. This of course hints at the underlying role of a convection and rotation driven dynamo in building such fields.

With a rudimentary picture of how spectropolarimetric observations operate, some of its recent results can be examined. One relevant to this thesis is the detection of polarity reversals on the planet-hosting F-type star τ Boötis. Figure 2.10, shows the morphology of the magnetic fields on this star as extracted with the Zeeman-Doppler imaging (ZDI) technique. The exciting realization is that it seems to have a polarity cycle, with the sign of the the radial magnetic field changing at the visible pole on a fairly regular interval of about a year (e.g., Donati et al., 2008b; Fares et al., 2013). The resolved field is quite weak, being at most about 10 G. However, if τ Boötis is like the Sun, the measured surface-averaged field is likely greatly reduced due to cancellation of small-scale structure surface fields. The radial field dominates the signal, but there are contributions of about 3 G from azimuthal and

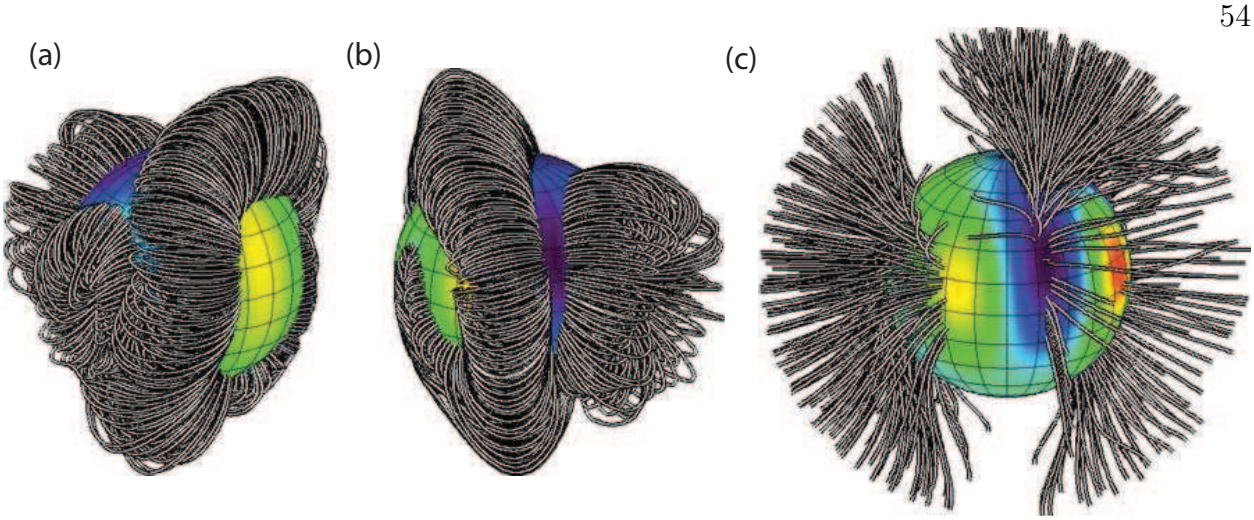

Figure 2.11: Magnetic field line extrapolations for the 15 $M_\odot$ main-sequence B0V star τ Scorpii, showing (a) the closed field line solutions at two points during the star's 41 day rotation and (b) the open field line solution extrapolated to twice the star's radius. The rotation axis is aligned with the page height (Images from Donati et al. (2006b)).

longitudinal components as well. The magnetic signal is entangled with Doppler information. This information is dominated by the substantial bulk rotation of 2 days, with the differential rotation between the fast equator and the slow poles being 0.4 days.

The atmospheres of massive stars present their own set of challenges such as a large thermal broadening and often a strong rotational broadening of their spectral lines. For some of these stars, particularly those with a lower rotation rate, the fields can be reconstructed as shown for τ Scorpii in Figure 2.11. This 5 Myr old 15 $M_\odot$ star exhibits a large-scale magnetic field topology, with a strength of about 1 kG (Donati et al., 2006b). Surprisingly, the closed field lines indicate that the magnetic equator is nearly aligned with the rotation axis. The open field lines would direct the hot winds streaming from the photosphere in a roughly dipolar fan.

2.4 X-Ray Variability and Luminosity

Observations of X-ray spectra and total bolometric luminosities offer a measure of stellar activity similar to that of the Ca H and K lines, though it is much more sensitive to

energetic events such as flares. However, such observations probe regions with much higher temperatures of millions of Kelvin, as in the solar corona rather than just a few thousand Kelvin as in the solar chromosphere. After more than 30 years of X-ray observations, which are only possible from space, X-ray emission has been found to be ubiquitous across the Hertzsprung-Russell (HR) diagram. The bulk of the this X-ray emission may have origins that are independent of the mass of the star. Appealing to the Sun, it is well known that the solar corona emits X-rays from this region of high temperature, rarefied, and magnetically confined plasma. Nearly all classes of low-mass stars show variable X-ray emission, which has likewise been attributed to stellar coronal plasmas (e.g., Vaiana et al., 1981; Schmitt & Liefke, 2004). While higher mass stars do not have the same degree of variability, it is still likely that they too possess a corona. Age also seems to impact X-ray luminosity. Young low-mass stars tend to be among the most X-ray luminous, where $L_X/L_{bol} \sim 10^{-3}$ is common (e.g., Telleschi et al., 2007). Older stars typically have lower X-ray luminosities, dropping several orders of magnitude relative to young stars at the same mass. This profound decrease in stellar X-ray luminosity between the zero-age main sequence (ZAMS) and the terminal age main sequence (TAMS) is widely supported among many stellar populations in our galaxy (e.g., Güdel et al., 1997; Wright et al., 2010).

The space-borne X-ray missions of the 1970s and 1990s, such as the High Energy Astronomy Observatory (HEAO) series and later the Röntgensatellit (ROSAT), found that X-ray luminosity scales with the bolometric luminosity as $L_X/L_{bol} \sim 10^{-7}$ for young massive O and B stars (e.g., Harnden et al., 1979; Pallavicini et al., 1981; Berghöfer et al., 1997; Nazé et al., 2011). For some time the primary X-ray emission mechanism for these massive stars was considered to be quite different from that occurring in lower mass stars, potentially being produced in shocks that arise from instabilities in their radiatively driven stellar winds (e.g., Lucy & White, 1980; Owocki & Cohen, 1999). Since the stars generally show little X-ray variability, these shocks could be occurring more frequently than the cadence of observation which would imply that they are numerous and fairly homogeneous. About a decade ago,

spectroscopic observations from Chandra and XMM-Newton confirmed this basic picture with X-ray emission in the extended wind giving rise to broadened lines at different depths (temperatures) within the wind (Schulz et al., 2000; Kahn et al., 2001; Waldron & Cassinelli, 2001).

Yet evidence is growing that magnetically confined hot plasma either near the photosphere or in the wind plays a significant role (Babel & Montmerle, 1997; Waldron & Cassinelli, 2001; Oskinova et al., 2011). Higher resolution instruments could provide the smoking gun for the hypothesis that these stars also have a corona and that the lack of variability largely arises from the nature of the bulk magnetic field. The fields visible at their surfaces are the observable portion of the fossil field remaining from their birth. However, the impacts of such a field depend sensitively upon the ratio of kinetic energy to magnetic energy as $\eta = B^2R^2/\dot{M}v_\infty$ (e.g., Güdel & Nazé, 2009), with B the rms magnetic field, R the stellar radius, and the product $\dot{M}v_\infty$ the terminal wind momentum. What may be crucial is the rotation rate, since the stars that appear to have coronal activity rotate much more slowly than the average rotation rate for O and B type stars. Raising the complexity of this is the observed trend that slow rotators also tend to have strong magnetic fields, which may be of some significance as it would either mean that there was (or is) some dynamo action building the field or that the fossil field has substantially braked the rotation of the star. In Petit et al. (2013), a large catalog of massive stars has been compiled by the MiMeS project. The character of the outer atmospheres of these stars has been categorized by the behavior of their magnetospheres as either magnetodynamically or centrifugally dominated. The magnetodynamical class have an Alfvén radius smaller than the Keplerian corotational radius, whereas the centrifugally dominated atmospheres possess the converse. The magnetodynamical atmospheres have large meridional flows guided by the magnetic field that more uniformly distribute high energy emission from UV and X-rays. The centrifugally dominated winds have equator migration of flows and field that forms a thin disk at the magnetic equator, which significantly modifies the character of the emission. These distinctions likely have

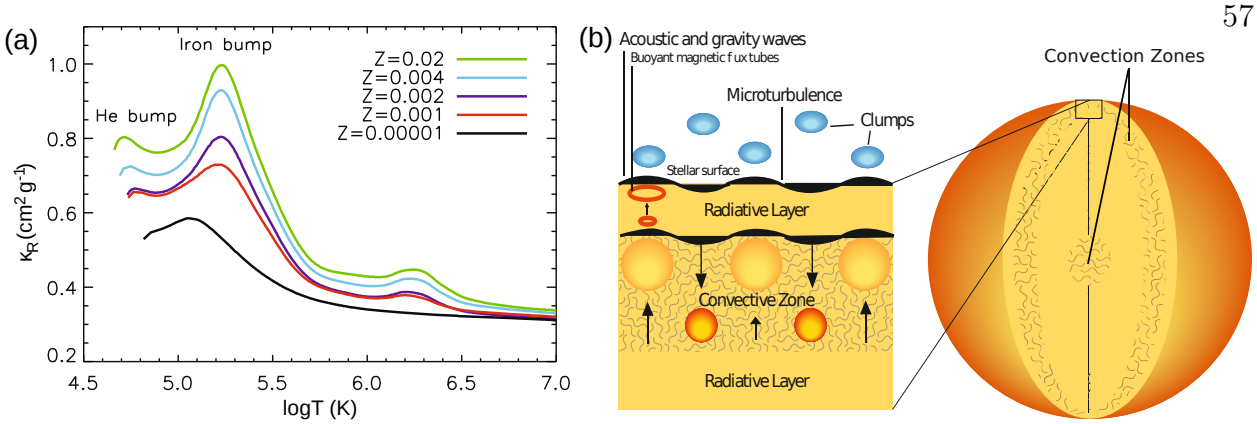

Figure 2.12: An illustration of the formation of convection zones due to distinct opacity bumps from helium and iron. (a) Metallicity and temperature dependence of the Rosseland mean opacity. (b) A sketch of the outer iron opacity driven convection zone in a massive star (Figures from Cantiello et al. (2009)).

some bearing on the plateau and scatter in the x-ray emission of intermediate mass stars as in Figure 2.13.

While there is not a large degree of X-ray variability in many of these massive stars, there is variability in both the visible photometric observations and in observations using other bandpasses (Petit et al., 2013). This has been attributed to possible dynamo action in the near-surface Fe-opacity bump convection zone present in stars with masses greater than about 5 or 6 $M_\odot$ (Cantiello & Braithwaite, 2011), which is highly metallicity dependent given that it arises from the peak in opacity from iron-group elements as seen in Figure 2.12a (Stothers & Chin, 1993; Cantiello et al., 2009). The character of this near-surface convection zone is illustrated in Figure 2.12b, with the Fe-bump convection zone sitting atop the deep radiative envelope that is sandwiched between the convective core and this layer. Convection in this layer can excite acoustic and gravity modes above it, which may be detected using asteroseismology. Moreover, applying a repurposed Cartesianism "Je convectent, donc je suis une dynamo" (I convect, therefore I am a dynamo), it may be running an interface-type dynamo like the Sun with buoyant flux tubes rising through to the surface. This opacity bump is due to millions of spectral lines many of arising from relativistic spin-orbit coupling in

the iron-group elements. The iron-group alone accounts for about 50% of the total Rosseland mean opacity in the iron bump (Iglesias et al., 1992). Additionally, there is a zone of weak convection in the more prevalent region of the He-opacity. It too could run a dynamo as it is much more rotationally constrained than the Fe-opacity bump convection. Depending upon the magnetic Prandtl number there, it may build large-scale magnetic fields.

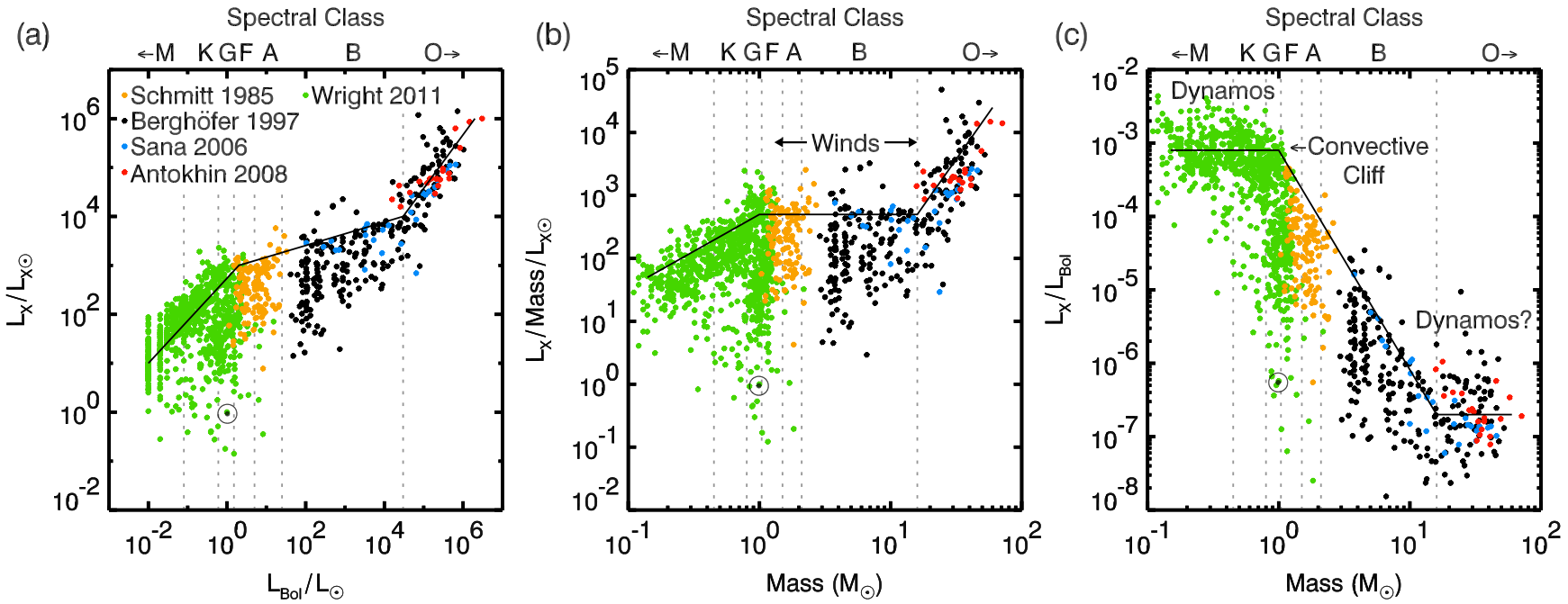

Figure 2.13: X-ray luminosity observations are displayed, showing such observations over the mass range of the main-sequence. (a) Average X-ray luminosity, $L_{\rm X}$ versus bolometric luminosity $L_{\rm Bol}$, both normalized by their respective solar values. Spectral type is indicated along the top abscissa and demarked with thin dotted lines. The black line is meant to illustrate the mean slope of the three distinct ranges of behavior. The sources for the data are indicated in (a). (b) $L_{\rm X}$ to mass ratio plotted versus mass. This serves to highlight the region where $L_{\rm X}$ depends linearly on mass and is likely wind driven. (c) The ratio $L_{\rm X}/L_{\rm Bol}$ versus mass, highlighting the mass range where $L_{\rm X}$ is linearly related to the $L_{\rm Bol}$. The location of the Sun is plotted with its symbol $\odot$, showing its relatively low X-ray luminosity.

Some of the behavior exhibited by low, intermediate, and high mass stars is displayed in Figure 2.13. The data for the low mass stars is from Wright et al. (2011), which presents a catalog of 824 X-ray sources with masses between 0.1 and 2.1 $M_\odot$ and are shown as green points in Figure 2.13. The black data points are from the ROSAT all-sky-survey (RASS) catalog of intermediate and high mass stars (Berghöfer et al., 1997), whereas the orange data points are from an Einstein survey of F-type and A-type stars (Schmitt et al., 1985). The other two sets of data are from XMM-Newton observations of NGC 6231 (Sana et al., 2006, blue points) and Carina OB1 (Antokhin et al., 2008, red points). There appear to be three distinct mass (or luminosity) ranges where there are changes in the power law relationship between X-ray luminosity (L_X) and bolometric luminosity (Figure 2.13a).

In the standard picture of stellar dynamo theory, an interaction of convection with rotation produces a magnetic dynamo within a star's convection zone. Stars less massive than about 1.6 $M_\odot$ spectral type A possess an outer convective envelope above a radiative zone, whereas very low mass stars are fully convective. The generation of magnetic field is responsible for a plethora of magnetic phenomena in or above the stellar photosphere such as starspots, a heterogeneous chromosphere, a magnetically constrained coronal plasma, flares, and coronal mass ejections. The study of a nearby example of a cool star, the Sun, has provided a robust framework with which to interpret the X-ray emissions of other cool stars (Peres et al., 2000). Indeed, most cool stars except cool giant stars have been found to exhibit characteristics grossly similar to what we know from the Sun. Most of these stars have variable X-ray emission at temperatures of at least 1-2 MK and occasional flaring. Thus the scatter in the X-ray data for lower mass stars seen in Figure 2.13 is primarily due to the interactions between rotation, convection and magnetism.

The L_X-Mass ratio in Figure 2.13b shows that the intermediate mass range between the low-mass A-type stars and the higher mass B-type stars has $L_{\rm X} \propto M$, which is likely due to the dominance of shocks in their winds. When scaled by $L_{\rm Bol}$, as in Figure 2.13c, two other regimes become evident, with one for the lower mass stars and another for the massive O-type

stars where $L_{\rm X} \propto L_{\rm Bol}$. The lower mass stars have a relatively high level of X-ray emission, whereas the relative X-ray emission declines significantly with higher mass and becomes nearly constant beyond about $16\,{\rm M}_{\odot}$. The saturation of $L_{\rm X}$ at low masses is potentially a result of the strong magnetic confinement of the wind, which in turn is likely due to the rotation of the star and dynamo action in its exterior convective envelope. The saturation at higher mass could be due to two mechanisms: one could be dynamo action in the Fe- and He-opacity bump convection zones; the other may be due to changing properties of the winds and mass loss for the O-type stars. It would be most interesting if the mass required for these near-surface convective layers to arise corresponds to the transition in the X-ray luminosity behavior of the O-type stars, which may be ascertained through asteroseismic measurements of this class of stars looking for a change in the balance of power between g-modes and p-modes.

2.5 Magnetic Activity-Rotation Correlation

In his article "On the Nature and Construction of the Sun and the Fixed Stars," William Herschel appeals to the rotation of the Sun and the planets in his proposition that other stars must also rotate (Herschel, 1795). He later clarifies his logic in a paper regarding the periodic brightness changes in α Herculis, wherein it is stated that other stars may have spots and that the periodic light curves he observed were the result of them rotating in and out of the line-of-sight (Herschel, 1796). Nearly 80 years after his musings on the possible axial rotation of other stars, a method for measuring stellar rotation using spectral lines was suggested by William Abney (Abney, 1877a). Shortly thereafter Abney applied this technique in photographing the line broadening due to the Sun's rotation (Abney, 1877b). Half a century after these Doppler measurements of the solar rotation, studies of stellar rotation shed light on two regimes of stellar rotation along the main-sequence that depends upon mass (e.g., Shajn & Struve, 1929; Struve, 1930; Huang, 1953; Abt & Hunter, 1962; Wilson, 1966). In particular, they found that stars more massive than about $1.6\,{\rm M}_{\odot}$ rotate

fairly rapidly at an average speed of around $140\,\mathrm{km\,s^{-1}}$, with a slow increase with mass and reaching a plateau above about $10\,\mathrm{M_\odot}$. Stars less massive than $1.6\,\mathrm{M_\odot}$, on the other hand, show a steep decline in $v \sin i$ with decreasing mass. There is a distribution of their projected equatorial rotation speed ($v \sin i$) about this mean, as the statistics in the above references show. The fact that most massive main-sequence stars are rapid rotators is partly due to their short lifespans, since only the lower mass stars have the time necessary to be rotationally braked by their winds.

Spectroscopic surveys of nearby field stars and clusters revealed a potential reason for this rapid decline in rotation. In a 1963 paper, Olin Wilson hypothesized, based on Ca H and K observations of young clusters and old field stars, that magnetic activity declines with age (Wilson, 1963). He further describes the link between rotation, convection, and magnetic activity in Wilson (1966), attempting to ascertain why stars less massive than about $1.5\,\mathrm{M_\odot}$ (spectral type F5V) rotate so slowly compared to their more massive brethren. He suggests that the reason is the loss of the outer convection zone and thus the loss of the ability to generate a strong, large-scale magnetic field that can efficiently brake the rotation of a star (Wilson, 1966). Though, this would not hold for the most massive stars as they have outer convection zones. This argument was put on a more quantitative footing with a survey of rotation in young stellar clusters that correlated with some of Wilson's Ca H and K measurements (Kraft, 1967). Figure 3 of that paper illustrates that F-type stars near the canonical $v \sin i$ transition that also show Ca H and K emission have larger rotational velocities at a given mass than stars without such emission. Shortly after which Kraft states that: "for stars less massive than $1.25\,\mathrm{M_\odot}$, the largest rotational velocities are associated with the stars having active chromospheres." In a concise letter, Andy Skumanich put this in perspective and formulated what is now widely accepted as the "Skumanich $t^{-1/2}$ law" for the decay of rotation and chromospheric magnetic activity (Skumanich, 1972). Thus the link between rotation, convection, magnetic activity, and age is made for low mass stars. Building upon this early chromospheric activity work, it was found that there may be two

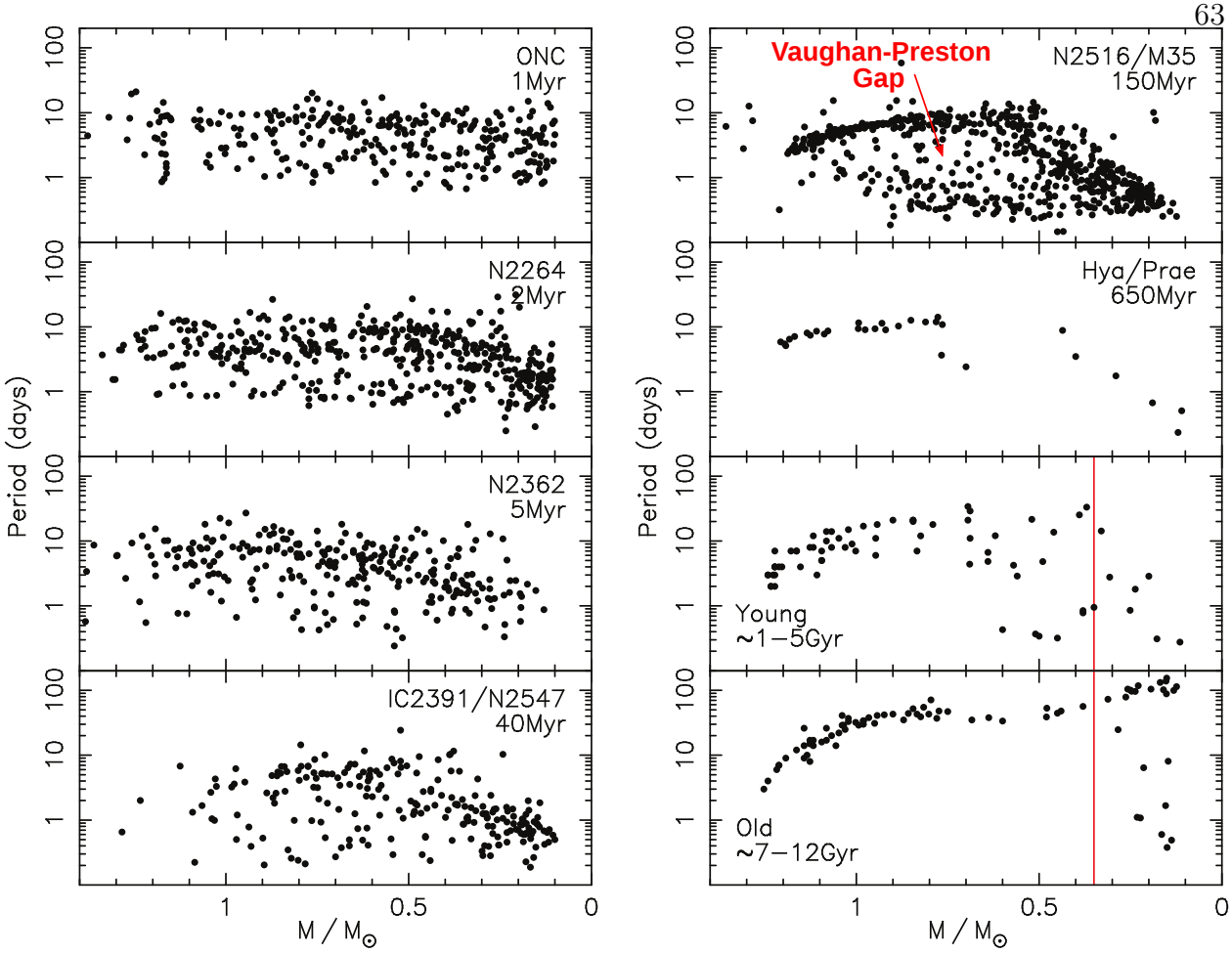

Figure 2.14: Rotation period distributions of stellar populations of differing ages and mass, showing the initially uniform distribution of a very young 1 Myr old cluster that evolves toward slower rotation with greater age. The panel in the upper right illustrates the Vaughan-Preston Gap, with a population of slow rotators, of fast rotators, and very few stars between them. The red line in the lower right two panels denotes the transition at 0.35 $M_\odot$ from stars with a radiative interior to those that are fully convective (Adapted from Stassun et al. (2011)).

regimes of dynamo behavior along the main sequence. As the star spins down, there is a transition between two regimes of chromospheric activity, with a sparsely populated gap between the two dubbed the "Vaughan-Preston Gap" after Vaughan & Preston (1980) and which can be seen most easily in Figure 2.14. It is also somewhat evident in the Ca H and K data plotted in Figure 2.15, with a small gap between the most active and a second branch of less active stars. The underlying cause of this is the spin down of stars which is why it is

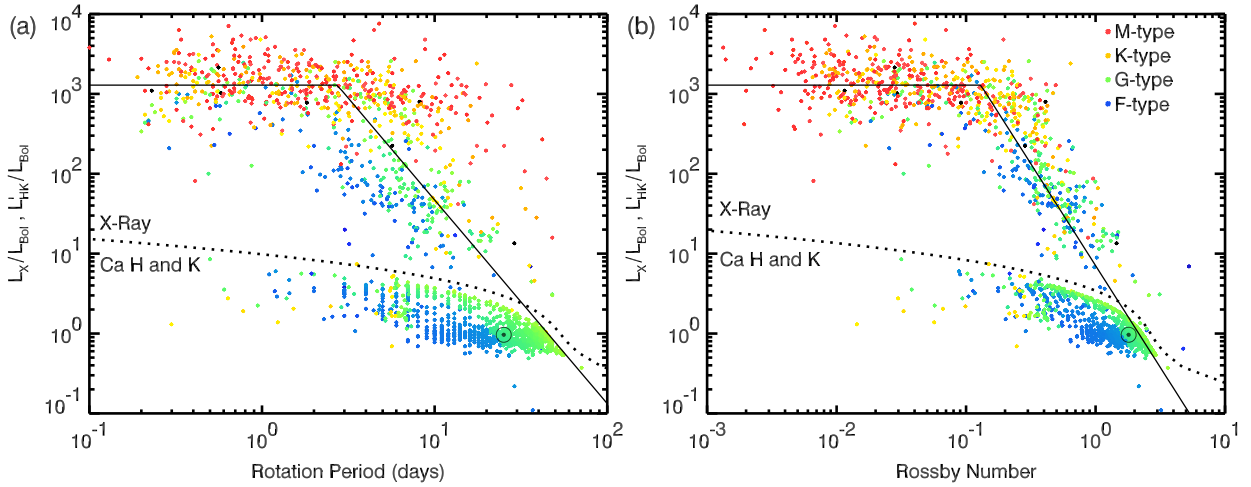

Figure 2.15: X-ray and Ca H and K observations of individual stars are shown, which cover a range of rotation rates and masses for lower mass stars. (a) Ratios of X-ray luminosity $L_{\rm X}$ and chromospheric Ca H and K luminosity ($L'_{\rm HK}$) to the bolometric value $L_{\rm Bol}$ (normalized so that these ratios are unity for the Sun; $L_{\rm X}/L_{\rm Bol} \approx 10^{-6}$ and $L'_{\rm HK}/L_{\rm Bol} \approx 10^{-5}$), displayed with rotation period in days as abscissa. The color indicates a star's mass, with M-type in red, K-type in yellow, G-type in green, and F-type in blue. The dotted line demarks the boundary between X-ray and Ca H and K measurements. The solid line shows an estimated fit for the rotation [or Rossby number in (b)] scaling of L_X. (b) L_X and L'_{HK} plotted versus an empirical Rossby number. The location of the Sun is shown with its symbol ($\odot$), again indicating its relatively low X-ray and chromospheric Ca H and K luminosity [Constructed with Ca H and K data from Soderblom et al. (1993a); Wright et al. (2004) and X-ray data from Wright et al. (2011)].

prominently labeled in Figure 2.14. This picture has been extended to provide a new way of measuring stellar ages, based on a relation between the spin down of the star and its waning activity, called gyrochronology (Barnes, 2007).

Beyond the connection between age and activity, the evidence began to mount that the mechanisms behind the activity were coupled to dynamo action that depends sensitively upon the rotation rate of the star (Vaughan et al., 1981; Noyes et al., 1984). Indeed, the relationship between stellar rotation and proxies of magnetic activity remains an important diagnostic of the dynamo processes likely responsible for stellar magnetism in low mass stars. Chromospheric variability measured in Ca H and K, and other chromospheric lines, as well as the X-ray observations that probe stellar coronae, indicate that there is a monotonic

increase in activity with rotation rate. This increase is halted as the rotation rate reaches a critical point, after which either these indicators of magnetic activity or these star's dynamos become saturated. Indeed, both coronal and chromospheric activity measures show such a saturation (Figure 2.15), though it is more prominent in the X-ray observations. The first tentative connection between X-ray luminosity and rotation was established by Pallavicini et al. (1981), reporting that X-ray luminosity scaled as $L_X \propto (v \sin i)^{1.9}$ for low mass stars and that the X-ray luminosities of higher mass stars depends only on the bolometric luminosity. The scaling with rotation for low mass stars suggested that, like the Sun, X-ray emitting coronal magnetic activity is linked to the magnetic dynamo running in the outer convection zones of these stars, whereas stars of ever greater mass (thereby lacking convective envelopes) produce X-rays primarily through their increasingly powerful winds.

Yet with more data the nearly quadratic proportionality between L_X and $v \sin i$ was found to have a limited domain of applicability, since the ratio of X-ray to bolometric luminosity reaches a peak saturation of about 10^{-3} that is effectively independent of spectral type (e.g., Vilhu, 1984; Micela et al., 1985; Vilhu & Walter, 1987). The rotational period at which this saturation level is reached, however, does depend upon spectral type, with lower mass stars reaching this state at longer periods than higher mass stars (Figure 2.15a). This can be attributed to the decrease in the vigor of the convection as one moves down the range of masses (Pizzolato et al., 2003). It is unclear whether the constancy of the X-ray luminosity is derived of a fundamental limit on the dynamo itself (e.g. Vilhu, 1984), a quenching arising from the pervasion of strong magnetic structures across much of the stellar surface (Vilhu, 1984), or a centrifugal stripping of the corona caused by the high rotation rates (Jardine & Unruh, 1999). There could also be changes in the X-ray production mechanisms as well as their X-ray spectral content. If these rapidly rotating stars support a Parker-like spiral magnetic field driven away from the star by strong winds, another possible explanation is, given the limiting behavior of the toroidal magnetic field is $B_\phi/B_r \sim (\Omega\lambda)/v_{\rm wind}$ (where Ω is the bulk rotation rate of the star, λ is the cylindrical radius, and $v_{\rm wind}$ is the wind speed),

that the radius at which the field becomes tightly wound in azimuth occurs within the hot corona itself. This would cause a transition close to the star where the wind is no longer strong enough to advect the field, due to the plasma β becoming unity, and secondary plasma effects cause a destabilization of the flow and magnetic field, creating a boundary layer that may be an X-ray absorber. However, a wind could still escape along a polar route, creating a strong polar jet. Yet once saturation occurs, the X-ray emission becomes a function of only the bolometric luminosity (Pizzolato et al., 2003), or effectively the mass, color, or radius of the main-sequence star.

Such characteristics also hold for chromospheric measures of magnetic activity as can be seen in Figure 2.15. This figure shows the ratio of chromospheric Ca H and K luminosity $L'_{\rm HK}$ to bolometric luminosity for 1328 main-sequence stars ranging in mass between 0.33 and 1.60 $\rm M_{\odot}$, with data from Soderblom et al. (1993a) and Wright et al. (2004). The ratio of X-ray luminosity and bolometric luminosity, also plotted with data from Wright et al. (2011), has a much greater dynamic range, spanning six orders of magnitude compared to the roughly 1.5 orders of magnitude for the Ca H and K observations. Yet both show an increase of activity with decreasing rotation period and an eventual saturation. It is of note that the chromospheric activity seems to saturate at longer periods and that there are few stars that are rotating rapidly that show Ca H and K emission, at least in this sample. As seen in many previous papers regarding the empirical nature of dynamo action, these proxies for magnetic activity seem to collapse into a more coherent structure when the stellar Rossby number is considered. This behavior follows from considering simple scaling arguments of the MHD equations and assuming that the dynamo mechanism draws its energy from the differential rotation. The work of Noyes et al. (1984) showed that such a relationship tightens the rotation-activity correlation. An empirical Rossby number was used there that relies upon stellar models to provide the convective overturning time for each star in the sample, given its observed $\log g$ and $T_{\rm eff}$. The resulting convective overturning times for the whole sample are then fit with a cubic function, from which the Rossby number may be estimated given

the rotation rate of a star and its B-V value. The behavior of the rotation-activity curve can be seen in Figure 2.15b, with the X-ray observations being more strongly affected. The rather meager impact on the Ca H and K data is a result of ill-determined rotational periods, which have been reconstructed using the cubic fits from Noyes et al. (1984), rather than a spectroscopically determined value. Moreover, there is a distinct paucity of Ca H and K data for more rapidly rotating stars, though it is unclear whether this is an artifact due to biased observational sampling or due to some intrinsic lack of chromospheric emission in the more rapidly rotating stars.

If we now disassemble the X-ray observations, breaking them out by spectral type, individual trends and scaling become more obvious as in Figure 2.16. Speaking broadly, the low mass stars of K, G, and F-type share similar characteristics in their X-ray emission involving increasing emission with more rapid rotation and a regime of saturated emission. What differs between them is the rapidity of the onset of this state of constant emission with rotation, the rotation period at which it saturates, and the maximum luminosity. The maximum luminosity seems to be determined by the bolometric luminosity, as surmised from Figure 2.15 where the data collapse onto the same fit. The rotation period at which it saturates may be related to the maximum achievable dynamo action, wherein the dynamo can no longer extract energy from the star's differential rotation due to strong Lorentz feedbacks. The rate of increase of X-ray emission with descreasing rotation period suggests a direct link to the Rossby number of the flows within these stars in that it measures the efficiency of the interaction of rotation and convection in building both the differential rotation and the magnetic field. In particular, there appears to be a change in the slope of the decrease of X-ray emission with rotation period, from 1.7 to 2.5 between the F- and K-type stars (Figure 2.16a-c). This may indicate that the K-type stars have the most efficient conversion of kinetic to magnetic energy. An interesting feature of stars about the mass of the Sun, namely the G and F type stars, is that there seems to be a regime of super-saturation with the X-ray luminosity decreasing at the rates of greatest rotation, which is a topic of ongoing research.

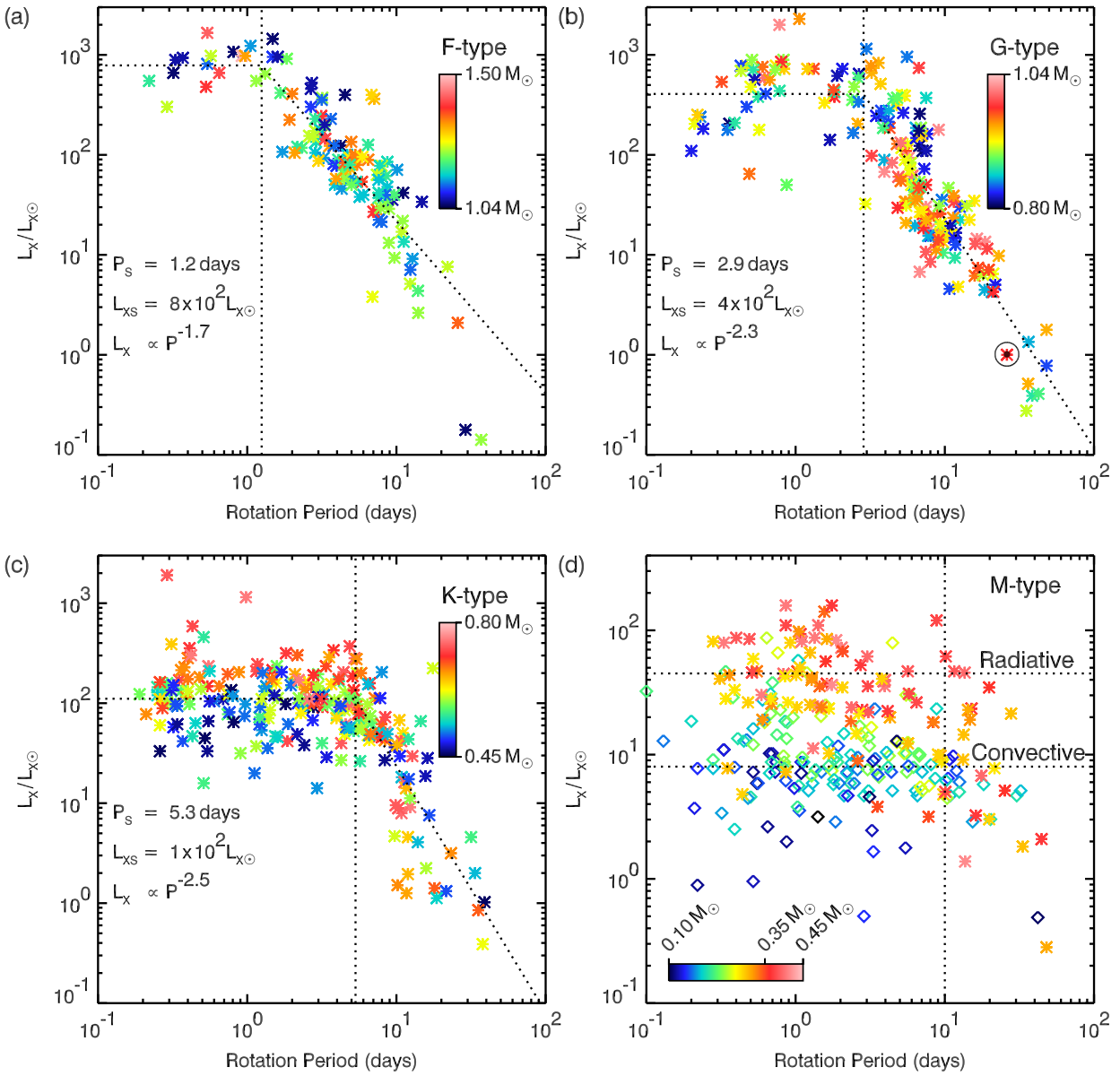

Figure 2.16: X-ray observations are shown for individual stars that are binned by their spectral type, which cover a range of rotation periods and masses. X-ray luminosity (L_X) normalized by the solar value and displayed with rotation period in days as abscissa. The color indicates a star's mass within the spectral type. (a) Spectral type F stars. (b) Spectral type G stars, with the Sun's position indicated. (c) Spectral type K stars. (d) Spectral type M stars, with stars above 0.35 $M_\odot$ as starred symbols and those below this mass as diamonds. In (a-c), the dotted lines indicate fits to the data for the scaling with period, the saturation value, and the rotation period corresponding to the beginning of the saturation (Constructed with data from Wright et al. (2011)).

What is also evident from all of these observations is that the Sun, while thought of as a magnetically active and robustly influential object, is in fact hundreds of times less active in both chromospheric and coronal proxies than some of its more rapidly rotating brethren, which serves to accentuate the overwhelming activity that must be present at the surfaces of these other stars.

What is possibly more remarkable in the X-ray data is the transition between stars that possess a radiative core and those that are fully convective (Figure 2.16d). Indeed, most of the stars in our galaxy are less massive than our Sun, with more than half of all stars being M-dwarfs. These are stars that are less than half the mass of the Sun and thus between tens and thousands of times less luminous than it. These low-mass stars had been believed to harbor magnetic dynamos quite distinct from those in Sun-like stars. It seems appropriate that there should be a difference between stars that have an interface-type dynamo, with a region of penetration and convective overshoot, and those that are fully convective.

In the Sun, the tachocline is a site of strong radial shear revealed by helioseismology , which is a matching layer between the differentially rotating outer convection zone and an interior rotating as a solid body (see §3.5). Other stars with a radiative interior may also have a tachocline. In an interface-type dynamo, the tachocline is thought to play a major role in the overall dynamo action. Such a layer below the convection zone can store and, through the radial differential rotation, comb small-scale magnetic field into a larger toroidal structure. When the magnetic field strength is sufficiently large, this field can become buoyant and thus could provide the seed magnetic field for the convective dynamo in the exterior convection zone (Spiegel & Weiss, 1980; Parker, 1993).

However, stars less massive than about $0.35\,\mathrm{M}_\odot$ are entirely convective (Chabrier & Baraffe, 1997), and so do not have such an internal boundary layer. Thus it was expected that these stars would possess magnetic behavior different from more massive stars, with only small-scale field being generated (Durney et al., 1993). Recent observations have instead shown that such stars can instead have both small- and large-scale fields, which means that

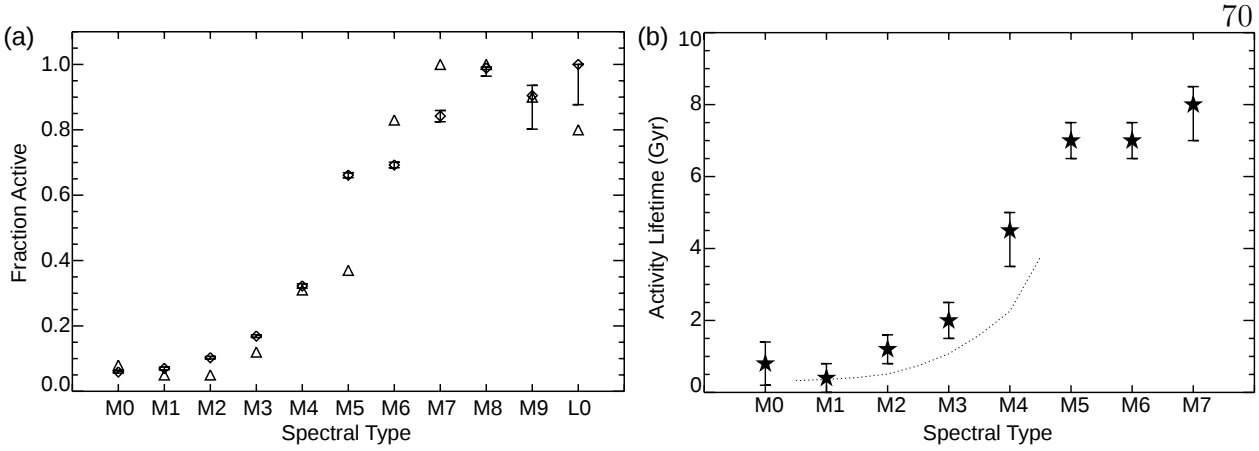

Figure 2.17: Magnetic activity properties of spectral type M stars from an Hα catalog of 38,000 such stars (West et al., 2008). (a) Fraction of active stars as a function of spectral type for the West et al. (2008) spectroscopic sample (diamonds). Older survey data are shown as triangles. (b) Activity lifetime with spectral type as abscissa. This plot serves to illustrate that M-type stars with masses greater than about 0.35 $M_\odot$ spin down and become less active, whereas their lower mass counterparts remain active for much longer periods of time. A theoretical age-activity relationship from Hawley et al. (2000) is shown as the dotted line (Adapted from West et al. (2008)).

these low mass stars can build magnetic fields with global-scale structure. Indeed, one of the great surprises emerging from studies of stellar magnetism has been that even low-mass stars can build large-scale magnetic fields. Zeeman-Doppler imaging has clearly established that rapidly rotating fully-convective stars can build large-scale magnetic fields (see Figure 2.9), while lacking any signs of latitudinal differential rotation (Donati et al., 2006a). This behavior is in stark contrast to the expectation that such large-scale fields are only possible with a measurable differential rotation. Yet some aspects of magnetism in low-mass stars does depend upon mass, as is manifest in Figures 2.16d and 2.17. There is a distinct and smooth transition between M-type stars with a radiative core and those that are fully convective occurring at 0.35 $M_\odot$ (spectral type M5). This is borne out in multiple observations: from the Hα and Ca H and K chromospheric activity proxies to X-ray emission (e.g., West et al., 2008; Morin et al., 2008; Browning et al., 2010; Morin et al., 2010). Figure 2.17a indicates that only about 8% of the more massive M-type stars are currently active, whereas the lower

mass M-type stars are nearly all active. This likely occurs because the higher mass M-type stars are able to spin down in only a few hundred million years, which eventually reduces their activity due to decreased dynamo action. The fully convective stars, on the other hand, seem to remain active for at least ten times as long (Figure 2.17b). One potential explanation is that, in direct contradiction to interface dynamo theory, the majority of surface magnetic features emerge from the near-surface regions (Brandenburg & Subramanian, 2005). Thus these stars provide an interesting theoretical and observational playground for testing crucial elements of stellar dynamo theory. For instance, one can ask what role a tachocline might play? Since these stars are birthed with a fairly uniform distribution of rotation periods, as visible in Figure 2.14, why does it seem that stars with a possible tachocline are able to efficiently spin down whereas those without do not?

2.6 Conclusion

In summary, there is a rich observational history for both the Sun and other stars that spans nearly four centuries and to which modern astrophysics owes its current success. There are a multitude of observable time and spatial scales of solar magnetism, which provides the keystone in our understanding of stellar magnetism as well as the properties of magnetism in many other astrophysical contexts. Yet despite the rapid advances in observing techniques and technology over the last century reviewed in this chapter, we have only begun to shed light on the mysteries of stellar magnetism. For instance, it is still unclear what establishes the magnetic cycles seen in activity measures of many stars, including the Sun, or the orderly large-scale fields present at their surfaces as determined by spectropolarimetry. Indeed, how long-term periodicity and large-scale, organized structures emerge from the chaos and turbulence present in stars is the central theme of dynamo theory. The following chapter will attempt to build the theoretical framework necessary to understand the processes that lead to the observed behaviors of stellar magnetism.

Chapter 3

Stellar Dynamo Theory

"TO LEARN: Non-linear Classical Hydro" – Feynman's Last Blackboards

Dynamo theory has its roots in geophysics where an explanation was sought for the migration of the Earth's magnetic pole, which was well known from four centuries of compass measurements and calibrations. The first such theory of the Earth's magnetism, in which the Earth is considered a permanent magnet, was put forward in William Gilbert's 1600 treatise on "The Magnet and Magnetic Bodies, and on That Great Magnet the Earth" ("De Magnete, Magneticisque Corporibus, et de Magno Magnete Tellure"). Carl Gauss established a much more complete theory, which even incorporated the idea of flowing currents. Gauss considered the field as potential and likely due to galvanic currents contained within the Earth's volume (Gauss, 1838). The debate on the origins of the magnetic field that followed would, however, not be settled for about a century. Prior to the certainty of dynamo processes being at work within the Earth, the tentative theories for the properties of the Earth's magnetism were laid out in 1911 by Arthur Schuster. This included the idea that eventually emerged as dynamo theory, which he dismissed as impossible (Schuster, 1911). Schuster and many others of the era often presumed that, due to the coincidence of the Earth's magnetic moment and its rotation axis, the terrestrial magnetic field was directly related to its rotation. This theory posited that the Earth's rotation directly influenced atomic and electronic motions, thus creating polarization. Another hypothesis was that independently rotating magnetized iron spheres within the Earth's interior produced the observed geomag-

netism. Some also thought that the fundamental equations of electromagnetism required some obscure relativistic modifications.

Although such theories were refuted by many scientists, Joseph Larmor is largely credited with planting the seeds from which modern dynamo theory grew. His idea that mean flows and fields could be self-inducting, though later proven incorrect, provided a basis for disestablishing earlier theories. These ideas were succinctly presented in a two page letter, following the 87th meeting of the British Association for the Advancement of Science (Larmor, 1919). It bears repeating his words here as it summarizes parts of the theory nicely: "In the case of the sun, surface phenomena point to the existence of a residual internal circulation mainly in meridian planes. Such internal motion induces an electric field acting on the moving matter: and if any conducting path around the solar axis happens to be open, an electric current will flow round it, which may in turn increase the inducing magnetic field. In this way it is possible for the internal cyclic motion to act after the manner of the cycle of a self-exciting dynamo, and maintain a permanent magnetic field from insignificant beginnings, at the expense of some of the energy of the internal circulation." The penultimate sentence of Larmor's paper states that, while the mechanism he proposed for the Sun is reasonable there, if it were to operate within the Earth it would require fluidity and a residual circulation in deep-seated regions. This was prescient since seven years later seismic measurements of the Earth's interior definitively showed it is indeed a liquid (Jeffreys, 1926), though it had been suggested earlier (Oldham, 1906). In summary, Larmor describes two dynamos operating in the Sun: one mechanism for the large-scale field is like a flux transport dynamo, while the other mechanism is akin to a local dynamo primarily acting in sunspots.

Following Larmor's insight, there were rapid developments in dynamo theory. Two prominent physicists, Thomas Cowling and Walter Elsasser, provided much of the progress in dynamo theory throughout the 1930s and 1940s. Indeed, Thomas Cowling's interpretation of Larmor's sunspot dynamo (Cowling, 1933) was strongly influential in the field, though it was written in a way that emphasized the perceived flaws in kinematic dynamos and ele-

vated a more obscure theory in its place. In that paper, Cowling proved by example that the currents established by an axisymmetric magnetic field of a sunspot cannot be a self-sustaining dynamo. More generally, he showed that a field which resembles an axisymmetric field cannot be maintained without an additional EMF. After early beginnings in quantum theory, Walter Elsasser began a long study of the Earth's modes of dynamo action. In a 1939 Physical Review article, Elsasser details the role of the Coriolis force in inducing statistical correlations between temperature and velocity at all turbulent scales in the Earth's liquid mantle, which in turn drive an electromotive force (EMF) and thermoelectric currents. Although Elsasser found thermoelectric currents to be the dominant factor in the Earth's dynamo, he states at the end of this article that the fields in sunspots must instead be maintained by a strong EMF. This, while not perhaps true of sunspots, is certainly true in the current understanding of global-scale dynamos. After being involved in the second world war with the US Signal Corps, Elsasser published a second work showing that toroidal flows alone cannot sustain a field (Elsasser, 1946). Continuing their collaborative efforts, Cowling permitted Elsasser to publish a more rigorous and general proof, elucidating why axisymmetric flows cannot sustain an axisymmetric magnetic field. This is the commonly cited "anti-dynamo theorem" (Elsasser, 1947). It does not, however, preclude the maintenance of non-axisymmetric fields by an axisymmetric flow.

At this point, most of the work in dynamo theory had been aimed at showing how a dynamo could not exist under various conditions of symmetry. Though in the 1947 article, Elsasser builds upon his earlier ideas in describing a mechanism whereby a mean toroidal magnetic field can be built through the inductive coupling of bulk fluid motions to the mean poloidal field. This operates by the stretch-and-fold mechanism, with the toroidal motions of the fluid acting to stretch poloidal field lines repeatedly over many rotation periods. These now toroidal field lines begin to accumulate in regions with a gradient in the bulk fluid motions. More importantly and in the same article, Elsasser states that the coupling of turbulent convection with rotation provides a statistical means by which the poloidal field

can be regenerated from a mean toroidal field, which is in contrast to the generation of the toroidal field. It is also pointed out that, while this turbulent field generation mechanism may be a second order effect, it is crucial to the overall maintenance of the dynamo process. These arguments are mostly qualitative and a more rigorous framework was still elusive.

Such a mechanism was confirmed to be possible with the calculations of Bullard & Gellman (1954), which evolved a kinematic dynamo in a 3D sphere with 10 radial grid points and four spherical harmonic degrees using an early supercomputer called ACE at the National Physics Laboratory in the UK. Their calculations showed that, if the flow field was that of elongated eddies aligned with the rotation axis, these structures can maintain and build poloidal and toroidal magnetic fields. They also illustrated, in painful detail, how energy was transferred between the various spherical harmonic modes. In 1955, Eugene Parker carried this further, describing more explicitly how a poloidal field can be regenerated from a toroidal field if there are cyclonic fluid motions present. Parker considered the interaction of cyclonic motions with a mean toroidal field, where the motions build small loops of magnetic field. The longitudinal field of these small-scale loops largely cancels, rather in aggregate they act to establish a poloidal field aligned with the rotation axis (Parker, 1955).

The efforts to establish a degree of mathematical precision were still frustrated even in 1955, where Elsasser states: "We have yet to come to grips with the one problem which, while rather arduous and frustrating from the purely mathematical viewpoint, is clearly basic for hydromagnetism, namely the question how the observed cosmic magnetic fields are actually created by amplificatory processes. This is the hydromagnetic dynamo problem." With a bit more patience, however, rigorous proofs of self-consistent dynamo action emerged for very idealized systems. For instance, a type of spherical dynamo was illustrated in Backus (1958). The primary result is the explicit construction of a large class of continuously differentiable velocity fields capable of indefinitely maintaining or amplifying the dipole moment of an external magnetic field even in the presence of resistive dissipation. Several important earlier results are also confirmed in this paper, namely that if the fluid motions have no

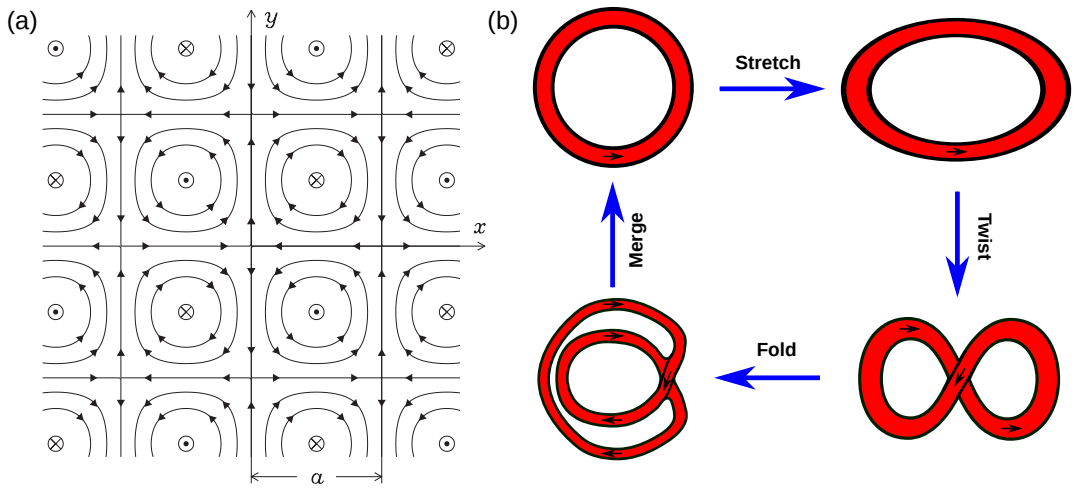

Figure 3.1: Examples of slow and fast dynamos. (a) The "slow" Roberts kinematic dynamo. (b) The "fast" stretch-twist-fold-merge dynamo.

radial component, the poloidal magnetic field decays as rapidly as if the fluid were at rest. Furthermore, if no poloidal field is initially present, the toroidal field decays as if the fluid were at rest. There it was also shown that dynamo maintenance is impossible if the local strain-rate of the fluid is always and everywhere less than the decay rate of the axisymmetric poloidal field. One important result is that fluid motions are bounded linear operators for the magnetic field on its Hilbert space equipped with a finite L_2 (energy) norm for the magnetic field.

Other authors independently built similar solutions, though they were often a bit more prosaic than Backus's work (e.g., Herzenberg, 1958). Herzenberg describes a solid, uniformly conducting medium with two or more conducting rotors in electrical contact with the other rotors. In this configuration, dynamo action is provably possible when the rotors spin faster than a critical value (Gailitis, 1973; Moffatt, 1978; Brandenburg et al., 1998). The Herzenberg dynamo belongs to the class of "slow" dynamos, with the other class being "fast" dynamos. Slow dynamos reach their largest growth rates for moderate values of conductivity, falling to zero in the limit of perfect conductivity. In contrast, fast dynamos, such as the Zeldovich stretch-twist-fold dynamo (see Figure 3.1b and Brandenburg & Subramanian (2005)), have

a finite and positive growth rate in the same limit. More to the point, the existence of such provably self-sustaining dynamos was essential to the development of dynamo theory, but the problem of greater interest became (and still is) how best to model the dynamo processes of the Earth, the Sun, as well as in other astrophysical bodies. It is prudent, at this stage, to introduce the mathematical and physical framework within which much of the more recent work has been set. This short mathematical diversion is contained in the next section.

3.1 The MHD Equations

The state of hydrodynamic turbulence, let alone magneto-hydrodynamic turbulence, is still best summed up by an apocryphal quote oft attributed to Werner Heisenberg: "I am an old man now, and when I die there are two matters on which I hope for enlightenment. One is quantum electrodynamics, and the other is the turbulent motion of fluids. And about the former I am rather optimistic." The underlying issue being that the equations of motion form a nonlinear, dissipative system. This inherently means that they can exhibit quasi-periodicity, multi-stability, and other chaotic behaviors, resulting in multiple basins of attraction in the phase space of the physical system.

There are many places from which one can begin to derive the single fluid MHD equations, say from geometrical arguments, from a Lagrangian standpoint, or from kinetic theory. The path that utilizes kinetic theory is tightly coupled to the classical theory of fields embodied by the Lagrangian approach. Since a Lagrangian framework is used in later sections and since kinetic theory provides the most general framework, the derivation will start there. Under Boltzmann's kinetic theory, statistical ensembles of large numbers of such particles map the otherwise 6-N_p dimensional phase space into a 6-S dimensional symplectic manifold, where S is the total number of particle species in the plasma. Appealing to differential geometry, we know that one-forms on this manifold are isomorphic to Hamiltonian vector fields. Moreover, such symplectomorphisms preserve volume on phase space and thus there must be an integral invariant on this space (Flanders, 1963; Bishop, 1968). This is

Liouville's theorem, which states generally that if a region of the N-dimensional phase space D_0 at time t_0 moves to a region D_1 at time t_1 then $\int_{D_0} \mu = \int_{D_1} \mu$, where μ is the phase space density. In more practical terms and given the phase space density $f_s(\mathbf{x}, \mathbf{v}, t)$ of species s, this density is constant along any trajectory in phase space and can be written as

$$\frac{\partial f_s}{\partial t} + \mathbf{v} \cdot \boldsymbol{\nabla}_{\mathbf{x}} f_s + \frac{\mathbf{F}_s}{m_s} \cdot \boldsymbol{\nabla}_{\mathbf{v}} f_s = \left.\frac{\partial f_s}{\partial t}\right|_{col}, \tag{3.1}$$

where $\mathbf{F}$ is the total force on species s and the collisional forces are included in the term on the right hand side. Relativistic effects and radiative transfer have been neglected as they are irrelevant to the dynamics considered here. The goal is to remove the velocity dependence by integrating over moments in velocity space and supplementing the resulting equations with a closure. The derivation of the full set of equations for a multi-species plasma coupled to an electromagnetic field that result from this approach is contained in Appendix A. These resulting equations need to be further reduced to the more manageable single fluid MHD equations. The MHD approximation assumes a single ion species, with a nearly equal number of electrons. The magnetic fields are considered weak enough that the total pressure tensor is isotropic and the time scales sufficiently long that the time variation of the electric field is negligible. These assumptions reduce the Boltzmann equation based framework of Appendix A to the following

$$\begin{aligned}
n &= n_i \approx n_e, \\
\varrho &= e(n_i - n_e) \approx 0, \\
\mathbf{u} &= \frac{\rho_e \mathbf{u}_e + \rho_i \mathbf{u}_i}{\rho_e + \rho_i} \approx \mathbf{u}_i, \\
\mathbf{J} &= \frac{e}{c}\left(n_i \mathbf{u}_i - n_e \mathbf{u}_e\right) \approx \mathbf{J}_w, \\
\Pi &= \frac{e}{c}\left(\frac{P_e}{m_e} + \frac{P_i}{m_i}\right)\mathbf{I} \approx \frac{e}{c m_e} P_e \mathbf{I}, \\
\dot{\mathbf{Q}}_e &= -\rho_e \nu_{ei}\left(\mathbf{w}_e - \mathbf{w}_i\right),
\end{aligned} \tag{3.2}$$

with c the speed of light, e the elementary charge, m_q the ion or electron mass, n_q the ion or electron number density, ρ_q the mass density of ions or electrons, P_q the partial pressures of the ions or electrons, and I the identity tensor. A linear conservative approximation to the momentum collision integrals $\dot{\mathbf{Q}}_q$ is used where ν_{ei} is the electron-ion collision rate and $\rho_e\nu_{ei} = \rho_i\nu_{ie}$, yielding $\dot{\mathbf{Q}}_e = -\dot{\mathbf{Q}}_i$. Thus the full collisional term in Equation A.41 is

$$\sum_s \frac{q_s}{m_s}\dot{\mathbf{Q}}_s = \frac{\varrho_e}{cnu_{ei}}(\mathbf{w}_e - \mathbf{w}_i)(1 + m_e/m_i) \approx -\nu_{ei}\mathbf{J}. \tag{3.3}$$

Utilizing the above assumptions and $\mathbf{w}_s = \mathbf{u}_s - \mathbf{u}$, the forces that yield changes in this scenario are

$$\begin{aligned}\sum_s \frac{q_s}{cm_s}\overline{\mathbf{F}} &= \sum_s \frac{q_s^2 n}{cm_s}\left(\mathbf{E} + \frac{\mathbf{u}_s}{c} \times \mathbf{B}\right) + \frac{q_s n}{c}\boldsymbol{\nabla}\Phi, \\ &= \frac{e^2 n}{cm_e}\left(\mathbf{E} + \frac{\mathbf{u}_e}{c} \times \mathbf{B}\right) + \frac{e^2 n}{cm_i}\left(\mathbf{E} + \frac{\mathbf{u}_i}{c} \times \mathbf{B}\right), \\ &\approx \frac{e^2 n}{cm_e}\left[\mathbf{E} + \frac{\mathbf{u}}{c} \times \mathbf{B}\right] - \frac{e}{cm_e}\mathbf{J} \times \mathbf{B}\end{aligned} \tag{3.4}$$

Finally, letting the conductivity be $\sigma = e^2 n/cm_e\nu_{ei}$ and upon substituting the above approximations into Equation A.41, Ohm's law for the simplified single-ion plasma becomes

$$\frac{1}{\nu_{ei}}\left(\frac{\partial \mathbf{J}}{\partial t} + \boldsymbol{\nabla} \cdot [\mathbf{J} \otimes \mathbf{u} + \mathbf{u} \otimes \mathbf{J}]\right) + \frac{\sigma}{ne}\boldsymbol{\nabla}P_e + \frac{\sigma}{en}\mathbf{J} \times \mathbf{B} = \sigma\left[\mathbf{E} + \frac{\mathbf{u}}{c} \times \mathbf{B}\right] - \mathbf{J}, \tag{3.5}$$

If we neglect the collisional timescale phenomenon, the electron pressure, and the Hall term this further simplifies to the often used form

$$c\mathbf{E} = c/\sigma\mathbf{J} - \mathbf{u} \times \mathbf{B}. \tag{3.6}$$

A further simplification is that of neglecting $\partial_t\mathbf{E}$, which can be done if the timescales of interest are long in comparison to $1/c\sigma \sim 10^{-15}\,s$ for solar interior conditions. Therefore, Maxwell's equations become

$$\boldsymbol{\nabla} \cdot \mathbf{E} = 0 \tag{3.7}$$

$$\boldsymbol{\nabla} \cdot \mathbf{B} = 0 \tag{3.8}$$

$$\boldsymbol{\nabla} \times \mathbf{B} \approx 4\pi\mathbf{J}, \tag{3.9}$$

$$\frac{\partial \mathbf{B}}{\partial t} \approx -c\boldsymbol{\nabla} \times \mathbf{E} = \boldsymbol{\nabla} \times [\mathbf{u} \times \mathbf{B} - \eta\boldsymbol{\nabla} \times \mathbf{B}], \tag{3.10}$$

with the magnetic diffusion $\eta = c/4\pi\sigma$. Thus, after combining a few terms and explicitly including the diffusive terms, the equation set under the standard MHD approximation are

$$\frac{\partial \rho}{\partial t} + \boldsymbol{\nabla} \cdot \rho \mathbf{u} = 0, \tag{3.11}$$

$$\frac{\partial \rho \mathbf{u}}{\partial t} + \boldsymbol{\nabla} \cdot \left[\rho \mathbf{u} \otimes \mathbf{u} + \left(P + \frac{\mathbf{B}^2}{8\pi} \right) \mathbf{I} - \frac{1}{4\pi} \mathbf{B} \otimes \mathbf{B} - \boldsymbol{\mathcal{D}} \right] = \rho \boldsymbol{\nabla} \Phi, \tag{3.12}$$

$$\frac{\partial E_M}{\partial t} + \boldsymbol{\nabla} \cdot \left[\mathbf{u}(E_M + P) + \mathbf{q} - \mathbf{u} \cdot \boldsymbol{\mathcal{D}} - \frac{1}{4\pi} \mathbf{u} \cdot \mathbf{B}\mathbf{B} + \frac{\eta}{4\pi} \left(\frac{1}{2} \boldsymbol{\nabla} \mathbf{B}^2 - \mathbf{B} \cdot \boldsymbol{\nabla} \mathbf{B} \right) \right] = 0, \tag{3.13}$$

$$\frac{\partial \mathbf{B}}{\partial t} = \boldsymbol{\nabla} \times [\mathbf{u} \times \mathbf{B} - \eta \boldsymbol{\nabla} \times \mathbf{B}], \tag{3.14}$$

$$E_M = \frac{1}{2} \rho \mathbf{u}^2 + \frac{\mathbf{B}^2}{8\pi} + \epsilon + \rho \Phi, \tag{3.15}$$

The viscous diffusion tensor is $\mathcal{D}_{ij} = \mu(e_{ij} - 2/3 \boldsymbol{\nabla} \cdot \mathbf{u} \delta_{ij})$, with e_{ij} being the linearized stress tensor and which assumes that the bulk viscosity is one third of the shear viscosity. The derivation of the molecular viscous diffusion is not carried out here, as one can establish this term through infinitesimal deformations and ascribe a force to it through a thermodynamically dependent coupling coefficient or compute the collisional integrals in kinetic theory as in Braginskii (1965). For LES, perhaps, a more general choice in the case of large velocities or strong gradients would be the Eulerian-Almansi finite strain tensor

$$E_{ij} = \frac{1}{2} \left[\frac{\partial u_i}{\partial x_j} + \frac{\partial u_j}{\partial x_i} + \sum_k \frac{\partial u_k}{\partial x_i} \frac{\partial u_k}{\partial x_j} \right]. \tag{3.16}$$

It might be considered as an alternative to more sophisticated schemes as it nonlinearly enhances dissipation in regions with strong gradients. More generally, the Israel-Stewart equations (Israel & Stewart, 1979) could be invoked and parameterized with finite time correlations as in (Pratt, 2008).

There is now a basis for comparison between the fairly general microscopic, species and distribution dependent magnetohydrodynamic flows and the macroscopic behavior of larger-scale MHD systems. Small spatial and short temporal scales are relevant in the former, wherein the coupled dynamics of the radiation field, magnetic and electric fields, as well as multiple ion and chemical species play dynamical roles. This is certainly critical in low

density and highly variable environments such as stellar chromospheres, coronae, and winds. In the MHD system, there is but a single ion and the free electrons that accompany it. This greatly simplifies matters, yet the system still has many facets such as two-component collisional dynamics, separate electron and ion pressures, and the Hall term electrons, and thus can be complex in its own regard. Even with these terms discarded, the remaining parameter regimes for turbulent magnetohydrodynamic flows are largely unexplored. Hence, despite being a much simpler system, the MHD regime permits the study of larger spatial and longer temporal scales, which are most applicable to the stellar dynamo problem. However, the transition between regimes is not at all clear, nor is it prudent to neglect the influence of one on another. This is especially true when considering the outer envelopes of stars, where there is a rapid change from the relatively dense low β plasma of stellar interiors and the low density high β plasma of their chromospheres, coronae, and winds.

This effectively brings us to the current era of dynamo theory. After the 1960s, the literature becomes intractably large to succinctly trace the roots of the various facets of the theory. There are currently three classes of methods in dynamo theory. The first class consists of 1D stochastic or continuous systems of equations that model certain aspects of dynamos. The second class utilizes the framework of mean-field electrodynamics, wherein the effects and feedback of turbulent motions upon the mean flows and mean magnetic fields are parameterized. The final class of methods attempt to directly simulate dynamo processes with fully 3D models of conducting fluids in various geometries and under a wide variety of conditions. All three of these methods seek to understand how the nonlinear interaction of turbulent flows and magnetic fields maintain magnetic fields against resistive decay. They also seek to comprehend what mechanisms determine the spatial and temporal scales for local and global fields. The following subsections will provide an overview of the systems that have relevance to stellar dynamo theory.

3.2 Dynamo Waves and Low-order Approximations

There are a few fundamental theories that reduce the magnetohydrodynamic (MHD) equations to more easily studied, low-order and yet still nonlinear systems of ordinary differential equations. These methods have been developed over the last 50 years. The first mention of dynamo waves arises from the last section of Parker's oxyblepsic 1955 paper in which there is a discussion of "migratory dynamos". In this model, a flow is prescribed and its impact upon the toroidal vector potential is parameterized as $\partial_t A = \Gamma B - \eta \boldsymbol{\nabla}^2 A$, with $\mathbf{B} = \boldsymbol{\nabla} \times A\hat{\boldsymbol{\phi}} + B\hat{\boldsymbol{\phi}}$ and with Γ measuring the "violence" of Parker's cyclones (Parker, 1955). The spatially varying functions of Γ, η, A, and B can be approximated by selecting particular modes, which reduces the set of equations to simple ODEs, and allowing their couplings to be examined. For instance, A could be chosen to be a pure dipole, and the particular modes that arise in B could then be found. Conversely, a toroidal field mode could be considered and its influence upon the poloidal field examined. More complicated fields can be constructed as well. The most rudimentary solutions of these equations eliminate one direction of motion. In doing so, these equations admit damped traveling wave solutions, if one considers motion only along the mean field direction. With other dimensions included, for instance in polar coordinates, the behaviors are more complex, but still can admit traveling wave solutions (Charbonneau, 2010). Some 3D simulations also show some aspects of this behavior, despite their turbulent conditions (e.g., Brown et al., 2010, 2011b; Käpylä et al., 2012, 2013). Some authors have extended such simple models and considered the nonlinear versions of this equation as well. These slightly more complex approximations to the induction equation have some bearing on the solar problem as they reveal quasi-periodic solutions, illustrating behavior similar to the deterministic chaos of the solar cycle (Weiss et al., 1984; Weiss & Tobias, 2000).

The Babcock-Leighton dynamo is one such nonlinear 1D model, in this case it is in latitude and time (Babcock, 1961; Leighton, 1969). These have quite a few ingredients and

parameters, but overall are still quite simple. The Babcock-Leighton mechanism considers spatially-averaged magnetic fields that vary in latitude and time. It is also assumed that the differential rotation is a function of latitude and depth, is constant in time, and acts only upon the poloidal magnetic field to modify the toroidal field, with the fluid assumed to be perfectly conducting and the flow laminar. If the toroidal field strength exceeds a critical threshold, the field erupts and a sunspot occurs. This eruption of the toroidal field induces radial fields with a net meridional magnetic moment due to the Joy's law and simultaneously weakens the toroidal field. The emerged radial field is then dispersed by a random walk. This model is well motivated by observations and produces solutions that mimic Hale's law quite well. It has also played a very prominent role in 2D mean-field modeling, which is the subject of the following subsection. Such a Babcock-Leighton mechanism has recently been incorporated into 3D models in order to assess the role of sunspots in the deeper dynamo more self-consistently (Miesch & Brown, 2012).

3.3 Mean-field Electrodynamics

There are many examples of "slow" dynamos, such as the Herzenberg dynamo or the Roberts flow, the latter of which consists of a steady 2D pattern in all three directional components of the velocity. The Roberts dynamo provides an important benchmark for a large-scale dynamo (see Figure 3.1a and Roberts (1970)), where magnetic fields are induced on scales larger than those of the velocity through the "α-effect." Returning to Parker's dynamo wave solutions discussed above, a close inspection of the evolution equation for the toroidal vector potential shows the first example of the scalar α-effect, which is equivalent to the First-Order Smoothing Approximation (FOSA) to turbulence (Brandenburg & Subramanian, 2005).

In work that paralleled that of Parker and many others in the West, though hidden behind the Iron Curtain, Steenbeck and colleagues were creating an effective field theory for the calculation of the mean Lorentz and electromotive forces for an electrically conductive,

rotationally influenced, and turbulent medium (Steenbeck et al., 1966; Moffatt, 1970). This work extended Parker's and showed that in general if the turbulent motions possess a mean helicity, then Ohm's law contains additional features that are aligned or anti-aligned with the mean field. The occurrence of this kind of electromotive force (EMF) has been dubbed the α-effect. If the time-averaged small-scale convective turbulent motions lacks reflectional symmetry such as when it has helicity, Ohm's law for the mean fields contains an EMF with a component directly proportional to the mean magnetic field.

The α-effect leads, as in Parker's model, to the generation of a poloidal magnetic field from a toroidal field and thus partially resolves the dynamo problem. Primarily, a broken symmetry leads to the possibility of overcoming resistive decay as well as producing an inverse cascade of magnetic energy and helicity that can organize into large-scale fields. Indeed, a mechanism to overcome the decay and build such fields is crucial for all dynamo theory. The early versions of α-only dynamos have since been extended to many geometries (e.g., Rädler, 1968), and have been modified so that the back-reaction of the magnetic field on the flow can be parameterized as in the Malkus-Proctor effect (e.g., Malkus & Proctor, 1975). These effects can be elucidated by considering first the azimuthally averaged induction equation in spherical coordinates (obtained by applying the Reynolds averaging rules to Equation 3.14), wherein, following from its solenoidal character, the magnetic field is expanded into poloidal and toroidal components as

$$\frac{\partial A}{\partial t} = \overbrace{\eta\left(\boldsymbol{\nabla}^2 - \frac{1}{\lambda^2}\right)A}^{\text{magnetic diffusion}} - \overbrace{\frac{1}{\lambda}\mathbf{u}_m \cdot \boldsymbol{\nabla}\left(\lambda A\right)}^{\text{meridional advection}} + \overbrace{\hat{\boldsymbol{\phi}} \cdot \overline{\mathbf{u}' \times \mathbf{B}'}}^{\text{poloidal generation}} \tag{3.17}$$

$$\frac{\partial B}{\partial t} = \underbrace{\eta\left(\boldsymbol{\nabla}^2 - \frac{1}{\lambda^2}\right)B}_{\text{magnetic diffusion}} + \underbrace{\frac{1}{\lambda}\frac{\partial \eta}{\partial r}\frac{\partial \lambda B}{\partial r}}_{\text{diffusive transport}} - \underbrace{\lambda \mathbf{u}_m \cdot \boldsymbol{\nabla}\frac{B}{\lambda}}_{\text{meridional advection}} \tag{3.18}$$

$$- \underbrace{B\boldsymbol{\nabla} \cdot \mathbf{u}_m}_{\text{compression}} + \underbrace{\lambda \boldsymbol{\nabla}\Omega \cdot \boldsymbol{\nabla} \times A\hat{\boldsymbol{\phi}}}_{\text{stretching}} + \underbrace{\hat{\boldsymbol{\phi}} \cdot \boldsymbol{\nabla} \times \overline{\mathbf{u}' \times \mathbf{B}'}}_{\text{toroidal generation}} \tag{3.19}$$

with $\mathbf{B} = \boldsymbol{\nabla} \times A\hat{\boldsymbol{\phi}} + B\hat{\boldsymbol{\phi}}$ and where $\lambda = r\sin\theta$ is the distance from the rotation axis, $\mathbf{u}_m = \mathbf{u}_m(r, \theta)$ is the meridional circulation, and $\Omega = \Omega(r, \theta)$ is the rotation rate. Note that

the axisymmetric velocity considered here is independent of time. With these equations, the features discussed in the first section of this chapter become quite evident. Namely, if the turbulent electromotive terms $\boldsymbol{\mathcal{E}} = \overline{\mathbf{u}' \times \mathbf{B}'} \approx \boldsymbol{\alpha}\mathbf{B}$ are omitted, the field simply decays away as there is nothing to regenerate A, since the equation for A is then a nothing more than an advection-diffusion equation. The $\boldsymbol{\alpha}$ tensor is the parameterization mentioned above, with the correlations between the fluctuating velocity and fluctuating magnetic field components being expressed as a spatially varying function that provide an instantaneous temporal correlation with the mean field. The mean-field evolution equations illustrate two new features that are intrinsic ingredients in the simulations presented in this thesis and to stellar dynamos in general. Chiefly, the stretching of the poloidal field by the differential rotation leads to the generation of toroidal field (the Ω-effect) and the turbulent generation of poloidal field that prevents the ohmic decay of the entire field. However, it is also of note that differential rotation is not necessary for a dynamo to run, only that there be some inherent symmetry breaking in the system that leads to a turbulent EMF and thus an inverse cascade. To put this in the nomenclature of mean-field theory (MFT), there are three primary types of dynamos. These are the $\alpha\Omega$, α^2, and $\alpha^2\Omega$, where the α^2 indicates that the α-effect is responsible for a substantial fraction, if not all, of the generation of both poloidal and toroidal field.

Solar models utilizing MFT reflect many of the observed magnetic phenomena (e.g., Petrovay, 2000; Charbonneau, 2010). The distribution of sunspots with respect to latitude and time can be reproduced under some assumptions for the somewhat arbitrary α-effect. To some degree, the solar angular velocity profile could be assessed through MFT in the deeper layers of the convection zone, which until about 1995 and the advances in helioseismology, were largely inaccessible to observations. Although the assumptions going into the theory initially were in contradiction with helioseismology, the coefficients of the $\boldsymbol{\alpha}$ tensor could be retuned to reproduce some solar phenomenon. Beyond solar dynamo models, MFT has also been successfully applied to the terrestrial dynamo including being in good agreement

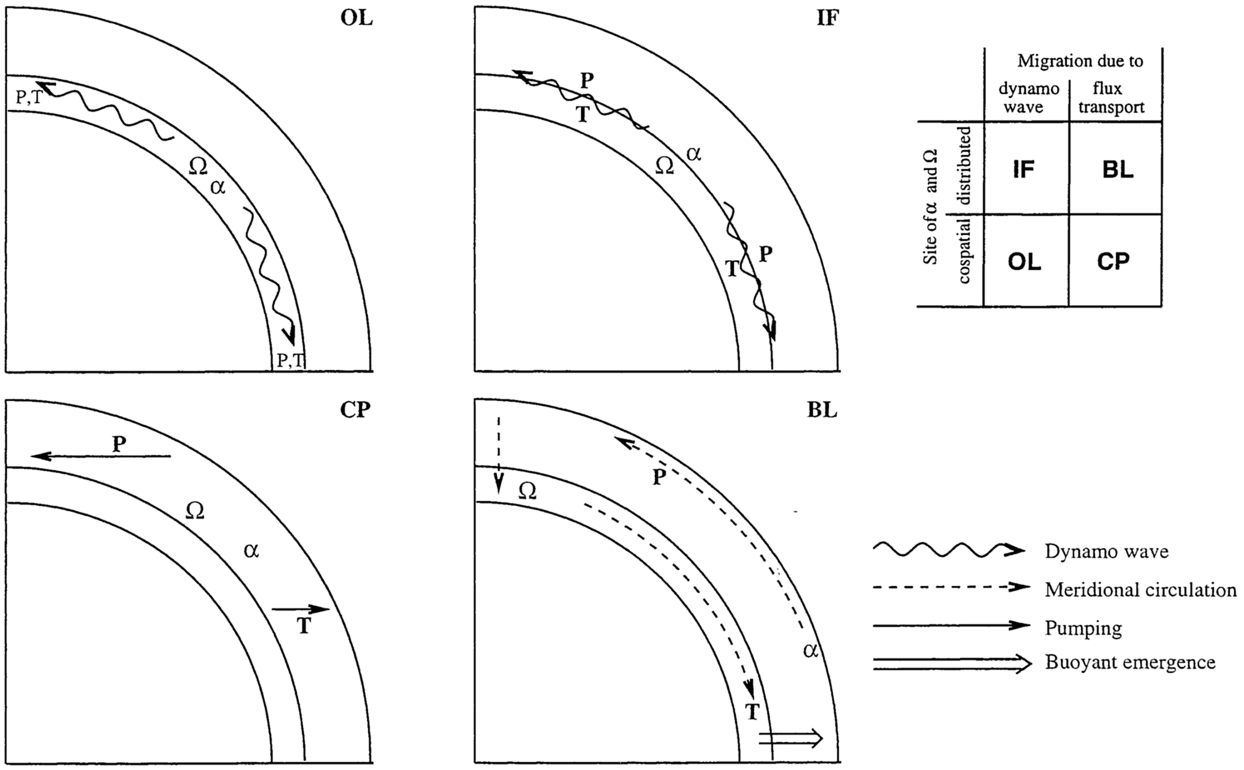

Figure 3.2: A diagrammatic illustration of the four primary mean-field dynamo modeling techniques. The sites of α and Ω effects as well as the magnetic flux transport mechanisms (and their respective directions) are shown for the northern hemisphere in a meridional plane. The four methods are: (OL) overshoot layer dynamos; (IF) interface dynamos; (CP) cospatial pumping models; and (BL) Babcock-Leighton-type models. The mechanisms at work in each model follow from the legend on the lower right, with some clarification given by the table in the upper right. [Adapted from Petrovay (2000)].

with 3D direct numerical simulations (Schrinner et al., 2007). While there is a bewildering variety of MFT solar models, they all can be effectively reduced to the mean-field equations as above with the exception of the approximation and construction of the turbulent EMF. The menagerie of MFT models are shown in Figure 3.2 for a visual reference of the mechanisms at work in each of them. The various models include: the usual α-type prescriptions described above (e.g. Ruediger & Brandenburg, 1995; Rüdiger & Arlt, 2003); flux-transport models that specify the meridional circulation apriori (e.g., Rempel, 2005, 2006b,a; Pipin & Kosovichev, 2013); interface dynamos, which circumvent the issues of α-quenching raised in simple $\alpha\Omega$

models by placing the region of toroidal field generation away from regions where the α-effect operates instead relying upon the radial shear of a tachocline (e.g., Parker, 1993; Dikpati & Gilman, 2001); and finally there is also the phenomenological Babcock-Leighton mechanism that parameterizes the formation and rise of buoyant flux tubes (e.g., Wang & Sheeley, 1991; Dikpati & Charbonneau, 1999; Charbonneau et al., 2005; Guerrero & de Gouveia Dal Pino, 2008).

The ultimate goal of solar dynamo theory is to account for the 11-year sunspot cycle (22-yr magnetic activity cycle) of the Sun, within the context of other observed phenomena such as the ubiquitous and rapidly-evolving small-scale flux that threads the solar photosphere. This striking manifestation of order amid chaos is a hallmark of solar magnetic activity and its explanation ultimately lies in detailed studies of convective dynamics that are inherently 3-D and nonlinear in nature. The computational challenges associated with such an undertaking have spurred the development of more tractable 2-D models of the solar dynamo, such as the popular flux transport models. Typically kinematic and mean-field in nature, flux transport models capture the effects of differential rotation and meridional circulation on the evolution of the axisymmetric magnetic fields. Most flux transport dynamo models are also Babcock-Leighton models in the sense that the destabilization, emergence, and subsequent dispersal of toroidal magnetic flux play an important role in generating the mean component of the poloidal magnetic field.

The coupling of mean transport effects to the emergence of magnetic structures captured by such coupled Babcock-Leighton flux transport models continues to play a prominent role in shaping the view of the solar cycle. In particular, the transport of toroidal magnetic field by meridional circulation in these models, and the subsequent destabilization and emergence of that flux is commonly thought to set the 11-year cycle period, accounting for the observed equatorward migration of sunspots over the solar cycle. Until recently this circulation could be treated as a free parameter, as helioseismology had yet to constrain it. Indeed, the widely adopted mono-cellular flow within each hemisphere now appears to be

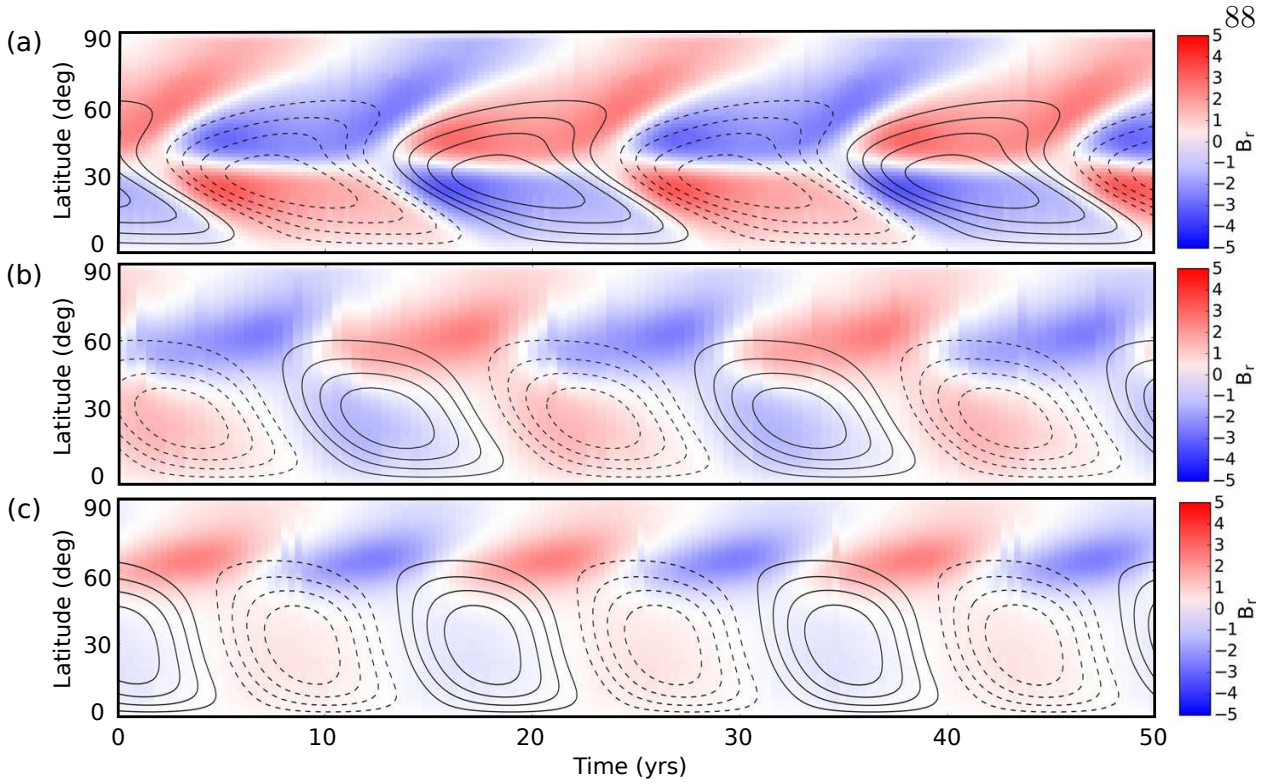

Figure 3.3: Babcock-Leighton flux transport dynamo with dual meridional cells dynamo, showing the impact of increasing meridional flow speed. The surface radial magnetic field is illustrated in a time-latitude diagram and in color, as in the colorbar on the right, for several meridional flow speeds (a) $u = 0\ m\,s^{-1}$, (b) $u = 10\ m\,s^{-1}$, and (c) $u = 20\ m\,s^{-1}$. The contours represent the toroidal field at $0.92\,R_\odot$, with steps of 25 G between ± 100 G. [Adapted from Pipin & Kosovichev (2013)].

at odds with recent results from helioseismology that suggest the existence of multiple cells within a hemisphere (Zhao et al., 2013). Such a multi-cellular profile may severely disrupt the operation of a flux transport dynamo (e.g., Jouve & Brun, 2007; Pipin & Kosovichev, 2013) as is visible in Figure 3.3. Moreover, it is impossible to gauge the self-consistency of the parameterized 3-D effects of flux emergence and turbulent transport with the prescribed mean flows in 2-D models.

One interesting result using MFT, beyond reproducing many aspects of the solar and terrestrial dynamos, some of these models can be reduced to a simple iterative map, which allows one to find possible basins of attraction for periodic solutions amidst those that are

chaotic. In particular, a large sample of MFT solar simulations have been assessed for solutions with periodic behavior as the dynamo number (effectively the magnetic Reynolds number) was increased and it shows a period-doubling bifurcation in magnetic energy that is very similar to the amplitude bifurcations of its corresponding in iterative map (Charbonneau, 2010). Despite its reputation of being terra incognita, such a mapping of parameter space may also be possible with global-scale 3D fully nonlinear simulations of rotating convective turbulence and has been undertaken, to a degree, by Gilman (1983), and more recently by Brown et al. (2011a); Gastine et al. (2012); and Yadav et al. (2013).

Mean-field theory does not end with the $\boldsymbol{\alpha}$ tensor, rather it can be extended to arbitrary derivative orders in the mean magnetic field provided that it is smooth enough. To that end, one of the other commonly used tensors is the rank three $\boldsymbol{\beta}$ tensor that links the components of the turbulent correlations that produce an effective magnetic diffusion to the gradient of the mean magnetic field. Given the ever larger degrees of freedom in choosing any of the coefficients for the $\boldsymbol{\alpha}$, $\boldsymbol{\beta}$, or higher rank tensors, there are obvious drawbacks to the theory, with one of them being the required scale separation between the regions of poloidal and toroidal regeneration, whether they be spatial or temporal. As the current theory stands, this requirement is a product of the assumption of the instantaneous correlation between the induction on the mean field and the mean field itself. These underlying requirement can be relaxed by including the temporal correlations in the mean field, akin to the more general theories constructed by Kazantsev (1968), Orszag (1970), Kleeorin et al. (2002), and Budaev et al. (2011). This could be done through a two time-scale separation, which doubles the number of equations. Such an approach is, in some ways, actually suggested in the FOSA, minimum-τ, and (Eddy-Damped Quasi-Normal Markovian) EDQNM theories (e.g., Pouquet et al., 1976). Indeed, recent work has attempted to incorporate results from local turbulence models and helicity cascades into the MFT framework (Kleeorin & Rogachevskii, 1999; Brandenburg & Subramanian, 2005; Brandenburg et al., 2012; Müller & Malapaka, 2013). Basically, this approach could account for the time scale for the inverse cascade from

small-scales where turbulent magnetic helicity and magnetic energy are generated to the large-scale mean fields.

Yet the theory is built upon shifting sands, with many underlying assumptions as mentioned above. For instance, consider the case of a moderately rotating system akin to a typical main sequence G-type star, which has a convective overturning time of 32 days but a rotation period of 12.6 days. The Coriolis number of this system is then 32. Under Kolmogorov scaling, the eddy correlation time is $\tau(k) = \tau_0(\ell_0 k/2\pi)^{-2/3}$, so it is possible that a large range of scales below the large-scale ℓ_0 are subject to the influence of the Coriolis force. Certainly, all the large scales of interest are under the influence of rotation. We can ask, under such conditions what is the mean-field model? Under the usual assumption of scale separation, the correlation tensors of fluctuating quantities $\mathbf{u}$ and $\mathbf{b}$ vary slowly with the large scale $\mathbf{R}$. Consider delta-correlated ensemble averages of products as $\overline{f(\mathbf{x}_1,t)g(\mathbf{x}_2,t)}$. In such a case, we have

$$\overline{f(\mathbf{x}_1,t)g(\mathbf{x}_2,t)} = \int\int \overline{\hat{f}(\mathbf{k}_1,t)\hat{g}(\mathbf{k}_2,t)} e^{i(\mathbf{k}_1\cdot\mathbf{x}_1+\mathbf{k}_2\cdot\mathbf{x}_2)} \mathrm{d}^3\mathbf{k}_1 \mathrm{d}^3\mathbf{k}_2, \tag{3.20}$$

where $\hat{f}$ and $\hat{g}$ are the Fourier transforms of f and g, respectively, and where such a notation will be used in general. A crucial and obvious step is to transform coordinates in physical and spectral space such that $\mathbf{r} = \mathbf{x}_1 - \mathbf{x}_2$ and $\mathbf{R} = \mathbf{x}_1 + \mathbf{x}_2$, which sets the stage for the separation of the rapid variation on the small scales $\mathbf{r}$ and slow variation on the large scales $\mathbf{R}$. The above correlation between f and g can then be expressed as

$$\overline{f(\mathbf{x}_1,t)g(\mathbf{x}_2,t)} = \int\int \overline{\hat{f}(\mathbf{k}+\mathbf{K},t)\hat{g}(-\mathbf{k}+\mathbf{K},t)} e^{i(\mathbf{k}\cdot\mathbf{r}+\mathbf{K}\cdot\mathbf{R})} \mathrm{d}^3\mathbf{k} \mathrm{d}^3\mathbf{K}, \tag{3.21}$$

$$= \int \Phi\left(\hat{f},\hat{g},\mathbf{k},\mathbf{R}\right) e^{i(\mathbf{k}\cdot\mathbf{r})} \mathrm{d}^3\mathbf{k}, \tag{3.22}$$

with $\mathbf{k} = \mathbf{k}_1 - \mathbf{k}_2$ and $\mathbf{K} = \mathbf{k}_1 + \mathbf{k}_2$. The velocity and magnetic correlations, as well as the turbulent electromotive force ($\overline{\mathcal{E}}$; EMF), are given by

$$v_{ij}\left(\mathbf{k},\mathbf{R}\right)=\Phi\left(\hat{u}_i,\hat{u}_j,\mathbf{k},\mathbf{R}\right),\quad \overline{\mathbf{u}^2}=\delta_{ij}\int v_{ij}\left(\mathbf{k},\mathbf{R}\right)\mathrm{d}^3\mathbf{k}, \tag{3.23}$$

$$m_{ij}\left(\mathbf{k},\mathbf{R}\right)=\Phi\left(\hat{b}_i,\hat{b}_j,\mathbf{k},\mathbf{R}\right),\quad \overline{\mathbf{b}^2}=\delta_{ij}\int m_{ij}\left(\mathbf{k},\mathbf{R}\right)\mathrm{d}^3\mathbf{k}, \tag{3.24}$$

$$\chi_{jk}\left(\mathbf{k},\mathbf{R}\right)=\Phi\left(\hat{u}_j,\hat{b}_k,\mathbf{k},\mathbf{R}\right),\quad \overline{\mathcal{E}}=\epsilon_{ijk}\int \chi_{jk}\left(\mathbf{k},\mathbf{R}\right)\mathrm{d}^3\mathbf{k}. \tag{3.25}$$

with implied sums over repeated indices. Consider the time derivative of the cross-correlation tensor

$$\frac{\partial\chi_{jk}}{\partial t}=\Phi\left(\dot{\hat{u}}_j,\hat{b}_k,\mathbf{k},\mathbf{R}\right)+\Phi\left(\hat{u}_j,\dot{\hat{b}}_k,\mathbf{k},\mathbf{R}\right), \tag{3.26}$$

which follows since the Fourier coefficients are assumed to only depend upon time. Consider the following small-scale field equations:

$$\frac{\partial\mathbf{b}}{\partial t}=\nabla\times\left[\overline{\mathbf{U}}\times\mathbf{b}+\mathbf{u}\times\overline{\mathbf{B}}+\mathbf{u}\times\mathbf{b}-\overline{\mathbf{u}\times\mathbf{b}}-\eta\mathbf{j}\right], \tag{3.27}$$

$$\frac{\partial\mathbf{u}}{\partial t}=-\nabla P_{eff}+\overline{\mathbf{B}}\cdot\boldsymbol{\nabla}\mathbf{b}+\mathbf{b}\cdot\boldsymbol{\nabla}\overline{\mathbf{B}}-2\boldsymbol{\Omega}\times\mathbf{u}+\mathbf{N}+\mathbf{f}+\nu\nabla^2\mathbf{u}, \tag{3.28}$$

$$\nabla\cdot\mathbf{u}=0, \tag{3.29}$$

where these small scale motions are assumed incompressible, the effective pressure P_{eff} contains the gas and magnetic pressures, $\mathbf{f}$ is the external force, and the nonlinear terms are collected in $\mathbf{N}=-\mathbf{u}\cdot\boldsymbol{\nabla}\mathbf{u}+\overline{\mathbf{u}\cdot\boldsymbol{\nabla}\mathbf{u}}+\mathbf{b}\cdot\boldsymbol{\nabla}\mathbf{b}-\overline{\mathbf{b}\cdot\boldsymbol{\nabla}\mathbf{b}}$. It is natural to make the further assumption that $\overline{\mathbf{U}}=0$, which is roughly valid for rapidly rotating systems. Since the system is incompressible, the pressure can be found by a Fourier solenoidal projection $P_{ij}=\delta_{ij}-\hat{k}_i\hat{k}_j$, with the unit vector $\hat{\mathbf{k}}=\mathbf{k}/|\mathbf{k}|$. Thus

$$\frac{\partial\hat{u}_i}{\partial t}=P_{ij}\left[\widehat{\left(\overline{\mathbf{B}}\cdot\boldsymbol{\nabla}\mathbf{b}\right)}_j+\widehat{\left(\mathbf{b}\cdot\boldsymbol{\nabla}\overline{\mathbf{B}}\right)}_j-2\epsilon_{jkl}\Omega_k\hat{u}_l+\hat{f}_j+\hat{N}_j-\nu k^2\hat{u}_j\right]. \tag{3.30}$$

where the nonlinear Lorentz force terms are convolutions in k-space. With the above definitions, we can largely proceed toward analyzing the structure of the mean-field equations. For some brevity, the reader is pointed to Brandenburg & Subramanian (2005) §10.3 for

the derivation of the time derivative of the cross-correlation tensor χ_{jk} (see Equation 3.25). Briefly, the underlying assumption behind this derivation is that the evaluation of correlation integrals in Fourier space is undertaken by expanding the velocity correlation tensor in a Taylor series. Only zeroth and first-order derivatives in $\mathbf{k}'$ are retained, in accord with the renormalization group analysis discussion above. This follows from the assumption that the mean field $\overline{\mathbf{B}}$ varies only on the large scales and hence small $\mathbf{k}$. The result is the following approximate equation for χ_{jk}, which is valid to first-order in large-scale spatial derivatives

$$\frac{\partial \chi_{jk}}{\partial t} = \mathcal{I}_{jk} - \mathcal{A}_{jl}\chi_{lk} - \mathcal{B}_{jlm}\frac{\partial \chi_{lk}}{\partial R_m} + \overline{\hat{u}_j \hat{G}_k} + \overline{\hat{H}_j \hat{b}_k} - (\eta + \nu)\, k^2 \chi_{jk} - i\,(\eta - \nu)\, \mathbf{k} \cdot \nabla \chi_{jk}, \tag{3.31}$$

$$\mathcal{A}_{jl} = -2\epsilon_{jlt}\hat{k}_t \hat{k}_s \Omega_s, \tag{3.32}$$

$$\mathcal{B}_{jlm} = \frac{i}{k}\hat{k}_s \Omega_s \epsilon_{jlt}\left[\delta_{mt} + \frac{k_t \Omega_m}{k_s \Omega_s} - 2\hat{k}_t \hat{k}_m\right], \tag{3.33}$$

$$\begin{aligned}\mathcal{I}_{jk} = {} & -i\mathbf{k} \cdot \overline{\mathbf{B}}\,(v_{jk} - m_{jk}) + \frac{1}{2}\overline{\mathbf{B}} \cdot \nabla\,(v_{jk} + m_{jk}) + \overline{B}_{j,l} m_{lk} - \overline{B}_{k,l} v_{jl} \\ & - \frac{1}{2}\overline{B}_{m,s} k_m \left[\frac{\partial v_{jk}}{\partial k_s} + \frac{\partial m_{jk}}{\partial k_s}\right] - 2\hat{k}_j \hat{k}_s \overline{B}_{s,l} m_{lk}.\end{aligned} \tag{3.34}$$

where $\nabla = \partial/\partial \mathbf{R}$ is the large-scale gradient operator in physical space and subscript indices with commas indicate a spatial derivative, for instance $\overline{B}_{j,l} = \partial \overline{B}/\partial R_l$. The first-order smoothing approximation, which says that averages of triple products of fluctuating or small-scale quantities are zero, could be applied here. However, this assumption has been proven to be highly inaccurate for nonself-adjoint systems such as the incompressible Navier-Stokes equation being considered here (Lerche, 1974). Instead, the minimum-τ approximation will be used, which says that the such triple products will be approximated by double products divided by a k-dependent correlation timescale $\tau(k)$. Thus, the triple product terms in Equation 3.34 are approximated as $\overline{\hat{u}_j \hat{G}_k} + \overline{\hat{H}_j \hat{b}_k} = -\chi_{jk}/\tau(k)$. Neglecting the microscopic viscosity and conductivity, the evolution of the cross-correlation tensor can be written as

$$\frac{\partial \chi_{jk}}{\partial t} = \mathcal{I}_{jk} - \frac{1}{\tau} D_{jl}\chi_{lk} - \mathcal{B}_{jlm}\frac{\partial \chi_{lk}}{\partial R_m}, . \tag{3.35}$$

where $D_{jl} = \delta_{jl} + \tau \mathcal{A}_{jl}$. If we average Equation 3.35 over a sufficiently long time, then the time-derivative should vanish, leaving

$$D_{jl}\chi_{lk} + \tau \mathcal{B}_{jlm}\frac{\partial \chi_{lk}}{\partial R_m} - \tau \mathcal{I}_{jk} = 0. \tag{3.36}$$

In the weakly inhomogeneous turbulence regime, this equation can be solved perturbatively in large-scale derivatives with the zeroth and first-order equations being

$$\chi^{(0)}_{jk} = D^{-1}_{jl}\tau \mathcal{I}^{(0)}_{lk}, \tag{3.37}$$

$$\chi^{(1)}_{jk} = D^{-1}_{jl}\tau \mathcal{I}^{(1)}_{lk} - \tau^2 D^{-1}_{jp}\mathcal{B}_{plm}\frac{\partial}{\partial R_m}\left(D^{-1}_{ls}\mathcal{I}^{(0)}_{sk}\right) \tag{3.38}$$

with the latter equation arising from substituting the zeroth-order equation into Equation 3.36 and noting that $\mathcal{I}^{(0)}_{lk} = -i\mathbf{k}\cdot\overline{\mathbf{B}}(v_{lk} - m_{lk})$. The matrix inverse of D is

$$D^{-1}_{jl} = \frac{1}{1 + Co^2(k)}\left[\delta_{jl} + \mathrm{Co}(k)\epsilon_{jlm}\hat{k}_m + \mathrm{Co}^2(k)\hat{k}_j\hat{k}_l\right], \tag{3.39}$$

where $\mathrm{Co}(k) \equiv 2\hat{k}_s\Omega_s\tau(k)$ is the scale dependent Coriolis number. As was instigated in the introduction of this derivation, we assume the Coriolis number is large over a significant range of scales, which is likely in rapidly rotating systems given that $\tau(k) \equiv \tau_0(\ell_0 k/2\pi)^{-2/3}$ for Kolmogorov turbulence. Thus $\mathrm{Co}(k) = \mathrm{Co}_0(\ell_0 k/2\pi)^{-2/3}$, with Co_0 the large-scale Coriolis number. In the limit that Co_0 is moderate, say around 32 as in the introductory example, $D^{-1}_{jl} \approx \hat{k}_j\hat{k}_l$ and so is actually independent of the spectrum of the motions. Before we can compute the mean-field expectation for the electromotive force $\mathcal{E}$, a form for the velocity and magnetic correlation tensors must be found. A form for these tensors in weakly inhomogeneous turbulence is given in either (Roberts & Soward, 1975) or Rädler et al. (2003). Let the kinetic energy and helicity spectra be independent of the large scale $\mathbf{R}$, then these correlation tensors simplify to

$$v_{lk} = P_{lk}(\mathbf{k})\,E(k) - \frac{i\hat{k}_q}{k}\epsilon_{lkq}F(k) \tag{3.40}$$

$$m_{lk} = P_{lk}(\mathbf{k})\,M(k) - \frac{i\hat{k}_q}{k}\epsilon_{lkq}N(k) \tag{3.41}$$

with the kinetic and magnetic energy spectra $E(k)$ and $M(k)$ as well as $F(k)$ and $N(k)$ the kinetic and current helicity spectra. Under this assumption the mean EMF becomes $\overline{\mathcal{E}} = \epsilon_{ijk}\int \mathrm{d}^3\mathbf{k}\tau(k)D_{jl}^{-1}\mathcal{I}_{lk} + \mathcal{O}(\nabla_{\mathbf{R}})$, or expanding using Equations 3.34, 3.40, and 3.41:

$$\overline{\mathcal{E}}_i = \epsilon_{ijk}\int \mathrm{d}^3\mathbf{k}\,\tau\hat{k}_j\hat{k}_l\left\{-ik_s\overline{B}_s\left[P_{lk}\left(E-M\right)-\frac{i\hat{k}_q}{k}\epsilon_{lkq}\left(F-N\right)\right]+\overline{B}_{l,p}\left[P_{pk}M-\frac{i\hat{k}_q}{k}\epsilon_{pkq}N\right]\right.$$
$$\left.-\overline{B}_{k,p}\left[P_{lp}E-\frac{i\hat{k}_q}{k}\epsilon_{lpq}F\right]-\frac{1}{2}\overline{B}_{m,s}k_m\left[\frac{\partial v_{lk}}{\partial k_s}+\frac{\partial m_{lk}}{\partial k_s}\right]-2\hat{k}_l\hat{k}_s\overline{B}_{s,p}\left[P_{pk}M-\frac{i\hat{k}_q}{k}\epsilon_{pkq}N\right]\right\}. \tag{3.42}$$

The most simple observation is that the EMF must be real so only one of the remaining terms depends upon the helicities. Furthermore, the spectral derivatives of v_{lk} and m_{lk} with respect to k_s, recalling the definition of P_{lk}, becomes the product of $(2\hat{k}_l\hat{k}_k\hat{k}_s-\hat{k}_k\delta_{ls}-\hat{k}_l\delta_{ks})/k$ and E or M, respectively. Thus the above integral reduces to

$$\overline{\mathcal{E}}_i = \epsilon_{ijk}\int \mathrm{d}^3\mathbf{k}\,\tau\hat{k}_j\hat{k}_l\left\{-\hat{k}_q\hat{k}_s\epsilon_{lkq}\left(F-N\right)\overline{B}_s+\overline{B}_{l,p}\left[\delta_{pk}-\hat{k}_p\hat{k}_k\right]M-\overline{B}_{k,p}\left[\delta_{lp}-\hat{k}_l\hat{k}_p\right]E\right.$$
$$\left.-1/2\overline{B}_{m,s}\hat{k}_m\left[2\hat{k}_l\hat{k}_k\hat{k}_s-\hat{k}_k\delta_{ls}-\hat{k}_l\delta_{ks}\right]\left(E+M\right)-2\hat{k}_l\hat{k}_s\overline{B}_{s,p}\left[\delta_{pk}-\hat{k}_p\hat{k}_k\right]M\right\}+\mathcal{O}(\nabla_{\mathbf{R}}). \tag{3.43}$$

Simplifying further and grouping the powers of $\hat{k}$ gives

$$\overline{\mathcal{E}}_i = \epsilon_{ijk}\int \mathrm{d}^3\mathbf{k}\,\tau\hat{k}_j\hat{k}_l\left[\hat{k}_q\hat{k}_s\epsilon_{lkq}\left(N-F\right)\overline{B}_s+1/2\left(E-M\right)\left(\overline{B}_{l,k}-\hat{k}_k\hat{k}_p\overline{B}_{l,p}\right)\right]+\mathcal{O}(\nabla_{\mathbf{R}}). \tag{3.44}$$

Using the identity that $\epsilon_{ijk}\epsilon_{lkq} = \delta_{iq}\delta_{jl}-\delta_{il}\delta_{jq}$, the first term in this integral vanishes. *This is quite dramatic as it means there is no α-effect!*

Indeed, the previous equation further reduces to

$$\overline{\mathcal{E}}_i = 1/2\,\epsilon_{ijk}\int \mathrm{d}^3\mathbf{k}\,\tau\hat{k}_j\hat{k}_l\left(E-M\right)\left(\overline{B}_{l,k}-\hat{k}_k\hat{k}_p\overline{B}_{l,p}\right)+\mathcal{O}(\nabla_{\mathbf{R}}). \tag{3.45}$$

The next observation is that $\overline{\mathbf{B}}$ is independent of k and that the spectra and eddy correlation time τ are isotropic and depend only on k. Noting that

$$\int \mathrm{d}^3\mathbf{k}\,\hat{k}_i\hat{k}_j\mathcal{F}\left(k\right) = 1/3\,\delta_{ij}\int \mathrm{d}^3\mathbf{k}\,\mathcal{F}\left(k\right), \tag{3.46}$$

$$\int \mathrm{d}^3\mathbf{k}\,\hat{k}_i\hat{k}_j\hat{k}_k\hat{k}_l\mathcal{F}\left(k\right) = 1/15\left(\delta_{ij}\delta_{kl}+\delta_{ik}\delta_{jl}+\delta_{il}\delta_{jk}\right)\int \mathrm{d}^3\mathbf{k}\,\mathcal{F}\left(k\right). \tag{3.47}$$

These identities allow the integrals to be evaluated, with the following result

$$\overline{\mathcal{E}}_i = 1/6\left[\epsilon_{ilk}+1/5\left(\epsilon_{ilp}+\epsilon_{ipl}\right)\right]\left(\tilde{E}-\tilde{M}\right), \tag{3.48}$$

where $\tilde{Q} = \int \mathrm{d}^3\mathbf{k}\,\tau(k)Q(k)$ and $Q = E,\,M$. The latter term in this integral vanishes as $\epsilon_{ilp} = -\epsilon_{ipl}$, thus the only remaining term in the mean-field EMF is

$$\begin{aligned}\overline{\mathcal{E}}_i &= 1/6\,\epsilon_{ilk}\left(\tilde{E}-\tilde{M}\right)\overline{B}_{l,k}+\mathcal{O}(\nabla_{\mathbf{R}}), \quad \text{so}\\ \overline{\boldsymbol{\mathcal{E}}} &= 1/6\left(\tilde{M}-\tilde{E}\right)\boldsymbol{\nabla}\times\overline{\mathbf{B}}+\mathcal{O}(\nabla_{\mathbf{R}}).\end{aligned} \tag{3.49}$$

Since we have assumed Kolmogorov scaling for the turbulent spectra, this coefficient can be evaluated with the further assumption that $M = B_0^2/8\pi(k\ell_0/2\pi)^{-\alpha}$ for some $\alpha \geq 0$. The mean EMF under this approximation is

$$\overline{\boldsymbol{\mathcal{E}}} = -\eta_t\overline{\mathbf{J}}+\mathcal{O}(\nabla_{\mathbf{R}}), \tag{3.50}$$

$$\eta_t = \frac{4E_0\tau_0}{9\ell_0}\left[1-\left(\frac{k_\nu\ell_0}{2\pi}\right)^{-4/3}-\frac{3\alpha B_0^2}{32E_0}\left(1-\left(\frac{k_\eta\ell_0}{2\pi}\right)^{1-\alpha}\right)\right], \tag{3.51}$$

with $\overline{\mathbf{J}} = \boldsymbol{\nabla}\times\overline{\mathbf{B}}$ being the mean current density. Since the global-scale ℓ_0 and both diffusive scales k_ν and k_η are large values, these terms are negligible. The remaining term is likely still positive provided that the magnetic fields are at most in equipartition with the kinetic energy, or more precisely that $ME < 4KE/3\pi\alpha \approx 0.1KE$ (with $ME = B_0^2/8\pi$ and $KE = E_0$), which tends to be the case within most global-scale convective dynamo simulations in the presence of strong rotational constraints. Perhaps, this is the physical mechanism underlying the saturation of the maximum magnetic energy in such simulations. Furthermore, the dependence only on $\overline{\mathbf{J}}$ is quite remarkable as it is not the kinetic helicity of the standard

MFT framework that provides the mechanism of poloidal field regeneration. Rather, it is the action of small-scale turbulence on $\overline{\mathbf{J}}$ that can lead to a constructive rather than destructive impact on the generation of mean magnetic fields.

It could then be asked whether or not the higher order terms proportional to $\nabla_{\mathbf{R}}$ better corroborate the standard field-theoretic picture at slow rotation. The short answer is no. The longer answer requires the calculation of

$$\overline{\mathcal{E}}_i^B = -\epsilon_{ijk} \int \mathrm{d}^3\mathbf{k}\, \tau^2 D_{jp}^{-1} \mathcal{B}_{plm} \frac{\partial}{\partial R_m} \left[D_{ls}^{-1} I_{sk}^{(0)} \right], \tag{3.52}$$

$$= -\Omega_n \frac{\partial \overline{B}_q}{\partial R_m} \int \mathrm{d}^3\mathbf{k}\, \tau^2 \hat{k}_n \hat{k}_j \hat{k}_p \hat{k}_l \hat{k}_s \hat{k}_q \epsilon_{ijk} \mathcal{C}_{plm} \left(v_{sk} - m_{sk} \right) \tag{3.53}$$

$$\mathcal{C}_{plm} = \epsilon_{plt} \left[\delta_{tm} + k_t/k_m - 2\hat{k}_t \hat{k}_m \right] \tag{3.54}$$

with $\mathcal{B}_{plm}$ given in Equation 3.33. Since there are no imaginary terms outside of the helicity contributions within v_{sk} and m_{sk}, these helicity contributions must be zero. This condition consequently leaves the kinetic and magnetic energy spectra as the significant contributors. However, the projection operator associated with them $P_{sk} = \delta_{sk} - \hat{k}_s \hat{k}_k$ correlates with the $\hat{k}_s$ term already present in the above Equation 3.53. *As a result, that entire expression is zero.* Hence there are no contributions to within second order in large-spatial derivatives, leaving the sole term above, or more appropriately

$$\overline{\boldsymbol{\mathcal{E}}} = -\eta_t \overline{\mathbf{J}} + \mathcal{O}\left(\frac{\partial^2 \overline{\mathbf{B}}}{\partial R_i \partial R_j} \right). \tag{3.55}$$

This relation is only approximate and relevant to only those scales that are under the influence of the Coriolis force. Below the threshold where the Coriolis number falls to around unity, the usual picture of an α-effect will again be relevant. Nonetheless, in dynamos that have significant rotational constraint, there could be a sizable range of scales over which the turbulent interactions between the flows and the mean current dominate. This problem has been looked at to some degree, though under a very different set of assumptions, in an another mean-field theory framework, and in the context of the Rädler $\boldsymbol{\Omega} \times \mathbf{J}$ effect

(Moffatt & Proctor, 1982; Moffatt, 1983). Those works suggest three further explorations to refine this picture: including inhomogeneities in the turbulent spectra, including anisotropic spectra, and perhaps employing a multi-scale expansion for such rotationally constrained dynamos. There may also be a less perturbative means to deriving such relations that instead rely on the robust framework of renormalization group analyses and symmetrical reductions constructed for quantum field theory.

Freeman Dyson was the first to formulate renormalization theory, creating a precise computational framework that seemed to magically cure the ills of the ultraviolet divergences in quantum electrodynamics (Dyson, 1949). Shortly thereafter, the renormalization group concept was introduced by Gell-Mann & Low (1954), where Dyson's renormalization theory was made more general and applicable beyond quantum field theory. Though, there was not yet a systematic way of using Gell-Mann's method and there were no clear links between effective field theories and the renormalization group. In both of these approaches, the prevailing practice had been to artificially introduce a short-distance (high-energy) cutoff in a field theory and then to renormalize the coupling constants of the theory, effectively wrapping the high-energy (ultraviolet) physics into the constant.

The insight of Kenneth Wilson was to, instead of waving one's hands and arbitrarily choosing a cutoff, take it seriously and regard it as part of the physical formulation of the field theory. Wilson imagined letting the cutoff shrink while simultaneously adjusting the theory to preserve its large-scale predictions, allowing the coupling constants to run apace with the changing cutoff (Wilson & Kogut, 1974). In this paper, he also clarified the renormalization group method, systematizing the process of integrating out short-distance degrees of freedom. While this procedure may seem complicated, Wilson's reasoning actually reveals something wonderful: the equations describing the processes occurring at large-scales become remarkably simple and completely characterized by just a few renormalized parameters. For instance using Wilson's approach, one recovers Dysons results in quantum electrodynamics and much more, while also establishing a robust and visually appealing picture of the

physics.

Thanks to Wilson's work, effective field theories are now first assessed through the renormalization group. Although this method alone is not sufficient to build an effective field theory, a renormalization group analysis serves to illustrate the domain of applicability of such theories. Indeed, such an analysis lends credence to the primary method of constructing effective field theories, which is using symmetries and Noether's theorem to restrict the manifold in which the broader theory rests, reducing its degrees of freedom. In particular, if there is a single energy scale with wavenumber k in the microscopic theory, such as the wavenumber above which a turbulent field has something akin to the Kolmogorov scaling (Kolmogorov, 1941), the effective field theory can be seen as an expansion in k.

Building an effective field theory accurate to some power of k requires an increasingly large set of free parameters at each order of the expansion that parameterize the degrees of freedom that have been integrated out. This technique is useful when the smallest scale has wave number K that satisfies the condition $k/K \ll 1$. This caveat holds true for mean-field electrodynamics if one considers K to be proportional to the inverse of the molecular dissipation scale. However, the effective field theory is not necessarily renormalizable as it is not valid at small length scales. Indeed, the increasingly large number of parameters admitted at each order in k of an effective field theory means that they are generally not renormalizable in the same sense as quantum electrodynamics, which requires the renormalization of only two parameters: the bare electron mass and charge. It is likely that the MHD equations are nonrenormalizable, but this will require some careful study.

Renormalization group analysis in wavenumber-space is usually carried out on a perturbation expansion. The standard derivation of mean-field electrodynamics does just this, being carried out as a perturbative expansion in the scale-separation limit. Yet the validity of such an expansion relies upon the hope that the underlying physics of the system is close to that of the non-interacting, free-field system. This is most likely untrue in general for mean-field electrodynamics except perhaps in the kinematic regime. In the case that it is

close to the free field system, collecting the leading order terms in the expansion permits calculations of quantities such as the mean-field. While the perturbative approach has been quite successful for many theories such as those of particle physics, it usually fails for systems whose physics is very far from any free system, for example systems with strong correlations. MHD systems fall into this latter category, given the nonlinear field interactions present in the MHD equations which allows for strong correlations between all scales that are unknown apriori. This fact renders the standard methods of mean-field electrodynamics rather dubious when applied to systems in the nonlinear regime, even when such correlations are approximated with the minimum-τ or second-order correlation approximations.

Yet there may be ways to skirt the current perturbative approach to the strongly coupled dynamics of turbulent MHD. Indeed, there have been several fairly recent attempts to look at aspects of mean-field electrodynamics utilizing the framework built for quantum chromodynamics, even to the extent of introducing a Feynman calculus (e.g., Adzhemyan et al., 1999; Vasil'ev, 2004; Jurčišinová et al., 2013). There may be a route to improving upon these direct applications of field theoretic methods to MHD, extending the results of Jurčišinová et al. (2013) for instance. Indeed, it may be possible to compute the all-order loop interactions (representing field self-interaction) and all-order tree interactions (representing interaction of the magnetic and velocity fields), utilizing a modified form of the amplituhedronic approach to quantum field theory (Arkani-Hamed et al., 2012). This latter work makes connections between algebraic geometry on the positive Grassmannian and the super-symmetric $\mathcal{N} = 4$ Yang-Mills quantum field theory that allow the the otherwise increasingly intractable Feynman calculus of higher order interactions to be reduced to calculations of the volume of simplices on the triangulated positive Grassmannian. A similar geometry might be constructed for the interacting fields of the Navier-Stokes MHD equations, allowing for a more accurate effective field theory of electrodynamics to be built.

3.4 Three-Dimensional Numerical Simulations of Nonlinear Dynamos

The greatest tool currently available to modern dynamo theorists are 3D numerical simulations, as there have been few breakthroughs in turbulence theory that would allow analytical or semi-analytical solutions to the fully nonlinear compressible MHD system. In direct numerical simulations (DNS), all the turbulent processes are fully captured, from the driving scale to the diffusion scales. Although these simulations are typically far removed from the length scales important to astrophysical processes, they can shed light on the small-scale dynamics that strongly influence the transport properties of the larger-scale system. The aim of these simulations is usually to try to make contact with theoretical predictions of turbulent spectra, such as the Kolmogorov scaling. However, as with large-eddy simulations (LES) that parameterize the small-scale physics, they are limited by computational resources in obtaining ever larger resolution and are constrained in their ability to run large suites of simulations that accurately probe large swaths of parameter space. Some of the largest DNS simulations to date have reached 1 trillion grid cells or roughly 10000 cells in each dimension, such as those of P. Maninni and A. Pouquet for Taylor-Green flow and those of P. Woodward for the National Ignition Facility.

There are many approaches to these problems: some that are true DNS in the sense that a particular physical system with its empirically determined diffusion coefficients are simulated, some that utilize other diffusive operators, and still others that employ only an implicit numerical diffusion. The first method assumes that the number of atoms within a grid cell is still large enough that the diffusion approximation to the collisional interactions is valid, whereas the last assumes effectively the same thing but with a numerically defined diffusion coefficient. This numerical diffusion could be considered a running coupling constant under the nomenclature of renormalization theory. The same can be said for LES schemes that explicitly and artificially increase the level of the Laplacian diffusion in the system. Thus there is some connection between these two schemes, though it may not be

simple. Indeed, it would be interesting to see if these two schemes act equivalently under some properly defined problem.

For those simulations that attempt to retain the diffusion approximation to collisional interactions, there are two dynamo regimes one of low magnetic Prandtl number (Pr_m) and another of large Pr_m. Theoretically, one should expect that at large Pr_m the magnetic Reynolds number is much greater than that of the fluid Reynolds number, which leads to the length scales of the magnetic field being smaller than that of the velocity field. At low Pr_m, the expectation should be the opposite that the generated magnetic fields roughly tend to be of larger scale than the velocity field. This does not preclude smaller scale intermittent fields for the low-Pr_m regime or vice versa for the converse, rather it is more a statement about which components of the magnetic field contain the most energy: the large-scales for low-Pr_m dynamos and the small-scales for high-Pr_m dynamos. Using the Braginskii definitions of the viscous and magnetic diffusivities and stellar models one, can determine the ranges of magnetic Prandtl numbers within a star. For dynamos in stars with convective exteriors, the low-Pr_m regime is of greatest interest. Using the Sun as an example, the molecular Pr_m ranges between about 10^{-1} in the core to roughly 10^{-6} at the photosphere, decreasing exponentially toward it. Other low mass stars are roughly similar, with a low Pr_m throughout the bulk of their domains. High mass stars, in contrast, have relatively large molecular values of Pr_m ranging from about 10 throughout the convective core and remaining nearly unity until the near-surface region is reached at which point it drops to about 10^{-2}. So, the convective cores of massive stars and the convective envelopes of low mass stars represent very different dynamo regimes with respect to the scales possessing the greatest magnetic energy, regardless of their myriad other differences.

At small scales, the Pr_m parameter regimes have been studied extensively with numerical simulations. The primary results of these simulations are that, at large magnetic Prandtl number, the magnetic field generation is of the stretch-twist-fold variety where its structures are of a smaller scale than the viscous dissipation scale (e.g., Schekochihin et al.,

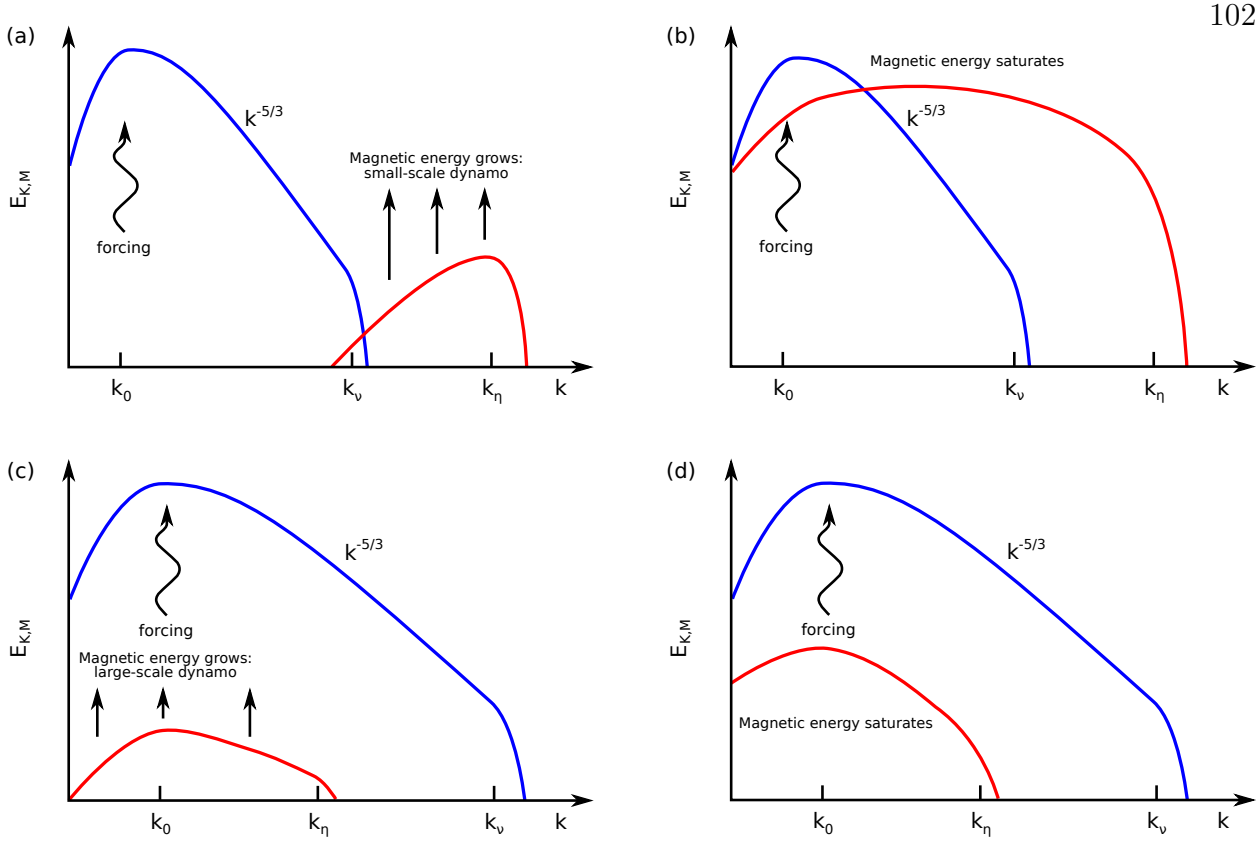

Figure 3.4: A sketch of energy spectra for low and high-Pr_m dynamos with wavenumber k. (a) Kinematic phase and (b) saturation phase of the high-Pr_m dynamo, with kinetic energy in blue and magnetic energy in red. (c) Kinematic phase and (d) saturation phase of the low-Pr_m dynamo. Here k_0 is the driving scale, k_ν the viscous dissipation scale, and k_η the magnetic energy dissipation scale.

2004). On the other side of the Prandtl number coin, the low Pr_m regime has the stretch-twist-reconnect mechanism, where the flows act similar to the large Pr_m regime, but instead of the flows dissipating and the magnetic field folding on itself, the magnetic field dissipates leading to reconnection (e.g., Schekochihin et al., 2007; Brandenburg, 2009). These two dynamo regimes are sketched in Figure 3.4, showing their kinematic and saturation phases. While such simulations are instructive for creating subgrid-scale models and understanding the small-scale physics, they lack a direct connection to the global-scale phenomena that are more directly observable for astrophysical objects.

Four large-scale dynamos have already been considered, or at least mentioned, those

of Parker, Backus, Herzenberg, and Roberts. These dynamos generate magnetic fields that have spatial scales greater than the velocity scales producing them. The Sun and the Earth, among many other astrophysical objects, seem to possess global-scale fields and as such they must be large-scale dynamos with a cascade of energy moving from small-scale turbulence to large-scale magnetic fields. For the helio- and geo-dynamos, the mechanisms building large-scale field is directly linked to their rotation. In these global-scale dynamos, one manner in which the rotation is crucial is that the Coriolis force induces a net kinetic helicity in the small-scale turbulent flows. Correlations between the fluctuating velocity components of the turbulence consequently yield Reynolds stresses that act to maintain the bulk differential rotation through an inverse cascade of kinetic helicity and energy. This inverse cascade is thus the indirect source of the differential rotation that fuels the generation of toroidal field as in Equation 3.19, whereas direct action of the convection is largely to transform this toroidal field into poloidal field as in an α-effect. Thus the structure of the convection and the differential rotation that it supports is key to the overall nature of the global-scale stellar dynamo.

3.5 Solar Convection and Differential Rotation

It is clear that both turbulent correlations in velocity and magnetic fields as well as rotation are necessary ingredients in the brew of the solar dynamo. The plasma in the interior of the Sun achieves its turbulence through nearly inviscid thermal convection driven by the enormous heat flux coming from fusion in its core and by the rapid cooling at its photosphere. Despite this extreme turbulence, the Sun manages to maintain both global-scale magnetic fields and the bulk flows of differential rotation and meridional circulation. These global-scale structures cannot emerge from only the interaction of intermittent turbulent vortices that produce a local spontaneous symmetry breaking. The coherency time for such vortices is simply too short in the solar context, being at most a few tens of eddy turnover times for a prominent outlier. Such spontaneous symmetry breaking consequently cannot account for

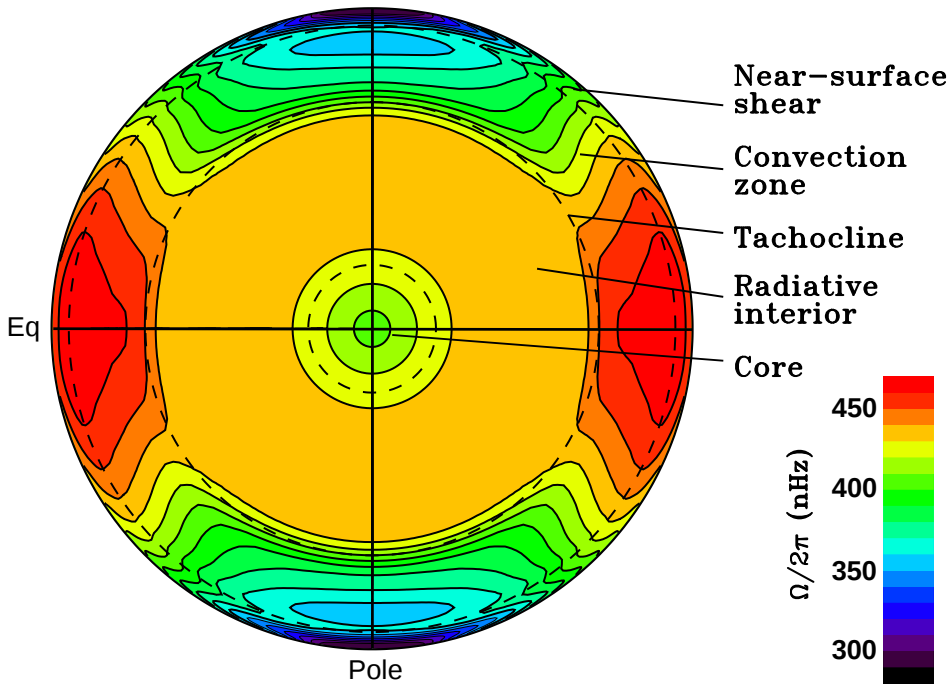

Figure 3.5: Helioseismically determined angular velocity profile Ω of the solar interior, with fast rotation (red) at the equator and slow (blue) at the poles. Important regions are indicated (Adapted from Howe (2009)).

the amount of upscale transfer of energy and helicity that is required to sustain the observed large-scale structures. Rather, the correlations induced by rotation are the only way that these flows and fields are possible.

It has long been known that the Sun exhibits turbulent phenomenon at its surface, yet the role that turbulent motions have in its interior remained fairly mysterious until the advent of helioseismology (e.g., Kahn, 1961; Leighton et al., 1962; Noyes & Leighton, 1963; Vandakurov, 1967; Deubner & Gough, 1984; Gough & Toomre, 1991; Thompson et al., 1996). Probing the interior of the Sun through seismology has established the surprising existence of two zones of strong rotational shear (e.g., Deubner et al., 1979; Brown et al., 1989; Schou et al., 1998; Christensen-Dalsgaard, 2002; Thompson et al., 2003; Howe, 2009). Moreover, the isorotational contours deduced from global inversions of the rotational are conical, as in Figure 3.5, which is in stark contrast to the cylindrical profiles one might expect from

the Proudman-Taylor theorem or from early global-scale simulations (Glatzmaier & Gilman, 1982). One of these zones of shear is the sharp transition between the radiative interior and the convection zone called the tachocline. In this region, there is a sharp change from the differential rotation in the convection zone to the uniform rotation of the deep interior, as was first adumbrated in Spiegel (1972) and later detected helioseismically in Brown et al. (1989). Three mechanisms have been proposed to explain this xyresic layer: highly turbulent horizontal motions just above the tachocline that prevent inward diffusion, as in Spiegel & Zahn (1992); magnetic confinement due to a relic magnetic field in the radiative interior (Gough & McIntyre, 1998); and that the skin-depth effect of a cycling magnetic field in a conductive medium prevents the spread of the tachocline (Petrovay, 2003). These notions are currently being put to the test in 3D simulations and in further theoretical work (e.g., Browning et al., 2006; Brun & Zahn, 2006; Zahn et al., 2007; Garaud & Garaud, 2008; Brummell et al., 2010; Strugarek et al., 2011; Wood et al., 2011)

A natural expectation for the profile of the angular velocity is one consistent with constant angular momentum, where the convection efficiently mixes angular momentum in the vertical direction and which yields $\Omega \propto r^{-2}$ (Wasiutynski, 1946; Kippenhahn, 1963). Evidence for an increasing angular velocity with increasing depth came from the proper motion of sunspots (e.g., Gilman & Foukal, 1979) and from the super-rotation of supergranulation (e.g., Gizon et al., 2003). So it was quite surprising to find that the second zone of strong shear occupied only the outer 5% of the Sun by radius. This region has thus been dubbed the near-surface shear layer. Yet how this layer arises naturally and blends continuously with the nearly conical isorotational contours of the deeper interior is still a bit of a mystery.

There are hints from simulations that the interaction of multi-scale flows and increasing rotational influences with depth regulate this behavior (Brandenburg, 2007; Augustson et al., 2011; Hurlburt et al., 2012; Guerrero et al., 2013). Indeed, photospheric convection simulations carried out over the last two decades have led to a picture of near-surface convection wherein cold, rapidly-descending, and small-scale plumes coalesce into a hierarchical

tree of convective downdrafts at greater depths (Nordlund et al., 2009). More precisely, the downflowing plumes originating at the photosphere interact and merge as they traverse many density scale-heights, which sets the spatial scale at which weak meandering upflows organize in response to the emergent downdrafts (Rast & Toomre, 1993). Such an effect has been suggested to persist deeper in the solar convection zone, with thin downdrafts resulting from the merger of plumes effectively determining the structure of giant cells (e.g., Spruit, 1997). Collectively, the above interpretation of the dynamics may be characterized as 'top-down' driving. This picture of solar dynamics, with a large asymmetry between upflows and downflows, has been posited as an explanation for the discrepancy between helioseismic estimates of convective velocity and those realized in global-scale convection simulations, in which these near-surface effects are necessarily omitted. There is also a sound theoretical reason for the structure of the near-surface shear layer, where there may be a transition from a baroclinic vorticity balance in the deep interior to a Reynolds stress balance in the near-surface layers (Miesch & Hindman, 2011). In other words, such a shear layer would arise from the smooth transition between the near-constant angular momentum one might expect near the photosphere to the rotationally constrained dynamics of the deeper solar interior where the time scales of the motions become commensurate with the rotation period.

Despite the large differential rotation and conical radial profiles, there have been time-distance analyses of solar Doppler velocity data that imply that the turbulent flow speeds are quite low (Hanasoge et al., 2010, 2012), being nearly 100 times less than those seen in 3D solar simulations. This helioseismic result, if confirmed, would have important implications for the maintenance of mean flows in the Sun. However, this result is eloquently argued against in Miesch et al. (2012). In this latter paper, lower bounds on convective velocities are derived using the MHD equations under the constraint that the turbulent flows must produce bulk flows consistent with those ascertained from global helioseismic inversions. This bound is not based on mixing-length theory nor on numerical simulations, though they are consistent with both. It is found that the amplitude of the turbulent flows in the upper solar

convection zone ($r \sim 0.95\,\mathrm{R}_\odot$) must be at least $30\,\mathrm{m\,s^{-1}}$ in order to be capable of sustaining the mean flows inferred from helioseismology. Similar estimates for the lower convection zone ($r \sim 0.75\,\mathrm{R}_\odot$) imply that motions there must be at least $8\,\mathrm{m\,s^{-1}}$. There are two possible reconciliations between the lower limits in Miesch et al. (2012) with the upper limits found by Hanasoge et al. (2012). One possibility is that there is an overestimate of the large-scale convective velocity amplitudes, with smaller scale turbulent flows being responsible for more of the angular momentum transport through inverse cascades and self-organization than previously realized. The second aspect, which is not considered in Miesch et al. (2012), is the impact that magnetic fields might have on the resulting convective amplitudes. In any case, the seeming inability of large-scale models to reproduce what should be a basic aspect of solar convection is a definite curiosity. For if the flows are indeed so slow, what is absorbing the kinetic energy or reducing the buoyancy of these flows as they descend into the depths of the Sun? If such measurements could be made for other stars, would they show a similarly low amplitude of convective motions?

3.6 Global-Scale Simulations

There is no doubt the transfer of kinetic and magnetic energy, momentum, and helicity from small to large scales is critical to the dynamo process operating within stars, with an inverse cascade arising from the breaking of certain symmetries with respect to isotropic homogeneous turbulence. Such symmetry breaking in stars primarily occurs due to the preferred directions introduced by rotation and stratification. Gravity and the resulting stratification that it creates break the global isotropic translational symmetry, being now only invariant in the directions perpendicular to the direction of the gravitational acceleration vector. The stratification makes the convection multi-scaled, with the convective scales at a given depth being roughly proportional to the density scale height. Naturally, the scales are then large at greater depths and smaller nearer the surface where the density scale height decreases.

Next one can ask are there spatial scales that are affected by rotation? The first observation is that, in a spherically-stratified rotating star, only the longitudinal direction remains translationally invariant as the radial direction is governed by gravity and the latitudinal direction by rotation. The above argument regarding stratification defines a large-scale symmetry breaking, but not a locally broken symmetry. So we may ask is the reflective symmetry breaking induced by global-scale rotation scale invariant? The answer lies within a simple argument: the MHD equations are rotationally symmetric when rotation is not present; in a rotating frame, however, the $\Omega \times \mathbf{u}$ term breaks this symmetry at all spatial scales as it transforms as a pseudo-vector with $\det(R)R\Omega \times \mathbf{u}$. The other term that might cause symmetry breaking is the Lorentz force, but since it involves two cross products it transforms as a polar vector and does not break the symmetry. However, this is only an argument for the spatial scales and says nothing of time scales. Indeed, there is a minimum time scale below which rotation has little influence which can roughly be characterized by $\tau < 4\pi \mathrm{Ro}\tau_c$, with τ_c the convective overturning time. There is some additional physics that also sets a length scale below which rotation matters increasingly less. Imagine a scenario in which the nominally intermittent temporal scales of local vorticity can be such that they overwhelm the global rotation. If Kolmogorov turbulence is again considered, one should expect $\ell < \ell_0(4\pi Ro_0)^{3/2}$, with ℓ_0 the maximum scale for which the scaling is valid. The breaking of translational and rotational symmetries are largely what set the minimum requirements for the time and spatial scales that must be resolved in global-scale MHD simulations of the solar interior.

In an ideal sense, a subset of these the large-scale dynamos are those that encompass large portions or effectively all of the scales relevant to the dynamics in most astrophysical systems. Clearly, this is a formidable task. The aim, therefore, is to self-consistently capture as many of the scales thought to be dynamically relevant to the global-scales as possible. For the Sun and other rotating bodies, this is a crucial issue due to the fact that the large-scale dynamics is strongly influenced by inverse cascades of energy and helicity. Hence there is no easy way to define the lower bound of relevancy, until the search reaches the dissipative

scales of the physical system. This question is quite apropos in light of the helioseismic results described above. So, one could ask what hope is there of ever being able to capture all the relevant scales? Moreover, how should the intermittent processes that play a significant dynamical role over many time and spatial scales be incorporated?

The answer is, as Neil deGrasse Tyson oxymoronically defines the pursuit of scientific research, the informed ignorance of subgrid-scale (SGS) models. Since the individual characteristics of a range of scales can be separately simulated, or at times theoretically surmised, models can be constructed that describe the SGS transport and diffusion of energy, momentum, and magnetic fields. Such methods prescribe a treatment for how processes occurring at the unresolved scales act upon the larger scales. The most commonly used method is that of eddy diffusion, wherein the natural diffusivities of a system are massively increased. For instance, in many stellar simulations the viscosity is some eleven orders of magnitude larger than its atomic value. However, this method does have a firm basis in renormalization analysis. The eddy diffusion scheme in these models implies that there is an enhanced Laplacian operator, or even multiple hyper-elliptic operators, acting in the system. The latter of these two is potentially more palatable than numerical and implicit diffusion, given that standard flow parameters such as a Prandtl or Reynolds number can be defined. However, the relevance of such numbers to the physical system is likely remote given the vast range of unresolved and thus ignored dynamical scales. Though, it should be kept in mind that the scales of interest are the largest possible.

To aid in resolving the smaller scale processes, the action of unresolved motions scales might be considered as hypo-elliptic, acting more hyperbolically than elliptically (Moffatt, 1983; Brandenburg et al., 2004). Indeed, one approach that has yet to be attempted is to coevolve a separate SGS eddy transport model [such as the test-field method (e.g., Kraichnan, 1972; Schrinner et al., 2007)] with a large-eddy simulation (LES). This SGS model would take the evolved fields at a grid point to be the mean test field, then a separate set of equations would evolve a local field using an eddy closure model that is appropriate to the

circumstances such as those found in Kazantsev (1968); Pouquet et al. (1976); Kleeorin et al. (2002); Brandenburg et al. (2012). Rather than acting only as a diffusion, it might allow local inverse cascades due to intermittent processes to be captured more accurately than a simple diffusive operator can. Alternatively, one could apply spectral boundary conditions that maintain a particular spectral slope and a flux of energy and helicity consistent with the system being studied. The class of Smagorinski-like diffusion schemes is somewhat like this approach where an extrapolation is made in spectral space from some presumed resolved scale in the inertial range to the grid scale (e.g., Germano et al., 1991; Meneveau & Katz, 2000; Nelson et al., 2013a). However, because the subgrid-scales are parameterized, global-scale simulations are necessarily sensitive to the treatment of diffusion, whether it is a numerical diffusion or a renormalized Laplacian diffusion. Nonetheless, global-scale simulations have had many successes in establishing how the solar differential rotation is sustained as discussed below in §3.7, in how magnetic fields may behave in the convection zone (§3.9), and how these fields can have long-term regular cycles as in Chapter 5.

3.7 Global-Scale Solar Hydrodynamics

Although cyclic solutions in 3D nonlinear global-scale dynamo simulations were found thirty years ago in the pioneering convection simulations of Gilman (1983) and Glatzmaier (1985), they were limited to laminar parameter regimes and made little contact with helioseismic observations of the solar differential rotation or with observations of the solar cycle, exhibiting short cycle periods and poleward-propagating dynamo waves. The picture began to change with the development of another anelastic code, which, as with Glatzmaier's code, captures the full spherical shell geometry. The first hydrodynamic models using this new code found that rotationally constrained convection produces correlations in the velocity field that transport momentum and drive mean flows such as differential rotation (e.g., Miesch, 1998), corroborating earlier studies and physical intuition. However, given the rapid growth of computing power since the first global-scale stellar dynamo models, the first models using

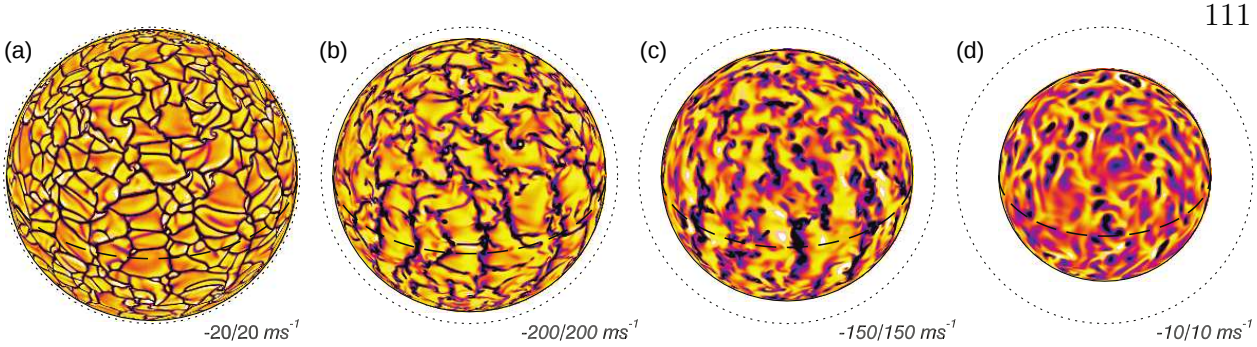

Figure 3.6: A high resolution simulation of solar convection. The changing convective patterns with depth are illustrated through orthographic projections of the radial velocity (v_r), which show giant cells (a) near the upper boundary at $0.98\,R_\odot$ and (b) in the upper convection zone at $0.92\,R_\odot$, and more plume-like flows at (c) mid convection zone ($0.85\,R_\odot$), and (d) near the base of the convection zone ($0.71\,R_\odot$). Adapted from (Miesch et al., 2008).

this new code had 500 times as many grid points and could take 50 times as many time steps for an overall increase of 25,000 in simulation fidelity. Over the last 15 years, there has been an additional increase leading to simulations with again 500 as many grid points compared to the those of Miesch (1998), though the number of time steps taken has only increased by a factor of four.

Under the somewhat more turbulent conditions of the much higher resolution simulations of (Miesch et al., 2000), relative to the Gilman and Glatzmaier simulations of the 1980s, the character of the transport mechanisms becomes increasingly complex, with large-scale coherent vortical structures and mean flows being influenced by small-scale turbulence through inverse cascades. Though, the dynamics of the highly turbulent solar convection zone is likely very different from these and the earlier global-scale numerical models, which are still limited to fairly laminar flows. In some of the first studies with this new code (Miesch et al., 2000), a region of overshoot was admitted by explicitly including a portion of the radiative interior below the convection zone. The convective structures built in the more turbulent simulation reported on in this paper had latitude and depth dependent structure with the mid to low-latitude regions of the simulation being tilted Busse columns or cresentoid cells, which arise in flows with strong rotational constraints. Connected with these

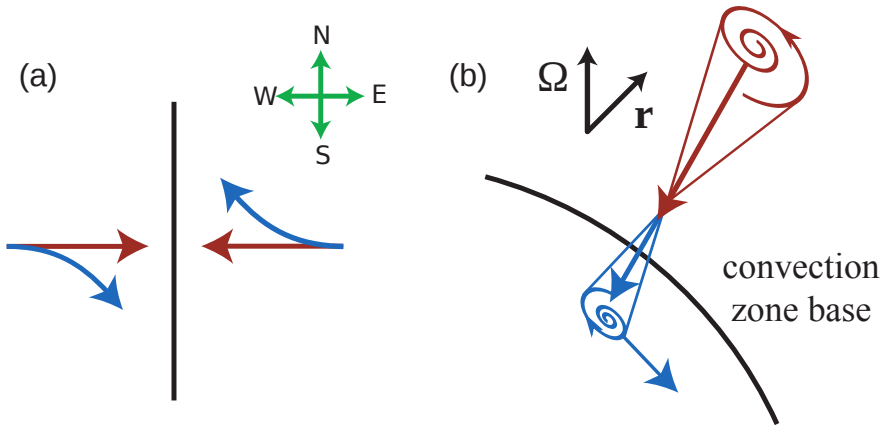

Figure 3.7: Sketches depicting the influence of Coriolis force. (a) Diagram of Coriolis influence on the horizontally converging flow associated with a downflow lane (vertical black line), with westward flows deflected poleward and eastward flows deflected equatorward. (b) Coriolis force acting on the vortical flows of a downflow plume, with cyclonic, converging flows in red and anti-cyclonic, diverging flows in blue [Adapted from Miesch (2005)].

more columnar flows are an intricate and rapidly evolving downflow network in the upper convection zone and plume-like structures at depth and in the overshooting layer. Such structure persists at even higher levels of turbulence and resolution as in Miesch et al. (2008), which details the dynamics of a simulation of solar convection that exhibits the patterns of giant-cells (large-scale eddies with sizes of about 200 Mm) that has a resolution of 256 points in radius, 1024 points in latitude, and 2048 points in longitude. Figure 3.6 displays those convective patterns, with downflow lanes aligned with the rotation axis at low latitudes and more isotropic convection at higher latitudes. The fluctuating kinetic helicity of these convective plumes tend to change sign at mid-convection zone, with the convergent flows in the upper convection zone being cyclonic and those in the lower convection zone being anti-cyclonic (Figure 3.7). Such behavior is evidence of further symmetry breaking, being in addition to the breaking of reflective symmetry by rotation, that is in turn due to density stratification and boundary conditions.

Relative to the local differential rotation established by the convection, the convective patterns themselves tend to propagate prograde at low latitudes and retrograde at high

latitudes. The profiles of the differential rotation established in the simulations of Miesch et al. (2000) and Elliott et al. (2000) show some similarity with helioseismic determinations of the solar rotation, yet, as with the early simulations of Gilman and Glatzmaier, they still exhibited significant cylindrical alignment. Nonetheless, there are significant differences between the dynamics of laminar flow and those in more turbulent regimes largely due to presence of strong, intermittent, vortical downflow lanes and plumes. In particular, the transport of momentum and energy are prominently modified as is the structure of the overshooting layer just below the convection zone (Miesch, 1998; Miesch et al., 2000; Brun & Toomre, 2002). Though these simulations are still quite sensitive to diffusion and the treatment of boundary conditions as described in the thermal Prandtl number studies of Elliott et al. (2000).

One of the goals of simulating the global-scale dynamics of the Sun is to accurately reproduce its differential rotation profile in latitude and radius. Prior to helioseismology, the solar differential rotation had many presumed forms and modeling efforts were geared towards predicting its potential profile. The presumed form of the differential rotation was often cylindrical after the Proudman-Taylor theorem and Gilman and Glatzmaier's simulations. So there was a bit of a theoretical scramble to try attempt to understand why the solar differential rotation is roughly constant on radial lines and has two boundary layers. There have been many attempts over the last 15 years to reproduce these basic features through 3D LES or implicit large eddy simulations (ILES), 2D mean-field hydrodynamics simulations, and analytical models.

Some of the more successful simulations and analytical models are shown compared to the solar profile in Figure 3.8. As mentioned above, the differential rotation achieved in early models and in those without a tachocline prove to have overly cylindrical isorotational contours, such as those in Figure 3.8d. This is known to be due to a lack of a latitudinal entropy gradient large enough to break the Proudman-Taylor constraint (e.g., Weiss, 1964; Thompson et al., 2003; Balbus et al., 2009). This was clearly shown in Rempel (2005), where

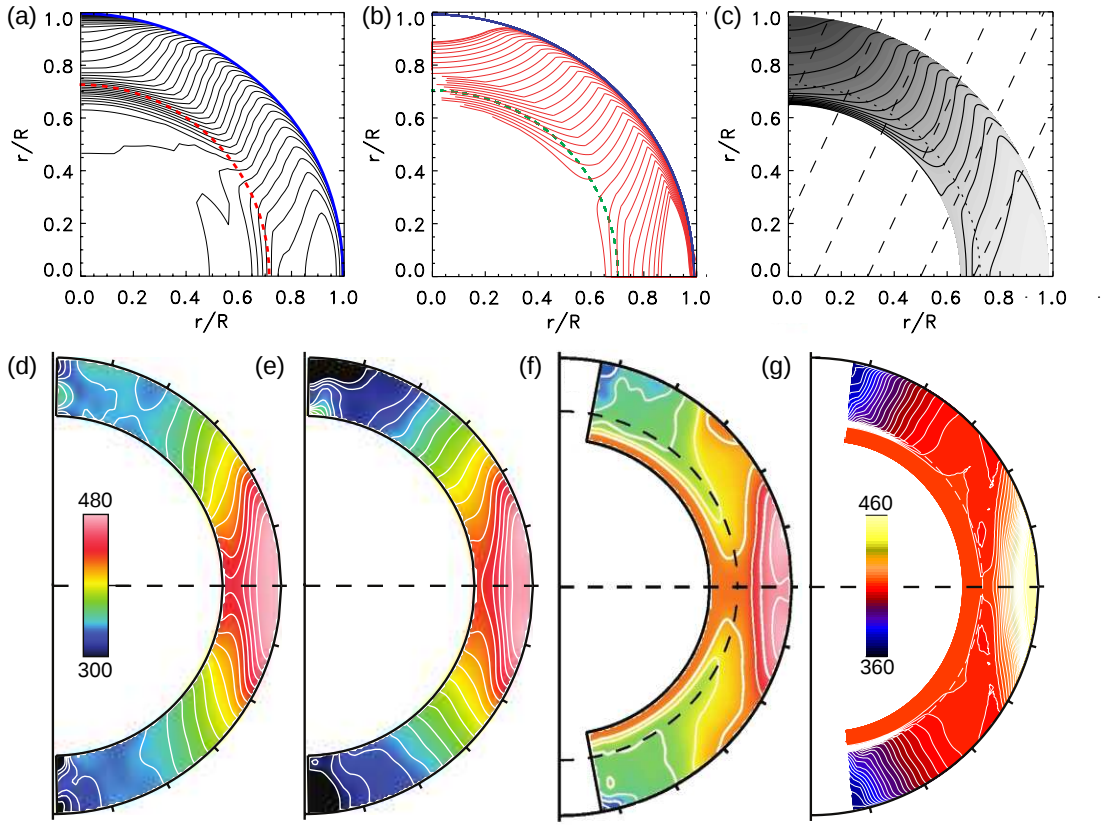

Figure 3.8: Solar differential rotation in observations and theory. (a) Isorotational contours from GONG data, solid blue line denotes the photosphere and the red dashed line the depth of the tachocline (courtesy R. Howe). (b) Isorotational contours from an analytical model, green dashed line indicates the tachocline and the blue curve the photosphere [Adapted from (Balbus et al., 2012)]. (c) Mean-field hydrodynamics simulation of solar differential rotation, dotted line indicates the tachocline and the long-dashed lines conical contours. Differential rotation established self-consistently in 3D simulations using the anelastic spherical harmonic (ASH) code as in (d) case AB from Brun & Toomre (2002), (e) case AB3 after Miesch et al. (2006), and (f) an AB-like case with its tachocline demarked with the black dashed line [Adapted from Browning et al. (2006)]. The colorbar of panel d is shared with panels (e-f). (g) The differential rotation established in an implicit large eddy solar simulation using the EULAG code. The tachocline is marked with a dashed white line [Adapted from Racine et al. (2011)].

2D mean-field models were applied to the solar convection zone and a portion of the subadiabatic radiative zone. The result of these calculations is shown in Figure 3.8c. Rempel found that the profile of the differential rotation is primarily influenced by the morphology of the entropy perturbation that thermally diffuses into the convection zone from the subadiabatic

region resulting. The weakness of the model is that it requires that the lower half of the convection zone to be weakly subadiabatic for good agreement with helioseismology. In the case of a weakly subadiabatic lower convection zone, the solar differential rotation can be explained through entropy perturbations arising from the nonadiabatic stratification. It is more likely, however, that the convection zone is nearly everywhere weakly superadiabatic, or adiabatic, due to the efficiency of convection. If the subadiabatic region has the small extent expected from the narrowness of the tachocline, additional effects such as the anisotropic heat transport advocated by Spiegel & Zahn (1992) are then required. Another important result from Rempel (2005) is that the meridional flow showed very little penetration beneath the base of the convection zone. This can be understood by invoking the concept of gyroscopic pumping, which that states that an angular momentum gradient is directly linked to a vergence in angular momentum fluxes (see Appendix B for details). It is unlikely that there is a significant Reynolds stress in the radiative zone, thus it is likewise unlikely that there is a meridional flow there, except perhaps one driven by the Eddington-Sweet mechanism.

The global-scale simulations presented in Miesch et al. (2006) provide a clear example of how sensitive the solar differential rotation may be to the thermal structure of the tachocline and overshoot region, though without explicitly resolving the penetrative or overshooting convection. Rather, this latitudinal thermal structure is imposed as a boundary condition, which provides information about the impact that a thermal wind balance (the zeroth-order azimuthal vorticity equation) within the tachocline can have on the resulting differential rotation and energy transport. The amplitude of the imposed entropy variations relative to the background entropy is of order 10^{-5}, corresponding to a latitudinal temperature variation of about 10 K. A second caveat is that these simulations also skirt the issue of how the sharpness of the tachoclinic transition impacts the overall character of the differential rotation and thermal structure. This does, however, have the benefit being that there is only a single tunable parameter. Regardless of its approximations, these simulations indisputably confirm that a baroclinic forcing, arising from tachocline-induced entropy variations, can break the

Proudman-Taylor theorem as one might suspect from the conservation of potential vorticity. Indeed, as the amplitude of the imposed variation is increased, initially cylindrical rotation profiles become increasingly conical, with nearly radial angular velocity contours at mid-latitudes (compare Figures 3.8d and 3.8e, for instance). In particular, Miesch et al. (2006) found that the conical rotation profiles are maintained primarily by the resolved convective heat flux, namely that diffusion was dominated by the transport of enthalpic variations from the lower boundary into the convective envelope. This sustains the baroclinicity of the fluid and its solar-like isorotational contours, which is also pointed out in Balbus et al. (2009).

The concomitant simulations of Browning et al. (2006) [and later ones by Brown (2009), Ghizaru et al. (2010), and Strugarek et al. (2011)] included the dynamics of a stable layer below the solar convection zone, which were attempted despite the formidable challenge that the conditions there pose to global convection simulations. To be specific, a high spatial and temporal resolution is required in and near the tachocline to reliably capture the relatively small-scale dynamics associated with convective overshoot, tachocline instabilities, internal waves, and other phenomena such as the magnetic boundary layers associated with some tachocline confinement models (e.g., Rüdiger & Kitchatinov, 1997; Gough & McIntyre, 1998; Wood et al., 2011). The global-scale 3D anelastic simulation of Browning et al. (2006) illustrated that most of the downflowing plumes overshoot into the underlying radiative region, where they are buoyantly braked. Due to the relatively high diffusivities of these simulations a strong differential rotation is established by the convection, which tends to hide the difficulties with the bistability of the latitudinal entropy gradients as the simulation attempts to establish a solar-like differential rotation in the presence of a stable region (private communication with N. Featherstone & B. Brown). Moreover, the tachocline was mechanically forced by artificially damping the angular velocity below the tachocline, which serves to prevent the diffusive spread of the layer.

Figure 3.8f depicts the mean angular velocity Ω with radius and latitude established by the convection of Browning et al. (2006). Within the bulk of the convection zone, there

is the expected increase of Ω from the pole to the equator. In comparison to Miesch et al. (2006), which had no penetrative region, the angular velocity contrast between the pole and the equator in Browning et al. (2006) is reduced and the isorotational contours are more cylindrical. Below the base of the convection zone (at $\sim 0.71\,R_\odot$), where the stratification is highly subadiabatic, Ω adjusts rapidly to uniform rotation due to the mechanical forcing. Nonetheless, the simulations of Miesch (1998) and Browning et al. (2006) represent the first attempts at including a stable layer below the convection zone in a high resolution global model, and they do a reasonable job at establishing a solar-like differential rotation. The recent simulations of a model solar convection zone using the ILES EULAG code also include a stiffly stratified stable region and due to the low dissipation of the numerical model the tachocline is prevented from spreading (Ghizaru et al., 2010; Racine et al., 2011). Figure 3.8g shows the differential rotation established in this MHD simulation, which like many of the anelastic models shows fairly cylindrical isorotational contours at low latitudes. The difference however is the conical alignment of the contours above about $\pm 45^\circ$ which more closely match the solar profile and the profile established in case AB3 from Miesch et al. (2006). However, there are issues with energy conservation within the anelastic approximation in regions with a stiff stable stratification as seen in Brown et al. (2012), Vasil et al. (2013), and Chapter 10.

A significant recent result is the construction of an analytical model describing the solar rotation profile (and perhaps the profiles of other main-sequence stars) that obeys a simple set of equations. The basic result of this model, as shown in Figure 3.8b, is that it appears much of the bulk dynamics of the solar convection zone may be governed by a reduced form of the vorticity equation, known as the thermal wind equation (e.g., Weiss, 1964; Thompson et al., 2003; Balbus et al., 2009). Though there are many more terms in this equation, one that may be the most important in the solar convection zone involves a balance between the cylindrical gradient of the square of the angular velocity and accelerations due to the misalignment of isopycnal and isobaric surfaces, the latter arising from latitudinal entropy

gradients, or mathematically $\lambda\partial_z\Omega^2 = g/\gamma r\partial_\theta S$, where λ is the lever arm from the rotation axis, g is gravity, and γ the adiabatic exponent.

Obviously, if both the angular velocity and the entropy are unknown, the thermal wind balance is underdetermined. However, the Balbus conjecture is that the entropy and angular velocity are nonlinearly and apriori related, which sidesteps the underdeterminedness of the thermal wind equation. For instance, it is noted in Balbus (2009) that, if the isentropic and isorotational surfaces are aligned or anti-aligned, a subset of magnetized baroclinic modes are marginally stable, those whose Alfvén speeds are slower than the fluid motions. However, the exact matching of the entropy and angular velocity surfaces in that case would quench any convection. The alternative is to take the hydrodynamic approach, which is less restrictive due to the gauge independence of the entropy thermal wind equation, where an arbitrary function of radius can be subtracted from the total entropy (Balbus et al., 2009). This allows the residual entropy to be separated from the mean entropy, whose gradient is responsible for much of the energy transport. The physical basis for this argument rests on the assumption that convective flows transport energy and momentum along surfaces of constant residual entropy, which then renders the total entropy profile effectively fixed in time, which the simulations of Miesch et al. (2006) corroborate. Hence there is no restriction on the radial gradient on the total entropy, which means convection can be quite vigorous as long as it is not so vigorous as to break the underlying assumption of the alignment of residual entropy and rotational surfaces. The last statement points out one weakness of the theory, with another being the exclusion of dynamo action and magnetic feed backs. Of greater import, one can ask how does the alignment of the residual entropy and rotational isosurfaces arise to being with, and how is it maintained. The results are necessarily dependent upon the boundary condition, which is the helioseismic data and thus the thermal wind equation is clearly not a unified theory of the solar differential rotation.

A recent paper set out to explore how such a relationship between the convective transport and the isentropic and isorotational surfaces is maintained (Balbus et al., 2012; Balbus

& Schaan, 2012). A surprising finding in this paper is that by using a fairly general calculation using linearized Lagrangian equations there is to leading order no poleward deflection of warm (relative to the background) fluid elements in the presence of a bulk rotation. Rather, it seems, such deflections occur only when a cylindrical gradient in angular velocity is already present. Though, this simply means the nonlinear transport terms must be acting when there is not yet a substantial angular velocity gradient, such as when a star is young, rotating rapidly, and thus possessing cylindrical isorotational surfaces. However, the results of Balbus & Schaan (2012) point out that once such a gradient is in place it is self-reinforcing and is to leading order the dominant dynamical process. The second point made in the paper has bearing on the order of magnitude of various processes, namely that the latitudinal entropy perturbations and the centrifugally induced baroclinicity in the tachocline are of the same order and as such the latter should not be neglected. They cite this latter processes as the origin of the vorticity necessary to promote the alignment of the residual entropy surfaces and the isorotational surfaces, though it could be suggested instead that a slight misalignment of these surfaces could produce sufficient nonlinear poleward enthalpy transport to sustain their near alignment. The latter processes is what occurs in the global-scale 3D numerical simulations and is certainly one of their salient features. Thus the equilibrium entropy and rotational profiles will depend sensitively upon the details of the convection, and chiefly upon how rotationally constrained it is. Yet once cylindrical gradients in the angular velocity form, according to Balbus & Schaan (2012), the differential rotation becomes almost self-sustaining, requiring only a weak source baroclinicity or vorticity. It will necessarily also evolve slowly with time as angular momentum is lost through stellar winds and magnetic breaking.

3.8 An Extension of Balbus' Theory

One potential extension of Balbus' theory, beyond what was expressed in Balbus & Latter (2010), is to include the latitudinal pressure gradient contribution to the thermal wind, in

order to better capture the tachocline and the stable region. The starting point for this is to assume the fluid is hydrostatic over a long time average, with bulk flows of meridional circulation and differential rotation that vary only in meridional planes (no azimuthal variation). If the meridional circulation is considered a first-order effect, the zeroth-order momentum equation, which includes the differential rotation, and the longitudinal component of its curl are

$$\boldsymbol{\nabla} P = -\rho \mathbf{g} + \lambda \Omega^2 \hat{\boldsymbol{\lambda}}, \tag{3.56}$$

$$\lambda \frac{\partial \Omega^2}{\partial z} = -\frac{1}{r\rho^2}\left[\frac{\partial P}{\partial \theta}\frac{\partial \rho}{\partial r} - \frac{\partial P}{\partial r}\frac{\partial \rho}{\partial \theta}\right] = \frac{1}{r\rho c_P}\left[\frac{\partial P}{\partial \theta}\frac{\partial S}{\partial r} - \frac{\partial P}{\partial r}\frac{\partial S}{\partial \theta}\right], \tag{3.57}$$

where the latter equation assumes an ideal gas with a radially varying pressure specific heat c_P, $\Omega(r,\theta)$ is the angular velocity $\mathbf{g}$ is assumed spherically symmetric and in the radial direction, $\lambda = r\sin\theta$, and $z = r\cos\theta$. A more thorough derivation of the averaged zonal vorticity equation can be found in Appendix B.3. The next step is to simply insert Equation 3.56 into Equation 3.57, yielding the simplified thermal wind equation

$$\begin{aligned} \lambda \frac{\partial \Omega^2}{\partial z} &= \frac{1}{c_P}\left[\lambda \cos\theta \Omega^2 \frac{\partial S}{\partial r} + \frac{1}{r}\left(g - \lambda \sin\theta \Omega^2\right)\frac{\partial S}{\partial \theta}\right], \\ c_P \lambda \frac{\partial \Omega^2}{\partial z} &= \lambda \Omega^2 \frac{\partial S}{\partial z} + \frac{g}{r}\frac{\partial S}{\partial \theta}. \end{aligned} \tag{3.58}$$

The concept upon which this fairly simple theory rests is the Balbus conjecture. This hypothesis states that $S(r,\theta) = f(\Omega^2) + \overline{S}(r)$, namely isentropes and isorotational surfaces are aligned to within an additive function. In Balbus' theory, this amounts to a gauge freedom. Here, however, the radial entropy gradient has been retained and this symmetry is lost, though the gauge freedom in Ω still remains at this stage. Thus Equation 3.58 can be simplified to

$$\lambda\left(c_P - f'\left(\Omega^2\right)\Omega^2\right)\frac{\partial \Omega^2}{\partial z} = \lambda \cos\theta \Omega^2 \sigma + \frac{g f'\left(\Omega^2\right)}{r}\frac{\partial \Omega^2}{\partial \theta}, \tag{3.59}$$

with $f'(\Omega^2) = df/d\Omega^2$ (so transforming the entropy gradients into derivatives in Ω) and $\sigma(r) = d\overline{S}/dr$. Note that here the full nonlinearity due to the centripetal acceleration is retained. For analysis, it is prudent to further reduce the notation to

$$\lambda \left(c_P - q' \left(u \right) \right) \frac{\partial u}{\partial z} = \lambda \cos\theta \Omega^2 \sigma + \frac{g e^{-u} q' \left(u \right)}{r} \frac{\partial u}{\partial \theta}, \tag{3.60}$$

where $u = \ln \Omega^2$ and $q'(u) = df(e^u)/du$. The final simplification is to convert to spherical coordinates and minimize the number of terms, wherein the previous equation becomes

$$\frac{\partial u}{\partial r} - \left(\frac{\tan\theta}{r} + \frac{g e^{-u} q'}{r^2 \sin\theta \cos\theta \left(c_P - q' \right)} \right) \frac{\partial u}{\partial \theta} - \frac{\sigma}{c_P - q'} = 0. \tag{3.61}$$

This is a highly nonlinear equation for the logarithm of the angular velocity u, and in general could be difficult to solve. The trick is to find a characteristic solution, which reduces this partial differential equation into an ordinary differential equation (ODE) along a particular path. The broader theory of implicit functions and the Lagrange-Charpit equations could be appealed to, but that is unnecessary in this case. It is sufficient to note that we can define a function $F(r, \theta, u, \frac{\partial u}{\partial r}, \frac{\partial u}{\partial \theta}) = 0$ that encapsulates Equation 3.61. Since we are only interested in the morphology of the characteristics, the solution along such paths that are equipped with a distance metric s reduces to

$$\frac{dr}{ds} = 1, \tag{3.62}$$

$$\frac{du}{ds} = \frac{\sigma}{c_P - q'}, \tag{3.63}$$

$$\frac{d\theta}{ds} = -\frac{\tan\theta}{r} - \frac{g e^{-u} q'}{r^2 \sin\theta \cos\theta \left(c_P - q' \right)}. \tag{3.64}$$

This system of characteristic ODEs exposes an issue, namely that the characteristics are no longer coincident with the isotachs, which arises because $du/ds \neq 0$. It is worth noting, however, this is not a problem in regions that are adiabatic. Such regions are the domain of Balbus' solutions, though here it is still extended to the nonlinear case and with a nonconstant c_P. As such, let us first find the equations for an adiabatic convection zone. First, note the equivalency between dr and ds and that $du/ds = 0$ when $\sigma = 0$ and for sensible values of $c_P - q'$. Thus, following a multiplication by $2r^2 \sin\theta \cos\theta$, the above system simplifies to characteristics along isotachs with

$$\frac{d\lambda^2}{dr} = -\frac{2ge^{-u}q'}{(c_P - q')}. \tag{3.65}$$

Since $du/ds = 0$, all terms involving u are constant along these curves and can be incorporated into a single constant $\beta(r_0, \theta_0, u(r_0, \theta_0))$ that depends only upon the initial position (r_0, θ_0) of a given characteristic. Hence, the general solution for the curve is

$$\lambda_0^2 - \lambda^2 = -\beta \int_r^{r_0} \mathrm{d}r \frac{g\,(r)}{(c_P\,(r) - q'\,(u_0))}. \tag{3.66}$$

This can be rendered independent of the choice of $q(u)$, which arises from the nonlinearity of the centripetal terms, in the limit that $q' \ll c_P$. This constraint is almost certainly true everywhere in the solar convection zone since the perturbations associated with the thermal wind are about one part in 10^5. Thus the above equation simplifies to

$$\lambda_0^2 - \lambda^2 = -\beta \int_r^{r_0} \mathrm{d}r \frac{g}{c_P} \approx B\left[1 - \frac{r_0}{r}\right]. \tag{3.67}$$

under the assumption that $g \propto r^{-2}$ and that $c_P = $ const. for the latter equation. Indeed, Balbus' solutions can be fully recovered after a division by r_0^2 and subtracting the equation from unity, as $\cos^2\theta_0(r, \theta; r_0) = 1 - r^2/r_0^2 \sin^2\theta - B\left[1 - \frac{r_0}{r}\right]$. This equation is then substituted into an appropriate fit to a rotation profile such as the common form for the Sun (e.g., $\Omega = a_0 + a_1 \cos^2\theta_0 + a_2 \cos^4\theta_0$), an example of which can be seen in Figure 3.9c. It is clear from Equation 3.67 that, if c_P varies significantly across the domain as it does in the solar convection zone due to the latent heats of ionization, there may be modifications in the rapidity with which the term involving β becomes negligible as the near-surface shear layer and the photosphere are approached from below. This is indeed what is found, though it has a minimal impact on the resulting profiles of the differential rotation. It is, however, a further indication that a thermal wind is restricted in validity to regions where turbulent stresses are small, which is not the case in the upper convection zone (see Appendix B, Miesch & Hindman (2011), and Balbus et al. (2012)).

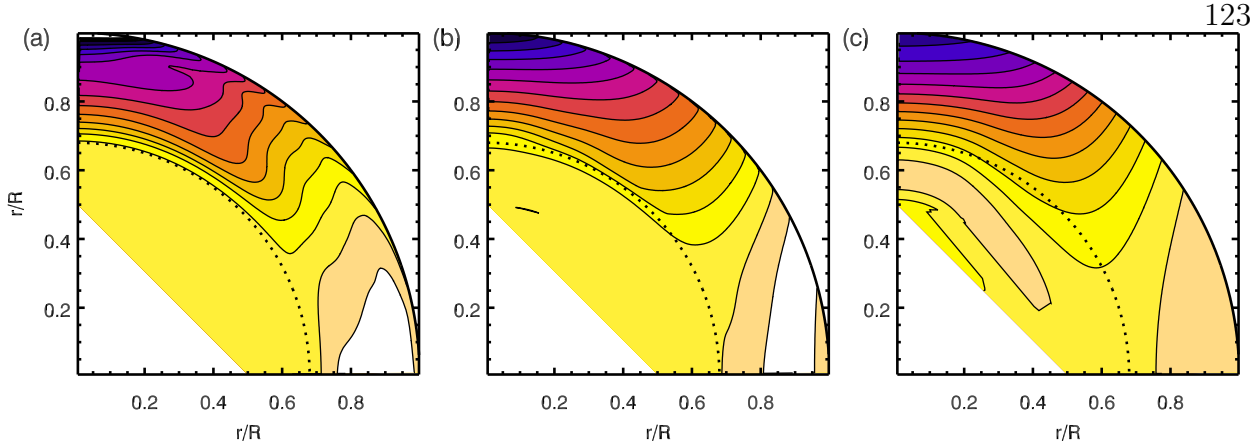

Figure 3.9: Solar differential rotation from helioseismic observations and theoretical isotachs. (a) Isorotational contours from a regularized least squares (RLS) inversion of the first 144 days of MDI data (publicly available at http://quake.stanford.edu/m̃jt/rls-mdi/; M. Thompson and R. Howe, 1997), solid black line denotes the photosphere and the dashed line the depth of the tachocline. (b) Isorotational contours from the analytical model that includes the effect of entropy gradients on the thermal wind (Equation 3.72). (c) The differential rotation resulting from Balbus' original thermal wind model as in Equation 3.67.

The intent now is to explore what happens when there is a significant mean radial entropy gradient, as in the radiative interior of the Sun. In this case, as seen in Equation 3.63, the characteristic solution does not precisely correspond to an isorotational contour. Rather, such curves are constant along isentropes modified by the pressure specific heat and by the form of the functional relationship between the angular velocity and the entropy. However, much can be improved by simply including the lower-order terms arising from the mean entropy gradient. If the centripetal terms are neglected, save for the mean entropy gradient term, the equations become

$$\lambda c_P \frac{\partial u}{\partial z} - \frac{g f'}{r} \frac{\partial u}{\partial \theta} = \lambda \cos\theta \sigma. \tag{3.68}$$

Thus the characteristic equations are then

$$\frac{du}{dr} = \frac{\sigma}{c_P}, \tag{3.69}$$

$$\frac{d\theta}{dr} = -\frac{\tan\theta}{r} - \frac{g f'}{r^2 c_P \sin\theta \cos\theta}. \tag{3.70}$$

Following the procedure above, this can be simplified to

$$\frac{d\lambda^2}{dr} = -\frac{2gdf/dr}{\sigma}. \tag{3.71}$$

Moreover, if $f'(u)$ is expanded in powers of the ratio of the mean entropy gradient over the pressure specific heat as $f' = \sigma/c_P \sum_k b_k(u_0)(\sigma/c_P)^k$, contact can be made with Equation 3.67, with

$$\lambda_0^2 - \lambda^2 = -\sum_{k=1}^{\infty} b_k \int_r^{r_0} \mathrm{d}r \frac{g\sigma^{k-1}}{c_P^k}. \tag{3.72}$$

The first term in the series corresponds to Equation 3.67, whereas the higher-order terms account for the entropy stratification. In fact, if only the second and third-order terms are retained, the fit to the differential rotation improves in the tachocline as one would expect given the rapid increase in the entropy gradient there (Figure 3.9b). This improves upon the ad hoc construction of tachoclinic isorotational contours in Balbus et al. (2012), though here omitting the near-surface approximation made in that paper.

3.9 Global-Scale Solar Magnetohydrodynamics

Having examined some of the basic principles of how differential rotation is built and maintained and examined how accurately global-scale models can capture such hydrodynamics, the topic of global-scale dynamo simulations in a solar setting must be addressed. To date, several different numerical models of solar convective dynamos have achieved cyclical polarity reversals, whether or not a tachocline is present. In all cases of such cycling global-scale dynamos, the interaction of convection, rotation, and magnetism are crucial ingredients. Though, precisely how the mechanisms are arranged so that a solar-like differential rotation can be maintained, and simultaneously yield a large-scale, periodic dynamo, has yet to be ascertained. Indeed, how the multiply-scaled convection of a thermaly driven system, like the Sun, sempiternally maintains a global-scale kinetic helicity and sustains the massively disparate scales of the Sun's magnetism is seemingly a mystery.

The earliest attempts to address these issues with global-scale solar dynamo simulations were those of Gilman and Glatzmaier, who used an anelastic and spherical harmonic based spectral code to simulate the dynamics (Glatzmaier, 1984) rather than the finite difference Boussinesq scheme of Gilman & Glatzmaier (1981). Gilman laid out a series of simulations in a 1983 Astrophysical Journal Supplement paper that aimed at assessing how varying the magnetic Prandtl number Pr_m and the rotation rate modified the character of the resulting dynamo. In general, it was found that magnetic cycles are a common feature, provided that there is sufficient energy in the bulk toroidal fields and that the Lorentz force feedback on the established differential rotation was not too large. Moreover, Gilman also noted that there is little preference for symmetry or anti-symmetry about the equator and that the toroidal bands of magnetic field tended to propagate toward the poles. It was also found that, for a fixed Rayleigh number (ratio of thermal driving to diffusion), Taylor number (ratio of the Coriolis force to viscous diffusion), and thermal Prandtl number (ratio of viscous to thermal diffusion), there is a peak dynamo efficiency with $Pr_m \sim 1$. For Pr_m below unity, the efficiency reached a plateau and for those cases with Pr_m above unity it decreased.

Yet the mismatch between those early simulations and helioseismic inferences effectively ended that line of investigation for about 15 years. A similar approach to simulating global-scale dynamos was, however, restarted roughly around 2004 with the inclusion of magnetic fields into the anelastic spherical harmonic (ASH) code (see Chapter 4 and Brun et al. (2004); hereafter B4). These 21st century global-scale convective solar dynamo simulations were carried out at moderate Pr_m, ranging between 2 and 4. Hence it was much more difficult for a large-scale dynamo to take hold. In keeping with that notion, the fluctuating fields dominated the magnetic energy, accounting for most of the back-reaction on the flow via Lorentz forces, whereas the mean fields were relatively weak. There were also no hints of periodic reversals or dynamo wave behavior. Again as expected with a large Pr_m dynamo, the magnetic fields exhibit a complex and small-scale spatial structure and highly-variable time evolution. The radial magnetic field is swept into the downflow lanes, being stretched

and folded there before reaching the resistive scale and reconnecting. The toroidal fields are organized into somewhat larger scales near the equator appearing as twisted ribbons, whereas they form smaller scales at higher latitudes (Figure 3.10a). In B4, it was also found that the convection maintained a solar-like angular velocity profile despite the influence of Maxwell stresses, which tend to extract energy from the differential rotation and thus reduce its contrast throughout the convection zone.

The next logical step was to include a stable region and to emulate a tachocline in order to assess its impact upon the global-scale dynamo (Browning et al., 2006). This simulation also employed the ASH code and its hydrodynamics are discussed above in §3.7. Both this simulation and that of B4 were fairly laminar with respect to the scales present in the velocity field. The dynamo action achieved in the convection zone of this simulation is also quite similar to the earlier calculation of B4, though with an even larger Pr_m. Thus, as one might expect the scales of magnetism become much smaller than the scales of the convection (Figure 3.10b), with the bulk of the magnetic energy appearing in the fluctuating magnetic fields and very little in the mean fields within the convection zone. The major difference between the dynamo action present in this simulation, as compared to that B4, is that the stable region provided a reservoir for storing magnetic energy and the tachocline may have provided a means of generation of large-scale magnetic field. Indeed, within the stable region, large-scale fields were able to persist, with the majority of the energy being in the mean magnetic fields. However, there was as yet no large-scale structure that might be able to appear at the surface (i.e. no magnetically buoyant structures) nor were there any cyclical polarity reversals.

Rapid progress over the last four years have confirmed the role that convection and rotation likely play in stellar dynamo action through global-scale dynamo simulations as well as suggested additional mechanisms that may be present in the solar dynamo. Several research

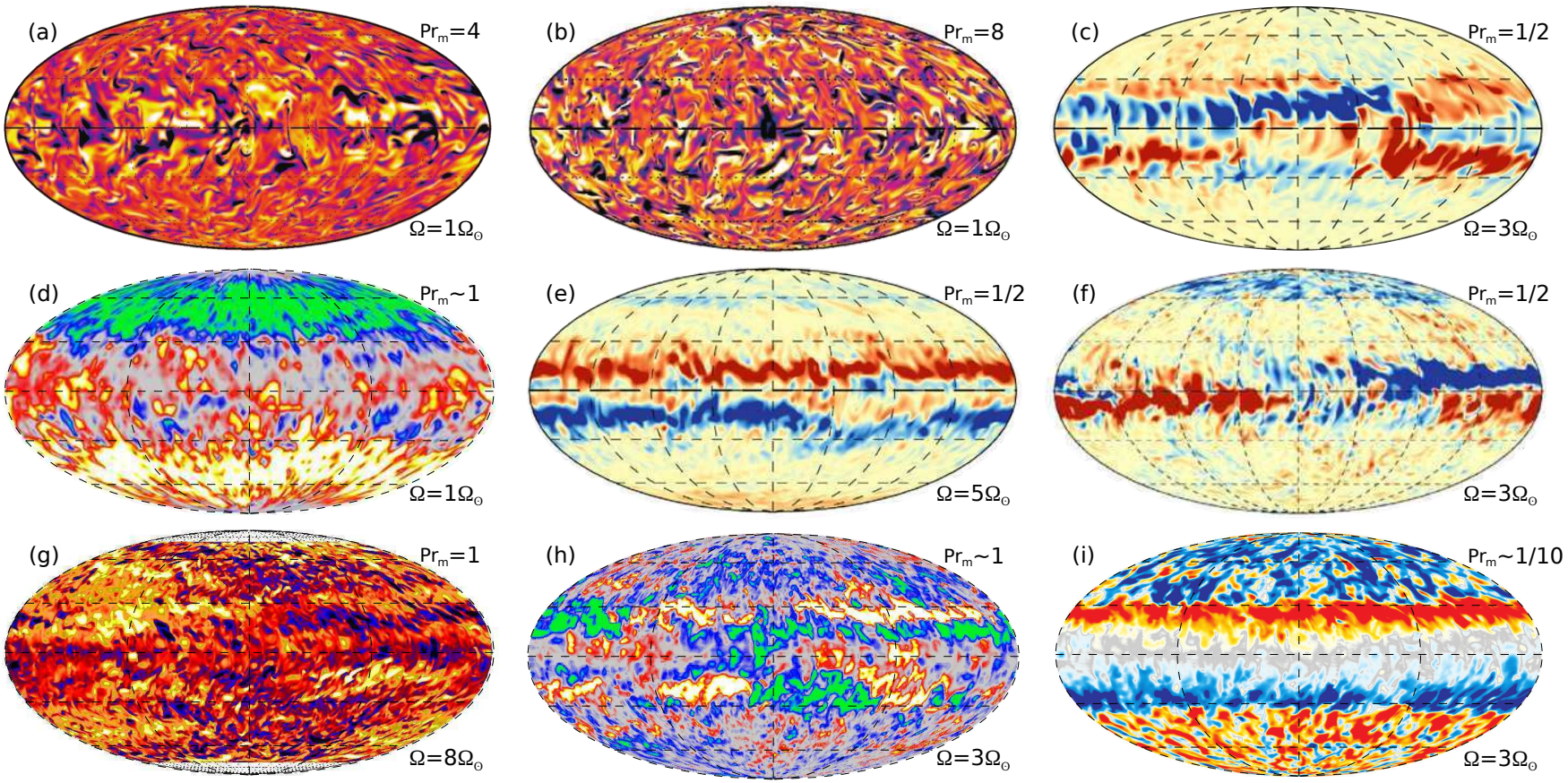

Figure 3.10: Modern 3-D global-scale convective dynamo simulations, showing snapshots of their toroidal magnetic fields in Mollweide projection. The effective magnetic Prandtl number (Pr_m) and rotation rate Ω of each simulation is indicated. (a) First dynamo simulation using ASH (Brun et al., 2004). (b) ASH simulation with a tachocline (Browning et al., 2006). (c) Large-scale, persistent toroidal structures dubbed wreaths maintained amidst moderately turbulent convection at lower Pr_m (Brown et al., 2010). (d) EULAG solution with regular decadal-time-scale magnetic reversals (Racine et al., 2011). (e) ASH simulation with quasi-periodic reversals (Brown et al., 2011b). (f) Recent continuation of (c) with lower diffusion and higher resolution. The greater levels of turbulence permits quasi-periodic cycles to emerge (Nelson et al., 2013a). (g) Cyclic dynamo solution with the Pencil code, showing wreath formation in a spherical segment (Käpylä et al., 2013). (h) EULAG solution rotating at $3\,\Omega_\odot$, for comparison with (c), (f), and (i) at the same rotation rate (Charbonneau, 2013). (i) Recent simulation using slope-limited diffusion in ASH exhibiting very regular cycles (see Chapter 5). Typical toroidal magnetic field strengths are between 1 and 10 kG in these simulations, with sense of fields suggested by color.

teams have concurrently made inroads into solar dynamo theory utilizing three distinct numerical techniques, but nonetheless realizing similar dynamo action. The Anelastic Spherical Harmonic (ASH) code has provided a framework for constructing and understanding the dynamos that produce and sustain coherent toroidal fields exhibiting quasi-cyclic behavior. The Eulerian-Lagrangian (EULAG) code has shown that solutions with very regular cycles can be achieved within its implicit large eddy simulation (ILES) framework. Third, the Pencil code that simulates compressive convection has also found cyclical solutions with large-scale toroidal field structures within its spherical wedge geometry.

The first 3D nonlinear convective dynamo simulation, beyond those of Gilman and Glatzmaier in the 1980s, that indicated that sustained large-scale toroidal magnetic field structures could be built within the solar convection zone was presented in Brown et al. (2010). A snapshot of this solution's toroidal magnetic field is shown in Figure 3.10c and its evolution is shown in Figure 3.13a. The persistence of such structures had previously been thought impossible, as one might expect that the highly turbulent convection should rapidly eviscerate it, transporting the magnetic flux to the boundaries of the domain. What separated this simulation from those undertaken a few years earlier was its higher rotation rate (or lower Rossby number) and its lower Pr_m, being about 16 times smaller. The salient point that this simulation brings forth was that the rate of generation of magnetic field through the mean shear of the differential rotation could overpower the rate of its destruction by convection and dissipation. Indeed, the convection instead acts to sustain the differential rotation through Reynolds stresses, which indirectly aids in the generation of the toroidal fields. The convection then in turn converts the toroidal field into poloidal field, creating a positive feedback loop that sustains the wreaths against resistive decay. Although this simulation hinted that perhaps fields could be sustained within the solar convection zone, it still did not have cyclical behavior. Furthermore, it was still quite laminar, so the ability to sustain such large-scale magnetic field structures at greater levels of turbulence and increased complexity of the velocity field was still in question.

That question was partly answered in concurrent dynamo calculations utilizing the EULAG code. The ILES implementation of this code allows it to minimize the impacts of diffusion and achieve more complex velocity and magnetic fields at a given resolution than ASH can achieve. The solar dynamo modeled with this computational framework exhibited many multi-decadal cycles of roughly 40 years that were quite regular and persisted for roughly 500 years of evolution despite the fairly complex flow fields permitted by the low numerical diffusion (Ghizaru et al., 2010; Racine et al., 2011). A snapshot of the toroidal magnetic field from this simulation is shown Figure 3.10d and its character in time and latitude is illustrated in Figure 3.13e. The turbulent EMF in these simulations is more amenable to a mean-field theory description than the earlier ASH simulations, which may in part be due to the greater complexity of the velocity field. Part of the reason for the greater agreement between these dynamos and mean-field theory may lie in the simple argument that as the number of convective cells becomes increasingly large the average poloidal magnetic field generation may approach a mean value. Such a characteristic might be expected if the averaging operator obeys the central limit theorem, or if the arguments given in Parker (1955) hold.

Further exploration of the rotation rate and Pr_m parameter space using the ASH code continued apace, with a quasi-periodic cycling dynamo solution published in Brown et al. (2011b) and a multitude of solutions explored in (Brown et al., 2011a). The toroidal fields of the cycling solution are shown in Figure 3.10, exhibiting the high degree of longitudinal connectivity that can be achieved within a low-Pr_m global-scale dynamo and also lending credence to their moniker of wreaths. These fields form at or near the regions of the greatest latitudinal shear in the differential rotation, which is why they tend to be generated closer to the equator. Such characteristics can be seen in several of the dynamo solutions from Brown et al. (2011a) as shown in Figures 3.13a–d. The dynamo behaviors exhibited within the menagerie of simulations in this latter paper seem to roughly correspond to the regimes described in Gilman (1983), as is illustrated in Figure 3.11. The Gilman picture suggests

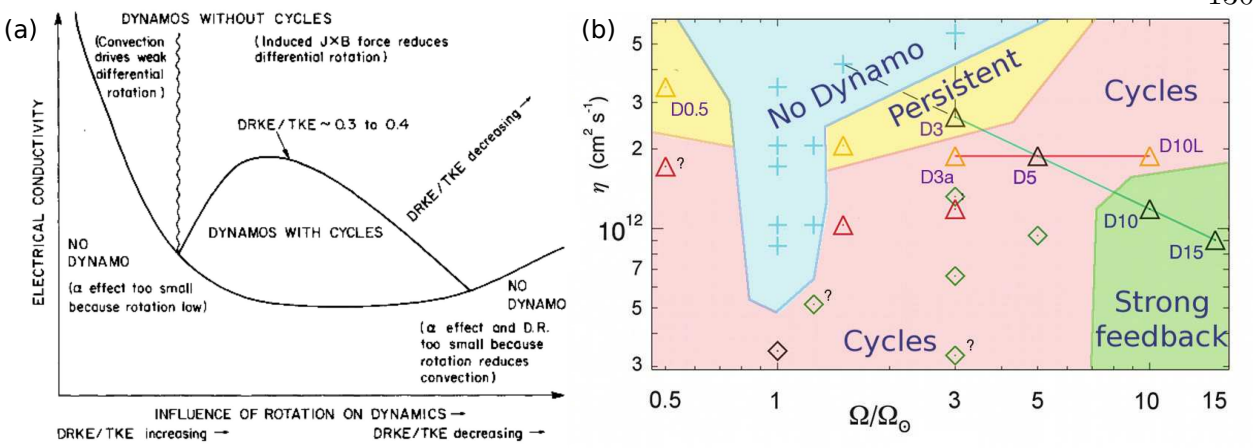

Figure 3.11: (a) A sketch of possible dynamo regimes with rotation rate and electrical conductivity, illustrating the cycling and persistent dynamo regimes as well as those without sustained dynamo action [adapted from Gilman (1983)]. (b) A set of numerical dynamo experiments carried out with varying Prandtl numbers and rotation rates, exhibiting many of the behaviors predicted in Gilman (1983) and some that were not, particularly at low rotation rate [adapted from Brown et al. (2011a)].

that, as the magnetic diffusivity is reduced, dynamo action becomes increasingly likely and that cycles become more likely over a small region. Eventually, however, Lorentz-force feedback quenches both the convection and differential rotation. Similarly, as the rotation rate is increased, cycles become more likely to a point and then past this threshold they become less likely due to the rotational suppression of convection. Yet another set of simulations that sought to determine the influence of the density scale height and convective driving has recently been carried out that finds distinct transitions between dipolarity, multi-polarity, and cyclic dynamos (Gastine et al., 2012), though in less of a solar context. Indeed, they found that their anelastic dynamo models produced a broad range of magnetic field geometries, with dipolar configurations for the least stratified and most rapidly rotating and a gradual transition to multipolar configurations if either the stratification or the rotation rate was increased. As the density stratification is increased the convective columns in their simulations become increasingly concentrated in a thin boundary layer near the upper boundary and at low latitudes. Such patterns of convection tended to be non-axisymmetric solutions.

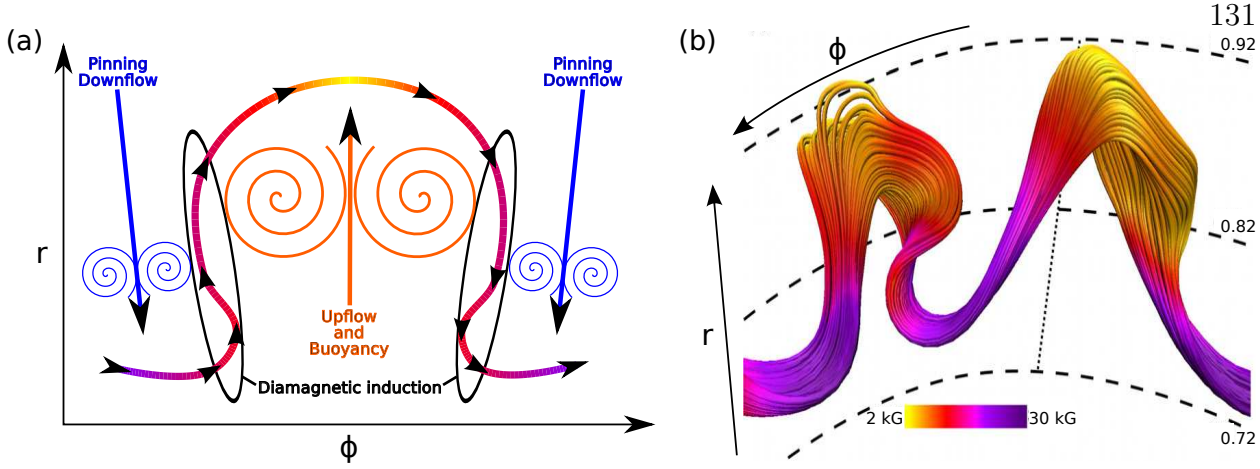

Figure 3.12: (a) A sketch of the processes leading to magnetic loop formation in ASH simulations with dynamic Smagorinski: downflows pin the foot points of the loops, shear between the upflow and downflow builds a large magnetic diffusivity gradient at the edge of the loop leading to diamagnetic induction that builds radial field of the correct sign, while advection and buoyancy lift the inner section of the toroidal field. (b) Two magnetic loops achieved in an ASH simulation utilizing a dynamic Smagorinski scheme shown in a field line rendering [adapted from Nelson et al. (2011)].

Furthermore, in multipolar solutions, zonal flows became more significant and led to the production of toroidal field through the Ω-effect. In those cases, dynamo waves seemed to then play an important role, leading to polarity reversing dynamos. The cycle frequency of those dynamos was

$$\omega \approx \left[\frac{\alpha}{D}\frac{du_{\rm rms}}{dr}\right]^{1/2}, \tag{3.73}$$

where α is roughly related to the kinetic helicity, and D is the depth of the domain.

Continuing the rapid pace in solar dynamo modeling and under the assumptions of dynamic Smagorinski, mildly buoyant magnetic structures have been realized in a cycling dynamo simulation (Figure 3.12; Nelson et al., 2011, 2013a). In this fortuitous simulation, the dynamic Smagorinski diffusion permits a greater degree of turbulence than can be achieved in the eddy viscosity model. It helps to establish a pattern of quasi-buoyant magnetic structures that form within the convection zone, which is in contrast to the common wisdom that they could only form in the tachocline as suggested in Parker (1993). Regardless of how

these structures come about, they tend to have statistics strikingly similar to the statistics of solar observations regarding Joy's and Hale's laws (Nelson et al., 2013b). These magnetic structures arise from the structure of the flow field, natural buoyancy, and partly from diamagnetic processes. The latter process has not yet been fully considered, so the logic of it will be expanded upon a bit here. The downflows help to pin down the foot points of the loop-like magnetic fields, whereas the upflow between two downflows advects a portion of the magnetic field toward the upper boundary of the simulation. The natural magnetic and thermal buoyancy of the structure further boost the forces compelling it to rise. Typically, there are downflows at the edges of the loop and upflow in its interior, so there is a strong velocity shear present at the boundaries of the loop. The dynamic Smagorinski diffusion coefficient is proportional to this shear and the magnetic diffusivity is simply the magnetic Prandtl number multiplied by this coefficient. Since the coefficient is proportional to the local shear, it is highly variable in space, increasing by at least an order of magnitude near the shearing interface of the upflows and downflows. At low latitudes where the convection is columnar and aligned with the rotation axis, the variation in the coefficient is largely radial and longitudinal. Two features consequently promote the formation of loops at low latitudes; one is the induction due to the mean shear acting on poloidal fields that builds strong toroidal fields there; the second is the strong longitudinal variation of the magnetic diffusion coefficient. The diamagnetic term is the cross product of the electric current with the gradient of the magnetic diffusivity. Under the circumstances arising in these simulations, the morphology of the electric current and the diffusivity gradient are arranged such that the diamagnetic induction reinforces a net positive growth of the radial magnetic field along the interfaces of upflows and downflows.

Other recent convective dynamo simulations carried out in spherical segments with the Pencil code have also manifested unprecedented magnetic self-organization, with strong mean field generation in nonlinear dynamo regimes, and cyclic activity on decadal time scales (Figure 3.10g; Käpylä et al., 2012). There have been more recent simulations that also ex-

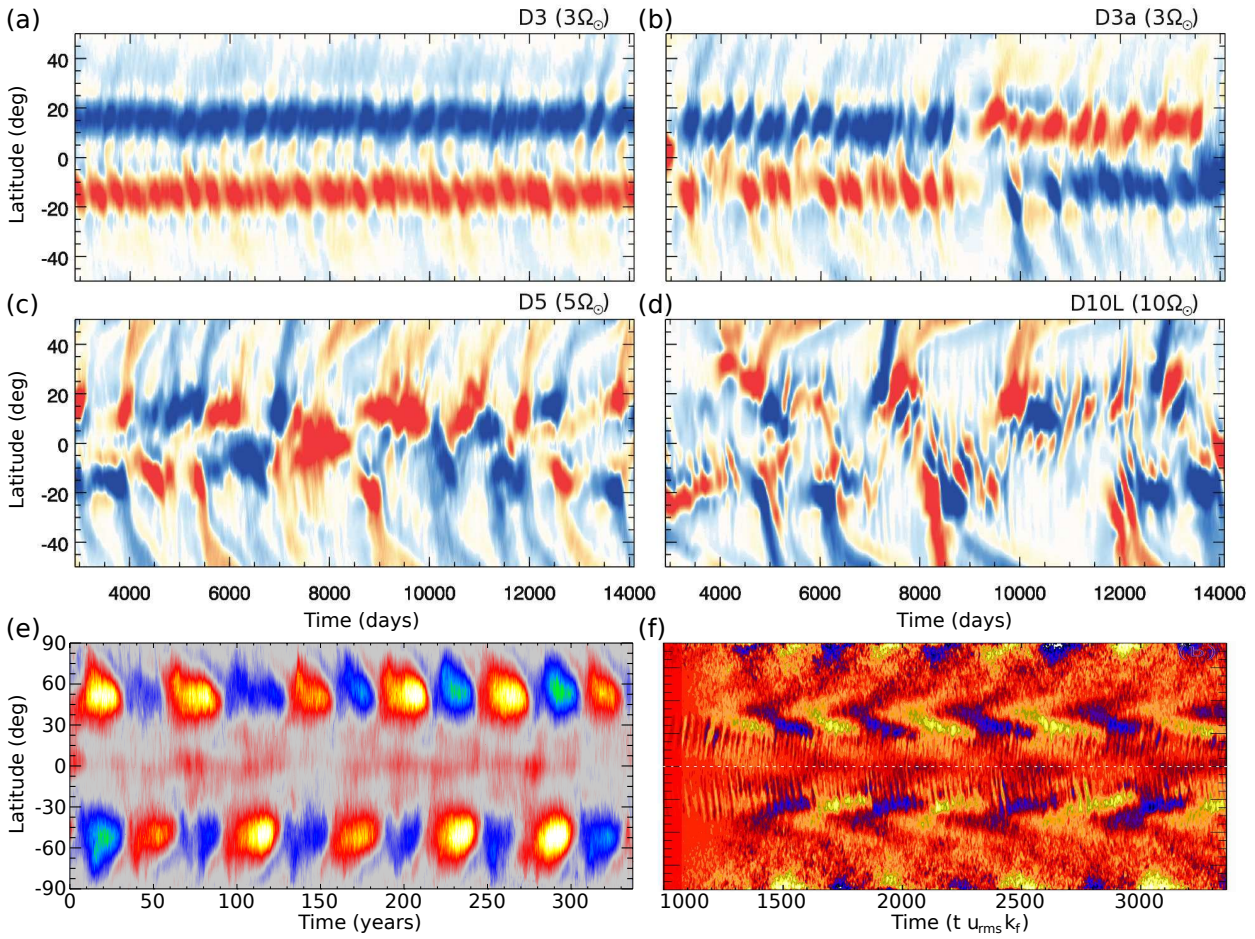

Figure 3.13: Time and latitude evolution of toroidal magnetic fields achieved in several global-scale convective dynamo solutions. (a-d) Dynamo calculations carried out with ASH showing four dynamo regimes arising from varying the rotation rate and magnetic diffusivity [adapted from Brown et al. (2011a)]. (e) Toroidal field evolution in a solar dynamo simulations utilizing EULAG, showing regular polarity reversals as in Racine et al. (2011). (f) A cycling case exhibiting polarward and equatorward branches of propagating dynamo waves in a Pencil code simulation described in Käpylä et al. (2013).

hibit two branches of propagating nonlinear dynamo waves one that is equatorward at low latitudes and another that is poleward at higher latitudes (Figure 3.13f; Käpylä et al., 2013). As was also seen in Gastine et al. (2012), they find that the density stratification of the simulation has a substantial impact on the overall character of the dynamo. In particular, one of their solutions exhibits both equatorward and poleward propagating dynamo waves (Figure 3.13f), though the reason for this is unclear. The propagation characteristics of the

dynamo are attributed to the stratification. Yet the number of density scale heights that are simulated in these calculations is only about 3 to 4.5 density scale heights, which is similar to those of previous ASH simulations. It may be that the differential rotation has a region of near-surface shear, which can promote equatorward propagation provided that the sign of the kinetic helicity does not reverse at the same time. Yet another set of Pencil code simulations have begun to investigate how the upper boundary can influence the operation of the dynamo, such as through the release of magnetic helicity (e.g., Brandenburg & Subramanian, 2005). The generation of large-scale fields in dynamos is often associated with an upscale transfer of magnetic helicity. In order to sustain this transfer, small-scale helicity must be either dissipated or removed from the system by passing through the boundaries. A possible manifestation of this on the Sun is that the magnetic helicity released in coronal mass ejections (Blackman & Brandenburg, 2003). Indeed, these recent simulations have demonstrated that convective dynamos can eject helicity through CME-like eruptions and separately form bipolar magnetic features akin to sunspots (Warnecke et al., 2012, 2013a,b), yet it is still unclear how such events effect the operation of the dynamo.

Though promising, all of these recent convective dynamo simulations are still in the early stages of discovery. They are also still quite sensitive to the treatment of diffusion where slight changes in the form and magnitudes of the diffusivities can lead to quite different behavior. Moreover, the physical mechanisms responsible for determining the cycle properties established within these various convection models remains unknown. What is clear is that these cyclic dynamos operate very differently than typical mean field dynamo models in that the meridional flow plays a minimal role in regulating the cycle period and flux emergence plays little or no role in poloidal field generation.

Chapter 4

Anelastic Formulations for Stable Stratification and Slope-Limited Diffusion

"Minima cura si maxima vis." – Il motto dell'Accademia dei Lincei

4.1 Sound-proofing Approximations

In studying compressible flows, particularly thermal convection in a rotating, electrically conductive, and compressible medium, many kinds of waves are encountered ranging from sound waves to gravity waves to Rossby and Alfvén waves. When pursuing numerical solutions of compressible convection, one must simultaneously resolve all the temporal scales of motion including the high frequency acoustic waves. Thus, it can be prohibitively expensive to simulate a numerical system for a long enough period to also capture the lower frequency convective modes.

One solution to this problem that manages to capture the dynamics in a stratified medium without prohibitively small time steps is to attempt to filter out the sound waves. This approach is not unreasonable given that the acoustic waves transport only a tiny fraction of the total energy in most convective systems at low Mach number. The energy contained in these waves, at least in linear theory, involve the fluctuating density components and are what we therefore a higher-order effect compared to the magnitude of the convective motions. The Boussinesq approximation (Boussinesq, 1903) suppresses sound wave propagation, but the effects of stratification are lost. Thus a more complete theory is needed if an understanding of the flows that span multiple density scale heights is to be constructed.

Meteorologists realized in the early 1950s that, in order to numerically model the weather, they would have to remove sound waves. The model that was used to do this is called the anelastic approximation. For meteorologists, it was crucial to have vertical variations in the background density stratification. The basic principle behind the anelastic approximation is to filter out sound waves by removing the time dependence of the background density stratification, leaving a solenoidal condition on the momentum density. There are, however, significant differences between geophysical fluid dynamics and stellar convection modeling, particularly in the processes involved in heating the compressible medium. So a few questions are raised: what is the model that must be used for stellar interiors, how is the system linearized about a background state, and how is this state chosen?

The early meteorological work on anelastic theory (Batchelor, 1953; Ogura & Charney, 1962; Ogura & Phillips, 1962) all linearize the hydrodynamic equations about local values in a stratified atmosphere, admitting only adiabatic motions. These models are restricted to layers with a very limited range of potential temperature variation. In a seminal work (Gough, 1969), an anelastic formulation is derived in which the hydrodynamic equations are linearized about a mean state obtained in a fully convective atmosphere, with the mean state defined by horizontal averages of the thermodynamic variables. This formulation was used in some of the first 3-D convection simulations, wherein the second convection zone in A-type stars is simulated (Toomre et al., 1976) using modal expansions of the anelastic equations in a plane parallel layer (Latour et al., 1976).

In a series of papers (Gilman, 1977) leading up to the creation of a 3D spherical anelastic model, some of the effects of stratification and rotation were examined in Boussinesq models of the Sun. A few years later, the anelastic equations were derived for convection of a compressible fluid in a deep rotating spherical shell with the solar convection zone in mind (Gilman & Glatzmaier, 1981). In this work, the anelastic equations in spherical coordinates were linearized, and the numerical method used to solve them is explained. In this numerical recipe, the equations of motion are expanded in spherical harmonics and

a radial basis function and then discretized in time. This model was used to extensively study the patterns of global-scale stellar convection and dynamos (Gilman, 1983; Glatzmaier, 1984, 1985). The numerical method and processes described in those early papers have been adapted for massively parallel computation and for dimensional quantities. Indeed, the governing equations and solution method are very similar to those developed and applied to stellar convection zones by Glatzmaier. This modern massively parallel numerical code is called the Anelastic Spherical Harmonic (ASH) code (Miesch, 1998; Clune et al., 1999; Brun et al., 2004). The latest versions of the ASH code utilize a slightly different set of equations that conserve energy and momentum in regions where the background stratification is not adiabatic. In ASH, this is the Lantz-Braginksy-Roberts (LBR) formulation that solves for a kinematic pressure rather than a thermodynamic pressure (Lantz, 1992; Braginsky & Roberts, 1995; Brown et al., 2012; Vasil et al., 2013). The latter paper provides a general Lagrangian framework in an astrophysical context that allows for constraints to be placed upon the ideal MHD equations in ways that are assured to conserve energy and that go beyond the earlier formulations.

4.2 Constrained Lagrangian Dynamics

It is worth a small digression to assess the derivation of the anelastic equations from a Lagrangian point of view, as it is implicitly energy conserving in non-adiabatic stratifications. Indeed, energy and momentum conservation were violated in earlier perturbative derivations of the equations in non-adiabatic stratifications. As is well known from classical mechanics, one can best construct and understand phase space attractors and the dynamics of a system as whole from a Lagrangian framework. Moreover, taking the classical approach to fields allows other constraints on the system to be more easily imposed, such as imposing an anelastic-like pressure or density constraint. Having derived the MHD equations in Chapter 3 and Appendix A, other paths to their construction can be expounded upon and their results compared. However, one outstanding problem remains: how does one establish the

existence and robustness of a suitable Lagrangian for the Navier-Stokes equations, among other dissipative systems. This has been a pernicious problem for decades. Many approaches have been taken while building the Hamiltonian for various simplified Navier-Stokes systems, including the local potential method, while others have relied on either entropy minimizing or maximizing principles to build an energy functional. In contrast, it is fairly straight forward to construct a Lagrangian system for the ideal equations, which may eventually provide a platform for extending this approach to the dissipative regime.

First consider an ideal system wherein phase space maps possess a preserved total volume, with compensating increases in either spatial or velocimetric volumes. One of the most simple dynamical system to consider is one of compressible and adiabatic magnetohydrodynamics, wherein

$$\frac{Ds}{Dt} = 0, \tag{4.1}$$

$$\frac{D\rho}{Dt} = -\rho\nabla\cdot\mathbf{u}, \tag{4.2}$$

$$\frac{D}{Dt}\left(\frac{\mathbf{B}}{\rho}\right) = \frac{\mathbf{B}}{\rho}\cdot\nabla\mathbf{u}. \tag{4.3}$$

Indeed, the flow of a fluid can be considered a time dependent map of an infinitesimal fluid element from one position to the next over some time interval t. A fluid element can be mapped from some set of initial coordinates that label a fluid element to some other set of coordinates, being a map from Lagrangian label space to Eulerian path space. Thus, the simple symplectic structure of the Lagrangian allows the equations to be integrated exactly between one time and another. Specifically, a diffeomorphic map exists between the labeling Lagrangian coordinates $\boldsymbol{\ell}$ and the Eulerian coordinates $\mathbf{x}(\boldsymbol{\ell}, t)$. Let this tensor be $E_{ij} = \partial x_i/\partial \ell_j$, which has an inverse $\Lambda_{ij} = \partial \ell_i/\partial x_j$, and a determinant $E = \det(E_{ij})$. The Lagrangian solution for the entropy is trivial $s(\boldsymbol{\ell}, t) = s_0(\boldsymbol{\ell})$, as it is only an advected scalar and so retains its value for all time in Lagrangian coordinates. The solution for the density (or the specific volume) requires a bit more work. First, note that one can define the

determinant of some matrix M as an expansion of matrix cofactors: $\det(M) = \sum_k M_{kj} C_{kj}$ for an expansion along the jth column. Thus one can define

$$\frac{\partial E}{\partial E_{ij}} = \sum_k \delta_{ik} C_{kj} = C_{ij}. \tag{4.4}$$

Using the identity that $C = E(E_{ij}^{-1})^{\mathrm{T}} = E\Lambda_{ji}$, where C is the matrix of cofactors and T denotes the matrix transpose, it is easily seen that

$$\frac{\partial E}{\partial E_{ij}} = E\Lambda_{ji}. \tag{4.5}$$

Another useful quantity is the Lagrangian derivative of the deformation tensor E_{ij}

$$\frac{DE_{ij}}{Dt} = \frac{D}{Dt}\frac{\partial x_i(\boldsymbol{\ell}, t)}{\partial \ell_j} = \frac{\partial^2 x_i(\boldsymbol{\ell}, t)}{\partial t \partial \ell_j} = \frac{\partial u_i}{\partial \ell_j}, \tag{4.6}$$

which uses the fact that $u_i(\boldsymbol{\ell}, t) = \partial x_i / \partial t$. Now consider the logarithmic Lagrangian derivative of the determinant of the deformation tensor

$$\frac{D \ln E}{Dt} = E^{-1}\frac{DE}{Dt} = E^{-1}\frac{\partial E}{\partial E_{ij}}\frac{DE_{ij}}{Dt} = \Lambda_{ji}\frac{\partial u_i}{\partial \ell_j} = \frac{\partial \ell_j}{\partial x_i}\frac{\partial u_i}{\partial \ell_j} = \boldsymbol{\nabla} \cdot \mathbf{u} \tag{4.7}$$

With Equation 4.2 and the above quantities, the Lagrangian solution for the density follows from

$$\frac{D \ln \rho}{Dt} = -\boldsymbol{\nabla} \cdot \mathbf{u} = -\frac{D \ln E}{Dt} = \frac{D \ln E^{-1}}{Dt}. \tag{4.8}$$

Integrate both sides to see that $\ln \rho/\rho_0 = \ln E^{-1}$, which of course implies that $\rho(\boldsymbol{\ell}, t) = E^{-1}\rho_0(\boldsymbol{\ell})$, with ρ_0 the initial density configuration. This also elucidates the geometrical connection between the density and the volume element, namely that the volume form is invariant $\rho \, \mathrm{d}^3\mathbf{x} = \rho_0 \, \mathrm{d}^3\boldsymbol{\ell}$.

The evolution of the magnetic field can also be found analytically. The first thing to note is that the pushforward mapping of the density normalized magnetic field vector, given the deformation tensor E_{ij}, is

$$\frac{B_i(\boldsymbol{\ell}, t)}{\rho(\boldsymbol{\ell}, t)} = E_{ij}\frac{B_j^0(\boldsymbol{\ell})}{\rho_0(\boldsymbol{\ell})}. \tag{4.9}$$

Using the earlier solution for the density, the above equation implies that

$$B_i\left(\boldsymbol{\ell},t\right)=E^{-1}E_{ij}B_j^0\left(\boldsymbol{\ell}\right). \tag{4.10}$$

The density normalized vorticity has exactly the same solution. The underlying geometrical connection is that both quantities transform like a line element.

The next step is to find perturbative solutions for a 3-space displacement vector. Consider two flows one with an Eulerian map $\mathbf{x}(\boldsymbol{\ell},t)$ and another with the map $\mathbf{y}(\boldsymbol{\ell},t)$ for which the initial values of s_0, ρ_0, and $\mathbf{B}_0$ are identical. The diffeomorphism that maps $\mathbf{x}$ to $\mathbf{y}$ is $J_{ij}=\partial y_i/\partial x_j$, hence if X_{ij} is the deformation tensor on $\mathbf{x}$ and Y_{ij} the same for $\mathbf{y}$ then $Y_{ij}=J_{ik}X_{kj}$. If the Eulerian deformation tensor E used above is equated with X, the composition of maps then takes the X fields to those fields with the deformation tensor Y as

$$\begin{aligned} s_Y\left(\boldsymbol{\ell},t\right)&=s_X(\boldsymbol{\ell},t),\\ \rho_Y\left(\boldsymbol{\ell},t\right)&=J^{-1}\rho_X\left(\boldsymbol{\ell},t\right),\\ B_i^Y\left(\boldsymbol{\ell},t\right)&=J^{-1}J_{ij}B_j^X\left(\boldsymbol{\ell},t\right). \end{aligned} \tag{4.11}$$

The Lagrangian displacement of the two flows is $\boldsymbol{\xi}=\mathbf{y}-\mathbf{x}$. Therefore,

$$J_{ij}=\delta_{ij}+\frac{\partial\xi_i}{\partial x_j}, \tag{4.12}$$

$$\det\left(J_{ij}\right)=1+\frac{\partial\xi_i}{\partial x_j}+\mathcal{O}\left(\xi^2\right), \tag{4.13}$$

$$\det\left(J_{ij}^{-1}\right)=1-\frac{\partial\xi_i}{\partial x_j}+\mathcal{O}\left(\xi^2\right). \tag{4.14}$$

The Lagrangian perturbations $\Delta Z=Z_Y(\boldsymbol{\ell},t)-Z_X(\boldsymbol{\ell},t)$ in a quantity Z are then easily found from Equations 4.11, with

$$\Delta s = 0, \tag{4.15}$$

$$\Delta\rho = \rho_Y - \rho_X = \left(Y^{-1} - X^{-1}\right)\rho_0 = \left(J^{-1} - 1\right)X^{-1}\rho_0 = -\rho_X \frac{\partial \xi_i}{\partial x_i} + \mathcal{O}\left(\xi^2\right), \tag{4.16}$$

$$\begin{aligned}\Delta B_i &= B_i^Y - B_i^X = \left(Y^{-1}Y_{ij} - X^{-1}X_{ij}\right)B_j^0 = \left(J^{-1}J_{ij} - 1\right)B_j^X \\ &= \left[\delta_{ij}\left(1 - \frac{\partial \xi_i}{\partial x_i}\right) + \frac{\partial \xi_i}{\partial x_j} - 1 + \mathcal{O}\left(\xi^2\right)\right]B_j^X = B_j^X \frac{\partial \xi_i}{\partial x_j} - B_i^X \frac{\partial \xi_k}{\partial x_k} + \mathcal{O}\left(\xi^2\right),\end{aligned} \tag{4.17}$$

$$\Delta u_i = \frac{Dy_i}{Dt} - \frac{Dx_i}{Dt} = \frac{D\xi_i}{Dt}. \tag{4.18}$$

The Eulerian perturbations $\delta Z = Z_Y(\mathbf{x}, t) - Z_X(\mathbf{x}, t)$ (note that the perturbations are at a fixed coordinate) for some quantity Z crucially link the perturbative Lagrangian and Eulerian frameworks. They can be connected through a Taylor expansion of the Lagrangian perturbations in powers of ξ. In particular, let Z be some scalar, vector, or tensor quantity that has a Lagrangian value $Z_Y^L(\boldsymbol{\ell}, t)$ for the Y flow and $Z_X^L(\boldsymbol{\ell}, t)$ for the X flow. The corresponding Eulerian values are $Z_Y^E(\mathbf{y}, t)$ for the Y flow and $Z_X^E(\mathbf{x}, t)$ for the X flow. Therefore, the Taylor expansion about $\mathbf{x}$ is

$$\begin{aligned}\Delta Z = Z_Y^L - Z_X^L &= Z_Y^E(\mathbf{x} + \boldsymbol{\xi}, t) - Z_X^E(\mathbf{x}, t) = Z_Y^E(\mathbf{x}, t) - Z_X^E(\mathbf{x}, t) + \boldsymbol{\xi} \cdot \boldsymbol{\nabla} Z_Y^E(\mathbf{x}, t) + \mathcal{O}\left(\xi^2\right) \\ &= \delta Z + \boldsymbol{\xi} \cdot \boldsymbol{\nabla} Z_Y^E(\mathbf{x}, t) + \mathcal{O}\left(\xi^2\right) = \delta Z + \boldsymbol{\xi} \cdot \boldsymbol{\nabla}\left(Z_X^E + \delta Z\right) + \mathcal{O}\left(\xi^2\right) = \delta Z + \boldsymbol{\xi} \cdot \boldsymbol{\nabla} Z + \mathcal{O}\left(\xi^2\right),\end{aligned} \tag{4.19}$$

where in the last equation we take the X flow to be the reference. To second order in ξ, the Eulerian perturbations are thus $\delta Z = \Delta Z - \boldsymbol{\xi} \cdot \boldsymbol{\nabla} Z$, which for individual quantities become

$$\delta s = -\boldsymbol{\xi} \cdot \boldsymbol{\nabla} s + \mathcal{O}\left(\xi^2\right), \tag{4.20}$$

$$\delta\rho = -\rho \boldsymbol{\nabla} \cdot \boldsymbol{\xi} + \mathcal{O}\left(\xi^2\right), \tag{4.21}$$

$$\delta\mathbf{B} = \mathbf{B} \cdot \boldsymbol{\nabla}\boldsymbol{\xi} - \boldsymbol{\xi} \cdot \boldsymbol{\nabla}\mathbf{B} - \mathbf{B}\boldsymbol{\nabla} \cdot \boldsymbol{\xi} + \mathcal{O}\left(\xi^2\right), \tag{4.22}$$

$$\delta\mathbf{u} = \frac{D\boldsymbol{\xi}}{Dt} - \boldsymbol{\xi} \cdot \boldsymbol{\nabla}\mathbf{u} + \mathcal{O}\left(\xi^2\right). \tag{4.23}$$

Note that the Eulerian perturbation for the magnetic field can be simplified through the vector identity $\boldsymbol{\nabla} \times (\mathbf{A} \times \mathbf{B}) = \mathbf{B} \cdot \boldsymbol{\nabla}\mathbf{A} - \mathbf{A} \cdot \boldsymbol{\nabla}\mathbf{B} + \mathbf{A}\boldsymbol{\nabla} \cdot \mathbf{B} - \mathbf{B}\boldsymbol{\nabla} \cdot \mathbf{A}$, and also since $\boldsymbol{\nabla} \cdot \mathbf{B} = 0$, $\delta\mathbf{B} = \boldsymbol{\nabla} \times (\boldsymbol{\xi} \times \mathbf{B})$. In index notation this is

$$\delta B_i = \epsilon_{ijk}\epsilon_{klm}\frac{\partial \xi_l B_m}{\partial x_j} = \left(\delta_{il}\delta_{jm} - \delta_{im}\delta_{jl}\right)\frac{\partial \xi_l B_m}{\partial x_j}, \tag{4.24}$$

where the last expression arises from the properties of the Levi-Civita symbol ϵ.

The general Lagrangian formulation for an ideal compressible conducting fluid can now be obtained. Let the Lagrangian density of the system be $\mathcal{L} = \mathcal{L}(\Phi)$, where $\Phi = (\mathbf{B}, \mathbf{u}, \rho, s)$, then Hamilton's principle states that the Eulerian path of motion is the one that minimizes the action functional $A[\Phi] = \int\int \mathrm{d}t\ \mathrm{d}^3\mathbf{x}\ \mathcal{L}$. Namely, the functional derivative of A is minimized by a particular path arising from the solution of the resulting Euler-Lagrange equations. In the ideal compressive MHD case, this principle yields

$$\delta A = \int\int \mathrm{d}t\ \mathrm{d}^3\mathbf{x}\ \left[\frac{\partial \mathcal{L}}{\partial \mathbf{B}}\cdot\delta\mathbf{B} + \frac{\partial \mathcal{L}}{\partial \mathbf{u}}\cdot\delta\mathbf{u} + \frac{\partial \mathcal{L}}{\partial \rho}\delta\rho + \frac{\partial \mathcal{L}}{\partial s}\delta s\right] = 0. \tag{4.25}$$

The Eulerian perturbations $\delta\Phi$ are constrained above in Equations 4.1-4.3, and are parameterized to second order with Equations 4.20-4.23. Substituting these expressions into the variation of the action and using the convention that repeated indices are summed over, it is found that

$$\delta A = \int\int \mathrm{d}t\ \mathrm{d}^3\mathbf{x}\ \left[\epsilon_{ijk}\epsilon_{klm}\frac{\partial \xi_l B_m}{\partial x_j}\frac{\partial \mathcal{L}}{\partial B_i} + \frac{\partial \mathcal{L}}{\partial u_i}\left(\frac{\partial \xi_i}{\partial t} + u_j\frac{\partial \xi_i}{\partial x_j} - \xi_j\frac{\partial u_i}{\partial x_j}\right) - \frac{\partial \mathcal{L}}{\partial \rho}\frac{\partial \rho\xi_j}{\partial x_j} - \xi_j\frac{\partial \mathcal{L}}{\partial s}\frac{\partial s}{\partial x_j}\right] = 0. \tag{4.26}$$

To isolate the displacement vector integrate by parts and swap a few indices to see that

$$\delta A = \text{B.T.} - \int\int \mathrm{d}t\ \mathrm{d}^3\mathbf{x}\ \xi_i\left[\frac{\partial s}{\partial x_i}\frac{\partial \mathcal{L}}{\partial s} - \rho\frac{\partial}{\partial x_i}\left(\frac{\partial \mathcal{L}}{\partial \rho}\right) + \frac{\partial}{\partial t}\left(\frac{\partial \mathcal{L}}{\partial u_i}\right) + \frac{\partial}{\partial x_j}\left(u_j\frac{\partial \mathcal{L}}{\partial u_i}\right) + \frac{\partial u_j}{\partial x_i}\frac{\partial \mathcal{L}}{\partial u_j} + B_j\frac{\partial}{\partial x_j}\left(\frac{\partial \mathcal{L}}{\partial B_i}\right) - B_j\frac{\partial}{\partial x_i}\left(\frac{\partial \mathcal{L}}{\partial B_j}\right)\right] = 0. \tag{4.27}$$

The boundary terms (B.T.) can have several interpretations depending upon the problem at hand. These terms must vanish if the system under consideration is infinite in extent or fully periodic. If instead the system has a finite domain, these terms should be treated very carefully, especially when they are porous, permeable, or otherwise deformable. For completeness, the boundary terms resulting from the integration by parts are

$$\text{B.T.} = \sum_i \int\int \mathrm{d}t \prod_{k\neq i} \mathrm{d}x_k \left[u_i \xi_j \frac{\partial \mathcal{L}}{\partial u_j} - \xi_i \rho \frac{\partial \mathcal{L}}{\partial \rho} - \epsilon_{ijk}\epsilon_{klm}\xi_l B_m \frac{\partial \mathcal{L}}{\partial B_j} \right]_{x_i = x_i^0}^{x_i^1} + \int \mathrm{d}^3\mathbf{x} \;\; \xi_i \frac{\partial \mathcal{L}}{\partial u_i}\bigg|_{t_0}^{t_1} \tag{4.28}$$

The beauty of this is that the impact of boundary conditions on the underlying system can be systematically studied, particularly when placing greater constraints on the system. One interesting feature is that an implicit assumption in the typical construction of Hamilton's principle used here becomes apparent with the temporal boundary condition seen in the equation for the boundary terms. While Hamilton's principle can be used to derive equations that function for initial conditions, it really is a boundary value problem in time. A recent paper has reformulated Hamilton's principle to be an initial value problem in time rather than a boundary value problem, which provides one potential method for creating suitable Hamiltonians and Lagrangians for dissipative systems (Galley, 2013).

For the time being the system will be considered to be fully periodic and to exist for an infinite amount of time. In this case, the boundary terms vanish and the following Euler-Lagrange equations are recovered for the velocity field under the constraints of an entropy and mass conserving system with the induction equation as

$$\begin{aligned} \frac{\partial s}{\partial x_i}\frac{\partial \mathcal{L}}{\partial s} - \rho \frac{\partial}{\partial x_i}\left(\frac{\partial \mathcal{L}}{\partial \rho}\right) + \frac{\partial}{\partial t}\left(\frac{\partial \mathcal{L}}{\partial u_i}\right) + \frac{\partial}{\partial x_j}\left(u_j \frac{\partial \mathcal{L}}{\partial u_i}\right) + \frac{\partial u_j}{\partial x_i}\frac{\partial \mathcal{L}}{\partial u_j} \\ + B_j\left[\frac{\partial}{\partial x_j}\left(\frac{\partial \mathcal{L}}{\partial B_i}\right) - \frac{\partial}{\partial x_i}\left(\frac{\partial \mathcal{L}}{\partial B_j}\right)\right] = 0, \end{aligned} \tag{4.29}$$

or in vector notation with $\mathbf{p} = \partial\mathcal{L}/\partial\mathbf{u}$ (momentum) and $\mathbf{H} = -\partial\mathcal{L}/\partial\mathbf{B}$ (magnetic field)

$$\frac{\partial \mathcal{L}}{\partial s}\boldsymbol{\nabla} s - \rho \boldsymbol{\nabla}\frac{\partial \mathcal{L}}{\partial \rho} + \frac{\partial \mathbf{p}}{\partial t} + \boldsymbol{\nabla}\cdot(\mathbf{u}\otimes\mathbf{p}) + \sum_j (p_j \boldsymbol{\nabla} v_j) - (\boldsymbol{\nabla}\times\mathbf{H})\times\mathbf{B} = 0. \tag{4.30}$$

This so far is fairly general with no Lagrangian yet specified. We know from the derivation of the MHD equations in Chapter 3 that the total energy density, and thus the Hamiltonian density $\mathcal{H}$, is

$$\mathcal{H} = \frac{1}{2}\rho\mathbf{u}^2 + \frac{\mathbf{B}^2}{8\pi} + \epsilon + \rho\Phi = \mathbf{u}\cdot\frac{\partial \mathcal{L}}{\partial \mathbf{u}} - \mathcal{L}. \tag{4.31}$$

Since the only first term involves $\mathbf{u}$, the Lagrangian density must be

$$\mathcal{L} = \rho\left[\frac{1}{2}\mathbf{u}^2 - e\left(\rho, s\right) - \Phi\left(\mathbf{x}\right)\right] - \frac{\mathbf{B}^2}{8\pi}, \tag{4.32}$$

with e the specific energy. Using this Lagrangian, Equation 4.30 becomes

$$\frac{\partial \mathcal{L}}{\partial s} = -\rho \left.\frac{\partial e}{\partial s}\right|_{\rho} = -\rho T, \tag{4.33}$$

$$\frac{\partial \mathcal{L}}{\partial \rho} = \frac{1}{2}\mathbf{u}^2 - e - \Phi - \rho \left.\frac{\partial e}{\partial \rho}\right|_{s} = \frac{1}{2}\mathbf{u}^2 - e - \Phi - \frac{p\left(\rho, s\right)}{\rho}, \tag{4.34}$$

$$\frac{\partial \mathcal{L}}{\partial \mathbf{u}} = \rho\mathbf{u}, \tag{4.35}$$

$$\frac{\partial \mathcal{L}}{\partial \mathbf{B}} = \frac{\mathbf{B}}{4\pi}, \tag{4.36}$$

$$-\rho T\boldsymbol{\nabla} s - \rho\boldsymbol{\nabla}\left(\frac{1}{2}\mathbf{u}^2 - h - \Phi\right) + \frac{\partial \rho\mathbf{u}}{\partial t} + \boldsymbol{\nabla}\cdot\left(\rho\mathbf{u}\otimes\mathbf{u}\right) + \frac{1}{2}\rho\boldsymbol{\nabla}\mathbf{u}^2 - \frac{1}{4\pi}\left(\boldsymbol{\nabla}\times\mathbf{B}\right)\times\mathbf{B} = 0, \quad \text{or} \tag{4.37}$$

$$\frac{\partial \rho\mathbf{u}}{\partial t} + \boldsymbol{\nabla}\cdot\left(\rho\mathbf{u}\otimes\mathbf{u}\right) + \boldsymbol{\nabla} p + \rho\boldsymbol{\nabla}\Phi - \frac{1}{4\pi}\left(\boldsymbol{\nabla}\times\mathbf{B}\right)\times\mathbf{B} = 0, \tag{4.38}$$

where the specific enthalpy is $h = e + p/\rho$ and with the thermodynamic identities $\partial e/\partial s|_{\rho} = T$ and $\partial e/\partial \rho|_{s} = P/\rho^2$. The last line uses the second law of thermodynamics to simplify it ($\rho T\boldsymbol{\nabla} S - \rho\boldsymbol{\nabla} e + P/\rho^2\boldsymbol{\nabla}\rho = 0$). It can be reduced further with the use of the continuity equation to the usual form

$$\frac{D\mathbf{u}}{Dt} = -\frac{1}{\rho}\boldsymbol{\nabla} p - \boldsymbol{\nabla}\Phi + \frac{1}{4\pi\rho}\left(\boldsymbol{\nabla}\times\mathbf{B}\right)\times\mathbf{B}. \tag{4.39}$$

There are several techniques that allow dissipative processes to be included in a Lagrangian framework, but they typically require perturbations about a set of fixed and doubled variables that represent an equilibrium flow such as with the methods of Mobbs (1982). As a consequence, such techniques cannot be valid for large excursions from equilibrium. A more recent insight establishes a covariant action principle in multi-fluid general relativity to non-perturbatively find dissipative Lagrangians (Andersson & Comer, 2013). The main idea in this approach is to treat the entropy field as a separate fluid from the matter field,

with the interactions between them being parameterized as interaction coefficients (diffusion coefficients). Heat conduction is then an effective thermodynamic force within the entropy fluid, transporting entropy from one place in the entropy coordinate space to another. The viscous diffusion terms arise from variations in the metric leading to a generalized pressure tensor that incorporates the shear-strain tensor. This latter variation suggests a new way of varying the Lagrangian in the non-relativistic limit. Namely, the Eulerian coordinates should be allowed to vary, equivalently that the volume measure should not be fixed. This should not be surprising given the direct relationship between the Lagrangian and Eulerian frames through the volume element, since dissipative processes change the internal energy and thus both the density and entropy, the volume element should be varied to accommodate the dissipative processes. This may possibly be sketched as the following action principle

$$\delta A = \int \int \mathrm{d}\tilde{t}\ \mathrm{d}^3\mathbf{a}\ \left[\frac{\partial \mathcal{L}}{\partial t}\delta t + \frac{\partial \mathcal{L}}{\partial \mathbf{x}} \cdot \delta \mathbf{x} + \frac{\partial \mathcal{L}}{\partial \mathbf{B}} \cdot \delta \mathbf{B} + \frac{\partial \mathcal{L}}{\partial \mathbf{u}} \cdot \delta \mathbf{u} + \frac{\partial \mathcal{L}}{\partial \rho}\delta \rho + \frac{\partial \mathcal{L}}{\partial s}\delta s\right] = 0. \quad (4.40)$$

with $\mathcal{L} = \mathcal{L}(t, \mathbf{x}, \mathbf{B}, \mathbf{u}, \rho, s)$ and where $\tilde{t}$ is a generalized "time" coordinate that should be thought more of as a thermodynamic time that has a link to the perceived time $t = t(\mathbf{a}, \tilde{t})$, the space coordinates $\mathbf{a}$ correspond to the thermodynamic displacements of the fields, and the variable Eulerian coordinates are $\mathbf{x} = \mathbf{x}(\mathbf{a}, \tilde{t})$. The way to think of this integral, in order to make connection to recent work in mathematics, is to consider the thermodynamic displacements more as a phase space path density, with the density of traversable paths equivalent to the entropy. If the number density of such physical paths is governed by the second law of thermodynamics, the metric on the thermodynamic space must be convex with $ds^2 = g_{\mu\nu} da^\mu da^\nu \geq 0$. This implies that a system in equilibrium would have $ds^2 = 0$, with the entropy of the system being maximum. It is also the only time-like curve available to the system. In this condition, the physical time and space merge wherein no further evolution is possible and the system is totally isotropic and homogeneous. If the metric is positive, the physical time and space instead emerge from the microscopic physics that are parameterized in the thermodynamic space and through the dynamics that it drives.

A very refreshing work regarding anti-self-dual systems (ASDS; such as the Navier-Stokes equations) has yielded a greater mathematical formalism for variational principles within such systems (Ghoussoub & Moameni, 2005; Ghoussoub, 2008; Ghoussoub & Moameni, 2009; Stuke, 2011). The basic premise is that the underlying manifolds of the ASDS are monotone and convex, and that time-dependent Lagrangians must be lifted to path space as noted above. The Lagrangian is then constructed by identifying the proper dual space and forming a functional on the product of the dual and physical spaces, one might note the similarities among this approach, the earlier fixed point variational methods, and the creation of dual matter thermodynamic spaces above. Indeed, these notions point out the subtle problems with the Euler-Lagrange functional minimization approach. For instance, one must show the regularity of that functional minimum, the existence of which is often obtainable only under a weak set of assumptions. This implies that the space of admissible functions must be chosen very carefully, which is quite evident in the "choice" of a Lagrangian for the Lantz-Braginsky-Roberts formulation (see the following section) or in the choice of an equilibrium state as in Mobbs (1982). Furthermore, not all stationary points are minima of the action in the sense that there could be multiple and nearly equal extrema. This weakens the overarching framework as the existence of stationary, non-minimizing points is quite difficult if not impossible to show in general.

Moreover, as described in Olver (1993), the vast majority of partial differential equations fall outside the purview of the Euler-Lagrange formalism. In this paper, Bäcklund's theorem [which states that the most general contact (canonical) transformations are extended point (coordinate) transformations whenever both the number of independent and dependent variables exceed unity (Edelen, 1984)] is generalized to formally characterize the internal versus external symmetries of canonical transformations relatable to the exceptional simple Lie group G_2. This group is particularly apropos to the general internal symmetries of the Navier-Stokes MHD equations that have eight continuous fields, with two vector fields and two thermodynamic quantities. The solenoidal restriction of the the magnetic field re-

duces this to seven total fields, which is the lowest order representation of the G_2 group. In this sense, perhaps some insight into the broader symmetries of the Navier-Stokes equations could be found in the construction an octonionic Hamiltonian as an alternative framework for analyzing the properties of conducting fluids, considering that the fundamental representation of G_2 is the set of automorphisms of the octonionic algebra $\mathbb{O}$. Such considerations may be linked to the earlier equilibrium and extremally entropic variational principles of Onsager (1931), Mobbs (1982), and Glansdorff & Prigogine (1954) through the consideration of doubled fields or dual spaces, which would fall into the 14-dimensional representation of G_2. More generally, it could be that all the possible approaches to asking fundamental questions about the nature of the structure of the dissipative Hamiltonian are branches of a deeper formalism. Indeed, an abstraction of the variational action principle may be in accord with the initial value formulation of Hamilton's principle as suggested in Galley (2013), though the systems considered in that work were not continuous fields.

4.3 ASH and the Lantz-Braginsky-Roberts Equation

With all the lovely Lagrangian machinery for ideal MHD at one's fingertips, the steps to deriving an energy conserving anelastic formulation are straight forward. To derive the energy conserving LBR equation two pieces are needed. The first piece is to linearize the thermodynamics, and the second is to constrain the compressive Lagrangian with a Lagrange multiplier λ that enforces the constraint $\rho/\rho_0 - 1 = 0$, which is the underlying assumption of the anelastic formulation. Thus the Lagrangian can be written down as

$$\mathcal{L} = \frac{1}{2}\rho\mathbf{u}^2 - e\left(\rho_0, s_0\right) - P_0 - \rho T_0 s - \rho_0\Phi - \frac{\mathbf{B}^2}{8\pi} - \lambda\left(\rho/\rho_0 - 1\right), \tag{4.41}$$

with the internal energy expanded to first order in ρ and s. The terms retaining the full density cancel after substituting this Lagrangian into Equation 4.30. So, the following is found

$$\frac{D\mathbf{u}}{Dt} = -\boldsymbol{\nabla}\frac{\lambda}{\rho_0} - s\boldsymbol{\nabla}T_0 + \frac{1}{4\pi\rho_0}\left(\boldsymbol{\nabla}\times\mathbf{B}\right)\times\mathbf{B}. \tag{4.42}$$

The Lagrangian multiplier λ/ρ_0 can thus be identified as the kinematic pressure p'/ρ_0 or ϖ. Secondly, in a purely adiabatic atmosphere the hydrostatic background state has the following equations $P_0 = K\rho_0^\gamma$, $P_0 = R\rho_0 T_0$, and $\boldsymbol{\nabla} P_0 = -\rho_0 \boldsymbol{\nabla}\Phi$, which together imply that $\boldsymbol{\nabla} T_0 = -R^{-1}K^{1/\gamma(\gamma-1)}\boldsymbol{\nabla}\Phi = -C\mathbf{g}$. Therefore the connection is made between the more familiar form with gravity rather than temperature gradients in nearly adiabatic atmospheres

$$\frac{D\mathbf{u}}{Dt} \approx -\boldsymbol{\nabla}\varpi - Cs\mathbf{g} + \frac{1}{4\pi\rho_0}(\boldsymbol{\nabla}\times\mathbf{B})\times\mathbf{B}. \tag{4.43}$$

This is accompanied by the continuity equation $\boldsymbol{\nabla}\cdot\rho_0\mathbf{u} = 0$ and the induction equation as well as a modified entropy advection equation $Ds/Dt = -\mathbf{u}\cdot\boldsymbol{\nabla}s_0$. These are roughly the equations solved in ASH, but what sets them apart is that the above equations lack diffusive processes.

Appealing to the derivation of the LBR equation of motion above and to the earlier derivation of the MHD equations in Chapter 3, the equations evolved in ASH with diffusion included and moving to the rotating frame are

$$\frac{\partial\mathbf{u}}{\partial t} = -\mathbf{u}\cdot\boldsymbol{\nabla}\mathbf{u} - \boldsymbol{\nabla}\varpi - Cs\mathbf{g} + 2\mathbf{u}\times\boldsymbol{\Omega} + \frac{1}{4\pi\rho_0}(\boldsymbol{\nabla}\times\mathbf{B})\times\mathbf{B} + \boldsymbol{\nabla}\cdot\left[2\rho_0\nu\left(\mathbf{e} - \frac{1}{3}\boldsymbol{\nabla}\cdot\mathbf{u}\mathbf{I}\right)\right], \tag{4.44}$$

$$\frac{\partial s}{\partial t} = -\mathbf{u}\cdot\boldsymbol{\nabla}(s_0+s) + \frac{1}{\rho_0 T_0}\boldsymbol{\nabla}\cdot(\rho_0 T_0\kappa_s\boldsymbol{\nabla}s) + \frac{4\pi\eta}{\rho_0 T_0 c^2}\mathbf{J}^2 + \frac{2\nu}{T_0}\left[\mathbf{e}:\mathbf{e} - \frac{1}{3}(\boldsymbol{\nabla}\cdot\mathbf{u})^2\right] + \epsilon, \tag{4.45}$$

$$\frac{\partial\mathbf{B}}{\partial t} = \boldsymbol{\nabla}\times[\mathbf{u}\times\mathbf{B} - \eta\boldsymbol{\nabla}\times\mathbf{B}], \tag{4.46}$$

$$\boldsymbol{\nabla} P_0 = -\rho_0\mathbf{g}, \tag{4.47}$$

$$\boldsymbol{\nabla}\cdot\rho_0\mathbf{u} = 0, \tag{4.48}$$

$$\boldsymbol{\nabla}\cdot\mathbf{B} = 0, \tag{4.49}$$

Here $\boldsymbol{\Omega}$ is the angular velocity of the rotating frame. The diffusion coefficients are the viscous diffusion ν, the entropy diffusion κ_s, and the magnetic diffusion η. The viscous diffusion acts linearly to reduce velocity gradients through its action on the stress tensor

$\mathbf{e} = 1/2(\boldsymbol{\nabla}\mathbf{u} + (\boldsymbol{\nabla}\mathbf{u})^{\mathrm{T}})$ and on compressive motions through the velocity divergence. The symbol $\mathbf{I}$ is the unit tensor and $\mathbf{J}$ is the electric current. The last term in the entropy equation ϵ incorporates all spherically symmetric heating and cooling terms such as the volumetric heating arising from the diffusion of radiation down the mean temperature gradient. Both ν and η have direct links to the microscopic fluid equations through their multiplicative renormalization.

The role of entropy diffusion more subtle. Its primary motivation is to parameterize the impact of unresolved flows on the energy transport in the system. The first assumption is that the net action of the small-scale flows is to transport energy outward in a spherically symmetric fashion, with a diffusion carrying the energy that is not transported by the larger scales along the mean entropy gradient. For the spherically symmetric component, this is simply the mixing length argument where the energy carried by the convection is parameterized as a diffusive flux $F_{conv} = -\rho T K ds_0/dr$ (e.g., Zahn, 1999). However, how much energy the larger scales should carry is an open question, and one that is somewhat independent of the question of how much momentum they should carry. So, the level of diffusion is very arbitrary ranging from the "let the large scales try to do everything" approach to the case where the resolved convection carries only a fraction of the total energy flux through the system.

This entropy diffusion also acts at all other resolved scales, becoming increasingly important at smaller scales where entropy gradients tend to be steeper and due to the k^2 wavenumber dependence of the diffuse operator. This can be considered as an increased entropy mixing at moderate scales due to the larger influence of the unresolved motions on them. The increased influence of the small scales is in turn due to the the relative magnitudes of the integrated kinetic energy of the small scales and the kinetic energy at moderate scales. However, its role is physically only valid in regions that are convectively unstable. Thus it must be carefully applied. In regions where the stratification is stable and stiff, this diffusion can violate the second law of thermodynamics. Physically, one should not expect the mixing

length argument to be valid in stable regions as there nominally is no convection and nothing as direct to mix entropy. Instead, photons and waves take over the role of diffusion. The action of the photons is to diffuse temperature gradients, whereas waves transport energy and momentum in a highly nonlocal fashion that is difficult to parameterize and is thus neglected.

ASH solves these 3-D anelastic MHD equations of motion in a rotating spherical shell using a pseudo-spectral method. The numerical methods and parallelization were first documented after its construction in (Miesch, 1998) and shortly thereafter in (Clune et al., 1999). The first version of the code solved the anelastic equations as defined in (Gough, 1969), which are not fully energy conservative particularly away from adiabatic stratifications. This formulation was still in use when magnetism was included as in (Brun et al., 2004). More recently, the energy conserving formulation has been implemented, allowing greater freedom in the choice of background states and more accurately capturing the dynamics of stable regions.

As described in Brun et al. (2004), the velocity and magnetic fields are expanded into poloidal and toroidal potentials. This formulation ensures that both the mass flux and the magnetic fields remain divergence free to within machine precision. It also reduces the number of fields that must be kept in memory, but increases the order of the spatial derivatives in the equations, which for spectral methods is usually not a problem. Thus the kinematic pressure, entropy, and the four potentials are expanded in spherical harmonics $Y_\ell^m(\theta,\phi)$ to resolve their horizontal structures and in either Chebyshev polynomials $T_n(r)$ or with finite difference methods to resolve their radial structures. This requires a spatial collocation mesh with $n_r \times n_\theta \times n_\phi$ points, or in spectral space this is equivalent to maximum spherical harmonic degree of $\ell_{\max} = 2(n_\theta + 1)/3$ with an equivalent maximum in azimuthal wavenumber m. The spherical harmonic transform therefore relies on a triangular truncation for which the maximum m is equal to the maximum ℓ, as opposed to other schemes such as the rhomboidal truncation.

Temporal discretization is accomplished using a semi-implicit Crank-Nicolson time-stepping scheme for the linear terms and a second-order explicit Adams-Bashforth method for nonlinear terms such as the convective derivative and the dissipative terms in the entropy equation. The Adams-Bashforth method is simple, being

$$\mathbf{y}^{n+1} = \mathbf{y}^n + \frac{1}{2}\Delta t \left(3\mathbf{f}_{NL}\left(t_n, \mathbf{y}^n\right) - \mathbf{f}_{NL}\left(t_{n-1}, \mathbf{y}^{n-1}\right)\right), \tag{4.50}$$

with $\mathbf{y}$ is the vector of values at each point on the spatial grid for each of the six evolved fields and the nonlinear terms and at each grid point are contained in $\mathbf{f}_{NL}$. This scheme is stable, but restricted by the CFL on any of the flow, Coriolis forces, Lorentz force, or the dissipative processes. In contrast, the linear terms involving the diffusion, pressure gradients, buoyancy, and volumetric heating terms are advanced with the implicit Crank-Nicholson scheme. This scheme for the linear portions of the time derivatives are

$$\mathbf{y}^{n+1} = \mathbf{y}^n + \frac{1}{2}\Delta t \left(\mathbf{f}_L\left(t_{n+1}, \mathbf{y}^{n+1}\right) - \mathbf{f}_L\left(t_n, \mathbf{y}^n\right)\right), \tag{4.51}$$

This equation is advanced in spectral space where small $n_r \times n_r$ matrices are solved for each ℓ and m. This requires a careful load balancing for optimal communication and computation. The Crank-Nicholson step implicitly determines the kinematic pressure. This character of the pressure has the benefit of moderating any instabilities that might arise from the less than ideal explicit time stepping scheme for the nonlinear terms, which have provided an estimate for the nonlinear portions of the solution at time t_{n+1}. It also ensures that the solenoidality constraint on the mass flux and the anelastic constraint on the density are maintained. The basic layout of the ASH time evolution algorithm is that there is a stored time step to be used for the Adams-Bashforth method, the nonlinear terms are computed and the current Adams-Bashforth as well as the explicit portion of the Crank-Nicholson operators are updated, then the implicit portion of the time step is computed.

4.4 Diffusion Methods in ASH

There are currently three methods for stabilizing the numerics in ASH, which is inherently unstable without a sufficient level of explicit diffusion. The first is that described above with a renormalization of the diffusion coefficients, the second is the spectral extrapolation method as in the dynamic Smagorinski method, and most recently the numerically stabilizing slope-limited diffusion (SLD) scheme. SLD has many possible formulations, with the one employed in ASH is similar to that found in Rempel et al. (2009) and Fan et al. (2013). At its heart, the SLD method attempts to push the solution toward a state that is monotonically smooth. This does not, however, guarantee the same smoothness of the first order derivatives. The smoothed solution is obtained through the following steps: a slope-limited piecewise linear reconstruction of the solution is made; the difference between the left and right reconstructed values at a cell edge is computed; this difference is then multiplied by a diffusion rate speed to create a diffusive flux at the cell edge; finally, the divergence of this flux is computed and added to the solution. Since this diffusion is nonlinear and a finite-volume scheme, it is computed in physical space and so must be transformed into spectral space before being added to the other nonlinear terms of the Adams-Bashforth time-stepping scheme described above. This incurs non-trivial overhead costs in memory and communication.

Effectively, SLD acts to minimize the cell-edge discontinuities arising in the piecewise linear reconstruction of the solution between adjacent cells so that the numerical method remains stable. Thus, in a sense, the SLD operator acts more as a spatial filter than as a diffusion operator. While this model of diffusion is not physically motivated like the eddy diffusion model or the dynamic Smagorinski scheme, it holds many computational advantages. Indeed, with SLD in ASH, one achieves a much higher level in the complexity of a solution for a given resolution than is possible in other methods. There is also no need to evaluate second-order derivatives or perform multiple transforms between spectral and

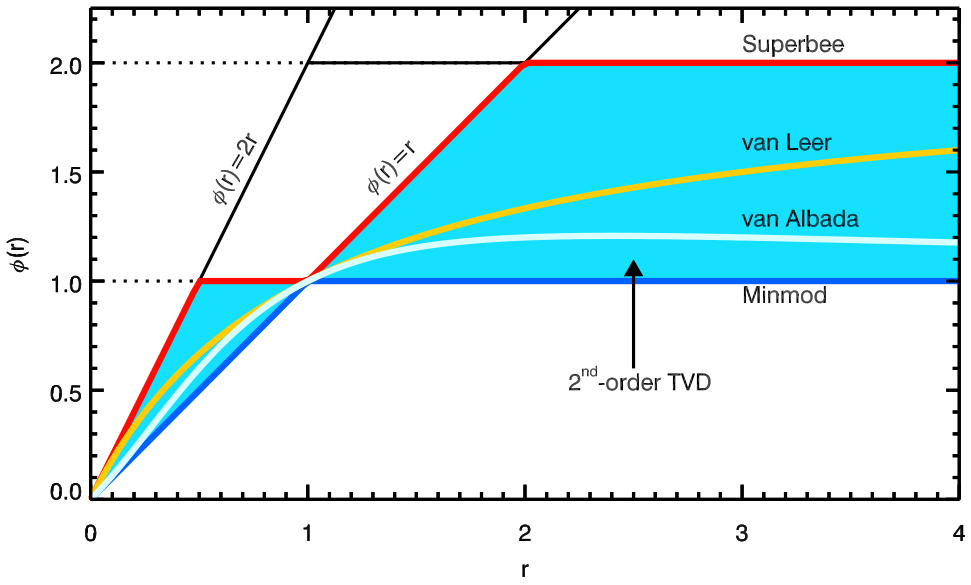

Figure 4.1: The space of second order total variation diminishing schemes is shaded in light blue, being bounded above by the superbee limiter (red) and from below by the minmod limiter (dark blue). The van Leer limiter is plotted in orange, and the van Albada limiter in gray. The abscissa r is the value of the ratio of adjacent derivatives and the ordinate ϕ is the value of the limiter.

physical space. Furthermore, under certain choices of slope-limiting functions and diffusion coefficients, the SLD scheme reduces to a fourth-order accurate approximation to a Laplacian operator as is used in the eddy diffusion model.

Before delving into the details of SLD, it is probably worth an aside to describe slope limiters and total variation diminishing schemes. Flux or slope limiters have been employed for hyperbolic conservation laws for over 50 years, starting with the pioneering work of Godunov (1954, 1959) and that of van Leer (1973, 1979). Those early methods are unified in the work of Sweby (1984), which provides a clean mathematical framework for understanding and linking all of the previous flux limiting schemes. Such formulations of hyperbolic partial differential equations are also known as total variation diminishing, which amounts to three constraints on the physical properties of a solution: there must not be any artificial entropy decreases in expansion shocks, monotonicity must be preserved, and the total variation of

any physically admissible solution must not grow in time. Generally, such terms were used to create a bounded anti-diffusive flux to counteract the excessively diffusive nature of the first order approximations to the hyperbolic equations, which is particularly important near regions of sharp gradients. For the SLD method presented here, this notion is inverted as the goal is a bounded diffusion rather than an anti-diffusion due to the use of a high-order numerical scheme.

The definition of total variation diminishing is that at a time step $n+1$ the total variation is less than the previous time step with $TV(t_{n+1}) \leq TV(t_n) = \sum_i |q_{i+1}^n - q_i^n|$ for some quantity q at cell center i (Lax, 1973). The limiters that yield this property do so in the context of second-order high-resolution flux-conservative numerical methods, such as those considered in Sweby (1984). Indeed, Sweby showed that if a second-order TVD scheme is desired then the values that the limiter can assume are fairly restricted and in general they must also possess a symmetry property so that forward and backward gradients are treated equally. The region over which this property is satisfied is shown in Figure 4.1. Also illustrated in this figure are four examples of slope limiters: the minmod limiter that is the lower bound of the region, the superbee limiter that is its upper bound, the van Leer limiter that smoothly bisects it, and the van Albada limiter that is commonly used in higher-order methods. Each of these limiters can change the character of the solution, with the superbee limiter being more compressive (leading to more cusped structures) and the minmod limiter being the most diffusive.

A piecewise reconstruction of values at the cell edge that are concurrent with the cell center value takes the general form of a Taylor series as

$$q_{i+1/2} = q_i + \sum_{k=1} \left(x_{i+1/2} - x_i\right)^k \left.\frac{\widetilde{\Delta^k q}}{\Delta x^k}\right|_i , \tag{4.52}$$

where each order of the numerical derivative is limited in some fashion to maintain monotonicity as is indicated with the tilde. There are a few techniques for computing these higher-order derivatives and their limited values, but they become increasingly complex

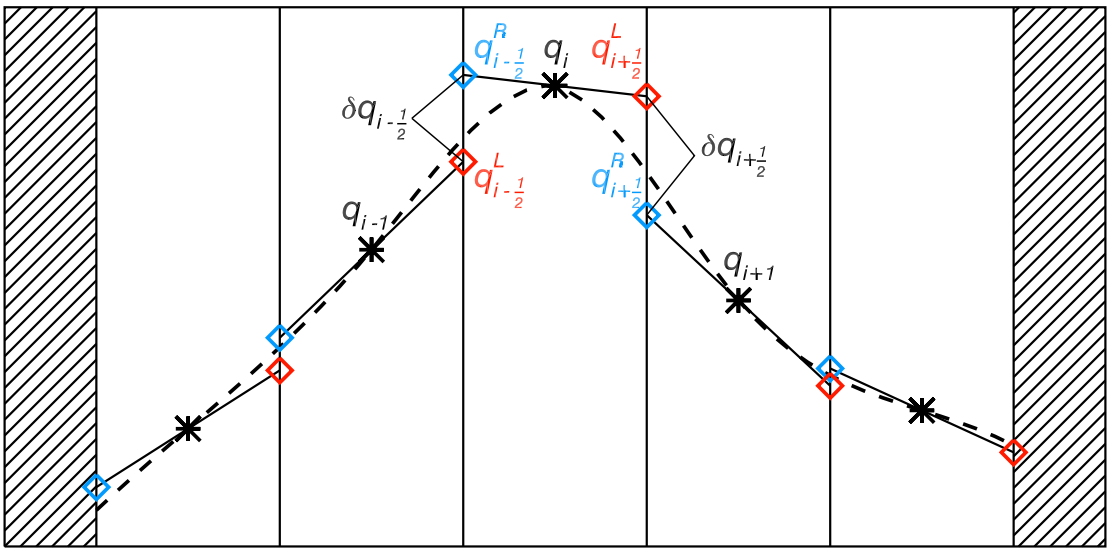

Figure 4.2: An illustration of the piecewise linear reconstruction used in slope-limited diffusion.

with each increasing order of polynomial approximation (e.g., Jiang, 1996; Suresh & Huynh, 1997; Borges et al., 2008; Čada & Torrilhon, 2009; Mignone et al., 2010). The most well studied schemes are linear reconstructions, which would be a poor approximation if the full flux were treated treated with it. However, for creating a diffusive operator they will suffice.

The piecewise linear reconstruction at the cell edges requires three derivative values (calculated using the spatial derivatives internal to a given numerical method) and three quantity values at adjacent cell centers of a given quantity q in a particular direction. Each direction is treated equally, so the following will focus only on one of them; call it coordinate x with index i. First define the cell-edge derivative approximation as

$$\left.\frac{\partial q}{\partial x}\right|_{i+1/2} = \frac{1}{2}\left[\left.\frac{\partial q}{\partial x}\right|_{i+1} + \left.\frac{\partial q}{\partial x}\right|_{i}\right] \tag{4.53}$$

Next define the the average cell-centered derivative with

$$\left\langle \left.\frac{\partial q}{\partial x}\right|_{i} \right\rangle = \frac{2}{2 + w_{i+1} + w_{i-1}}\left[w_{i+1}\left.\frac{\partial q}{\partial x}\right|_{i+1/2} + w_{i-1}\left.\frac{\partial q}{\partial x}\right|_{i-1/2}\right], \tag{4.54}$$

$$= \frac{1}{2 + w_{i+1} + w_{i-1}}\left[w_{i+1}\left(\left.\frac{\partial q}{\partial x}\right|_{i+1} + \left.\frac{\partial q}{\partial x}\right|_{i}\right) + w_{i-1}\left(\left.\frac{\partial q}{\partial x}\right|_{i} + \left.\frac{\partial q}{\partial x}\right|_{i-1}\right)\right]. \tag{4.55}$$

where the weights w are

$$w_{i-1} = \text{minmod}\left[q_i, q_{i-1}\right], \tag{4.56}$$

$$w_{i+1} = \text{minmod}\left[q_i, q_{i+1}\right], \tag{4.57}$$

$$\text{minmod}\left[x, y\right] = \begin{cases} \min\left[1, \frac{x}{y}\right] & \text{for } xy > 0 \\ 0 & \text{otherwise} \end{cases}. \tag{4.58}$$

Such a weighting minimizes the overshoot and undershoot of the solution near a discontinuity, allowing greater monotonicity. Let the slope-limiting function be defined so that

$$\phi_i = \phi\left[\left\langle \left.\frac{\partial q}{\partial x}\right|_i \right\rangle \left(\left.\frac{\partial q}{\partial x}\right|_i \right)^{-1}\right] \tag{4.59}$$

and bounded so that $0 \leq \phi_i \leq 1$. The limited slope at cell center is then constructed as

$$\left.\widetilde{\frac{\partial q}{\partial x}}\right|_i = (1-\phi_i)\left\langle \left.\frac{\partial q}{\partial x}\right|_i \right\rangle + \phi_i \left.\frac{\partial q}{\partial x}\right|_i \tag{4.60}$$

Therefore, the slope-limited and linearly reconstructed the values of q on the left and right sides of a cell edge are

$$q^L_{i+1/2} = q_i + \frac{1}{2}\Delta x_i \left.\widetilde{\frac{\partial u}{\partial x}}\right|_i, \tag{4.61}$$

$$q^R_{i+1/2} = q_{i+1} - \frac{1}{2}\Delta x_{i+1} \left.\widetilde{\frac{\partial u}{\partial x}}\right|_{i+1}. \tag{4.62}$$

with $\Delta x_i = x_i - x_{i-1}$. Thus the cell-edge difference is

$$\delta q_{i+1/2} = \Delta q_{i+1/2} - \frac{1}{2}\left[\Delta x_{i+1} \left.\widetilde{\frac{\partial u}{\partial x}}\right|_{i+1} + \Delta x_i \left.\widetilde{\frac{\partial u}{\partial x}}\right|_i\right], \tag{4.63}$$

where $\Delta q_{i+1/2} = q_{i+1} - q_i$. In this case, the diffusive flux is then controlled with a coefficient that sets the rate at which the solution achieves a state that is linearly smooth and monotonic. The diffusive flux in direction x at the cell edge $F^x_{i+1/2}$ is then

$$F^x_{i+1/2} = c_{i+1/2}\delta q_{i+1/2}, \tag{4.64}$$

with the diffusion speed at the cell edge defined as

$$c_{i+1/2} = \beta\left(\delta q_{i+1/2}, \Delta q_{i+1/2}; \alpha\right)\sqrt{v_{\min}^2 + \mathbf{v}'^2 + \mathbf{v}_A'^2}. \tag{4.65}$$

Here $v_{\min}$ is a minimum speed that sets the base level of diffusion and the fluctuating velocities and magnetic fields (through fluctuating Alfvén velocities) are

$$\mathbf{v}'^2 = \mathrm{v_r}'^2 + \mathrm{v}_\theta'^2 + v_\varphi'^2 = \frac{1}{2}\left[\left(\mathbf{v} - \langle\mathbf{v}\rangle\right)^2\Big|_{i+1} + \left(\mathbf{v} - \langle\mathbf{v}\rangle\right)^2\Big|_{i}\right], \tag{4.66}$$

$$\mathbf{v}_A'^2 = \frac{\mathbf{B}'^2}{4\pi\rho} = \frac{1}{2}\left[\left.\frac{\left(\mathbf{B} - \langle\mathbf{B}\rangle\right)^2}{4\pi\rho}\right|_{i+1} + \left.\frac{\left(\mathbf{B} - \langle\mathbf{B}\rangle\right)^2}{4\pi\rho}\right|_{i}\right]. \tag{4.67}$$

The function β further isolates the diffusion to regions of the largest discontinuities and prevents anti-diffusion. It is defined as

$$\beta\left(\delta q_{i+1/2}, \Delta q_{i+1/2}; \alpha\right) = \left(\mathrm{minmod}\left[\delta q_{i+1/2}, \Delta q_{i+1/2}\right]\right)^\alpha, \tag{4.68}$$

with α some positive value. If the value is too great, the solution may not be stable. Let r_i be the cell center in radius of a grid cell, θ_j the center in colatitude, and φ_k the center in longitude. Following the definition of finite volumes, the rate of change induced in the quantity q through the diffusive flux is

$$\left.\frac{\partial q}{\partial t}\right|_{\text{Diff}} = \frac{1}{V}\int \boldsymbol{\nabla}\cdot\mathbf{F}_q dV = \frac{1}{V}\sum_m \int \mathbf{F}_q \cdot \mathrm{d}\mathbf{S}_m \tag{4.69}$$

The divergence of the diffusive flux for a scalar quantity q, which is the same for vector components arising from tensor quantities, is

$$\begin{aligned}\frac{1}{V_{i,j,k}}\sum_m \int \mathbf{F}_q \cdot \mathrm{d}\mathbf{S}_m = \frac{1}{V_{i,j,k}}\big[&A_{i+1/2,j,k}c_{i+1/2,j,k}\delta q_{i+1/2,j,k} - A_{i-1/2,j,k}c_{i-1/2,j,k}\delta q_{i-1/2,j,k} \\ &+ A_{i,j+1/2,k}c_{i,j+1/2,k}\delta q_{i,j+1/2,k} - A_{i,j-1/2,k}c_{i,j-1/2,k}\delta q_{i,j-1/2,k} \\ &+ A_{i,j,k+1/2}c_{i,j,k+1/2}\delta q_{i,j,k+1/2} - A_{i,j,k-1/2}c_{i,j,k-1/2}\delta q_{i,j,k-1/2}\big],\end{aligned} \tag{4.70}$$

The volume of a given cell is $V_{i,j,k}$ and the surface area of a given face is A. In spherical coordinates this becomes

$$\left.\frac{\partial q}{\partial t}\right|_{\text{Diff}} = 3\frac{r_{i+1/2}^2 F_{i+1/2}^r - r_{i-1/2}^2 F_{i-1/2}^r}{r_{i+1/2}^3 - r_{i-1/2}^3} + \frac{3}{2}\frac{r_{i+1/2}^2 - r_{i-1/2}^2}{r_{i+1/2}^3 - r_{i-1/2}^3}\frac{\sin\theta_{j+1/2}F_{j+1/2}^\theta - \sin\theta_{j-1/2}F_{j-1/2}^\theta}{\cos\theta_{j-1/2} - \cos\theta_{j+1/2}}$$
$$+ \frac{3}{2}\frac{r_{i+1/2}^2 - r_{i-1/2}^2}{r_{i+1/2}^3 - r_{i-1/2}^3}\frac{\theta_{j+1/2} - \theta_{j-1/2}}{\cos\theta_{j-1/2} - \cos\theta_{j+1/2}}\frac{F_{k+1/2}^\varphi - F_{k-1/2}^\varphi}{\varphi_{k+1/2} - \varphi_{k-1/2}}, \tag{4.71}$$

where unchanging indices have been suppressed.

Since this diffusion scheme is derived from finite volumes, it is conservative to within machine precision, with the adage "one cell's loss is another's gain" holding here. It is useful to show that this diffusion reduces to a Laplacian diffusion under certain assumptions. Assume first that the diffusion speed is set to the constant $c = v_{\min}$. Second, let the function $\beta = 1$ and further let there be no discontinuities in the domain (so that the weights w are all unity). For simplicity, also assume a uniform mesh in one dimension, thus the divergence of the diffusive flux in Equation 4.64 is

$$\boldsymbol{\nabla}\cdot\mathbf{F} = \frac{1}{\Delta x}\left(c\delta q_{i+1/2} - c\delta q_{i-1/2}\delta\right), \tag{4.72}$$
$$= \frac{c}{\Delta x}\left(\Delta q_{i+1/2} - \frac{1}{2}\Delta x\left[\left.\widetilde{\frac{\partial u}{\partial x}}\right|_{i+1} + \left.\widetilde{\frac{\partial u}{\partial x}}\right|_{i}\right] - \Delta q_{i-1/2} + \frac{1}{2}\Delta x\left[\left.\widetilde{\frac{\partial u}{\partial x}}\right|_{i} + \left.\widetilde{\frac{\partial u}{\partial x}}\right|_{i-1}\right]\right), \tag{4.73}$$
$$= c\Delta x\left(\frac{q_{i+1} - 2q_i + q_{i-1}}{\Delta x^2} - \frac{1}{2\Delta x}\left[\left.\widetilde{\frac{\partial u}{\partial x}}\right|_{i+1} - \left.\widetilde{\frac{\partial u}{\partial x}}\right|_{i-1}\right]\right). \tag{4.74}$$

Notice that the first term is just the second-order approximation to the second derivative, whereas the second is the slope-limited approximation to the second derivative. So, this may be expressed as

$$\boldsymbol{\nabla}\cdot\mathbf{F} = c\Delta x\sum_{k=0}^{N}\frac{\Delta x^{2k}}{(2k+1)!}\left[\frac{1}{k+1}\frac{\partial^{2k+2}q}{\partial x^{2k+2}} - \widetilde{\frac{\partial^{2k+2}q}{\partial x^{2k+2}}}\right]_i, \tag{4.75}$$
$$= c\Delta x\left[\frac{\partial^2 q}{\partial x^2} - \widetilde{\frac{\partial^2 q}{\partial x^2}} + \mathcal{O}\left(\Delta x^2\right)\right]_i. \tag{4.76}$$

where N is the exponent of the truncation error in the computation of the derivatives within the numerical scheme minus two and then divided by two. For instance in ASH, $N = 1$ as

the finite differences in the radial direction have truncation error of order four. Equation 4.75 elucidates the behavior of the slope-limited diffusion operator. The difference between the unfiltered and the filtered Laplacian operators reduces the overall diffusion by subtracting off the smoothed average Laplacian, which is by construction always less than the local Laplacian. This leaves only the local fluctuations to be diffused away with the coefficient $c\Delta x$. In the ASH simulation described below, this value is of the order of $10^{12}\,\mathrm{cm}^2\ \mathrm{s}^{-1}$, which is quite typical of the diffusivities used in the turbulent eddy viscosity model. If the higher order terms are retained, it is clear that the unfiltered hyperelliptic operators act hyper-diffusively. In contrast, the higher-order filtered operators now act anti-diffusively and with increasing influence at ever higher orders given the $1/(k+1)$ coefficient multiplying the unfiltered operators. This might be problematic if the derivatives were not limited, but, in addition to the slope limiting, the function β eliminates the possibility of anti-diffusion. Some additional aspects of the SLD operator will be further explored in later Chapters.

In order to conserve energy in the domain, the diffusive processes must be accounted for. Since the entropy diffusion is automatically energy conserving, only the dissipative exchange of energy from the magnetic and velocity fields to the entropy field need be examined. One caveat is that the SLD operator does not preserve solenoidality of a vector field on its own. The projection operator from physical space into spectral space preserves this property for the vector fields, but not for the fluxes available for calculating the dissipation. The way around this is to project forward into spectral space, and then project back into physical space and use the transformed fields for computing the dissipation. Such forward and backward projections would be very costly as it would need to be done for each component of the SLD viscous and magnetic diffusion tensors. For now, it is assumed that the departures from solenoidality from time step to time step are very small given that the vector fields themselves are solenoidal upon every entry into the SLD routine. With this in mind, the viscous component of the entropy production due to SLD is

$$\rho_0 T_0 \left.\frac{\partial s}{\partial t}\right|_{\rm sld}^{\nu} = \boldsymbol{\nabla}\cdot\left(\rho_0\mathbf{u}\cdot\boldsymbol{\tau}^{\rm T}\right) - \rho_0\mathbf{u}\cdot\boldsymbol{\nabla}\cdot\boldsymbol{\tau}, \tag{4.77}$$

where $\boldsymbol{\tau}$ is the SLD tensor that is inherently non-symmetric and where ρ_0 and T_0 are the background density and temperature in an ASH simulation. Writing this in terms of the antisymmetric component of $\boldsymbol{\tau}$, the lack of symmetry can be emphasized

$$\rho_0 T_0 \left.\frac{\partial s}{\partial t}\right|_{\rm sld}^{\nu} = \boldsymbol{\tau}^{\rm T} : \boldsymbol{\nabla}\rho_0\mathbf{u} - 2\rho_0\mathbf{u}\cdot\boldsymbol{\nabla}\cdot\boldsymbol{\tau}^{\rm A}, \tag{4.78}$$

with $\boldsymbol{\tau}^{\rm A}$ the antisymmetric part and the colon denoting the full contraction of $\boldsymbol{\tau}$ and the gradient of the momentum. The tensor for magnetic diffusion can be treated the same way, so the resulting total entropy gain from dissipation arising from SLD is

$$\rho_0 T_0 \left.\frac{\partial s}{\partial t}\right|_{\rm sld}^{\nu} = \boldsymbol{\tau}^{\rm T} : \boldsymbol{\nabla}\rho_0\mathbf{u} + \frac{1}{8\pi}\boldsymbol{\mu}^{\rm T} : \boldsymbol{\nabla}\mathbf{B} - 2\rho_0\mathbf{u}\cdot\boldsymbol{\nabla}\cdot\boldsymbol{\tau}^{\rm A} - \frac{1}{4\pi}\mathbf{B}\cdot\boldsymbol{\nabla}\cdot\boldsymbol{\mu}^{\rm A}. \tag{4.79}$$

Here $\boldsymbol{\mu}$ is the magnetic SLD tensor. For the latter two terms, the tensor values must be interpolated to the cell center for the products to be valid in the context of the ASH solution. One further note on the implementation of SLD in ASH is that, because of the converging longitudinal grid near the poles, the diffusion is filtered in longitude. This is accomplished through two processes. First the full grid-wise SLD is computed; a second SLD is computed with a continuously increasing cell size as the poles are approached, which incorporates a greater number of points in a given cell. The cell size increases as $\csc\theta$, with the requirement that there be no fewer than eight large cells at high latitudes. The slope is reconstructed over the larger cell such that the individual points within the cell see the same slope. The two diffusive fields are weighted with $\sin^2\theta$ for the first field and by $\cos^2\theta$ for the second field. This allows more uniform resolution of the SLD operator over the nonuniform griding of the sphere. The application of this numerical diffusion technique as implemented in ASH will be explored in Chapter 5.

Chapter 5

Achieving Regular Cycles in ASH

"[Rediscovering the Maunder Minimum] was one more defeat in our long and losing battle to keep the Sun perfect, or, if not perfect, constant, and if inconstant, regular. Why we think the Sun should be any of these when other stars are not is more a question for social than for physical science." – Jack Eddy

In this Chapter, the global-scale dynamo action achieved in a simulation of a Sun-like star rotating at thrice the solar rate is assessed. The 3-D MHD Anelastic Spherical Harmonic code, modified with a viscosity minimization scheme, is employed to capture convection and dynamo processes in such a young Sun. The simulations are carried out in spherical shells that encompass 3.8 density scale heights of the solar convection zone. We find that dynamo action with a high degree of time variation occurs, with many periodic polarity reversals occurring roughly 6.2 years. The magnetic energy also rises and falls with a regular period, with two magnetic energy cycles required to complete a polarity cycle. These magnetic energy cycles arise from a Lorentz-force feedback on the differential rotation, whereas the polarity reversals are present due to the spatial separation of the equatorial and polar dynamos. Moreover, an equatorial migration of toroidal field is found, which is linked to the changing differential rotation and to a nonlinear dynamo wave. This simulation also enters a grand minimum lasting roughly 20 years, after which the dynamo recovers its regular polarity cycles. This chapter is based on work that is soon to be published in Augustson et al.

(2013a)[1] and will shortly be submitted to Astrophysical Journal Letters in a much more condensed form. I implemented slope-limited diffusion into ASH, conducted the testing of those routines, performed the simulation presented here, and wrote the paper. Sacha Brun provided careful comments to this paper and suggested the dynamo-wave analysis. Mark Miesch advised looking into the nonlinear and nonlocal effects as possible suspects for the equatorward propagation. Juri helped with revising some of the magniloquent wording and providing guidance on how to reformulate sections for greater clarity.

5.1 Introduction

The Sun exhibits many time scales from the ten minute lifetimes of granules to multi-millennial magnetic activity modulations. One of the most prominent of these scales is the 11-year sunspot cycle, during which the number of magnetically active regions waxes and wanes. The Sun also possesses longer-term variability of its magnetic activity such as the 88-year Gleissberg cycle (Gleissberg, 1939) and less frequent phenomenon commonly described as grand extrema (Usoskin, 2013). Other main-sequence stars also exhibit cyclical magnetic phenomenon in Ca II, photometric, spectropolarimetric, and X-ray observations (e.g., Baliunas et al., 1996; Hempelmann et al., 1996; Favata et al., 2008; Metcalfe et al., 2010; Fares et al., 2013; Mathur et al., 2013). These observations include solar-mass stars younger than the Sun that also possess magnetic activity cycles, yet they rotate more rapidly than the Sun as a consequence of the low rate of angular momentum loss in such stars (Barnes, 2007). Furthermore, there are hints from both observations and from theory that a star's magnetic cycle period is closely linked to its rotation rate (e.g., Saar, 2009; Jouve et al., 2010; Morgenthaler et al., 2011). This may imply that the dynamo regime achieved in our simulation of a young sun, which rotates three times faster than the Sun and has a nearly constant magnetic polarity cycle of 6.2 years, can scale up to the solar rotation rate with a

[1] Augustson, K. C., Brun, A. S., Miesch, M. S., & Toomre, J., 2013b, "Cycling Dynamo in a Young Sun: Grand Minima and Equatorward Propagation", ApJL, to be submitted

polarity cycle period closer to the 22 year cycle of the Sun.

In addition to its large range of time scales, observations of the magnetic field at the solar surface reveal complex, hierarchical structures existing on a vast range of spatial scales. Despite these chaotic complexities, large-scale organized spatial patterns such as Maunder's butterfly diagram, Joy's law, and Hale's polarity laws suggest the existence of a structured large-scale magnetic field within the solar convection zone. On the Sun's surface active regions initially emerge at mid-latitudes and appear at increasingly lower latitudes as the cycle progresses, thus exhibiting equatorward migration. As the low-latitude field propagates toward the equator, the diffuse field that is comprised of small-scale bipolar regions migrates toward the pole, with the global-scale reversal of the polar magnetic field occurring near solar maximum (e.g., Hathaway, 2010; Stenflo & Kosovichev, 2012).

Consequently, the large-scale field must vary with the solar cycle, likely being sustained through dynamo action deep in the solar interior. It has been suspected for at least 60 years that the crucial ingredients for the solar dynamo are the shear of the differential rotation and the helical nature of the small-scale convective flows present in the solar convection zone (e.g., Parker, 1955; Steenbeck & Krause, 1969; Parker, 1977). Yet even with the advancement to fully nonlinear global-scale 3-D MHD simulations (e.g., Gilman, 1983; Glatzmaier, 1985; Brun et al., 2004; Browning et al., 2006), achieving dynamo action that exhibits the basic properties of Sun's magnetism has been quite challenging. Nonetheless, recent global-scale simulations of convective dynamos have begun to make substantial contact with some of the properties of the solar dynamo through a wide variety of numerical methods (e.g., Brown et al., 2011b; Racine et al., 2011; Käpylä et al., 2012; Nelson et al., 2013a). It is within this vein of modern global-scale modeling that we report on a global-scale 3D MHD convective dynamo simulation utilizing the ASH code that possesses some features akin to those observed during solar cycles.

5.2 Computational Methods and Modifications

The simulation of convection and dynamo action presented here uses the ASH code to evolve the anelastic equations for a conductive calorically perfect gas in a rotating spherical shell. ASH solves these equations with a spherical harmonic decomposition of the entropy, magnetic field, pressure, and mass flux in the horizontal directions. Either a Chebyshev polynomial representation (Clune et al., 1999; Miesch et al., 2000), or a fourth order non-uniform finite difference in the radial direction, resolve radial derivatives. The radial finite difference derivative scheme is used here. The solenoidality of the mass flux and magnetic vector fields is maintained through the use of a stream function formalism (Brun et al., 2004). The Crank-Nicholson implicit time-stepping method advances the linear terms in the MHD equations including eddy diffusion, pressure gradients, and buoyancy. Nonlinear terms such as the convective derivatives, Lorentz forces, and dissipative processes are handled with a second-order Adams-Bashforth time step. The boundary conditions used are impenetrable on radial boundaries, with a constant entropy gradient there as well. The magnetic boundary conditions are perfectly conducting at the lower boundary and extrapolated as a potential field at the upper boundary. Furthermore, we employ the latest version of the ASH code that overhauls the necessary MPI communication pathways and memory layout (Featherstone, private communication).

The authors have implemented a slope-limited diffusion (SLD) mechanism similar to the scheme presented in Rempel et al. (2009) and Fan et al. (2013) into the reformulated ASH code. The SLD acts locally to achieve a spatially monotonic solution by limiting the linearly reconstructed slope in each coordinate direction. The scheme minimizes the steepest gradients through the action of the minmod limiter as described in 4.58, while the rate of diffusion is regulated by the local velocity. The rate of diffusion is further reduced through a function ϕ of the ratio of the cell-edge difference δq_i and the cell-center difference Δq_i in a given direction i for the quantity q. Similar to Rempel et al. (2009), this function

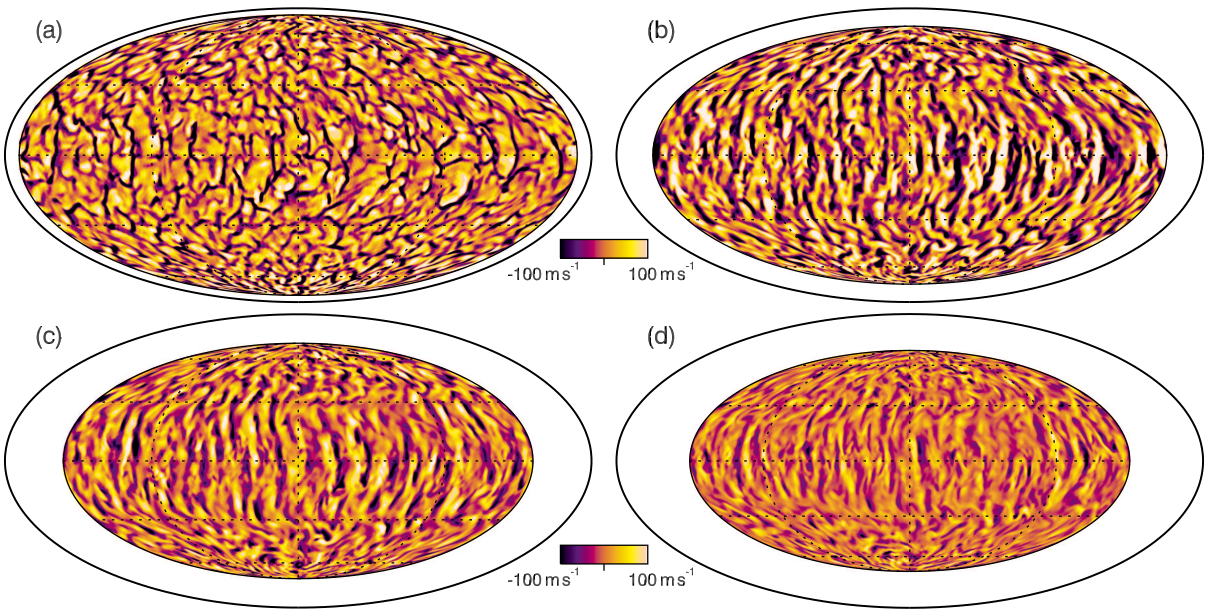

Figure 5.1: Snapshots of the horizontal convective patterns arising in the radial velocity v_r from the ASH simulation presented here that uses slope-limited diffusion are shown in Mollweide projection and are sampled at four depths: (a) $0.95\,\mathrm{R}_\odot$, (b) $0.87\,\mathrm{R}_\odot$, (c) $0.80\,\mathrm{R}_\odot$, (d) $0.75\,\mathrm{R}_\odot$. The patterns possess larger-scale columnar convection at low latitudes and the smaller-scales at higher latitudes, with downflows dark and upflows in lighter tones. The velocity range is the same for each panel, as indicated with the color bar.

is defined as $\phi_i = (\mathrm{minmod}[\delta q_i, \Delta q_i])^8$. This function limits the action of the diffusion to regions with large differences in the reconstructed solutions at cell-edges. Since SLD is a nonlinear operator, it is computed in physical space, incurring the cost of smaller time steps due to the convergence of the grid at the poles. The resulting diffusion fields are projected back into spectral space and added to the solution through the Adams-Bashforth scheme for the other nonlinear terms.

The simulation encompasses the bulk of the solar convection zone and the full spherical geometry, though the rotation rate of the frame is $\Omega_0 = 3\Omega_\odot$. The domain stretches from the base of the convection zone at $0.715\,\mathrm{R}_\odot$ to $0.965\,\mathrm{R}_\odot$, omitting the tachocline and the deep radiative interior as well as the complex physics of the near-surface layers and approximating their action with an impenetrable boundary. The SLD has been restricted to act only on

the velocity field in this simulation. This mimics a lower thermal and magnetic Prandtl number ($\mathrm{Pr_t}$, $\mathrm{Pr_m}$) than otherwise obtainable through an elliptic diffusion operator. Yet the entropy and magnetic fields remain under the influence of an anisotropic and inhomogeneous eddy diffusion, with both a radially dependent entropy diffusion coefficient κ_S and magnetic diffusivity η. The magnitude and form of these two diffusion coefficients are similar to those of case D3 from Brown et al. (2010), with $\kappa_S, \eta \propto \overline{\rho}^{\,-1/2}$, with $\overline{\rho}$ the spherically symmetric density. However, the stratification in this case has about twice the density contrast across the domain, being 45 rather than 26, and has a resolution of $N_r \times N_\theta \times N_\phi = 200 \times 256 \times 512$. In keeping with the ASH nomenclature for the simulations explored in Brown et al. (2010), Brown et al. (2011b), and Nelson et al. (2013a), this dynamo solution has been called D3S.

5.3 Dynamics and Cyclical Convective Dynamo Action

Global-scale convective dynamo simulations in rotating spherical shells have recently achieved the long-sought goal of cyclical magnetic polarity reversals with a multi-decadal period. Moreover, some of these simulations have illustrated that large-scale dynamo action is possible within the bulk of the convection zone, even in the absence of a tachocline (Brown et al., 2010). Global-scale MHD simulations of a more rapidly rotating Sun with the pseudo-spectral Anelastic Spherical Harmonic (ASH) code have produced polarity reversing dynamo action that possesses strong toroidal wreaths of magnetism that propagate poleward as a cycle progresses (Brown et al., 2011b; Nelson et al., 2013a), much like the earlier work of Gilman (1983) and Glatzmaier (1985). These fields are seated deep within the convection zone, with the bulk of the magnetic energy near the base of the convection zone. The perfectly conducting lower boundary condition used here and in those simulations requires the field to be horizontal there, which tends to promote the formation of longitudinal structure in the presence of a differential rotation.

A recent simulation with ASH employs a dynamic Smagorinski diffusion scheme, wherefore a greater level of turbulent complexity is achieved than in those simulations employing

Newtonian diffusion as seen in the comparison of Figures 3.10c and 3.10f. Those simulations show that the large-scale toroidal wreaths persist despite the pummeling they endure from the more complex and vigorous convection (Nelson et al., 2013a). Not only do the toroids of field persevere, but portions of them can be so amplified that the combination of upward advection and magnetic buoyancy create giant arcs of magnetic field that balloon upwards and span hundreds of mega-meters (Nelson et al., 2013b). This lends credence to the classical picture of a Babcock-Leighton or Parker interface dynamo (Leighton, 1969; Parker, 1993), with semi-buoyant flux structures that rise toward the solar surface, leading to active regions and helicity ejection. There is the caveat that the magnetic fields in the simulation are instead built in the convection zone.

Contemporaneously, implicit large-eddy simulations (ILES) have paved the road toward more orderly long-term cycles in a setting that mimics the solar interior. Indeed, simulations utilizing the Eulerian-Lagrangian (EULAG) code produce regular polarity cycles occurring roughly every 80 years in the presence of a tachocline and with the bulk of the magnetic field existing at higher latitudes (Ghizaru et al., 2010). This simulation showed radial propagation of structures but little latitudinal variation during a cycle. More recent simulations of a Sun-like star rotating at $3\,\Omega_\odot$ also produce low-latitude poleward propagating solutions (Charbonneau, 2013). In both cases, such dynamo action is accomplished through two mechanisms: first by reducing the enthalpy transport of the largest scales through a deliberately simple sub-grid-scale (SGS) model that apriori diminishes thermal perturbations over a roughly 1.5 year time scale, serving to moderate the global Rossby number, and second through the ILES formulation of the semi-implicit EULAG MHD code that maximizes the complexity of the flows and magnetic fields for a given Eulerian grid resolution.

Inspired by these recent ASH and EULAG results, we have attempted to make contact with both numerical methods through the incorporation of SLD into ASH with the express goal of achieving a low effective $\mathrm{Pr_t}$ and $\mathrm{Pr_m}$ dynamo. Thus an attempt is made to better mimic the low Prandtl number solar setting, while keeping the eddy-diffusive approximation

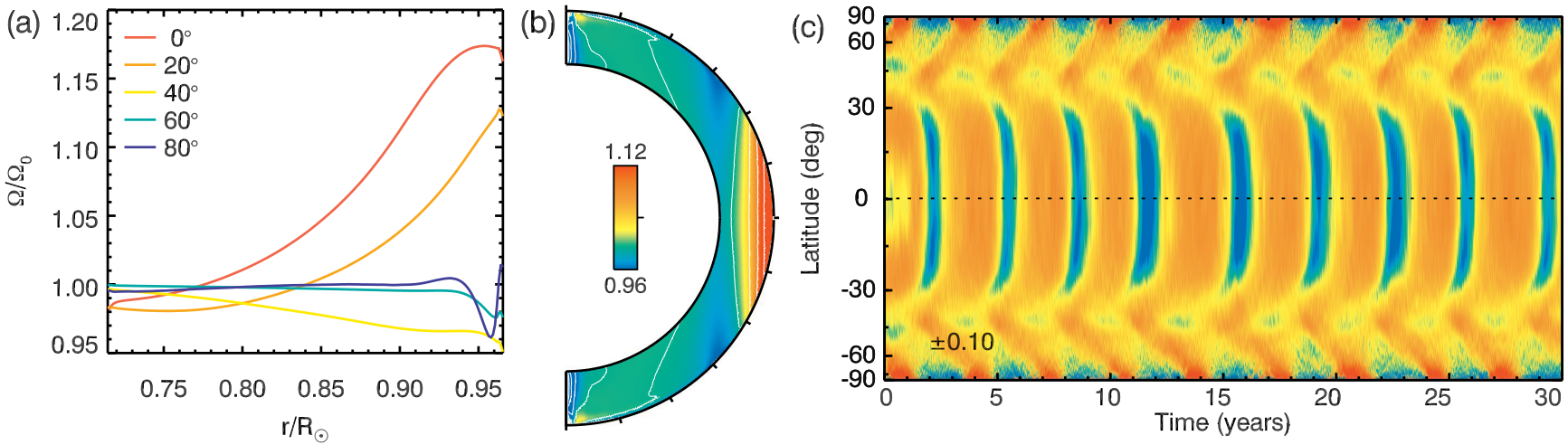

Figure 5.2: The properties of the differential rotation in D3S. (a) Cuts at constant latitude through the time-averaged, azimuthally-averaged, and normalized angular velocity $\langle\langle\Omega\rangle\rangle/\Omega_0$ (double brackets indicating dual averages and Ω_0 the frame rotation rate of $3\Omega_\odot$), showing a fast equator and slow poles. (b) $\langle\langle\Omega\rangle\rangle/\Omega_0$ shown in the meridional plane, illustrating the nearly cylindrical rotation profile. (c) A time-latitude diagram of azimuthally-averaged $\langle\Delta\Omega\rangle = \langle\Omega\rangle - \langle\langle\Omega\rangle\rangle$ in cylindrical projection, elucidating the propagation of equatorial and polar branches of a torsional oscillation arising from strong Lorentz-force feedback. The color indicates enhanced differential rotation in red and periods of slower rotation in blue, with variations of up to $\pm 10\%$ of the bulk rotation rate.

for entropy mixing and treating the reconnection of small-scale magnetic field as diffusive. This effort minimizes the effects of viscosity, and so extends the inertial range as far as possible for a given resolution. Thus SLD permits more scales to be captured before entering the dissipation range, allowing more scale separation between the larger magnetic and and smaller kinetic scales participating in the low $\mathrm{Pr_m}$ dynamo (Ponty et al., 2005; Schekochihin et al., 2007; Brandenburg, 2009). Subsequently, the kinetic helicity is also greater at small scales than otherwise would be achieved, which has been shown to have a large influence on the dynamo efficiency (Malyshkin & Boldyrev, 2010). Indeed, with this newly implemented diffusion minimization scheme, we have happened upon a solution that possesses four fundamental features of the solar dynamo: a regular magnetic energy cycle period, and an orderly magnetic polarity cycle with a period of $\tau_C = 6.2$ years, equatorward propagation of magnetic features, and poleward migration of oppositely signed flux. Furthermore this equilibrium is punctuated by an interval of relative quiescence, after which the cycle is recovered.

Some aspects of the nature of the convective dynamics achieved within D3S are visible in Figure 5.1. In the upper convection zone, the downflows are roughly twice as fast as the upflows, with the rms upflow being about $100\,\mathrm{m\,s^{-1}}$ and the downflow roughly $-200\,\mathrm{m\,s^{-1}}$. This decreases with depth, with the asymmetry between the up and downflows nearly vanishing and with the typical velocity being about $10\,\mathrm{m\,s^{-1}}$. The convection is very columnar reflecting the strength of the Coriolis force acting upon them, which tends to tilt the convective structures toward the rotation axis. In particular, the convective structures are elongated and north-south aligned flows at low latitudes and smaller scales at higher latitudes. In aggregate, the spatial structure and flow directions along these cells produce strong Reynolds stresses that act to accelerate the equator and slow the poles. The Reynolds stresses arising from these turbulent structures are the dominant mechanism that maintains the differential rotation, as the viscous stresses are quite small in this simulation. However, the Maxwell stresses are certainly important during the latter phases of a magnetic energy cycle where

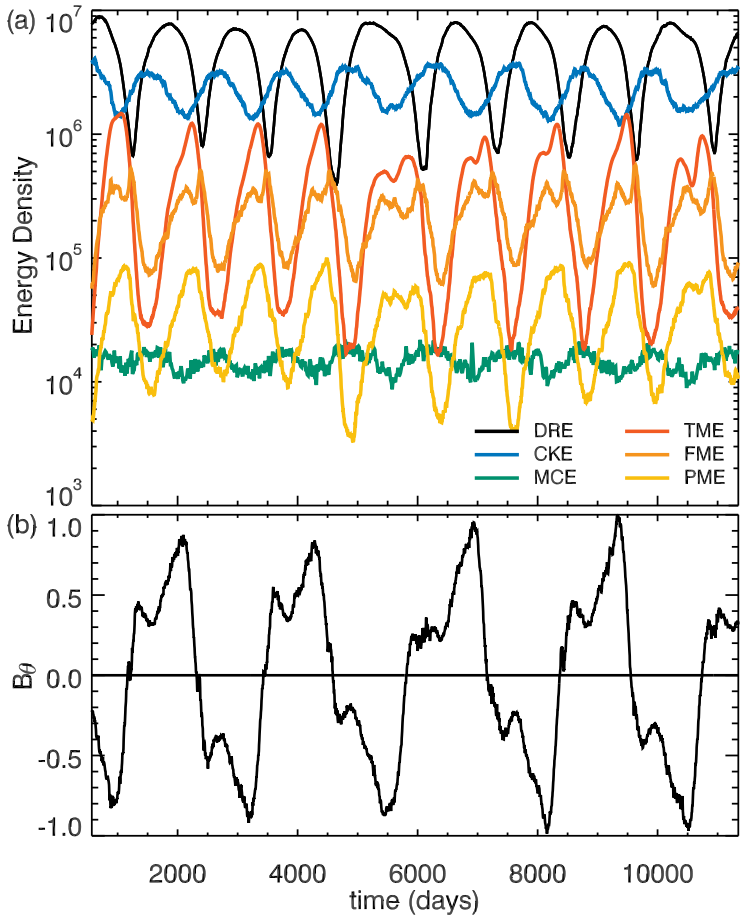

Figure 5.3: Volume-averaged energy densities and latitudinal magnetic field in Case D3S. (a) Time traces of volume-averaged energy densities associated with the differential rotation (DRE), turbulent convective kinetic energy (CKE), meridional circulation (MCE), toroidal magnetic field (TME), fluctuating magnetic field (FME), and the poloidal magnetic field (PME). The magnetic energy cycle is evident. (b) The horizonally-averaged and normalized latitudinal magnetic field shown at mid-convection zone, showing the magnetic polarity cycle.

they act to quench both the convection and the differential rotation, which is apparent in the volume averaged energy traces of Figure 5.3. Indeed, a substantial differential rotation is established and maintained here, as can be seen in Figure 5.2. It is also apparent at higher latitudes that this simulation has a negative radial gradient in the angular velocity Ω, akin to the near-surface shear layer that is well-known from helioseismology. The reason for its formation is likely a numerical boundary layer effect rather than capturing the physical

processes present in the solar near-surface shear layer. The collective action of these cells also leads to a significant latitudinal enthalpy flux that heats the poles and sustains the thermal wind balance between the differential rotation and the latitudinal entropy gradient. The thermal wind in concert with the Reynolds stresses serves to rebuild and maintain the differential rotation during each cycle.

The variable nature of the convective patterns over a cycle is an important piece of the story of the dynamo of D3S. Indeed, the magnetic fields disrupt the alignment and correlations of these cells through Lorentz forces. Particularly, as the field gathers strength during a cycle, the strong azimuthally-connected toroidal fields tend to create a thermal shadow that weakens the thermal driving of the equatorial cells. Thus their angular momentum transport is also diminished, which explains why the differential rotation seen in Figure 5.2(b) cannot be fully maintained during the cycle. This is captured in the modulation of the kinetic energy contained in the fluctuating velocity field, which here varies by about 50% throughout the cycle as is visible in Figure 5.3(a). Such a mechanism is in keeping with the impacts of strong toroidal fields in the convection zone suggested by Parker (1987). Moreover, strong nonlinear Lorentz force feedbacks have been seen in other convective dynamo simulations as well (Brown et al., 2011b), and they have been theoretically realized for quite some time (Malkus & Proctor, 1975).

Figure 5.4 illustrates the morphology of the toroidal fields in space and time. The presence of large-scale and azimuthally-connected structures is evident in Figures 5.4(a, d). Such toroidal structures have been dubbed wreaths (Brown et al., 2010). In D3S, there are two counter-polarized, lower-latitude wreaths that form near the point where the tangent cylinder intersects the spherical surface at a given radius. This point is also where the peak in the latitudinal gradient of the differential rotation exists for much of a magnetic energy cycle. There are also polar caps of magnetism of the opposite sense of those at lower latitudes. These caps serve to moderate the polar differential rotation, which would otherwise tend to accelerate and hence establish fast polar vortices. The average structure

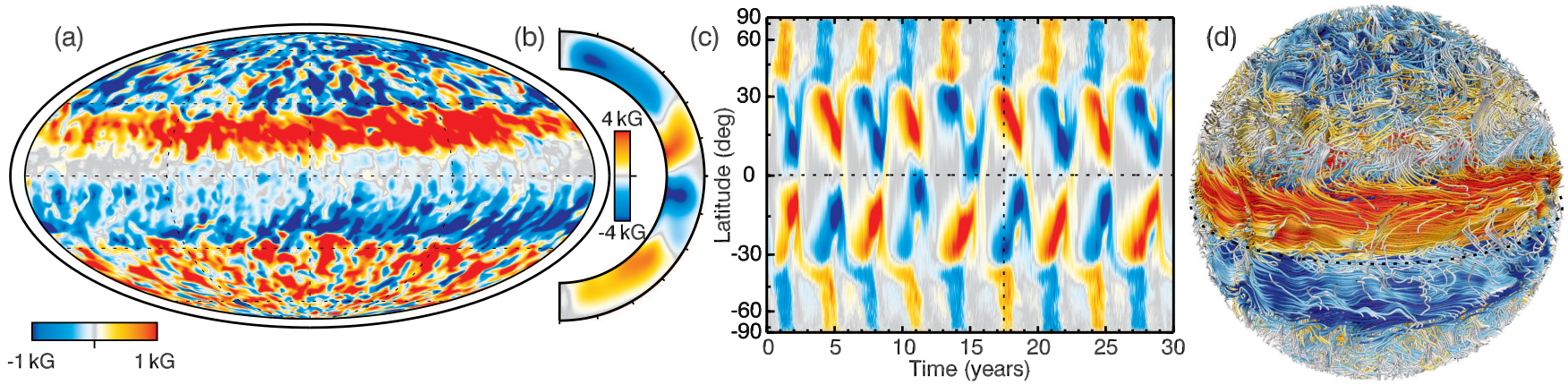

Figure 5.4: Nature of the toroidal magnetic field B_ϕ. (a) Snapshot of the horizontal structure of B_ϕ at $0.95\,\mathrm{R}_\odot$ shown in Mollweide projection, at the time corresponding to the vertical dashed line in (c). This illustrates the azimuthal connectivity of the magnetic wreaths, with the polarity of the field such that red (blue) tones indicate positive (negative) toroidal field. (b) Azimuthally-averaged $\langle B_\phi \rangle$ also time-averaged over a single energy cycle, depicting the structure of the toroidal field in the meridional plane. (c) Time-latitude diagram of $\langle B_\phi \rangle$ at $0.95\,\mathrm{R}_\odot$ in cylindrical projection, exhibiting the equatorward migration of the wreaths from the tangent cylinder at roughly 38° and the poleward propagation of the higher latitude field. The color is as in (a). (d) A rendering of magnetic field lines in the domain colored by the magnitude and sign of B_ϕ, with strong positively oriented field in red, and the strong oppositely directed field in blue.

of the wreaths and caps is apparent in Figure 5.4(b), which is averaged over a single energy cycle or 3.1 years. The wreaths appear rooted at the base of the convection zone, whereas the caps have the bulk of their energy in the lower convection zone above its base. This is somewhat deceptive as the wreaths are initially generated higher in the convection zone, while the wreath generation mechanism (primarily the Ω-effect) migrates equatorward and toward the base of the convection zone over the course of the cycle. The wreaths obtain their greatest amplitude at the base of the convection zone and thus appear seated there.

5.4 Grand Minima and Long-Term Modulation

As with some other dynamo simulations (e.g., Brown et al., 2011b; Augustson et al., 2013b), there is also a degree of long-term modulation of the magnetic cycles in case D3S. Figure 5.5 shows an interval of about 20 years where the polarity cycles are lost, though the magnetic energy cycles resulting from the nonlinear interaction of the differential rotation and the Lorentz force remain. During this interval, the magnetic energy in the domain is about 25% lower, whereas the energy in the volume encompassed by the lower-latitudes is decreased by 60%. However, both the spatial and temporal coherency of the cycles are recovered after this interval and persist for the last 40 years of the 100 year-long simulation. Prior to entering this quiescent period, there was an atypical cycle with only the northern hemisphere exhibiting equatorward propagation. This cycle also exhibits a prominent loss of the equatorial anti-symmetry in its magnetic polarity. The subsequent four energy cycles do not reverse their polarity, which is especially evident in the polar regions, whereas the lower latitudes do seem to attempt such reversals.

Similar quasi-periodic dynamo action has been realized in quite a few instances, though only in mean-field models and in reduced dynamo models not in fully nonlinear 3D MHD simulations. Some of the most well-studied quasi-periodic systems utilize reduced dynamo models that couple only a few modes of the overall system, such as those models of Weiss et al. (1984). Weiss uses a simple $\alpha\Omega$ dynamo model. This is accomplished through systems

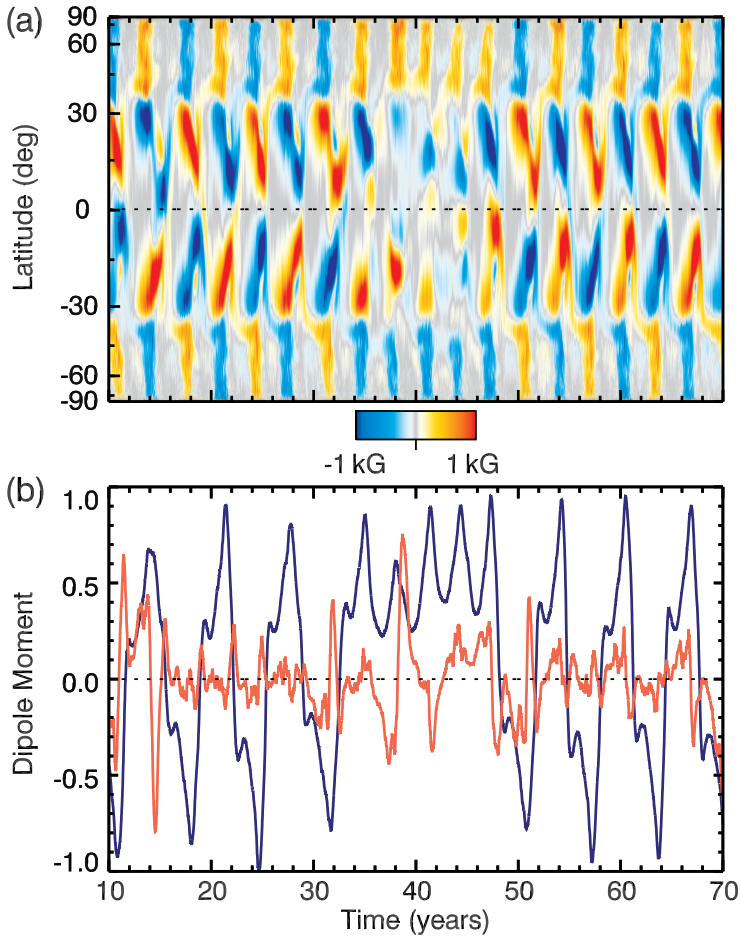

Figure 5.5: An interval of magnetic quiescence. (a) Time-latitude diagram of $\langle B_\phi \rangle$ at $0.95\,\mathrm{R}_\odot$ in cylindrical projection, picturing the loss and reappearance of cyclical polarity reversals as well as the lower amplitude of the wreaths. Strong positive toroidal field is shown as red, negative in blue. (b) Normalized magnetic dipole moment (blue) and quadrupole moment normalized by the dipole absolute maximum (red). There is a significant rise in the quadrupole moment near reversals, suggesting a brief coupling between families of dipolar and quadrupolar dynamo modes.

of coupled nonlinear ordinary differential equations, where the number of included modes is varied. This results in models that range from fourth to sixth-order in their time derivative. These models admit simple nonlinear oscillatory solutions. The highest-order model with the largest number of dynamic modes exhibits transitions from periodic oscillations to chaotic behavior with longer-term modulation akin to the grand minima in the solar activity cycle.

Later work explored alternative dynamo feedback mechanisms in these low order sys-

tems (Tobias, 1997). Tobias explored the impacts that modulations in the toroidal magnetic field energy and that Lorentz-force feedback on the large-scale flows have on the character and evolution of nonlinear $\alpha\Omega$ dynamo solutions. The former mechanism is shown to affect the parity of the dynamo, whereas the latter can reduce the efficiency of both the α and Ω effects in the limit of low magnetic Prandtl numbers. With an appropriate choice of parameters, some solutions exhibit a long-term evolution that produces grand extrema, while retaining the basic cycle periods, as the Sun is observed to do. In particular, it is shown that the magnetic field can be substantially modulated and effectively remain dipolar. During grand minima the magnetic field is weak and is no longer a simple dipole. Such behavior is also seen in the simulation here, where its grand minimum is associated with a much stronger quadrupole moment, as is evident in Figure 5.5b. It also worth noting that the quadrupole component tends to briefly spike during the polarity reversal, which may be a signal of the reversal mechanism. Indeed, recent work has explored solar observations over the past three solar cycles to assess the magnetic energy contained in a large range of spherical harmonic modes (DeRosa et al., 2012). It is seen there that the coupling between the dipolar and quadrupolar families of modes correlates well with the large-scale polarity reversals of the Sun.

5.5 Generating Global-Scale Magnetism

The toroidal field shown in Figure 5.4 is initially generated and then maintained by similar processes. During the growth phase of the magnetic field, the shear of the differential rotation acts to fold and wind the initial poloidal field into toroidal structures. During this kinematic phase, the mean shear and meridional flows are largely unaffected and can be considered stationary relative to the time scales of the growing field. However, once the magnetic fields are strong enough they begin to quench the convective flows that cross them. The magnetic field strength becomes saturated as the back reaction of the Lorentz forces increases the alignment of the velocity field and the magnetic field, which reduces both its

generation and at times leads to its partial destruction.

This configuration of fields establishes a new balance between the various mechanisms of angular momentum transport needed to sustain the differential rotation when compared to a hydrodynamic simulation. Here magnetic fields both transport angular momentum as well as block formerly open channels of transport. For instance, the strong toroidal field serves to reduce the latitudinal transport of angular momentum by Reynolds stresses, which modifies both the differential rotation and the meridional circulations within the simulation relative to what would be achieved in a hydrodynamic simulation.

Since the dynamo running within D3S waxes and wanes as time marches forward through many polarity reversals, the balance between magnetic field generation mechanisms is not instantaneous nor is it the same at any given time within the cycle. When averaged in time over the full span of the simulation, an analysis of the terms contributing to the generation and destruction of magnetic energy can illustrate those mechanisms that have the greatest overall influence on the dynamo. The evolving magnetic fields arise through many competing processes that both produce and destroy magnetic field through the shearing and advection of field, through compressive motions, and dissipation through resistive processes. These production and dissipation terms are most easily understood through an evolution equation for the magnetic energy contained in the mean magnetic fields. This equation can be broken into its poloidal and toroidal components $\mathrm{P_{ME}}$ and $\mathrm{T_{ME}}$ as

$$\frac{\partial \mathrm{T_{ME}}}{\partial t} = \frac{\langle B_\phi \rangle}{8\pi}\Bigg[\overbrace{\left(\left(\langle \mathbf{B}\rangle \cdot \boldsymbol{\nabla}\right)\langle \mathbf{v}\rangle\big|_\phi\right)}^{\mathrm{T_{MS}}} + \overbrace{\left\langle \left(\mathbf{B}'\cdot\boldsymbol{\nabla}\right)\mathbf{v}'\right\rangle\Big|_\phi}^{\mathrm{T_{FS}}} - \overbrace{\left(\left(\langle \mathbf{v}\rangle \cdot \boldsymbol{\nabla}\right)\langle \mathbf{B}\rangle\big|_\phi\right)}^{\mathrm{T_{MA}}} - \overbrace{\left\langle \left(\mathbf{v}'\cdot\boldsymbol{\nabla}\right)\mathbf{B}'\right\rangle\Big|_\phi}^{\mathrm{T_{FA}}} + \overbrace{\langle B_\phi \mathrm{v_r}\rangle \frac{\partial \ln \overline{\rho}}{\partial r}}^{\mathrm{T_{CC}}} - \overbrace{\boldsymbol{\nabla}\times\left(\eta\boldsymbol{\nabla}\times\langle\mathbf{B}\rangle\right)\big|_\phi}^{\mathrm{T_{RD}}}\Bigg], \tag{5.1}$$

$$\frac{\partial \mathrm{P_{ME}}}{\partial t} = \frac{\langle \mathbf{B}_P \rangle}{8\pi}\cdot\Bigg[\overbrace{\left(\left(\langle \mathbf{B}\rangle \cdot \boldsymbol{\nabla}\right)\langle \mathbf{v}\rangle\right)}^{\mathrm{P_{MS}}} + \overbrace{\left\langle \left(\mathbf{B}'\cdot\boldsymbol{\nabla}\right)\mathbf{v}'\right\rangle}^{\mathrm{P_{FS}}} - \overbrace{\left(\left(\langle \mathbf{v}\rangle \cdot \boldsymbol{\nabla}\right)\langle \mathbf{B}\rangle\right)}^{\mathrm{P_{MA}}} - \overbrace{\left\langle \left(\mathbf{v}'\cdot\boldsymbol{\nabla}\right)\mathbf{B}'\right\rangle}^{\mathrm{P_{FA}}} + \overbrace{\langle \mathbf{B}_P \mathrm{v_r}\rangle \frac{\partial \ln \overline{\rho}}{\partial r}}^{\mathrm{P_{CC}}} - \overbrace{\boldsymbol{\nabla}\times\left(\eta\boldsymbol{\nabla}\times\langle\mathbf{B}\rangle\right)}^{\mathrm{P_{RD}}}\Bigg], \tag{5.2}$$

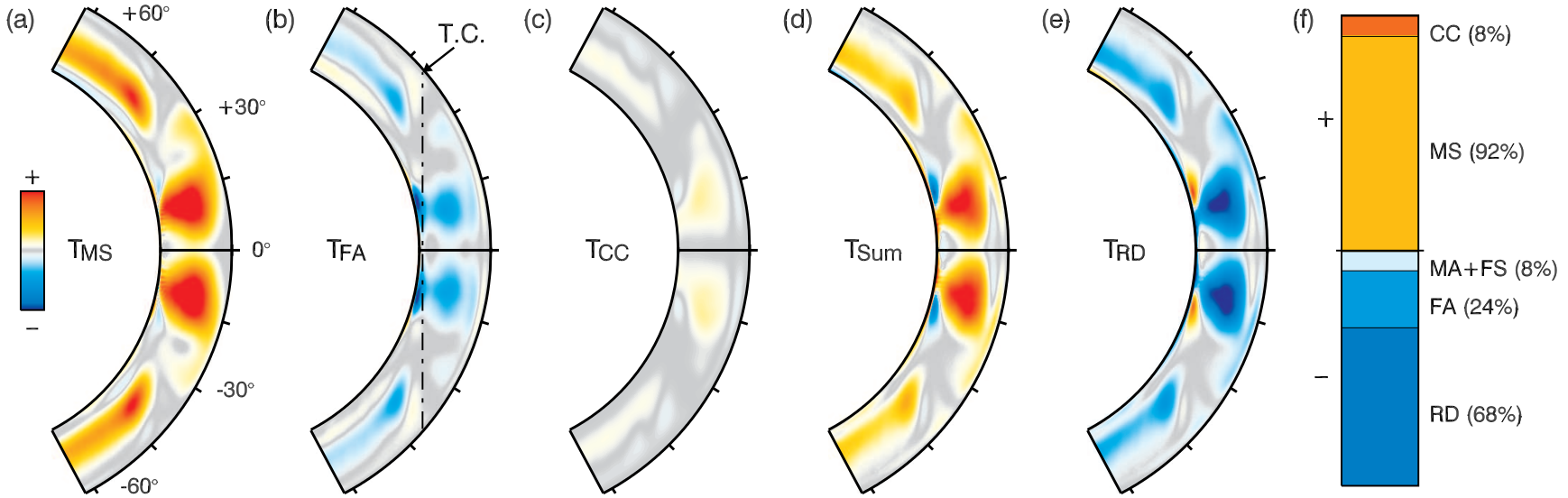

Figure 5.6: Generation of mean toroidal magnetic energy (T_{ME}) in D3S. The view is from $\pm 60^\circ$ to emphasize the equatorial regions. Here only the dominant production terms are shown, namely (a) mean shear (T_{MS}), (b) fluctuating advection (T_{FA}), with a cylinder tangent to the bottom of the domain (T. C.) is indicated (dashed line), (c) compressive correlations (T_{CC}), (d) the sum $T_{MS} + T_{FS} + T_{MA} + T_{FA} + T_{CC}$, which largely act in concert to balance (e) the resistive diffusion of field (T_{RD}). All panels have identical scaling. The mean generation terms shown here contribute to the T_{ME} when positive (red), and destroy it if they are negative (blue). (f) The relative contribution of each term, with terms in red toned regions adding to the volume and time-averaged toroidal energy generation and those in blue dissipating energy.

with the $\langle\rangle$ denoting an average in longitude, $\mathbf{v}' = \mathbf{v} - \langle\mathbf{v}\rangle$ the fluctuating velocity, $\mathbf{B}' = \mathbf{B} - \langle\mathbf{B}\rangle$ the fluctuating magnetic field, and $\langle\mathbf{v}\rangle$ and $\langle\mathbf{B}\rangle$ the axisymmetric velocity and magnetic field respectively. A detailed derivation of the mean-field production terms in spherical coordinates is provided in Appendix A of Brown et al. (2010). Here T indicates a toroidal magnetic energy generation term and P a poloidal energy generation term. The subscript of these monikers denote production in turn by mean shear (MS), fluctuating shear (FS), mean advection (MA), fluctuating advection (FA), compressional correlations (CC), and resistive diffusion (RD).

Over a long time average, the time variability of the production of $\mathrm{T_{ME}}$ is removed, leaving a balance between terms that produce and terms that destroy field. Figure 5.6 presents such a time average of these mean generation terms, involving the entire evolution of case D3S over an 80 year interval (3300 rotations). In this statistically steady state, the maintenance of the toroidal wreaths of magnetic field is largely governed by a balance between the production of field by both the mean shear and the dissipation of field through resistive processes. By comparing Figures 5.6(a) and 5.6(d), it is clear that the mean shear $\mathrm{T_{MS}}$ of Equation (5.1) is primarily responsible for maintaining the strength of the wreaths. The production due to the compressibility of the downflows, which can be seen from the form of $\mathrm{T_{CC}}$, plays a weak but supporting role. In keeping with the dominance of the Ω effect ($\mathrm{T_{MS}}$ above), the toroidal magnetic energy generation is greatest at latitudes where the latitudinal gradients in the differential rotation are at their largest. This maximum occurs at latitudes outside the tangent cylinder in a roughly 15° swath, though there is also generation of toroidal field at higher latitudes just inside the tangent cylinder. The resistive dissipation and fluctuating advection of field act in tandem to destroy toroidal field. Given the spatial distribution of $\mathrm{T_{FA}}$ in Figure 5.6b, the action of the fluctuating advection could be considered as part of an α-effect with the small-scale flows tearing at the large-scale wreaths, transferring energy from the toroidal to the poloidal magnetic fields.

The relative contributions of each term have been measured by integrating it over time

and space $\langle T_i \rangle = \int T_i dV$, where i is any of the terms in Equation (5.1). This allows the net action of a given term to be assessed, indicating whether it on average is productive or destructive of toroidal magnetic energy. As indicated in Figure 5.6(f), the bulk of the production is accomplished by $\mathrm{T_{MS}}$, being about 92% of the total. The remaining 8% of the mean production is due mostly to the compressive motions of the downflows ($\mathrm{T_{CC}}$). In contrast, the averaged $\mathrm{T_{RD}}$, $\mathrm{T_{FA}}$, $\mathrm{T_{MA}}$, and $\mathrm{T_{FS}}$ processes act in concert to dissipate magnetic energy, with $\mathrm{T_{RD}}$ responsible for 68% of the dissipation and $\mathrm{T_{FA}}$ 24%.

The mechanisms generating the poloidal fields and its associated magnetic energy $\mathrm{P_{ME}}$ are given in Equation 5.2. In Figure 5.7, the temporal and longitudinal averages of the generation terms with the largest average contributions are shown. The average is again carried out over 80 years. Figure 5.7(g) shows that in the spatially integrated sense and unlike in the toroidal energy generation, the fluctuating shear $\mathrm{P_{FS}}$ is the dominant contributor to the production of poloidal field, generating on average 79% of the poloidal energy, while the resistive diffusion $\mathrm{P_{RD}}$ again is the largest dissipator, destroying 75% of it. However, other processes contribute to the generation of poloidal field as well. The production of poloidal field arises through the joint action of the fluctuating shear $\mathrm{P_{FS}}$ and mean advection $\mathrm{P_{MA}}$, whereas the dissipation of poloidal magnetic energy arises from the combination of resistive diffusion $\mathrm{P_{RD}}$ and mean shear $\mathrm{P_{MS}}$. The bulk of the production occurs near the lower boundary and inside the tangent cylinder, being associated with the fluctuating velocities and magnetic fields of the more isotropic convective cells at higher latitudes. The generation of poloidal field has two primary balances: the first is between production through the fluctuating shear and resistive decay; the second is between the mean shear and the mean advection. The overall balances of magnetic energy generation are subtle given the spatial separation between the primary regions of toroidal and poloidal field generation, with poloidal field being built near the base of the convection zone and at higher latitudes and the toroidal field being produced at low latitudes in the upper convection zone.

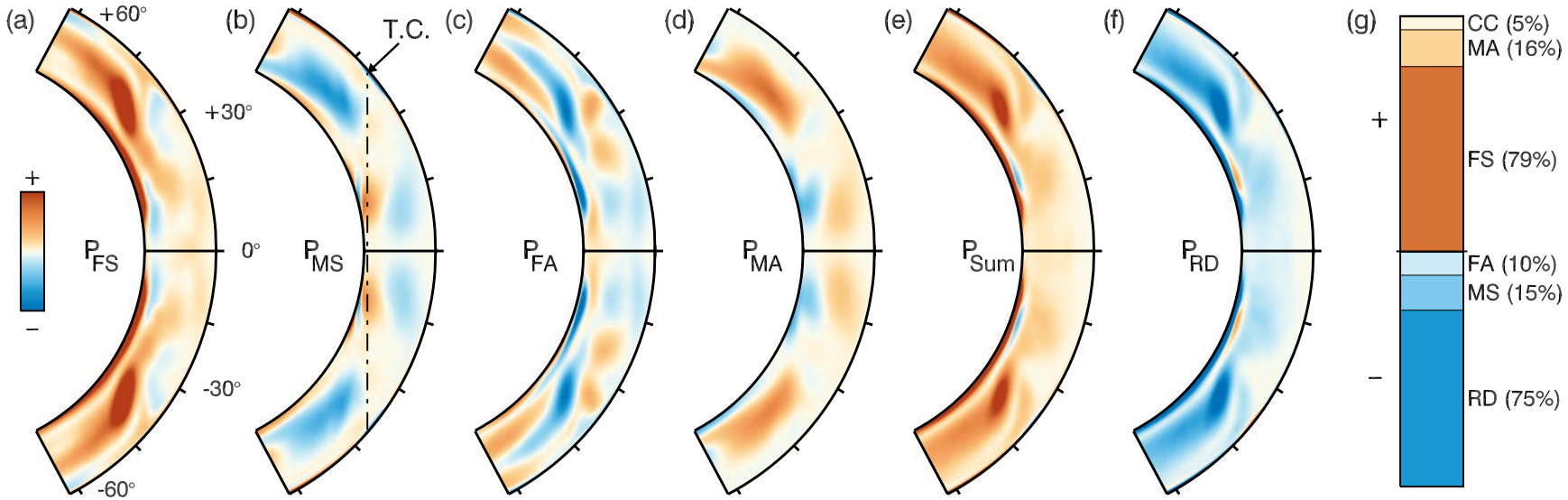

Figure 5.7: Generation of mean poloidal magnetic energy (P_{ME}) in D3S. The dominant production/destruction terms are shown, namely (a) fluctuating shear (P_{FS}), (b) mean shear (P_{MS}), (c) fluctuating advection (P_{FA}), (d) mean advection (P_{MA}) and (e) the sum $P_{MS} + P_{FS} + P_{MA} + P_{FA} + P_{CC}$, with (f) the resistive diffusion of field (P_{RD}). The mean generation terms shown contribute to the P_{ME} when positive (red), and destroy it if negative (blue). (g) The relative contribution of each term, with those in red adding to the volume- and time-averaged poloidal energy generation and those in blue dissipating energy.

5.6 What Might Be Setting Cycle Periods?

There are a large set of possible and often interlinked time scales that could be relevant to the processes setting the pace of the cyclical dynamo established in D3S. For instance, there are resistive time scales that depend upon the length scale chosen. One such time scale is the resistive decay of the poloidal field at the upper boundary as it propagates from the tangent cylinder to the equator, which would imply that the length scale is $\ell = r_2 \Delta\theta$ and so $\tau_\eta = \ell^2/\eta_2 \approx 6.7$ years and is close to the polarity cycle period, where the subscript two denotes the value of a quantity at the outer boundary of the simulation. However, this is likely not dynamically dominant as the the polarity reversal occurs in half that time. The same is true of the diffusion time across the convection zone, being 4.6 years. Since the cycle is likely not resistively controlled it must be the interplay of dynamical processes. Another mechanism to consider is the cycle time related to flux transport by the meridional flow, with the transit time of a magnetic element along its circuits possibly being relevant. In D3S, the mean meridional flow is anti-symmetric about the equator and has two cells, with a polar branch and a lower latitude cell that are split by the tangent cylinder. The circulation time of the polar branch is about 0.7 years, whereas that of the equatorial cell is about a year. So it is also unlikely that the meridional flow is setting the cycle period.

The dynamical coupling of azimuthally-averaged magnetic fields $\langle \mathbf{B} \rangle$ and the mean angular velocity $\langle \Omega \rangle$ (Figure 5.2(b)) plays a crucial role in regulating the cycle, though it alone cannot be the sole actor as is well known from Cowling's anti-dynamo theorem. The significant anti-correlation of $\langle B_\phi \rangle$ and angular velocity variations $\langle \Delta\Omega \rangle$ during reversals becomes apparent when comparing Figures 5.4(c) and 5.2(c), revealing the strong nonlinear coupling of the magnetic field and the large-scale flows. The dynamics that couples these two fields is the toroidal field generation through the mean shear ($\mathrm{S} = \lambda \langle \mathbf{B}_P \rangle \cdot \boldsymbol{\nabla} \langle \Omega \rangle$, with $\langle \mathbf{B}_P \rangle$ the mean poloidal field) and the mean azimuthal Lorentz-force ($L_\phi = \hat{\boldsymbol{\phi}} \cdot \langle \mathbf{J} \rangle \times \langle \mathbf{B} \rangle$), which acts to decrease $\langle \Omega \rangle$. The auto-correlation of each of these components of the MHD system

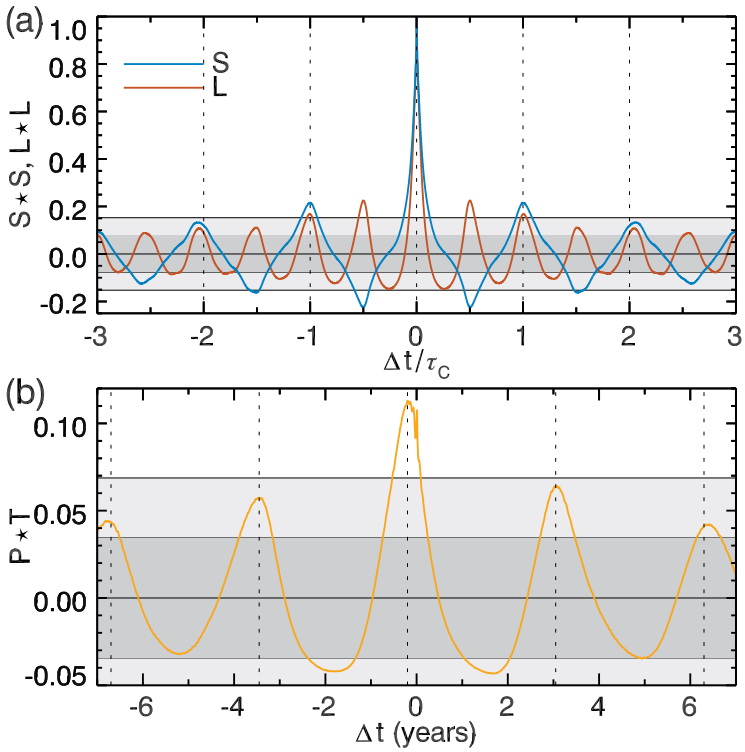

Figure 5.8: (a) Volume-averaged temporal auto-correlation of toroidal magnetic energy generation by mean shear ($\mathrm{S} = \lambda\langle\mathbf{B}_P\rangle \cdot \boldsymbol{\nabla}\langle\Omega\rangle$, blue curve) and the same for the mean Lorentz force impacting the mean angular velocity (L_ϕ, red curve) plotted against temporal lags Δt normalized by the polarity cycle period $\tau_C = 6.2$ years. Confidence intervals are shown as shaded gray regions, with the 67% interval in darker gray and 95% in lighter gray. (b) Cross-correlation of the mean poloidal energy production $\mathrm{P} = \mathbf{B}_P \cdot \boldsymbol{\nabla} \times \mathcal{E}'_\phi$ through the fluctuating EMF and the toroidal magnetic energy production due to the mean shear $\mathrm{T} = \langle B_\phi \rangle S$, showing the nonlinear dynamo wave character of the solution.

reveals that L_ϕ varies with a period corresponding to the magnetic energy cycle, whereas S varies on the polarity cycle period (Figure 5.8). It also shows the high degree of temporal self-similarity between cycles, with the auto-correlation of both quantities remaining significant with 95% confidence for a single polarity cycle and with 67% confidence for three such cycles.

Appealing to Figure 5.4(c), it is evident that $\mathbf{B}$ exhibits a high degree of spatial and temporal self-similarity, though with reversing polarity. Thus the period apparent in the auto-correlation for L_ϕ might be expected. Furthermore, if we simply let $\langle\mathbf{B}\rangle \approx \mathbf{B}_0(r,\theta)\exp(i\omega_C t)$, the Lorentz forces could be characterized very roughly as $L_\phi \propto L_{\phi,0}\exp(i\omega_L t) \sim$

$\mathbf{B}_0 \cdot \mathbf{B}_0/\ell \exp(2i\omega_C t)$, with cycle frequency $\omega_C = 2\pi/\tau_C$ and some length scale ℓ. Hence, the magnetic energy or Lorentz cycle frequency $\omega_L = 2\pi/\tau_L$ implies that $2\tau_L = \tau_C$. What is potentially more curious is that S varies on the cycle period. While Figure 5.2(c) might suggest a reversal in the solar-like character of the differential rotation, this in fact does not occur. Rather, the shear is significantly weakened but maintains the positive latitudinal gradient that sustains the toroidal magnetic field, which renders the sign of $\boldsymbol{\nabla}\Omega$ independent of time. Therefore, the polarity reversals in $\langle \mathbf{B}_P \rangle$ require that S vary with the polarity cycle period τ_C.

Therefore, the mechanism that sets the time scale for the reversal of the poloidal field is responsible for the reversal period. This mechanism is more difficult to assess as it requires information about the collective action of the turbulent convection upon existing magnetic structures. It is inherently nonlocal in space as magnetic energy from the local and small-scale action of helical motions upon a large-scale toroidal magnetic structure leads to a large-scale poloidal field, and thus is also nonlocal in time as the large-scale structures evolve on longer time scale than the convection. However, several components of the turbulent production of poloidal magnetic field can be illustrated. In particular, the axisymmetric collective action of the turbulent velocity on the magnetic field that produces poloidal field $\mathcal{E}'_\varphi$ and its evolution can be seen in Figures 5.9 and 5.10. In these figures and those that follow, the average cycle is shown, which has been formed by identifying the common structures in each cycle, obtaining the times of the beginning and end of each cycle as defined through these structures, and then stretching each cycle to be the same length in time and co-adding them. This is greatly aided by the extreme regularity of the cycle, which varies by only a few weeks from cycle to cycle.

In Figures 5.7, 5.9, and 5.10, two primary regions of production of poloidal magnetic field are visible: one at low latitudes and another at high latitudes. The low latitude regions of poloidal energy production are associated with convective cells acting upon the equatorially migrating toroidal wreaths. While the mechanism is somewhat similar for the

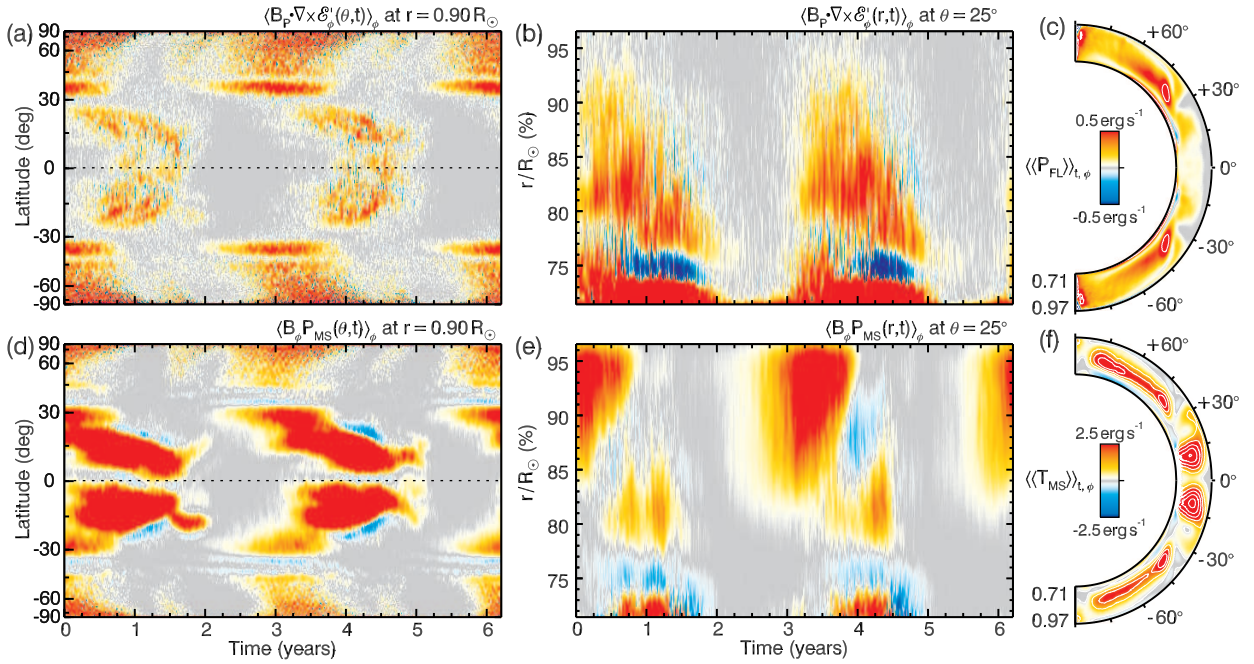

Figure 5.9: A comparison of the temporal evolution of the poloidal magnetic energy production through the fluctuating EMF as $P = \mathbf{B}_P \cdot \boldsymbol{\nabla} \times \mathcal{E}'_\phi$ and toroidal magnetic energy production by mean shear with $T = B_\phi P_{MS}$ in D3S. All cycles have been stretched to the the same time span and then averaged to allow the progression of an average cycle to be ascertained. (a) Poloidal magnetic energy generation P in the upper convection zone shown with latitude and time in cylindrical projection, illustrating the strong field generation above about $\pm 30°$ and the weak generation that accompanies the equatorward propagation of the large toroidal wreaths. (b) P plotted with depth $r/\,\mathrm{R}_\odot$ at a latitude of 25°. The tapering with depth arises from the strong radial dependence of $\mathbf{B}_P$, with a downward direction of propagation. (c) P averaged over the entire cycle rendered in the meridional plane. (d) Toroidal magnetic energy generation T exhibited over the average cycle and with latitude in cylindrical projection, showing the equatorward migration of field generation. (e) T in depth and time at a latitude of 25°, with two zones of migration evident. (f) T averaged over the entire cycle, where the equatorial and polar regions represent spatially separated zones of generation.

high-latitude poloidal field, it primarily originates in the helical action of convection on the high-latitude wreaths, which themselves are built from the differential rotation brought to the poles through torsional oscillations. In turn, these oscillations arise from the transport of angular momentum to the poles through Maxwell stresses and from the increased vigor of the convection there at the beginning of a magnetic energy cycle leading to Reynolds

stresses that spin up the pole. The spatial and temporal separation of poloidal and toroidal field generation is particularly evident when comparing Figures 5.9a and 5.9d. The greatest generation of poloidal field is concentrated in the polar regions and near the tangent cylinder, with the low latitudes playing much less of a role. In contrast, the generation of toroidal magnetic field is greatest at low latitudes throughout the bulk of the cycle. In Figures 5.9b and 5.9e, the reversal in the sign of the kinetic helicity of the convection is largely responsible for the thin region of destruction of magnetic field in the lower convection zone, where there is an anti-correlation between the fluctuating velocity field and the fluctuating magnetic field.

At the beginning of the cycle, when the magnetic fields are weakest (Figure 5.10a) and after the differential rotation has recovered (Figure 5.2c), toroidal field begins to grow at roughly $\pm 30^{\circ}$. The turbulent action of the convection on this newly generated wreath sustains the EMF on the polar edge of the wreath, which is near the tangent cylinder (Figure 5.9a). In combination with the polar EMF that emerges from the action of convection on the toroidal fields there, this serves the purpose of sustaining the poloidal field that in turn allows the wreaths to be maintained through the action of the differential rotation. However, once the polar differential rotation has been quenched the EMF that had been quite prominent at the tangent cylinder vanishes. The EMF that remains moves equatorward, advancing with the migration of the wreaths; yet it is still on the polar edge of the wreath. At this point, the strong toroidal magnetic field at low latitudes has begun to significantly feedback on the equatorial differential rotation, modifying the structure of the convection and diminishing the differential rotation. Furthermore, in D3S, as a cycle progresses the centroid for the greatest dynamo action propagates both equatorward as evident in the time-latitude diagram Figures 5.9e and downward in radius as is suggested in the time-radius diagrams of Figure 5.9f. Hence, the equatorial migration begun at the surface makes its way deeper into the domain as the cycle progresses.

The wreaths eventually lose their azimuthal coherence through the lack of sufficient

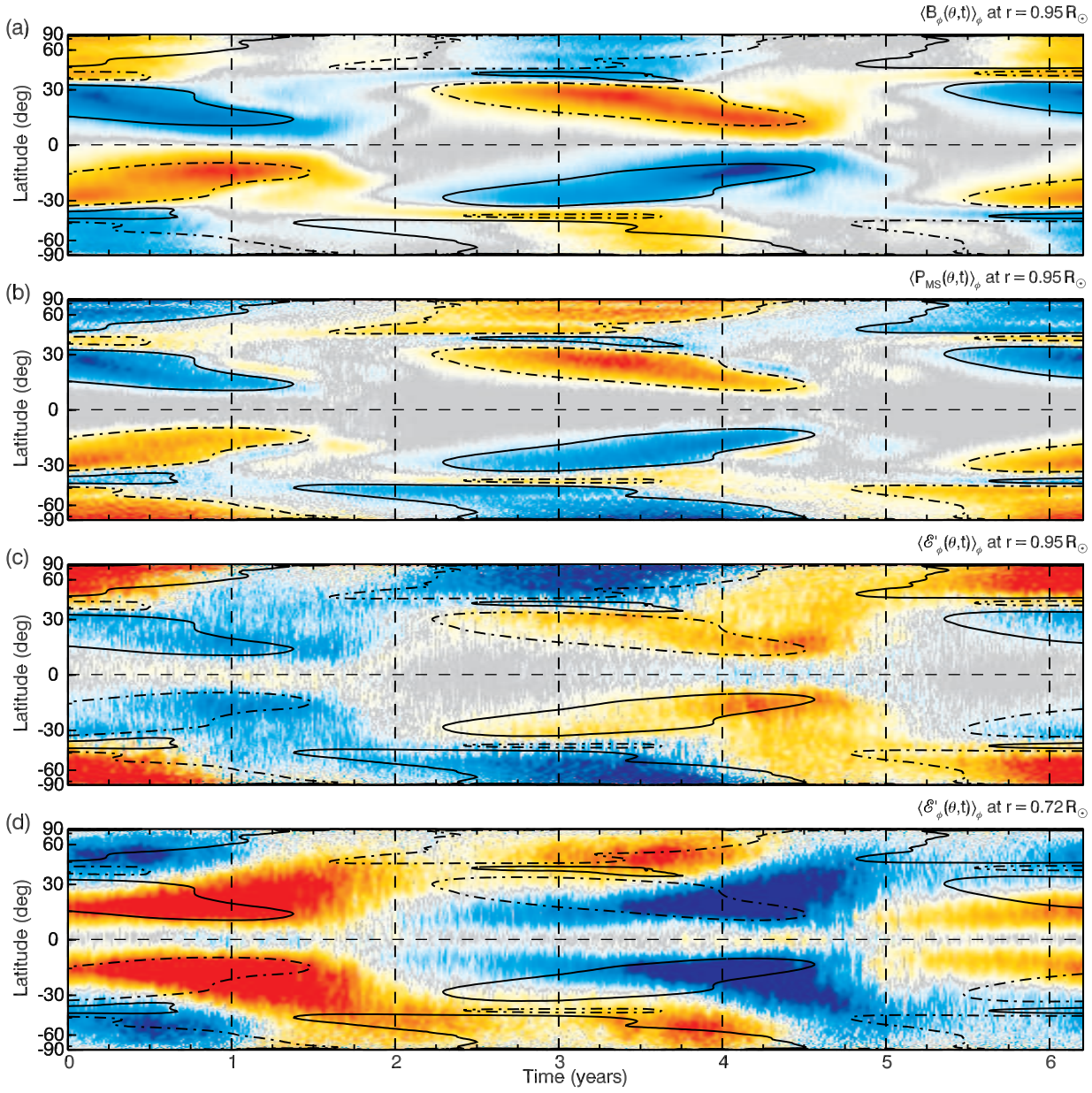

Figure 5.10: A comparison of the time and latitudinal evolution of the poloidal field production by fluctuating EMF $\mathcal{E}'_\phi$ and the toroidal field production by mean-shear $P_{\rm MS}$ over an average cycle of D3S. (a) Azimuthally-averaged toroidal field B_ϕ near the upper boundary at $0.95\,{\rm R}_\odot$, with the contours of $P_{\rm MS}$ overplotted with negative values as solid contours and dash-dotted contours as positive values of $P_{\rm MS}$. (b) Toroidal magnetic field production through mean shear $P_{\rm MS}$ at $0.95\,{\rm R}_\odot$. The turbulent EMF $\mathcal{E}'_\phi$ is shown (c) at $0.95\,{\rm R}_\odot$ and (d) $0.72\,{\rm R}_\odot$. The contours are a visual aid to help assess the dynamo wave character of the solution.

differential rotation to sustain them, the destructive influence of the convection, and also due to cross-equatorial flux cancellation. Together these processes lead to a rapid dissemination of the remaining flux by the convection. This is evident in Figure 5.4(c), where at the end of each cycle the wreaths converge on the equator and their resulting destruction leads to the poleward advection of field. This advected field is of the opposite sense of the previous cycle's polar cap and, being of greater amplitude compared to the remaining polar field, establishes the sense of the subsequent cycle's polar field. The sense of the subsequent poloidal field seems however to be determined by the weak EMF generated at the equator, as was also seen in Nelson et al. (2013a). This EMF begins to be generated as the toroidal fields start their equatorward migration and is sustained throughout the rest of the cycle (Figures 5.10c, d), leading to enough field generation there for these freshly minted and oppositely signed poloidal fields to overcome the dissipative collapse that the fields elsewhere in the domain succumb to. This EMF originates in the action of convection on the equatorward edge of the wreaths, which leads to a weak but influential cross-equatorial poloidal linking of the wreaths as is marginally visible in Figure 5.4.

All of these processes suggest that the reversal time scale is set by three time scales: the rate of production of differential rotation kinetic energy, the effective rate of conversion of differential rotation kinetic energy into toroidal magnetic energy, and the rate of conversion of toroidal magnetic energy into poloidal magnetic energy that in turn sustains the toroidal field. The latter rate is related to the dynamo efficiency of the convection, which Figure 5.6f suggests to be about 24% and is close to value found in Augustson et al. (2013b). This level of efficiency is what one might expect given the factor of 5 between the rate of toroidal energy generation and poloidal energy generation seen in Figures 5.9c, f. This is more or less constant throughout the cycle, though it requires toroidal field to be present. However, the other two processes are more difficult to pin down given that they vary throughout the cycle due to the nonlinear feedback of the Lorentz force.

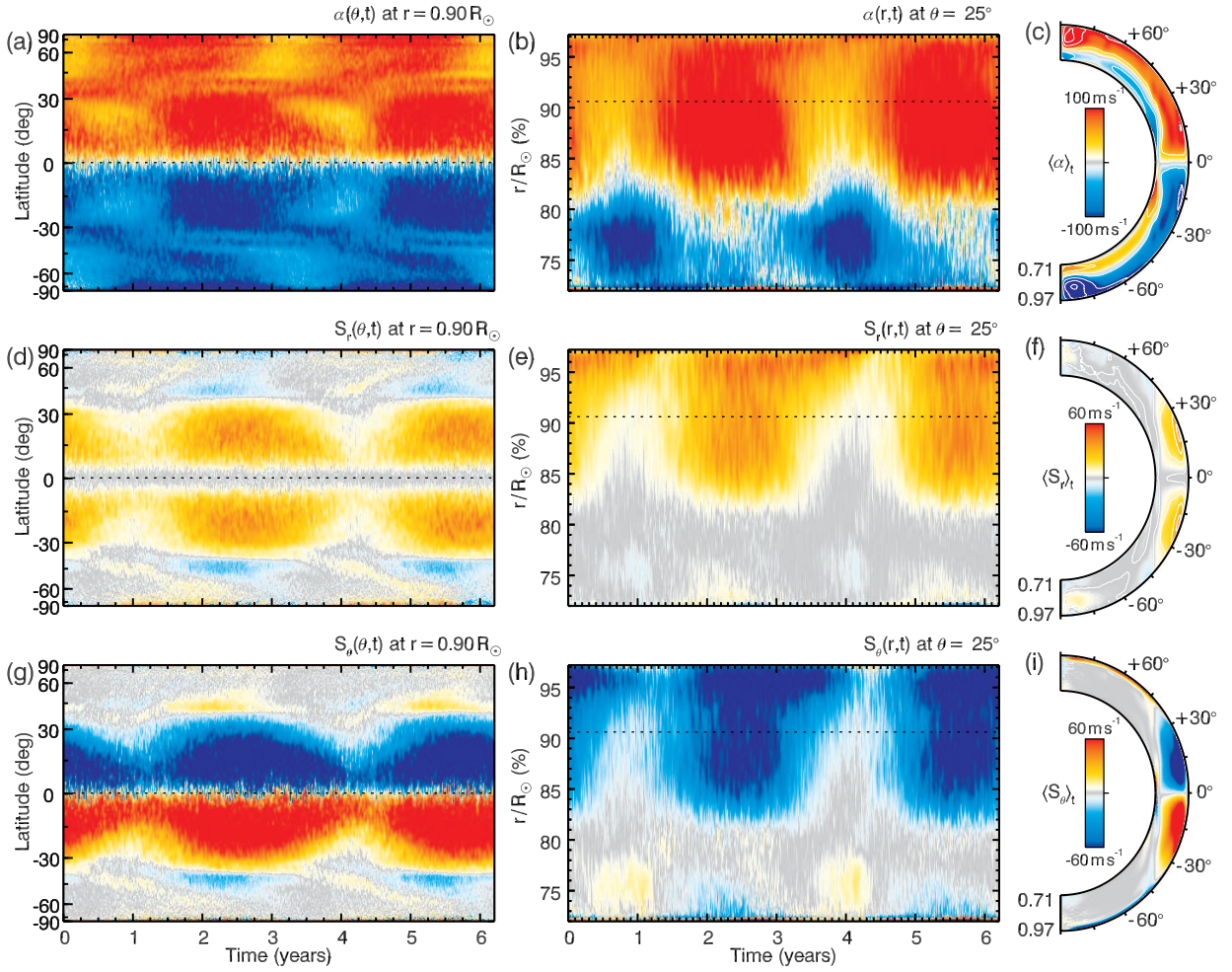

Figure 5.11: A mean-field interpretation of the D3S dynamo over the average cycle. The isotropic α-effect arising from the kinetic helicity is shown (a) with latitude and time, (b) with radius and time, and (c) averaged over the cycle. The radial velocity S_r and latitudinal velocity S_θ of the dynamo wave propagation within the context of the Parker-Yoshimura mechanism are exhibited in (d-i). (d) A radial cut at $0.90\,R_\odot$ through the radial propagation S_r of the dynamo wave, outward propagation is in red and downward in blue. (e) A latitudinal cut through S_r, colors as in (d) and the dotted line indicates the depth of the radial cut in (d). (f) S_r averaged over the cycle and shown in the meridional plane. Figures (g-i) are as in (d-f), but for S_θ, with the latitudinal propagation is equatorward at latitudes above 30° and largely poleward at lower latitudes (blue in the northern hemisphere and red in the south).

5.7 Equatorward Dynamo Wave Propagation

As with ASH and EULAG, simulations in spherical segments that employ the Pencil code have also obtained regular cyclical magnetic behavior. Some of these polarity reversing

solutions exhibited equatorward propagating magnetic features (Käpylä et al., 2012, 2013), magnetic flux ejection (Warnecke et al., 2012), and 33-year magnetic polarity cycles (Warnecke, 2013). Currently, however, the mechanism for the equatorward propagation of the magnetic structures in those simulations remains unclear. Perhaps the mechanism is similar to that seen here.

The equatorward propagation of magnetic features observed in this case, as in Figures 5.4(c) and 5.5(a), arises through two mechanisms. The first process is the nonlinear feedback of the Lorentz force that acts to quench the differential rotation, disrupting the convective patterns and the shear-sustaining Reynolds stresses they possess. Since the latitudinal shear serves to build and maintain the magnetic wreaths, the latitude of peak magnetic energy corresponds to that of the greatest shear. So the region with the largest magnetic potential energy in the form of latitudinal shear moves progressively closer to the equator as the Lorentz forces of the wreaths locally weaken the shear. Such a mechanism explains the periodic modifications of the differential rotation seen in Figure 5.2(c). However, it does not explain how this propagation is initiated and sustained, as one might instead expect an equilibrium to be established with the magnetic energy generation balancing the production of shear and which is further moderated by cross-equatorially magnetic flux cancellation as the distance between the wreaths declines as seen in earlier simulations (Brown et al., 2011b; Nelson et al., 2013a).

There are two possibilities for the second mechanism that promotes the equatorward propagation of toroidal magnetic field structures. If we may consider the dynamo action in this case as a dynamo wave, the velocity of the dynamo wave propagation is sensitive to the gradients in the angular velocity and the kinetic helicity in the context of an $\alpha\Omega$ dynamo (e.g., Parker, 1955; Yoshimura, 1975). This dynamo-wave velocity is given as $\mathbf{S} = -\lambda\alpha\hat{\boldsymbol{\phi}} \times \boldsymbol{\nabla}\Omega$, where $\lambda = r\sin\theta$. The basic α-effect has $\alpha = \tau_o\langle \mathbf{u} \cdot \boldsymbol{\omega} \rangle/3$, and so depends on the convective overturning time τ_o and the kinetic helicity. These quantities are shown in Figure 5.11 with time-latitude, time-radius, and time-averaged plots over the average cycle. This simple

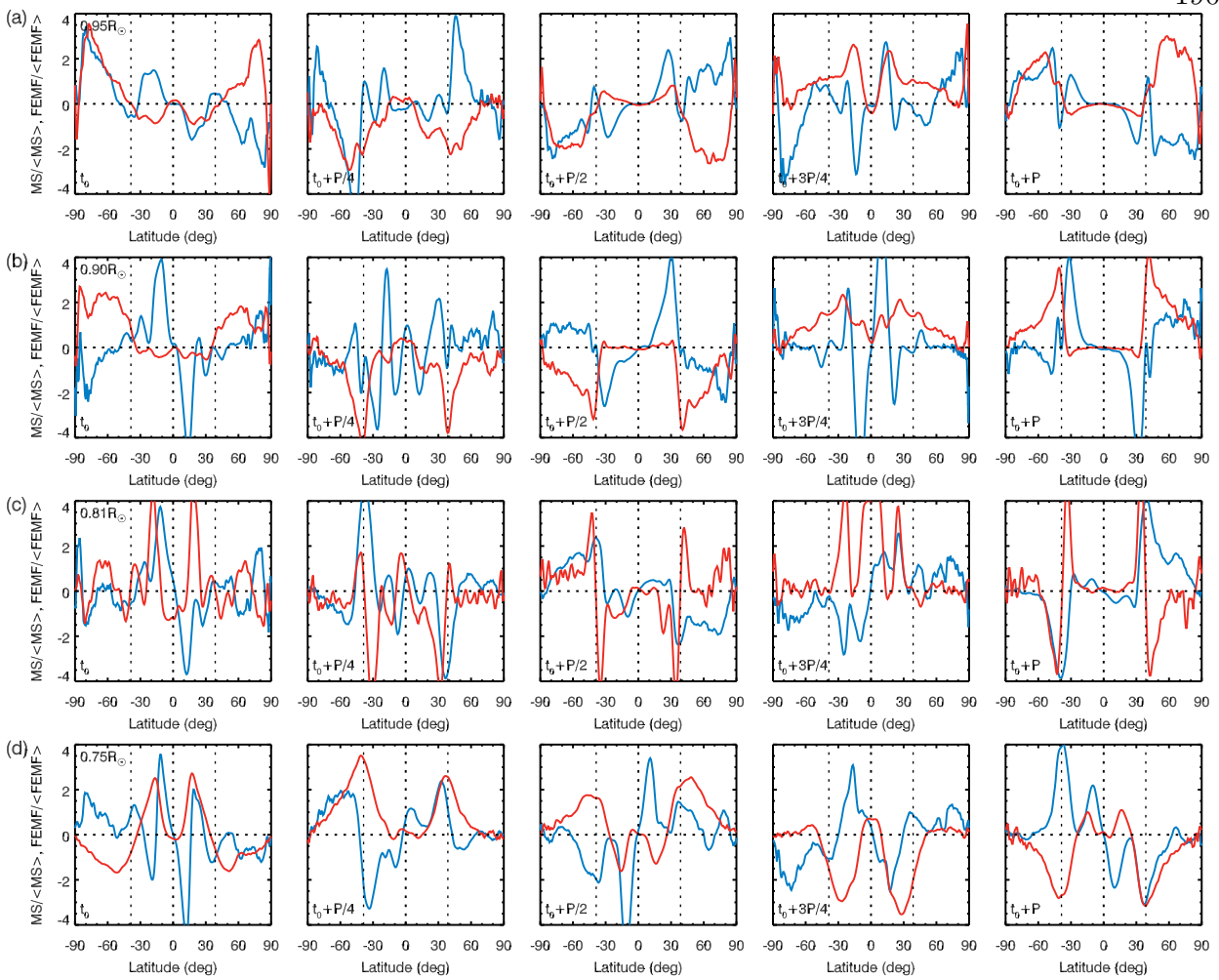

Figure 5.12: A comparison of the latitudinal regions of generation by the two primary toroidal and poloidal field production mechanisms at intervals of a quarter of the polarity cycle period in the average cycle. This serves to show the relative displacement of the two mechanisms, which may assist the wreaths in their equatorward propagation. The production of toroidal field is shown in blue, and the fluctuating azimuthal EMF is in red. The time series begins at t_0 and increments by a quarter of the polarity cycle period as one proceeds to the right. This is repeated for four depths: (a) $0.95\,\mathrm{R}_\odot$, (b) $0.90\,\mathrm{R}_\odot$, (c) $0.81\,\mathrm{R}_\odot$, (d) $75\,\mathrm{R}_\odot$.

analysis indicates that near and poleward of the edge of the low-latitude wreaths the sign of the Parker-Yoshimura mechanism is correct to push the dynamo wave toward the equator, but the effect is marginal elsewhere. The second possibility is that the spatial and temporal offsets between the fluctuating EMF and the mean-shear production of toroidal field leads to a nonlinear inducement to move equatorward. This mechanism relies on the concurrent

movement of the turbulent production of the poloidal field that continues to destroy gradients in angular velocity through the production of toroidal magnetic through the action of the differential rotation on the renewed low-latitude poloidal field as is visible in Figures 5.9 and 5.12.

5.8 Conclusions

The simulation presented here is the first to self-consistently exhibit four prominent aspects of solar magnetism: regular magnetic energy cycles during which the magnetic polarity reverses, akin to the sunspot cycle; magnetic polarity cycles with a period of 6.2 years, where the orientation of the dipole moment returns to that of the initial condition, the equatorward migration of toroidal field structures during these cycles, and an interval of magnetic quiescence after which the previous polarity cycle is recovered. Furthermore, this simulation may capture some aspects of the influence of a layer of near-surface shear, with a weak negative gradient in $\langle\Omega\rangle$ within the upper 10% of the computation domain (3% by solar radius). The magnetic energy cycles with the time scale $\tau_C/2$ arise through the nonlinear interaction of the differential rotation and the Lorentz force. We find that the nonlinear feedback of the Lorentz force on the differential rotation disestablishes its primus inter pares role in the generation of toroidal magnetic energy. The magnetic fields further quench the differential rotation by impacting the convective angular momentum transport during the reversal. Furthermore, despite the nonlinearity of the case, there is an eligible influence of a dynamo wave in the fluctuating production of poloidal magnetic field linked to the shear-produced toroidal field. The possible mechanisms producing the equatorward propagation of the toroidal fields have been elucidated, with the nonlinear dynamo wave character of the solution and the nonlocal interaction of the turbulent EMF and the mean-shear production of toroidal field all playing a role. However, the dominant mechanism behind the equatorward propagation is the nonlinear feedback of the Lorentz force on the differential rotation. This simulation has also exhibited grand minima, similar to a Maunder minimum. Indeed,

there is an interval covering 20% of the cycles during which the polarity does not reverse and the magnetic energy is substantially reduced. Hence, despite rotating three times faster than the Sun and parameterizing large portions of its vast range of spatio-temporal scales, some of the features of the dynamo that may be active within the Sun's interior have been seen in this global-scale ASH simulation.

Chapter 6

Global-scale Hydrodynamic Simulations of F-type Stars

"No man ever steps in the same river twice, for it's not the same river and he's not the same man." – Heraclitus

Differential rotation is a common feature of main-sequence spectral F-type stars. In seeking to make contact with observations and to provide a self-consistent picture of how differential rotation is achieved in the interiors of these stars, we use the 3-D Anelastic Spherical Harmonic (ASH) code to simulate global-scale turbulent flows in 1.2 and 1.3 $M_\odot$ F-type stars at varying rotation rates. The simulations are carried out in spherical shells that encompass most of the convection zone and a portion of the stably stratified radiative zone below it, allowing us to explore the effects of overshooting convection. We first explore the general properties of the hydrodynamics within these thin convection zones here. Additionally, three of the simulations exhibit a global-scale shear instability within their stable regions that persists for the duration of the simulations. The flow structures associated with the instabilities have a direct coupling to and impact upon the flows within the convection zone.

In Chapter 7, we examine a case in detail as well as the scaling of the mean flows and thermal state with rotation rate and mass, and link these scalings to fundamental parameters of the simulations. These two chapters are based on work published in Augustson et al. (2012)[1] and are largely restatements of that paper, though with some new material

[1] Augustson, K. C., Brown, B. P., Brun, A. S., Miesch, M. S., & Toomre, J., 2012, "Convection and Differential Rotation in F-type Stars", ApJ, 756, 169

included (see §6.4). As the primary author of the paper, I conducted all of the simulations, performed all of the analysis, and wrote the paper. The coauthors provided advice and guidance throughout this process, with Sacha Brun encouraging the scaling analysis during a delightful trip to Paris and Ben Brown kindly providing his data for the G-type stars. This first peek into the possible scaling of hydrodynamic parameters such as differential rotation and thermal gradients with both rotation and mass has since been carried over to a larger mass range in Olivier Do Cao's thesis work.

6.1 Introduction: Stellar Convection and Rotation

Star-forming molecular clouds are generally endowed with angular momentum and magnetic fields. As a star forms, gases from the cloud fall into a proto-stellar region. Since the initial position of this gas is far from the stellar core, the initial angular momentum of the gas is amplified many orders of magnitude before it is incorporated into the star. The fact that most young stars are observed to have large rotation rates implies that, regardless of the complicated processes that initiate and eventually lead to the formation of a main-sequence star, some of this angular momentum must be transferred to the star. During the early evolution of these stars, it is thought that they lose their initially high angular velocity. Stellar winds and magnetic braking acting throughout the lifetime of the star may lead to such angular momentum loss (Bouvier et al., 1997). However, even after several billion years of angular momentum loss, stars such as the Sun still possess a substantial angular velocity. Indeed, stars with convective envelopes exterior to their radiative envelopes are believed to behave in qualitatively similar ways, where the complex interaction between the convection and the star's rotation likely yields non-uniform rotation. Hence, most stars may be differentially rotating, with the angular velocity varying with depth and latitude. The Sun is one such star, where the equator rotates 30% faster than the poles.

Main-sequence stars of all masses appear to have convection zones in some portions of their interiors. What makes F-type stars of particular interest is that they bridge a

gap between stars that have external convection zones, like the Sun, and those that have convective cores, such as A-type stars. They actually possess two regions of convective instability, one exterior to their radiative envelope and a convective core. Being slightly more massive than the Sun, F-type stars span the mass range between 1.1 and 1.6 $M_\odot$. With increasing mass, the convection zones of these stars become increasingly narrow and contain less of the star's total mass, ranging from 25% to 2% of the radius of the star compared to the Sun's 30%. The luminosity of the F-type stars increases from about 1.4 $L_\odot$ at 1.1 $M_\odot$ to 6.0 $L_\odot$ at 1.6 $M_\odot$, while the stellar radius only increases by about 27% over the same range of masses. Thus, the amount of energy flux that must be transported through ever thinner convection zones increases by a factor of 2.4. To accommodate the increasing flux, the convection must become more vigorous in order to efficiently transport the heat from the bottom of the convection zone to the photosphere. Such properties place F-type stars in an interesting position to address questions of how convection interacts with rotation and convection-zone geometry to produce differential rotation.

6.1.1 Observations of Differential Rotation

Detecting differential rotation in stars is very difficult, as stars other than the Sun generally cannot be spatially resolved. However, recent observations using spectropolarimetry permits some information about both the differential rotation and the magnetic field to be mapped out on the surface of the star (e.g., Donati et al., 1997; Marsden et al., 2005). Several additional techniques exist to extract information about the rotational behavior of a star from spectra (e.g., Reiners & Schmitt, 2003b; Reiners, 2006), photometry (e.g., Henry et al., 1995; Collier Cameron et al., 2002; Silva-Valio & Lanza, 2011), and asteroseismology (e.g., Thompson et al., 1996; Schou et al., 1998; Verner et al., 2011). For the F-type stars, a Fourier analysis technique using stellar spectra has produced the largest number of detections of differential rotation to date (Reiners, 2007). In this method, many spectral lines from a target star are averaged to produce a mean line-profile which is then Fourier transformed.

Table 6.1
Properties of Cases A and B

Cases	M	L	R	T_{eff}	$\log_{10}g$	r_1/R	r_2/R
A	1.20	2.00	1.19	6300	4.54	0.80	0.98
B	1.30	2.93	1.33	6540	4.48	0.86	0.98

Table 6.1: The mass of the star being simulated (M) is given in units of $M_\odot$ (1.98×10^{33} g); luminosity (L) in units of $L_\odot$ (3.86×10^{33}); stellar radius (R) in units of $R_\odot$ (6.96×10^{10} cm); the stellar effective temperature (T_{eff}) in Kelvin; the logarithm of gravity in cm s^{-2}. The lower and upper radial boundaries of the simulation domains are in turn r_1 and r_2.

The ratio of the first two minima, which are denoted as q_1 and q_2, of the resulting power spectrum of this line is used to determine whether or not the star is differentially rotating, and if so by how much.

In Figure 6.1 the absolute differential rotation of F-type stars is shown to increase with rotation rate, reach a maximum, and then to decrease slowly with ever faster rotation; a trend that is more clear with the use of more rapidly rotating stars in Reiners (2006). For Figure 6.1 we have only shown stars with masses between 1.15 and 1.45 $M_\odot$ that have both a measurement of the differential rotation and its uncertainty. It is likely, however, that rather more of the stars cataloged in Reiners (2006) rotate differentially as it is difficult to detect when a star rotates too rapidly or too slowly. Indeed, stars with a projected rotational velocity ($v \sin i$) greater than 50 km s^{-1} have a relative differential rotation that often falls below the detection threshold. Similarly, when using the method of Reiners & Schmitt (2002c), stars with $v \sin i \leq 10$ km s^{-1} rotate too slowly to accurately measure the bulk rotation rate further restricting the range of detection. Those stars identified as differentially rotating exhibit a wide range of relative differential rotation. There is even the suggestion that several stars may possess anti-solar differential rotation, where the pole rotates more rapidly than the equator, and which may also be interpreted as cool polar spots.

There appears to be a trend in the observations of Reiners (2006) in which the number of stars that rotate differentially seems to decrease with decreasing B-V color. However, this

could be a two-fold selection effect. The first effect is from the non-uniform color (effective temperature) sampling of stars. The distribution is roughly Gaussian between B-V values of 0.2 and 0.6, or spectral types A7 and G1 respectively, with a peak at a B-V of 0.4 (spectral type F4). The second effect arises from the fact that higher mass stars tend to rotate more rapidly and thus their $q_2 - q_1$ values fall below the differential rotation detection threshold. Of the stars that do rotate differentially, the results for the F-type stars with the largest differential rotation in Reiners (2006) are consistent with the trend of increasing absolute differential rotation found in Barnes et al. (2005) where they find that absolute differential rotation increases strongly with effective temperature or increasing mass, as seems to be the case in our simulations as well (Figure 6.1 and §7.5).

6.1.2 Global Models of F-type Star Convection

How the angular momentum in a star is redistributed to produce and maintain a stable angular velocity profile appears to involve subtle dynamical balances. The highly turbulent nature of stellar convection coupled with rotation involves a vast range of scales, making it quite challenging to directly model such dynamic processes. Yet these issues must be explored if the behavior of stellar rotation is to be understood. Rapid advances in supercomputing have enabled global-scale 3-D simulations of convection coupled with rotation that are shedding light on the dynamics of the flow achieved within stars (Bessolaz & Brun, 2011; Brown et al., 2008; Miesch et al., 2008). In a similar spirit, we are reporting on the dynamics of turbulent global-scale convection in a realistically stratified computational domain in two main-sequence F-type stars that are each studied over a range of rotation rates. The two stars investigated here are a $1.2\,\mathrm{M}_\odot$ star (*Case A* simulations) and a $1.3\,\mathrm{M}_\odot$ star (*Case B* simulations) that possess the same central hydrogen abundance resulting in main-sequence ages of 1.15 Gyr and 1.00 Gyr respectively (see Table 6.1). As mentioned above, convection zone depth and luminosity change rapidly with mass in F-type stars. Indeed, the tenth of a solar mass difference between the two stars simulated here leads to

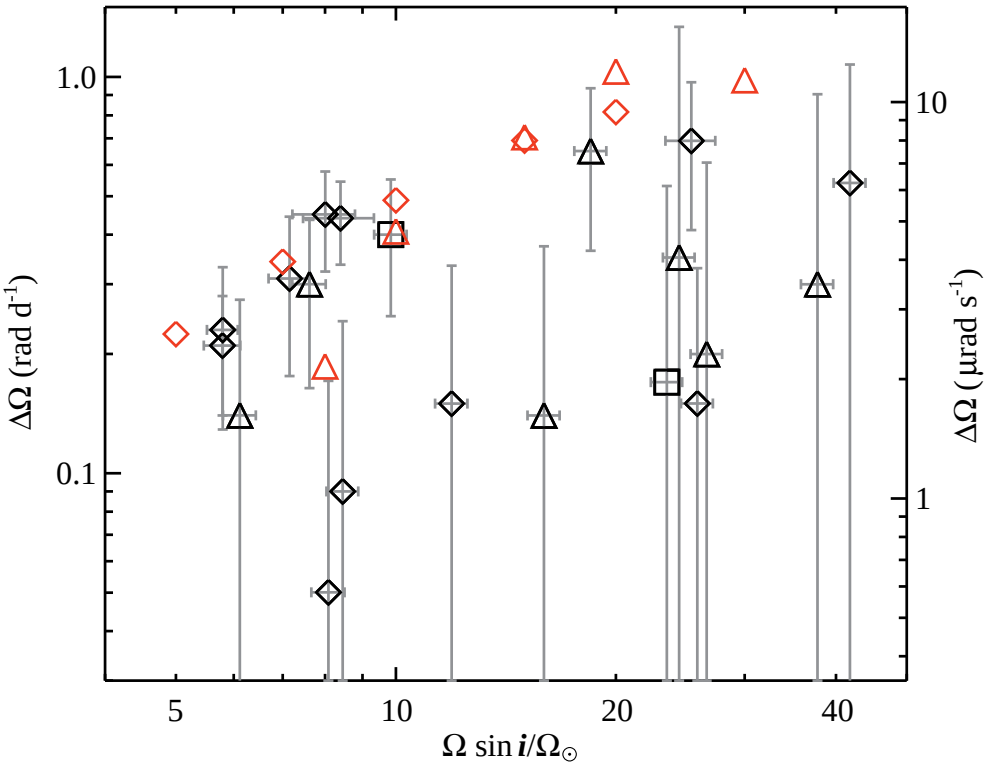

Figure 6.1: Absolute differential rotation contrast ($\Delta\Omega$) seen in simulations and observed on F-type stars. The observational uncertainties of the contrast and rotation rate are shown as gray lines. The values of the $\Delta\Omega$ realized in our simulations are shown in red symbols, while those observed on F-type stars with masses between 1.15-1.25 $M_\odot$ shown as diamonds, 1.25-1.35 $M_\odot$ as triangles, and 1.35-1.45 $M_\odot$ as squares. Observational data from Table B.1 of Reiners (2006).

a 50% increase in luminosity and a 50% decrease in convection zone depth, allowing us to also probe how the vigor of the convection and convection zone geometry impact the mean properties of the flows established in these stars.

In our analysis of these simulations, we first provide details about the anelastic equations solved, the formulation of the numerics, and the setup the numerical experiments in §6.2. The general properties of the convective patterns and mean flows of selected cases are discussed in §6.3. We look at the dynamics in detail for a particular case in §7.1. The effects of overshooting convection are addressed in §7.2. The link between the thermal properties of the simulations and the differential rotation is probed in §7.3. The connection between

the two mean flows, the differential rotation and the meridional circulation, is examined for these two cases in §7.4. Finally, in §7.5, the scaling of the magnitudes of the mean flows and the thermal signatures of the flows are presented.

6.2 Formulating the Problem

The convection zones of most stars are extremely turbulent with very small values of viscosity and thermal diffusivity. A direct numerical simulation that effectively captures all of the relevant scales of motion in a stellar convection zones are currently, and for the foreseeable future, impossible. Therefore, a model that eliminates the fast time-scales of sound waves and parametrizes the dynamics at small spatial scales is necessary in order to capture the large number of rotational periods and the full spherical geometry. Such features are thought to be crucial in establishing an equilibrium state that maintains a differential rotation. To this end, we use the 3-D anelastic spherical harmonic (ASH) simulation code. ASH is a mature modeling tool which solves the anelastic MHD equations of motion in a rotating spherical shell using a pseudo-spectral method. ASH simulations capture the entire spherical shell geometry and allow for zonal jets, large scale vortices, and structures with connectivity such as convective plumes. The simulated turbulence is still many orders of magnitude removed from the intensely turbulent conditions present in stellar convection zones. Despite this discrepancy, simulations of the solar convection zone using ASH have been successful in matching helioseismic constraints upon differential rotation within the solar convection zone (Miesch et al., 2000; Brun & Toomre, 2002; Miesch et al., 2006, 2008; Brun et al., 2011).

6.2.1 Anelastic Equations

In the anelastic approximation, the time derivative of the density in the continuity equation is eliminated. This approximation is employed to capture the effects of density stratification without having to resolve the rapidly varying sound waves. In this approxima-

tion, the Courant-Friedrichs-Lewy condition on the time step will then be governed by the subsonic flow velocity rather than the sound speed. The anelastic equations evolved within ASH are fully nonlinear in the velocity variables, but the thermodynamic variables are linearized about the spherically symmetric and evolving mean stratification comprised of the quantities $\overline{\rho}$, $\overline{S}$, $\overline{P}$, and $\overline{T}$ for the density, entropy, pressure, and temperature respectively. The fluctuations of thermodynamic variables are taken about the mean stratification and are denoted ρ, S, P, and T. These fluctuations are generally of the order $\epsilon = (\gamma - 1) M^2$ where M is the Mach number of the flow at a given depth, which in the simulations here gives $\epsilon \approx 10^{-6}$. The resulting equations in physical units, in spherical coordinates (r, θ, ϕ), and with time t are (Glatzmaier, 1984; Clune et al., 1999)

$$\overline{\rho}\frac{\partial \mathbf{u}}{\partial t} = -\overline{\rho}\mathbf{u}\cdot\boldsymbol{\nabla}\mathbf{u} - \boldsymbol{\nabla}P - \rho\mathbf{g} + 2\overline{\rho}\mathbf{u}\times\boldsymbol{\Omega}_0 + \boldsymbol{\nabla}\cdot\mathcal{D} - \Lambda\hat{\mathbf{r}}, \tag{6.1}$$

$$\overline{\rho}\overline{T}\frac{\partial S}{\partial t} = -\overline{\rho}\overline{T}\mathbf{u}\cdot\boldsymbol{\nabla}\left(\overline{S}+S\right) - \nabla\cdot\mathbf{q} + \Phi, \tag{6.2}$$

$$\frac{\partial \overline{P}}{\partial r} = -\overline{\rho}g_r + \Lambda, \tag{6.3}$$

$$\boldsymbol{\nabla}\cdot\overline{\rho}\mathbf{u} = 0, \tag{6.4}$$

where $\mathbf{u} = u_r\hat{\mathbf{r}} + u_\theta\hat{\boldsymbol{\theta}} + u_\phi\hat{\boldsymbol{\phi}}$ is the velocity vector, $\boldsymbol{\Omega}_0 = \Omega_0\hat{\mathbf{z}}$ is the angular velocity of the rotating frame, $\hat{\mathbf{z}}$ is the axial unit vector, and c_P is the specific heat at constant pressure. The gravitational acceleration is taken to be $\mathbf{g} = -g(r)\hat{\mathbf{r}}$. As the simulation evolves, a turbulent pressure pushes the system slightly away from the initial hydrostatic equilibrium, Λ in Equation (6.3) is the radial gradient of the spherically symmetric component of this turbulent pressure. The components of the viscous stress tensor $\mathcal{D}$ are Newtonian and Φ is the viscous heating, which are given by

$$\mathcal{D}_{ij} = 2\overline{\rho}\nu\left[e_{ij} - \frac{1}{3}\boldsymbol{\nabla}\cdot\mathbf{u}\delta_{ij}\right], \tag{6.5}$$

$$\Phi = 2\overline{\rho}\nu\left[e_{ij}e_{ij} - \frac{1}{3}\left(\boldsymbol{\nabla}\cdot\mathbf{u}\right)^2\right], \tag{6.6}$$

where e_{ij} is the stress tensor and ν is the effective kinematic viscosity. The energy flux $\mathbf{q}$ is composed of two diffusive components

$$\mathbf{q} = \kappa_r \overline{\rho} \mathrm{c_P} \boldsymbol{\nabla} \left(\overline{T} + T \right) + \kappa \overline{\rho} \overline{T} \boldsymbol{\nabla} S + \kappa_0 \overline{\rho} \overline{T} \frac{\partial \overline{S}}{\partial r} \hat{\mathbf{r}}, \tag{6.7}$$

where the first component is a radiation diffusion flux with the molecular radiation diffusion coefficient κ_r, The second component is an anisotropic entropy diffusion flux, with κ acting on the non-axisymmetric entropy fluctuations and another κ_0 acting only on the spherically symmetric component of the entropy.

Ideally, the system would adjust to a new equilibrium by modifying the Rosseland mean opacity and the thermal stratification. The overshooting convection realized in our simulations modifies the mean stratification in the overshooting region. However, to fully adjust the mean thermal state, and thus the radiative flux, would require evolving the simulation for a thermal relaxation time. This timescale is about $E_i/L \approx 2400$ yr for the $1.2\,\mathrm{M}_\odot$ F-type stars and about 160 years for the $1.3\,\mathrm{M}_\odot$ F-type stars, where E_i is the total internal energy of the plasma in the stable region and L is the luminosity. Since achieving these timescales is currently beyond our computational resources, we accelerate this process by first simulating the stars with the Rosseland mean opacity (κ_{Ros}) and the 1-D thermodynamic state from the stellar model, and then updating this opacity using the evolved thermodynamic state of the simulation. This is accomplished by Taylor expanding the opacity using the partial derivatives of the opacity with respect to the density and temperature extracted from the stellar model, and then updating the radiative diffusion coefficient with the mean thermal state as

$$\kappa'_{\mathrm{Ros}} = \kappa^0_{\mathrm{Ros}} + \left.\frac{\partial \kappa_{\mathrm{Ros}}}{\partial \rho}\right|_0 (\overline{\rho} - \overline{\rho}_0) + \left.\frac{\partial \kappa_{\mathrm{Ros}}}{\partial T}\right|_0 \left(\overline{T} - T_0\right),$$
$$\kappa_r = \frac{4ac\overline{T}^3}{3\mathrm{c_P}\overline{\rho}^2 \kappa'_{\mathrm{Ros}}},$$

where the subscript 0 indicates that these quantities are taken from the stellar model. This scheme is typically applied only once, but can be used as frequently as necessary to achieve an equilibrium. Updating the diffusion coefficient in this fashion ensures that the radiative

energy flux and the enthalpy flux are properly balanced in the stable region, providing for a nearly constant total flux throughout the domain and also avoiding the long time evolution that would otherwise be required (see §7.1.2). Finally, a linearized equation of state closes the set of equations for the fluctuations, while the ideal gas law closes the equations for the mean state

$$\rho/\overline{\rho} = P/\overline{P} - T/\overline{T} = P/\gamma\overline{P} - S/\mathrm{c_P}, \tag{6.8}$$

$$\overline{P} = (\gamma - 1)\mathrm{c_P}\overline{\rho}\overline{T}/\gamma, \tag{6.9}$$

where γ is the adiabatic exponent. A stellar evolution code, MESA (Paxton et al., 2011), is employed to evolve a realistic 1-D stellar model at the solar metallicity and helium mass fraction from the pre-main sequence to a central hydrogen mass fraction of 0.54. This places these models at about 20% of their main-sequence lifetime. This model is then used to establish the initial mean stratification for an ASH simulation. For the numerical experiments conducted here, we neglect the effects of stellar evolution. A single initial stellar structure model is used for each of the two simulated F-type stars shown in Table 6.1.

6.2.2 Numerics and Experimental Configuration

In the ASH code, the mass-flux remains divergence-free through a poloidal-toroidal streamfunction decomposition. These streamfunctions and the variations in the entropy and pressure are expanded in spherical harmonics $Y_\ell^m(\theta, \phi)$, with spherical harmonic degree ℓ and azimuthal order m, to resolve their horizontal structures and in Chebyshev polynomials $T_n(r)$ to resolve their radial structures. Temporal discretization is accomplished using a semi-implicit Crank-Nicolson time-stepping scheme for linear terms and an explicit Adams-Bashforth scheme for nonlinear terms. ASH is designed with modern programming constructs to yield efficient performance and scaling on massively parallel supercomputers (e.g., Clune et al., 1999). Several codes numerically solving for anelastic magnetohydrodynamics, including ASH, have recently been thoroughly tested on the same suite of nonlinear

problems, in which the accuracy of several numerical methods has been probed extensively and shown to be robust (Jones et al., 2011).

The studies here explore a range of rotation rates for each mass, from $5\,\Omega_\odot$ to $20\,\Omega_\odot$ for the $1.2\,\mathrm{M}_\odot$ case *Case A* simulations and from $8\,\Omega_\odot$ to $30\,\Omega_\odot$ for the $1.3\,\mathrm{M}_\odot$ *Case B* simulations. All cases at a given mass use the same initial stellar structure and are initialized with random perturbations in the fluctuating entropy. These ranges of rotation rates are chosen so that all the cases exhibit solar-like differential rotation, where the poles rotate more slowly than the equator, as is discussed in §7.5. Note that the nomenclature for the cases is: *Case A* or *Case B* depending upon the mass followed by the bulk rotation rate quoted in integer multiples of the solar rotation rate. So, *Case A10* is a $1.2\,\mathrm{M}_\odot$ F-type star rotating at 10 times the solar rate. Cases that omit the stable layer, simulating only the convectively unstable region, are denoted with an i after the case's name.

While most parameters and the initial stratification are taken from the stellar model, a perfect gas is assumed (Equation (6.9)). Therefore, the He and H ionization zones that occur in the outer 1% by radius of these stars cannot be properly captured. Additionally, ionization coupled with radiative losses drive very intense convection on small scales. These small scale flows are nearly sonic, so sound waves play an important role in the dynamics and cannot be neglected. Thus, the radius of the upper boundary (r_2) in our simulations is taken to be below this region, where the Mach number is generally very small, so that the assumptions made in the formulation of the anelastic approximation remain valid.

The simulations being reported on here include a portion of the stable radiative zone below the convection zone as seen in Figure 6.2, in a manner similar to the simulations have been carried out in a solar setting in Browning et al. (2006); Brun et al. (2011). Such a layer has been shown to play a large role in determining the radial and latitudinal structure of the differential rotation (Rempel, 2005). Indeed, the dependence of the morphology of the differential rotation upon the amplitude of a weak latitudinal entropy gradient imposed at an impenetrable lower boundary has been explored within ASH simulations of the Sun.

The simulations in Miesch et al. (2006) use this latitudinal entropy gradient to emulate a tachocline that is in a thermal wind balance. It was found that this gradient spurred an adjustment of the contours of constant angular velocity from an alignment with the rotation axis to a radial alignment. The impetus behind these various efforts is to understand why the helioseismically determined angular velocity of the Sun has nearly conical contours (Schou et al., 1998), as is also found in the angular velocity contours of the simulations explored here (see §6.3.1 and §6.3.2).

The position of the radius of the lower boundary (r_1) is determined by how deep the overshooting motions occurring within the simulations penetrate into the stable zone and by how much resolution is necessary to fully resolve the steep entropy gradient that arises below the convection zone. The radial extent of the stable region in these simulations is set to be roughly twice the penetration depth of the overshooting motions. This choice reduces the need for a high radial resolution and allows these simulations to capture the effects that convective overshooting and a stable layer have upon the mean flows and thermodynamic properties of the convection. However, it does restrict the ability of the simulations to capture the full spectrum of gravity waves excited by the convection as some of the modes are trapped within this cavity (see Brun et al., 2011).

6.2.3 Diffusion and Sub-grid-scale Models

The anelastic system of hydrodynamic equations requires eight boundary conditions in order to be well posed. One of the primary goals of this work is to assess the redistribution of angular momentum and energy in our simulations. Thus, we have opted for the following torque-free and flux transmitting boundary conditions

$$u_r = \frac{\partial}{\partial r}\left(\frac{u_\theta}{r}\right) = \frac{\partial}{\partial r}\left(\frac{u_\phi}{r}\right) = \left.\frac{\partial S}{\partial r}\right|_{r_2,\, r_1} = 0, \tag{6.10}$$

where the constant flux boundary condition on the entropy fluctuations implies that the mean entropy gradient remains unchanged on the boundaries throughout the simulation.

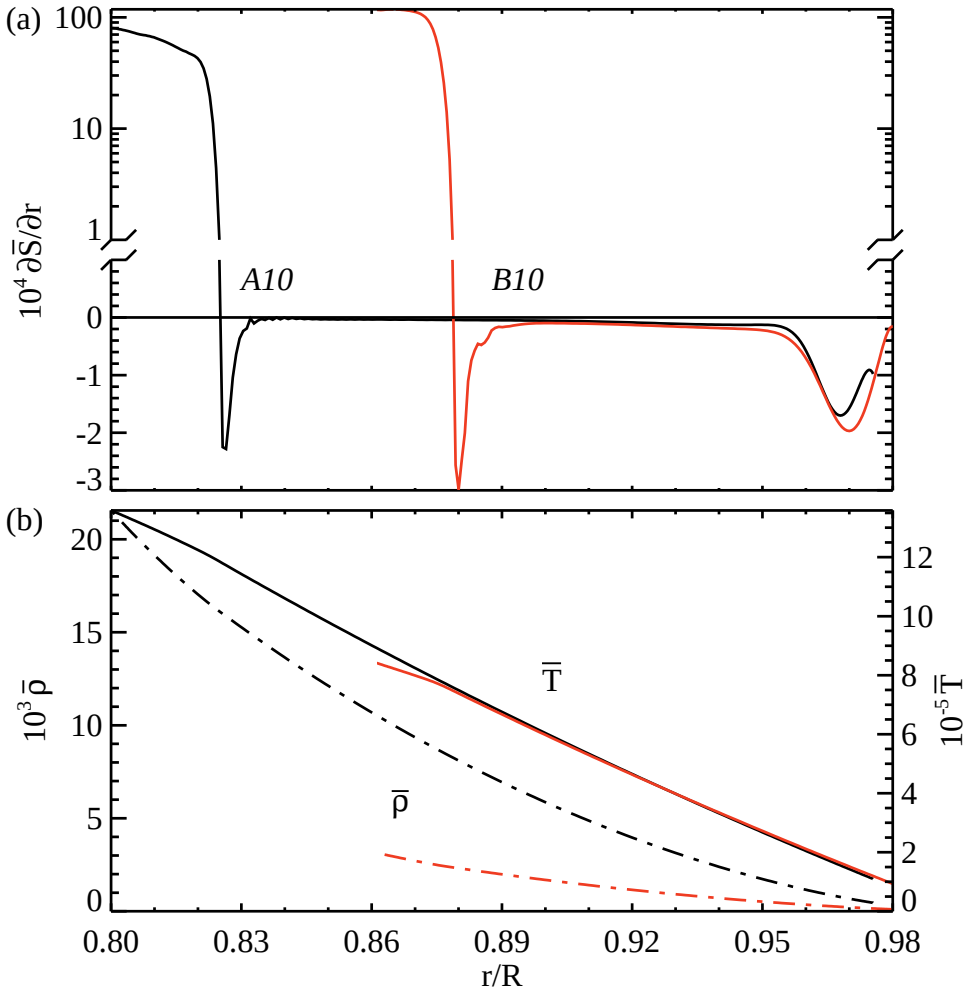

Figure 6.2: Time-averaged mean stratification established in *Case A10* (black lines) and *Case B10* (red lines). (a) The entropy gradient ($\partial\overline{S}/\partial r$ in units of $10^{-4}\,\mathrm{erg\,cm^{-4}\,K^{-1}}$); the break in the y-axis denotes the change from linear to logarithmic scaling. (b) The density ($\overline{\rho}$ in units of $10^{-3}\,\mathrm{g\,cm^{-3}}$, *dash-dot*) and temperature ($\overline{T}$ in units of 10^5K, *solid*).

The stress-free boundary conditions used in the simulations here ensure that the volume-integrated transport terms nearly vanish. Indeed, the total angular momentum is conserved to within the global accuracy of the radial derivatives at each time step. Over the course of the entire simulation where the mean stratification is allowed to change, it is conserved to within the order ϵ, roughly the order to which the anelastic approximation is valid.

Current and foreseeable computing resources, render simulations that directly capture all scales of stellar convection from global to molecular dissipation scales unattainable. The

simulations reported on here resolve nonlinear interactions among a large range of scales both in the convective and radiative zones of two F-type stars. Motions and waves within the actual star exist on scales smaller than our grid resolution, and in this sense our models should be regarded as large-eddy simulations (LES). These sub-grid scale motions are parameterized as effective viscous and thermal diffusivities (ν and κ respectively), which are meant to emulate the mixing properties of the unresolved turbulent eddies. These diffusivities are allowed to vary in radius only and evolve slowly in time as they are dependent upon the profile of the mean density $\overline{\rho}$. The radial profile of κ and κ_0 are given by

$$\kappa(r) = \frac{\kappa_{top}\left(\overline{\rho}/\overline{\rho}_{top}\right)^{-1/2}}{1+\exp\left[\alpha\left(r_\kappa - r\right)/\left(r_2 - r_1\right)\right]} + \kappa_{min}, \tag{6.11}$$

$$\kappa_0(r) = \frac{\kappa_0^{top}\exp\left[\beta\left(r_2 - r\right)/\left(r_2 - r_1\right)\right]}{1+\exp\left[\delta\left(r_{\kappa_0} - r\right)/\left(r_2 - r_1\right)\right]} + \kappa_0^{min}, \tag{6.12}$$

where κ_{top} is the thermal diffusivity at the upper boundary, κ_{min} is the floor value of this diffusivity, and α controls the steepness of the quenching of the diffusion below a particular radius r_ν. This allows the diffusion to be greatly reduced in stable regions, where motions have a small amplitude and the expected SGS motions are subsequently smaller. The Prandtl number is $\mathrm{Pr} = \nu/\kappa = 1/4$ and is fixed throughout the domain, so $\nu = \mathrm{Pr}\kappa$. In both the *Case A* and *Case B* simulations, $\alpha = 300$ and the minimum levels of diffusion $\nu_{min} =$ and κ_{min} are set to be 1000 times smaller than ν_{top} and κ_{top}. The radius below which the diffusion drops rapidly is $r_\kappa = 6.7 \times 10^{10}\,\mathrm{cm}$ for *Case A* simulations and $r_\kappa = 8 \times 10^{10}\,\mathrm{cm}$ for *Case B* simulations. This allows the convective motions to carry the majority of the flux throughout the convection zone and avoids an inward diffusive energy flux in sub-adiabatic regions. The diffusion acting on the mean entropy has the coefficient κ_0, which is set so that this unresolved eddy flux carries the stellar luminosity through the upper boundary but is exponentially tapered with depth below r_2. It is further quenched below the radius r_κ, with the rapidity of the decrease controlled by δ. In the *Case A* simulations, $\beta = 60$, $\delta = 200$, and $r_{\kappa_0} = 6.95 \times 10^{10}\,\mathrm{cm}$, while in the *Case B* simulations $\beta = 100$, $\delta = 200$, and $r_{\kappa_0} = 8.22 \times 10^{10}\,\mathrm{cm}$.

The unresolved eddy diffusion associated with the spherically symmetric diffusion component acts to conduct the full stellar flux through the upper boundary. Thus, almost by definition it has a substantial influence on the spherically symmetric component of the entropy. The monotonically decreasing initial entropy gradient from the stellar model is significantly steepened near the upper boundary by the cooling induced by the unresolved eddy flux, as is clearly seen as a large dip near the upper boundary in Figure 6.2. This has the effect of enhancing the buoyancy driving in the upper convection zone relative to what might be expected if the upper boundary were open and the surface convection allowed to influence the deeper flows. Recent 3-D surface convection simulations have shown a sizable change in the entropy gradient in the surface layers of various stars when compared to the gradient expected from standard mixing length theory (Trampedach & Stein, 2011). While the total integrated entropy deficit across the convection zone remains the same, as the luminosity is the same, its radial distribution is somewhat different. The gradient of the entropy becomes more superadiabatic near the surface and more adiabatic in the bulk of the convection zone. Therefore, the total entropy contrast across the domain in these simulations may be too high relative to the actual stratification, especially in simulations at lower rotation rates where the steepest superadiabatic gradients arise. This results in flows that begin to feel the effects of rotation at depths greater than otherwise might occur. The transition between flows that strongly feel the bulk rotation and those that do not takes place where the fluctuating Rossby number of the flows drops below one. Thus, we attempt to temper the influence of the upper boundary on the dynamics of the interior by ensuring that the fluctuating Rossby number throughout the convection zone is less than one. This requires that the rotation rate be high enough to attain $\mathrm{Ro}' < 1$ as is the case for the simulations here as indicated in Table 6.2.

Table 6.2

Diagnostic Flow Parameters

Mass	Case	$\Omega_0/\,\Omega_\odot$	$N_r \times N_\theta \times N_\phi$	Ra	Ta	Re	Re$'$	Ro	Ro$'$	$\mathrm{Ro_{DR}}$	$\mathrm{Ro_{mc}}$	$\nu/10^{13}$	τ_c	τ_ν
	A5	5	$257 \times 512 \times 1024$	1.75×10^5	2.40×10^5	84	37	0.69	0.48	0.29	0.017	0.87	2.8	101
	A7	7	$257 \times 512 \times 1024$	2.62×10^5	7.36×10^5	140	44	0.52	0.35	0.24	0.014	0.69	3.0	126
	A10	10	$257 \times 512 \times 1024$	4.22×10^5	2.41×10^6	240	52	0.39	0.25	0.21	0.008	0.55	3.3	159
$1.2\,\mathrm{M}_\odot$	*A15*	15	$257 \times 512 \times 1024$	7.64×10^5	9.32×10^6	451	75	0.28	0.18	0.19	0.004	0.42	3.7	209
	A20	20	$257 \times 512 \times 1024$	1.60×10^6	2.42×10^7	644	102	0.25	0.15	0.16	0.004	0.35	3.9	252
	A5i	5	$97 \times 512 \times 1024$	1.22×10^5	2.29×10^5	82	38	0.63	0.44	0.23	0.016	0.81	3.2	96
	A20i	20	$97 \times 512 \times 1024$	1.04×10^6	2.30×10^7	410	76	0.23	0.14	0.14	0.002	0.32	4.2	241
	B8	8	$193 \times 512 \times 1024$	4.32×10^4	9.21×10^4	62	41	0.99	0.73	0.07	0.021	1.29	1.1	39
	B10	10	$193 \times 512 \times 1024$	6.45×10^4	1.90×10^5	108	44	0.84	0.61	0.11	0.012	1.12	1.2	44
$1.3\,\mathrm{M}_\odot$	*B15*	15	$193 \times 512 \times 1024$	1.19×10^5	7.34×10^5	207	57	0.56	0.40	0.12	0.009	0.85	1.3	59
	B20	20	$193 \times 512 \times 1024$	2.34×10^5	1.91×10^6	363	76	0.46	0.31	0.13	0.009	0.71	1.5	71
	B30	30	$193 \times 512 \times 1024$	4.25×10^5	4.31×10^6	324	73	0.28	0.19	0.09	0.004	0.71	1.7	71
	B20i	20	$97 \times 512 \times 1024$	9.49×10^4	1.43×10^6	248	58	0.51	0.30	0.21	0.001	0.72	1.5	60

Table 6.2: The depth of the convection zone ($\mathrm{d} = \mathrm{r_2} - \mathrm{r_b}$, where r_b is the radius of the bottom of the convection zone) is the relevant length scale in the following parameters and is 1.3×10^{10} cm for *Case A* simulations and 9.2×10^9 cm for *Case B* simulations. We estimate and quote the following diagnostic parameters at mid-convection zone: the Rayleigh number $\mathrm{Ra} = \Delta\overline{S}\mathrm{gd}^3/\mathrm{c_P}\nu\kappa$, Taylor number $\mathrm{Ta} = 4\Omega_0^2\mathrm{d}^4/\nu^2$, Reynolds number $\mathrm{Re} = v_{\mathrm{rms}}\mathrm{d}/\nu$, fluctuating Reynolds number $\mathrm{Re}' = v'_{\mathrm{rms}}\mathrm{d}/\nu$, Rossby number $\mathrm{Ro} = \overline{|\omega|}/2\Omega_0$, fluctuating Rossby number $\mathrm{Ro}' = \overline{|\omega'|}/2\Omega_0$, where the $\langle\rangle$ denotes a horizontal average and ω is the vorticity vector. The differential rotation and meridional circulation Rossby numbers at mid-convection are $\mathrm{Ro_{DR}} = \overline{|\lambda\boldsymbol{\nabla}\ln\Omega|}$ and $\mathrm{Ro_{mc}} = \overline{|\omega_\phi|}/2\Omega_0$, respectively. The bar denotes the horizontal average. Kinematic viscosity (ν) values are given in units of $10^{13}\mathrm{cm}^2\mathrm{s}^{-1}$. The mid-convection zone local overturning time τ_c and the viscous diffusion time τ_ν across the convection zone are quoted in days.

6.2.4 Scaling Diffusion with Rotation

In the Boussinesq approximation, convection becomes possible above a critical Rayleigh number, which scales with rotation rate as $\mathrm{Ra_c} \propto \Omega_0^{4/3}$ (e.g., Chandrasekhar, 1961; Dormy et al., 2004). Anelastic systems have a similar constraint upon the minimum Rayleigh number that is necessary for the flows to be convective (Glatzmaier & Gilman, 1981; Jones et al., 2009). We seek here to explore the effects of rotation on stellar convection in the global spherical geometry at a representative point of time within the main-sequence lifetime of these two F-type stars. This goal means that the simulations must be highly supercritical so that the level of turbulence dominates diffusion. With unlimited computer resources, we ideally would maintain a constant level of supercriticality, but this requires scaling the effective diffusivities ν and κ as Ω_0^{-2}. However, lower diffusivities lead to both longer viscous and thermal diffusion timescales and to flows possessing finer spatial scales. Achieving equilibrated states in these systems requires high-resolution simulations carried out over extended periods, which would be prohibitively expensive if we followed this path. We have attempted to balance the level of supercriticality and the resolution requirements necessary to resolve the flow in our path through parameter space. Thus, our trajectory through the parameter space of Ω_0, ν, and κ attempts to maintain strongly nonlinear dynamics without having the increased rotation rate laminarize the convection. In our simulations, we have constrained this trajectory to be 1-D by requiring that the Prandtl number be 1/4 and that the value ν_{top} be set relative to the most rapidly rotating case, and subsequently scaled according to $\nu_{top} \propto \Omega_0^{-2/3}$, as seen in Table 6.2.

The Rayleigh numbers at mid-convection zone are about 50 times the critical Rayleigh number (Jones et al., 2009) for the *Case A* simulations about 25 for the *Case B* simulations. These levels of supercriticality are equivalent to ASH simulations of lower mass stars (e.g., Brown et al., 2008; Matt et al., 2011). The lower level of supercriticality in the $1.3\,\mathrm{M}_\odot$ simulations is primarily due the stronger driving of the convection and larger superadiabatic

gradient, both of which are in turn due to the higher luminosity and narrower convection zones of the higher mass F-type stars. This requires that the diffusion in the *Case B* simulations be about two times larger than the lower mass *Case A* simulation at the same rotation rate. This is done to ensure numerical stability at a chosen resolution as the downflows tend to be faster with larger temperature deficits in *Case B* simulations due to the higher luminosity of the star. The radial extent of the convection zone is taken to be the representative scale for determining the flow parameters seen in Table 6.2. This in combination with a larger diffusion results in lower Reynolds and Rayleigh numbers for *Case B* simulations. As a matter of definition, an evolved case is one in which the volume averaged differential rotation and kinetic energies vary by less than 0.1% relative to an initial value over a span of about 1000 days of simulation time. The differential rotation and other quantities are measured in these evolved cases to ensure that the time averages taken are essentially stationary.

6.3 Convective Patterns and Mean Structure

The variation of convective patterns of selected *Case A* simulations with increasing rotation rate Ω_0 is illustrated in the first column of Figure 6.3 (Panels (a), (e), and (i)), while the same is shown for three *Case B* simulations in Figure 6.4. These snapshots of the radial velocity near the top of the domain (0.96 R) are shown in Mollweide projection for three cases in Figure 6.3: *Case A5*, *Case A10*, and *Case A20*. The radial velocities exhibit the complex, evolving, and global-scale nature of the convection established in these simulations. The convective cells that comprise these complex patterns are outlined by the dark downflows. A distinctive transition in the morphology of the convective cells occurs between the columnar equatorial cells, which are essentially viewed from the side given the spherical geometry, and the polar columns where they are viewed from the top down. Equatorial convective columns march around the equator in a prograde sense, constantly jockeying for position as they collide and overtake one another. Cells of convection at higher latitudes continually form and reform as they interact with one another and are shuffled

along by the mean flows in a retrograde sense. The mean zonal flow makes its presence felt at mid-latitudes where there is an obvious shear between the prograde equatorial flows and the retrograde polar flows. These flows exhibit somewhat different time scales over which they maintain their coherence. The convective cells at the poles can last a few days, and those at the equator last even longer.

6.3.1 Case A: $1.2\,M_\odot$ Simulations

In Figure 6.3, there is a juxtaposition between high and low latitudes in both the scale and structure of the convection especially for more rapidly rotating cases. The latitudinal variation of convection patterns can be in part understood by considering a cylinder tangent to the base of the convection zone whose axis of symmetry is aligned with the rotation axis. Within the geometry of the *Case A* simulations, the top of such a cylinder intersects upper boundary at latitudes of $\pm 32^\circ$. Outside the tangent cylinder, downflows are deflected equatorward by Coriolis forces and can connect across the equator before they are strongly braked in the stable region. For downflows inside the tangent cylinder, they generally encounter the stable region before they can be paired with a flow from the opposite hemisphere. Such constraints on the convection become more severe as the rotation rate of the frame is increased.

The flows outside the tangent cylinder organize into large-scale sheared cylindrical rolls aligned with the rotation axis. Individual convective cells remain coherent for roughly the global overturning time which is between 15-30 days for these $1.2\,M_\odot$ simulations. These convective structures are very similar to the linearly unstable columnar modes arising in the presence of a significant density gradient and a convex boundary (Busse, 2002; Jones et al., 2009). The convective columns form a thermal Rossby wave that has a phase velocity larger than the local rotation rate, leading to downflows that propagate prograde faster than the local differential rotation. In a linear regime, the effects of compressibility counteract the tendency of the convection to occur along the tangent cylinder where it instead increasingly

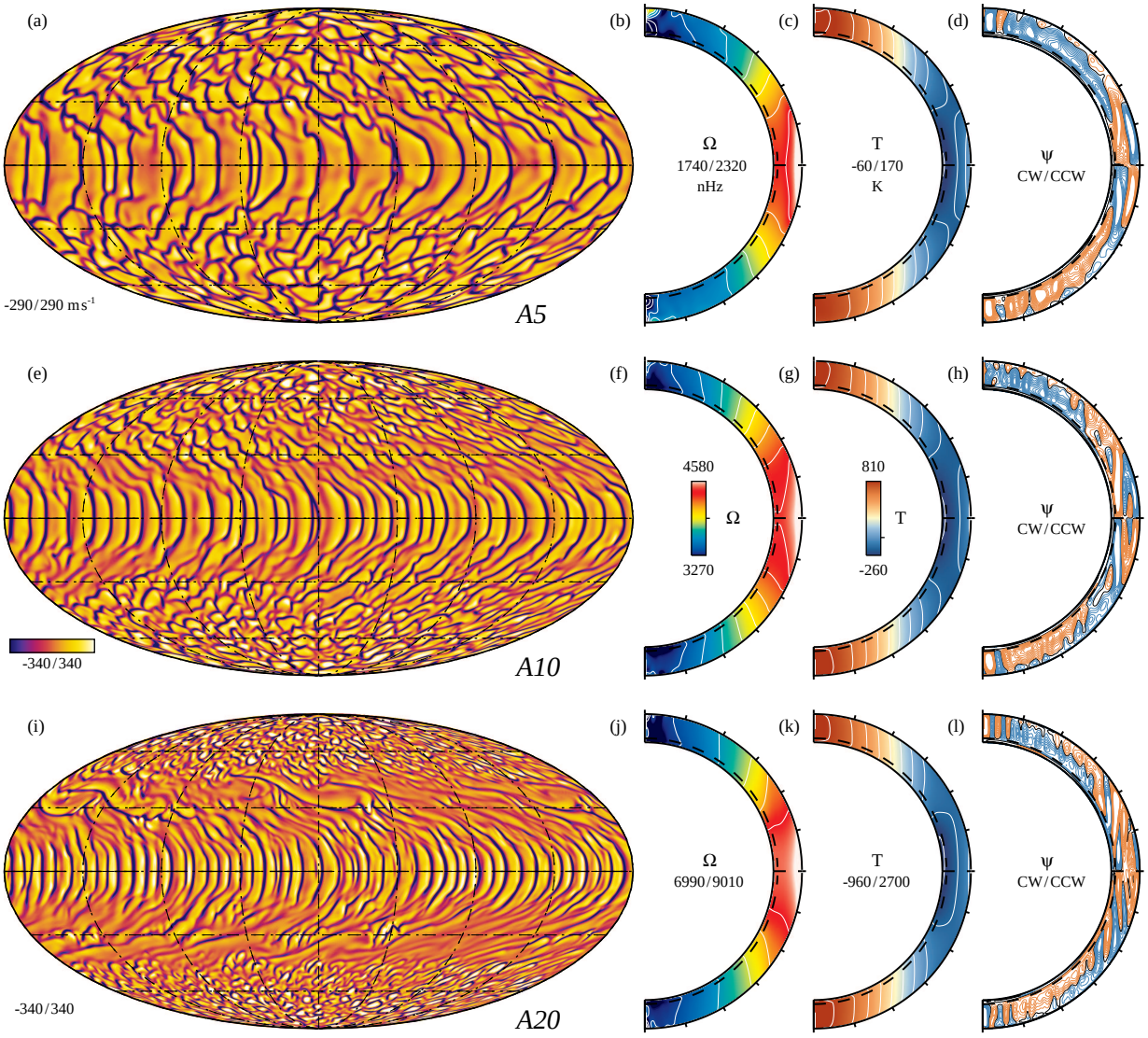

Figure 6.3: Overview of convective patterns, mean flows, and mean temperature fluctuations in selected *Cases A*. The first column of figures (a, e, i) display convective patterns in radial velocities near the upper boundary in turn for *Case A5*, *Case A10*, and *Case A20*. (b, f, j) the second column presents the time- and azimuthally-averaged angular velocity with radius and latitude, with the fast prograde equator in red and slower poles in blue. (c, g, k) azimuthally- and time-averaged temperature fluctuations (where the $\ell = 0$ component has been removed) with the warm poles in red tones and the cool equator in blue tones. (d, h, l) the streamfunction of the meridional flow (ψ), clockwise (CW) flows in red and counter-clockwise (CCW) flows in blue. The dashed line in the second, third and fourth columns delineates the beginning of the stable region.

occupies the outermost portions of the domain (Jones et al., 2009). In our simulations,

however, these effects often lead to two sets of columnar structures, one being somewhat more confined to larger radii and another that occurs deeper along the tangent cylinder. The primary difference in the simulations here is that they are highly supercritical with a realistic stratification, yet these structures largely persist despite their nonlinear interaction with turbulent flows.

The downflows sheaths surrounding the upflows are elongated in azimuth forming thin sheets that spiral outward from the base of the convection zone in a prograde direction. Such structures are largely due to vortex stretching near the upper boundary that is enhanced by the effects of compressibility, both of which are in turn due to our choice of a Prandtl number that is less than unity (Zhang, 1992; Jones et al., 2009). This prograde spiraling leads to strong Reynolds stresses that act in concert with the thermal state to help build the strong zonal flow and thus the differential rotation seen in these simulations (see §7.3.2 and §7.4). The radial differential rotation, as seen in panels (b), (f), and (j) of Figure 6.3, which increases with larger rotation rates also must play a role in stretching out these columns. The latitudinal differential rotation tends to shear the columns, creating the so called "banana cells." There also tends to be less latitudinal connectivity in the downflow networks than in more slowly rotating cases. This enhanced connectivity at lower angular velocities can prevent the formation of the columnar structures so prevalent in cases with a larger angular velocity.

The number of such convective modes that can fit within the circumference of the star increases with rotation rate, and thus the Taylor number (Gilman & Glatzmaier, 1981; Dormy et al., 2004; Jones et al., 2009). This means that at a given radius these modes will have less longitudinal extent as exhibited in panels (a), (e), and (i) of Figure 6.3. Analysis carried out using the modal equations of rotating Boussinesq convection within tangent cylinders (Dormy et al., 2004) and numerical computations of linear modes in compressible anelastic convection (Gilman & Glatzmaier, 1981; Jones et al., 2009) reveal that the azimuthal wavenumber of the most unstable mode increases as $m = m_c \mathrm{Ta}^{1/6}$, where m_c is the critical wavenumber.

For our cases, the viscosity scales as $\Omega_0^{-2/3}$, thus the most unstable mode is only a function of the rotation rate, where $m = m_c \left(\Omega_0/\Omega_\odot\right)^{5/9}$. The critical mode is determined by using a value estimated from those given in Jones et al. (2009) as $\hat{m}_c$ and the values of convection zone depth, viscosity in *Case A5* and its rotation rate in the Taylor number, which yields $m_c \approx 2^{1/3}5^{-2/9}\hat{m}_c d^{2/3}\nu_{A5}^{-1/3}\Omega_\odot^{1/3} = 9$. The resulting wavenumbers agree well with the modes that are most visible at the equator in cases *Case A5*, *Case A10*, and *Case A20* have azimuthal order of $m = 22$, 32, and 54, where as the brief analysis here yields $m = 22$, 32, and 47. There is likely a discrepancy between the order of the two modes for the fastest rotators because an instability arises in these cases that may change this scaling (see §6.4).

At higher latitudes inside of the tangent cylinder, the convection is more isotropic and the downflow networks organize on scales smaller than in the equatorial regions, as is seen in panels (a), (e), and (i) of Figure 6.3. These convective cells are intricate and dynamic, with cells constantly evolving as they interact with one another and the bulk motions. When viewed on a spherical shell, the downflows of the high latitude convective cells take on a crescent-like shape and precede the upflows as both are carried along by the differential rotation. As described by the Taylor-Proudman theorem, the tendency for these flows to align with the rotation axis becomes more pronounced at higher rotation rates. Indeed, as the angular velocity of the frame increases the high latitude downflows form into cylindrical sheaths nearly aligned with the rotation axis. Such convective structures have a strong vertical vorticity. The sense of this vorticity in the downflow plumes is cyclonic above the middle of the convection zone: counterclockwise in the northern hemisphere and clockwise in the southern. As the plumes descend deeper into the convection zone, their vorticity changes sign and the downflows become anti-cyclonic Miesch et al. (2000, 2008). The upflows, on the other hand, are anti-cyclonic at all depths outside the tangent cylinder and at latitudes above about $\pm 60°$. However, at mid-latitudes the upflows are anti-cyclonic in the upper convection zone but are cyclonic in the lower portion.

In Table 6.2, flow diagnostics for the last two $1.2\,\mathrm{M}_\odot$ F-type star simulations (*Case*

A5i and *Case A20i*) are shown. The computational domain of these two simulations is restricted in radius to be only in the convectively unstable portion of the domains of the other $1.2\,M_\odot$ F-type star simulations. Placing the lower boundary of the domain at the bottom of the convection zone is tantamount to having an infinitely stiff entropy gradient there, eliminating penetrative motions. While the convective patterns are largely unchanged in these simulations, the rate of deceleration of downflow plumes generally increases as they approach the lower boundary. This alters the Reynolds stress correlations and turbulent enthalpy flux, which in turn changes the differential rotation, meridional circulation, and temperature structures established in these simulations and will be discussed further in §7.2.

6.3.2 Case B: $1.3\,M_\odot$ Simulations

Three $1.3\,M_\odot$ F-type star simulations are shown in Figure 6.4, *Case B10*, *Case B20*, and *Case B30*. The two *Case B* simulations carried out at 10 and 20 times the solar rate allow for an easy comparison to the two *Case A* simulations at the same rotation rate. The third simulation (*Case B30*) exhibits modulated convection that is not seen in the other cases, and therefore is shown for its inherent interest. A striking similarity is seen between the convective patterns established in the *Case B* simulations and the *Case A* simulations (Figures 6.4(a), (e), and (i)). There is still a transition from columnar convection outside the tangent cylinder, to more isotropic and smaller scale convective cells inside of it. For these simulations, the edges of the tangent cylinder intersect the upper boundary at latitudes of $\pm\,26°$, six degrees closer to the equator than in the $1.2\,M_\odot$ F-type stars.

Careful scrutiny reveals that the columnar equatorial convective modes, as seen in the Mollweide projections of the radial velocity (Figures 6.4(a), (e), and (i)), have less of a latitudinal extent when compared to the $1.2\,M_\odot$ simulations. The radial velocities are about 15% larger on average than in the *Case A* series of simulations, but the tails of the radial velocity distribution extend out even further to several $\mathrm{km\,s^{-1}}$ in the downflows. The difference in temperature fluctuations between the center of an upflow and the downflows at

its edges is about 120 K, 50% larger than in the 1.2 $M_\odot$ F-type stars. These somewhat larger velocities and temperature fluctuations are expected given that both the lower background density is lower and that the luminosity is 50% higher in the 1.3 $M_\odot$ simulations. As seen in Table 6.2, there is a single case that captures only the convectively unstable region, *Case B20i*. This case is meant to be a point of comparison for assessing the role of overshooting in maintaining a strong differential rotation.

The mean angular velocities and temperature variations for *Case B10*, *Case B20*, and *Case B30* are shown in the second and third column of Figure 6.4. The nine panels in the last three columns of Figure 6.4 all demonstrate the convection zone geometry of the *Case B* simulations. The convection zone is much narrower than in both the Sun and the 1.2 $M_\odot$ F-type stars. This narrowing of the convectively unstable region and the increased luminosity of the higher mass stars play a role in the behavior of the differential rotation established in these simulations.

6.3.3 Mean Zonal and Meridional Flows

Shown in the second column of Figure 6.3 are the mean radial and latitudinal profiles of angular velocity ($\Omega = \Omega(r, \theta)$) achieved in *Case A5*, *Case A10*, and *Case A20*. These profiles are averaged in longitude and in time, over 150 days. All of the 1.2 $M_\odot$ F-type star simulations exhibit solar-like differential rotation profiles, with prograde (fast) equators and retrograde (slow) poles. Contours of constant angular velocity, black lines in Figures 6.3(b), (f), and (j), are largely radial but become increasingly aligned with the rotation axis with more rapid rotation.

More specifically, the average rotation profile in depth and latitude established in *Case A10* is shown in Figure 6.3(f). The red and white tones indicate a fast prograde equator, while the black and blue tones indicate a pole rotating more slowly than the frame rate; this is considered solar-like differential rotation. The color associated with the frame rate of 4240 nHz is yellow. The rotational shear averaged over the convection zone between the

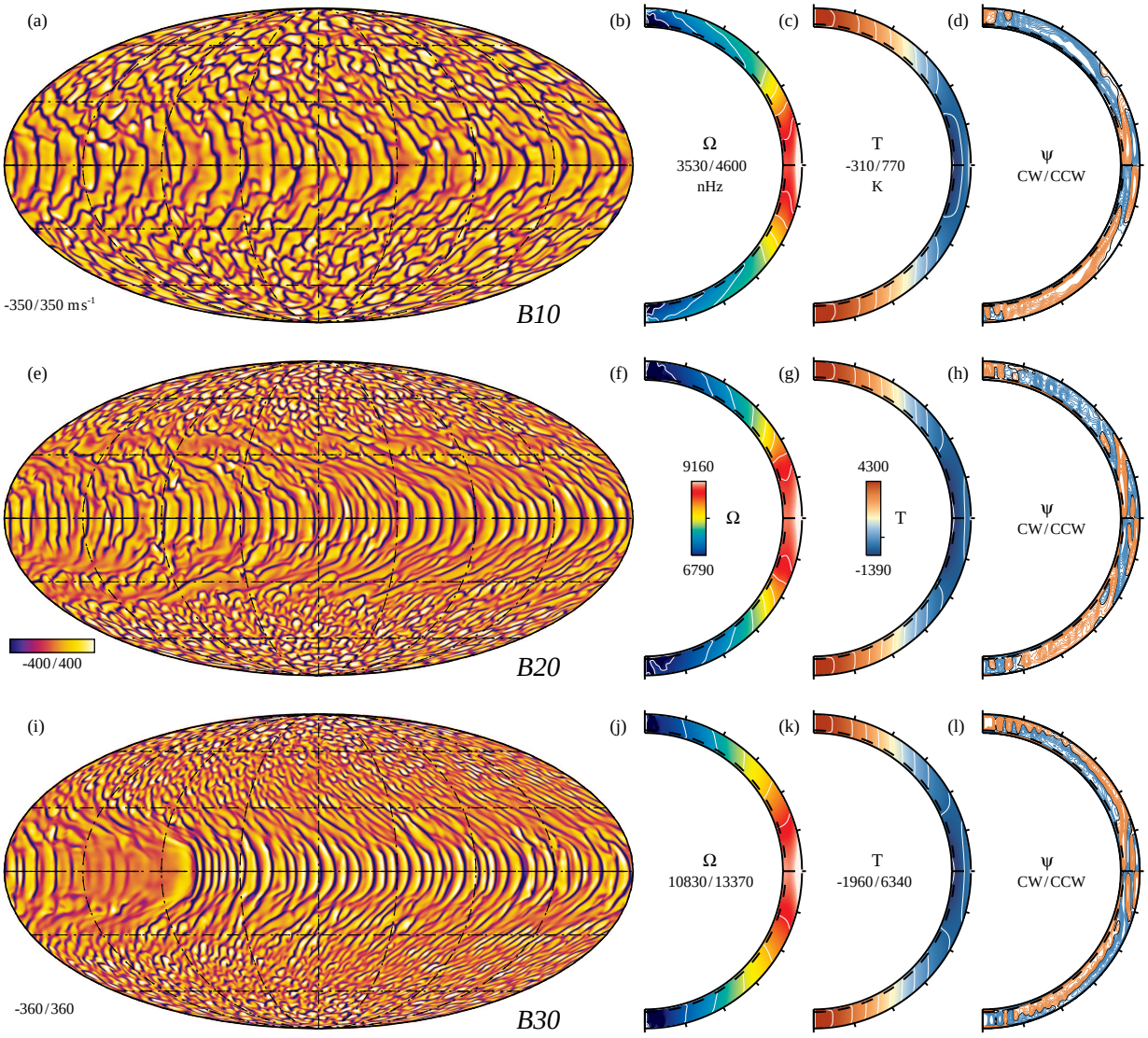

Figure 6.4: Overview of convective patterns, mean flows, and mean temperature fluctuations in selected *Cases B*. The first column of figures (a, e, i) display convective patterns in radial velocities near the upper boundary in turn for *Case B10*, *Case B20*, and *Case B30*. (b, f, j) the second column presents the time- and azimuthally-averaged angular velocity with radius and latitude, with the fast prograde equator in red and slower poles in blue. (c, g, k) azimuthally- and time-averaged temperature fluctuations (where the $\ell = 0$ component has been removed) with the warm poles in red tones and the cool equator in blue tones. (d, h, l) the streamfunction of the meridional flow (ψ), clockwise (CW) flows in red and counter-clockwise (CCW) flows in blue. The dashed line in the second, third and fourth columns delineates the beginning of the stable region.

equator and the pole is $\Delta\Omega = 1290\,\mathrm{nHz}$, corresponding to a relative latitudinal shear of

$\Delta\Omega/\Omega_0 = 34\%$. Thus, this simulation has a latitudinal shear that is quite similar to that observed at the solar surface. Similarly, *Case A5* and *Case A20* possess a equator to pole absolute differential rotation of $\Delta\Omega = 560\,\mathrm{nHz}$ or $\Delta\Omega/\Omega_0 = 26\%$ and $\Delta\Omega = 2330\,\mathrm{nHz}$ or $\Delta\Omega/\Omega_0 = 27\%$. Though we have attempted to drop the diffusion within the stable region, we are restricted both in the depth of the layer and the magnitude of the motions that still require some diffusion. This leads to a slow spread of the differential rotation into the stable region, which can be seen in Figures 6.3(b), (f), and (j).

A trend is readily discernible; the absolute contrast of angular velocity grows in latitude and radius with more rapid rotation. These profiles show some weak asymmetry between the northern and southern hemispheres, but only at lower rotation rates and at high latitudes. This behavior would likely disappear if very long time averages were taken. Variation between the hemispheres should be expected as the patterns of convection, and thus the mean zonal flows, are not symmetric about the equator.

The streamlines of the time-averaged meridional mass flux (ψ) are shown in the last column of Figure 6.3. The streamfunction ψ is defined such that $\langle\rho\mathbf{u}_m\rangle = \boldsymbol{\nabla}\times\psi\hat{\boldsymbol{\phi}}$. The sense of the flow is counterclockwise (CCW) for the blue contours and clockwise (CW) for the red. There is typically a CCW cell of meridional flow in the northern hemisphere, and a CW cell in the southern hemisphere, that stretches from the inner edge of the tangent cylinder to the pole, indicating a poleward meridional flow in the upper convection zone and an equatorward flow near the base of the convection zone. These high latitude cells are very large-scale flows and are thus constrained by the global spherical geometry. These flows reside mostly on contours of constant radius and possess weaker meridional flows than the low latitude cells. Outside the tangent cylinder the mean meridional flow is dominated by the columnar structures seen in the Mollweide projections of the radial velocity in Figures 6.3(a), (e), and (i).

The meridional flows associated with these structures have streamlines that are quite complicated, having multiple cells in radius and latitude. The trend is that the number

of cells increases with rotation rate, primarily with more cells in radius. These cells are aligned with the rotation axis and extend from the upper radial boundary to the equator where they close, indicating that there is very little mean cross-equatorial flow or flow across the tangent cylinder. The net effect of these low latitude cells is to largely isolate the equatorial region from higher latitudes inside the tangent cylinder. This behavior can be understood by considering the latitudinal connectivity of the downflow networks established in the convection, at low rotation rates there is a tendency for a large degree of latitudinal connectivity that is reduced at higher rotation rates due to the influence of the Coriolis forces. The meridional circulations established within the *Case B* simulations are similar in morphology to those in the *Case A* simulations. They are multi-cellular at low latitudes and single celled at high latitudes, as seen in the streamlines of the meridional flow (ψ) shown in Figures 6.4(d), (h), and (l).

6.3.4 Mean Temperature Profiles

The azimuthally- and time-averaged profiles of temperature fluctuations about the spherical mean are shown for cases *Case A5*, *Case A10*, *Case A20* (Figures 6.3(c), (g), and (k)). A clear pattern arises in these simulations, where the poles are warm and the equator is cool, while mid-latitudes are cooler yet, relative to the background temperature. These fluctuations are nearly constant on cylinders, especially at high latitudes. Such a pattern has also been found in simulations of global-scale convection in G-type stars (Brown et al., 2008). The origins of these fluctuations are discussed in detail in §7.3.

These fluctuations about the spherical mean are generally still small, but become more significant for more rapid rotation rates. In *Case A20* for instance, the temperature fluctuations near the top of the simulation are about 3% of the background value or about 3000 K. All of the cases presented here have similar latitudinal profiles in temperature. The latitudinal temperature contrast between the equator and 60° latitude increases markedly at higher rotation rates as shown in Table 7.1. Indeed, the primary difference between the *Case B*

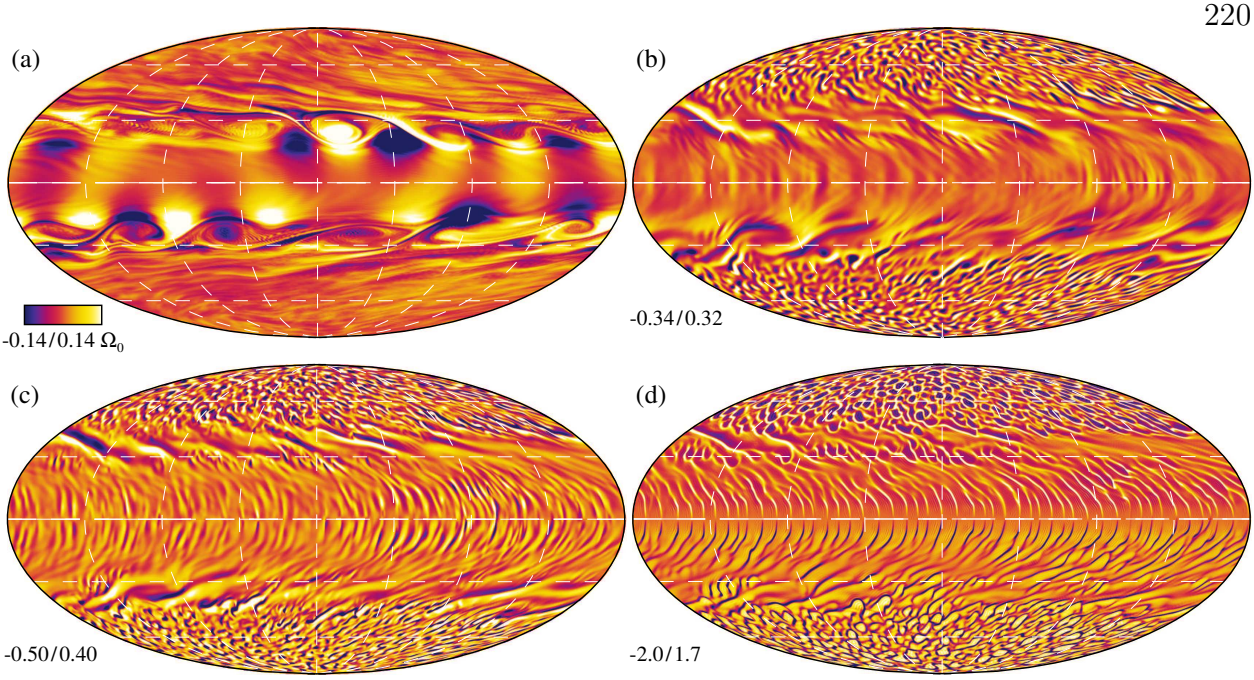

Figure 6.5: Large-scale shear instability existing within the stable region prints through the convection zone as evident in *Case A20*. Mollweide projections of the radial vorticity (ω_r) are shown relative to the vorticity of the reference frame (Ω_0) and at four depths with the $m = 0$ component removed (a) 0.81 R, (b) 0.86 R, (c) 0.91 R, (d) 0.96 R. Dark tones indicate negative radial vorticity.

simulations and those shown for the *Case A* simulations are that the absolute latitudinal contrasts of differential rotation and temperature fluctuations are larger (see §7.5), but the structure is largely the same with slow, warm poles and a cool, fast equator (Figure 6.4(c), (g), and (k)).

6.4 Modulated Convection and Shear Instabilities

Spatially modulated convection, such as that discussed in Brown et al. (2008), becomes readily apparent in *Case B30* (Figure 6.4(i)). The convection in the equatorial region is less vigorous at certain longitudes and more so at others. In this simulation, there is a roughly $m = 1$ modulation in the equatorial convection. This modulation is increasingly pronounced with depth and is most evident in the stable region where the overshooting convection and gravity waves are confined to a horizontal region covering roughly a quarter of the sphere

at the equator and converging at the poles. This localized overshooting convection feeds back on to the upflows initiated at the base of the convection giving them a substantially larger temperature perturbation than elsewhere on the sphere generating faster flows. This case is also slightly off the path in parameter space followed in the other cases in that the diffusivity is the same as in *Case B20* and thus is about 25% higher than expected given its bulk rotation rate. This is to avoid the high cost of increasing the resolution of the simulation and the subsequently longer evolution time.

The presence of a sufficiently large differential rotation within a convectively stable region can give rise to a global, shear instability similar to Rossby-Haurwitz or planetary waves (Haurwitz, 1940; Longuet-Higgins, 1964; Kitchatinov, 2010). These waves can efficiently transport energy and angular momentum between the equatorial region and the poles. Such an instability has arisen in the radiative zone of *Case A15*, *Case A20*, and *Case B20*, where several low degree spherical harmonic modes are unstable as are visible for *Case A20* in Figure 6.5 and for *Case B20* in Figure 6.6. These motions have a pressure and vorticity signature that print through the convection zone, surviving despite the vigorous convection present there as in Figure 6.6(b). The instability of these modes is sensitive to the magnitude of the differential rotation and to its latitudinal profile (Watson, 1981; Kitchatinov, 2010). Furthermore, it has significant impact upon the overshooting convection, allowing mixing to greater depths (Figure 7.3(c)).

To assess the character and the stability of the saturated state of the instability established within our simulations, we consider the simplified problem of a two-dimensional (horizontal) inviscid shear instability of a differentially rotating fluid as in Watson (1981); Kitchatinov (2010). In such an approximation, the radial fluid motions are assumed to be small compared to the horizontal flows and the effects of sound waves are ignored (Watson, 1981, hereafter W81). The neglect of radial fluid motions is justified given that the ratio of the standard deviations of the radial velocity and the latitudinal velocity is less than 0.02 throughout the stable region in cases *Case A20* and *Case B20*, which agrees well with the

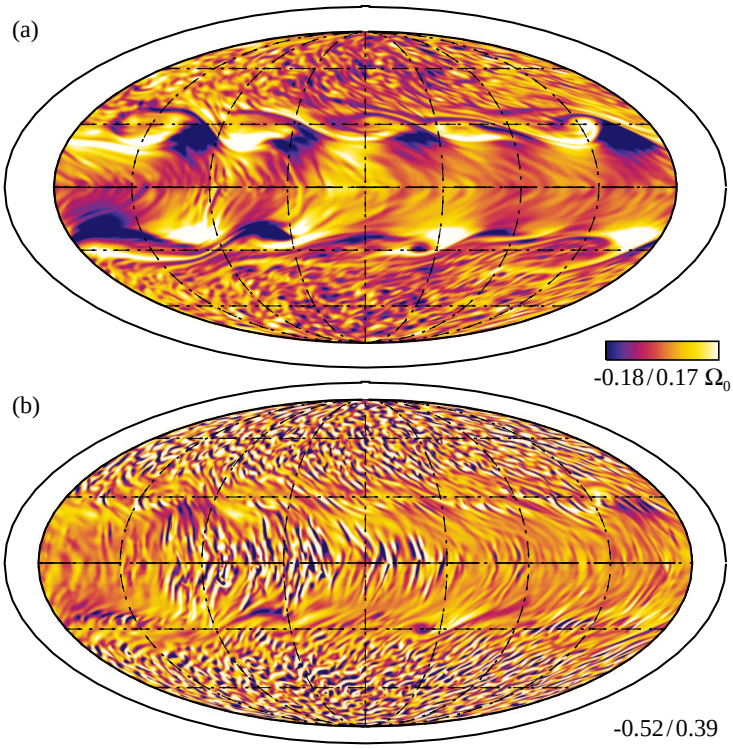

Figure 6.6: Large-scale shear instability existing within the stable region prints through the convection zone as evident in *Case B20*. Mollweide projections of the radial vorticity (ω_r) are shown relative to the vorticity of the reference frame (Ω_0) and at four depths with the $m = 0$ component removed (a) 0.86 R and (b) 0.92 R. Dark tones indicate negative radial vorticity.

assumption in W81 that this ratio is proportional to Ω^2/N^2, where N is the Brunt-Väisälä frequency and Ω is the angular velocity as a function of latitude. Therefore, the dominant source of energy for any instability is the kinetic energy of the shear rather than the baroclinic potential energy. These approximations leave us with three equations: the continuity equation and the θ and ϕ momentum equations. These equations can be reduced to one by the introduction of a toroidal streamfunction ξ, such that $\overline{\rho}\vec{u} = \boldsymbol{\nabla} \times \xi\hat{r}$. If we further consider only normal modes, with a time and longitudinal dependence of $\exp\left[im\left(\phi - \sigma t\right)\right]$, we are left with a Sturm-Liouville problem that solves for the latitudinal dependence of the stream function ξ:

$$\left[\left(1-\mu^2\right)\xi'\right]' + \left(K\left(\mu\right) - \frac{m_c^2}{1-\mu^2}\right)\xi = 0, \tag{6.13}$$
$$K\left(\mu\right) = -\frac{\left[\Omega\left(\mu\right)\left(1-\mu^2\right)\right]''}{\Omega - \Omega_1},$$

where Ω_1 is the value of Ω for which $\left[\Omega\left(\mu\right)\left(1-\mu^2\right)\right]'' = 0$. From Equation (6.13) it is clear that a version of Rayleigh's necessary criterion plays a role for this instability. This criterion is that $\left[\Omega\left(1-\mu^2\right)\right]''$ must change sign somewhere, where $\mu = \cos\theta$ and primes denote derivatives with respect to μ. This alone, however, is not enough to ensure instability. Indeed, the magnitude of the differential rotation plays a key role in determining the stability of a given mode [W81]. The full solution of this problem for an arbitrary differential rotation is given in Appendix C. As a further restriction upon which modes may be unstable, there exists a critical longitudinal wave number m_c above which the modes are stable. Thus, only the longest waves may be unstable. This critical value is shown in W81 to be the largest eigenvalue of the Sturm-Liouville problem of Equation (6.13).

Figure 6.7(a) shows the differential rotation profile for *Case B20*. There is only a small latitudinal region where the mean angular velocity satisfies the Rayleigh criterion that triggers this instability (Figure 6.7(b)). The most unstable modes are of azimuthal order $m = 5$, 6, and 7, as can be ascertained from Figure 6.7(c). This agrees well with the spherical harmonic modes of the radial vorticity that have the most power within the stable region. A program that solves these linearized equations for the eigenvalues and eigenfrequencies produces very similar results (see Appendix C), with the magnitude of the imaginary part of the mode set peaking at $m = 2$ for *Case B20*. A similar analysis for *Case A20* shows peaks at $m = 3$ and $m = 5$, with the latter being the maximum.

Of further interest is that not only do these modes arise, but they are sustained by the convection. These unstable modes will grow until the instability is saturated, at which point they become efficient at transporting angular momentum in latitude between the equator and the poles. This mechanism quenches further growth of the modes, and without a mechanism

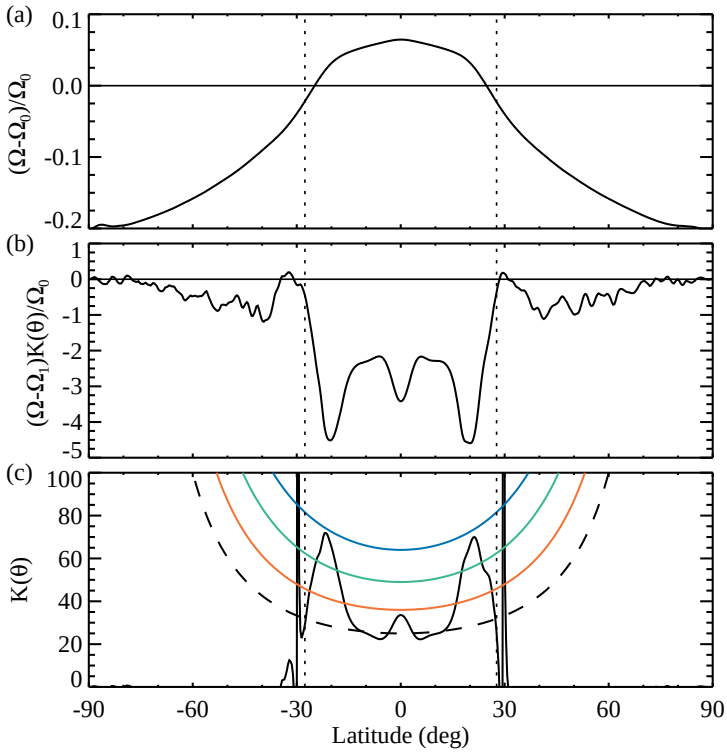

Figure 6.7: (a) The radially and time-averaged differential rotation profile $(\Omega - \Omega_0)/\Omega_0$ within the stable region of *Case B20*. (b) The latitudes at which the Rayleigh criterion is satisfied can be seen where the function $(\Omega - \Omega_1) K(\mu)$ crosses the horizontal line, which indicates zero. (c) The function $K(\mu)$ associated with this differential rotation profile is plotted with the four most likely excited modes of $m = 5$, 6, 7, and 8 shown as dashed, red, green, and blue lines respectively.

to sustain the profile of the angular velocity that satisfies the Rayleigh criterion the amplitude of the flows associated with the instability would decay. However, the turbulent overshooting convection continually resupplies angular momentum to the stable region, thus maintaining a differential rotation with a shear unstable profile. This leads to the shear instability persisting throughout the statistically steady portion of the time evolution of these simulations.

Since the shear unstable modes are saturated and persist, they impact the convection by coupling into buoyantly unstable upflows near the lower boundary. The upflows rise carrying some of the vorticity imparted upon them toward the surface, as can be clearly seen in the radial vorticity shown at several radial levels starting in the stable region in Figure

6.5(a), and then proceeding into the convection zone and toward the upper boundary in Figures 6.5(b-d).

Chapter 7

Examining the Convection Zone Dynamics of F-type Stars

After the broad overview of results in Chapter 6, the focus is narrowed to a single case (*Case A10*) in order to illustrate the detailed dynamics occurring within each of the cases. The chapter then concludes with scaling results with mass and rotation rate. Indeed, it is found that the differential rotation becomes much stronger with more rapid rotation and larger mass, scaling as $\Delta\Omega \propto \mathrm{M}^{3.9}\Omega_0^{0.6}$. Accompanying the growing differential rotation is a significant latitudinal temperature contrast, with amplitudes of 1000 K or higher in the most rapidly rotating cases. This contrast in turn scales with mass and rotation rate as $\Delta\mathrm{T} \propto \mathrm{M}^{6.4}\Omega_0^{1.6}$. On the other hand, the meridional circulations become much weaker with more rapid rotation and with higher mass, with their kinetic energy decreasing as $\mathrm{KE_{MC}} \propto \mathrm{M}^{-1.2}\Omega_0^{-0.8}$.

7.1 Examining Dynamics within Case A10

The convective patterns, like those discussed in §6.3.1, are complex and time dependent with asymmetries between upflows and downflows due to mass conservation in a stratified medium. The downflows are cold, fast, narrow and border their more leisurely ascending counterparts. The convective cells are outlined by the dark downflows visible in the radial velocities shown in the top four panels of Figure 7.1.

7.1.1 Typical Flows and Thermal Properties

The archetypal convective cell is defined by a central broad upflow bordered by narrow downflows. Indeed, the color tones in Figures 7.1(a)-(d) are meant to construe both the sign of the temperature fluctuations (Figures 7.1(e)-(h)) associated with these structures as well as the direction of the flow. Namely, the upflows are warm and the downflows are cool relative to the mean temperature. Radial velocities that are within one σ of the mean at mid-convection zone for the flows in *Case A10* are between $-230\,\mathrm{m\,s^{-1}}$ for downflows and $190\,\mathrm{m\,s^{-1}}$ for upflows, where the rms radial velocities are $150\,\mathrm{m\,s^{-1}}$. Large and small scale thermal structures are visible in Figures 7.1(e)-(h), where the large $m = 0$ temperature perturbations arising from the thermal wind balance have been removed. The average difference of temperature fluctuations between the central upflow and the bordering downflows defining the convective cell are about 45 K at mid-convection zone and increases with height. A large scale structure corresponding to a $m = 1$ spherical harmonic mode is also visible. This global scale pattern persists for long periods of time and is most evident in the more rapidly rotating cases.

The effects of the stratification are visible in the patterns of the convection in Figures 7.1(a)-(c). The convective cells near the surface in panel (a), show the greatest asymmetry in areal coverage and rms radial velocity between the upflows and the downflows. This asymmetry is reduced at greater depths as in panel (c) as the upflows and downflows become increasingly symmetrized both in the rms velocities achieved and in areal extent due to the larger local density scale height. The temperature field appears slightly more diffuse than the radial velocity due to the thermal diffusion being four times greater, as reflected in the Prandtl number being 1/4 at all depths. However, it shows the changes in the morphology of the convection that are similar to those of the radial velocity, where the longitudinal extent and magnitude of the temperature fluctuations of the convective cells decreases with depth.

The areal filling factors of the upflow and downflows are roughly 2/3 and 1/3, re-

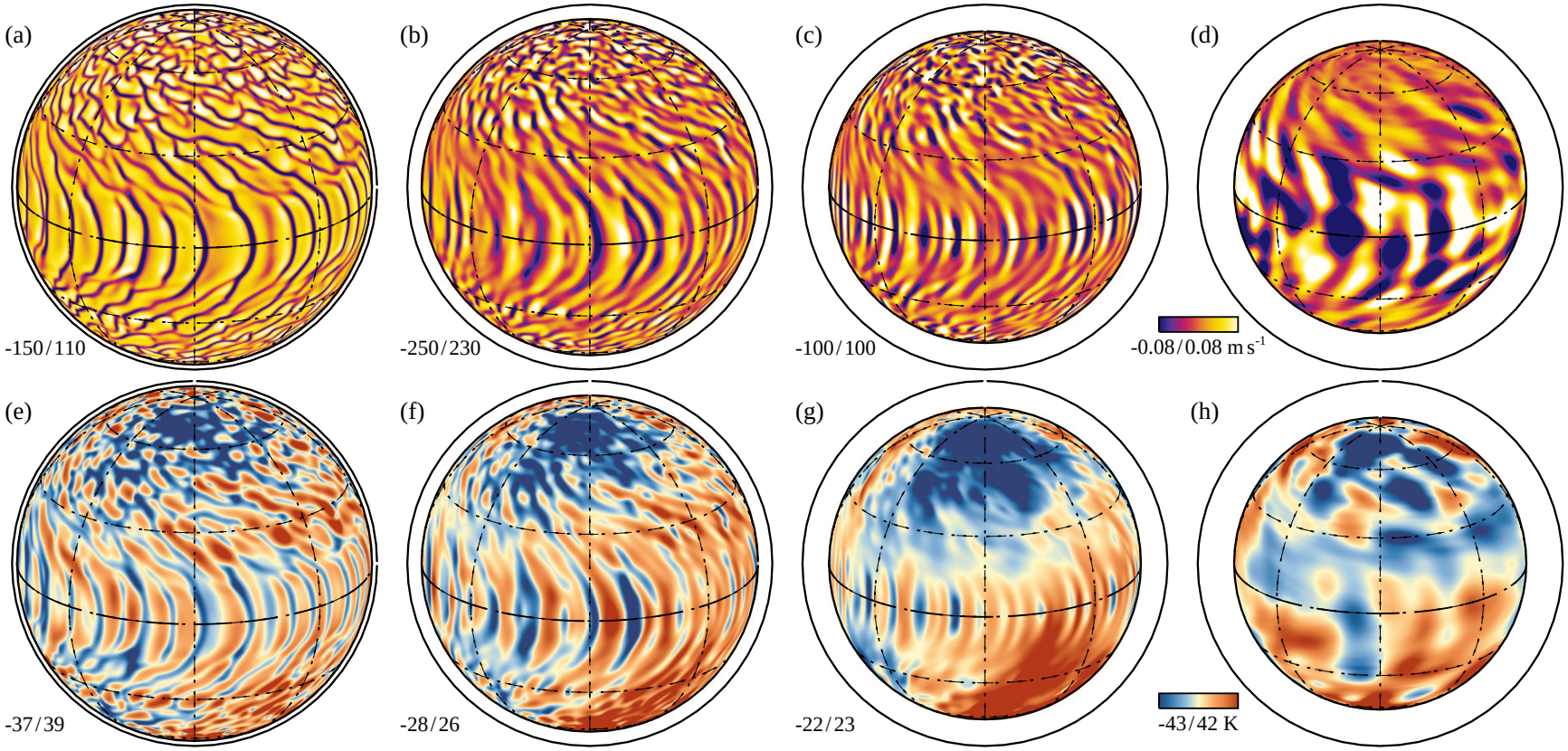

Figure 7.1: Radial velocities (u_r) and temperature fluctuations (T') at several depths in *Case A10*. The temperature fluctuations are taken about the $m = 0$ component, removing the largest-scale variations. The quantities u_r and T' are shown in orthographic projection at several radial levels with r/R equal to (a, e) 0.97, (b, f) 0.92, (c, g) 0.85, (d, h) 0.80. Light tones are warm upflows, while dark tones are cool downflows. Panels (d) and (h) show flows within the radiative zone.

spectively, when averaged over the convection zone. There is a further asymmetry in the magnitudes of the radial velocity within these flows, with the downflows being faster than the upflows. Indeed, the distribution of the radial velocities has a large negative skewness within the convection zone. The distribution of radial velocities in the downflows has a tail that is about twice as long as the distribution of velocities in the upflows. These properties are similar to the flows established in solar simulations detailed in Miesch et al. (2008). Further, the mean negative radial velocity is about twice as large as the mean positive radial velocity. This asymmetry in the radial velocities reflects the density stratification and mass conservation, with the caveat that the degree of asymmetry is dependent upon the level of turbulence within a simulation where higher Reynolds numbers lead to more asymmetry.

The downflows, visible as dark lanes in (Figure 7.1(a)-(c)), are initiated by cooling near the surface and sustained through buoyancy driving within the bulk of the convection zone. The cooler and more dense downflows entrain fluid from the surrounding upflows through mass conservation and diffusion. These processes act to erode the density contrast between the downflow and the surrounding fluid. Thus, the downflows experience less buoyancy driving as they fall deeper into the convection zone. Even without a significant buoyancy to provide a downward acceleration, they have enough momentum to continue under their own inertia. Once the downflows reach the bottom of the convection zone, they become buoyantly braked as they enter the stable region. However, they continue into the uppermost reaches of the radiative zone through their own inertia, as in Figures 7.1(d) and 7.1(h). Eventually they are fully braked, but not before they have penetrated a significant distance into the stable region. Such overshooting motions can excite gravito-inertial waves that propagate within the stable region. These waves are eventually dissipated through diffusive processes, but can play a role in the redistribution angular momentum and energy (Rogers & Glatzmaier, 2006; Brun et al., 2011).

7.1.2 Energetics of the Convection

These flows give rise to the transport of energy and momentum throughout the domain. The energy transport by resolved convective motions will not in general be equivalent to the mixing-length prescriptions assumed in the 1D solar structure model, so the simulation must adjust accordingly. In a steady state, an equilibrium is reached that balances the different components of the mean radial transport of energy.

The large outward enthalpy flux L_{en} seen in Figure 7.2(a) exceeds the luminosity of the star at its peak and is balanced primarily by the unresolved eddy flux L_{ed} near the top of the domain and by the radiative flux L_{rd} below mid-convection zone to produce a nearly constant stellar luminosity throughout the domain. While the upflows contribute about 10% of the enthalpy flux, the dominant factor contributing to the enthalpy flux are the downflows. These flows are cool relative to the mean value as seen in the temperature fluctuations of Figure 7.1; this correlation between the negative fluctuating temperature and the negative radial velocities leads to a radially outward enthalpy flux. There is significant latitudinal variation in the enthalpy flux, with the largest positive flux in the polar regions and with fluxes that are about 30% less outside of the tangent cylinder. Near the base of the convection zone, indicated by the dashed line in Figure 7.2, the enthalpy flux becomes negative due to the overshooting convection as will discussed in the following section. The overshooting enthalpy flux attains its most negative value near the poles, though when integrated over the stable and overshooting regions it peaks at the tangent cylinder. This variation in the enthalpy flux reflects the latitudinal variation in the depth of the overshooting.

The asymmetrically larger velocities in the downflows give rise to an inward kinetic energy L_{ke} (inside the tangent cylinder) that is due to the cubic dependence on the velocity. Outside the tangent cylinder, the columnar equatorial flows produce a net outward kinetic energy flux, dominated by the large zonal velocity component, that are on average slightly larger than the higher latitude components and lead to a small net outward flux for *Case*

A10 (Figure 7.2(a)).

7.2 Convective Overshooting

The Péclet number (Pe = Re′Pr) of the radial flows is of essential importance in determining the properties of the overshooting convection (e.g., Brummell et al., 2002; Brun et al., 2011). Small values of Pe give rise to convective overshoot, in the sense that the stratification remains sub-adiabatic. Large Pe values, those much greater than one, promote efficient entropy mixing such that the stratification becomes nearly adiabatic, and the base of the convection zone can spread downward in time if nothing acts to oppose the spreading. In the stable region, the Peclet number is about 1/40 at the lower boundary, around 1 in the overshooting region and approximately 10 in the bulk of the convection zone. Therefore, it is expected that the motions at the base of the convection zone are overshooting rather than penetrative. This is indeed the case; as demonstrated in Figure 6.2(a), where the evolved mean entropy gradient is shown for cases *Case A10* and *Case B10*. However, all the cases reported on here possess a strongly sub-adiabatic region below the convection zone that is essentially fixed in time. It extends from the lower boundary to the radius at which the entropy gradient changes sign, or the bottom of the convection zone. The mixing there is inefficient and the stratification remains largely unchanged as indicated by the Peclet number there (Zahn, 1991; Spiegel & Zahn, 1992; Brummell et al., 2002). The width of this layer is likely overestimated because this width scales as the square root of the filling factor of the downflowing plumes, which are likely larger in these simulations than in the actual stars (Zahn, 1991; Rempel, 2004).

In the region of overshooting, on the other hand, the entropy gradient is steepened significantly compared to the stellar model. This is a consequence of the downflows within the convection dragging cool fluid to the bottom of the domain, where they are then quickly heated due to buoyancy braking in the region of overshooting as will be seen in the following section. While there is not a physical boundary at the bottom of the convection zone,

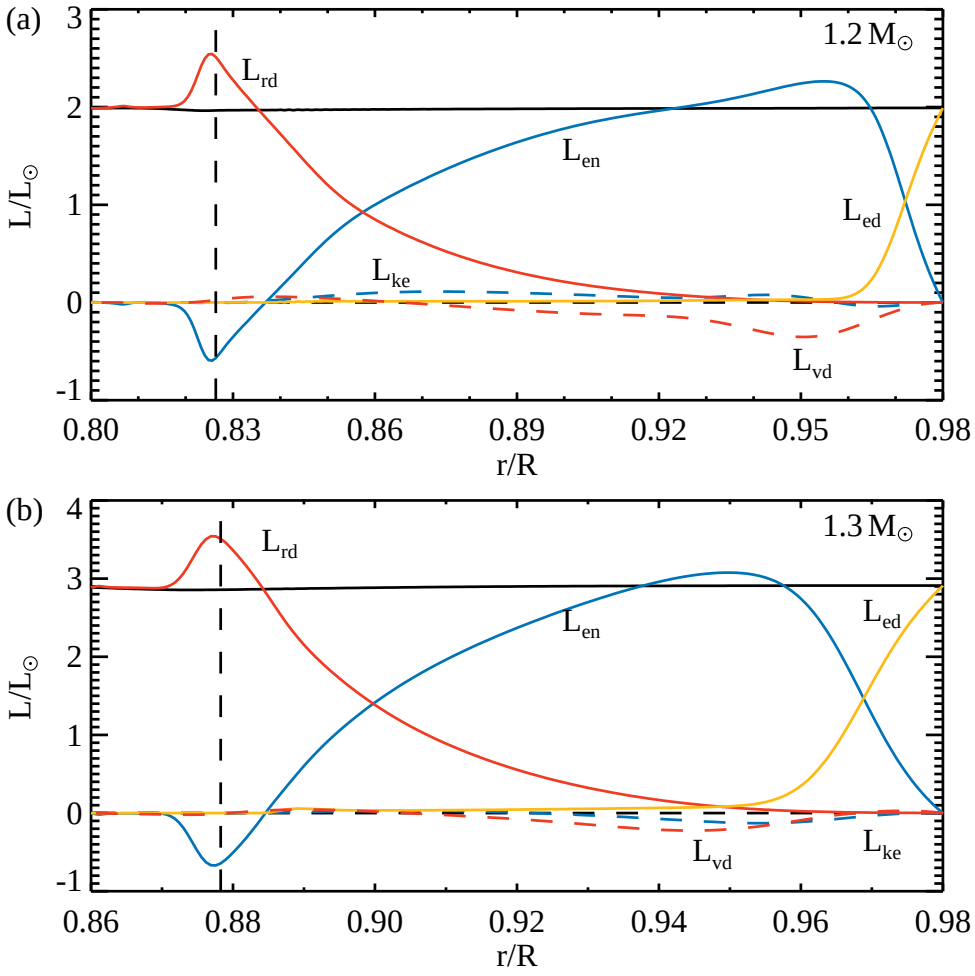

Figure 7.2: Time- and horizontally-averaged radial energy fluxes for (a) *Case A10* and (b) *Case B10*. Fluxes are shown as luminosities ($L = 4\pi r^2 F$) and taken relative to the solar luminosity with the total (L_{tot}) shown as a *solid black* line. The components of the total flux are the kinetic energy flux (L_{ke}, *dashed blue*), enthalpy flux (L_{en}, *solid blue*), radiative flux (L_{rd}, *solid red*), unresolved eddy flux (L_{ed}, *solid orange*), viscous diffusive flux (L_{vd}, *dashed red*). The vertical dashed line indicates the radius at which the mean entropy gradient changes sign.

the rapid increase in the entropy gradient acts very much like a wall that rapidly slows downflows. However, these flows overshoot into the stable region where the work done by buoyancy rapidly brakes and heats them. This allows the fluid to thermally equilibrate with the surrounding fluid. The stronger downflows, those that are cooler and faster than the majority in the convection zone, retain enough inertia to flow past the bottom of the

convection zone and continue to be buoyantly heated. They quickly become warmer than the surrounding fluid but are still traveling into the stable region. Thus, correlations between the fluctuating temperature and the radial velocity in the overshooting convection gives rise to a substantial negative enthalpy flux as seen in Figure 7.2 where it reaches around half of a solar luminosity. This is in contrast to 1-D stellar structure models, where there is either a small, negative overshooting enthalpy flux or none depending upon how the overshooting is parameterized.

In Figure 7.3, we quantify the beginning of the overshooting region by the radius r_c where the enthalpy flux becomes negative, the radius at which the entropy gradient equals zero (r_{bcz}) is demarked by the dashed line, and the bottom of the overshooting region occurs at a radius where the negative enthalpy flux of the overshooting convection equals one percent of the most negative value (r_o). It is clear from Figure 7.3(a) that the convection zone in *Case A10* is most shallow around $\pm 20^\circ$ (at about 3% of the stellar radius R), and is deepest at the equator ($0.0075\,R$), with an average width of $0.015\,R$. The overshooting region in *Case B10* is 1.5% of the stellar radius at its deepest around $\pm 20^\circ$, $0.009\,R$ at its most shallow at the equator, and $0.0125\,R$ on average. The depth of overshooting at the equator is reduced as the centroid of the region of the overshooting occurs at a greater depth due to the penetration of the convection, resulting in convection that feels a much more stiff stratification. At higher latitudes, the centroid of the overshooting region occurs at a larger radius, which results in a larger region of overshooting as the convection feels a less stiff stratification.

The bottom of the overshooting region is deepest at low latitudes and most shallow at the poles in *Case A10*, which implies that the radiative zone is slightly prolate. In *Case B10*, the bottom of the overshooting region is essentially spherically symmetric. This is also true of the radius of the base of the convection zone (r_{bcz}), which has almost no latitudinal variation in both cases. The radius at which the enthalpy flux becomes negative (r_c) is everywhere larger r_{bcz}. This property arises from some of the downflow plumes having a change in the sign of their fluctuating temperature (from cool to warm) that precedes their arrival at r_{bcz}.

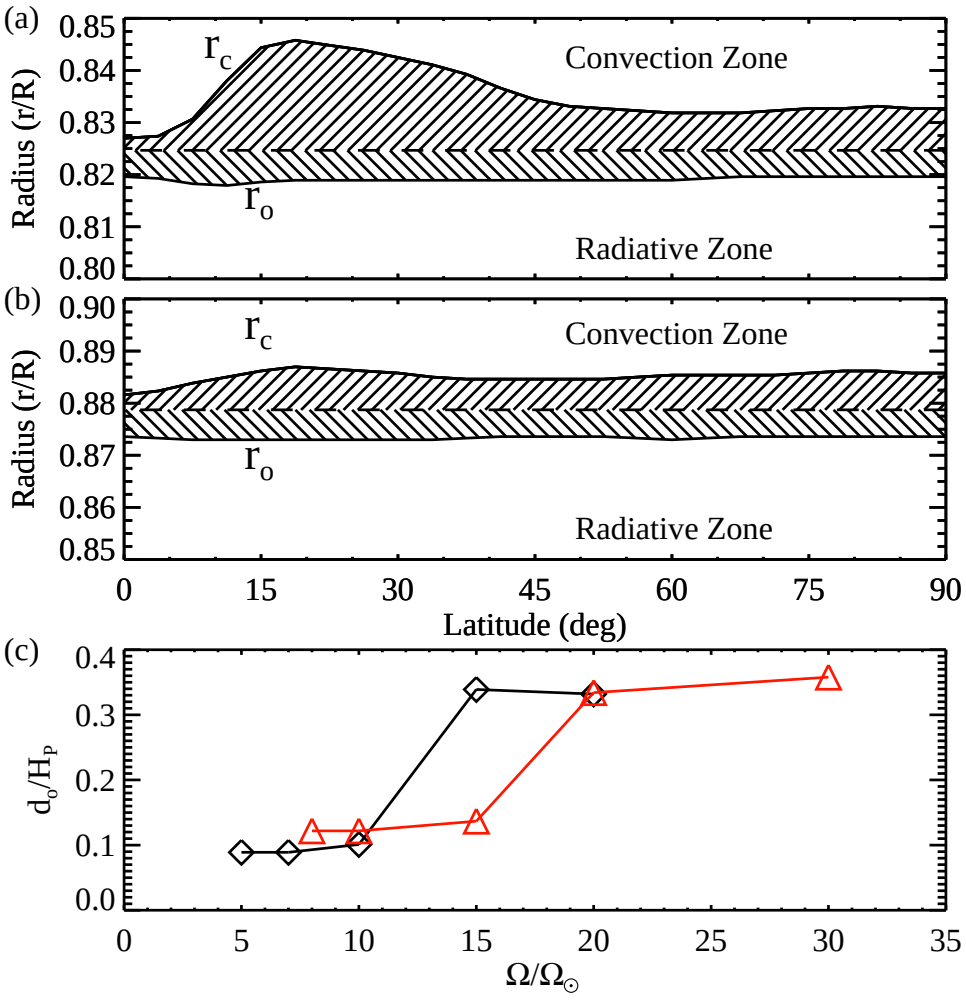

Figure 7.3: Changes in the radial extent of overshooting motions with latitude. Shown as a shaded region below r_{bcz} for case (a) *Case A10* and (b) *Case B10*. The radii where the enthalpy flux is negative encompasses the full shaded region. The radius at which there is a transition to the convection zone is denoted by r_c. The lower boundary of the overshooting motions is denoted by r_o. The scaling with rotation rate of the depth of the overshooting region relative to the pressure scale height at r_{bcz} (d_o/H_P) for cases *A* and *B*.

The downflows are diffusively heated by the warm upflows that surround them, which occurs because the time for the downflow to cross the distance between r_c and r_{bcz} is longer than the horizontal diffusion time across the downflow. This results in a negative enthalpy flux that begins before the bottom of the convection zone and builds to its most negative values as the downflows continue into the stable region where they are buoyantly heated.

We have conducted simulations with the same initial stellar model, but without the region of penetration, these are *Case A5i*, *Case A20i*, and *Case B20i*. It is clear from Table 7.1 that these simulations have much weaker latitudinal entropy and temperature contrasts than their counterparts with a stable region. However, the equator to 60° differential rotation contrast is only slightly lower. Hence, the inclusion of a stable region alters several aspects of the mean thermal state and flows, where it primarily leads to a tilting of the contours of the angular velocity toward being conical. It also leads to a stronger scaling of the latitudinal temperature gradient with rotation rate. The primary driver behind this is that there is an enhanced equatorward latitudinal enthalpy flux relative to the cases that have a stable region. The meridional circulation kinetic energy, on the other hand, is lower in cases with a region of overshooting than those without. This behavior arises due to a change in the axial torque near the lower boundary. The impenetrable lower boundary imposes a much stronger constraint upon the flows, indeed all flows must halt at this point. This means that the divergence of both the Reynolds and the viscous stresses must be larger in simulations with an impenetrable boundary when compared to simulations with a region of overshooting, as is indeed the situation in *Case A5i*, *Case A20i*, and *Case B20i*. The equation of gyroscopic pumping (Equation (7.6)), implies that this leads to a larger meridional circulation kinetic energy as is evident in the energies given in Table 7.1.

7.3 Thermal Structuring

As an example of the mean thermal structure established in these simulated stars, consider the time- and azimuthally-averaged temperature fluctuations for *Case A10* (Figure 7.4(a)). It is clear that the perturbations do not have a zero mean, as expected from the broken spherical symmetry arising from the rotation of the system. The temperatures range from the hot poles at 840 K to the cool equator at -280 K with yet cooler mid-latitudes. This equator to pole temperature contrast is slightly more than two orders of magnitude greater than the observational limits on the latitudinal temperature profile of the Sun (Rast

et al., 2008). However, these variations are taken relative to the mean temperature that varies between 1.3×10^6 K at the bottom of the domain and 10^5 K at the top, so they are still relatively small being of order one percent. These averaged temperature fluctuations are nearly constant on cylinders at latitudes above $\pm 45°$, while it has a positive radial gradient at lower latitudes. This distribution of temperature fluctuations impacts the local energy flux balance, and is intimately linked to the differential rotation and meridional flows, such as those seen for *Case A10* in Figures 6.3(f) and 6.3(h).

7.3.1 Principal Contributions to Temperature

The time- and azimuthally-averaged temperature fluctuations are decomposed into the fluctuating pressure and entropy components ($T = P/\overline{\rho} c_P + \overline{T} S/c_p$), from which it becomes apparent that the pressure is the largest contributor (Figure 7.4(b) and 7.4(c)). This is especially true at latitudes above 45°, where the pressure perturbation has nearly radial contours and contains about 80% of the amplitude of the temperature fluctuations. At these higher latitudes, the entropy contribution tilts the contours of the temperature fluctuations to be nearly cylindrical. At low latitudes, the two components play more equal roles, at least within the deep convection zone. Figure 7.4(d) exhibits the latitudinal structure of the mean temperature fluctuations at several depths: near the top of the domain, at mid-convection zone, and in the stable region. There is a substantial change in the temperature structure with depth outside the tangent cylinder where it swings from -280 K in the stable region to almost 0 K near the top of the domain at the equator. The entropy and pressure act in tandem to depress its value at the base of the convection zone and the pressure drives its value above zero near the surface where the entropy contribution wanes. Figure 7.4(e) shows the mean entropy fluctuations at the same depths as in panel (d). The entropy fluctuations increase nearly monotonically in latitude and have little radial variation.

In *Case A10*, the background temperature decreases by about a factor of 10 across the convection zone, and since it weights the entropy fluctuations it causes an equivalent decrease

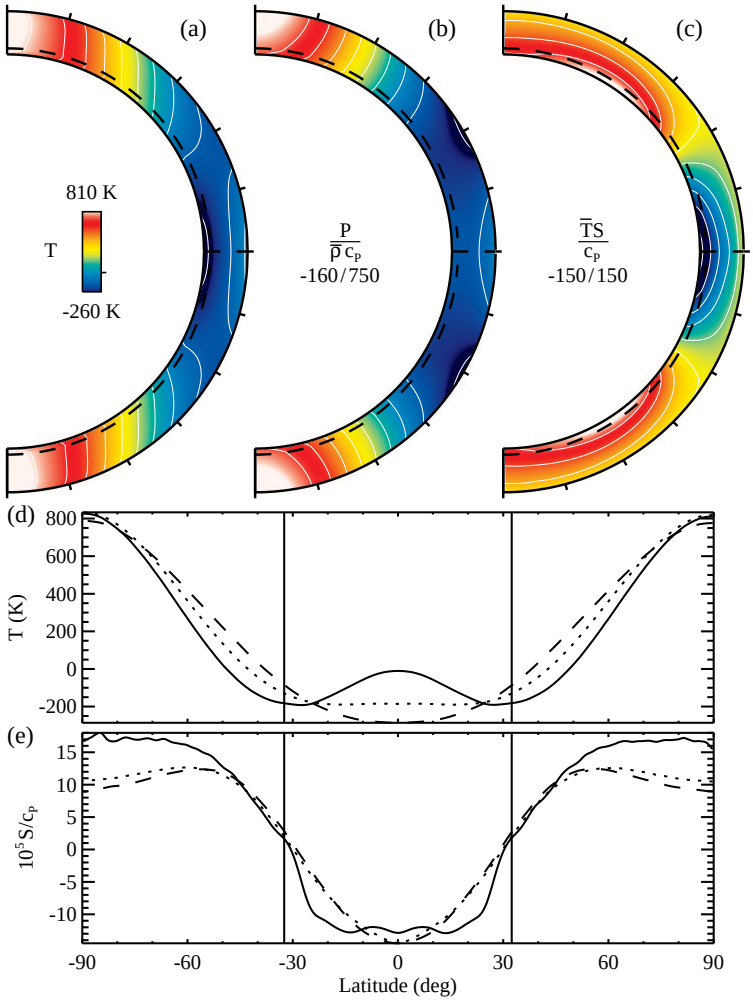

Figure 7.4: Fluctuating thermal structures found within *Case A10*. Azimuthally-averaged variations are shown for the temperature (a) and the scaled contributions from the fluctuations of (b) pressure $[P/\overline{\rho}c_P]$ and (c) entropy $[\overline{T}S/c_P]$. Cuts through (d) the averaged temperature fluctuations and (e) the averaged entropy fluctuations are displayed at fixed radii: at the top of the domain (*solid line*, 0.98 R), at mid-convection zone (*dotted line*, 0.89 R), and in the stable region (*dashed line*, 0.80 R). The vertical lines denote the edges of the tangent cylinder.

in them (Figure 7.4(c)). The decrease is in part due to the weak radial differential rotation in *Case A10* (Figure 6.3(f)). Indeed, a time steady meridional force balance leads to a linking of the entropy to the ageostrophic component of the differential rotation (see §7.3.2), which implies that a strong radial differential rotation could lead to a larger entropy contribution. But as is evident in Figure 7.4(e), the entropy perturbations have little variation in radius, reflecting the weak radial differential rotation. In an azimuthal and time average of the momentum equation (Equation (6.1)), the time and azimuthal derivatives of the mean flows vanish, leaving the advection, viscous, Coriolis, buoyancy, and pressure gradient terms. If we keep only the largest contributing terms, the gradient of the zonally averaged pressure fluctuations is then primarily balanced by three terms: the buoyancy arising from the mean density fluctuations, the Coriolis forces acting on the mean zonal flow, and the centripetal force due to the differential rotation arising from the largest of the advection terms. These terms combine to give

$$\boldsymbol{\nabla}\langle P\rangle \approx \overline{\rho}\lambda\left(\Omega^2 - \Omega_0^2\right)\hat{\lambda} - \langle\rho\rangle g\hat{\mathbf{r}}, \tag{7.1}$$

where $\Omega = \Omega(r,\theta)$ is the angular velocity and $\lambda = r\sin\theta$ is the distance from the rotation axis. When integrated over the domain, the relative difference between the pressure gradient and the terms on the right hand side ($\mathbf{R}$) of the Equation (7.1), which is given by $\|\boldsymbol{\nabla}\langle P\rangle - \mathbf{R}\|/\|\boldsymbol{\nabla}\langle P\rangle\|$, shows that this balance is satisfied to within 2% over the entire domain. The agreement is best at higher latitudes, but is significant everywhere. The Coriolis and the advection terms comprise about 66% of the magnitude of the gradient, while the buoyancy terms make up about 34%. Thus, the structure of the pressure arises primarily from the geostrophy of the flow (Pedlosky, 1982), which is particularly important for the low latitude peak in the pressure and temperature in the upper reaches of the convection zone. The buoyancy arising from the mean density fluctuations, however, is also important. This term follows from the equation of state (Equation (6.8)), and arises from the baroclinicity of the flow. Indeed, the differential rotation plays a crucial role in determining the structure of

these fields.

7.3.2 Thermal Signature of Differential Rotation

If the planetary vorticity of a system is large relative to the turbulent vorticity, the Rossby number is small, which is the case in the simulations conducted in this paper (see Table 2). In these systems, the dynamics that arise tend to minimize variations across cylinders aligned with the rotation axis. Indeed, in constant density settings, the Taylor-Proudman theorem states that there is no variation along these cylinders. On the other hand, the density and pressure isosurfaces can lose alignment in stratified flows, leading to baroclinicity and flows that can violate this constraint as is seen in the cylinder crossing meridional circulation in Figures 6.3 and 6.4. One might suspect that, given the large equator to pole thermal contrast established in these simulations, a strong meridional circulation would arise to homogenize the temperature. However, as will be shown in the following section (§7.4), the differential rotation and turbulent Reynolds stresses mediate the mean meridional flow. Thus another mechanism must act to maintain this large thermal contrast. In the simulations reported on here, there is a balance between latitudinal enthalpy flux and entropy diffusion that establishes the thermal contrast, which in turn evolves in conjunction with the meridional flow and differential rotation. It is clear from the previous section that quasi-geostrophic flow accounts for a portion of the average temperature fluctuations, where the differential rotation leads to temperature perturbations, while another mechanism is responsible for the ageostrophic component.

The bulk rotation of these simulations is sufficiently rapid to increase the axial alignment of the convective structures, which leads to a more cylindrically aligned transport of enthalpy and angular momentum. The domains are highly stratified and thus baroclinicity plays an important role in them. These tendencies lead to a mean thermodynamic state and the two mean flows (the meridional circulation and the differential rotation) that are closely coupled and maintained through the time-averaged properties of the turbulent trans-

port of energy and momentum. We here explore the connection between the mean thermal structures and the differential rotation by examining the zonal vorticity equation, which is the azimuthal component of the curl of the momentum equation divided by the background density as detailed in Brun et al. (2011). We begin with the time- and azimuthally-averaged zonal vorticity equation that has been divided by Ω_0^2 in order to aid our assessment of how the various terms scale with rotation rate. It is important to note that the advection terms can be split into three contributing pieces, those due to the mean zonal velocity, the mean meridional circulation, and the Reynolds stresses arising from the fluctuating velocities. The advection term arising from the mean zonal velocity cancels the contribution from the Coriolis force leaving the quadratic dependence upon the angular velocity seen on the left hand side (LHS) of the following equation

$$\overbrace{\frac{\lambda}{\Omega_0^2}\frac{\partial \Omega^2}{\partial z}}^{\mathrm{Ro_{DR}}} = \overbrace{\frac{g}{\Omega_0^2 r C_P}\frac{\partial \langle S\rangle}{\partial \theta} + \frac{1}{\Omega_0^2 r \overline{\rho} C_P}\frac{\partial \overline{S}}{\partial r}\frac{\partial \langle P\rangle}{\partial \theta}}^{Baroclinicity} + \underbrace{\frac{1}{\Omega_0^2}\langle \mathrm{RS}\rangle}_{\mathrm{Ro'^2}} + \underbrace{\frac{1}{\Omega_0^2}\langle \mathrm{MC}\rangle}_{\mathrm{Ro_{mc}^2}} + \underbrace{\frac{1}{\Omega_0^2}\langle \mathrm{VS}\rangle}_{\mathrm{Ek\ Ro}}, \tag{7.2}$$

where $z = r\cos\theta$ is the axial coordinate and the overbraces and underbraces indicate the scaling of a particular term with its associated Rossby number (Ro) and label the baroclinic terms. The baroclinic terms have been simplified using Equation 6.3. The viscous stresses $\langle \mathrm{VS}\rangle$ scale as the Ekman number ($\mathrm{Ek} = \mathrm{Ta}^{-1/2}$) times the Rossby number. The turbulent Reynolds stresses $\langle \mathrm{RS}\rangle$ arising from the fluctuating velocity component subsequently are proportional to the fluctuating Rossby number (Ro'), and the advection of the meridional vorticity by the meridional circulation $\langle \mathrm{MC}\rangle$) vary with $\mathrm{Ro_{mc}}$. These stresses are given explicitly by

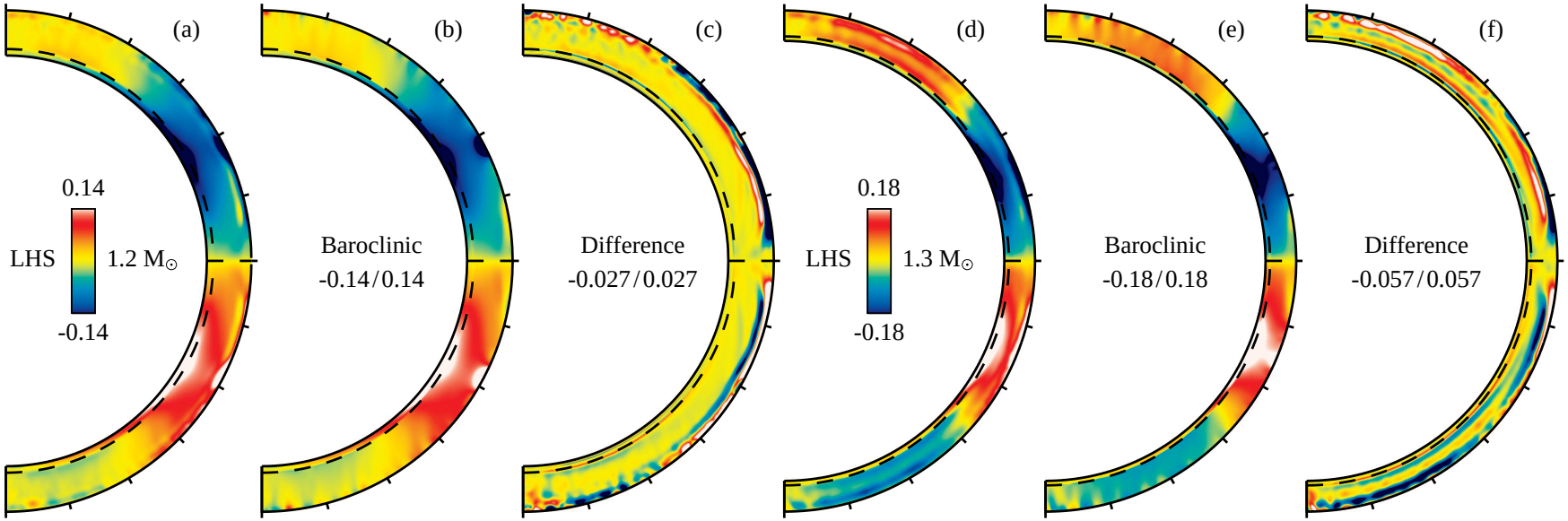

Figure 7.5: Components of the time- and azimuthally-averaged zonal vorticity balance. (a) Depicts the left hand side of Equation (7.2), (b) the baroclinic terms, and (c) their difference, which is composed of the viscous and Reynolds stresses, for *Case A10*. (d, e, f) Show the same quantities for *Case B10*. The color tables used in each panel are scaled by the indicated values.

$$\langle \mathrm{RS} \rangle = \left\langle \mathbf{u}' \cdot \boldsymbol{\nabla} \omega'_\phi \right\rangle + \left\langle \frac{u'_\phi \omega'_\lambda}{\lambda} \right\rangle - \left\langle \boldsymbol{\omega}' \cdot \boldsymbol{\nabla} u'_\phi \right\rangle - \left\langle \frac{u'_\lambda \omega'_\phi}{\lambda} \right\rangle - \left\langle \omega'_\phi u'_r \frac{\partial \ln \overline{\rho}}{\partial r} \right\rangle, \tag{7.3}$$

$$\langle \mathrm{MC} \rangle = \langle \mathbf{u}_{\mathrm{mc}} \rangle \cdot \boldsymbol{\nabla} \langle \omega_\phi \rangle - \frac{\langle \omega_\phi \rangle \langle u_\lambda \rangle}{\lambda} - \langle \omega_\phi \rangle \langle u_r \rangle \frac{\partial \ln \overline{\rho}}{\partial r}, \tag{7.4}$$

$$\langle \mathrm{VS} \rangle = \frac{1}{\overline{\rho} r} \left\langle \frac{\partial}{\partial \theta} \boldsymbol{\nabla} \cdot \mathcal{D} \cdot \hat{\mathbf{r}} \right\rangle - \left[\frac{1}{r} - \frac{\partial \ln \overline{\rho}}{\partial r} + \frac{\partial}{\partial r} \right] \left\langle \boldsymbol{\nabla} \cdot \mathcal{D} \cdot \hat{\boldsymbol{\theta}} \right\rangle. \tag{7.5}$$

Here λ is the cylindrical radius; ω_λ and u_λ are the cylindrically radial directed vorticity and velocity, respectively. Within the convection zone of these simulations, the pressure contribution to the baroclinic terms is small, but it becomes appreciable in the stable region and is retained. The Reynolds stresses of the fluctuating velocities ($\mathbf{u}'$) in Equation (7.3) possess two primary components of stretching and advection. The first two terms of this equation are the advection of the zonal vorticity and the second two are the vortical stretching of the zonal velocity, and the last term arises from the compressibility of the flows. The terms associated with the meridional circulation ($\mathbf{u}_{mc}$, Equation (7.4)) are similar in that the meridional flow advects meridional vorticity and retains the effects of compressibility, but they lack vortical stretching with contributions from only the component due to the geometry ($\langle \omega_\phi \rangle \langle u_\lambda \rangle / \lambda$). The definition of $\mathcal{D}$ from Equation (6.5) is used here for the viscous stress terms given in Equation (7.5).

Consistent with the strong thermal gradients seen in Table 3 and discussed in §7.3, Figure 7.5 demonstrates the extent to which the baroclinic terms are linked to the differential rotation through a meridional force balance. Indeed, from Equation (7.2) it is clear that the cylindrical gradient of the square of the angular velocity (labeled LHS in Figures 7.5(a) for case *Case A10* and 7.5(d) for *Case B10*) is almost entirely balanced by the latitudinal gradients of the entropy and pressure. These two thermal gradients arise due to the baroclinicity of the flows and are labeled as such in Figures 7.5(b) and 7.5(e). The entropy gradient dominates the meridional force balance within the convection zone because

the pressure gradient is weighted by the nearly adiabatic mean entropy gradient. Within the stable region, however, the mean entropy gradient is about four orders of magnitude larger than in the convection zone, leading to a significant contribution form the latitudinal gradient of the pressure. The baroclinic terms in the bulk of the convection zone change sign at higher latitudes. This reversal in sign occurs at a lower latitude in the $1.3\,\mathrm{M}_\odot$ cases, at about $\pm 45^\circ$ rather than $\pm 60^\circ$ as in the $1.2\,\mathrm{M}_\odot$ cases. The presence of the latitudinal pressure gradient causes the large negative structure that occurs around the tangent cylinder in the northern hemisphere (positive in the south) to stretch to the poles in the stable region.

The balance, however, is not perfect as there are effects near the upper boundary that are primarily due to the Reynolds stresses associated with the turbulent velocity field, as has been seen in previous simulations of G-type stars (e.g., Brun et al., 2011; Brown et al., 2008; Brun & Toomre, 2002). These departures from a pure thermal wind balance are easily seen in Figures 7.5(c) and 7.5(f), where the difference between the angular velocity gradient and the baroclinic terms are shown for *Case A10* and *Case B10*. It is also apparent that the turbulent Reynolds stresses play more of a role in the $1.3\,\mathrm{M}_\odot$ simulations than in those of the $1.2\,\mathrm{M}_\odot$ F-type stars, where the rms values of the Reynolds stresses contribute to about 10% of the balance versus 5% for the lower mass $1.2\,\mathrm{M}_\odot$ F-type stars. This is expected given that the fluctuating Rossby number in *Case B10* is larger than in *Case A10* as seen in Table 2. There are additional contributions from the viscous stresses and the advection terms associated with the meridional circulation, but they play a much smaller role in the meridional force balance than the baroclinicity and turbulent Reynolds stresses. Indeed, the importance of these various terms scale well with the values of the Rossby numbers given in Table 2, with the viscous stresses being proportional to $\mathrm{Ek}\,\mathrm{Ro} \approx 10^{-4}$ and $\langle \mathrm{MC} \rangle$ varying as $\mathrm{Ro}_{\mathrm{mc}}^2 \approx 10^{-4}$. For comparison, $\langle \mathrm{RS} \rangle$ scales as $\mathrm{Ro}'^2 \approx 10^{-1}$. Accordingly, we may safely neglect these small contributions to the meridional force balance due to $\langle \mathrm{MC} \rangle$ and $\langle \mathrm{VS} \rangle$. This leads to an expected proportionality of the baroclinic terms in Equation (7.2) of $\mathrm{Ro}_{\mathrm{DR}} + \mathcal{O}\left(\mathrm{Ro}'^2\right) \approx \mathrm{Ro}$.

7.4 Maintaining Mean Flows

The convective motions in these simulations are influenced by the bulk rotation, spherical geometry, and stratification of the domain. The mean flows and thermodynamic structures, such as those described above, are established and maintained by the transport of momentum and energy supported by these motions. Here we will consider how the transport of angular momentum leads to a co-evolution of and a direct link between the meridional circulation and the differential rotation. To illustrate the subtle balances achieved within this turbulent convection that lead to the maintenance of these mean flows, consider the time and azimuthally averaged zonal component of the momentum equation (Miesch & Hindman, 2011), which yields the evolution equation for the specific angular momentum

$$\langle \rho \mathbf{u} \rangle \cdot \boldsymbol{\nabla} \mathcal{L} = -\boldsymbol{\nabla} \cdot \left[F_\lambda \hat{\boldsymbol{\lambda}} + F_z \hat{z} \right] \equiv \mathcal{T}, \tag{7.6}$$

$$F_\lambda = \overline{\rho} \lambda \langle u'_\lambda u'_\phi \rangle - \overline{\rho} \nu \lambda^2 \frac{\partial \Omega}{\partial \lambda}, \tag{7.7}$$

$$F_z = \overline{\rho} \lambda \langle u'_z u'_\phi \rangle - \overline{\rho} \nu \lambda^2 \frac{\partial \Omega}{\partial z}, \tag{7.8}$$

where $\mathcal{L} = \lambda^2 \Omega = \lambda \left(\langle u_\phi \rangle + \lambda \Omega_0 \right)$, $\lambda = r \sin\theta$ is the cylindrical radius, and $\mathbf{u}' = \mathbf{u} - \langle \mathbf{u} \rangle$ is the fluctuating velocity, $\hat{\boldsymbol{\lambda}}$ is the cylindrical radial unit vector, and $\langle \mathbf{u} \rangle$ is the axisymmetric velocity. The advection of angular momentum by the meridional flow could be incorporated into the flux, but is retained separately for later analysis. The axial torque $\mathcal{T}$ is the divergence of the sum of both the radial and cylindrical angular momentum fluxes, which are due to the viscous stresses arising from the mean zonal velocity and the Reynolds stresses produced by the turbulent alignment of the cylindrical and radial velocity components with the fluctuating longitudinal component. These transport mechanisms act in concert during the evolution of a case to accelerate the equator and decelerate the poles until a steady state is reached in which the axial torques act to balance the meridional advection of angular momentum, while also helping to maintain the differential rotation. The axial torque for *Case A10*, as well as the angular momentum fluxes that contribute to it, are shown in Figure 7.6.

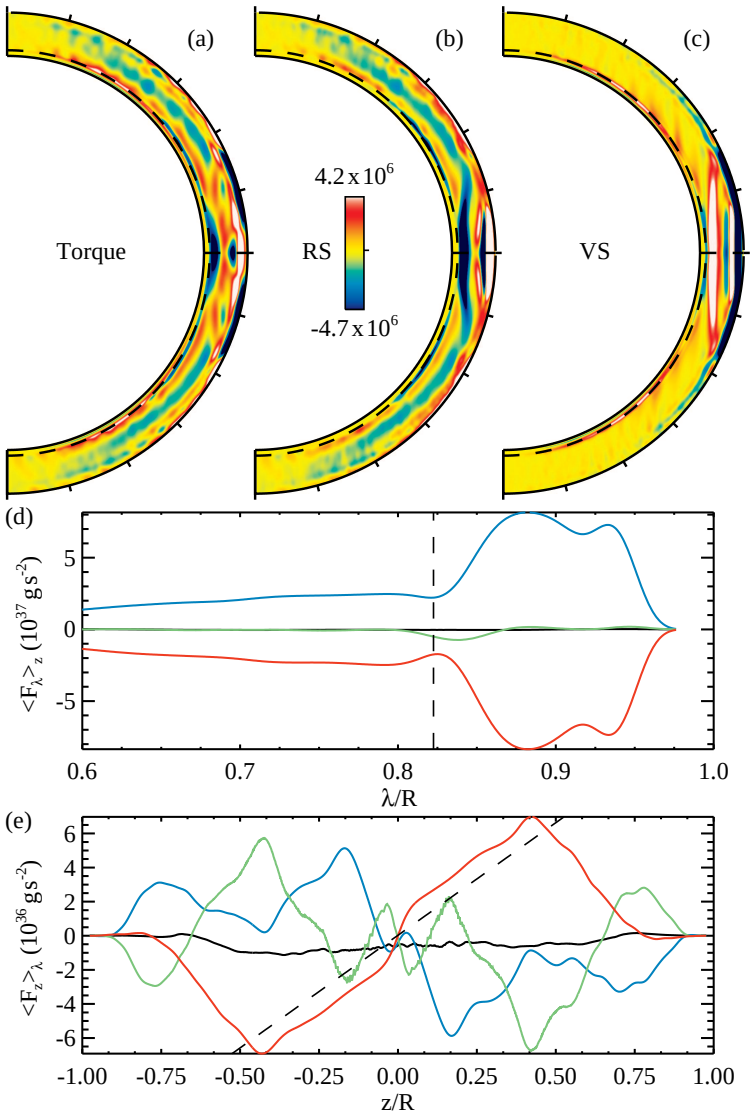

Figure 7.6: The axial torques that balance the meridional advection of angular momentum are shown for *Case A10*. (a) The net axial torque of the right hand side of Equation (7.6). (b) The axial torque due to Reynolds stresses (RS). (c) The axial torque due to viscous stresses (VS). (a)-(c) are scaled relative to the net torque and shown in units of $\mathrm{g\,cm^{-1}\,s^{-2}}$. (d) Vertically integrated angular momentum fluxes in the cylindrical radial direction ($\langle F_\lambda \rangle_z$) and (e) cylindrical angular momentum fluxes integrated over the cylindrical radius ($\langle F_z \rangle_\lambda$) with Reynolds stresses as blue lines, transport by the meridional circulation in green, viscous stresses in red, and the total in black. The dashed line in (d) indicates the value of λ at the tangent cylinder at the base of the convection zone. In (e) the dashed line shows the values of z along the tangent cylinder until it intersects the upper radial boundary.

In a statistically steady state where $\partial\mathcal{L}/\partial t \approx 0$, the angular momentum advected by the meridional flows must balance the net torque $\mathcal{T}$ as in Equation (7.6). Although the angular velocity profile Ω of these simulations is roughly conical at most latitudes, as shown in Figures 6.3 and 6.4, the specific angular momentum $\mathcal{L}$ is much more cylindrical, increasing away from the rotation axis due to the weighting by the square of the lever arm. For some intuition, Equation (7.6) can be understood by considering the largest component of the left hand side, $\langle\rho u_\lambda\rangle\partial\mathcal{L}/\partial\lambda \approx 2\Omega_0\lambda\langle\rho u_\lambda\rangle$. This approximate relationship implies that the axial torque is balanced largely by the cylindrically radial component of the meridional flow. Moreover, this can be interpreted as $\langle\rho u_\lambda\rangle \approx \mathcal{T}/2\Omega_0\lambda$ namely that an axial torque induces a meridional flow either toward or away from the rotation axis depending on its sign. Thus, Equation (7.6) implies that a net prograde torque ($\mathcal{T} > 0$) will induce a steady meridional flow away from the rotation axis, while a retrograde torque ($\mathcal{T} < 0$) will generate a flow toward the rotation axis. Thus, the steady state meridional circulation is achieved in part through the Coriolis force acting on the mean zonal flow, a process referred to as gyroscopic pumping (e.g., McIntyre, 1998; Wood & McIntyre, 2007; Miesch & Hindman, 2011).

7.4.1 Decrypting the Axial Torques

Figure 7.6 depicts the balance of the axial torques expressed in Equation (7.6) that is established in *Case A10*, averaged over approximately 30 rotation periods. The sum of the torques due to the Reynolds and viscous stresses (Figures 7.6(b) and (c)) balances the meridional advection of angular momentum so closely that it is visually indistinguishable from Figure 7.6(a), and thus the left hand side of Equation (7.6) is not included in the figure. This indicates that the mean flows have indeed reached an equilibrium state, as can be deduced from the very small departure from zero of the integrated total cylindrical radial and axial angular momentum fluxes shown in Figures 7.6(d) and (e). The net axial torque shown in Figure 7.6(a) illustrates that there is a prograde equatorial torque and retrograde torque inside the tangent cylinder as one would expect given the sense of the

differential rotation (see §6.3.1 and §6.3.2). The mean net torque is sustained over a long period of time, as the average taken here is over several hundred rotational periods. Given that energy is conserved within the system, this implies that energy is being transferred from the thermal state to the kinetic energy of the system and through dissipation it is transferred back to the thermal reservoir.

By comparing Figures 7.6(a) and (b), it is apparent that the Reynolds stresses are the dominant mode of angular momentum transport inside of the tangent cylinder. In the regions above 45° latitude, the axial component of the Reynolds stress transports angular momentum outward along cylinders and is balanced by the meridional circulation advecting angular momentum inward, as is seen in Figures 7.6(a) and (e). At mid-latitudes between the tangent cylinder and about 45°, the radial component of the Reynolds stress angular momentum flux is positive, so angular momentum is transported toward the surface, but it then reverses sign above 45°. The torque resulting from the divergence of these Reynolds stress angular momentum fluxes is negative at mid-depth, decelerating the mid-convection zone, and positive at the boundaries, thus accelerating the upper convection zone and the overshooting region (Figure 7.6(b)). Inside the tangent cylinder, the downflow plumes are nearly aligned with the rotation axis and tend to conserve their angular momentum. This supports an inward angular momentum transport and results in the zonal deceleration seen at higher latitudes and throughout the bulk of the convection zone. However, the downflows are buoyantly braked and diverge as they approach the bottom of the convection zone and enter the overshooting region. During this process the flows begin to dilate and become anti-cyclonic so that they accelerate the lower convection zone and overshooting region. This torque results in an a gyroscopically pumped meridional flow that is equatorward near the base of the convection zone and poleward closer to the surface, where it must cross $\mathcal{L}$ contours (Figures 6.3(h) and 7.6(b)).

Outside the tangent cylinder, where the columnar convective structures are so prominent, the viscous and the Reynolds stresses are of nearly equal importance. The integrated

Table 7.1
Global Properties of the Evolved Convection

Mass	Case	$KE/10^6$	$KE_{DR}/10^6$	$KE_{MC}/10^3$	$KE_C/10^6$	$\Delta\Omega_r/\Omega_0$	$\Delta\Omega_{60}/\Omega_0$	ΔT_{60}	ΔS_{60}	d_o/H_P
	A5	7.46	6.35 (85.1%)	5.39 (0.072%)	1.10 (14.8%)	0.065	0.195	-117	-20750	0.088
	A7	15.0	13.9 (92.9%)	4.31 (0.029%)	1.07 (7.11%)	0.063	0.212	-246	-44830	0.089
	A10	29.4	28.4 (96.6%)	3.68 (0.013%)	1.01 (3.42%)	0.054	0.211	-501	-93010	0.101
$1.2\,M_\odot$	*A15*	67.1	65.3 (97.4%)	2.44 (0.004%)	1.74 (2.60%)	0.043	0.200	-1048	-184400	0.339
	A20	91.9	90.4 (98.4%)	1.99 (0.002%)	1.51 (1.65%)	0.037	0.177	-1635	-290300	0.332
	A5i	6.92	5.65 (81.7%)	6.04 (0.087%)	1.26 (18.2%)	0.057	0.199	-101	-13900	—
	A20i	28.5	27.5 (96.5%)	2.48 (0.009%)	0.99 (3.47%)	0.049	0.114	-714	-44940	—
	B8	2.23	1.41 (63.1%)	2.93 (0.131%)	0.82 (36.8%)	0.030	0.101	-190	-31000	0.121
	B10	6.70	5.99 (89.3%)	2.46 (0.037%)	0.71 (10.7%)	0.038	0.177	-613	-111670	0.122
$1.3\,M_\odot$	*B15*	15.5	14.6 (94.4%)	1.97 (0.013%)	0.86 (5.55%)	0.041	0.204	-1444	-267900	0.137
	B20	35.0	33.8 (96.5%)	1.53 (0.004%)	1.22 (3.49%)	0.036	0.224	-2799	-503200	0.334
	B30	26.4	25.6 (97.2%)	0.88 (0.003%)	0.75 (2.83%)	0.024	0.142	-3745	-812000	0.358
	B20i	15.3	14.6 (95.5%)	1.43 (0.009%)	0.69 (4.51%)	0.038	0.182	-1797	-224100	—

Table 7.1: Total (KE), differential rotation (KE_{DR}), meridional circulation (KE_{MC}), and convective (KE_C) kinetic energy densities are both averaged in time and volume and are shown in units of $\mathrm{erg\,cm^{-3}}$, and relative to the total kinetic energy in parentheses. The spatial averages are taken over only the convection zone to allow comparison between the cases with and without overshooting. The relative radial and latitudinal differential rotation ($\Delta\Omega_r/\Omega_0$ and $\Delta\Omega_{60}/\Omega_0$), the latitudinal temperature difference (ΔT_{60}, in K) the latitudinal entropy difference (ΔS_{60}, in $\mathrm{erg\,K^{-1}\,cm^{-3}}$) are measured between the equator and 60° latitude (averaged over both hemispheres). The depth of the overshooting region (d_o) is shown measured relative to the pressure scale height (H_P) at the base of the convection zone and is horizontally averaged.

fluxes shown in Figures 7.6(d) and (e) reflect this balance. A strong columnar feature saturates the color table and is visible in the viscous and Reynolds stress torques (Figures 7.6(b) and (c)), where it nearly follows the tangent cylinder as is clear in Figure 7.6(e). The Reynolds stresses arise from the thin, spiraling, columnar equatorial convective cells. The properties of the torque due to Reynolds stresses associated with these structures are clear; they act to reduce the angular momentum at depth and increase it nearer the surface, while the viscous stresses attempt to counteract this action but are slightly weaker. The axially aligned equatorial flows seen in these simulations are strongly affected by the boundary geometry. In Busse (2002), it is shown that the convex curvature of the caps of the cylindrical annular convective domain geometry leads to prograde tilted columnar cells. These tilted columns transport prograde momentum outward and retrograde angular momentum inward, as occurs with the equatorial convection cells here. This occurs because the thermal Rossby wave associated with the columnar convection tends to propagate faster in the upper convection zone and slower in the lower convection zone (Busse & Hood, 1982). The prograde torque of the Reynolds stresses above the mid-convection zone and the retrograde torque in the lower convection zone and overshooting region, visible in Figure 7.6(b), indicate that these equatorial convective structures do indeed play a crucial role in the angular momentum transport. This is manifest in the radial dependence of the angular velocity (Figures 6.3 and 6.4.

There are two sets of equatorial columns in this simulation. One set of columns are confined to the deep convection zone, terminating at the base of the convection and extending up to the middle of the convection zone. A second set of columns exists at the upper boundary and extend down to the middle of the convection zone. This situation arises because the radial differential rotation is large enough to shear the columns and because the density scale height acts to confine columns near the upper boundary, which can be understood as a result of a large Taylor number. This configuration of columns manifests itself in the axial torque as a region of negative torque at the base of the convection zone, a positive torque just below

the middle of the convection zone, a negative torque at the base of the outer columns and a positive torque near the upper boundary as in Figure 7.6(b).

In the limit that the outer boundary becomes spherical, the equatorial columns described in Busse (2002) become increasingly sheared in longitude with increasing latitude, where the fastest prograde flows are at the equator and are slower near the latitude at which the tangent cylinder intersects the upper boundary. This process is accentuated by the thin-shell geometry of the F-type stars, where the spherical upper boundary has an increasing slope as one approaches the equator, which in turn causes the phase speed of the thermal Rossby waves to increase. This leads to faster equatorial flows and slower flows at higher latitudes. The net axial torque reflects these effects, with a retrograde torque (flux divergence) at low latitudes between the tangent cylinder and about $\pm 8^\circ$ and a prograde torque (flux convergence) near the equator (Figure 7.6(a)).

7.4.2 Meridional Flows Induced by Axial Torques

The Reynolds stresses arising from the convective cells outside the tangent cylinder are not perfectly cylindrical and have a convergent structure, where the latitude of the outer boundary of the cell is dependent on the spherical radius as is evident in Figures 7.6(a) and (b). On the other hand, the viscous stresses in the bulk of the convection zone are nearly cylindrical. The slight misalignment of these two torques gives rise to the net torque, as they almost cancel one another outside of the tangent cylinder (Figure 7.6(d)). Indeed, the complicated morphology of the net torque gives rise to four reversals in the sign at the equator, resulting in four cells of low-latitude meridional flow (Figures 7.6(a) and 6.3(h)). These cells close on the equator and end either at very low latitudes or merge and stretch up to the tangent cylinder. At latitudes below the tangent cylinder, but above the lowest latitudes, there are two meridional cells. In the northern hemisphere, a clockwise circulation is centered on the tangent cylinder and the counter-clockwise circulation at larger cylindrical radii is a combination of a cylindrical cell at mid-convection zone and a curved cell that

stretches along the outer boundary.

A similar balance of angular momentum fluxes is realized in both the *Case B* simulation at $10\,\Omega_\odot$ and also at other rotation rates. The trend is that there are a larger number of meridional circulation cells outside the tangent cylinder with faster bulk rotation rates, while the equatorial region remains isolated from the higher latitudes by the meridional circulation cells at the tangent cylinder. At higher latitudes inside the tangent cylinder, the Reynolds stresses support a dual celled meridional circulation at higher rotation rates. These two cells are split in radius, one nearer the surface and one at depth. The upper cell connects with the cell that sits on the tangent cylinder, moving fluid with lower angular momentum from the upper layers at high latitudes to the base of the convection zone which is then whisked poleward by the polar circulation cell at the base of the convection zone. However, in cases with the shear instability (§6.4) there is a substantial peak in both the diffusive and Reynolds stress components of the angular momentum transport at higher latitudes inside the tangent cylinder not seen in other cases. The time dependence of the instability leads to angular momentum fluxes that fluctuate much more than in the cases that do not have this instability.

7.5 Scaling with Rotation and Mass

With our choices in the scaling of the diffusivities with rotation rate, the parameter space covered by these simulations is essentially restricted to varying the rotation rate (or Rossby number) and mass of the system. Thus, we explore the variation of the differential rotation ($\Delta\Omega$), meridional circulation ($\mathrm{KE_{MC}}$), and latitudinal temperature gradient (ΔT) with these parameters. The latitudinal differential rotation is not known apriori and is fit for, however, the latitudinal temperature gradient follows directly from $\Delta\Omega$ given the quasi-geostrophy and thermal wind balance of the flow. The energy associated with the meridional circulation also follows from the differential rotation, but through the mechanism of gyroscopic pumping and the influence of the Reynolds stresses.

The Rossby numbers of these simulations and those in Brown et al. (2008) (see Table 6.2 and Figure 7.7(a)) are fit as a function of mass (with M between $1.0\,M_\odot$ and $1.3\,M_\odot$) and bulk angular velocity (Ω_0), which yields

$$\mathrm{Ro} = \frac{\langle|\boldsymbol{\omega}|\rangle}{2\Omega_0} \propto \mathrm{M}^{5.7}\Omega_0^{-0.77} \tag{7.9}$$

This is close to the value expected from mixing length theory, where $\mathrm{Ro}_{\mathrm{mlt}} = v_{\mathrm{mlt}}/\mathrm{R}\Omega_0$ and $v_{\mathrm{mlt}} = (\mathrm{L}/\mathrm{R}^2\rho_{\mathrm{cz}})^{1/3}$. In the mass range of stars covered here, the depth of the convection zone decreases rapidly so we restrict our consideration to stellar masses between $1\,M_\odot$ and $1.3\,M_\odot$. In this range, the mean density of the convection zone scales as $\rho_{\mathrm{cz}} \propto \mathrm{M}^{-15.5}$, while the radius and luminosity of the stars simulated here are proportional to $\mathrm{R} \propto \mathrm{M}$ and $\mathrm{L} \propto \mathrm{M}^4$. This implies that the mixing length velocity scales as $v_{\mathrm{mlt}} \propto \mathrm{M}^{5.8}$, which leads to a an estimate of the Rossby number that scales as $\mathrm{Ro}_{\mathrm{mlt}} \propto \mathrm{M}^{4.8}\Omega_0^{-1}$. The exponents of the mass and rotation rate for this estimate are close to the fit to the Rossby number shown above, but imply a slightly smaller dependence upon the mass and more dependence upon the rotation rate.

Numerical simulations, on the other hand, suggest that the Rossby number is inversely proportional to a power of the rotation rate that is less than unity. This scaling is exhibited here, in G-type star simulations using ASH (Brown et al., 2008), in spherical shell segments (Käpylä et al., 2011), and in Cartesian f-plane simulations (Käpylä et al., 2004). The rotational scaling of the Rossby number in these simulations, with a power less than one, is expected given the influences of rotation upon the convective patterns and the rms velocities of the flow, effects that mixing length theory does not explicitly treat. One can see this directly from the convective flux in the simulations, where it can be greater or less than the luminosity of the star depending upon the rotation rate. This leads to a mixing length velocity that varies with rotation rate, and thus a more complicated dependence of the Rossby number upon the rotation rate.

On our path through parameter space, a complication arises, where there is a threshold bulk rotation rate Ω_{th} below which the differential rotation becomes anti-solar. Such behavior

is seen in both simulations of spherical domains and Cartesian domains at various levels of turbulence in both the ASH simulations (Brun & Palacios, 2009; Matt et al., 2011) and in simulations carried out in Cartesian domains (Käpylä et al., 2004) as well as in spherical segments (Käpylä et al., 2011). We observe that this transition between solar-like and anti-solar-like differential rotation occurs within flows that have a Rossby number of nearly one. It is also apparent that this change in the rotational behavior of the simulations is a function of mass, as it occurs around $0.8\,\Omega_\odot$ for $1.0\,M_\odot$ G-stars in Brown et al. (2008), near $4\,\Omega_\odot$ for the $1.2\,M_\odot$ F-type stars, and at about $7\,\Omega_\odot$ for the $1.3\,M_\odot$ F-type stars. We have been working to understand how and why there is this branch solutions possessing anti-solar-like differential rotation, and will be subsequently reporting on it with models of F-, G-, and K-type stars. Briefly, this transition arises from over-driven convection occurring due to our choices of boundary conditions, diffusion profiles, and initial stratification, all of which result in a Rossby number is greater than one throughout the bulk of the convection zone and a reversal in the sign of the Reynolds stresses for rotation rates below the threshold. However due to this existence of this branch of solutions, we have chosen the bulk rotation rates of the simulations reported on here to be above this threshold rotation rate.

7.5.1 Differential Rotation

The relative latitudinal differential rotation ($\Delta\Omega/\Omega_0$) established in these simulations is measured between the equator and 60° latitude (Table 7.1). The relative radial differential rotation measured between the bottom of the domain and the top at the equator is also shown in Table 7.1. The trend for increasing relative latitudinal differential rotation at lower rotation rates, and decreasing $\Delta\Omega/\Omega_0$ at higher rotation rates is clear. There is a peak in $\Delta\Omega/\Omega_0$ in both of the $1.2\,M_\odot$ and the $1.3\,M_\odot$ simulations, with the former achieving a maximum around $7\,\Omega_\odot$ and the latter at $20\,\Omega_\odot$. In Brown et al. (2008), a peak in the latitudinal differential rotation is reached at about $2\,\Omega_\odot$. These maxima, however, are sensitive to the level of turbulence in both the simulations as shown in Brown et al. (2008), which is likely

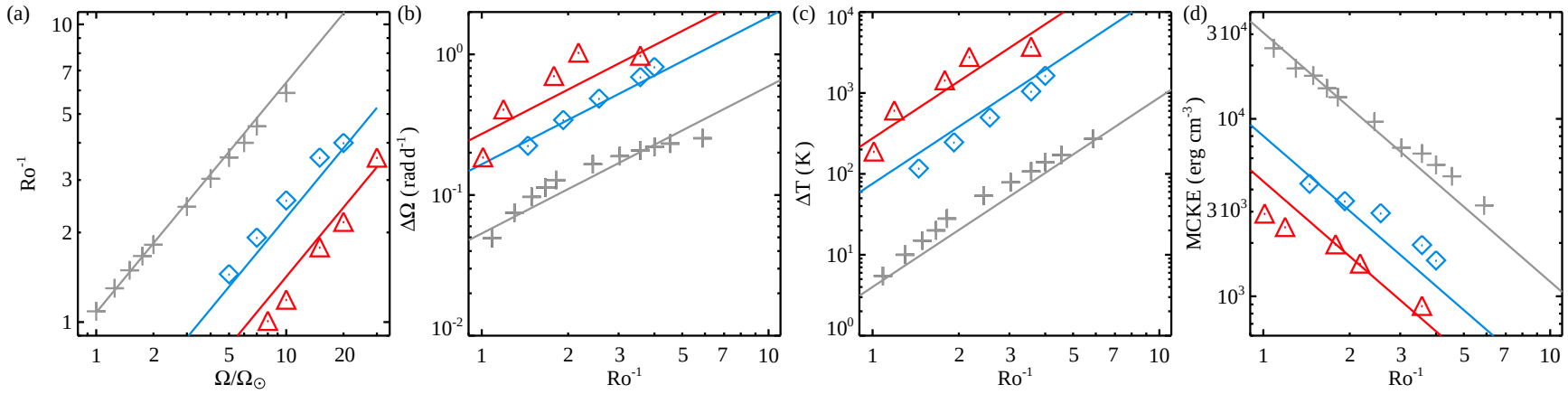

Figure 7.7: Scaling of the inverse Rossby number with mass and rotation rate, as well as latitudinal differential rotation ($\Delta\Omega$), latitudinal thermal contrasts (ΔT), and the volume averaged meridional circulation kinetic energy (KE_{MC}) with mass and inverse Rossby number. (a) inverse Rossby number for F-type star *Case A* simulations (diamonds) and *Case B* simulations (triangles), and for 1.0 $M_\odot$ G-type star simulations (crosses) [from Brown et al. (2008)]. The fit to the Rossby number is shown as solid colored lines blue, red, and gray for the *Case A*, *Case B*, and G-type star simulations respectively. These symbols and colored lines are employed in the following panels: (b) $\Delta\Omega$ with the solid lines as in Equation (7.10). (c) ΔT with the lines given in Equation (7.14). (d) KE_{MC} with lines given in Equation (7.21).

also the case here but is not explicitly explored.

An intriguing feature of these simulations is that the absolute differential rotation in both radius and in latitude increases with rotation rate (decreasing Rossby number), as seen in Figure 7.7. It is also apparent that the mass of the star plays an important role through its influence upon the depth of the convection zone as well as the strength of the convective driving arising from the increased luminosity of the star. Indeed, we find here that the absolute latitudinal differential rotation $\Delta\Omega_{60}$ established in these simulations, and measured between the equator and 60° latitude, scales with the mass of the star and the inverse of the Rossby number as

$$\Delta\Omega_{60} = 5.3 \times 10^{-2}\,\mathrm{rad\,d^{-1}} \left(\frac{\mathrm{M}}{\mathrm{M}_\odot}\right)^{6.2} \mathrm{Ro}^{-1.05}. \tag{7.10}$$

This scaling of the absolute latitudinal differential rotation with Rossby number and mass is shown in Figure 7.7(b). Although the differential rotation decreases consistently with increasing Rossby number among all the cases studied here, there is some indication from the levels of differential rotation achieved in Brown et al. (2008) that there may be a change in the rate of increase of the absolute differential rotation at larger rates of rotation. This may arise either because there is a maximum in absolute differential rotation or simply slower growth at larger rotation rates. However, probing these higher rotation rates is beyond the current capabilities of ASH due to the exclusion of centrifugal forces.

Mass also plays a crucial role in building increasingly strong differential rotation in higher mass stars. The strong mass dependence of the fit in Equation (7.10) reflects the more vigorous convection and consequently larger Reynolds stresses that arise during the transition from the Sun to the slightly more massive F-type stars. The dependence of the magnitude of the differential rotation upon the mass, or more concretely the dependence upon effective temperature, is also clear in observations over a large range of temperatures Barnes et al. (2005); Reiners (2006); Collier Cameron (2007). The scaling of the latitudinal differential rotation in Collier Cameron (2007) is $\Delta\Omega \propto {\mathrm{T}_{\mathrm{eff}}}^{8.6} \propto \mathrm{M}^{4.3}$, where $\mathrm{T}_{\mathrm{eff}} \propto \mathrm{M}^{1/2}$.

When the latitudinal differential rotation is fit for mass and bulk rotation rate, it scales as

$$\Delta\Omega_{60} = 8.3 \times 10^{-2}\,\mathrm{rad\,d^{-1}} \left(\frac{\mathrm{M}}{\mathrm{M}_\odot}\right)^{3.9} \left(\frac{\Omega_0}{\Omega_\odot}\right)^{0.6}, \tag{7.11}$$

and is therefore close to the observational mass scaling, within the bounds of the uncertainty of the observational data. The reason for the discrepancy in the expected mass scaling between Equation (7.10) and Equation (7.11) is that the above fit is applied to shifted data, making the mapping between rotation rate and Rossby number more complicated. This is due to the fact that the rotation rate mass fit to the differential rotation of our models crosses zero and becomes negative below a particular value of the rotation rate that depends upon the mass of the star. We remove this variation by shifting the data so that they may be fit consistently as in Equation (7.11).

7.5.2 Latitudinal Temperature Gradient

A striking property of the meridional force balance in Equation (7.2) is that increasing Ω_0 leads to increasingly cylindrical rotation profiles, as one would expect from gyroscopic pumping (§7.4). In the absence of baroclinicity, gyroscopic pumping will produce a meridional circulation that acts to make the contours of the angular momentum, and thereby the angular velocity, more cylindrical (Miesch & Hindman, 2011). We find, however, that the baroclinicity of the flows increases with more rapid rotation. The scaling of the latitudinal gradients in temperature and entropy increase at a rate that nearly keeps pace with the quadratic scaling of the rotation rate, reducing the tendency for increased alignment with the rotation axis. This variation of the temperature with mass and Rossby number is shown in Figure 7.7(b), where $\Delta\mathrm{T}_{60}$ decreases substantially with increasing Rossby number (increase with increasing rotation rate) as

$$\Delta\mathrm{T}_{60} = 5.3\,\mathrm{K} \left(\frac{\mathrm{M}}{\mathrm{M}_\odot}\right)^{16.1} \mathrm{Ro}^{-2.3} = 5.3\,\mathrm{K} \left(\frac{\mathrm{M}}{\mathrm{M}_\odot}\right)^{6.4} \left(\frac{\Omega_0}{\Omega_\odot}\right)^{1.6}. \tag{7.12}$$

To understand the origin of these scalings, consider the latitudinal gradients of the entropy and pressure that scale with the ageostrophic component of the angular velocity, which in turn scales as the Rossby number. To find how the latitudinal gradient of the temperature should vary with rotation rate, we combine the geostrophic pressure balance (Equation (7.1)) and the ageostrophic thermal wind (Equation (7.2)), which leads to the following

$$\frac{\partial \langle \mathrm{T} \rangle}{\partial \theta} = \frac{r \lambda \overline{T}^2}{g} \frac{\partial}{\partial z} \left[\frac{\Omega^2 - \Omega_0^2}{\overline{T}} \right]. \tag{7.13}$$

This allows a simple homology relationship to be developed with the assumptions that the effective temperature and the radius of the star depend upon only the mass of the star as mentioned above. We find that when integrated over latitude the temperature gradient becomes

$$\Delta \mathrm{T}_{60} \approx \Delta \mathrm{T}_0 \left(\frac{\mathrm{M}}{\mathrm{M}_\odot} \right)^{2.5} \left(\frac{\Omega_0}{\Omega_\odot} \right) \Delta\Omega = \Delta \mathrm{T}_0 \left(\frac{\mathrm{M}}{\mathrm{M}_\odot} \right)^{9.6} \mathrm{Ro}^{-1.3} \Delta\Omega. \tag{7.14}$$

The solid curves in Figure 7.7(b) depict this homology relationship, where it overlays the actual values of the temperature contrast in the simulations.

7.5.3 Meridional Circulation Kinetic Energy

Volume-averaged energy densities for our simulations are shown in Table 7.1. At the lowest rotation rate, fluctuating convective kinetic energy (defined as $0.5\overline{\rho}\langle u'^2 \rangle$, $\mathrm{KE_C}$) and the kinetic energy in the average differential rotation ($0.5\overline{\rho}\langle u_\phi \rangle$, $\mathrm{KE_{DR}}$) are comparable. As the rotation rate is increased, the $\mathrm{KE_{DR}}$ grows strongly and the convective energy decreases slightly, leading the $\mathrm{KE_{DR}}$ to dominate the total kinetic energy. The energy in meridional circulations ($0.5\overline{\rho}(\langle v_r \rangle + \langle v_\theta \rangle)$, $\mathrm{KE_{MC}}$) is always small and decreases in both magnitude and percentage of the total energy with more rapid rotation.

The volume averaged meridional circulation kinetic energy clearly decreases with rotation rate in both these simulations and those of (Brown et al., 2008). If we fit for this scaling, as we have for the absolute differential rotation, we find that

$$\mathrm{KE_{MC}} = 2.4 \times 10^4 \,\mathrm{erg\,cm^{-3}} \left(\frac{\mathrm{M}}{\mathrm{M}_\odot}\right)^{-7.4} \mathrm{Ro}^{1.04}, \tag{7.15}$$

$$= 2.4 \times 10^4 \,\mathrm{erg\,cm^{-3}} \left(\frac{\mathrm{M}}{\mathrm{M}_\odot}\right)^{-1.2} \left(\frac{\Omega_0}{\Omega_\odot}\right)^{-0.8}. \tag{7.16}$$

We can understand this scaling by returning to the equations of gyroscopic pumping and considering the scaling of the axial torques. First, though, it is useful to extract the dependence of the streamfunction upon the gradients of the angular momentum and the torques. Since the mean poloidal mass flux is divergence-less, the meridional flow can be represented as a stream function ψ such that $\langle \rho \mathbf{u} \rangle = \boldsymbol{\nabla} \times \psi \hat{\boldsymbol{\phi}}$. Expressing Equation (7.6) in terms of this streamfunction and then integrating the result clockwise from the lower boundary along $\mathcal{L}$ contours we arrive

$$\psi = \frac{1}{\lambda} \int_C \frac{\lambda \mathcal{F}}{|\boldsymbol{\nabla} \mathcal{L}|} ds, \tag{7.17}$$

where C is the contour of integration. The denominator in this equation is dominated by the λ component such that $\boldsymbol{\nabla}\mathcal{L} \approx 2\Omega_0 \lambda$. This reduces Equation (7.17) to the following

$$\psi \approx \frac{1}{2\lambda\Omega_0} \int_C \mathcal{F} ds \propto \mathrm{M}^{-7.4} \mathrm{Ro}^{1.3} \mathcal{F}\left[\mathrm{M}, \mathrm{Ro}\right]. \tag{7.18}$$

The meridional circulation kinetic energy is consequently proportional to

$$\mathrm{KE_{MC}} = \frac{1}{V} \int_V \frac{\left(\boldsymbol{\nabla} \times \psi \hat{\boldsymbol{\phi}}\right)^2}{\rho} dV \propto \mathrm{M}^{-1.3} \mathrm{Ro}^{2.6} \mathcal{F}\left[\mathrm{M}, \mathrm{Ro}\right]^2. \tag{7.19}$$

The proportionality of the torque $\mathcal{F}$ is difficult to predict apriori. One could assume that the Reynolds stresses follow the Λ effect (Rüdiger, 1989), in which case the axial torque associated with the Reynolds stresses in our parameter regime should scale as $\rho_{\mathrm{cz}} v_{\mathrm{mlt}}^2 {\mathrm{Ro}_{\mathrm{mlt}}}^{-1} \propto \mathrm{M}^{-4} {\mathrm{Ro}_{\mathrm{mlt}}}^{-1} \propto \mathrm{M}^{9.8} \Omega_0$. However, this would lead to a $\mathrm{KE_{MC}}$ that is constant with the rotation rate, which is clearly not the case here. Thus, without guidance to predict the scaling of the torque, it must be fit for. Indeed, we find that the Reynolds stress axial torque scales as

$$\mathcal{F} \propto \mathrm{M}^{-3}\mathrm{Ro}^{-0.6}. \tag{7.20}$$

Therefore, the $\mathrm{KE_{MC}}$ that arises from gyroscopic pumping (Equation (7.6)) is proportional to

$$\mathrm{KE_{MC}} \propto \mathrm{M}^{-7.3}\mathrm{Ro}^{1.4}. \tag{7.21}$$

which correlates well with the $\mathrm{KE_{MC}}$ found in our simulations as seen in Figure 7.7(d) and Equation (7.15). That is that the torque associated with the Reynolds stresses increases with rotation rate, rather than decreases as expected from mean-field theory.

7.6 Conclusions

As is apparent from the observation of F-type stars, they rotate on average much more rapidly than does the present Sun. In these stars, rotation must strongly influence the convective motions and lead to differential rotation. Such differential rotation has been observed in many F-type stars (e.g., Reiners, 2007). To assess how this differential rotation may arise, we have explored here the effects of rotation rate, convective overshooting, and stellar mass upon the patterns and mean properties of the global-scale convection in simulations of two F-type stars.

We have found that the mean zonal flows of differential rotation become much stronger with more rapid rotation and larger mass, scaling as $\Delta\Omega \propto \mathrm{M}^{3.9}\Omega_0^{0.6}$ or as $\Delta\Omega/\Omega_0 \propto \mathrm{M}^{3.9}\Omega_0^{-0.4}$ (§7.5). This corresponds well with observational detections of differential rotation for increasing rotation rate (Reiners, 2007) and with mass (Barnes et al., 2005; Reiners, 2006; Collier Cameron, 2007). Accompanying the growing differential rotation is a significant latitudinal temperature contrast, with amplitudes of 1000 K or higher in the most rapidly rotating cases. This contrast in turn scales with mass and rotation rate as $\Delta\mathrm{T} \propto \mathrm{M}^{6.4}\Omega_0^{1.6}$. The maximum temperature contrast near the surface occurs between the hot poles and the cool

mid-latitudes at about $\pm 30^{\circ}$, near the tangent cylinder. These temperature fluctuations about the spherically symmetric mean temperature are decomposed into its geostrophic and ageostrophic components, both of which are linked to the rotation of the star and its baroclinicity (§7.3). If this latitudinal temperature contrast prints through the vigorous convection at the stellar surface, it may appear as an observable latitudinal variation in intensity. The thermal contrast would presumably persist for long periods compared to stellar activity, offering a way to disentangle this intensity signature from that caused by spots of magnetism at the stellar poles.

Additionally, we have seen that the mean meridional circulation becomes much weaker with more rapid rotation and with higher mass, consistent with the concept of gyroscopic pumping, where the energy contained in these circulations drops approximately as $\mathrm{KE_{MC}} \propto \mathrm{M}^{-1.2}\Omega_0^{-0.8}$. However, the scaling of these quantities are sensitive to the variation Reynolds stresses, and thus their variation with the level of turbulence in the simulations must be better understood. As suggested in Brown et al. (2010, 2008), the weaker meridional circulations in more rapidly rotating stars will have a strong impact on many theories of stellar dynamo action, including the Babcock-Leighton flux-transport model favored for Sun-like stars as recently investigated (Jouve & Brun, 2007; Jouve et al., 2010; Miesch & Brown, 2012). Indeed, the lack of large single cells of meridional circulation at all latitudes in many models of more rapidly rotating stars suggests that the most common profile used for these flows may be oversimplified, and is actually associated with anti-solar-like differential rotation.

The simulations here include a portion of the stably stratified radiative interior below the convection zone. It has been shown here and in previous works to have a significant impact upon the morphology of the mean flows, and upon the magnitude of the latitudinal thermal contrast. The largest impact is upon the thermal field, where it leads to about a 50% greater latitudinal temperature contrast but only about 10% more differential rotation. However, its inclusion does lead to a tilting of the angular velocity contours to be more conical than cylindrical, as occurs in cases without a stable region. The convection exhibited

in the simulations with a stable zone yield a region of overshooting that is very slightly prolate and occupy about 1% of the star by radius.

Three of the cases presented here have exhibited a global-scale shear instability that operates within the stable region and persists for the duration of our simulations. This instability is sensitive to the magnitude and the latitudinal profile of the differential rotation, and is present in both mass stars but only at higher rotation rates. It has a significant impact upon the convection, causing greater depths of overshooting (§7.2) and prints through into the convection zone (§6.4). The instability and angular momentum transport and mixing properties associated with it will be examined in a subsequent paper (Augustson et al., 2012).

Our simulations are hydrodynamic, and it is possible that the inclusion of magnetism may alter the scalings of differential rotation and latitudinal temperature contrast with rotation rate. Prior MHD simulations of stellar convection have demonstrated that in some parameter regimes, strong dynamo-generated magnetic fields can react back on the differential rotation, acting to lessen angular velocity contrasts as energy is transferred into the magnetic fields (e.g., Brun et al., 2005; Browning, 2008). Magnetic F-type star simulations will be examined in the following Chapter 8. Unfortunately, the computational cost of such simulations is too great to run simulations at each roration rate examined in Chapters 6 and 7, which would allow the assessment of whether the scaling trends identified here for differential rotation and latitudinal temperature contrasts as a function of Ω_0 survive. Given previous experience with G-type stars it is likely that the general functional dependence with rotation rate is retained (Brown et al., 2010, 2011b). Our simulations stop short of the turbulent stellar surface, and it is thus difficult to estimate how all of the properties of the convection seen here may affect stellar observations in detail. However, we have found that the strong differential rotation and large thermal contrasts are a robust feature over a range of parameters, and it is likely that they will have observable consequences.

Chapter 8

Global-scale Simulations of Dynamo Action in F-type Stars

"There are, it seems, two muses: the Muse of Inspiration, who gives us inarticulate visions and desires, and the Muse of Realization, who returns again and again to say 'It is yet more difficult than you thought.' This is the muse of form. It may be then that form serves us best when it works as an obstruction, to baffle us and deflect our intended course. It may be that when we no longer know what to do, we have come to our real work and when we no longer know which way to go, we have begun our real journey. The mind that is not baffled is not employed. The impeded stream is the one that sings." – Wendell Berry

Magnetic activity and differential rotation are commonly observed features on main-sequence F-type stars. We seek to make contact with such observations and to provide a self-consistent picture of how differential rotation and magnetic fields arise in the interiors of these stars. The 3-D MHD anelastic spherical harmonic (ASH) code is employed to simulate global-scale convection and dynamo processes in a $1.2\,M_\odot$ F-type star at two rotation rates. The simulations are carried out in spherical shells that encompass most of the convection zone and a portion of the stably stratified radiative zone below it, allowing us to explore the effects a stable zone has upon the morphology of the global-scale magnetic fields. In this chapter, we examine the more slowly rotating case *Case A10m* that rotates at $10\,\Omega_\odot$ and possesses persistent wreaths of magnetism established and maintained by dynamo action. Compared to their hydrodynamic progenitors seen in the previous two chapters, the dynamo states here involve a marked reduction in the exhibited latitudinal differential rotation, which

also vary during the course of a cycle.

In Chapter 9, a cycling dynamo in the presence of a tachocline will be explored. These two chapters represent work recently published in Augustson et al. (2013b)[1] and are thus largely restatements of those results, though with some additional thoughts included in §9.11. As the primary author of the paper, I conducted all of the simulations, performed all of the analysis, and wrote the paper. The coauthors provided advice and guidance throughout this process, with Sacha Brun providing detailed comments and helpful conversations, as well as suggesting some lines of analysis for the polar-slip instability and the α-effect. Juri Toomre had to bear reading through many drafts of the paper, and both his suggestions for the text and for ways of pinning down the reversal mechanism were quite useful.

8.1 Introduction: Stellar Magnetic Fields and Rotation

Observations of main sequence stars across the Hertzsprung-Russell diagram indicate that most stars rotate and that many possess both substantial magnetic variability and strong axisymmetric magnetic fields (e.g., Donati & Landstreet, 2009). In particular, main-sequence late-type stars such as the F-type stars exhibit a positive correlation between the stellar rotation rate and surface magnetism (e.g., Pizzolato et al., 2003; Wright et al., 2011). The precise origins of this magnetic activity and its correlation with rotation, however, remain unclear. Convection and differential rotation are likely crucial elements in the dynamo action that manifests itself as starspots, coronal emission, and variable magnetic fields seen on the surfaces of these stars (e.g., Noyes et al., 1984; Berdyugina, 2005; Miesch & Toomre, 2009; Reiners, 2012).

The polarity reversals observed on the Sun occur roughly every 11 years and are the clearest evidence for cyclical magnetic field regeneration by dynamo processes. However, there have recently been detections of magnetic cycles in other stars as well. Advances

[1] Augustson, K. .C, Brun, A. S., & Toomre, J. 2013, Dynamo Action and Magnetic Cycles in F-type Stars", ApJ, 777, 153

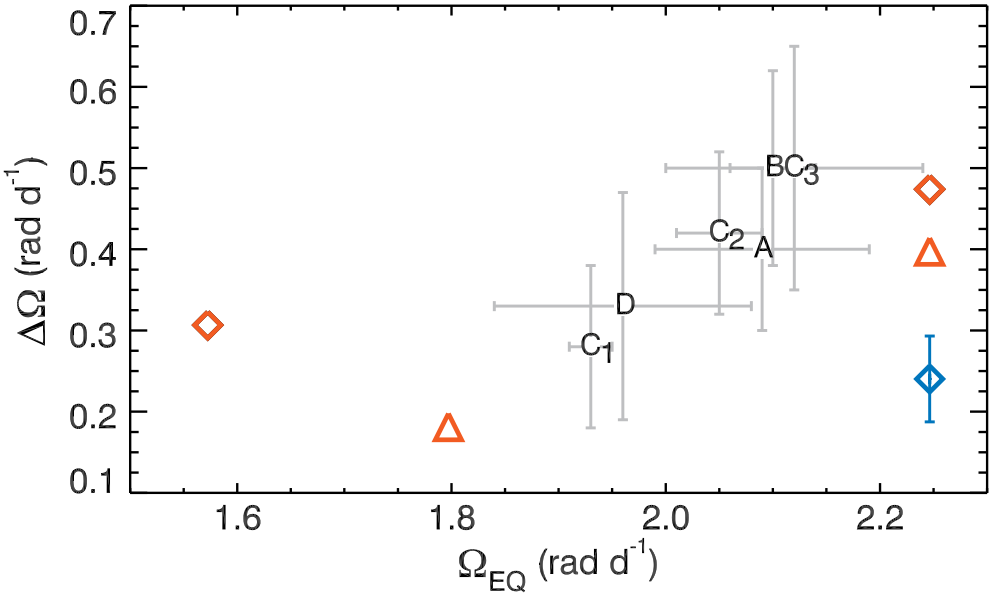

Figure 8.1: Observed latitudinal differential rotation ($\Delta\Omega$) of τ Boötis, and of 1.2 $M_\odot$ and 1.3 $M_\odot$ main sequence F-star models. Observed $\Delta\Omega$ and equatorial rotation rate Ω_{EQ} from A (Catala et al., 2007), B (Donati et al., 2008b), C_1-C_3 (Fares et al., 2009), and D (Ammler-von Eiff & Reiners, 2012), with uncertainties in gray. For comparison, hydrodynamic simulations of 1.2 $M_\odot$ (red diamonds) and 1.3 $M_\odot$ (red triangles) stars from Chapters 6 & 7, and our *Case A10m* involving the MHD simulation of a 1.2 $M_\odot$ star rotating at 10 $\Omega_\odot$ (blue diamond).

in asteroseismology enabled by the Kepler and CoRoT missions and in Zeeman-Doppler spectropolarimetric imaging (ZDI) techniques have enabled long-term observations of many magnetically active stars. Such measurements have revealed that cyclic magnetic reversals are not a unique feature of the Sun, but seem to be a fairly common feature of late-type stars. Some of the stars with the best observational coverage are F-type stars, being that they are fairly luminous and have a large mean rotation rate. Several F-type stars have observations indicating that they may harbor magnetic cycles, including τ Boötis, HD 49933, HD 52265, and HD 181420, (Fares et al., 2009; Mathur et al., 2010, 2013).

Given the crucial role that differential rotation likely plays in the dynamo action occurring within these stars, we note that spectropolarimetric observations not only permit a mapping of the surface magnetism of these stars, but also reveal information about the differential rotation on the surface of the star (e.g., Donati & Landstreet, 2009; Reiners, 2012).

Other methods can also shed light on the nature of the differential rotation of stars. For instance, high resolution observations of stellar absorption lines can be processed to produce an average line profile that is then Fourier transformed. The ratio of the values of the first two zero crossings of this transform give a measurement of the differential rotation (e.g., Reiners, 2006, 2012). Starspot modeling of photometric data can also be used to infer the inclination angle and differential rotation profile (e.g., Berdyugina, 2005; Strassmeier, 2009). In another technique, photometric data can be analyzed for their asteroseismic signatures, yielding information about the rotational behavior of a star (e.g., Gizon & Solanki, 2004; Cunha et al., 2007). For the F-type stars, the Fourier analysis technique using stellar spectra has produced the largest number of detections of differential rotation to date (Ammler-von Eiff & Reiners, 2012). In this work, 18 F-type stars are identified as having differential rotation and it is shown that the horizontal shear expressed as a latitudinal angular velocity contrast $\Delta\Omega$ increases both with increasing effective temperature and with increasing angular rotation rate Ω, extending and corroborating earlier work (Barnes et al., 2005; Reiners, 2006). These data are shown in Figure 8.2 along with the differential rotation achieved in our earlier hydrodynamic simulations and the two MHD simulations presented here.

It is instructive to look in detail at one specific F-type star, namely τ Boötis, a $1.3\,\mathrm{M}_\odot$ star rotating at about $10\,\Omega_\odot$. This star is magnetically active and appears to reverse its magnetic polarity with a period of about 2 years (Fares et al., 2009). The first measurement of the differential rotation of this star was made using the line profile analysis technique (Reiners, 2006), and again a year later in Catala et al. (2007). Subsequent measurements were made using spectropolarimetric techniques as in Donati et al. (2008b). Three separate observations were made in Fares et al. (2009) over the course of several months in 2008, showing a potential variation in the magnetic field. Subsequent observations suggest that τ Boötis does indeed possess stable, periodic reversals (Vidotto et al., 2012; Fares et al., 2013).

In Figure 8.1 it appears that in addition to the possible time varying magnetism of

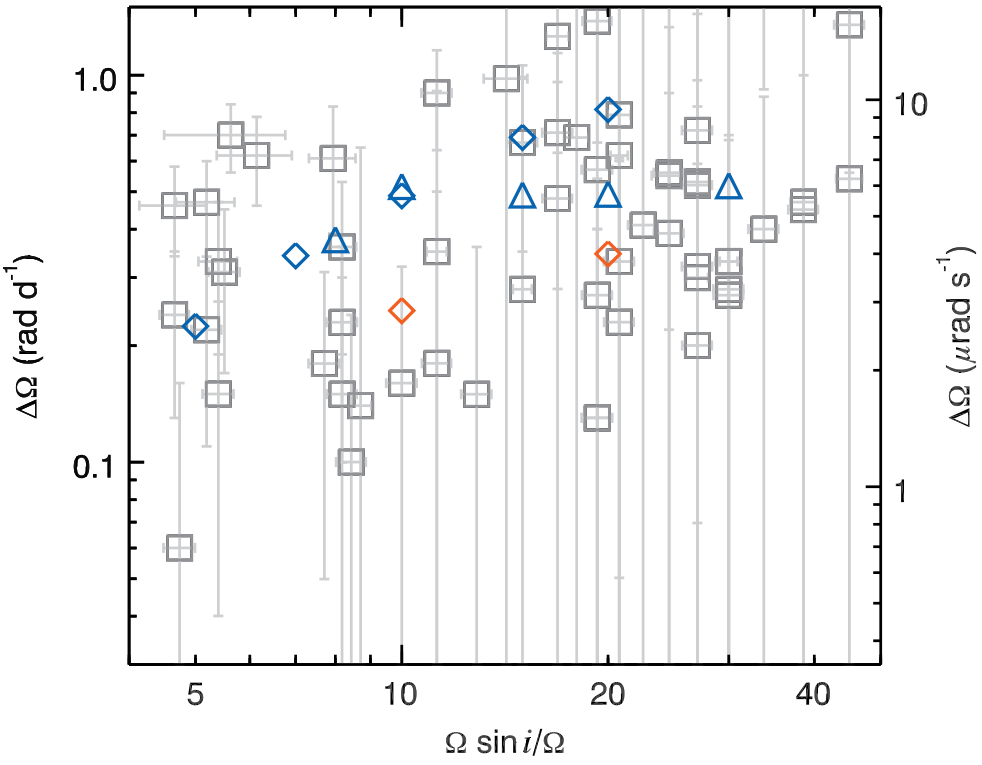

Figure 8.2: Absolute differential rotation contrast ($\Delta\Omega$) seen in simulations and observed on F-type stars. The observational uncertainties of the contrast and rotation rate are shown as gray lines. The values of the $\Delta\Omega$ realized in hydrodynamic simulations are shown in blue symbols (diamonds are 1.2 $M_\odot$ simulations and triangles 1.3 $M_\odot$), MHD simulations presented here in red, and the observed F-type stars are shown as gray squares. Observational data from online sources provided by Ammler-von Eiff & Reiners (2012).

τ Boötis deduced from the ZDI studies, there may also be temporal variation in the differential rotation. Such variations have been observed using ZDI methods on more rapidly rotating stars such as AB Doradus (Donati et al., 2003). It could be that the dynamo action likely occurring within the star is impacting the differential rotation achieved at its surface. Indeed, global simulations of G-type stars rotating faster than the Sun (Brown et al., 2010, 2011b, hereafter B10 & B11), as well as the simulations of F-type stars being reported upon here, show similar behavior. More precisely, the differential rotation achieved in these simulations varies in accord with the waxing and waning strength of the magnetic fields built by dynamo action in their convection zones.

8.1.1 Global Simulations of Convection

The hydrodynamic behavior of F-type stars has recently been explored for a range of masses and rotation rates using the anelastic spherical harmonic (ASH) code as in Augustson et al. (2012), hereafter Chapters 6 & 7. It was found that the both the magnitude and the scaling of the differential rotation with rotation rate achieved in the simulations of Chapters 6 & 7 have a quantitatively good agreement with those observed in the F-type stars. We show in Figure 8.1 a comparison of the latitudinal differential rotation $\Delta\Omega$ observed on τ Boötis to those achieved in our simulations from Chapters 6 & 7 and this work with rotation rates closest to τ Boötis. We here will extend the results of Chapters 6 & 7 by explicitly admitting dynamo processes, so that we might assess the impact of magnetism on the differential rotation achieved in these stars and comment upon what time scales of magnetic variability arise in them. To assess the role that magnetism may have in the internal dynamics of these stars, we have selected two of the hydrodynamic $1.2\,M_\odot$ simulations from Chapters 6 & 7 that have differing rotation rates and have evolved them with magnetic dynamo processes enabled. The latitudinal differential rotation in one of these magnetic cases is shown in Figure 8.1 for comparison to both τ Boötis and our previous models, with the minimum and maximum of its time varying value indicated by the error bar.

Helioseismology has presented detailed observational evidence for the presence of differential rotation in both latitude and radius in the Sun, and asteroseismology is beginning to provide estimates of differential rotation in other stars (e.g., Thompson et al., 2003; Cunha et al., 2007; Chaplin & Miglio, 2013). The definitive evidence for substantial differential rotation in the Sun and advances in supercomputing technology spurred a major series of numerical experiments using global-scale simulations. These simulations aimed to establish which mechanisms might be sustaining the Sun's differential rotation. Utilizing the global-scale ASH code, early work revealed the role of turbulent Reynolds stresses and the meridional circulation in transporting angular momentum to the equator to yield rotation

profiles in the bulk of the convection zone largely in accord with helioseismic findings (Miesch et al., 2000; Brun & Toomre, 2002; Miesch et al., 2006). Higher resolution simulations have enabled detailed study of the dynamics of the giant cells of convection seen in these simulations (Miesch et al., 2008). Deeper 3-D models that capture both the solar convection zone and much of the radiative interior are feasible and exhibit the nonlinear coupling between the overshooting convection and the gravity wave field in the Sun's interior (Brun et al., 2011).

8.1.2 Stellar Dynamo Modeling

A major focus of the global-scale 3-D simulations has been the solar dynamo and its accompanying 22-year reversal period. Early simulations of the global-scale solar dynamo with the magnetohydrodynamic (MHD) version of the ASH code showed that complex magnetic field structures were built through sustained dynamo action, with irregular polarity reversals, and that the solar differential rotation profile was maintained despite the influence of Maxwell stresses (Brun et al., 2004). The role of a tachocline of shear at the base of the convection zone upon the dynamo action was examined by Browning et al. (2006). Other 3-D MHD simulation codes also capture aspects of the Sun's complex behavior, for instance cyclical magnetic polarity reversals have been found in solar convective dynamo simulations (Ghizaru et al., 2010; Käpylä et al., 2012). There is yet no definitive answer as to what sets the cycle period and its variability nor how it links to surface magnetic activity.

Recent MHD studies of G-type stars that rotate more rapidly than the Sun, reminiscent of the younger Sun, were conducted using ASH (B10; B11). The dynamo action in these simulations generated significant mean fields as large-scale bands of toroidal field, dubbed wreaths, in their convection zones without the need for a tachocline. These wreaths of magnetism were robust features over a range of rotation rates and diffusivities in these Sun-like G-type stars. The dynamo action in these simulations involves a rich set of behavior depending upon rotation rate, variously exhibiting intermittency, persistence, or cyclic

polarity reversals. Most recently, buoyant magnetic structures have been obtained in low dissipation simulations of such a G-type star rotating at $3\,\Omega_\odot$, where they buoyantly rise away from strong wreaths of magnetism built in its convection zone (Nelson et al., 2011, 2013a,b).

The ASH code has also been used to simulate the dynamics of turbulent global-scale hydrodynamic and MHD convection in a range of main-sequence stars, spanning the mass range between the M dwarfs and the more massive A-type stars. At the lower end of the mass range, the global MHD simulations of fully convective M dwarfs have shown that they likely possess little latitudinal differential rotation and strong axisymmetric fields (Browning, 2008), a finding that is commensurate with observations of differentially rotating and magnetically active M dwarfs (Donati & Landstreet, 2009; Reiners, 2012). In studies of core convection in A-type stars, the ASH simulations showed that dynamo action can support magnetic fields in equipartition with the convective kinetic energy, with peak field strengths of about 100 kG (Brun et al., 2005). When this convective core dynamo was threaded with a poloidal fossil field, it can achieve a ten-fold superequipartition dynamo state (Featherstone et al., 2009). Such prior work with global simulations using ASH provides perspectives to the dynamo processes that we now considers in F-type stars.

In turning to our two F-type star dynamo simulations, we provide in §8.2 the MHD equations solved in ASH and the details of the setup of our numerical experiments. The general properties of the convective patterns and mean flows established within the MHD simulations are discussed in §8.4, where they are also compared to their hydrodynamic counterparts described in Chapters 6 & 7. We then examine in §8.5 the magnetic simulation of a $1.2\,M_\odot$ F-type star rotating at ten times the solar rate ($10\,\Omega_\odot$) and its resulting persistent magnetic wreaths. We explore in §8.6 the dynamo mechanisms maintaining these wreaths, and in §7.4 the impact such structures have upon the transport of angular momentum and upon their thermal structure. We then examine in §9.1 the dynamo action with reversing fields achieved in the more rapidly rotating ($20\,\Omega_\odot$) of our two cases. In §9.2 we consider the

magnetic field morphologies achieved during the course of a polarity reversal, in §9.8 analyze the evolving toroidal and poloidal field generation terms and examine the many time scales involved in the cycles. In §9.13 we reflect upon the significance of these F-star dynamo simulations.

8.2 Formulating the Problem

The generation of the global-scale magnetism and the maintenance of the large-scale flows observed in the Sun and other stars involve the continuous transfer of energy and momentum amongst a vast range of spatio-temporal scales. This requires that subtle balances arise between the dynamical components present within stars that both builds and sustains strong, organized magnetic fields and bulk flows. Capturing all the relevant time and spatial scales existing within stars from the global spherical geometry through the true dissipation range within a direct numerical simulation in a single simulation is currently intractable. Yet, studying carefully selected portions of these complex systems can yield insight into the observed behavior of stellar magnetism and rotation.

Therefore, a modeling tool is required for stellar dynamo studies that parameterizes unresolved spatial scales and eliminates processes that occur on time scales much faster than the relevant dynamics, along with taking account of the spherical geometry of the star. The 3-D ASH simulation code is one such approach and it is employed in our study of the two F-type star models here. ASH solves the anelastic MHD equations of motion in a rotating spherical shell using a pseudo-spectral method with spherical harmonic expansions in the horizontal and Chebyshev polynomials in radius. Simulations using ASH capture the entire spherical shell geometry, allowing for global connectivity of magnetic structures and turbulent flows. However, the simulated turbulence is still quite removed from the intensely turbulent conditions likely present in actual stellar convection zones.

Table 8.1
Diagnostic Flow Parameters in the Four Cases

Case	$\Omega_0/\,\Omega_\odot$	$N_r \times N_\theta \times N_\phi$	Ra	Ta	Re	Re$'$	$\mathrm{Re_m}$	$\mathrm{Re'_m}$	Ro	κ_{top}	τ_c	τ_ν
A10	10	$257 \times 512 \times 1024$	4.22×10^5	2.41×10^6	240	52	–	–	0.39	6.35	3.3	159
A10m	10	$257 \times 512 \times 1024$	4.11×10^5	2.41×10^6	141	52	46	17	0.37	6.35	3.2	159
A20	20	$257 \times 512 \times 1024$	1.96×10^6	2.41×10^7	592	79	–	–	0.24	4.00	3.8	252
A20m	20	$257 \times 512 \times 1024$	1.60×10^6	2.42×10^7	236	78	78	26	0.25	4.00	3.4	253

Table 8.1: The depth of the convection zone $\mathrm{d} = \mathrm{r_2} - \mathrm{r_b}$ (where r_b is the radius of the bottom of the convection zone) is the relevant length scale in the following parameters and is 1.3×10^{10} cm. We estimate the following diagnostic parameters at mid-convection zone: the Rayleigh number $\mathrm{Ra} = \Delta\overline{S}\mathrm{gd}^3/\mathrm{c_P}\nu\kappa$; Taylor number $\mathrm{Ta} = 4\Omega_0^2\mathrm{d}^4/\nu^2$; Reynolds number $\mathrm{Re} = \mathrm{v_{rms}d}/\nu$; fluctuating Reynolds number $\mathrm{Re}' = \mathrm{v'_{rms}d}/\nu$; magnetic Reynolds number $\mathrm{Re_m} = \mathrm{Pr_m Re}$; fluctuating Reynolds number $\mathrm{Re}' = \mathrm{Pr_m Re}'$; Rossby number $\mathrm{Ro} = \overline{\xi}/2\Omega_0$, where $\overline{\xi}$ is the rms enstrophy. Thermal diffusion (κ_{top}) values are in units of $10^{13}\mathrm{cm^2 s^{-1}}$. The mid-convection zone local overturning time τ_c and the viscous diffusion time τ_ν across the convection zone are quoted in days.

8.2.1 Anelastic Equations

In the anelastic approximation, the effects of a mean density stratification and Alfvén waves are retained, while high frequency sound waves are filtered out. Thus the Courant-Friedrichs-Lewy condition on the time step will be governed by the subsonic flow velocity and Alfvén waves rather than the sound speed. In ASH, the anelastic MHD equations solved are fully nonlinear in the momentum and magnetic variables (Glatzmaier, 1984; Clune et al., 1999; Brun et al., 2004). However, the density, entropy, pressure, and temperature are linearized about their spherically symmetric and evolving means $\overline{\rho}$, $\overline{S}$, $\overline{P}$, and $\overline{T}$ respectively, which are functions of the radial coordinate only. These linearized thermodynamic variables are denoted ρ, S, P, and T. The equations solved in ASH retain physical units, are in spherical coordinates (r, θ, ϕ), and are evolved in time t. These equations are

$$\text{continuity:} \quad \boldsymbol{\nabla} \cdot \overline{\rho}\mathbf{v} = 0, \tag{8.1}$$

$$\text{solenoidal:} \quad \boldsymbol{\nabla} \cdot \mathbf{B} = 0, \tag{8.2}$$

$$\text{hydrostatic:} \quad \frac{\partial \overline{P}}{\partial r} = -\overline{\rho} g_r + \Lambda, \tag{8.3}$$

$$\begin{aligned}\text{momentum:} \quad \overline{\rho}\frac{\partial \mathbf{v}}{\partial t} &= -\overline{\rho}\mathbf{v} \cdot \boldsymbol{\nabla}\mathbf{v} - \boldsymbol{\nabla} P + \left(\frac{1}{\gamma \overline{P}} + F_{BVZ}\right) P\mathbf{g} \\ &\quad + 2\overline{\rho}\mathbf{v} \times \boldsymbol{\Omega}_0 + \frac{1}{4\pi}\left(\boldsymbol{\nabla} \times \mathbf{B}\right) \times \mathbf{B} + \boldsymbol{\nabla} \cdot \mathcal{D} - \Lambda \hat{\mathbf{r}},\end{aligned} \tag{8.4}$$

$$\text{energy:} \quad \overline{\rho}\overline{T}\frac{\partial S}{\partial t} = -\overline{\rho}\overline{T}\mathbf{v} \cdot \boldsymbol{\nabla}\left(\overline{S} + S\right) - \nabla \cdot \mathbf{q} + \Phi, \tag{8.5}$$

$$\text{induction:} \quad \frac{\partial \mathbf{B}}{\partial t} = \boldsymbol{\nabla} \times \left[\mathbf{v} \times \mathbf{B} - \eta \boldsymbol{\nabla} \times \mathbf{B}\right], \tag{8.6}$$

with the velocity field being $\mathbf{v} = \mathrm{v_r}\hat{\mathbf{r}} + \mathrm{v}_\theta\hat{\boldsymbol{\theta}} + \mathrm{v}_\phi\hat{\boldsymbol{\phi}}$, and the magnetic field being $\mathbf{B} = B_r\hat{\mathbf{r}} + B_\theta\hat{\boldsymbol{\theta}} + B_\phi\hat{\boldsymbol{\phi}}$. $\boldsymbol{\Omega}_0 = \Omega_0\hat{\mathbf{z}}$ is the angular velocity of the rotating frame, $\hat{\mathbf{z}}$ is the direction along the rotation axis, and the gravitational acceleration is $\mathbf{g} = -g(r)\hat{\mathbf{r}}$.

The term $F_{BVZ} = (g\overline{\rho})^{-1} d\overline{S}/dr$ ensures that the motions in regions where the entropy gradient is large are energy conserving (Brown et al., 2012). The $\Lambda(r)$ term in Equation (8.3) is a radial gradient of the mean turbulent pressure that maintains hydrostatic equilibrium as the mean state evolves. The viscous diffusion tensor $\mathcal{D}$ and the diffusive heating Φ are

$$\mathcal{D}_{ij} = 2\overline{\rho}\nu\left[e_{ij} - \frac{1}{3}\boldsymbol{\nabla}\cdot\mathbf{v}\delta_{ij}\right], \tag{8.7}$$

$$\Phi = 2\overline{\rho}\nu\left[e_{ij}e_{ij} - \frac{1}{3}\left(\boldsymbol{\nabla}\cdot\mathbf{v}\right)^2\right] + \frac{4\pi\eta}{c^2}\mathbf{J}^2, \tag{8.8}$$

involving the stress tensor e_{ij}, the effective kinematic viscosity ν, the magnetic resistivity η, and the current density $\mathbf{J} = c/4\pi\boldsymbol{\nabla}\times\mathbf{B}$. The energy flux $\mathbf{q}$ is comprised of a radiation flux (in the diffusion approximation) and a two-term anisotropic turbulent entropy diffusion flux,

$$\mathbf{q} = \kappa_r\overline{\rho}\mathrm{c_P}\boldsymbol{\nabla}\left(\overline{T}+T\right) + \kappa\overline{\rho}\overline{T}\boldsymbol{\nabla}S + \kappa_0\overline{\rho}\overline{T}\frac{\partial\overline{S}}{\partial r}\hat{\mathbf{r}}, \tag{8.9}$$

with κ_r the molecular radiation diffusion coefficient, and c_P the specific heat at constant pressure. The entropy diffusion flux has the effective thermal diffusivity κ acting on the entropy fluctuations with spherical harmonic degree $\ell > 0$ and another κ_0 acting only on the spherically-symmetric ($\ell = 0$) entropy. The form and impact of these diffusive transport coefficients are discussed in §8.2.2. A calorically perfect gas equation of state is used for the mean state, about which the fluctuations are linearized as

$$\overline{P} = (\gamma-1)\mathrm{c_P}\overline{\rho}\overline{T}/\gamma, \tag{8.10}$$

$$\rho/\overline{\rho} = P/\overline{P} - T/\overline{T} = P/\gamma\overline{P} - S/\mathrm{c_P}, \tag{8.11}$$

with γ the adiabatic exponent. The anelastic system of MHD equations requires 12 boundary conditions in order to be well posed. One of the primary goals of this work is to assess the generation of magnetic field and how it impacts the organization of angular momentum and energy in our simulations. Thus we have opted for the following impenetrable, torque-free, and flux transmitting boundary conditions

$$\mathrm{v_r} = \frac{\partial}{\partial r}\left(\frac{\mathrm{v}_\theta}{r}\right) = \frac{\partial}{\partial r}\left(\frac{\mathrm{v}_\phi}{r}\right) = \frac{\partial S}{\partial r} = 0, \quad \text{on } r = r_1 \text{ and } r_2. \tag{8.12}$$

The magnetic boundary conditions are perfectly conducting at the lower radial boundary (r_1) and matching to a potential field at the upper radial boundary (r_2), implying that

$$B_r|_{r_1} = 0 \quad \text{and} \quad \mathbf{B}|_{r_2} = \nabla\Psi \Rightarrow \triangle\Psi = 0, \tag{8.13}$$

with Ψ the magnetic potential. The solution of Laplace's equation defines the three components of $\mathbf{B}$ at the upper boundary. Further details of the implementation and formulation of the ASH code can be found in Clune et al. (1999) and Brun et al. (2004).

8.2.2 Experimental Configuration

The studies here explore two $1.2\,\mathrm{M}_\odot$ stars, one rotating every 2.72 days or $10\,\Omega_\odot$ (*Case A10m*) and the other every 1.36 days or $20\,\Omega_\odot$ (*Case A20m*), as summarized in Table 8.1. These cases were initialized from the evolved hydrodynamic *Case A10* and *Case A20* from Chapters 6 & 7, after introducing a weak 10^{-4} G oblique dipolar field oriented at 45° relative to the rotation axis. The hydrodynamic progenitor cases were originally initialized from a realistic 1-D stellar model evolved using the stellar evolution code MESA (Paxton et al., 2011). The convective dynamics in these simulations slightly modifies the 1-D stellar structure, establishing a mean thermodynamic state as shown in Figure 6.2. The radial boundaries of the original hydrodynamic simulations, and thus in the simulations presented here, are carefully chosen locations within the star. The upper boundary is located below the surface to avoid the very intense convection driven by radiative losses and ionization in the uppermost layers of the actual star. Our models include a realistically stratified stable zone and possess a greater luminosity and a geometrically thinner convection zone than in the solar models with wreaths studied as in B11. Despite being stable against convective instability, a broad spectrum of motions arise in this region due to overshooting motions and waves.

The strongly nonlinear interactions are resolved up to spherical harmonic degree $\ell = 340$ in the simulations here. However, because the convective motions and waves within the actual star exist on scales smaller than our grid resolution, these models should be regarded

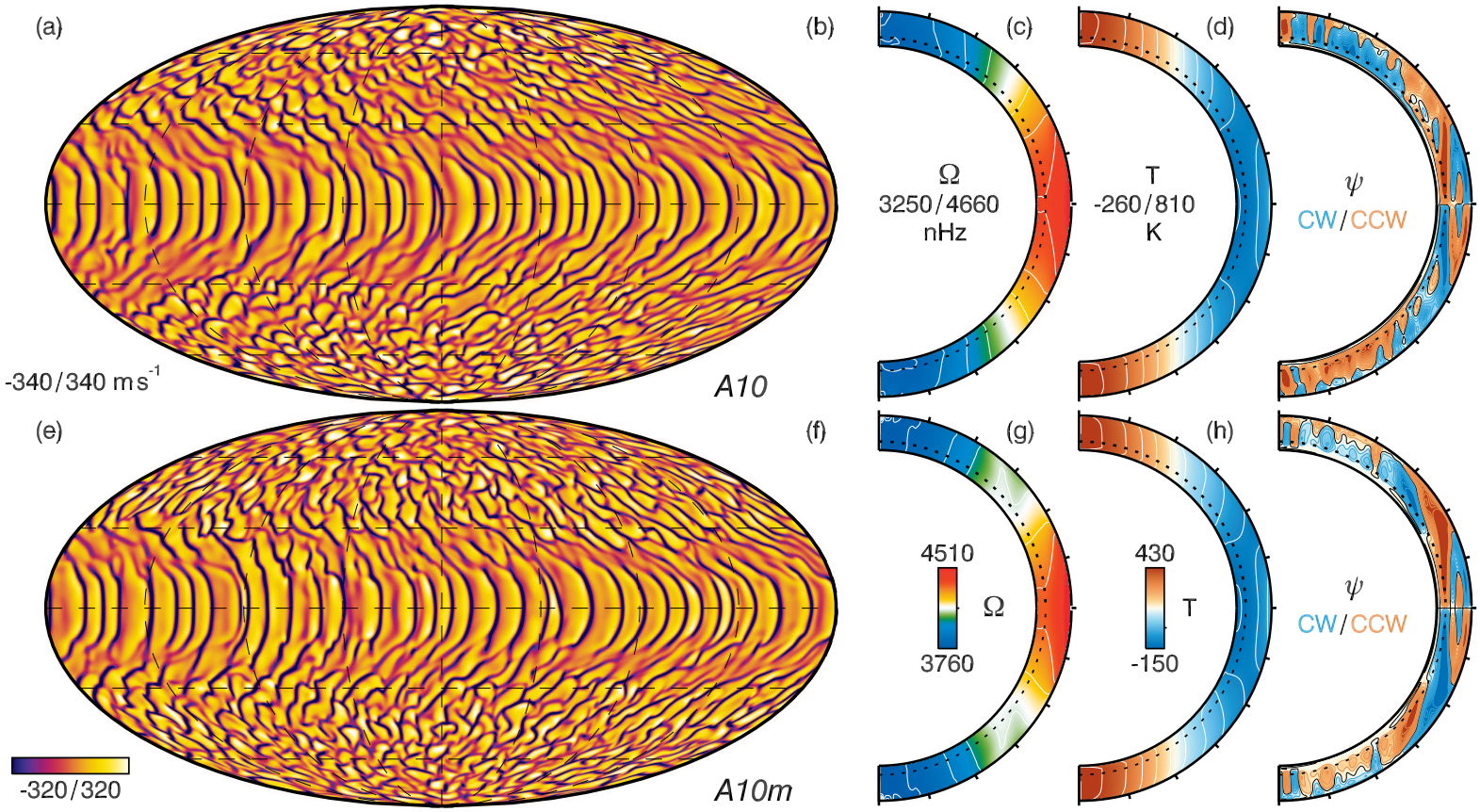

Figure 8.3: Overview of convective patterns, mean flows, and mean temperature fluctuations in the hydrodynamic case *Case A10* (above) and its magnetic counterpart *Case A10m* (below). This serves to illustrate the modified and reduced latitudinal differential rotation in the magnetic case, and accompanying changes in the temperature and meridional circulation. (a, e) Convective patterns in radial velocities (v_r) near the upper boundary in global Mollweide projection, with downflows in dark tones and amplitude ranges indicated. (b, f) Time- and azimuthally-averaged angular velocity (Ω) with radius and latitude, with the fast, prograde equator in reddish and slower poles in bluish tones. (c, g) Azimuthally- and time-averaged temperature fluctuations (T, with the $\ell = 0$ component removed), with the warm poles in red tones and the cool equator in blue. (d, h) Streamfunction of the meridional flow (ψ), with clockwise (CW) flows blue and counter-clockwise (CCW) flows red. The dashed line in the second, third and fourth columns delineates the beginning of the stable zone.

as large-eddy simulations (LES). We parameterize the effects of these sub-grid scale motions as effective viscous and thermal diffusivities and magnetic resistivity (ν, κ, and η respectively). Our parameterization of these motions are meant to mimic the mixing properties of unresolved turbulent eddies. The functional form with radius of these diffusivities are as in Chapters 6 & 7, where they are proportional to $\overline{\rho}^{-\frac{1}{2}}$ and are tapered in the stable zone by a factor of 1000 below the radius (0.83 R). An effective magnetic resistivity is also introduced. The magnetic Prandtl number $\mathrm{Pr_m} = \nu/\eta = 1/3$ is fixed throughout the domain, hence $\eta = \mathrm{Pr}/\mathrm{Pr_m}\,\kappa$. The thermal Prandtl number is $\mathrm{Pr} = \nu/\kappa = 1/4$. These diffusive parameters give rise to radial variations in the Rayleigh, Taylor, and Reynolds numbers. Table 8.1 provides representative values of these parameters, which are sampled at mid-convection zone depth.

8.3 Overview of Primary Findings

The global-scale convective hydrodynamics of F-type stars of differing masses were explored in Chapters 6 & 7, with an emphasis on the sensitivity of the simulations to the bulk rotation rate. We found that the latitudinal differential rotation $\Delta\Omega$ increased both with mass and with rotation rate. The increasing differential rotation induced a decreasing meridional circulation kinetic energy because of weakened Reynolds stresses and an increasing latitudinal temperature gradient due to a strong thermal wind effect. The differential rotation achieved in those models, however, was near the upper bound of the reported observational data over the range of rotation rates examined in Chapters 6 & 7. In addition to general interest in dynamo processes, this encouraged us to explore the effects of magnetism upon the mean properties of F-type stars.

By admitting MHD processes in two of these simulations, we find that both models rapidly build strong toroidal magnetic structures through dynamo action. These prominent toroidal magnetic fields (as in Figures 8.5, 9.2, and 9.3) may be called wreaths due to their longitudinal connectivity and filamentary latitudinal structure. Particularly in *Case A10m*,

the wreaths are persistent in their polarity, with their toroidal field sense maintained, though they vary in time and in magnitude. In both of our magnetic cases, the differential rotation is reduced by at least 50% compared to their hydrodynamic counterparts. This prominent change in rotation profile means that the latitudinal temperature contrasts are also sharply diminished. As is discussed in §8.7, the meridional flow is significantly modified, for it is difficult for such flows to cross the toroidal bands of field due to the Lorentz force back-reaction upon them.

Much as in the studies by B11 of young G-type stars, we find here that lower diffusivities and more rapid rotation leads to field reversals in both the toroidal and poloidal polarities of the wreaths. The toroidal fields of *Case A20m* possess a dipolar character (wreaths of opposite polarity) in the stable zone and have a more complex latitudinal structure within the convection zone. Indeed, in the convection zone the toroidal structures are fairly long-lived octopolar wreaths. These multipolar wreaths slowly slip poleward, are eviscerated by the small scale polar convection, and then are dissipated. The linking between this polar slip, the poloidal field, and the wreaths generated in the convection zone that together lead to field reversals is explored in detail in §§9.2-9.12.

8.4 Convective Patterns and Mean Structures

Our hydrodynamical simulations of F-type stars in Chapters 6 & 7 revealed that the convection involved structures that depend upon the location of a convective cell relative to the tangent cylinder of the convection zone. This tangent cylinder is centered on and extends along the rotation axis of the simulation, and touches the bottom of the convection zone. For the $1.2\,M_\odot$ star simulations, this cylinder extends through the upper boundary at $\pm 32^\circ$ latitude. There is a distinct transition in the nature of the convection inside (at higher latitudes) and outside the tangent cylinder. Outside the tangent cylinder (at low latitudes) the convective structures are columnar rolls that possess an elliptical cross-section in the equatorial plane that is tilted prograde by Coriolis forces and that are aligned with the

rotation axis. However, the convective motions associated with these equatorial columns are largely perpendicular to the rotation axis. Inside the tangent cylinder (at higher latitudes), the convective structures are also columnar and aligned with the rotation axis, but in contrast to their low-latitude counterparts have convective motions mainly aligned with the rotation axis.

This change of convective structure with latitude leads to differing transport properties of the flows, wherein the low latitude structures have Reynolds stresses that act to accelerate the mean zonal flow in a prograde direction, whereas the high latitude structures act to accelerate flows in the retrograde direction. When in a statistically steady state, the mean angular momentum transport properties of the convection maintains both a steady zonal flow and a steady meridional flow through gyroscopic pumping as discussed in Chapters 6 & 7. In turn, it is shown there that this steady zonal flow establishes a largely geostrophic pressure balance and a thermal wind balance that leads to the latitudinal temperature contrast.

In Figure 8.3, the hydrodynamic progenitor *Case A10* from Chapters 6 & 7 and its magnetic counterpart *Case A10m* are compared in terms of their radial velocity convective patterns and the profiles in radius and latitude of the mean angular velocity, mean temperature fluctuations, and meridional circulation streamfunction ψ. The same is shown for *Case A20* and *Case A20m* in Figure 8.4. It is clear from the snapshots of the radial velocities shown in Figures 8.3(a, e) and 8.4(a, e) that the convective patterns of the magnetic cases are only moderately changed relative to the hydrodynamic progenitor cases. As in the non-magnetic simulations, the convection is largely isotropic inside the tangent cylinder (high latitudes), whereas outside of this cylinder the convective structures are prograde-tilted columns roughly aligned with the rotation axis (low latitudes). This is particularly true for *Case A10m*, where only small changes in the convective patterns are evident visible at low latitudes. This is a result of the weakened latitudinal shear, which leads to less disruption of the poleward edges of the low-latitude columnar convective cells.

For *Case A20m*, the convective columns at low-latitudes are of a smaller scale compared

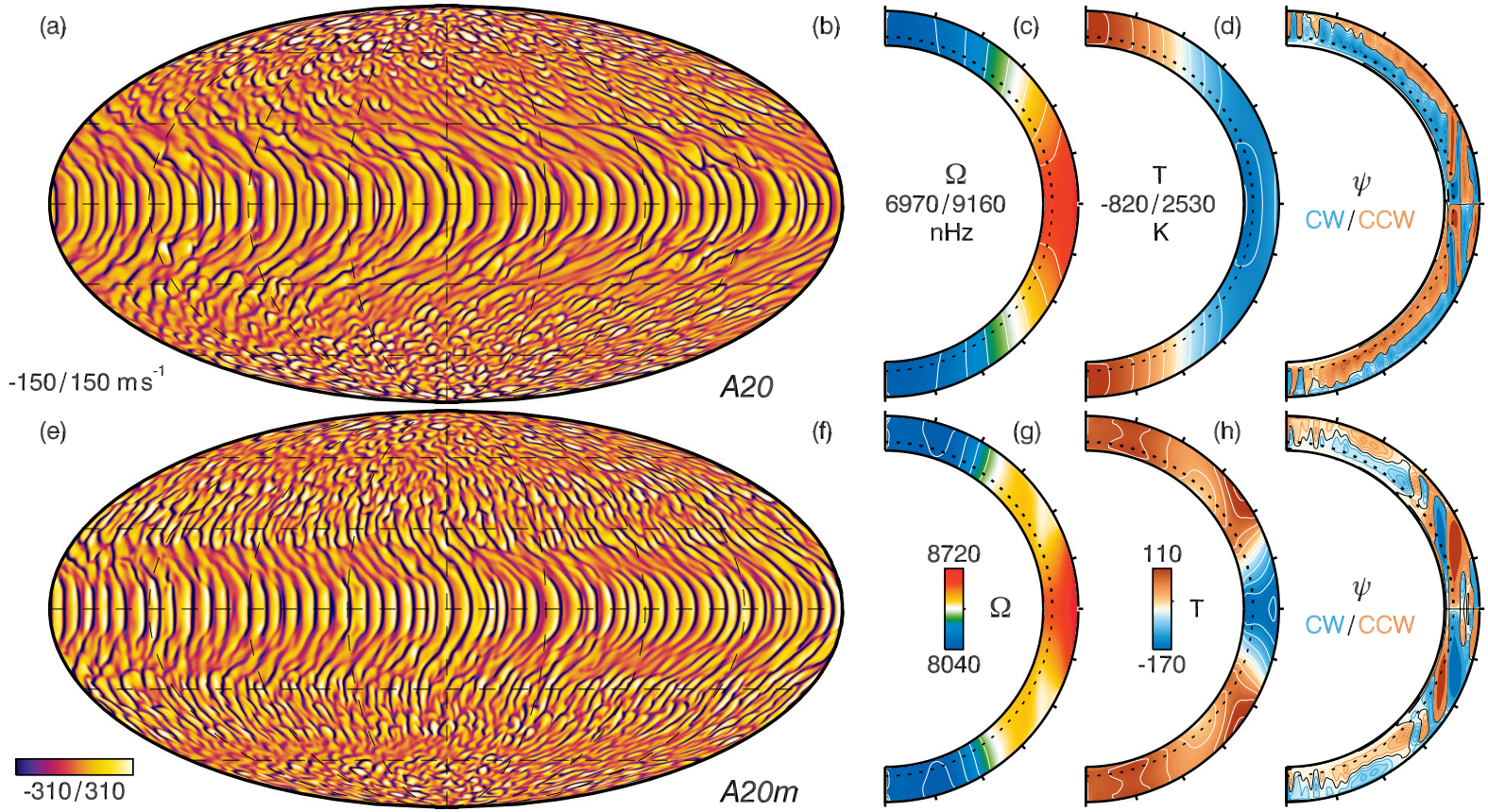

Figure 8.4: As in Figure 8.3, but for *Case A20* and and its magnetic companion *Case A20m*. (a, e) Although the radial velocity patterns are similar, *Case A20m* involves two-fold faster convective flows. (b, f) There are substantial differences in the latitudinal differential rotation ($\Delta\Omega$), here reduced by a factor of 3.2 between the hydrodynamic and magnetic case. (c, g) This reduction in $\Delta\Omega$ leads to a thermal contrast reduced by a factor of 10, and in (d, h) to significantly modified meridional flows.

to *Case A20*. The regions that had latitudinal shear strong enough to suppress convection now have elongated convective cells with radial velocities nearly twice as large in the magnetic case and with much greater connectivity between the equatorial regions and mid-latitudes extending to about $\pm 30^\circ$. Also evident are the bands of weakened convection that coincide with the locations of the strong toroidal wreaths at about $\pm 60^\circ$ and $\pm 20^\circ$ in latitude. These wreaths tend to suppress convection where they are strongest due to the Lorentz force feedback on the rising and descending flows.

The magnetic fields also have a more indirect impact on the mean flows and the thermodynamic state of the simulations. For instance, the angular velocity is decreased in amplitude for *Case A10m* and is both diminished and banded in character for *Case A20m* (Figures 8.3(b, f) and 8.4(b, f)). As shown in Table 8.2, the mean difference in angular velocity between 60° and the equator is reduced by 50% in *Case A10m* and by 60% in *Case A20m* relative to their hydrodynamic counterparts. This leads to a substantial reduction in the strength of the thermal wind, with the latitudinal temperature contrast (Figures 8.3(c, g) and 8.4(c, g)) dropping from 500 K to 300 K (a factor of 1.7) in *Case A10m* and from 1600 K to 250 K (a factor of 6.4) in *Case A20m*.

Moreover, due to the modified Reynolds stresses and an introduction of the Maxwell stresses, the meridional flow also changes in structure. In *Case A10m*, it is changed only slightly with the cells occupying slightly larger extents in latitude (Figure 8.3(d, h)). The hydrodynamic *Case A20* has meridional flows that are multi-celled and possess a strong polar cell that stretches between the tangent cylinder and the pole, while in contrast the magnetic case has a very weak polar cell with only two low latitude cells, one roughly at the tangent cylinder and another of the opposite sense at lower latitudes near the equator (Figure 8.4(d, h)).

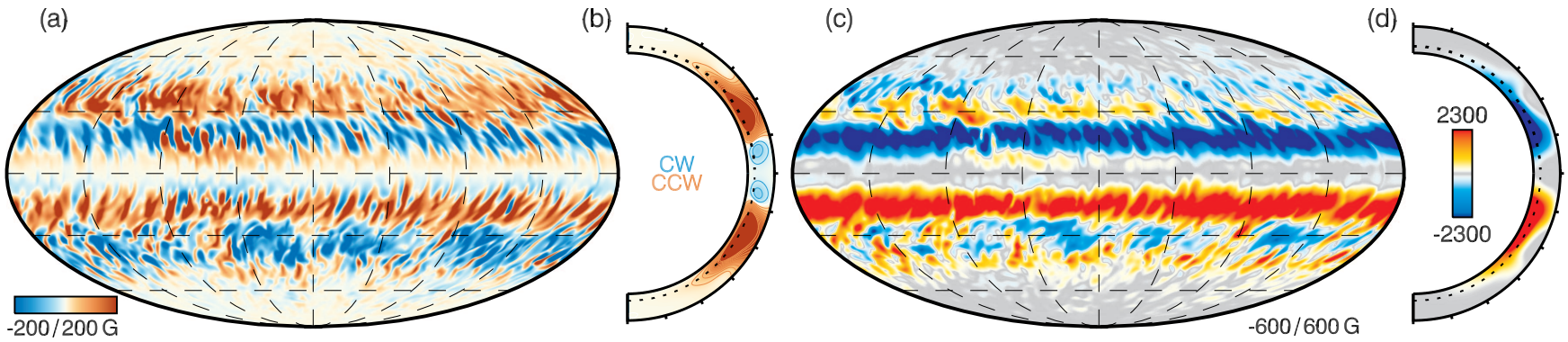

Figure 8.5: Snapshot of the magnetic field in *Case A10m*, coincident with radial velocities in Figure 8.3(e). (a) Radial component of the magnetic field (B_r) shown near the upper boundary, where multiple zonal bands are visible in the convection zone, (b) Mean poloidal field lines shown with radius and latitude, exhibiting the quadrupolar nature of the poloidal field. (c) Toroidal magnetic field (B_ϕ) in the convection zone displaying the primary wreaths occupying lower latitudes and the secondary bands of field at higher latitudes. (d) Time- and azimuthally-averaged $\langle B_\phi \rangle$. The toroidal fields obtain their greatest amplitudes in the stable zone, where the peak strength of $\langle B_\phi \rangle$ is 11 kG. Also evident is the radial dependence of the latitudinal connectivity of B_ϕ, where the wreaths are connected in the stable zone but are disrupted in the convection zone by the presence of weak field of the opposite sense at mid-latitudes, as in (c).

8.5 Dynamics within Case A10m

We begin with a detailed analysis of *Case A10m*, for it has the least temporal variability in its magnetic structures. This allows us to more readily assess the various processes that maintain the mean magnetic fields and the mean flows. After considering here the general properties of the fields, we then turn in §8.6 to the generation of the strong toroidal wreaths, examining the role of the various production terms in the mean induction equation. Then in §8.7 we consider the impact of the magnetic field on the balance of angular momentum transport terms and the thermal wind that accompanies it.

The magnetic fields as shown in Figure 8.5 for *Case A10m* are prominent longitudinal structures, with the B_ϕ field within the stable zone positively oriented in longitude in the southern hemisphere and oppositely directed in the northern hemisphere as in panels (c, d). The radial fields B_r show the same sense, but are more tessellated with fine structure (panels (a, b)). In the convection zone, there are two toroidal magnetic structures at low latitudes. The strongest of these two wreaths resides at about $\pm 20^\circ$ and is of the same sense as the fields in the stable zone. There is also a weaker wreath situated at mid-latitudes in the convection zone that rests on top of the strong, latitudinally-extended wreaths that are seated in the stable zone. The toroidal fields have peak field strengths that range between about 1.2 kG at the upper boundary and 16 kG in the stable zone. The longitudinal component of the vector potential is traced with streamlines in Figure 8.5(b). These streamlines show the orientation of the poloidal field, namely whether it is clockwise (CW) or counter-clockwise (CCW) in the meridional plane. The magnitude of the poloidal field is generally weaker than the toroidal field, with about 600 G peak radial field strength and 2 kG peak meridional field strength.

The magnetic fields built and maintained through dynamo action in *Case A10m* wax and wane in strength by about a factor of two with a period of about 1000 days. Similarly, the latitudinal differential rotation varies by up to 20% on the same time scale (Figure 8.1). The variations arise primarily from the interplay of the Lorentz forces acting on the mean flow

and the resulting reduced magnetic field generation due to the diminished shear. However, while the magnetic fields vary in magnitude, they do not reverse their polarity during the 3000 day evolution of this case. This time span covers 1100 rotation periods, 15 magnetic diffusion times, and many hundreds of convective overturnings. Thus these toroidal wreaths are remarkably persistent magnetic structures.

In *Case A10m*, the strongest bands of toroidal field are established in the relatively quiescent stable zone and extend into the churning convection zone. Given their long-lived nature, these fields have both mean magnetic helicity and cross-helicity, which is achieved by the enshrouding character of the poloidal fields and to the stretching and twisting of field due to differential rotation and meridional flows. Due to the perfectly conducting lower boundary, the magnetic helicity is somewhat suppressed in the stable zone. It is instead largest at the base of the convection zone where the toroidal magnetic field and the toroidal component of the vector potential (representing the poloidal fields) have the greatest overlap. The cross-helicity on the other hand is largest in the stable zone, where the fields and mean flows are able to align given that they are free of the convective pummeling occurring in the convection zone.

8.6 Generating Global-Scale Magnetism

The mean toroidal field shown in Figure 8.5(d) was initially generated and then maintained by similar processes. During the growth phase of the magnetic field, the shear of the differential rotation acts to fold and wind the initial poloidal field into toroidal structures. During this kinematic phase, the mean shear and meridional flows are largely unaffected and can be considered stationary relative to the time scales of the growing field. However, once the magnetic fields are strong enough they begin to quench the convective flows that cross them. The magnetic field strength becomes saturated as the back reaction of the Lorentz forces increases the alignment of the velocity field and the magnetic field, which reduces both its generation and at times leads to its partial destruction.

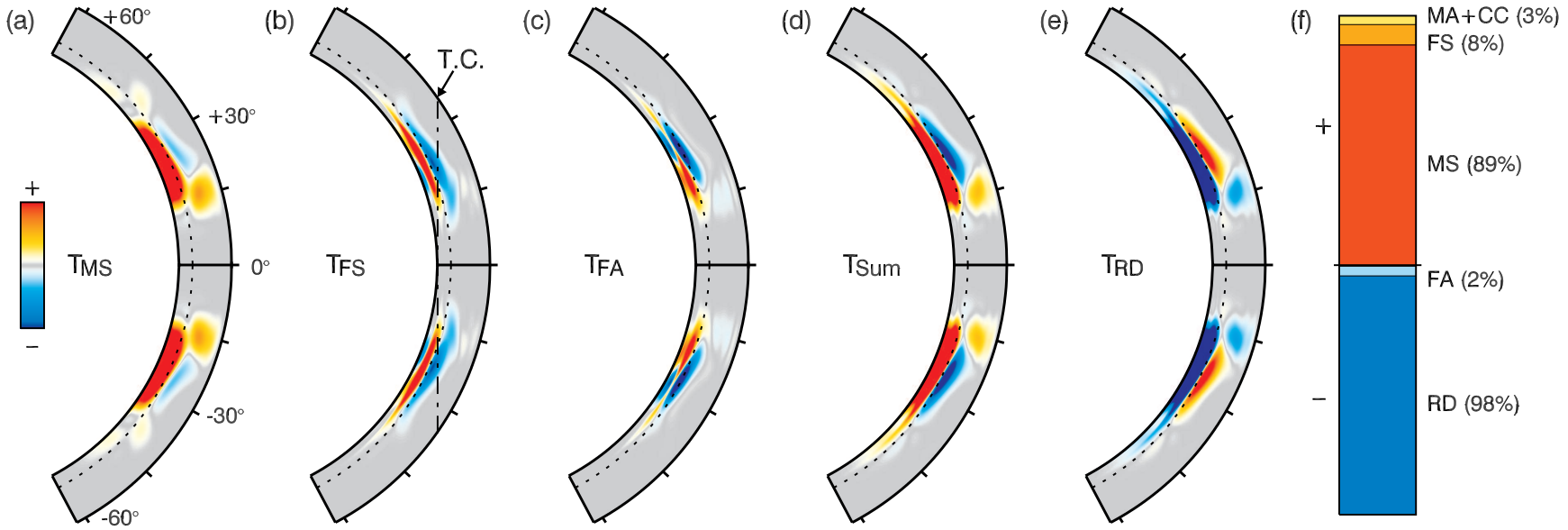

Figure 8.6: Generation of mean toroidal magnetic energy (T_{ME}) in *Case A10m*. The view is from ±60° to emphasize the equatorial regions. Here only the dominant production terms are shown, namely (a) mean shear (T_{MS}), (b) fluctuating shear (T_{FS}), a cylinder tangent to the bottom of the domain (T. C.) is indicated (dashed line), (c) fluctuating advection (T_{FA}), (d) the sum $T_{MS} + T_{FS} + T_{MA} + T_{FA} + T_{CC}$, which largely act in concert to balance (e) the resistive diffusion of field (T_{RD}). All panels have identical scaling. The mean generation terms shown here contribute to the T_{ME} when positive (red), and destroy it if they are negative (blue). (f) The relative contribution of each term, with terms in red adding to the volume- and time-averaged toroidal energy generation and those in blue dissipating energy.

This configuration of fields establishes a new balance between the various mechanisms of angular momentum transport needed to sustain the differential rotation when compared to the hydrodynamic cases. Here magnetic fields both transport angular momentum as well as block formerly open channels of transport. For instance, the strong toroidal field serves to reduce the latitudinal transport of angular momentum by Reynolds stresses, which modifies both the differential rotation and the meridional circulations within the simulation.

8.6.1 Toroidal Generation

The mean magnetic field strengths in *Case A10m* wax and wane as time marches forward, so this balance is not instantaneous. This time evolving dependence of the mean fields is due to many competing processes that both produce and destroy magnetic field through the shearing and advection of field, through compressive motions, and dissipation through resistive processes. These production and dissipation terms are most easily understood through an evolution equation for the mean magnetic energy. We break this equation into its poloidal and toroidal components $\mathrm{P_{ME}}$ and $\mathrm{T_{ME}}$ as

$$\begin{aligned}\frac{\partial \mathrm{T_{ME}}}{\partial t} = \frac{\langle B_\phi \rangle}{8\pi}\Bigg[&\overbrace{\left(\left(\langle \mathbf{B}\rangle \cdot \boldsymbol{\nabla}\right)\langle \mathbf{v}\rangle\big|_\phi\right)}^{\mathrm{T_{MS}}} + \overbrace{\left\langle \left(\mathbf{B}' \cdot \boldsymbol{\nabla}\right)\mathbf{v}'\right\rangle\Big|_\phi}^{\mathrm{T_{FS}}} \\ &- \overbrace{\left(\left(\langle \mathbf{v}\rangle \cdot \boldsymbol{\nabla}\right)\langle \mathbf{B}\rangle\big|_\phi\right)}^{\mathrm{T_{MA}}} - \overbrace{\left\langle \left(\mathbf{v}' \cdot \boldsymbol{\nabla}\right)\mathbf{B}'\right\rangle\Big|_\phi}^{\mathrm{T_{FA}}} \\ &+ \overbrace{\langle B_\phi \mathrm{v_r}\rangle \frac{\partial \ln \overline{\rho}}{\partial r}}^{\mathrm{T_{CC}}} - \overbrace{\boldsymbol{\nabla} \times \left(\eta \boldsymbol{\nabla} \times \langle \mathbf{B}\rangle\right)\big|_\phi}^{\mathrm{T_{RD}}}\Bigg], \end{aligned} \tag{8.14}$$

$$\begin{aligned}\frac{\partial \mathrm{P_{ME}}}{\partial t} = \frac{\langle \mathbf{B}_P \rangle}{8\pi} \cdot \Bigg[&\overbrace{\left(\langle \mathbf{B}\rangle \cdot \boldsymbol{\nabla}\right)\langle \mathbf{v}\rangle}^{\mathrm{P_{MS}}} + \overbrace{\left\langle \left(\mathbf{B}' \cdot \boldsymbol{\nabla}\right)\mathbf{v}'\right\rangle}^{\mathrm{P_{FS}}} - \overbrace{\left(\langle \mathbf{v}\rangle \cdot \boldsymbol{\nabla}\right)\langle \mathbf{B}\rangle}^{\mathrm{P_{MA}}} \\ &- \overbrace{\left\langle \left(\mathbf{v}' \cdot \boldsymbol{\nabla}\right)\mathbf{B}'\right\rangle}^{\mathrm{P_{FA}}} + \overbrace{\langle \mathbf{B}_P \mathrm{v_r}\rangle \frac{\partial \ln \overline{\rho}}{\partial r}}^{\mathrm{P_{CC}}} - \overbrace{\boldsymbol{\nabla} \times \left(\eta \boldsymbol{\nabla} \times \langle \mathbf{B}\rangle\right)}^{\mathrm{P_{RD}}}\Bigg], \end{aligned} \tag{8.15}$$

with the $\langle\rangle$ denoting an average in longitude, $\mathbf{v}' = \mathbf{v} - \langle \mathbf{v}\rangle$ the fluctuating velocity, $\mathbf{B}' = \mathbf{B} - \langle \mathbf{B}\rangle$ the fluctuating magnetic field, and $\langle \mathbf{v}\rangle$ and $\langle \mathbf{B}\rangle$ the axisymmetric velocity and

magnetic field respectively. A detailed derivation of the mean field production terms in spherical coordinates is provided in Appendix A of B10. Here T indicates a toroidal magnetic energy generation term and P a poloidal energy generation term. The subscript of these monikers denote production in turn by mean shear (MS), fluctuating shear (FS), mean advection (MA), fluctuating advection (FA), compressional correlations (CC), and resistive diffusion (RD).

Over a long time average, the time variability of the production of T_{ME} is removed, leaving a balance between terms that produce and terms that destroy field. Figure 8.6 presents such a time average of these mean generation terms, involving a 500 day interval or 180 rotations. In this statistically steady state, the maintenance of the toroidal wreaths of magnetic field is largely governed by a balance between the production of field by both the mean shear and the dissipation of field through resistive processes. By comparing Figures 8.6(a) and 8.6(d), it is clear that the mean shear T_{MS} of Equation (8.14) is primarily responsible for maintaining the strength of the wreaths, with the production due to fluctuating fields T_{FS}, T_{MA}, and T_{CC} playing weak but supporting roles.

The relative contributions have been measured by integrating over time and space to give a mean production or destruction of toroidal magnetic energy $\langle T_i \rangle = \int T_i dV$, where i is any of the terms in Equation (8.14). As indicated in Figure 8.6(f), the bulk of the production is accomplished by T_{MS}, being about 89% of the total. The remaining 11% of the mean production is due mostly to the T_{FS} term. In contrast, the averaged T_{RD} and T_{FA} terms act in concert to dissipate magnetic energy, with T_{RD} being the 98% partner.

In keeping with the dominance of the Ω effect (T_{MS} above), the spatial distribution of toroidal magnetic energy generation is greatest at latitudes where the latitudinal gradients in the differential rotation are at their largest. This maximum occurs in a 15° swath just inside the tangent cylinder in the stable zone at about $\pm 25°$ and in a patch centered at $\pm 15°$ in the convection zone. The toroidal sense of the wreaths shown in Figure 8.5 are maintained throughout the simulation by these same mechanisms. Indeed the sign of the gradient of the

latitudinal differential rotation gives rise to the sign of the wreaths, provided the poloidal field does not change its sense during this extended simulations, which it does not.

The fluctuating shear (T_{FS}) plays less of a role because it both creates and destroys field, with the field being built where the tangent cylinder intersects the bottom of the convection zone with regions of destruction above and below it. This can be regarded as the result of small variations in the differential rotation as it migrates northward and southward in latitude as each of the convective cells varies somewhat in its latitudinal extent and in the strength of its resulting Reynolds stresses. These variations can produce field when their gradients are aligned with the fluctuating poloidal field, and destroy it when anti-aligned with it. The local variations in the differential rotation also induce changes in the meridional flow as seen in the fluctuating advection terms (T_{FA}), which can similarly build or destroy field when the gradients of the fluctuating toroidal field are anti-aligned or not with the fluctuating meridional flow. The resistive diffusion (T_{RD}) acts to maintain an energetic balance in the saturated state whereby it effectively counteracts the sum of all the other terms in Equation (8.14).

8.6.2 Poloidal Generation

We next examine the mechanisms generating the poloidal fields and its associated magnetic energy P_{ME} as in Equation 8.15. Figure 8.7 shows the temporal and longitudinal averages of the these generation terms, displaying the terms with the largest average contributions. The averaging window is here also 500 days. The primary balance of poloidal magnetic energy generation in the stable zone is between the mean shear P_{MS} and the mean advection P_{MA} (Figures 8.7(a, b)). In particular, at latitudes inside the tangent cylinder, mean shear produces field, while it destroys it at lower latitudes. In contrast, advection by the mean flow creates poloidal field in a small but diffuse region about where a tangent cylinder intersects the base of the convection zone and it acts to destroy poloidal field inside this cylinder. The physical mechanism behind this balance is that the mean Lorentz force

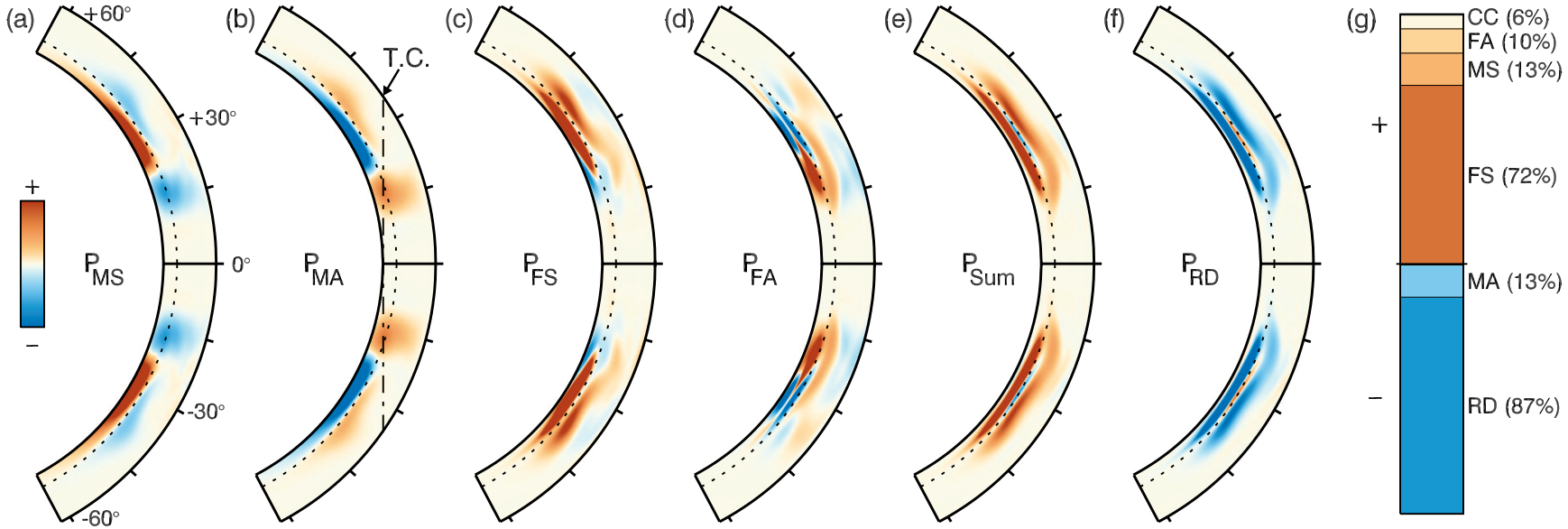

Figure 8.7: Generation of mean poloidal magnetic energy (P_{ME}) in *Case A10m*. The dominant production terms are shown, namely (a) mean shear (P_{MS}), (b) mean advection (P_{MA}), a cylinder tangent to the bottom of the domain (T. C.) is indicated (dashed line), (c) fluctuating shear (P_{FS}), (d) fluctuating advection (P_{FA}) and (e) the sum $P_{MS}+P_{FS}+P_{MA}+P_{FA}+P_{CC}$, with (f) the resistive diffusion of field (P_{RD}). The mean generation terms shown contribute to the P_{ME} when positive (red), and destroy it if negative (blue). (g) The relative contribution of each term, with those in red adding to the volume- and time-averaged poloidal energy generation and those in blue dissipating energy.

is directed such that the mean poloidal field in the northern hemisphere is nearly aligned with the mean meridional flow in the stable zone (anti-aligned in the southern hemisphere). Given this, the sign difference between the P_{MS} and the P_{MA} terms ensures their balance. Further, this alignment of meridional velocity and poloidal field give rise to the particular quadrupolar nature of the poloidal field seen in Figure 8.5(b), with counter-clockwise field at higher latitudes and clockwise field at lower latitudes.

In the convection zone itself, the story is quite different. Here the predominant balance is between fluctuating shear P_{FS}, fluctuating advection P_{FA}, and resistive diffusion P_{RD} (Figures 8.7(c), (d), (f)). These terms are associated with the fluctuating velocities and magnetic fields of the more isotropic convective cells at higher latitudes, with the bulk of the production occurring at the interface between the convection zone and the stable zone. The fluctuating shear produces field inside the tangent cylinder, whereas the fluctuating advection destroys field there. Yet just outside the tangent cylinder their roles are reversed.

Figure 8.7(g) shows that in the spatially integrated sense and unlike in the toroidal energy generation, the fluctuating shear P_{FS} is the dominant contributor to the production of poloidal field, generating on average 72% of the poloidal energy, while the resistive diffusion P_{RD} again is the largest dissipator, destroying 87% of it. However, the balances are more subtle given the distinction between the spatial localities of the energy generation in the convection zone versus the stable zone.

8.7 Maintaining the Mean Flows

The transport of momentum, energy, and magnetic field effected by the convective motions in these simulations establish and maintain the mean flows, mean magnetic fields, and thermodynamic structures. Here we focus on the transport of angular momentum in a statistically steady state, in which a direct link between the meridional circulation and the differential rotation can be found. The balance of angular momentum transport fluxes gives rise to the statistical time invariance of the angular velocity, with those fluxes arising

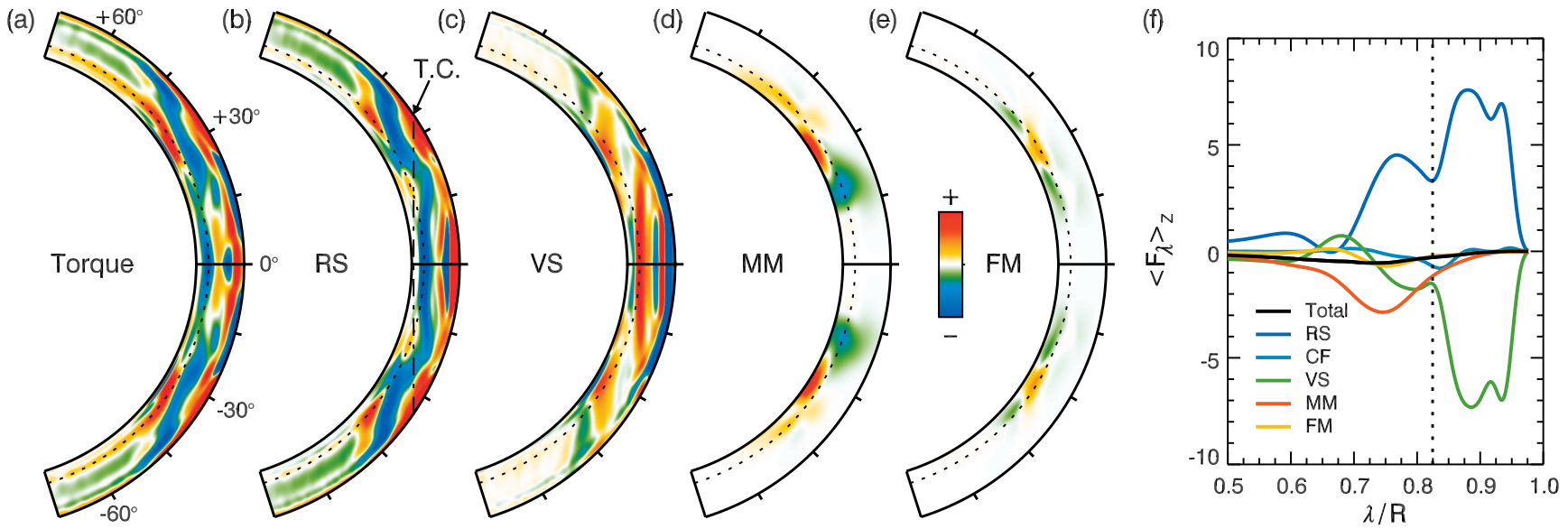

Figure 8.8: The balance of axial torques in *Case A10m*. (a) The net axial torque ($\mathcal{T}$), as in Equation (8.16), is in near pointwise agreement with the advection of angular momentum by the meridional flow (not shown). The components of the net axial torque are in turn (b) Reynolds stresses (RS), a cylinder tangent to the bottom of the domain (T. C.) is indicated (dashed line), (c) viscous stresses (VS), (d) mean magnetic stresses (MM), and (e) fluctuating magnetic stresses (FM). (a)-(e) are scaled relative to the net torque with units of $5.4 \times 10^6\,\mathrm{g\,cm^{-1}\,s^{-2}}$. (f) Vertically integrated angular momentum fluxes in the cylindrical radial direction ($\langle F_\lambda \rangle_z$ in units of $10^{37}\,\mathrm{g\,s^{-2}}$) showing near perfect balance, with fluxes due to RS (dark blue), Coriolis forces on the meridional circulation (CF, light blue), VS (green), MM (red), FM (yellow), and the total in black. The dashed line in (f) indicates the radius of the cylinder tangent to the base of the domain.

from the Reynolds, Maxwell, and viscous stresses. In a time-averaged sense, these transport mechanisms act in sum to balance the advection of angular momentum by the meridional circulation, while also maintaining the differential rotation. To elucidate the individual contributions of these fluxes, consider the evolution of the mean specific angular momentum as

$$\frac{\partial \mathcal{L}}{\partial t} + \langle \rho \mathbf{v} \rangle \cdot \boldsymbol{\nabla} \mathcal{L} = -\overbrace{\boldsymbol{\nabla} \cdot \left[F_\lambda \hat{\boldsymbol{\lambda}} + F_z \hat{z} \right]}^{\mathcal{T}}, \tag{8.16}$$

$$F_\lambda = \overline{\rho} \lambda \langle \mathrm{v}'_\lambda \mathrm{v}'_\phi \rangle - \overline{\rho} \nu \lambda^2 \frac{\partial \Omega}{\partial \lambda} - \frac{\lambda}{4\pi} \langle B_\lambda \rangle \langle B_\phi \rangle - \frac{\lambda}{4\pi} \langle B'_\lambda B'_\phi \rangle, \tag{8.17}$$

$$F_z = \underbrace{\overline{\rho} \lambda \langle \mathrm{v}'_z \mathrm{v}'_\phi \rangle}_{\mathrm{RS}} - \underbrace{\overline{\rho} \nu \lambda^2 \frac{\partial \Omega}{\partial z}}_{\mathrm{VS}} - \underbrace{\frac{\lambda}{4\pi} \langle B_z \rangle \langle B_\phi \rangle}_{\mathrm{MM}} - \underbrace{\frac{\lambda}{4\pi} \langle B'_z B'_\phi \rangle}_{\mathrm{FM}}, \tag{8.18}$$

with $\mathcal{L} = \lambda^2 \Omega = \lambda \left(\langle \mathrm{v}_\phi \rangle + \lambda \Omega_0 \right)$, $\lambda = r \sin\theta$ the cylindrical radius, $\mathbf{v}' = \mathbf{v} - \langle \mathbf{v} \rangle$ the fluctuating velocity, $\mathbf{B}' = \mathbf{B} - \langle \mathbf{B} \rangle$ the fluctuating magnetic field, $\hat{\boldsymbol{\lambda}}$ the cylindrical radial unit vector, and $\langle \mathbf{v} \rangle$ and $\langle \mathbf{B} \rangle$ the axisymmetric velocity and magnetic field respectively.

The axial torque $\mathcal{T}$ is the divergence of the angular momentum flux $\mathbf{F} = F_\lambda \hat{\boldsymbol{\lambda}} + F_z \hat{z}$. There are four components to this flux: the Reynolds stresses produced by the turbulent alignment of the fluctuating poloidal and toroidal velocity components which are the first terms in Equations (8.17) and (8.18) (RS), the second term being the viscous stresses associated with the mean zonal velocity VS, and the mean and fluctuating Maxwell stresses (MM and FM) are the third and fourth terms in these equations. These fluxes are integrated in z and are shown in Figure 8.8(f). The divergence of each of these components of the fluxes, resulting in axial torques, are shown in Figures 8.8(b)-(e).

In a statistically steady state, the advection of mean angular momentum by the meridional circulation, the left hand side of Equation (8.16), then acts against this torque so as to produce no net torque. Therefore, the meridional flow may be considered an extrinsic property of the system that depends upon the angular momentum fluxes and the overall profile of the angular momentum that are in turn established by the convection present in these simulations. This framework for understanding the linking of the angular momentum,

meridional flow, and angular momentum transport processes is called gyroscopic pumping (e.g., McIntyre, 1998; Miesch & Hindman, 2011). The basic idea of gyroscopic pumping is that axial torques induce meridional circulations that act to balance the total torque. Such an approach allows us to focus on the transport properties established by the convection with the influence of the meridional flow removed. However, the assumption of statistical steadiness is not required for much of this understanding to apply. Indeed, one need only retain the explicit time dependence of the angular momentum in Equation (8.16) to have greater generality, which can be of importance when considering the time variability of the mean magnetic fields due to cyclic activity for instance.

8.7.1 Feedback of Magnetism on Mean Flows

In Figure 8.8(a), the axial torque $\mathcal{T}$ gives an indication as to where the zonal flow is being sustained in prograde and retrograde directions and by which transport mechanism. There are two regions to consider in detail, one is the convection zone and the other is the stable zone below it. We first examine the convection zone, where, by comparing Figures 8.8(a) and 8.8(b), it is clear that the Reynolds stresses dominate the torque inside of the tangent cylinder and act to accelerate the zonal flow in a retrograde direction (negative). Outside the tangent cylinder, the Reynolds stresses and viscous stresses act to nearly oppose each other. The Reynolds stresses of the low latitude columnar convective structures are yet somewhat larger, leading to prograde zonal flow in the bulk of the interior. This balance in the convection zone is most evident in Figure 8.8(f), where the dark blue and green lines mirror each other to the right of the dashed line that indicates the base of the convection zone.

The mean Maxwell stresses (MM) displayed in Figure 8.8(d) contributes to the retrograde torque on the low-latitude, equatorward edge of the wreaths (as in Figure 8.5(c)) and to the positive torque at latitudes above 35° in the lower convection zone where the magnetic field strength is greater. While the Reynolds and viscous stresses align very closely

Table 8.2
Global Properties of the Evolved Convection

Case	$KE/10^6$	$KE_{DR}/10^6$	$KE_C/10^6$	$KE_{MC}/10^3$	$ME/10^5$	$TME/10^5$	$FME/10^5$	$PME/10^5$	$\Delta\Omega_{60}/\Omega_0$	ΔT_{60}
A10	29.4	28.4 (97%)	1.01 (3.4%)	3.68 (0.013%)	–	–	–	–	0.211	-501
A10m	8.84	7.87 (89%)	0.97 (11.%)	3.06 (0.035%)	3.05 (3.4%)	2.46 (80%)	0.49 (17%)	0.10 (3.1%)	0.107	-285
A20	80.1	78.8 (98%)	1.33 (1.7%)	1.95 (0.002%)	–	–	–	–	0.177	-1635
A20m	6.43	5.60 (86%)	0.83 (14.%)	1.82 (0.028%)	5.41 (9.4%)	4.44 (82%)	0.71 (14%)	0.25 (4.4%)	0.075	-255

Table 8.2: Total kinetic energy density (KE) and those of differential rotation (KE_{DR}), meridional circulation (KE_{MC}), and convective (KE_C). Total magnetic energy density (ME) and of toroidal (TME), fluctuating (FME), and poloidal (PME). Both energies are averaged in time and volume and are shown in units of erg cm^{-3}, and component percentages in parentheses, with the exception of ME which is shown relative to KE. The relative latitudinal differential rotation is $\Delta\Omega_{60}/\Omega_0$, and the latitudinal temperature difference (ΔT_{60}, in K) are both measured between the equator and 60° latitude (averaged over both hemispheres), with the latter providing a more stable measure in contrast to the pole.

along the cylinder tangent to the base of the convection zone, both the mean and fluctuating Maxwell stresses (MM and FM) act together to balance the hydrodynamic stresses (RS and VS) along a cylinder that is tangent to the bottom of the domain in the stable zone. This leads to the tilting of the net retrograde torque away from the rotation axis and to a small inclusion of prograde torque approximately where this latter cylinder meets the base of the convection zone.

In comparing the mean angular velocities in the convection zones of *Case A10* and *Case A10m* (Figures 8.3(b, f)), the tilt of contours in the polar regions have transitioned from the cylindrical and almost lenticular alignment in *Case A10* to a radial alignment in *Case A10m*. This is in keeping with Ferraro's theorem, which states that the isorotational contours become aligned with the poloidal field as can be seen in Equation 8.14. Given the radial field present at high latitudes in *Case A10m* (Figure 8.5) and that there is very little net production of azimuthal magnetic field (Figure 8.6), a situation arises that promotes the conical alignment of the isorotational contours.

In the stable zone, the axial torque is confined to a roughly 45° band in latitude where the toroidal magnetic fields reach their greatest strength. In this region, that is predominantly inside the tangent cylinder, the Maxwell stresses and diffusion are the largest sources of the torque $\mathcal{T}$. The mean Maxwell stresses decelerate the lowest latitudes and act to accelerate higher latitudes. This torque is due to the Lorentz force feedback of the wreaths on the differential rotation, where they are acting to minimize the latitudinal gradients of the angular velocity in the stable zone. Yet, the magnitude of the latitudinal shear of the differential rotation and the higher density in the stable zone lead to a balance between the diffusion and the magnetic stresses, and thus to a stable net torque and steady induced meridional flow.

The result of these torques, beyond maintaining the rotation profile Ω, is to also sustain the meridional flow through the mechanism of gyroscopic pumping. With the addition of magnetism in these F-type star models, a new cell of meridional flow is built and maintained

through the interaction of the magnetic fields and the relatively unchanged convective flow patterns. This cell stretches from about $\pm 30^\circ$ to $\pm 55^\circ$ and occupying much of the convection zone (Figures 8.3(d, h)). The primary action of this cell is to short circuit the transport of angular momentum by the meridional flow between higher latitudes and the equator, isolating it somewhat from the poles. Instead high angular momentum fluid from the poles is now most efficiently advected to this mid-latitude cell along the base of the convection zone. So, not only do Lorentz forces keep angular momentum from being easily advected across the strong toroidal wreaths by deflecting the meridional flow, but they also set up a meridional circulation that further weakens this transport.

The magnetic disruption of the formerly efficient equatorward angular momentum transport means that more angular momentum is trapped and recirculated in the polar regions. It is a situation markedly different from the hydrodynamic solutions, where momentum slips more easily equatorward to enhance the differential rotation. This suggests that the latitudinal differential rotation can be significantly reduced in the magnetic *Case A10m*, as is indeed evident in the sharply reduced differential rotation kinetic energy and latitudinal differential rotation $\Delta\Omega_{60}$ in Table 8.2.

8.7.2 Thermal Wind Balances

The convective structures in these simulations are largely axially aligned due to the influence of the bulk rotation, which leads to both the enthalpy and angular momentum fluxes also being aligned on cylinders. Baroclinicity arises from the misalignment of pressure and density surfaces and becomes increasingly important in regions that are stratified, such as the domains in the simulations here where we capture roughly four density scale heights. It is these tendencies that lead to a linking of the mean flows and the mean thermodynamic state through the time-averaged properties of the turbulent transport of energy and momentum. This linking becomes more explicit when considering the time- and azimuthally-averaged zonal vorticity equation, which is the longitudinal component of the curl of Equation (8.4)

divided by background density $\overline{\rho}$. Here, we show only the dominant balance in the zonal vorticity equation, omitting the small amplitude Reynolds, magnetic, and viscous zonal torques that are covered in greater depth in Chapters 6 & 7. This leads to the approximate thermal wind equation

$$\lambda \frac{\partial \Omega^2}{\partial z} = \frac{g}{r C_P} \frac{\partial \langle S \rangle}{\partial \theta} + \frac{1}{r \overline{\rho} C_P} \frac{\partial \overline{S}}{\partial r} \frac{\partial \langle P \rangle}{\partial \theta}. \tag{8.19}$$

As is evident from Equation (8.19), the latitudinal thermal perturbations depend quadratically on the magnitude of the differential rotation. Thus, the diminished latitudinal differential rotation in *Case A10m* compared to *Case A10* requires less poleward enthalpy flux and results in a reduced thermal contrast. This strong dependence of the mean temperature perturbations upon the differential rotation is realized when comparing the latitudinal differential rotation $\Delta\Omega_{60}$ and the thermal contrast ΔT_{60} between these two cases in Table 8.2.

Although the magnetic torques do contribute to the thermal wind, it is a very minor effect as they constitute only about 10^{-3} of the total balance. Indeed as seen in Chapters 6 & 7, the baroclinic terms are by far the largest contributors outside of a small region near the upper boundary, where the Reynolds stresses play the dominant role. The two baroclinic terms contribute in different regions, wherein the entropy gradient is the dominant term in the convection zone, whereas the pressure term largely controls the balance in the stable zone.

Chapter 9

Cyclic Dynamo Action in a Rapidly Rotating F-type Star

Following the detailed analysis of *Case A10m*, this chapter focuses on *Case A20m* as it is found that dynamo action with a high degree of time variation occurs in this $1.2\,\mathrm{M}_\odot$ star rotating more rapidly at $20\,\Omega_\odot$. Indeed, the polarity of the mean field reverses on a timescale of about 1600 days. Between reversals the magnetic energy rises and falls with a fairly regular period, with three magnetic energy cycles required to complete a reversal. The magnetic energy cycles and polarity reversals arise due to a linking of the polar-slip instability in the stable region and dynamo action present in the convection zone.

9.1 Exploring Case A20m

Unlike its more diffusive and more slowly rotating partner, *Case A20m* has not only oscillations in the total magnetic energy, but it also exhibits global scale changes in the polarity of the poloidal and toroidal magnetic fields. Such transitions to some form of cyclical and polarity reversing dynamo action have been realized in explorations of the Sun-like stars at varying rotation rates (B11), though unlike here those simulations did not incorporate a stable zone. Figure 9.1(a) presents the time evolution of the volume averaged energy densities of *Case A20m*, with the time-averaged values given in Table 8.2 for reference. The simulation has been evolved for a total of 14200 days (10450 rotations), with the first 8000 days being the evolution of the hydrodynamic case. We have not shown the kinematic growth and saturation phases of the field evolution, a process that occupies about 1000 days

in the early evolution. Starting at about day 9000, the magnetic field cyclically waxes and wanes in strength while also undergoing occasional polarity reversals. At later times, after about 13000 days, the system enters a more quiescent state, during which a relatively high magnetic energy and weaker differential rotation are maintained. It may be beginning a renewed phase of cycles as was seen in case D5 of B11, but this behavior could not be pursued further at this stage due to the high cost of the simulation.

The energy density of the convection and of the meridional flows show only modest temporal variations, with changes on the order of at most 20%. In contrast, the differential rotation and magnetic energy densities possess major swings, with the strong nonlinear feedback between the differential rotation and the magnetic fields. The energy density of the differential rotation oscillates by about a factor of three between roughly $3 \times 10^6 \, \mathrm{erg \, cm^{-3}}$ and $9 \times 10^6 \, \mathrm{erg \, cm^{-3}}$, which is indicative of up to 70% changes in the magnitude of the differential rotation. The minima and maxima of the differential rotation kinetic energy is about 90° out of phase with the magnetic energies. The magnetic energy densities can change even more substantially, with the poloidal energy dropping by more than an order of magnitude between cycles and the toroidal energy decreasing by up to a factor of six. The fluctuating magnetic energies are somewhat less variable, but still show swings of about a factor of two.

As illustrated in Figure 9.1(b), three global-scale polarity changes in the toroidal and poloidal fields are realized during the simulation, occurring roughly every 1600 days. There are also several failed reversals. Additionally, there is a lag of about 150 days in these reversals between the convection zone and the stable zone. This phase difference is reflected in the relative timing of both the local minima and maxima of the toroidal and poloidal magnetic energy densities. However, further time evolution would be necessary to assess the consistency and periodicity of such cycles and reversals. The interval containing the second reversal and the times t_1 through t_5 indicated in Figure 9.1 will be examined in detail to elucidate the reversal mechanism and the properties of the field generation.

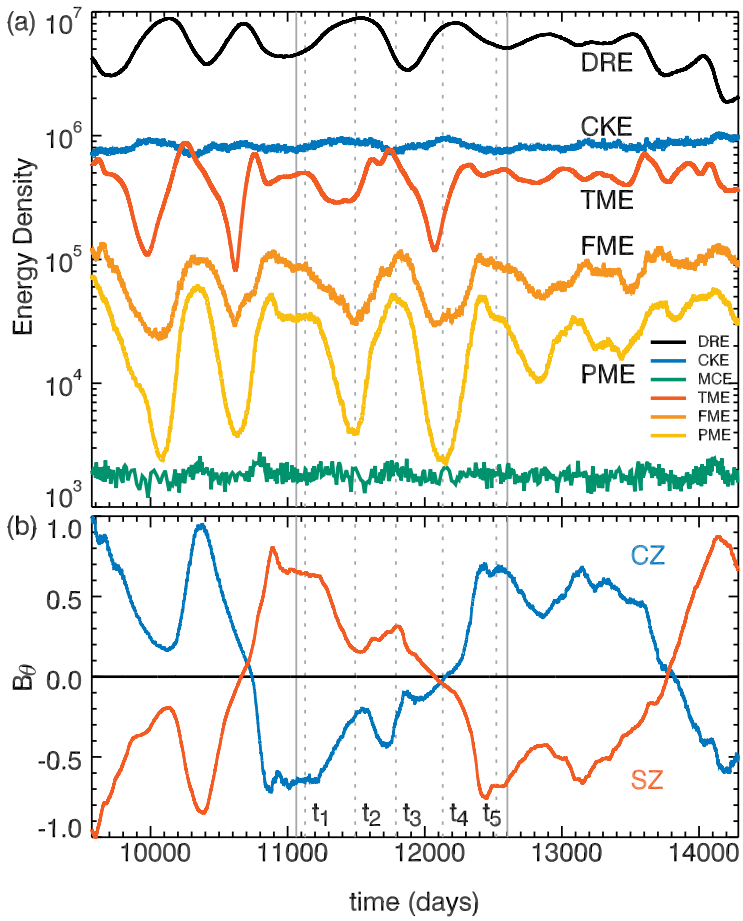

Figure 9.1: Time variation of volume-integrated energy densities for *Case A20m*. (a) Time traces of kinetic and magnetic energies in units of erg cm^{-3} over 4500 days of evolution (3200 rotation periods), showing the differential rotation kinetic energy (DRE, black), convective kinetic energy (CKE, dark blue), meridional circulation kinetic energy (MCE, light blue), toroidal magnetic energy (TME, red), fluctuating magnetic energy (FME, orange), and poloidal magnetic energy (PME, yellow). (b) Time variation of the sign and magnitude of the horizontally-averaged latitudinal magnetic field B_θ, indicating poloidal polarity reversals, with separate averages at mid-convection zone (blue) and in the stable zone (red). The labels t_1 through t_5 indicate the times at which we examine the solution in detail (dashed gray lines), while the solid gray lines indicate the reversal interval studied in detail.

9.2 Morphology of a Reversal

Case A20m clearly shows strong variability in both its magnetic fields and its mean flows. We seek perspective on how a reversal is achieved and identify the mechanisms responsible for destroying and building field around the time of a reversal, which in the example reversal discussed here occurs at t_4. We begin by emphasizing the global connectivity of the magnetic field in this system as shown in Figure 9.2. We then turn to a detailed analysis of this reversal sampled at times t_1 through t_5 in Figure 9.3 that provides a reasonable proxy for what may be occurring more generally in this simulation. In studying a reversal, we first examine the evolution of the mean toroidal field, then turn to successive samplings of full global views of the toroidal fields at two depths, and then consider the evolving properties of the poloidal field. To help pull all of this together, we summarize in §9.12 the elements involved in the reversal, and forward reference these enumerated elements in presenting our results here.

9.3 Wreaths of Magnetism

The dynamo generated magnetic fields of *Case A20m* have global connectivity not only in their mean components, but also possesses long distance links between more localized fields. Figures 9.2(a, b) show the field lines extended outside of the surface of the star using a force-free potential field extrapolation (Schatten et al., 1969). This serves to accentuate the global-scale linkage of the fields built by dynamo action within this simulation of an F-type star. The field is shown at two times, near times t_1 and t_5. The coloring of the lines indicates the polarity of the magnetic field. Given that at the upper radius our boundary condition is a potential field, this extrapolated field is close to the exterior field that implicitly links the magnetic fields in the interior.

At time t_5, there are distinct bridges of field between individual adjacent wreaths, and the magnetic fields share longer distance connections as well. For instance if we focus on the

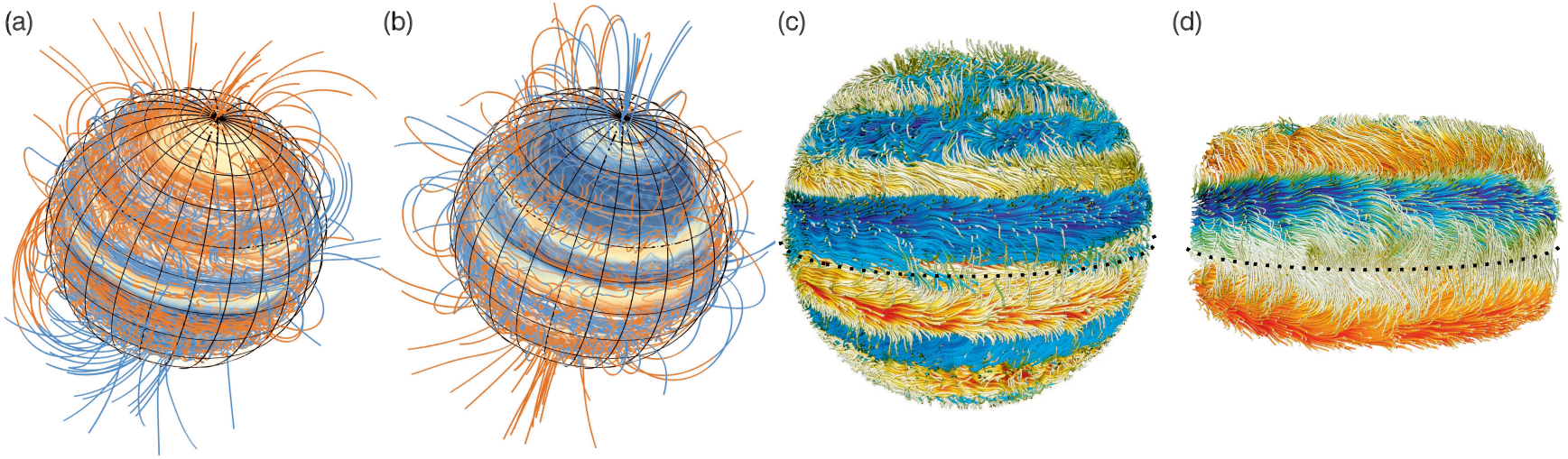

Figure 9.2: Field line tracings of banded magnetic wreaths in *Case A20m* near the top of the convection zone. (a) A snapshot of the 3-D force-free magnetic potential field line extrapolation at time t_1. Lines trace the magnetic fields and color denotes the polarity of the radial field B_r (red, positive; blue, negative). Here the view is orthographic and tilted so the northern pole is visible, showing the global connectivity of the magnetic field. Meridians and circles of latitude are solid black lines. Field lines bridge the wreaths at higher latitudes and connectivity is evident across much of the sphere. (b) The same is shown after a polarity reversal at time t_5. (c) A snapshot of multiple wreaths at t_5 in a volume rendering of the upper convection zone, when magnetic fields reach maximum strength. Lines trace the magnetic fields and color denotes the amplitude and polarity of the longitudinal field B_ϕ (red, positive; blue, negative), showing the global connectivity of the magnetic field and the oppositely-directed wreath at mid-latitudes with the equator marked by a dashed line. (d) A view restricted to $+30^\circ$ and -10° about the equator detailing the cross-equatorial linkages and the magnetic field bridging the wreaths at higher latitudes.

the bottom right of Figure 9.2(b), there are field lines linking the low-latitude wreaths with a polar wreath. This is also the case in the bottom left of Figure 9.2(a), where there is a strong long-distance connection between the low-latitude wreath in the southern hemisphere and the pole. Given the global-scale interconnectedness and spatial complexity of the field built in *Case A20m*, it is no surprise that local changes in the structure of the field and flows can influence the global topology of the entire magnetic field.

To have a clearer impression of the 3-D structure of the magnetism and its connectivity within its convection zone, we show a field-line tracing of the magnetic structures at time t_5 in Figure 9.2(c) where the field lines are colored by the strength and sign of the toroidal field. The multiple bands in latitude of large-scale toroidal field are most prominent, where at this time there is octopolar symmetry in the convection zone. The cross-linking of these toroidal bands of field includes an equatorial bridging of the two wreaths with the greatest strength.

Also visible are the remnant wreaths that have slipped poleward and are being recycled into poloidal field by the vigorous small-scale convection there. Figure 9.2(d) shows the details of the fields linking the two strongest wreaths that straddle the equator. The imprint of the low-latitude convective columns is visible on the blue-toned wreath in the northern hemisphere, where the upflows and downflows alternately draw field upward and punch it down resulting in the corrugation seen there. Weak poloidal field also threads through these columns, field that arises from the stretching of toroidal field into poloidal field by the rotation-axis-aligned helical flows of the columns. Thus the convection gives the wreaths their braided character.

9.4 Mean Toroidal Field Evolution

In Figures 9.3(a, b), the time-latitude diagrams show the evolution of the mean toroidal magnetic field at two depths, one near the top of the simulation in the convection zone and another in the stable zone. Comparing these two panels, it is clear that the the morphologies

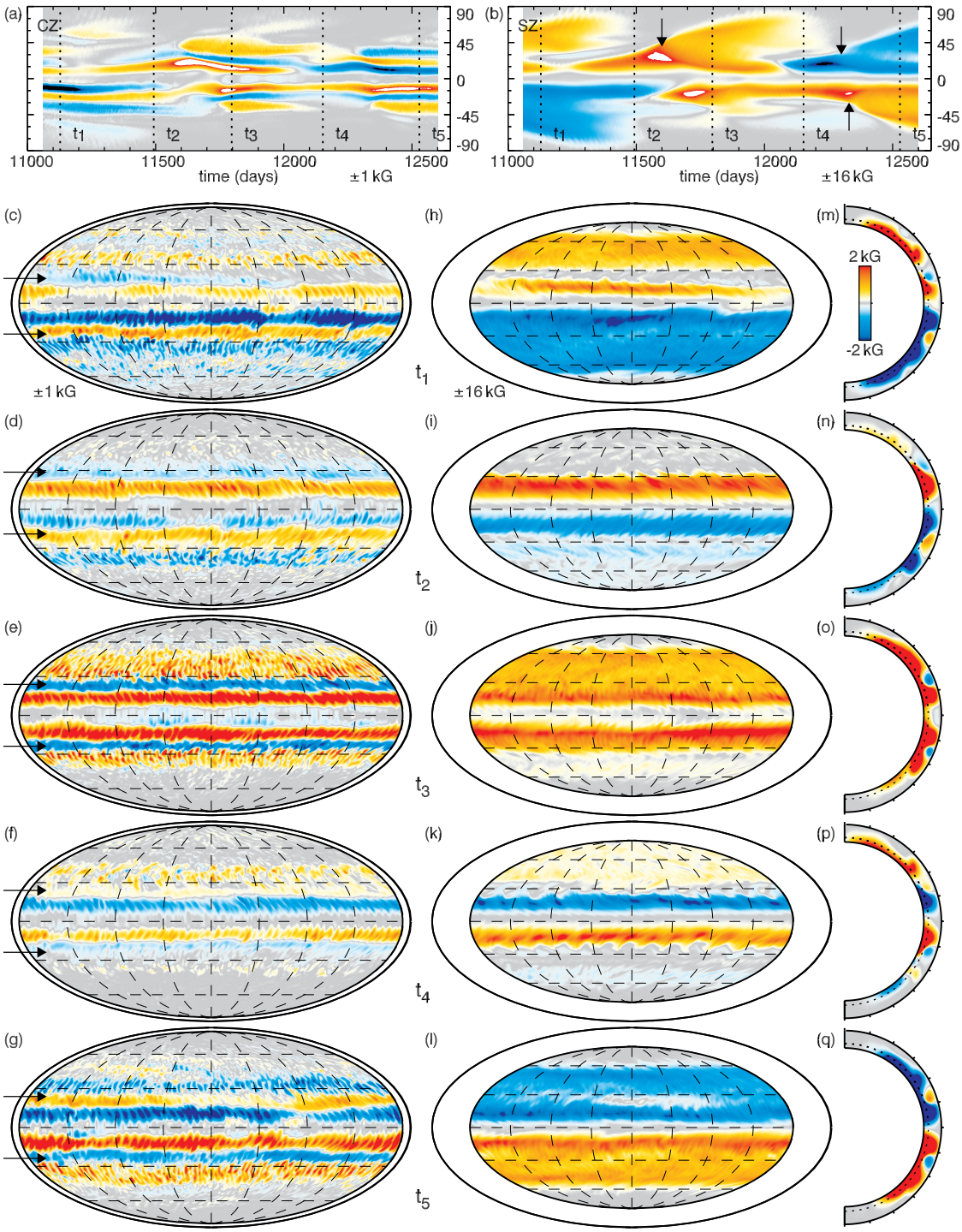

Figure 9.3: Global magnetic field morphology evolving during a cycle in *Case A20m*. Time-latitude diagrams showing the time evolution with latitude of the mean toroidal magnetic field $\langle B_\phi \rangle$ over a cycle at (a) in the convection zone near the upper boundary and (b) in the stable zone near the lower boundary (polar-slip onset indicated by arrows). (c-g) Left column shows successive snapshots of the toroidal magnetic field B_ϕ in the convection zone at times t_1-t_5, with arrows here indicating the "oppositely-directed" wreaths; those wreaths in the convection zone that are directed opposite of the wreaths in the stable zone. (h-l) Middle column shows B_ϕ in the stable zone. (m-q) Right column presents $\langle B_\phi \rangle$ averaged over 10 days (7 rotation periods) centered on times t_1 through t_5 respectively. Uniform color scaling is used with scales indicated in panels (c, h, m).

of the fields are related, but have very different latitudinal dependencies. The multipolar arrangement of the field in the convection zone is evident, where a wreath of the opposite sense (as in Figure 9.2(c) and indicated with arrows in Figure 9.3(c-g)) is nestled between the radially extended lobes of the more latitudinally extended fields seated in the stable zone. These toroidal fields merge and dissipate as time evolves, with some of them propagating poleward and others equatorward.

Within the stable zone in Figure 9.3(b), toroidal field begins as two weak wreaths of opposite sense in each hemisphere, these wreaths gain strength as the cycle proceeds and begin to slowly rise along cylinders due to magnetic buoyancy. The Lorentz forces pulling on the fluid within the wreath become strong enough to break off the poleward facing portion of it [see Element 2, §9.12]. This leaves a new toroidal segment of field that, as we show in §9.6, undergoes a polar slip instability (Spruit & van Ballegooijen, 1982b; Moreno-Insertis et al., 1992). The onset of these polar slip events are indicated by arrows. Indeed, once this poleward branch of field breaks away, it propagates poleward with the meridional Alfvén speed, with the polar branch of the toroidal wreaths slipping from about 30° to the pole in roughly 480 days. The remaining field, with its buoyancy and Lorentz forces reduced, is then pulled equatorward by the meridional circulation and Coriolis forces. This also impacts the fields in the convection zone, as they can also be seen propagating equatorward with a time delayed response.

The hemispheres do not change their polarity at the same time, as the poloidal field connecting the wreaths across the equator is too weak to rapidly affect such changes. In particular, at time t_2 the northern hemisphere reaches a maximum in field strength, while the southern hemisphere is undergoing a polarity reversal. There was a failed reversal at time t_1 in the northern hemisphere, leading to the quadrupolar symmetry maintained in the portion of the cycle between times t_1 and t_4. Likewise, the southern hemisphere fails to reverse at time t_4 leading again to a dipolar symmetry in the toroidal field. When the field does reverse its polarity, the time scale for the reversal at a given latitude is very short on the

order of a few days. The reversal begins at mid-latitudes where the latitudinally extended swaths of toroidal magnetic field seen in Figure 9.3(b) begin to break apart [Element 4], as occurs around day 11350 in the southern hemisphere and at about day 12000 in the northern hemisphere. This reversal then propagates poleward and equatorward, though at different rates for each direction with the equatorial reversal taking about 150 days and the higher-latitude reversal about 300 days.

9.5 Successive Toroidal Field Samplings During a Reversal

The variations in the toroidal field configurations, their waxing and waning field intensities, and the impacts of small-scale convection and MHD instabilities are shown as the cycle proceeds between day 11000 and 12650 at times t_1 through t_5 in the left column of Figures 9.3(c-g) for the convection zone and in the middle column of Figures 9.3(h-l) for the stable zone. For reference, the right column of Figures 9.3(m-q) shows a time- and azimuthal-average of B_ϕ over 10 rotation periods centered at each time t_i, which displays the latitudinal and radial dependence of the wreaths as well as their overall sense. These mean toroidal field snapshots reveal that the fields have their greatest strength in the stable zone, much as in *Case A10m*. During most of the cycle, they possess a large degree of latitudinal connectivity as the deeper field slips toward the poles [Figures 9.3(e, k, q) and Elements 2 & 4]. They also extend radially into the convection zone nearly reaching the upper boundary of the simulation. Weak, oppositely-directed wreaths are generated at about $\pm 25^\circ$ where the latitudinal shear of the differential rotation is large [Elements 3 and 6].

The left column of panels in Figure 9.3 shows Mollweide views of B_ϕ in the upper convection zone. The impact of convection on the wreaths gives rise to the complex patterns of magnetic field seen there. The high-latitude convection destroys much of the signature of the deeper wreaths, leaving small-scale yet still persistently polarized toroidal magnetic fields. Similarly, the downflows of the low-latitude convective columns imprint themselves as alternating and latitudinally inclined dark and light patterns on the stronger equatorially

seated wreaths. All of these panels share the same color scaling, thus providing an overall impression of the increase and decrease of the global field strength over the time samples here. The strongest fields occur at the sample times t_1, t_3, and t_5 (Figures 9.3(c, e, g)), which correspond to local maxima in the total magnetic energy. The bands of magnetic field in the convection zone whose toroidal sense is opposite that of the fields in the stable zone play critical roles during a reversal are indicated with arrows in these panels [Elements 3 and 6].

The middle column of panels shows a global view of the toroidal field at the base of the stable zone, where the strongest fields in the simulation reside. These fields can at times encompass nearly the entire horizontal surface in the stable zone, as a portion of the strong low-latitude wreaths slips poleward leaving a sheet of fairly strong toroidal field in its wake [Element 2]. While the field interior to the edges of this sheet is still quite strong, it is a tenuous enmeshment of field lines held together by magnetic tension. This field connecting the equatorial and polar-slipping wreaths is stretched over the sphere and possesses membrane Alfvén modes arising from the interaction with the fluid motion present in the stable zone, which leads to a natural thinning and strengthening in places (Figures 9.3(h, j, l)). Therefore, there is small-scale, fibril structure contained within this latitudinally extended toroidal field.

At times t_1 and t_5 (Figures 9.3(h, l)), the detachment of the polar sheet of toroidal field from the primary low-latitude wreath can be seen. This process begins at an isolated latitude and longitude where the latitudinal tension force is near a minimum. But is an inherently non-local phenomenon, as the reason the field detaches is due to the strong shear experienced by the polar wreath, which acts through the Ω effect to build stronger field on the poleward side of the sheet. However, this shear also advects field on a time scale faster than the Alfvén travel time across the sheet, leading to a loss of cohesion in the toroidal sheet. Thus, without magnetic tension to hold the sheet together, the polar and equatorial wreaths contract in on themselves. This process leads to a reconnection of the poloidal field

as discussed in the following section [Element 4].

There is also evidence for an intermittent global-scale shear instability occurring at an azimuthal order m of about 14 at times t_2 and t_4, though most prominently at time t_4. This arises from the latitudinal shear satisfying the Rayleigh criterion for instability at certain latitudes, which leads to a rapid mixing of potential vorticity at these and nearby latitudes (Watson, 1981; Gilman & Fox, 1997). Hence, this instability can significantly reduce the latitudinal gradient of the differential rotation, but occurs only intermittently when its instability criteria are met.

9.6 Polar-Slip Instability

In a non-rotating frame, the equations of motion of a toroidal flux tube are coupled in a plane parallel to the tube. Motions out of this plane, which are in latitude, are independent of the other directions and in a quiescent medium depend only upon the tension in the magnetic field (Spruit & van Ballegooijen, 1982b). Thus the latitudinal motion of such a tube satisfies the dispersion relationship $\omega^2 = v_A^2(m^2-1)/2r_0^2$, with v_A the local Alfvén speed and r_0 the radius of the centroid of the tube. This relation implies that only $m = 0$ flux tubes are unstable to the polar-slip instability.

This instability may still occur for such axisymmetric flux tubes in the presence of rotation. Yet rotation does place some constraints on when the instability can occur as it couples longitudinal and latitudinal motions. These coupled motions of the flux tube lead to the dispersion relationship $\omega^2 = -v_A^2/r_0^2 + \Omega_0^2 - \Omega_e^2$, which must be negative for the polar-slip instability to arise (Ferriz-Mas & Schüssler, 1993; Schüssler et al., 1994). In this dispersion relationship Ω_0 is the rotation rate of gas within the flux tube and Ω_e the rotation rate outside the tube. In *Case A20m*, the fields in the stable region satisfy the constraint $v_A^2 > r_0^2(\Omega_0^2 - \Omega_e^2)$ about 75% of the time. However, given the paucity of polar slip events realized in the simulation, there must be other processes that inhibit the instability from occurring more often. Having accounted for rotational influences above, the only other latitudinal force to

contend with in the stable zone is advection due to the meridional circulation.

Overcoming the equatorward meridional return flow in the stable zone is much more difficult than satisfying the above constraint. It requires that the magnetic field strengths be in energy superequipartition with this flow. More precisely, the magnetic tension forces need to be at least as large as the force arsing from advection, which means that the field strength must satisfy the following $B^2 \gtrsim 4\pi\rho_0 v_{MC}^2$. In *Case A20m*, the minimum field strength required to overcome the meridional advection is therefore 19 kG. The peak field strengths achieved in this case on the other hand are 30 kG, so it is possible for these strongest fields to slip toward the pole. Hence it is no coincidence that the fields slip poleward when the low latitude torii of field reach their peak strengths. We find that the mean fields satisfy this constraint only 0.2% of the time, which implies that the slip instability should occur roughly every 500 days. This is very close to the average time between the slip events and roughly the energy cycle time in *Case A20m*. This time should be expected given that it is equivalent to the time for a meridional Alfvén wave to propagate from the latitude of the slip to the pole in this simulation ($\tau \approx \pi r/3v_A \approx 480$ days). In *Case A10m*, the kinetic energy in the meridional circulation is about twice as large as that in *Case A20m*. Following the arguments above, this requires a minimum field strength of 27 kG to have the magnetic tension overcome meridional advection. However, the peak field strength achieved in this more slowly rotating case is only 16 kG, which may explain why the polar-slip is not seen there.

Next we assess the buoyancy of these wreaths using the following thin flux tube instability criterion for axisymmetric fields with motions in the plane parallel to the flux tube

$$\frac{1}{2}\beta\delta - f^2\left(1-s\right) + \frac{2}{\gamma}f - \frac{1}{\gamma}\left(\frac{1}{\gamma} - \frac{1}{2}\right) > 0, \tag{9.1}$$

where β is the ratio of gas pressure to magnetic pressure, δ is a measure of the adiabaticity of the stratification, f is the ratio of the scale height to the local radius of curvature, and γ is the adiabatic exponent as in Spruit & van Ballegooijen (1982a). In *Case A20m* the plasma

β is fairly large, being at minimum about 10^6 near the stable zone and at maximum 10^7 near the upper boundary. The stratification is quite sub-adiabatic in the stable zone with $\delta = \nabla - \nabla_{ad} \approx -0.1$ throughout much of it. Hence in the bulk of the stable zone, the field is very stable to radial motions. Yet as shown above, the field can still slip toward the pole along horizontal surfaces. In the upper portion of stable zone and in the convection zone of *Case A20m* this criterion is easily satisfied where $|\delta| \leq 10^{-6}$, meaning that fields have the possibility of radial buoyancy.

9.7 Evolution of Poloidal Field

The variability of the poloidal field over this reversal interval is presented in Figure 9.4, showing both the field in our computational domain and a potential field extrapolation of it into the atmosphere above. The field begins at time t_1 in a quadrupolar state with clockwise-oriented field wrapped around the deep-seated wreaths in the stable zone. The asymmetric field reversals are also visible, with the southern hemisphere reversing between times t_1 and t_3, followed by the northern hemisphere between t_3 and t_5. As the simulation evolves through the global polarity reversal between t_1 and t_5, this quadrupolar field begins to transition to a dipolar configuration as the toroidal field begins to weaken. It then again migrates toward a quadrupolar symmetry as the dipolarity of the toroidal wreaths is reasserted.

During the detachment process of the poleward propagating wreaths in the stable zone, large portions of the wreath eventually break away from the equatorial wreath. These toroidal fields have enshrouding poloidal fields associated with them, as can be deduced by comparing Figures 9.3(m-q) and the panels of Figure 9.4. Hence, as the sheet of toroidal field is torn in two, the poloidal field reconnects. If the polar branch retains its polarity, the poloidal field associated with the equatorial wreath usually reconnects with the oppositely-signed equatorial poloidal field and vice versa. The failure or success of a reversal hinges on which branch reconnects with the poloidal field of the oppositely-directed wreath present at mid-latitudes in the convection zone. This occurs at times t_2 in the northern hemisphere

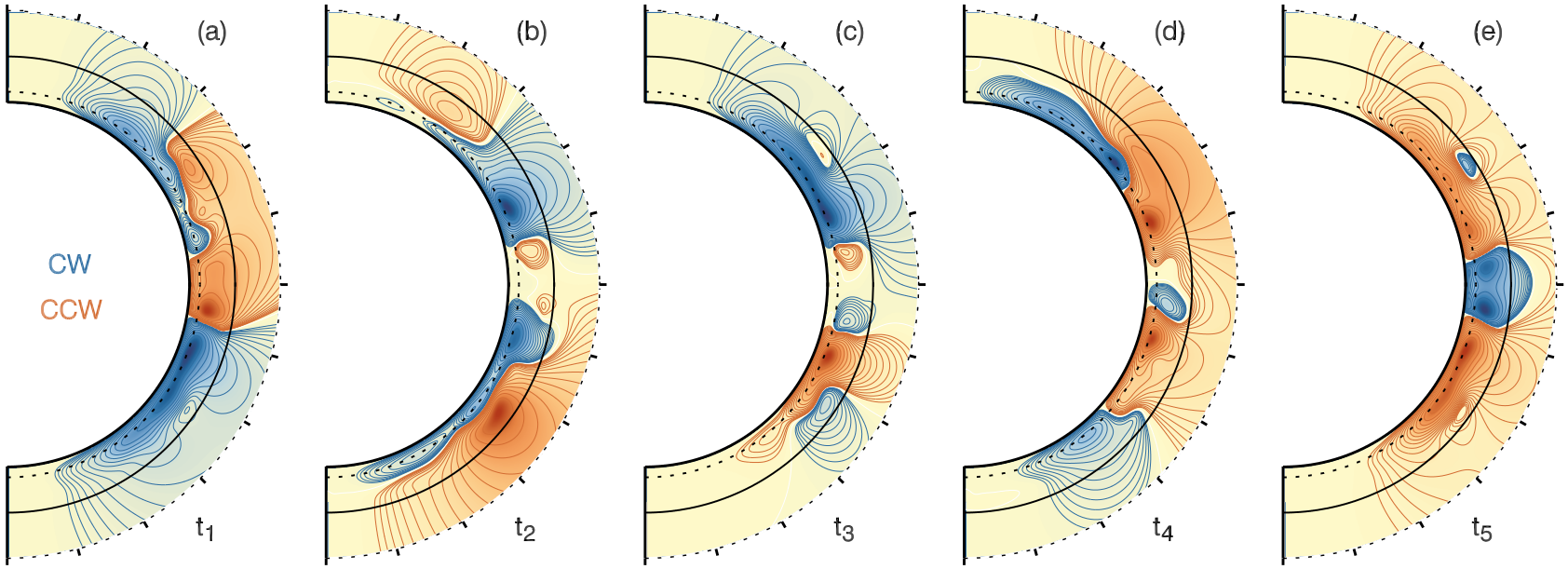

Figure 9.4: Azimuthally-averaged poloidal field at times (a) t_1, (b) t_2, (c) t_3, (d) t_4, and (e) t_5 showing the quadrupolar reversal and a transitory dipolar state. The field lines are extended to 1.2 R using a potential field extrapolation, indicated with a dashed line, whereas the surface of the star is shown with a solid line. The base of the convection is also illustrated with a dashed line. The magnitude of the poloidal field is given by the depth of the color, while its orientation is given by the color sense. Namely, blue regions are oriented clockwise, whereas those in red are counter-clockwise.

(Figure 9.4(b)) and t_4 in the southern hemisphere (Figure 9.4(d)). When this occurs, the T_{MS} that had been acting to build the field now acts in concert with resistive diffusion to rapidly dissipate field and to later build toroidal field of the opposite sense [Elements 4 and 5].

The oppositely-directed wreaths have weak poloidal fields also of the opposite sense associated with them. Yet once the poloidal field of the deeper wreaths weaken, these fields can become dominant as in Figures 9.4(b, d). Hence, despite being usually weaker than the fields associated with the primary toroids of field in the stable zone, these poloidal fields provide the seed field for a reversal [Element 6].

The potential field extrapolation to 1.2 R in Figure 9.4 provides some idea of what the field structure outside of the star might look like if the dynamo action seen here is occurring in real stars. Namely, one may detect transitions between dipolar and quadrupolar dominance in ZDI of more rapidly rotating F-type stars. In addition, as a star transitions between dynamo states, many of the magnetic field lines become open possibly leading to a stellar wind with oscillatory behavior.

9.8 Assessing the Production of Magnetic Energy

The toroidal magnetic energy (T_{ME}) generation in *Case A20m* is shown in Figure 9.5, with the stable zone and the convection zone analyzed individually. Much as in *Case A10m*, the dominant balance is between the production of field due to the mean shear (T_{MS}) and its destruction by resistive dissipation (T_{RD}). The former responsible on average for 90% of the field generation and the latter for 95% of its annihilation, with such a dominant balance achieved in both zones. However, the stable zone contributes about three times greater energy production than the convection zone, reflecting the stronger fields present there.

The oscillation in toroidal magnetic field energy (Figure 9.1(a)) follows naturally from the variation in the toroidal magnetic energy generation terms seen in Figure 9.5. The generation rises and falls depending upon the strength of the mean poloidal field and the

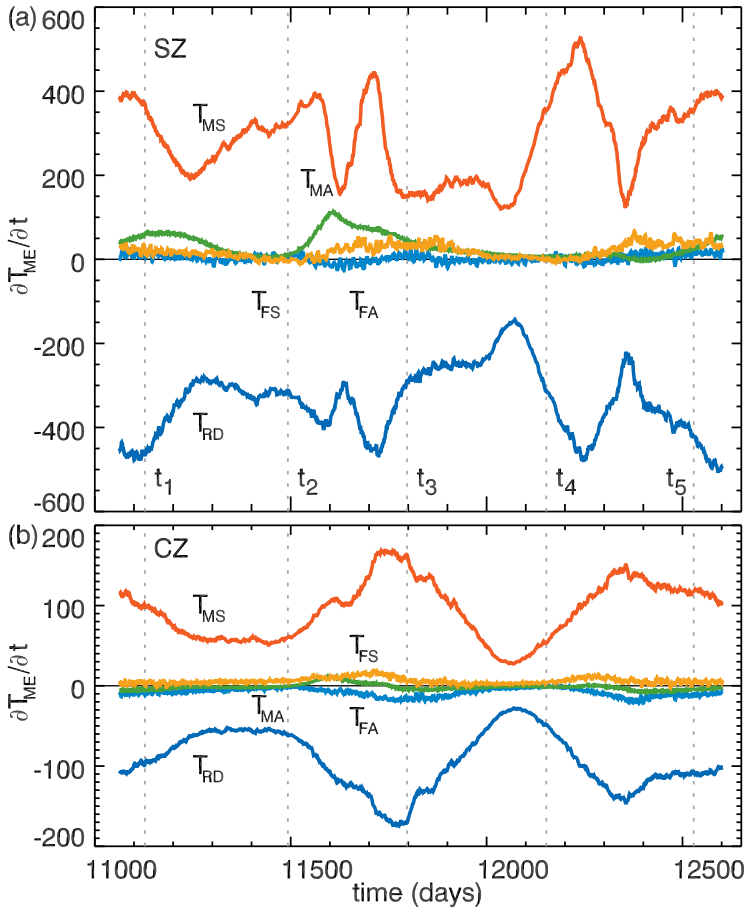

Figure 9.5: Volume-integrated toroidal magnetic energy (T_{ME} in units of erg cm^{-3} s^{-1}) generation terms traced in time for *Case A20m*. (a) T_{ME} generation for the stable zone (SZ), with a dominant balance between production through T_{MS} (red) and dissipation by T_{RD} (dark blue) evident. The remaining terms are T_{MA} (green), T_{FS} (orange), and T_{FA} (light blue). (b) The same quantities in the convection zone (CZ). The average production in the SZ is three times greater than the CZ due to the weaker field present there.

steepness of the gradients of the differential rotation. The production of mean toroidal field in the stable zone appears less periodic than in the convection zone. This is due to the polar slip instability and the resulting detachment events, which occur somewhat stochastically and cause shifts in the magnetic energy cycle period. The timing of peak generation by T_{MS} in the stable zone tends to precede that in the convection zone.

The poloidal magnetic energy (P_{ME}) generation is displayed in Figure 9.6, with the production terms shown separately for the stable and convection zones. The P_{CC} term (omitted) is negligible at all times. The dominant production term in the convection zone (Figure 9.6(a)) is the fluctuating shear (P_{FS}), and is counteracted by resistive dissipation (P_{RD}). The time averaged generation of P_{ME} by P_{FS} accounts for 82% of the total, whereas P_{RD} makes up 88% of its total dissipation. The time lag between this production and the production of toroidal field arises from the advection and rise time of the field moving from the stable zone into the convection zone. Once this toroidal field rises into the convection zone, it is pummeled by the convection and shredded into poloidal field. Hence there is a rapid increase in the turbulent production terms [Element 3], where this deeper-seated toroidal and poloidal field serves as a source of magnetic energy for the more complex field developed in the convection zone.

In contrast, in the stable zone there is a balancing act between P_{MS} and P_{MA}. This arises from the alignment of the poloidal field and meridional flows in the stable zone. The mean shear here accounts for 50% of the production in a time averaged sense. In comparing Figures 9.5(a) and 9.6(a), it is clear that the peak in T_{ME} production by T_{MA} and the peak in P_{ME} production by P_{MS} occur at identical times. It is no coincidence that this also accompanies a minimum in T_{ME} production, as it coincides with the detachment of the poleward side of the toroidal field in the stable zone and thus to the reconnection of the poloidal field.

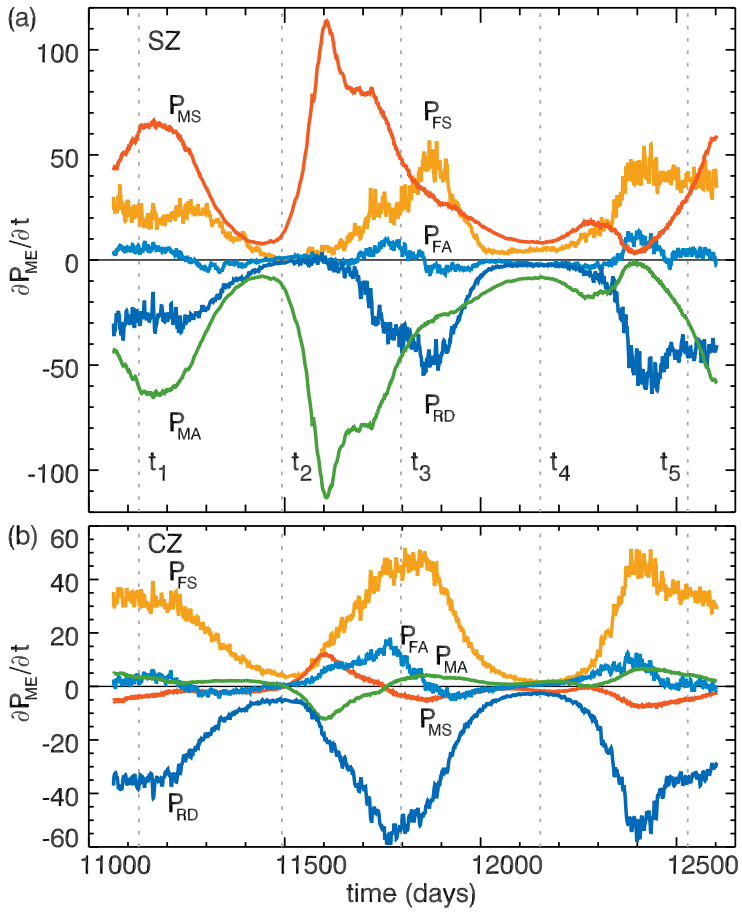

Figure 9.6: Volume-integrated poloidal magnetic energy (P_{ME} in units of erg cm^{-3} s^{-1}) generation terms traced in time for *Case A20m*. (a) P_{ME} generation in the stable zone (SZ), with a phase lag between two production mechanisms: production by P_{MS} (red) and field destruction by P_{MA} (green) precedes the balance between P_{FS} (orange) and P_{RD} (dark blue). P_{FA} (light blue) plays a minor role. (b) The same quantities in the convection zone (CZ). Here the dominant contributors are P_{FS} and P_{RD}.

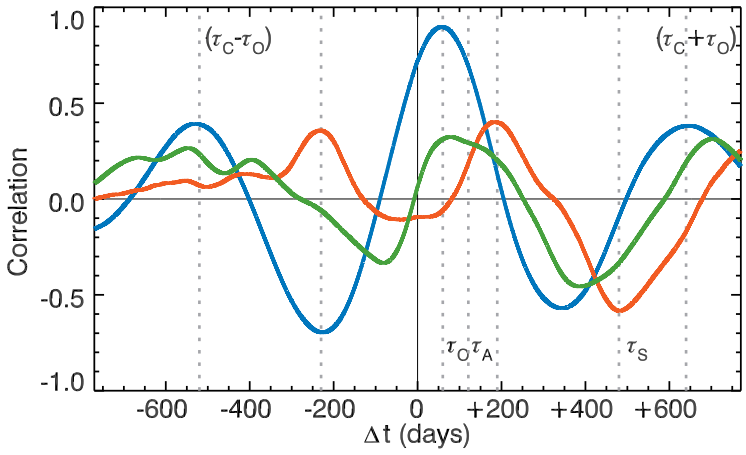

Figure 9.7: Temporal cross-correlations of volume-averaged magnetic energy generation rates for *Case A20m*. Cross-correlation of T_{MS} and P_{FS} in the stable zone (red) and convection zone (blue). Cross-correlation of T_{MS} between the stable and convection zones (green). Relevant time scales are indicated as average magnetic energy cycle time τ_C, convective overturning time over the entire convection zone τ_O, radial Alfvén wave τ_A crossing time across the shell, and the polar-slip time τ_S.

9.9 Dynamo Time Scales

To elucidate the relevant time scales for the dynamics of the global magnetic field, we examine cross-correlations of the magnetic energy generation terms as in Figure 9.7. The underlying magnetic energy cycle in *Case A20m* is somewhat obscured by other signals in Figures 9.5 and 9.6, but is revealed in the cross-correlation of T_{MS} and P_{FS} in the convection zone (blue curve). Here the average cycle period is 580 days (τ_C). There is also a 60 day shift τ_O at no temporal offset. This is likely related to the convective overturning time in the convection zone that can link the deeper wreaths with poloidal field in the convection zone.

The energy cycle period is not the sole time scale governing this system. In particular, the same cross-correlation in the stable zone (red curve) indicates three relevant time scales, with a prominent anti-correlation between T_{MS} and P_{FS} at 480 days (τ_S). This time scale corresponds to the time it takes the poleward branch of the magnetic field to slip from low latitudes to the pole [Element 2]. This is an anti-correlation because T_{MS} is often at a minimum when P_{MS} is growing or near a maximum. This itself may be linked to the time

required for an Alfvén wave to circumnavigate the toroidal sheet of field in the stable zone, which also happens to be about 480 days.

Another important time scale is that which separates the energy cycle period and the polar-slip time scale. This roughly 100 day time scale is a lagged response of the convection zone to the destruction of the polar wreath in the stable zone through dissipation and instabilities. To make this time scale more evident, we have shown the volume-averaged T_{MS} production terms cross-correlated between the convection zone and the stable zone in Figure 9.7 (green curve). There is a peak at the time scale labeled τ_A in this correlation. This is approximately the Alfvén wave crossing time from the lower boundary at the base of the stable zone to the upper boundary of the simulation. These waves travel along these field lines and serve to link the convection zone in regions where the radial field threads through both zones (Figure 9.4).

We conclude that in *Case A20m* it is the underlying dynamics of the poleward slip instability and Alfvénic waves that act together to set the magnetic energy cycle period $\tau_C = \tau_S + \tau_A$. This gives rise to the time scales for reversal Elements 2-4. However, τ_C of course is not the polarity reversal timescale. The transitions between field polarities are accompanied by minima in the magnetic field strength, each of which are separated by an average period of τ_C. We find here that the polarity reversal time scale of 1600 days typically involves three magnetic energy cycles.

9.10 Characterizing the Dynamo

To place the prior analysis in perspective, it is useful to make a connection to the mean-field theory (MFT) of electrodynamics (e.g., Moffatt, 1978; Krause & Raedler, 1980; Brandenburg & Subramanian, 2005). It is fairly simple to understand the mechanisms building the mean toroidal field, where the presence of a poloidal field and differential rotation readily generate it. The origin of the axisymmetric poloidal field is more subtle, with the turbulent convection being primarily responsible for its generation. The meridional circula-

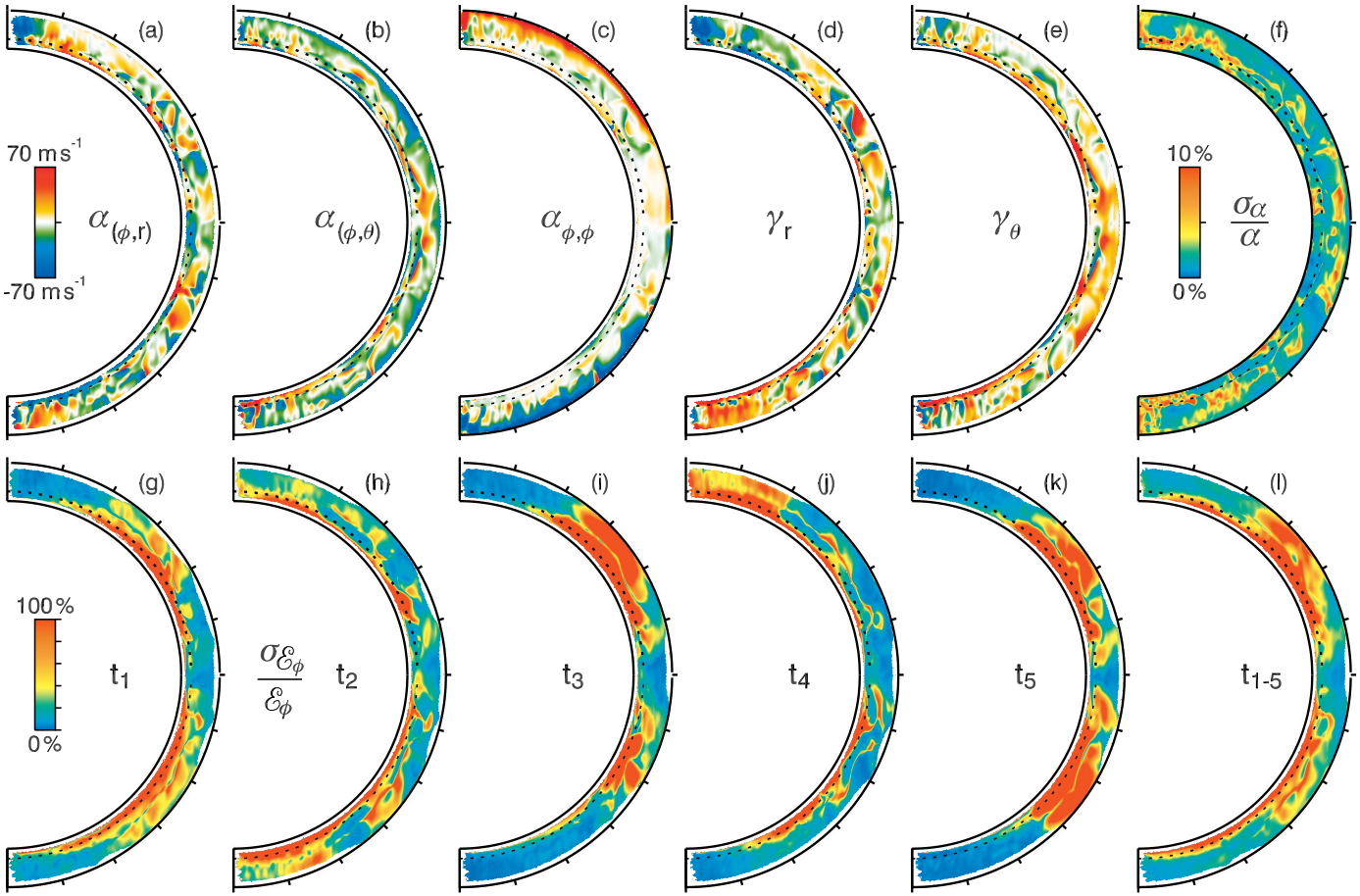

Figure 9.8: Reconstructed components of the mean-field α effect and its accompanying relative uncertainties. (a-e) Components of α that contribute to the turbulent EMF ($\mathcal{E}_\phi$) are shown in the meridional plane. (f) Relative uncertainty of the contracted α tensor, a measure of goodness of fit. (g-k) Relative uncertainty in the reconstructed EMF as measured against the EMF of the simulation in 20 day intervals centered on each of the sample times t_1-t_5, a measure of effectiveness and reproducibility. (l) The same but measured over the entire reversal interval of 1600 days.

tion, turbulent pumping, and diffusion on the other hand bring it into the stable zone. Thus we examine a constant in time but spatially varying α-effect. This provides a quantitative measure of the influence of the turbulent properties of the flow on the turbulent electromotive force (EMF, $\mathcal{E}$), which is defined as $\langle\mathcal{E}\rangle = \langle\mathbf{v}' \times \mathbf{B}'\rangle$.

As just seen in §9.8, $\mathcal{E}$ is largely responsible for the generation of poloidal magnetic field in the convection zone and also at times in the stable zone (Figure 9.6(a),(b)). Therefore we will concentrate on the generation of poloidal field in terms of the azimuthal component of the mean vector potential $\langle A_\phi\rangle$ under the Coulomb gauge, which evolves as

$$\frac{\partial\langle A_\phi\rangle}{\partial t} = \hat{\boldsymbol{\phi}} \cdot (\langle\mathbf{v}\rangle \times \langle\mathbf{B}\rangle + \langle\mathcal{E}\rangle) + \eta\nabla^2\langle A_\phi\rangle. \tag{9.2}$$

We now explore the connection between MFT and the EMF achieved in our simulations by first noting that the first-order expansion of $\mathcal{E}$ around the mean magnetic field is

$$\langle\mathcal{E}\rangle = \alpha\langle\mathbf{B}\rangle + \beta\nabla\langle\mathbf{B}\rangle + \mathcal{O}\left(\partial\langle\mathbf{B}\rangle/\partial t, \nabla^2\langle\mathbf{B}\rangle\right), \tag{9.3}$$

where α is a rank two pseudo-tensor and β is a rank three tensor. We approximate the β tensor by including only its action on the anti-symmetric part of $\nabla\langle\mathbf{B}\rangle$, which is the current $\langle\mathbf{J}\rangle = \boldsymbol{\nabla} \times \langle\mathbf{B}\rangle$, so that

$$\beta_{ijk}\frac{\partial\langle B_j\rangle}{\partial x_k} \approx -\chi_{im}\epsilon_{mkj}\frac{\partial\langle B_j\rangle}{\partial x_k} = -\chi_{im}\left(\boldsymbol{\nabla} \times \langle\mathbf{B}\rangle\right)_m = -\chi\langle\mathbf{J}\rangle \tag{9.4}$$

with the sign of χ chosen to conform to the standard notation mean-field theory, ϵ_{mkj} the Levi-Civita symbol, and with an implied sum over repeated indices. In our analysis α is expanded as $\alpha\langle\mathbf{B}\rangle = \alpha_S\langle\mathbf{B}\rangle + \boldsymbol{\gamma} \times \langle\mathbf{B}\rangle$, with α_S being the symmetric portion of α and $\boldsymbol{\gamma}$ the anti-symmetric portion. The latter is also known as the turbulent pumping velocity. For the diffusion tensor χ, we apply the first order smoothing approximation and take only the lowest order moments, wherein χ becomes purely isotropic as $\chi_{ij} \approx 1/3\tau_0\langle\mathbf{v}' \cdot \mathbf{v}'\rangle\delta_{ij}$ (e.g., Brandenburg & Subramanian, 2005). While χ becomes isotropic under these assumptions, it may still be inhomogeneous through both τ_0 and $\langle\mathbf{v}' \cdot \mathbf{v}'\rangle$. We define τ_0 to be the local

convective overturning time $\tau_0(r) = H_\rho / u_{\mathrm{r,rms}}$, which here ranges between 40 days at the base of the convection zone to about one day near the upper boundary of the simulation.

To reconstruct the α tensor from our data, its individual components are solved for from a temporal sequence of data at each radial and latitudinal grid point using a method similar to the least-squares singular value decomposition (SVD) methodology described in Racine et al. (2011). This local fitting technique assumes that each point may be treated independently, which precludes the capture of temporally and spatially displaced correlations that can influence the dynamo action achieved in our simulations (B11, Nelson et al. (2013a)). Yet it has the advantage that the magnetic fields and electric currents from the simulation constrain the components of α. The higher-order tensor components neglected here can be found using test field methods (e.g., Kraichnan, 1972; Schrinner et al., 2007), or calculated analytically as in (Brandenburg & Subramanian, 2005). The reconstruction is carried out over the entire reversal interval, and then its applicability at a given stage of the reversal is assessed. To this end, Figures 9.8(a-e) show the five components of α that contribute to $\mathcal{E}_\phi$. The magnitude of the components of the α tensor is fairly large in comparison to solar simulations (Racine et al., 2011; Nelson et al., 2013a; Simard et al., 2013), being about five to ten times greater. This is due to the intrinsically faster flows present in the F-type stars, which in turn arises from their higher luminosity and the lower density in their convection zones. The dynamo efficiency of these flows can be estimated by finding the average magnitude of the α-effect relative to the rms value of the fluctuating velocity field. We find that this measure of efficiency is roughly

$$\langle \frac{\alpha}{v_{\mathrm{rms}}} \rangle \sim \frac{3}{2\left(r_2^3 - r_1^3\right)} \iint \mathrm{d}r\mathrm{d}\theta r^2 \sin\theta \sqrt{\frac{\alpha_{\phi,j}\alpha^{\phi,j}}{\langle \mathbf{v}' \cdot \mathbf{v}' \rangle}} \approx 0.3. \tag{9.5}$$

The spatial structure of $\alpha_{\phi,r}$, $\alpha_{\phi,\phi}$, and γ_r visible in Figures 9.8(a, c, d) is roughly asymmetric between the two hemispheres, with the other two components being nearly north-south symmetric. The former attribute arises from the influence of Coriolis forces on the flows, with the cyclonic turbulence present at higher latitudes being an important

contributor to the sign and magnitude of these fields. All of the components shown also have structures that know about the bottom of the convection zone, where there is a change in sign as one moves from the upper boundary to the bottom of the domain. This is particularly evident in $\alpha_{\phi,\phi}$. The divergence and dilution of vortical downflows and the convergence of swirling upflows gives rise to this feature. Not surprisingly there is a latitudinal dependence to these structures, where a distinct transition in flow morphology across the tangent cylinder makes itself known. The amplitude of these components is fairly low in the stable zone except near the poles, which is consistent with the fluctuating velocities being relatively small in this region. The impact of the β-effect is largest near the upper boundary, within the viscous boundary layer, and within the stable region, where the eddy correlation time becomes large. The diffusion coefficient is nearly independent of latitude, with small variations of the order of 1% at a given radius. However, it increases by about three orders of magnitude from about 10^{13} in the bulk of the convection zone to 10^{16} near the upper boundary and in the stable zone.

Figure 9.8(f) indicates the quality of the fit over a reversal, with σ_α being the standard deviation of a scalar contraction of the α tensor $\sqrt{\alpha_{i,j}\alpha^{i,j}}$ as follows

$$\sigma_\alpha^2 = \sum_{i,j} \left[\alpha_{i,j}^2 \sigma_{\alpha_{i,j}}^2\right] / \sum_{i,j} \alpha_{i,j}^2, \tag{9.6}$$

with the standard deviations of each component $\sigma_{\alpha_{i,j}}^2$ computed using the least-squares merit function and components from the SVD decomposition. Under this measure, the accuracy of the SVD fit to α over the interval t_1-t_5 has an uncertainty that is at worst about 5 $\mathrm{m\,s^{-1}}$, and is on average about 1 $\mathrm{m\,s^{-1}}$. Given the small values of the fluctuating velocity and magnetic field in the stable zone, it is no surprise that the fits are most uncertain there. It is of note that, when the contributions of the β-effect and the current are included, the accuracy of the fit to the α tensor is increased by about 20%.

The lower row of Figure 9.8 shows the relative uncertainty in the reconstructed EMF averaged over 20 day intervals surrounding times t_1-t_5, with panel (l) showing the average

over an entire reversal. The agreement between the mean-field estimate of the EMF and the EMF of the simulation is highly time dependent, with some instances showing agreement and other times being more poorly represented by the temporally constant α and β tensors. Yet the longer term agreement between the two is reasonably good, as in Figure 9.8(l), with the mean uncertainty being only about 30%. If only the α-effect is taken into account, the average uncertainty of the mean-field estimate relative to the EMF of the simulation is larger at about 50%. This indicates that the combination of the α and β-effects is capturing the rough outlines of the reversal, though the EMF resulting from mean-field theory tends to be much less spatially variable than the EMF in the simulation.

Under a L_2 norm, no single one of the components of α is overtly dominant in the mean-field estimate of the turbulent EMF generating poloidal field, rather they each contribute almost equally to the total EMF. The one exception is the $\alpha_{\phi,\phi}$ component, which contributes about 40% to the total α-effect, whereas the other quantities are nearly evenly split in importance and sustain the other 60% of the α-effect. This balance is sensitive to whether or not the β-effect is included, with a lower overall contribution of the $\alpha_{\phi,\phi}$ component when it is not included. In either case, however, this means that the turbulent production of mean poloidal field by an α-effect achieved through the action of convection chewing away at the mean toroidal field is not the sole effect. Indeed, as the above analysis indicates, the mean poloidal field is also generated through the action of the smaller-scale vortical turbulence at high latitudes and the columnar convection at low latitudes amplifying existing poloidal field.

From the above analysis it is evident that the action of convection on both the poloidal and toroidal fields effectively sustains and regenerates the mean poloidal field, whereas the toroidal fields are primarily built through the interaction of the poloidal field and the rotational shear. In Figure 9.5, there is a weak influence of the α-like T_{FS} and T_{FA} terms, which are roughly a factor of ten smaller than the Ω-effect (T_{MS}). Yet this is only the case for the toroidal magnetic energy. The difference between the same terms for the generation of the

Figure 9.9: Reconstructed components of the mean-field α and β-effects and their accompanying relative uncertainties. (a-e) Components of α that contribute to the turbulent EMF ($\mathcal{E}_\phi$) are shown in the meridional plane. (f) Relative uncertainty of the contracted α tensor, a measure of goodness of fit. (g-k) Components of χ that contribute to $\mathcal{E}_\phi$. (l) A measure of fit to χ. (m-q) Relative uncertainty in the reconstructed EMF as measured against the EMF of the simulation in 20 day intervals centered on each of the sample times t_1-t_5, a measure of effectiveness and reproducibility. (r) The same but measured over the entire reversal interval of 1600 days.

field itself is only a factor of three. Therefore, given the presence of the differential rotation to sustain the toroidal field and the secondary but non-negligible action of the EMF, the dynamo operating in this simulation could be characterized as an α^2-Ω dynamo.

9.11 A Second Fitting Approach

We now explore higher-order mean-field approximations, noting that the second-order expansion of $\mathcal{E}$ around the mean magnetic field is $\langle\mathcal{E}\rangle = \alpha\langle\mathbf{B}\rangle + \beta\nabla\langle\mathbf{B}\rangle + \mathcal{O}\left(\partial\langle\mathbf{B}\rangle/\partial t, \nabla^2\langle\mathbf{B}\rangle\right)$, where α is a rank two pseudo-tensor and β is a rank three tensor. This is the logical extension of the first-order approximation used above. We approximate the β tensor by including only its action on the anti-symmetric part of $\nabla\langle\mathbf{B}\rangle$, which is the current $\langle\mathbf{J}\rangle = \boldsymbol{\nabla}\times\langle\mathbf{B}\rangle$, so that

$$\beta_{ijk}\frac{\partial\langle B_j\rangle}{\partial x_k} \approx -\chi_{im}\epsilon_{mkj}\frac{\partial\langle B_j\rangle}{\partial x_k} = -\chi_{im}\left(\boldsymbol{\nabla}\times\langle\mathbf{B}\rangle\right)_m = -\chi\langle\mathbf{J}\rangle \tag{9.7}$$

with the sign of χ chosen to conform to the standard notation mean-field theory, ϵ_{mkj} the Levi-Civita symbol, and with an implied sum over repeated indices. The notation for α is as in §9.10. The diffusion tensor χ can also be decomposed into symmetric and anti-symmetric components as $\chi\langle\mathbf{J}\rangle = \chi_S\langle\mathbf{J}\rangle + \boldsymbol{\xi}\times\langle\mathbf{J}\rangle$, which can be interpreted as an anisotropic conductivity χ_S and a helicity interaction term $\boldsymbol{\xi}$.

To reconstruct these two tensors from our data, both of their individual components are simultaneously solved for from a temporal sequence of data at each radial and latitudinal grid point using a method that extends the SVD technique used in §9.10. The difference is that both α and χ are reconstructed from the simulation data, which we find improves the overall numerical agreement between the mean-field theoretic EMF and the EMF from the simulation. It has the advantage that the magnetic fields and electric currents from the simulation constrain the components of α and χ. We again carry out the reconstruction over the entire reversal interval, assessing its applicability at a given stage of the reversal, with Figures 9.9(a-e) showing the five components of α that contribute to $\mathcal{E}_\phi$ and with Figures 9.9(g-k) displaying the equivalent components of χ.

The spatial structure of $\alpha_{\phi,r}$, $\alpha_{\phi,\phi}$, and γ_r visible in Figures 9.9(a, c, d) shares roughly the same characteristics as in §9.10. Figure 9.9(f) indicates the quality of the fit over a reversal, with σ_α being the standard deviation defined in Equation 9.6. The same procedure is applied to the χ tensor to measure the accuracy of the SVD fit. Under this measure, the accuracy of the SVD fit to α over the interval t_1-t_5 has an uncertainty that is at worst about 5 $\mathrm{m\,s^{-1}}$, and is on average about 1 $\mathrm{m\,s^{-1}}$. The fit to χ is not as accurate as is apparent in Figure 9.9(l), with the median uncertainty being about 6% and with a relatively long tail of larger values in the PDF of the uncertainty. Given the small values of the fluctuating velocity and magnetic field in the stable zone, it is no surprise that the fits are most uncertain there. It is of note that, if the contributions of the β-effect and the current are neglected, the accuracy of the fit to the α tensor is reduced by about a factor of nine.

The component $\chi_{\phi,\phi}$ provides the most spatially uniform contribution to the EMF (Figure 9.9(i)). Since it is negative most everywhere, this component acts as a turbulent anti-diffusion. This is in marked contrast with the often used approximation that χ should be everywhere positive and fairly isotropic, which is valid in isotropic turbulence that is not rotationally constrained (e.g., Brandenburg & Subramanian, 2005). In Chapter 3 it was shown that under strong rotational constraints the isotropic components of β can in fact be negative. The common form of the β tensor has $\chi_{ij} \propto \tau \langle \mathbf{v}' \cdot \mathbf{v}' \rangle \delta_{ij}$, δ_{ij} the identity tensor, and τ an eddy correlation time, as is employed in §9.10. In this simulation, however, the components of χ_S and the $\boldsymbol{\xi}$ vector capture the impact of the anisotropy of the convection due to rotation and stratification. Such an underlying anisotropy in the small-scale turbulence leads to an anisotropic diffusion as well as to the anti-diffusive nature of some of the mean-field interactions. The anisotropic turbulent diffusion of the current arises from the off-diagonal components of the symmetrized χ tensor $\chi_{(\phi,r)}$ and $\chi_{(\phi,\theta)}$, as is evident upon inspection of Figures 9.9(g, h). However, the global influence of the kinetic helicity is captured by the north-south asymmetry in $\chi_{(\phi,\theta)}$ and ξ_θ, with the former acting diffusively in the northern hemisphere and anti-diffusively in the southern hemisphere.

The lower row of Figure 9.9 shows the relative uncertainty in the reconstructed EMF averaged over 20 day intervals surrounding times t_1-t_5 as in Figure 9.8, with panel (r) showing the average over an entire reversal. The agreement between the mean-field estimate of the EMF and the EMF of the simulation is highly time dependent, with some instances showing agreement and other times being more poorly represented by the temporally constant α and β tensors. Yet the longer term agreement between the two is reasonably good, as in Figure 9.9(r), with the mean uncertainty being only about 14%. If only the α-effect is taken into account, the average uncertainty of the mean-field estimate relative to the EMF of the simulation is much larger at about 40%. This indicates that the combination of the α and β-effects is capturing the rough outlines of the reversal, though the EMF resulting from mean-field theory tends to be much less spatially variable than the EMF in the simulation.

We find here that the overall α-effect accounts for about 43% of the generation of poloidal field through the azimuthal component of the turbulent EMF, whereas the β-effect is the other 57%. Under a L_2 norm, no single one of the components of α or χ is overtly dominant in the mean-field estimate of the turbulent EMF generating poloidal field, rather they each contribute almost equally to the total EMF. As in §9.10, the $\alpha_{\phi,\phi}$ component contributes about 40% to the total α-effect, with the other quantities evenly split in importance to sustain the other 60% of the α-effect. This balance is again sensitive to whether or not the β-effect is included, with a lower overall contribution of the $\alpha_{\phi,\phi}$ component when it is not included. In either case, however, this means that the turbulent production of mean poloidal field by an α-effect achieved through the action of convection chewing away at the mean toroidal field is not the sole effect. Indeed, as the above analysis indicates, the mean poloidal field is also generated through the action of the smaller-scale vortical turbulence at high latitudes and the columnar convection at low latitudes amplifying existing poloidal field. In contrast, the components of the β-effect that contribute to the azimuthal EMF are nearly all equal, with no dominant component. However, the existence of anti-diffusive values of the β-effect is of some significance for this dynamo. In particular, it indicates that

nonlinear processes involving the current (such as the Lorentz force) that lead to magnetic field production have been captured within our fitting procedure. Moreover, the dominant anti-diffusive character of the $\chi_{\phi,\phi}$ component is quite surprising as it is quite different from the expectation of how the diagonal components of the χ tensor should behave.

From these two approaches of mean-field theoretic analysis presented in §9.10 and §9.11, it is fairly evident that the dynamo processes active in *Case A20m* lead to an $\alpha^2\Omega$ type dynamo, as discussed above. Yet given the importance of the β-effect, it may be more apt to classify this MHD simulation as an $\alpha\beta\Omega$ dynamo. However, the spatio-temporal variation of the generation of poloidal field in the simulations makes an exact characterization of the dynamo in the context of mean-field theory difficult.

9.12 Reversal Elements

Having viewed the evolving properties of the toroidal and poloidal fields in a reversal, it may be useful to enumerate the elements that appear to be essential. We have cross-referenced these elements in our prior discussions and sketched them in Figure 9.10.

Element 1. At the beginning of each 580 day magnetic cycle, strong monolithic toroidal field is built through the Ω effect in the stable zone over the course of about 150 days, utilizing the remaining poloidal field from the previous cycle (Figure 9.10(a)).

Element 2. Continued dynamo action through the Ω-effect serves to strengthen the wreaths and to broaden them in latitude. Eventually the structure reaches a latitudinal extent and strength great enough for Lorentz forces to begin tearing it in two, with the poleward side of the wreath breaking away (Figure 9.10(b)). This field then accelerates toward the poles under the influence of the combined action of buoyancy, Lorentz, and Coriolis forces. Yet it retains some of its linkage with the primary low-latitude bound wreath, forming a sheet of toroidal field in the stable zone. The entire slip between low-latitudes and the pole takes about 480 days, which is the Alfvénic time-scale that characterizes the polar-slip instability.

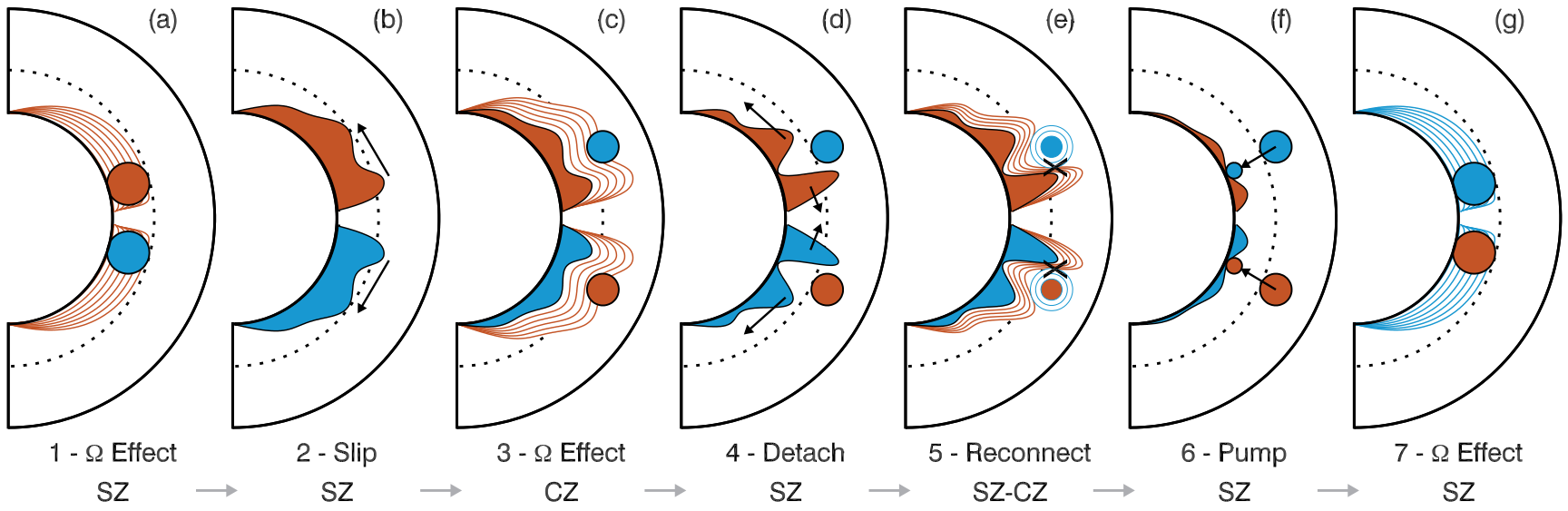

Figure 9.10: A sketch of the basic processes occurring during a reversal in *Case A20m*, with panels (a-g) depicting Elements 1-7. The radial extent is expanded by a factor of two for clarity and the dotted line indicate the base of the convection zone. Solid structures represent toroidal fields and isolated curves are meant to convey the poloidal field lines. The color gives the sense of the field with red positive and blue negative. The dotted line illustrates the bottom of the convection zone.

Element 3. Poloidal field wraps around the deeper wreaths, encasing them. The action of convection above the stable zone is to turn this poloidal field into toroidal field through shearing due to the differential rotation (T_{MS}). This builds and maintains a wreath at mid-latitudes in the convection zone over the course of a magnetic energy cycle, whose toroidal sense is opposite to that of the deeper field (Figures 9.3(c-g) and 9.10(c)).

Element 4. While the poleward branch of toroidal field in the stable zone slips further toward the pole, the toroidal sheet of field linking it to the low-latitude is shorn apart by the differential rotation. This initiates a reconnection of the poloidal field enshrouding both branches of toroidal field. During this reconnection event, either the equatorial or the polar branches of this field reverse their magnetic helicity (Figures 9.10(d, e)). This reconnection process takes only a few days at a given latitude.

Element 5. The fields whose helicity does not reverse continue to grow until the differential rotation weakens under Lorentz force feedbacks. The rate of magnetic field generation due to the mean shear then falls below the rate of resistive dissipation, eventually destroying the field. The field with the reversed helicity is more rapidly dissipated by the combined action of the resistive dissipation and the mean shear, which due to the reversed poloidal field sense now acts to destroy field. The reconnection and field dissipation migrates equatorward from the initial mid-latitude reconnection on a time scale of about 100 days (Figures 9.3(b) and 9.10(e, f)). It is this time scale and the polar-slip that are the dominant processes setting the 580 day energy cycle period.

Element 6. As the field decays away, the convection which is relatively unchanged during the cycle rebuilds the differential rotation on the timescale of a few global convective overturnings. As this is occurring, the poloidal field that had been sustained around the deeper wreaths is no longer available to build the weaker, oppositely directed toroidal field in the convection zone. This field is pumped into the stable region over a convective overturning

time scale (Figure 9.10(f)).

Element 7. There are now two paths to rebuilding field in the stable zone to begin an energy cycle anew. One path is that both the toroidal and poloidal field remnants of the weaker wreaths in the convection zone are pumped into the stable zone. This provides the seed of the polarity for the new cycle and gives rise to a polarity reversal, which is then built upon by the Ω effect. This appears to occur every three energy cycles, leading to the 1600 day reversal period. Typically following the end of the first cycle there is a failed reversal in which the polarity of the former wreaths is retained. In this cycle, the deeper field begins to strengthen before it had decayed sufficiently to be overcome by the remnant wreath pumped in from the convection zone (Figure 9.10(g)) .

9.13 Conclusions

We have explored the interaction of rotation, convection, and magnetism in a $1.2\,M_\odot$ star rotating at 10 and 20 times the solar rate with the 3-D MHD ASH code. We find that strong dynamo action occurs both in the convection zone and in the stable zone of these simulations. The magnetic fields resulting from this dynamo action are organized into large scale structures, forming strong toroidal bands (wreaths) of field with intricate fibril structure and with enshrouding poloidal fields that the serve to link the wreaths. The portion of the radiative zone present in the simulations here plays an active role in both storing and building these global-scale magnetic fields.

These MHD simulations of F-type stars reveal spatially complex and temporally dynamic behavior, with time variation in the magnetic energy arising in both cases. In our analysis of these two cases, the primary mechanism for building toroidal field is the Ω effect underlying T_{MS}, and that for building the poloidal field is P_{FS}. This corresponds well with prior simulations of G-type stars (B11; Nelson et al. (2013a)), where these are also the dominant sources of magnetic energy production. To put these simulations in the context of

mean-field theory electrodynamics, the dynamos in both *Case A10m* and *Case A20m* exhibit some characteristics similar to those seen in a classical α^2-Ω dynamo. We also find that the β-effect is an important factor in obtaining a reasonable agreement between the mean-field estimate of the turbulent EMF and the time-averaged turbulent EMF of the simulation.

The limited temporal variability of *Case A10m* allows us to examine time averages of these magnetic structures in terms of their generation, maintenance, and impacts upon the mean flow and thermal structure of the simulation. Unlike previous simulations of young G-stars that yield strong, coherent wreaths of magnetism in their convection zones, the simulations here explicitly include a stable zone. In our assessment of the generation of magnetic field in the stable zone, we find that the P_{MS} and P_{MA} poloidal magnetic energy generation terms are largely equal. This arises due to the alignment of the mean poloidal magnetic field and the meridional flow. This poloidal field is directly tied to the deep toroidal wreaths present in the stable zone. These structures act to block channels of angular momentum transport that had efficiently accelerated the equator in the hydrodynamic cases of Chapters 6 & 7, leading to a reduced latitudinal differential rotation in their MHD counterparts here.

In contrast to the modest variability of *Case A10m*, *Case A20m* exhibits a broad spectrum of dynamical time scales, with large variations in the magnetic energies and their generation rates. Indeed, we have found magnetic energy cycles with a roughly 580 day period and cyclical polarity reversals occurring roughly every 1600 days, or every three energy cycles. A mechanism for the polarity reversals in *Case A20m* has been enumerated, where the crucial elements are the coupling between the stable zone and the convection zone and the polar-slip instability. This reversal mechanism merits further investigation to better assess its statistical properties over many polarity reversals and to establish its potential role in other stellar configurations, such as in the Sun or τ Boötis.

The mean flows established in these 3-D MHD simulations are quite different from those of the purely hydrodynamic variety. The differential rotation and its accompanying thermal contrast of *Case A10m* and *Case A20m* are reduced relative to their hydrodynamic

counterparts *Case A10* and *Case A20* of Chapters 6 & 7. In particular, the average latitudinal differential rotation has dropped by a factor of 2.0 in *Case A10m* and by a factor of 2.4 in *Case A20m*. The global-scale magnetism established in both *Case A10m* and *Case A20m* leads to variations in the latitudinal differential rotation with time. Here the differential rotation varies by about 20% in *Case A10m* and by up to 70% in *Case A20m* on time scales commensurate with the variation of the magnetic fields. Time varying bulk flows have been seen in prior MHD simulations of the G-type stars (B11). Some modulation of the differential rotation with magnetic activity appears to be also observed on τ Boötis and several other stars (Donati et al., 2003).

The 3-D numerical simulations presented here and in Chapters 6 & 7 cover rotation ranges that are accessible to the line profile technique, and thus are directly comparable to recently expanded data sets of observed differential rotation in F-stars, such as those in (Ammler-von Eiff & Reiners, 2012). Indeed, the differential rotation achieved in the prior simulations of Chapters 6 & 7 tended to match the earlier observational data (Reiners, 2006), an agreement further improved upon here. The hydrodynamic models of Chapters 6 & 7 fell well within the uncertainties of the measured differential rotation, but often a given model had a $\Delta\Omega$ matching that of the stars with the greatest differential rotation at a given rotation rate. The time-averaged latitudinal differential rotation of the two magnetic models explored here, on the other hand, now follows the average trend line of the observed data for the F-type stars.

Our 3-D simulations of F-type star dynamo action reveal that quite complex processes can be at work, and that we have sampled only a small subset of them. However, tools in computational astrophysics such as ASH that study the interior dynamics of stars will continue to improve with rapid advances in supercomputing. This holds out the promise of increasing contact between global-scale simulations and observations of stellar magnetic variability.

Chapter 10

Convection and Dynamo Action within the Cores of B-type Stars

"When I had satisfied myself that no star of that kind had ever shone before, I was led into such perplexity by the unbelievability of the thing that I began to doubt the faith of my own eyes." – Tycho Brahe

In a first foray into the realm of massive star convection, the following brief paper was the first published ASH simulation of a B-type star. It is included here as an introduction (§10.1) into the possibilities of interesting dynamo states within the cores of B-type stars. Again this is my work, with wordsmithing assistance from Juri, and is published in Augustson et al. (2011)[1] . The remaining sections discuss the broader aspects of observations and simulations that build upon those first steps.

10.1 Introduction

Main-sequence massive stars possess convective cores that likely harbor strong dynamo action. To assess the role of core convection in building magnetic fields within these stars, we employ the 3-D anelastic spherical harmonic (ASH) code to model turbulent dynamics within a $10\,M_\odot$ main-sequence (MS) B-type star rotating at $4\,\Omega_\odot$. We find that strong (900 kG) magnetic fields arise within the turbulence of the core and penetrate into the stably stratified radiative zone. These fields exhibit complex, time-dependent behavior including reversals in magnetic polarity and shifts between which hemisphere dominates the total magnetic energy.

[1] Augustson, K. C., Brun, A. S., & Toomre, J., 2011, "Convection and dynamo action in B stars", Proc. IAU Symp., 271, 361

Surface magnetic fields have been found on a few MS massive stars (e.g., Donati & Landstreet, 2009). To some degree both the fossil fields and dynamo generated fields in these stars must coexist, although how they interact to produce and maintain these surface fields is unclear. Recent work has shed some light on the interaction between a superequipartition core dynamo and fossil magnetic fields in A-type stars (Brun et al., 2005; Featherstone et al., 2009). We extend this work to a much more luminous $10\,M_\odot$ star with a rotation period of seven days ($4\,\Omega_\odot$) which is typical for active MS B stars.

Using the 3-D ASH code, we study convection and dynamo action realized in the core and part of the surrounding radiative envelope of this $7200\,L_\odot$ B star. ASH is a mature modeling tool which solves the anelastic MHD equations of motion in a rotating spherical shell using a pseudo-spectral method (e.g., Brun et al., 2004). The mean structure in this ZAMS star is obtained from a stellar evolution code. We capture the full spherical geometry with a radial domain that occupies $0.6\,R$ (covering 7 pressure scale heights), with the inner $0.2\,R$ being convectively unstable. The innermost $0.02\,R$ is excluded to avoid the coordinate singularity at the origin in the ASH code. The upper and lower radial boundary conditions are stress-free and impenetrable for the velocity field and perfect conductor (lower) and potential field (upper) for the magnetic field.

The intricate and time-varying flows established in this simulation are largely aligned with the rotation axis. These columnar convection cells break the spherical symmetry due to equator-crossing meridional circulations and a north-south asymmetric differential rotation. A central columnar flow (occupying the inner $0.1\,R$ at the equator) stretches north-south across the entire core, rotates retrograde to the reference frame, and gently flares out to about 25° in latitude at the core boundary (Fig. 1a). Along the rotation axis within this column are strong vortical flows. Outside the central column, there are typically five columnar convection cells that rotate prograde to the reference frame. These cells transport angular momentum between the central column and the overshooting region, where there is a weak prograde equatorial flow. These flows maintain a mean rotation rate that increases monotonically

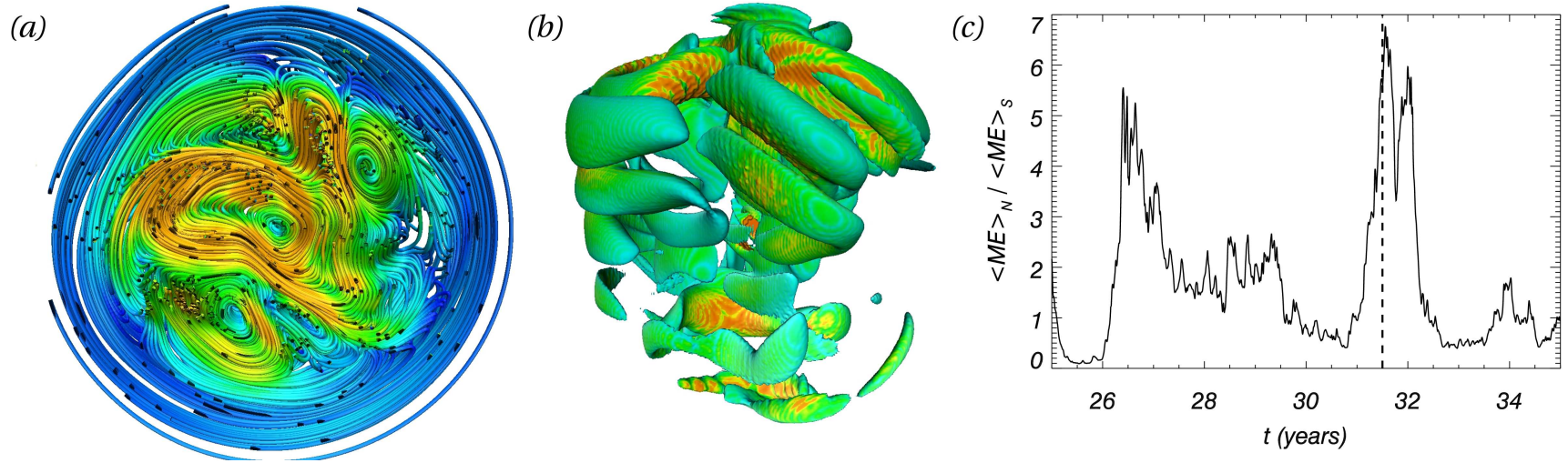

Figure 10.1: (a) Velocity streamlines within the core, cut along the equator. Fast core-crossing flows and several columnar flows are visible. Orange tones indicate fast flow speeds ($|v| > 300\,\mathrm{m\,s^{-1}}$, peak 1000 $\mathrm{m\,s^{-1}}$), slower speeds in blue tones. (b) An isocontour rendering of magnetic energy showing the dominance of the northern hemisphere and equatorward tilted magnetic structures (rotation axis vertical). (c) North to south ratio of hemispherical averages of ME shown for a decade of time evolution; (a) and (b) are rendered at 31.5 years (dashed line).

from the center of the star to become nearly uniform within the radiative envelope, with an overall radial differential rotation of 25%.

A strong dynamo operates within the core, generating magnetic fields with peak strengths reaching 900 kG (200 kG rms). These fields form equatorward tilted strands that encircle the core (Fig. 1b). The fluctuating component of the magnetic field comprises 76% of the total magnetic energy (ME) in the core, while 21% remains in the mean toroidal field and 3% in the mean poloidal field. On average the total ME is 55% of the convective kinetic energy, but there are intervals where it approaches 86% indicating that the ME is nearing equipartition.

The time evolution of magnetic field is complex and multi-periodic. When averaged over several decades, the ME of the northern hemisphere is 1.7 times greater than that of the southern hemisphere. There are intervals, however, when the southern hemisphere comes to dominate the magnetic energy (Fig. 1c), but only by a factor of at most 2.5. The northern hemisphere, on the other hand, dominates the ME for periods of up to two years by a factor as great as 6.7. These magnetic field configurations have quadrupolar and dipolar components that are nearly equal and opposite, which have been shown to exist when there is weak equatorial symmetry breaking (Gallet & Pétrélis, 2009).

The greatest extent of convective overshooting into the stable radiative envelope occurs at mid-latitudes. The sustained overshooting pushes magnetic field and lower entropy fluid into the stable layer, making the core prolate and stochastically exciting gravity waves. The strongest magnetic fields (900 kG) and fastest flows (1 $\mathrm{km\,s^{-1}}$) typically occur along the edge of the central column and are maximum where this column transects the core boundary. As this field is advected into the overshooting region it is combed into a large-scale toroidal field ($\sim$30 kG) by the flows in the stable region. Therefore, in this region, the velocity and magnetic fields are nearly aligned creating a force-free state.

To better understand the hemispherical dynamo state achieved within this B-star model, simulations at varying rotation rates and lower diffusivities must be run. Mini-

mal diffusion is especially important if buoyant magnetic structures that might arise from the strongest fields in these models are to be captured.

10.2 Recent Observational Studies of B-type Stars

The B-type stars span a range of stellar masses from about 2.1 to 16 $M_\odot$ (e.g., Habets & Heintze, 1981). When on the main sequence the radius of these stars is about 2 to 7 $R_\odot$. The fusion in their cores rapidly consumes hydrogen, with energy streaming from the stellar surface at luminosities of up to 30,000 times that of the Sun. This large energy output drives strong winds and ultra-violet radiation from their photospheres. Indeed, once these stars are born in a molecular cloud, they quickly erode the cocoon of nebular gas harboring them and in the process suppress nearby star birth. These rapidly evolving stars are also the crucibles in which the majority of the elements are forged. Their short and energetic lives of just a few million years soon end in a supernova, redistributing hydrogen and heavier elements throughout their environment. Thus these massive stars are the engines driving the evolution of galaxies.

Much is unknown about the dynamics occurring within the interiors of these stars. During their main-sequence lifetime, there is a convective core deep within a massive star and thin convective shells near the surface with a large radiative envelope between them. Yet how these regions interact through instabilities, convective driving, and magnetic linking remains largely unknown. A portion of this problem is addressed here by examining the core-envelope coupling and sustained dynamo action through 3-D MHD simulations of a 10 $M_\odot$ main-sequence B-type star.

10.2.1 Aspects of Convective Cores and Their Observed Properties

The convective core is usually spherical due to its large mass and density, except in the most rapidly rotating stars. The core also occupies up to 50% of the star by mass and 30% by radius. The energy burning of the CNO fusion cycle in the cores of massive stars

drives an energy flux that must be carried to the surface in order for the star to remain in pressure balance. However, neutrino and photon radiation can only carry a portion of the total energy flux due to their moderate opacities and the weak temperature gradient in the core. Thus, convective motions must carry the remaining flux through the core, which tends to be roughly 50% of the total luminosity. The convective flows are extremely turbulent and hence are inherently time-dependent and three-dimensional. The convective core has a strong influence on the structure and evolution of these massive stars, though little is known about its detailed properties. Beyond modifying the structure of the core itself, this core convection also influences the dynamics of the radiative zone above it and may influence the surface properties of the star through three primary mechanisms: convective overshooting, rotational mixing processes, and magnetic linkages.

In standard one-dimensional stellar models, the effects of stellar convection are usually calculated using simple mixing-length prescriptions (e.g., Claret, 2007), but such approaches involve considerable uncertainties. Mixing-length theory can only provide rough estimates of the turbulent properties of the convection, which has important consequences for compositional mixing and redistribution of angular momentum within massive stars. Overshooting from convection zones raises other problems. It has long been realized that convective motions do not halt at the boundary between the convection zone and the stable radiative zone above it (e.g., Saslaw & Schwarzschild, 1965; Maeder, 1975). Upward moving fluid parcels will penetrate into the stable zone, decelerating and mixing with their surroundings. Such overshooting motions may bring fresh nuclear fuel into the core, thereby prolonging the star's lifetime on the main sequence as well as increasing its luminosity and radius (Brott et al., 2011). Accurately estimating the character and extent of this overshooting is challenging, but 3-D simulations provide a route to understanding aspects of it such as turbulent entrainment.

Asteroseismology, enabled by current space-born missions as well as ground based photometric observing campaigns, has been very successful in multiple fronts. It has provided

precision measurements of the fundamental parameters of many massive stars such as their mass, age, radius, and metallicity (e.g., Handler et al., 2003; Degroote et al., 2010a; Aerts et al., 2011). For a few stars with well resolved modes, it has even been possible to detect and partially constrain the effects of overshooting at the core boundary (e.g., Aerts et al., 2003; Briquet et al., 2011).

10.2.2 Properties of Rotation in B-type Stars

Observations have shown that the majority of main sequence B-type stars are fairly rapid rotators (Abt et al., 2002). The average equatorial velocities of these stars are about $140\,\mathrm{km\,s^{-1}}$ on the main sequence, but have an equally large standard deviation. Indeed, spectroscopic measurements of single stars in the Small and Large Magellanic Clouds as well as those of field stars have determined a wide range of rotational velocities, between undetectably slow rotation to about 70% of breakup or about $450\,\mathrm{km\,s^{-1}}$ (e.g., Keller, 2004; Hunter et al., 2008). Younger B-type stars may rotate slightly more rapidly, but likely spin down quickly due to strong winds and magnetic torques.

The distribution of angular momentum achieved within the interiors of massive stars is quite uncertain. However, for a handful of B-type stars, asteroseismic inversions of the radial profile of angular velocity have shown that the core may be more rapidly rotating than its surrounding radiative envelope (e.g., Aerts et al., 2003), though the uncertainties in these measurements are fairly large. Yet the presence of a such a non-uniform rotation deep within these massive stars could have major consequences for their bulk properties.

Differential rotation can give rise to shear instabilities that stir and mix material, and may serve to build strong magnetic fields through sustained dynamo action. Stellar evolution codes attempt to capture these instabilities and the convection in the core using 1-D advection-diffusion approximations. Such approaches yield radial profiles of angular velocity that are flat in the core and fall off slowly toward the surface (e.g., Maeder & Meynet, 2012; Potter et al., 2012), which agrees with these few observed profiles.

In the solar convection zone, Reynolds stresses give rise to a prominent radial and latitudinal differential rotation that has been studied extensively through helioseismology (e.g., Thompson et al., 2003). Explaining this differential rotation within the Sun has been a major challenge for both theory and simulation, but 3-D spherical shell simulations of turbulent convection have made substantial contact with the helioseismic results (e.g., Miesch et al., 2000; Brun & Toomre, 2002; Miesch et al., 2006). If it also the case that there is a significant radial or latitudinal differential rotation either in the core or the radiative envelopes of the massive stars, 3-D simulations may again provide a basis for exploring how this may arise, as has been attempted with simulations of an A-type star (Browning et al., 2004; Brun et al., 2005; Featherstone et al., 2009).

10.2.3 Magnetism Observed on Massive Stars

Recent observational efforts have directly detected magnetic fields on the surfaces of about 10% of B-type stars using spectropolarimetric Zeeman Doppler Imaging techniques (e.g., Donati & Landstreet, 2009; Grunhut et al., 2013). There is also indirect evidence that a larger fraction may possess magnetic fields, but that they may be too weak to be found using spectropolarimetry. In particular, spectral Doppler measurements have shown that for a well selected sample population that there is a bimodal distribution of projected rotational velocity (Dufton et al., 2013). There it is clear that there are two populations of main sequence B-type stars, a more rapidly rotating one with an average rotational velocity of of about $160\,\mathrm{km\,s^{-1}}$ and another peaking near no detectable rotational velocity. It is likely that the stars in this latter population possess magnetic fields that act to spin them down.

What remains largely unknown is how these magnetic fields arise to begin with, nor is it clear how the magnetic fields in massive stars influence both their evolution and their environment. There are three complementary theories that attempt to address the origins of these magnetic fields: a strong core dynamo (Charbonneau & MacGregor, 2001), a shear-driven dynamo in the radiative zone (Mullan & MacDonald, 2005), or a fossil field remaining

from the birth of the star (Braithwaite & Nordlund, 2006).

There is observational support for each of those hypotheses. For core convection, one could appeal to the fact that correlations between magnetic fields and rotation have been inferred in main-sequence stars ranging from spectral type M through F (Wright et al., 2011). These observed magnetic fields are likely the result of convective dynamo action, though how thoroughly they permeate the interior beyond the convective envelope is unknown. However, massive stars with convective cores are likely to admit a similar form of dynamo action, for they too possess the necessary ingredients: intensely turbulent convection, a highly conductive medium, and the global effects of rotation which are all thought to be crucial for building magnetic fields.

How magnetic fields built through dynamo action in the core could be transported to the surface across the radiative zone of these stars remains unclear. If there is no expeditious means of such transport, the fields will take roughly the main sequence lifetime of the star to diffuse from the core to the surface. On the other hand, sufficient turbulence and shear in the radiative zone may allow the fields to rise to the surface on a reasonable timescale. In particular, if the Tayler-Spruit dynamo mechanism is operating in the radiative zone, it may be possible that a coupling between the core dynamo and a shear dynamo in the radiative zone allows strong magnetic fields to be transported to the surface.

The dynamo action within the cores of massive stars may produce buoyant fields, but they must overcome the compositional gradients and stiff stratification present at the core boundary (MacDonald & Mullan, 2004). One mechanism that partially circumvents this constraint, reducing the magnetic field strength required to buoyantly rise the surface, is convective overshooting and penetration into the stably stratified envelope above the core. This leads to mixing in this region, which reduces the compositional and sub-adiabatic gradients there. It also deposits magnetic field above the steepest gradients, where the field can be strengthened through further dynamo action and further deposition of field. This field may grow to strengths sufficient to become buoyant. A pre-existing magnetic field might

link the surface and the core, potentially providing a conduit for the buoyant fields to more readily move along. If so, the core dynamo may have direct bearing on the regions of strong magnetic field observed on the surfaces of magnetically-active massive stars.

Regardless of the detailed evolution of the star, the magnetic field present in the molecular cloud during the formation of a massive star will almost certainly be interred into its interior, providing the seed field for any dynamo action occurring there. During their main sequence lifetimes, dynamo action in the convective core likely amplifies these fossil magnetic fields and is linked to any field present in their radiative envelopes. As these stars evolve off the main sequence, they possess a convective exterior which will also serve to build magnetic field through dynamo action. When massive stars shed these envelopes during their explosive demise, the magnetic fields built and stored in their interiors over their lifetimes will be dispersed into the interstellar medium and a portion of it trapped in a stellar remnant. Such remnants provide the greatest evidence of magnetic fields being present in the deep interior of massive stars. Thus, given the many impacts that magnetism may have upon the evolution and observable properties of massive stars, a better understanding of the complex flows and magnetism established within their interiors should be sought.

10.3 Simulating Massive Stars with ASH

There are many difficulties to overcome when modeling the interiors of these stars. The nuclear reactions occurring in the core constantly change its isotopic composition. These lead to double diffusive instabilities and may hinder some of the penetrative convection and large scale circulations. In the Sun, it is thought that the tachocline plays a critical role in the global dynamo. It is possible that the differential rotation established in the radiative zone is different from that built in the convective core leading to a reverse tachocline at the boundary between the two regions further complicating the modeling of the interior.

The regions of strong magnetic field observed on the surfaces of some massive stars may be linked to a primordial large-scale interior magnetic field that extends through the stellar

surface. Studies of the interaction between such a relic magnetic field and the convective core of an A-type star have illuminated the richness of the dynamo behavior possible in massive stars (Featherstone et al., 2009). In these studies a coupled core-fossil field system has been constructed by placing a fossil fields with several morphologies in the radiative zone that link to the convective core of the A-type star. These simulations used the 3-D magnetohydrodynamic (MHD) simulation with global spherical geometry using the anelastic spherical harmonic (ASH) code.

The interaction between the existing dynamo and the fossil field has allowed the system to generate significantly higher (roughly tenfold) magnetic energy than kinetic energy. This remarkable super-equipartition state is characterized by an equatorial belt of magnetic field that has persisted for several magnetic diffusion times, along with complex fields built within the convective core. Peak field strengths in this torus reach as high as 500 kG. It was also found that such states depend upon the helicity of the initial configuration of the relic field, where states with the largest poloidal content increase the level of superequipartition. This behavior is in stark contrast to simulations in the absence of a fossil field where these stars generated magnetic energies that were only 70% of the convective kinetic energy (Brun et al., 2005). These studies give the general flavor of the structures and strengths of fields that may be built in B-type stars. However, the convection within the cores of the more massive B-stars is much more vigorous, where the average convective velocities are ten times those seen in a typical A-type star. Therefore, the field strengths and flow structures maintained within the core of these stars remain uncertain given the nonlinearity of the underlying physics.

10.4 Formulating ASH Simulations for B-type Stars

Turning to the $10\,M_\odot$ B-type star dynamo simulations, this section describes the MHD equations solved in ASH and elaborates on the details of how these numerical experiments are constructed. The subgrid-scale motions present in the simulation domain must be parameterized. The turbulent eddy diffusion model does so through renormalized effective

momentum, thermal, and magnetic diffusivities. For B-type stars, the sound speed in the core is on the order of $1000\,\mathrm{km\,s^{-1}}$, while the convective flows are about $0.5\,\mathrm{km\,s^{-1}}$. Thus the anelastic approximation is ideally suited for simulating the interior of these stars. The Courant-Friedrichs-Lewy condition on the time step thus depends either on the local subsonic flow velocity or the speed of Alfvén waves, rather than the local speed of sound.

The turbulence achieved in these models is still quite removed from the intensely turbulent conditions likely present in actual stellar convection zones. Yet with ASH, simulations of convection and dynamo action in many spectral types of stars have made significant contact with observations and led to new ways of thinking about stellar dynamos. In particular, it has been used to simulate a wide range of stars: from fully convective M dwarfs (Browning, 2008), to Sun-like stars (Brown et al., 2011b; Nelson et al., 2013a) and F-type stars (Chapters 6, 7, 8 & 9), and extended to the convective cores of an early A-type star (Brun et al., 2005; Featherstone et al., 2009).

The version of the ASH code utilized here implements the Lantz-Braginsky-Roberts co-density formulation (Lantz, 1992; Braginsky & Roberts, 1995), so that gravity waves are properly captured in the stably stratified, radiative envelope (Brown et al., 2012). The anelastic MHD equations evolved in ASH are still fully nonlinear in the momentum and magnetic variables (Brun et al., 2004). The thermodynamic variables (S, P, T, and ρ) are linearized about a spherically-symmetric and hydrostatic background state $\overline{S}$, $\overline{P}$, $\overline{T}$, and $\overline{\rho}$, which are functions of the radial coordinate only. The equation of state for this background state is a calorically perfect gas. The equations solved in ASH retain physical units, are in spherical coordinates (r, θ, ϕ), and are evolved in time t. These equations are

$$\partial\mathbf{v}/\partial t = -\mathbf{v}\cdot\boldsymbol{\nabla}\mathbf{v} - \boldsymbol{\nabla}\varpi + S\mathrm{c}_\mathrm{P}^{-1}\mathbf{g} - \Lambda\hat{\mathbf{r}} + 2\mathbf{v}\times\boldsymbol{\Omega}_0 + (4\pi\overline{\rho})^{-1}(\boldsymbol{\nabla}\times\mathbf{B})\times\mathbf{B} + \overline{\rho}^{-1}\boldsymbol{\nabla}\cdot\mathcal{D}, \tag{10.1}$$

$$\partial\mathbf{B}/\partial t = \boldsymbol{\nabla}\times\left[\mathbf{v}\times\mathbf{B} - \eta\boldsymbol{\nabla}\times\mathbf{B}\right], \tag{10.2}$$

$$\partial S/\partial t = -\mathbf{v}\cdot\boldsymbol{\nabla}\left(\overline{S}+S\right) + \left(\overline{\rho}\overline{T}\right)^{-1}\left[\nabla\cdot\mathbf{q} + \Phi + \epsilon\right], \tag{10.3}$$

with $\mathbf{v} = \mathrm{v_r}\hat{\mathbf{r}} + \mathrm{v}_\theta\hat{\boldsymbol{\theta}} + \mathrm{v}_\phi\hat{\boldsymbol{\phi}}$, $\mathbf{B} = B_r\hat{\mathbf{r}} + B_\theta\hat{\boldsymbol{\theta}} + B_\phi\hat{\boldsymbol{\phi}}$, and the co-density $\varpi = P\overline{\rho}^{-1}$. The solenoidality of the mass flux ($\boldsymbol{\nabla}\cdot\overline{\rho}\mathbf{v} = 0$) and the magnetic field ($\boldsymbol{\nabla}\cdot\mathbf{B} = 0$) are maintained through the use of a streamfunction formalism. The angular velocity of the rotating frame is $\boldsymbol{\Omega}_0 = \Omega_0\hat{\mathbf{z}}$. The gravitational acceleration is $\mathbf{g} = -g(r)\hat{\mathbf{r}}$. In Equation (10.1), $\Lambda(r)$ is the radial gradient of the mean turbulent pressure that maintains hydrostatic equilibrium as the spherically symmetric state evolves. In the induction equation, η is the magnetic resistivity. The volumetric heating arising from the combination of the CNO and PP nuclear reaction chains are parameterized in ϵ. The energy flux $\mathbf{q}$ is comprised of a spherically-symmetric, diffusive radiation flux and a turbulent entropy diffusion flux,

$$\mathbf{q} = -\kappa_r\overline{\rho}\mathrm{c_P}\boldsymbol{\nabla}\overline{T} - \kappa\overline{\rho}\overline{T}\boldsymbol{\nabla}S, \tag{10.4}$$

where κ_r the radiation diffusion coefficient, and c_P the specific heat at constant pressure. The entropy diffusion flux has an effective thermal diffusivity κ acting on the entropy fluctuations. The viscous diffusion tensor $\mathcal{D}$ and the diffusive heating Φ are

$$\mathcal{D}_{ij} = 2\overline{\rho}\nu\left[e_{ij} - 1/3\left(\boldsymbol{\nabla}\cdot\mathbf{v}\right)\delta_{ij}\right], \tag{10.5}$$

$$\Phi = 2\overline{\rho}\nu\left[e_{ij}e_{ij} - 1/3\left(\boldsymbol{\nabla}\cdot\mathbf{v}\right)^2\right] + \left(4\pi\right)^{-1}\eta\left(\boldsymbol{\nabla}\times\mathbf{B}\right)^2, \tag{10.6}$$

Here e_{ij} is the stress tensor, and ν is the effective kinematic viscosity. The use of this set of anelastic MHD equations requires 12 boundary conditions in order to be well posed. Since it is desirable to assess the generation of magnetic field and how it impacts the organization of angular momentum and energy in these simulations, the following boundary conditions are imposed: impenetrable, perfectly conducting, torque-free, and thermal flux transmitting boundary conditions at both the inner (r_1) and outer (r_2) radial boundaries of the simulation

$$\mathrm{v_r} = B_r = \frac{\partial}{\partial r}\left(\frac{\mathrm{v}_\theta}{r}\right) = \frac{\partial}{\partial r}\left(\frac{\mathrm{v}_\phi}{r}\right) = \left.\frac{\partial S}{\partial r}\right|_{r_1,\,r_2} = 0. \tag{10.7}$$

Table 10.1
Diagnostic Flow Parameters in the Four Cases

Case	$\Omega_0/\Omega_\odot$	$N_r \times N_\theta \times N_\phi$	Ra	Ta	Re	Re′	$\mathrm{Re_m}$	$\mathrm{Re'_m}$	Ro	Λ	κ_1	τ_c	τ_κ
H4	4	$500 \times 256 \times 512$	9.51×10^8	1.00×10^9	1850	610	–	–	0.48	–	8.0	75.	8600.
M4	4	$500 \times 512 \times 1024$	4.18×10^8	1.24×10^9	540.	520	2160	2080	0.35	330	7.2	87.	9600.
M8	8	$500 \times 512 \times 1024$	1.18×10^9	7.11×10^9	500.	490	2000	1960	0.16	493	6.0	114	11500
M16	16	$500 \times 512 \times 1024$	2.93×10^9	4.45×10^{10}	420.	410	1680	1640	0.06	383	4.8	165	14400

Table 10.1: The depth of the convection zone $\mathrm{d} = \mathrm{r_c} - \mathrm{r_1}$ (where r_c is the radius of the top of the convection core) is the relevant length scale in the following parameters and is 6×10^{10} cm. The following diagnostic parameters are estimated at mid-convection zone: the Rayleigh number $\mathrm{Ra} = \Delta\overline{S}\mathrm{gd}^3/\mathrm{c_P}\nu\kappa$; Taylor number $\mathrm{Ta} = 4\Omega_0^2\mathrm{d}^4/\nu^2$; Reynolds number $\mathrm{Re} = \mathrm{v_{rms}d}/\nu$; fluctuating Reynolds number $\mathrm{Re'} = \mathrm{v'_{rms}d}/\nu$; magnetic Reynolds number $\mathrm{Re_m} = \mathrm{Pr_m Re}$; fluctuating Reynolds number $\mathrm{Re'} = \mathrm{Pr_m Re'}$; Rossby number $\mathrm{Ro} = \overline{\xi}/2\Omega_0$, where $\overline{\xi}$ is the rms enstrophy. Elsasser number $\Lambda = \mathrm{B^2_{rms}Pr_m}/(\kappa_1\rho_0\Omega_0)$. Thermal diffusion ($\kappa_1$) values are in units of 10^{12} cm^2 s^{-1}. The mid-convection zone local overturning time τ_c and the thermal diffusion time τ_κ across the convective core are quoted in days.

10.4.1 Experimental Configuration

The inner 65% by radius of a young main-sequence B-type star of $10\,M_\odot$ is simulated at the three rotation rates of 4, 8, and $16\,\Omega_\odot$. These bulk angular velocities are equivalent to surface equatorial velocities of 28, 56, and $112\,\mathrm{km\,s^{-1}}$, or 0.16, 0.66, and 2.6% of the breakup velocity. The luminosity at the surface of the star is $5700\,L_\odot$. The model of the star consists of a convective core that occupies the inner 23% by radius of the star, or about 30% of the computational domain, and an overlying radiative exterior that extends to the outer radius of the domain. To avoid the small time steps required when including the coordinate singularity at origin, the innermost 1% of the core has been excluded. The stratification is taken from a MESA stellar evolution model that had evolved a $10\,M_\odot$ star from the pre-main sequence to about 1 Myr, or just past the beginning of its main-sequence life. The MESA code employs realistic microphysics and employs the mixing-length approximation to the convective dynamics within the core (Paxton et al., 2011). The volume-averaged values of $\partial \ln \epsilon / \partial \ln T$ and $\partial \ln \epsilon / \partial \ln \rho$ are computed in the core of the 1-D stellar model and then they are applied in ASH as a volumetric heating arising from nuclear burning, which gives $\epsilon = \epsilon_0 \overline{\rho}^2 \overline{T}_6^{15.33}$ and $\epsilon_0 = 2.31 \times 10^{-20}\,\mathrm{erg\,cm^3 g^{-2} s^{-1}}$. The initial conditions for these simulations are random entropy perturbations, and for magnetic cases there is also a very weak dipolar field confined to the core with an initial peak strength of 10^{-4} G.

A comparison between the 1-D stellar model and the background state used in these 3-D simulation of B-type stars is shown in Figure 10.2. The discrepancy between the nuclear energy generation rate ϵ and the Brunt-Väisälä frequency N displayed in Figure 10.2(b) arises from the use of a calorically perfect gas equation of state, where both Γ_1 and c_P have been required to be constant with radius. The logarithmic density and temperature are also required to be well fit. This leaves ϵ and N less well described, but still within about 10% of the stellar model.

The effective diffusivities ν, η, and κ vary in radius only. The diffusion is greatly

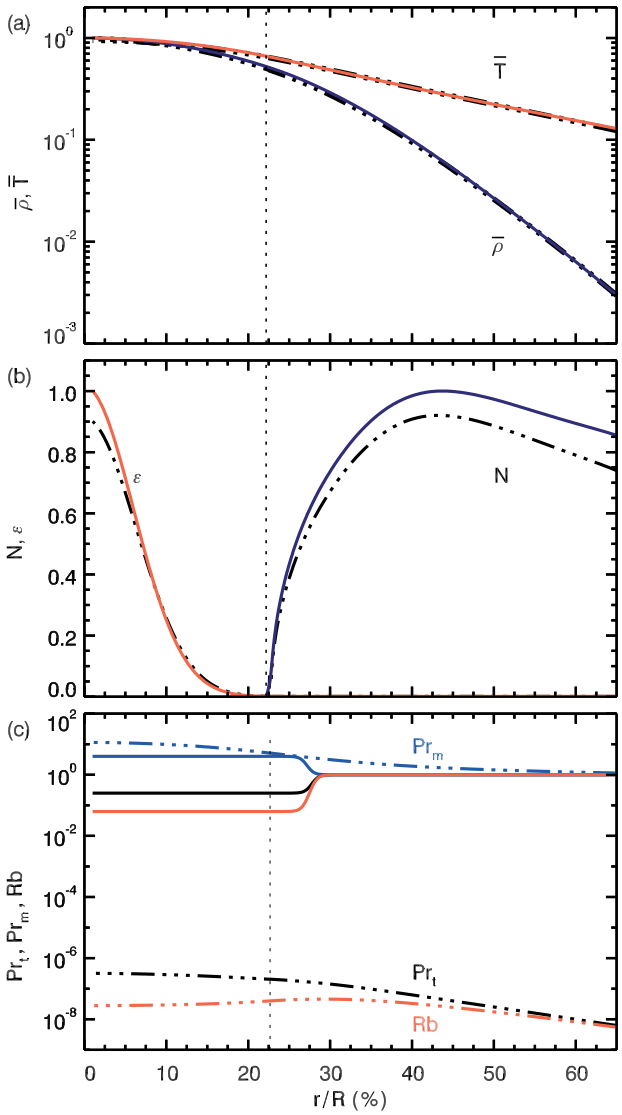

Figure 10.2: Mean stratification established in Case *M4* as a function of proportional radius r/R. (a) Density normalized to the central value ($\overline{\rho}$, solid blue) and normalized temperature ($\overline{T}$, solid red), with the stellar model density and temperature as black dash-dotted lines. (b) Normalized Brunt-Väisälä frequency (N, solid blue) and nuclear energy generation (ϵ, solid red), with stellar model values as black dash-dotted lines. The core boundary is indicated with a dashed vertical line. (c) Comparison of thermal (Pr_t, black) and magnetic Prandtl (Pr_m, blue) numbers and Roberts number (Rb, red) from the atomic values in Braginskii (1965) (dash-dotted lines) and from these B-star simulations (solid lines).

reduced in the stable region, where motions have a small amplitude and the expected SGS motions are subsequently smaller. In the convective core, the Prandtl number is fixed at

$\mathrm{Pr} = \nu/\kappa = 1/4$, so $\nu = \mathrm{Pr}\,\kappa$. Similarly, the Roberts number is constant in the core with $\mathrm{Rb} = \eta/\kappa = 1/16$, leaving $\eta = \mathrm{Rb}\,\kappa$. Outside of the core, the diffusion is tapered to profiles that give $\mathrm{Pr} = \mathrm{Rb} = 1$. The radial profile of the thermal diffusivity κ is given by

$$\kappa\left(r\right) = \left(\overline{\rho}/\overline{\rho}_1\right)^{-1/2}\left[\kappa_1\left(1+\exp\left[\alpha\left(r-r_\kappa\right)\right]\right)^{-1}+\kappa_2\right], \tag{10.8}$$

where $\overline{\rho}_1$ is the background density value at the lower boundary and κ_1 is the thermal diffusivity at the lower boundary. The values of κ_1 are shown in Table 10.1 for each simulation, along with many other diagnostic flow parameters from the middle of the convective core. The floor value of the diffusivity is κ_2. The steepness of the transition between κ_1 and κ_2 is controlled by α and occurs at the radius $r_\kappa = 6.7 \times 10^{10}\,\mathrm{cm}$, which is just outside the core. The minimum levels of diffusion are equal with $\kappa_2 = \nu_2 = \eta_2 = 4 \times 10^8\,\mathrm{cm^2 s^{-1}}$. As visible in Figure 10.2c, the magnetic Prandtl number Pr_m regime likely operating within the true stellar core is numerically accessible as the atomic values of the diffusivities yield $Pr_m \approx 10$. Being a fairly large magnetic Prandtl number, the dynamo that may be running within the star and within the simulations presented here should be expected to be a small-scale dynamo.

10.5 Hydrodynamics of the Core and Radiative Envelope

A very large heat flux is driven through the convective cores of massive stars, and the one being modeled here is no exception. Near the center of the star, the radius is quite small so the heat flux as plotted in terms of a "luminosity" in Figure 10.3 is corresponding small. Nonetheless, the volumetric heating due to nuclear fusion deposits a massive amount of heat in the lower half of the core as visible in Figure 10.2b. Given the small temperature gradient across the core, neither radiation or conduction are sufficient to carry the increasingly large flux throughout a large fraction of the core. Thus convection ensues that carries the equivalent of several thousand solar luminosities of heat flux through the core. This is accomplished through the turbulent alignment of fluctuating temperature and radial velocities

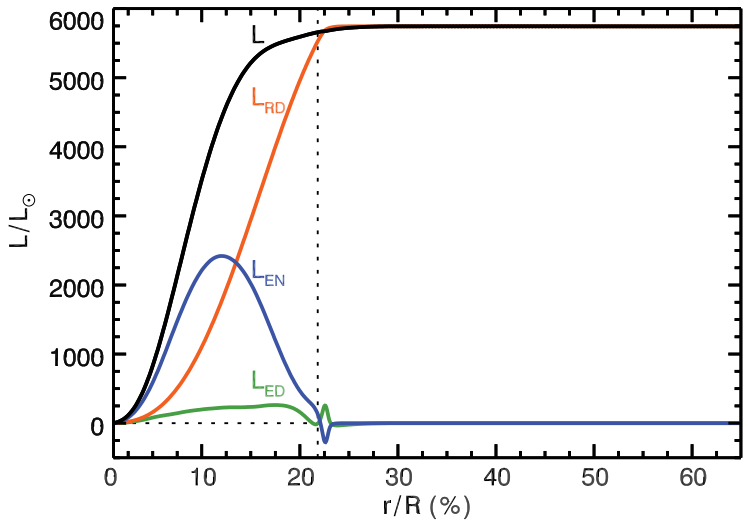

Figure 10.3: Horizontally and time-averaged energy flux balance in Case M4. The energy fluxes are shown as luminosities ($L = 4\pi r^2 F$) for the total flux (L, black), radiative flux (L_{RD}, red), enthalpy flux (L_{EN}, blue), and the flux due to unresolved motions (L_{ED}, green). The magnetic energy flux is minimal and not shown. The vertical dashed line indicates the core boundary, and the horizontal dashed line shows the zero ordinate.

that act in concert to produce a net outward enthalpy flux. However, as the outer portion of the core is reached, the temperature gradient steepens and radiation becomes more efficient than convection for carrying heat. This process acts somewhat like the solar photosphere where radiative losses halt the upflows, rapidly cooling them. Here that processes takes place over a much larger radius and involves a great deal more mass. These simulations employ a realistic stable stratification in the radiative envelope, whose stiffness helps to prevent the diffusive spread of the differential rotation and latitudinal thermal gradient from the core into the stable region. The small zone of overshoot is visible near the core-radiative zone boundary in Figure 10.3 near 0.22 R.

10.5.1 Convective Patterns and Mean Structures

Figures 10.4(a, d) show the enstrophy $\xi = |\nabla \times \mathbf{v}|$ of the flows from two simulations in their cores and their overshooting regions. Case *H4* is purely hydrodynamic and the other Case *M4* is an MHD simulation. The enstrophy in these cases show the tangled and

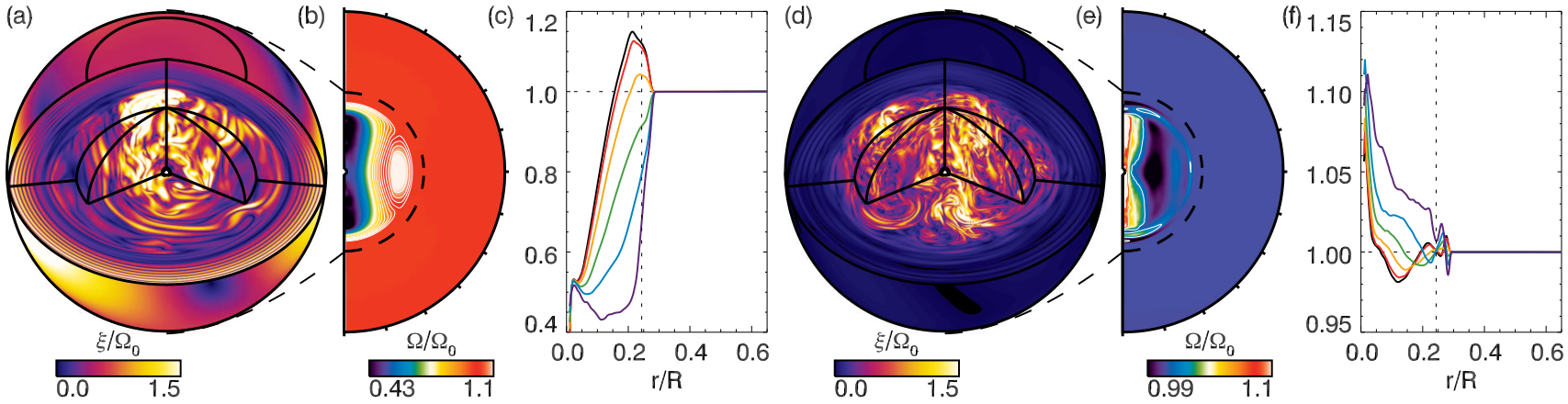

Figure 10.4: Comparison of the hydrodynamic Case *H4* in panels (a)-(c) and MHD Case *M4* in (d)-(f). (a, d) Orthographic volume projection of the rotation rate normalized enstrophy ξ/Ω_0 in the core. (b, e) Time- and azimuthally-averaged angular velocity Ω shown with radius and latitude. (c, f) Radial dependence of Ω at specific latitudes. The location of the projected volume projection is indicated with dashed lines.

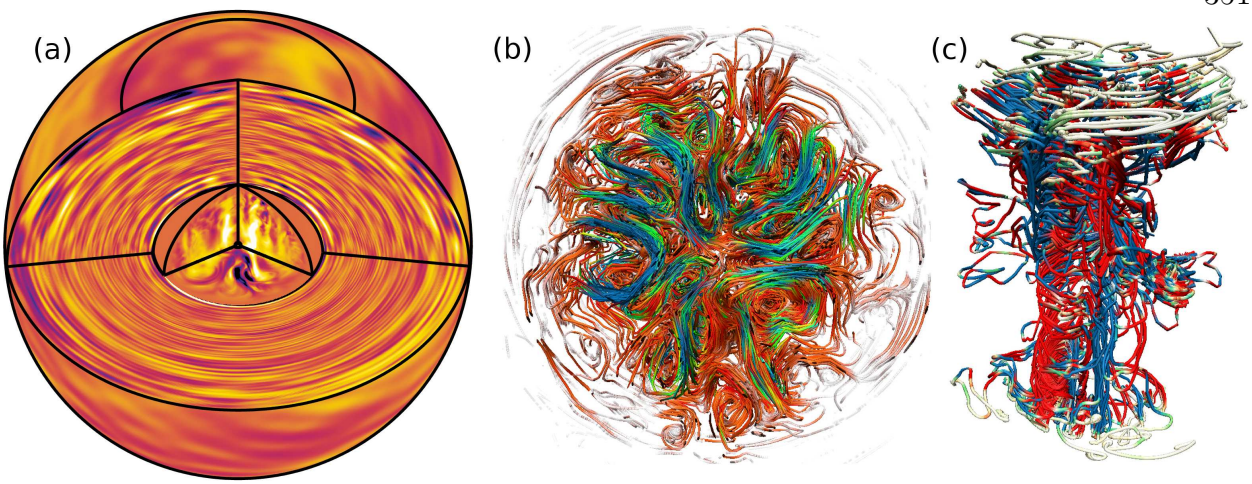

Figure 10.5: Radial velocity shown in an orthographic volume projection for Case *M4*, with the velocities outside the core scaled to $10\,\mathrm{cm\,s^{-1}}$ and those in the core scaled to $100\,\mathrm{m\,s^{-1}}$. Downflows are dark, upflows light. Gravity waves are visible in the radiative zone and columnar convective structures can be seen in the core. (b) Instantaneous velocity streamlines in the convective core, cut at the equator in Case *M16*. Color indicates the magnitude of the velocity, with slow flows of about $10\,\mathrm{m\,s^{-1}}$ in red and fast flows of about $500\,\mathrm{m\,s^{-1}}$ in blue. (c) Instantaneous velocity streamlines of single convective column, showing only a weak linking between adjacent columns and a helicity reversal across the equator. Color indicates the direction of the vertical velocity v_z, with red positive and blue negative.

filamentary nature of the flows within their cores and the high radial wavenumber gravity modes that the convective overshooting excites in their radiative exteriors. It also serves to highlight the dramatically different amplitude of the modes excited in the two cases, the hydrodynamic case shows modes with a fair amount of enstrophy, whereas the magnetic case has much less. The reason for this becomes clear when one considers Figures 10.4(c, f). Case *H4* has a profound radial differential rotation with the deepest portions of the core rotating 50% more slowly than the frame rate, and 70% more slowly than the more rapidly rotating flows near the overshooting region at 0.2 R. Thus the flows carrying energy in this simulation are also very effective at transporting angular momentum out of the core. The meridional profile of the angular velocity in this case is shown in Figure 10.4b, where a prominent Stewartson column is formed along the rotation axis. It is quite remarkable that

this situation is completely reversed in the magnetic case. The slow central column in Case *H4* becomes a region of more rapid rotation, though it rotates only about 7% more rapidly than the radiative exterior. The MHD Case *M4* shares all parameters with *H4*, save for the addition of magnetic fields and a higher horizontal resolution. Yet the radial contrast in differential rotation for *M4* is only about 10% that of the hydrodynamic case.

The flow patterns in Case *M4* become more clear in Figure 10.5a, where strong swirling columnar flows pervade the core and high radial order gravity modes are visible outside of it. These columns are also present at larger rotation rates as seen in the velocity field line tracing of Figure 10.5b, where the equatorial cut shows the cross-section of the convective columns in Case *M16*. There are many weaker columns that are fairly localized. The stronger flows in contrast have a much greater radial extent. These flows are the primary conduits for radial thermal angular momentum transport. An isolated convective column is shown in profile in Figure 10.5c. The color indicates the orientation of the vertical flows v_z. The reversal of the sign of the vertical flows mirrors the helicity reversal across the equator. Unlike earlier simulations in A-type stars, there is less cross-linking between adjacent columns. This is likely due to the much stiffer stable stratification in these simulations, with the entropy gradient being at least several hundred times greater.

The angular momentum flux balance for Cases *H4* and *M4* are shown in Figure 10.6. Only the fluxes in cylindrical radius $\lambda = r\sin\theta$ are shown as the vertical transport is relatively small. The fluxes are averaged in time and azimuth and then integrated cylindrically (with $z = r\cos\theta$). The hydrodynamic Case *H4* has only three possible fluxes of angular momentum: Reynolds stress $\overline{\rho}\lambda\langle v'_\lambda \mathrm{v}'_\phi\rangle$, angular momentum advection by meridional circulations $\langle\rho\mathbf{v}_{MC}\rangle\lambda\langle\mathrm{v}_\phi\rangle$, and those due to viscous stresses $\overline{\rho}\nu\lambda^2\frac{\partial\Omega}{\partial\lambda}$. The primary balance seen in Figure 10.6a is between the Reynolds stresses and the viscous stresses as is typical of a hydrodynamic ASH simulation with moderate levels of turbulence. The Reynolds stresses arising from the convective columns pushes angular momentum outward, whereas the viscous stresses transport it inward. The meridional flows play a passive role accounting for about

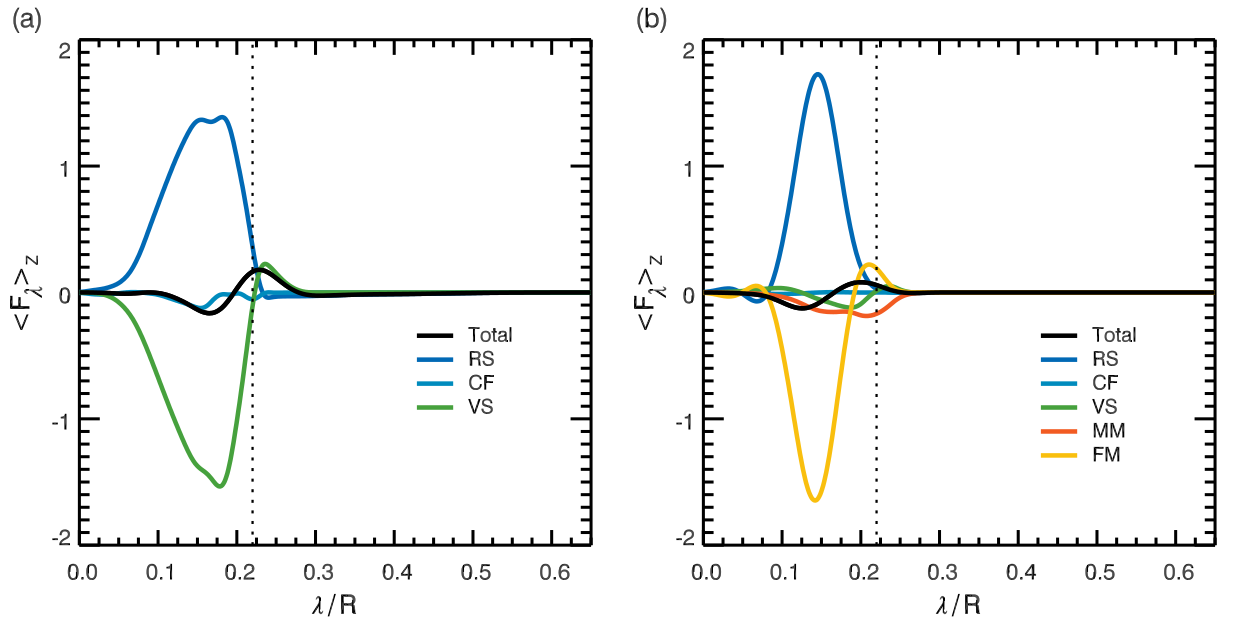

Figure 10.6: A comparison of angular momentum transport mechanisms in Cases *H4* and *M4*. The cylindrically-averaged angular momentum fluxes $\langle F_\lambda \rangle_z$ are shown with proportional cylindrical radius λ/R for (a) Case *H4* and (b) Case *M4*, in units of $10^{40}\,\mathrm{g\,s^{-2}}$. The flux components are the total flux (black), the Reynolds stress (RS; blue), the advection by the meridional circulation (MC; teal), viscous stresses (VS; green), mean Maxwell stresses (MM; red), and fluctuating Maxwell stresses (FM; orange).

5% of the overall transport. The flux balance is not perfect as the time scale for the viscous spread of the differential rotation into the stable region is many thousands of years, much longer than can be simulated.

Figure 10.6b exhibits the angular momentum fluxes in cylindrical radius for the MHD Case *M4*. The balance relative to the hydrodynamic case have been radically altered with the inclusion of magnetic fields and their associated angular momentum transport through Maxwell stresses. The primary balance is between the angular momentum flux arising from the fluctuating Maxwell stress $\frac{\lambda}{4\pi}\langle B'_\lambda B'_\phi \rangle$ and that of the Reynolds stress, with weaker contributions from the meridional circulation and the mean Maxwell stress $\frac{\lambda}{4\pi}\langle B_\lambda \rangle \langle B_\phi \rangle$. The Maxwell stresses transport angular momentum inward countering the outward transport by the Reynolds stress that arises from the rotationally constrained convective columns. Now

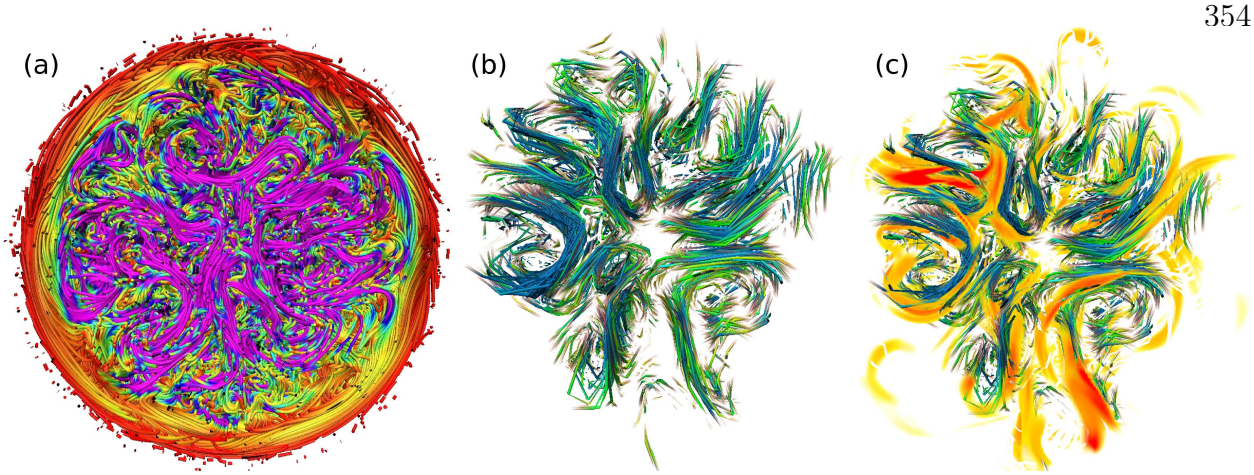

Figure 10.7: A comparison of magnetic and velocity fields in Case *M16*. (a) Magnetic field line tracing in a snapshot of Case *M16*, colored by field amplitude, looking down the rotation axis at the equatorial cross-section of the magnetic field structures. The peak fields seen here are 0.75 MG (purple, which are also the most coherent in the core) and the weakest fields about are 1 G (red). The strongest magnetic fields are the most interconnected, threading throughout the core. (b) Instantaneous velocity field lines for the strongest flows, and (c) with an overlay of magnetic energy for the strongest magnetic fields. This exhibits the slight spatial offset between the strongest flows and strongest magnetic fields.

comparing Cases *H4* and *M4*, the role of the magnetic field is very similar to that of the viscous diffusion, elucidating its visco-elastic nature in a convective dynamo. The difference in transport mechanisms in these two models is partly responsible for the differences in their distributions of angular momentum. However, it is only part of the story as the role of the magnetism is two-fold: first it provides an alternative channel for transport and second the presence of magnetism acts to reduce the mean shear utilizing it as an energy source for building magnetic field as seen in earlier chapters. In the core convection dynamos, the magnetic field acts to suppress the central Stewartson layer that otherwise becomes the dominant flow structure in the core as in Case *H4*.

10.6 Dynamo Action Achieved in a B-type Star Core

The magnetic fields built through dynamo action in the core is of an even finer scale than the velocity field, being twisted, braided, and pulled through the core by the strong

Table 10.2
Global Properties of the Evolved Convection

Case	KE	KE_{DR}	KE_{C}	KE_{MC}	ME	FME	TME	PME	ME/KE	B_{max}	$\Delta\Omega_r/\Omega_0$
H4	73.1	66.4 (91.%)	6.57 (8.9%)	13.0 (0.1%)	–	–	–	–	–	–	0.495
M4	3.91	0.17 (4.5%)	3.72 (95.%)	2.34 (0.6%)	4.08	3.71 (91.%)	0.30 (7.4%)	0.07 (1.7%)	1.06	0.76	-0.078
M8	2.20	0.14 (6.2%)	2.06 (94.%)	0.81 (0.4%)	4.52	4.19 (93.%)	0.20 (4.5%)	0.13 (2.8%)	2.07	1.06	-0.017
M16	1.42	0.09 (6.5%)	1.32 (93.%)	0.54 (0.4%)	5.42	5.17 (95.%)	0.15 (2.8%)	0.10 (1.9%)	3.86	1.17	-0.012

Table 10.2: Total kinetic energy density (KE) and those of differential rotation (KE_{DR}) and convective (KE_{C}) in units of $10^7\,\mathrm{erg\,cm^{-3}}$. The meridional circulation (KE_{MC}) kinetic energy is in units of $10^5\,\mathrm{erg\,cm^{-3}}$. Total magnetic energy density (ME) and of toroidal (TME), fluctuating (FME), and poloidal (PME). Both energies are averaged in time and volume and are shown in units of $10^7\,\mathrm{erg\,cm^{-3}}$, and component percentages in parentheses, with the exception of ME which is shown relative to KE which is shown as a ratio in the third to last column. The peak magnetic field strength in units of 10^6 G is B_{max}. The relative radial differential rotation across the core is $\Delta\Omega_r/\Omega_0$.

radial flows. The magnetic field is also stored in the overshooting region allowing it to be slowly amplified, forming a magnetic cocoon around the core as is somewhat visible in Figure 10.7a. The knotted and braided character of the field is established through successive core-crossing events where strong downdrafts knead the field into shape. Given the tangled filamentary field seen in Figure 10.7, it is no surprise that over 90% of the magnetic energy is contained in the fluctuating fields. This is largely due to the large Pr_m of the system, which tends to build small-scale field as seen in §3.4.

As the rotation rate is increased, the differential rotation becomes increasingly small in the cores of the simulated B-type stars (Table 10.2). While there is still a central region of differential rotation in each of these systems, the amount of energy contained in this mean flow becomes ever weaker. Combined with slightly weaker convective flows, this leads to the decreasing kinetic energy seen in the first column of Table 10.2. Accompanying this reduced differential rotation and total kinetic energy is an increase in magnetic energy. Indeed, the ease with which these core dynamos became superequipartition is remarkable, where the magnetic energy exceeds the kinetic energy by a factor of 1.06 for *M4*, 2.07 for *M8*, 3.86 for *M16*. The diffusivities within these simulations was decreased to maintain the level of supercriticality, and yet the amount of total kinetic energy in the system continues to decrease. It begs the question whether there is a point at which the fields become so strong as convection is no longer efficient enough to carry the heat building up in the core, leading to thermal pulses as convection is briefly reestablished. Further, given that superequipartition states in previous stellar dynamo simulations of A-type stars had only been achieved with the aid of a fossil field present in the radiative zone, it would be quite interesting to extend these simulations by admitting a model primordial field to assess whether states of even greater superequipartition might be achieved.

The magnetic field with the greatest amplitude tends to outline the convective columns, which are strongly rotationally constrained and aligned with the rotation axis. Similar structures have been seen in previous core dynamo simulations (Featherstone et al., 2009),

where there are spatio-temporal offsets between the magnetic structures and the velocity structures. Similarly, the convective dynamo action within the cores of these B-type stars builds magnetic fields that minimize the Lorentz forces through these offsets. Figure 10.7b shows a snapshot of the velocity field lines associated with the flow structures with the greatest kinetic energy. That image is meant to be compared directly with Figure 10.7c, which has an overlay of the magnetic energy. Together these figures exhibit the spatial offsets between the strongest flow structures and the strongest magnetic structures. Such structures arise in superequipartition systems, for if they did not the magnetic fields would quench the convection and disrupting its ability to transport heat. This arrangement must be more energetically favorable than an increased amplitude of the thermal perturbations, which would also increase the heat flux at the expense of enhanced buoyancy and thus faster flows. These two features are the underpinnings of the magneto-Archimedean-Coriolis force balance, wherein the magnetic, thermal, and vortical structures are arranged to minimize the sum of those forces. Here this is accomplished through the spatially offset magnetic fields, which reduce the impact of the Lorentz forces, while the Coriolis forces are minimized through a local baroclinic balance between thermal gradients and the local vortical structures.

10.7 Internal Gravito-Inertial Waves

The overshooting convection excites gravity waves as the flows are buoyantly braked as they enter the stable region. These waves propagate mostly in the horizontal directions, though they also have a weak radial component that allows them to carry energy through the radiative zone. The spectra of these waves are now considered at two radii in the radiative zone of Case *M4*. These modes nominally would propagate and be dissipated, but here this region is not captured and the waves reflect off of the upper boundary. This leads to trapped resonant modes and an enhanced discrete spectrum of modes at those resonant frequencies. Indeed, by comparing Figure 10.8a with Figures 10.8(b, c), it is clear that discrete gravity modes are being excited in Case *M4* within the radiative cavity above the

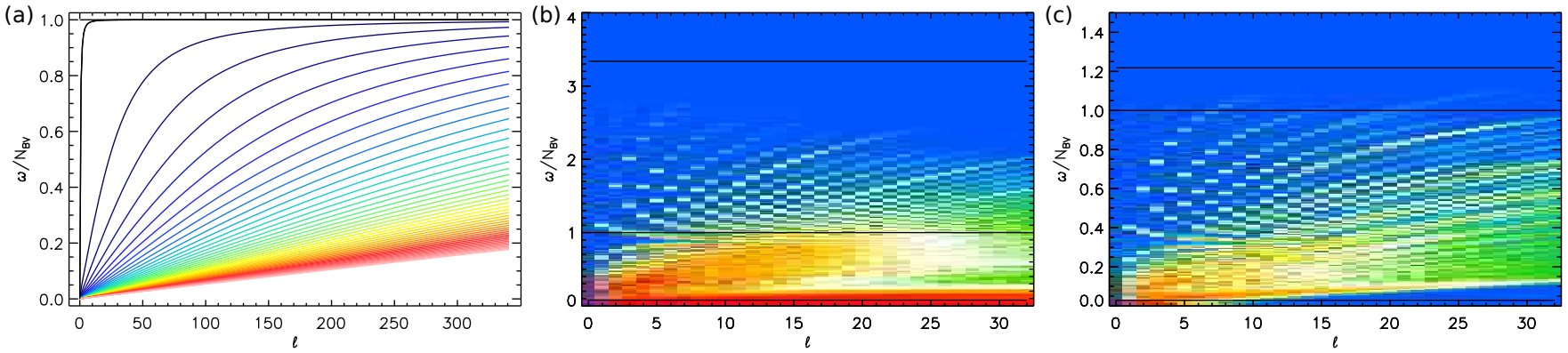

Figure 10.8: Horizontal power spectra of gravity waves excited in the radiative exterior of *M4*. (a) A reference gravity wave spectrum excited in an isothermal atmosphere, with the fundamental mode in black and increasingly larger radial wave numbers from blue to red. (b) The time and m-averaged power spectrum of radial velocities just above the overshooting region on a logarithmic color scale, a bar of low frequency power is visible as are ridges of power far above the local Brunt-Väisälä frequency. (c) The same as in (b) but mid-way through the radiative exterior. The lower black line is the rotation frequency, the black line at $\omega/N_{VB} = 1$ is the local Brunt-Väisälä frequency, and the upper black line is the upper limit of frequencies of modes present at a given radius.

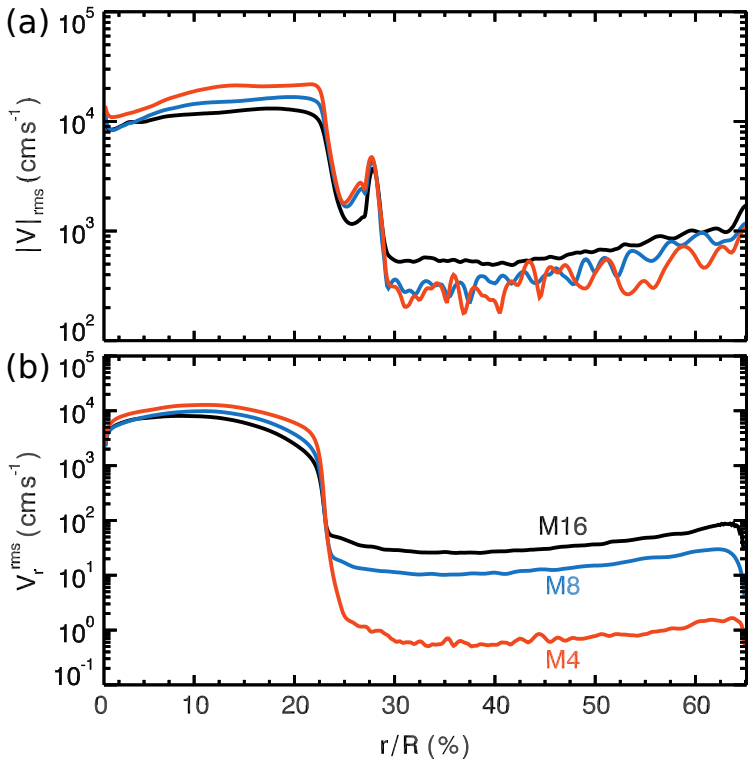

Figure 10.9: Shell and time-averaged rms velocities in the B-type star simulations. (a) The total rms velocity $v_{\rm rms}$, showing little overall change in rms velocity with rotation rate, with *M16* in black, *M8* in blue, and *M4* in red. (b) Rms radial velocity $v_r^{\rm rms}$, showing a 100-fold rise in radial velocity in the radiative exterior, color as in (a).

convective core. Figures 10.8b, c show the time and azimuthal-wavenumber averaged radial velocity power spectra at two depths one just above the overshooting region and another mid-way through the radiative envelope. The influence of the convection is still present near the overshooting region, as is visible in the low-frequency bar of power. The ridges of power extend far beyond the Brunt-Väisälä frequency, indicating that modes reflected from higher in the radiative envelope are propagating in the region. This seems to be more prevalent closer to the core where perhaps a broader spectrum of waves can be excited, or waves that have been reflected from the upper boundary and are now impinging on the core.

What is of potentially greater interest is the ability of those waves to transport energy and angular momentum from the core to near the surface or to a critical layer where they

may break. Figure 10.9 shows the total rms velocity for the three magnetic cases. The change in $v_{\rm rms}$ with a factor of four increase in rotation rate is fairly small, with slightly larger rms values in the core for slower rotation, and the converse in the radiative zone. If one examines the rms radial velocities, there are again modest differences in the core. Yet in stark contrast to the total rms velocities, the radial velocities climb substantially with rotation rate, being 100-fold greater for the same factor of four increase in rotation rate. This encourages a further analysis of the wave transport properties as they scale with rotation rate. Indeed, beyond the increase in the rms radial velocity, there is also an increase in the amplitude of the thermal perturbations. Together these perturbations establish an enthalpy or heat flux that increase with rotation rate

Figure 10.10a shows where $\log \Gamma_S$ (the growth rate of waves arising from entropy diffusion as described in Appendix D) is greater than zero over a range of frequencies varying between zero and 1.4 times the resonance frequency of the domain, which can loosely be defined as $\omega_0 = \int_{r_1}^{r_2} N/r dr$. The actual Brunt-Väisälä frequency divided by the resonance frequency is the black line. The growth rate is largest in the overshooting region where κ is still large, with a growth rate of about 6 hours. This is about on par with the the excitation rate, but it decays exponentially away from this region dropping to about 280 days at mid-radiative zone. Modes propagating near the upper boundary, whose local Brunt-Väisälä frequency is above resonance, can also grow due to entropy diffusion though very slowly. The most worrisome place to be is obviously when $\omega \approx N$ as the growth rate can be come very large.

The remedy for any possible issues arising from entropy diffusion would come from using only the thermal diffusion arising from the combination of the Braginskii conductivity and radiation under the diffusion approximation. The radiation diffusion dominates the thermal conductivity by at least three orders of magnitude in these stars, as seen in Figure 10.10b. The radiation is clearly doing the yeoman's work, smoothing out temperature perturbations. Moreover, replacing the entropy diffusion by the thermal diffusion looks very promising, as

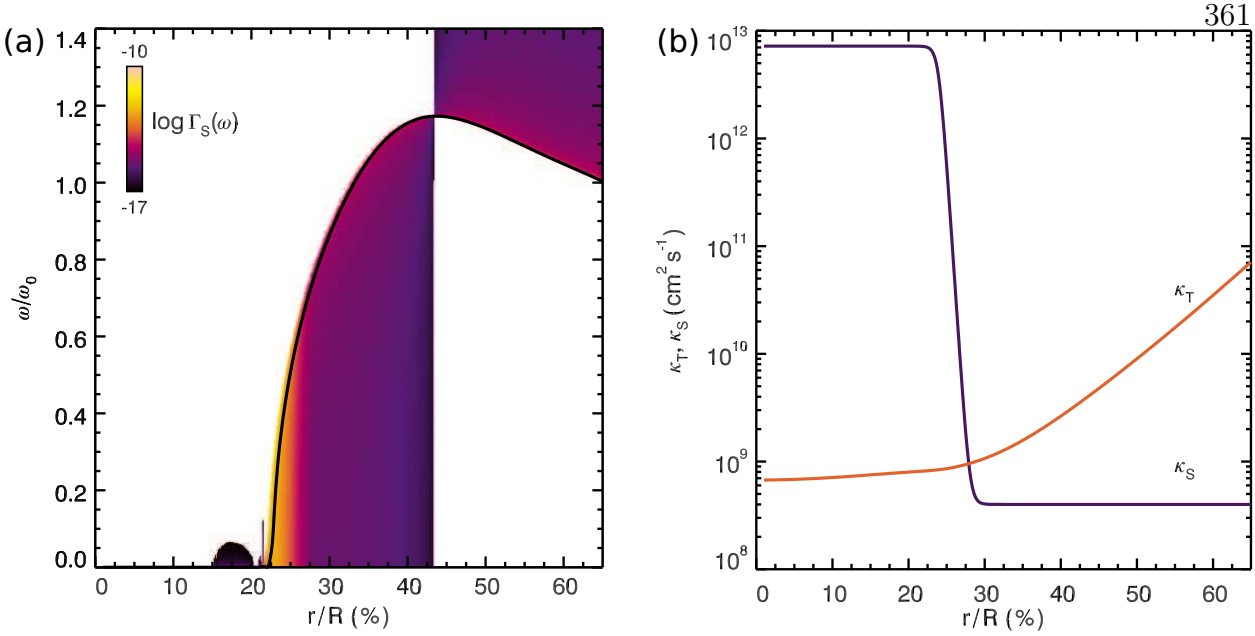

Figure 10.10: (a) Regions of wave instability due to entropy diffusion as evidenced through the wave growth rate Γ_S, indicating that waves with frequencies close to the Brunt-Väisälä frequency can grow faster than they are dissipated. (b) A comparison of the magnitudes of the entropy diffusion and the thermal diffusion coefficients, showing that the thermal diffusion is more than sufficient to maintain stability.

the thermal diffusion is actually quite a bit larger than the entropy diffusion. Surprisingly, the gravity waves should be much more damped than in the current models. Thus there is no reason one should be using entropy diffusion rather than the temperature diffusion for these models: it instead should be zero in the radiative zone. It may further be possible to remove this problem entirely by splitting the thermal diffusion into two components, one that uses the molecular values on the mean temperature and an artificially increased effective thermal diffusion that acts on temperature perturbations in the convection zone but is then tapered back to its molecular value in the radiative zone.

10.8 Conclusions

These preliminary results are promising, with superequipartition fields being built through dynamo action that reach MG strengths. It is likely that a number of different

superequipartition states can be realized. With recent experience with geodynamo studies and those with core convection in A-type stars, an external magnetic field that threads the core but that resides in a separate region can lead to strongly superequipartition states. These states may also be sensitive to the functional forms of the SGS diffusivities that are imposed. The ASH simulations of B-type stars presented here may set the groundwork for finding buoyant fields within more turbulent settings, particularly those that admit fossil fields in the radiative exterior. In keeping with previous results (Brun et al., 2005; Featherstone et al., 2009), there is a marked difference in the differential rotation between magnetic and hydrodynamic simulations. The gravity wave spectrum seen here shows discrete modes that may be trapped in the cavity of the truncated radiative envelope. Furthermore, to better assess the properties of the internal waves, there are hints about how to better handle diffusion in regions with stable stratifications within the context of the anelastic approximation.

There is much promise in studying the coupled core and radiative envelope dynamics of massive O and B-type stars. In order to make contact with the observed surface magnetism of those stars and to better understand their wind-driven mass-loss, simulations that capture the convective core and the internal waves that connect it to the surface of the star will require a unified treatment of both of these regions. The simulations presented here represent an initial description of such coupled dynamics, and thus it is anticipated that substantial advances in understanding the properties of this coupling and its observational implications will be made in the near future. These massive stars are the crucibles in which the elements are forged and they are the mechanism by which the galaxies are seeded with those elements. Hence it is of great interest to ascertain how they end their lives. Namely, do they explode as supernovae and distribute their elements in a single burst, or do their strong winds and the subsequent mass-loss provide a slow and steady means for that distribution. The relative importance of these mechanisms likely depends on the internal dynamics of these stars, which involves convection, rotation, magnetism, and internal gravity waves.

Chapter 11

Modeling the Solar Near-Surface Shear Layer

"Truth is much too complicated to allow anything but approximations." – John von Neumann

This chapter presents some aspects of the Compressible Spherical Segment (CSS) code, from its numerical foundations to some of its applications. The science goal that started work on this code was a project to assess the role of thermal plumes in the solar near-surface shear layer, which since blossomed into many other projects. The first version of the 2-D code was described in Hurlburt & Rucklidge (2000). However, the only remaining similarity between the two codes is the acronym. The original version of the code was not scalable and required large eddy diffusivities for stability. In the intervening time, the code has been completely rewritten (several times over) so as to be highly scalable, numerically stable at low levels of diffusion, and to have a wide range of features. Thus, there is no piece of the original code that remains.

The motivation for the chapter is to understand some aspects of the solar differential rotation. To that end, it is worthwhile to recap some of the highlights of features within the solar interior. While the radiative interior of the Sun rotates at a nearly uniform angular velocity, the convection zone rotates differentially with latitude and radius (e.g., Deubner et al., 1979; Brown et al., 1989; Thompson et al., 1996; Schou et al., 1998; Howe et al., 2000; Thompson et al., 2003). The interface between the two has come to be known as the tachocline (Spiegel & Zahn, 1992), a region important in determining both the global dy-

namics of the overlying convection zone (Miesch, 2005) and likely the operation of the cyclic solar dynamo (Charbonneau, 2010). The angular velocity in the bulk of the convection zone reflects departures from a cylindrically invariant Proudman-Taylor state. Such departures are likely due to the presence of radial shear in the stably stratified tachocline, which induces latitudinal temperature gradients there. This thermal structures is subsequently felt throughout the convection zone, where a thermal wind or baroclinic balance is established between cylindrical gradients in the differential rotation and the thermal field (Rempel, 2005; Miesch et al., 2006; Balbus et al., 2012). This yields an angular velocity profile in the bulk of the convection zone with only weak radial gradients bounded by the tachocline at the base and the near surface shear layer at the top. It is this the origin of the upper shear layer which is largely the scientific subject of this chapter.

As in Figure 3.5, the near surface shear layer (NSSL) occupies the upper $\sim 5\%$ of the Sun by radius. Within this region, the angular velocity increases by about 15 nHz from the photosphere to about $0.95\,\mathrm{R}_\odot$. The gradient close to the photosphere is fairly large, being consistent with angular momentum conservation per unit mass (Corbard & Thompson, 2002; Howe et al., 2006). The gradient becomes flatter with increased depth and with increasing latitude, with some suggestion, not shared by all analyses, that it may reverse in the uppermost layers for latitudes above $\sim 45 - 55^\circ$ (Corbard & Thompson, 2002; Howe et al., 2006). These features may imply that the near-surface differential rotation can have a substantial variation in time throughout the solar cycle. It is unknown what role the NSSL plays in the global dynamics of the Sun or in the operation of the solar dynamo, but torsional oscillations within it show strong cycle dependencies.

Much of the dynamics in the NSSL arises from the vigorous granular-scale convection driven by radiative cooling and large superadiabatic gradients in the photosphere. The collective interaction of granular-scale flows (typical size of 1 Mm, lifetime of 0.2 hr) is a major component in the formation of mesogranular (5-10 Mm, 5 hr) and supergranular (15-35 Mm, 24 hr) scales (Rast, 1995; Rieutord et al., 2000; Rast, 2003), and these in turn likely

interact in the NSSL with larger-scale motions generated below, possibly leaving signatures in the surface flows (Lisle et al., 2004). The shear layer depth is of the same order as the length scale of supergranulation, which is weakly influenced by rotation. This dynamical coupling between vigorous small-scale convection and larger-scale rotationally influenced motions results in angular momentum transport within the layer maintaining the observed radial shear (De Rosa et al., 2002). Finally, recent results using the latest HMI Dopplergram data have ascertained some information about the even larger scales of giant cells, including the Reynolds stresses that accompany them (Hathaway et al., 2013). Those results give some hope for contact between theory and observations that may disentangle the dynamical differences between the deep interior and the near-surface region.

11.1 Equations Solved in CSS

With §3.1 as a reference, consider the vector form of the resistive MHD system of equations in a rotating spherical coordinate system

$$\frac{\partial \rho}{\partial t} + \boldsymbol{\nabla} \cdot \rho \mathbf{u} = 0, \tag{11.1}$$

$$\frac{\partial \rho \mathbf{u}}{\partial t} + \boldsymbol{\nabla} \cdot \left[\rho \mathbf{u} \otimes \mathbf{u} + \left(P + \frac{\mathbf{B}^2}{8\pi} \right) \mathbf{I} - \frac{1}{4\pi} \mathbf{B} \otimes \mathbf{B} - \boldsymbol{\mathcal{D}} \right] = \rho \left[\boldsymbol{\nabla} \phi_{\text{eff}} + 2\mathbf{v} \times \boldsymbol{\Omega}_0 \right], \tag{11.2}$$

$$\frac{\partial E_M}{\partial t} + \boldsymbol{\nabla} \cdot \left[\mathbf{u}(E_M + P) + \mathbf{q} - \mathbf{u} \cdot \boldsymbol{\mathcal{D}} - \frac{1}{4\pi} \mathbf{u} \cdot \mathbf{B}\mathbf{B} + \frac{\eta}{4\pi} \left(\frac{1}{2} \boldsymbol{\nabla} \mathbf{B}^2 - \mathbf{B} \cdot \boldsymbol{\nabla} \mathbf{B} \right) \right] = 0, \tag{11.3}$$

$$\frac{\partial \mathbf{B}}{\partial t} = \boldsymbol{\nabla} \times [\mathbf{u} \times \mathbf{B} - \eta \boldsymbol{\nabla} \times \mathbf{B}], \tag{11.4}$$

$$E_M = \frac{1}{2} \rho \mathbf{u}^2 + \frac{\mathbf{B}^2}{8\pi} + \epsilon + \rho \phi_{\text{eff}}, \tag{11.5}$$

with Ω_0 the frame rotation rate, the effective gravitational potential $\phi_{\text{eff}} = \phi + \lambda^2 \Omega_0^2 / 2$, and λ the distance to the rotation axis. First the energy equation is reduced to an evolution equation for the entropy. This allows greater compatibility between the ASH and CSS codes, but one does lose some nice properties of the conservation equations. In any case, the entropy equation follows from the application of the second law of thermodynamics and through the substitution of Equations 11.1, 11.2, 11.4, and 11.5 into Equation 11.3, yielding

$$\frac{\partial s}{\partial t} = -\mathbf{u} \cdot \boldsymbol{\nabla} s - \frac{1}{\rho T} \left[\boldsymbol{\nabla} \cdot \mathbf{q} - \Phi - \rho \epsilon \right] + \mathrm{D}_s, \tag{11.6}$$

where D_s represents an entropy diffusion that will be defined later, ϵ is heating or cooling term, Φ is the combined ohmic and viscous heating, $\mathbf{q}$ is a heat flux. In addition to the entropy, the form of the equations evolved in CSS is slightly modified so as to keep the primitive variables to allow easier implementation of certain boundary conditions, speed computation, and to minimize communication, yet the conservative form is retained for most of the Eulerian terms as

$$\frac{\partial \rho}{\partial t} = -\boldsymbol{\nabla} \cdot \rho \mathbf{u} + \mathrm{D}_\rho, \tag{11.7}$$

$$\frac{\partial \mathbf{u}}{\partial t} = -\frac{\mathbf{u}}{\rho} \frac{\partial \rho}{\partial t} - \frac{1}{\rho} \boldsymbol{\nabla} \cdot \left[\rho \mathbf{u} \otimes \mathbf{u} + \frac{\mathbf{B}^2}{8\pi} \mathbf{I} - \frac{1}{4\pi} \mathbf{B} \otimes \mathbf{B} \right] - \frac{1}{\rho} \boldsymbol{\nabla} P + \boldsymbol{\nabla} \phi_{\mathrm{eff}} + 2\mathbf{v} \times \boldsymbol{\Omega}_0 + \mathbf{D}_\mathbf{u}, \tag{11.8}$$

$$\frac{\partial \mathbf{A}}{\partial t} = \mathbf{v} \times \mathbf{B} + \mathbf{D}_\mathbf{A}, \tag{11.9}$$

$$\mathbf{B} = \boldsymbol{\nabla} \times \mathbf{A}, \tag{11.10}$$

with D_ρ, $\mathbf{D}_\mathbf{u}$, and $\mathbf{D}_\mathbf{A}$ being diffusive terms whose form depend upon the choice of diffusion scheme. The pressure gradient is isolated to allow a variety of boundary conditions to be imposed. The vector potential form of the induction equation is employed to ensure that the solenoidality constraint on $\mathbf{B}$ is met to within the accuracy of the numerical scheme. Expanding these equations in spherical coordinates and reserving the diffusion related terms for a later section, the evolved equations are

$$\frac{\partial \rho}{\partial t} = -\frac{1}{r^2}\frac{\partial}{\partial r} r^2 \left[\rho u_r\right] - \frac{1}{r\sin\theta}\frac{\partial}{\partial \theta}\sin\theta\left[\rho u_\theta\right] - \frac{1}{r\sin\theta}\frac{\partial}{\partial \phi}\left[\rho u_\phi\right] + \mathrm{D}_\rho, \tag{11.11}$$

$$\begin{aligned}\frac{\partial u_r}{\partial t} = &-\frac{u_r}{\rho}\frac{\partial \rho}{\partial t} - \frac{1}{\rho r^2}\frac{\partial}{\partial r} r^2 \left[\rho u_r^2 + \frac{1}{8\pi}\left(B_\theta^2 + B_\phi^2 - B_r^2\right)\right] - \frac{1}{\rho r\sin\theta}\frac{\partial}{\partial \theta}\sin\theta\left[\rho u_r u_\theta - \frac{B_r B_\theta}{4\pi}\right] \\ &- \frac{1}{\rho r\sin\theta}\frac{\partial}{\partial \phi}\left[\rho u_r u_\phi - \frac{B_r B_\phi}{4\pi}\right] - \frac{1}{\rho}\frac{\partial P}{\partial r} - g + r\sin^2\theta\Omega_0^2 + 2\Omega_0\sin\theta u_\phi + \hat{\mathbf{r}}\cdot\mathbf{D}_\mathbf{u},\end{aligned} \tag{11.12}$$

$$\begin{aligned}\frac{\partial u_\theta}{\partial t} = &-\frac{u_\theta}{\rho}\frac{\partial \rho}{\partial t} - \frac{1}{\rho r^2}\frac{\partial}{\partial r} r^2 \left[\rho u_\theta u_r - \frac{B_\theta B_r}{4\pi}\right] - \frac{1}{\rho r\sin\theta}\frac{\partial}{\partial \theta}\sin\theta\left[\rho u_\theta^2 + \frac{1}{8\pi}\left(B_r^2 + B_\phi^2 - B_\theta^2\right)\right] \\ &- \frac{1}{\rho r\sin\theta}\frac{\partial}{\partial \phi}\left[\rho u_\theta u_\phi - \frac{B_\theta B_\phi}{4\pi}\right] - \frac{1}{\rho r}\frac{\partial P}{\partial \theta} + r\sin\theta\cos\theta\Omega_0^2 + 2\Omega_0\cos\theta u_\phi + \hat{\boldsymbol{\theta}}\cdot\mathbf{D}_\mathbf{u},\end{aligned} \tag{11.13}$$

$$\begin{aligned}\frac{\partial u_\phi}{\partial t} = &-\frac{u_\phi}{\rho}\frac{\partial \rho}{\partial t} - \frac{1}{\rho r^2}\frac{\partial}{\partial r} r^2 \left[\rho u_\phi u_r - \frac{B_\phi B_r}{4\pi}\right] - \frac{1}{\rho r\sin\theta}\frac{\partial}{\partial \theta}\sin\theta\left[\rho u_\phi u_\theta - \frac{B_\phi B_\theta}{4\pi}\right] \\ &- \frac{1}{\rho r\sin\theta}\frac{\partial}{\partial \phi}\left[\rho u_\phi^2 + \frac{1}{8\pi}\left(B_r^2 + B_\theta^2 - B_\phi^2\right)\right] - \frac{1}{\rho r\sin\theta}\frac{\partial P}{\partial \phi} - 2\Omega_0\left(\sin\theta u_r + \cos\theta u_\theta\right) + \hat{\boldsymbol{\phi}}\cdot\mathbf{D}_\mathbf{u},\end{aligned} \tag{11.14}$$

$$\begin{aligned}\frac{\partial s}{\partial t} = &-u_r\frac{\partial s}{\partial r} - \frac{u_\theta}{r}\frac{\partial s}{\partial \theta} - \frac{u_\phi}{r\sin\theta}\frac{\partial s}{\partial \phi} \\ &- \frac{1}{\rho T}\left[\frac{1}{r^2}\frac{\partial}{\partial r} r^2\left[q_r\right] + \frac{1}{r\sin\theta}\frac{\partial}{\partial \theta}\sin\theta\left[q_\theta\right] + \frac{1}{r\sin\theta}\frac{\partial}{\partial \phi}\left[q_\phi\right] - \Phi - \rho\epsilon\right],\end{aligned} \tag{11.15}$$

and the vector potential equations in component form are

$$\frac{\partial A_r}{\partial t} = u_\theta B_\phi - u_\phi B_\theta + \hat{\mathbf{r}}\cdot\mathbf{D}_\mathbf{A}, \tag{11.16}$$

$$\frac{\partial A_\phi}{\partial t} = u_\phi B_r - u_r B_\phi + \hat{\boldsymbol{\theta}}\cdot\mathbf{D}_\mathbf{A}, \tag{11.17}$$

$$\frac{\partial A_\phi}{\partial t} = u_r B_\theta - u_\theta B_r + \hat{\boldsymbol{\phi}}\cdot\mathbf{D}_\mathbf{A}. \tag{11.18}$$

The closure of the system is the equation of state given ρ and s, which arrives in the form of $P = P(\rho, s)$. For a calorically perfect gas this is $P = (\gamma - 1)\, C_V \rho T = \rho^\gamma e^{S/C_V}$. The physical heat flux is currently defined in the radiation diffusion approximation as

$$\mathbf{q} = -\frac{4acT^3}{3\rho\kappa_\mathrm{R}\left(\rho, s\right)}\boldsymbol{\nabla} T\left(\rho, s\right), \tag{11.19}$$

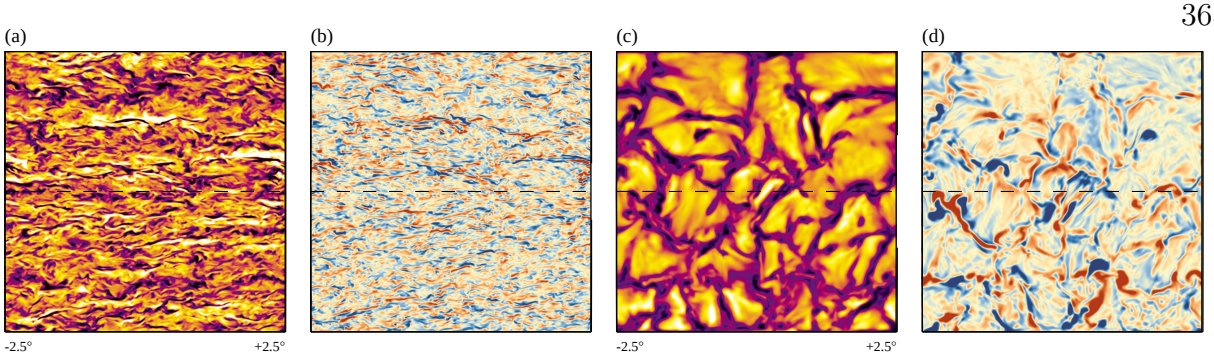

Figure 11.1: MHD simulations with CSS. Simulations of the magneto-rotational instability in spherical coordinates with (a) radial velocities and (b) radial magnetic field near the upper boundary of the simulation. An MHD convection simulation with (c) radial velocities and (d) radial magnetic field near its upper boundary.

where $\kappa_{\rm R}(\rho, s)$ is the Rosseland mean opacity. When not using the perfect gas equation of state, the temperature, pressure and opacity are interpolated within a tabular equation of state such as OPAL or the Milhalas-Hummer-Dappen equation of state. Finally, there is an additional feature in CSS that allows the artificial reduction of the sound speed by modifying the continuity equation as seen in Appendix E. Two example MHD calculations in local domains near the equator are shown in Figure 11.1. The simulation illustrated in Figures 11.1(a, b) had a stable stratification and admitted the magnetorotational instability, whereas the other simulation was in the same domain with an adiabatic stratification and is convectively unstable.

11.2 Boundary Conditions

There are several choices of boundary conditions within CSS. These choices are described in following two subsections, one regarding the radial boundaries and the other regarding the latitudinal boundaries. Currently, the only option for the longitudinal direction is periodicity.

11.2.1 Radial Boundaries

The entropy or its radial gradient may be specified at the radial boundaries as

$$\begin{cases} s(\theta,\phi,r_1) & = f(\theta,\phi) \quad \text{Dirichlet} \\ \dfrac{\partial s}{\partial r}(\theta,\phi,r_1) & = g(\theta,\phi) \quad \text{Neumann} \end{cases} \tag{11.20}$$

and similarly on the upper boundary

$$\begin{cases} s(\theta,\phi,r_2) & = f(\theta,\phi) \quad \text{Dirichlet} \\ \dfrac{\partial s}{\partial r}(\theta,\phi,r_2) & = g(\theta,\phi) \quad \text{Neumann} \end{cases} \tag{11.21}$$

where r_1 and r_2 are the lower and upper radial boundaries of the computational domain, and f and g are arbitrary functions of the horizontal coordinates.

The latitudinal velocity on radial boundaries may be stress-free or no-slip as follows:

$$\begin{cases} u_\theta|_{r_1,r_2} & = 0 \quad \text{No-Slip} \\ \left.\dfrac{\partial u_\theta}{\partial r}\right|_{r_1,r_2} & = \left.\dfrac{u_\theta}{r}\right|_{r_1,r_2} \quad \text{Stress-Free} \end{cases} \tag{11.22}$$

as is also the case for the longitudinal velocity

$$\begin{cases} u_\phi|_{r_1,r_2} & = 0 \quad \text{No-Slip} \\ \left.\dfrac{\partial u_\phi}{\partial r}\right|_{r_1,r_2} & = \left.\dfrac{u_\phi}{r}\right|_{r_1,r_2} \quad \text{Stress-Free} \end{cases} \tag{11.23}$$

If the boundaries are impenetrable, then $u_r|_{r_1,r_2} = 0$; the case of open boundaries is handled below. To ensure that the pressure gradient at the boundary is consistent with an impenetrable boundary to machine precision, it is set at the latitudinal and radial boundaries. For the radial boundaries, first all terms in the radial momentum equation except for the pressure gradient are evaluated, which yields

$$\begin{aligned} \delta u_r = &-\frac{u_r}{\rho}\frac{\partial \rho}{\partial t} - \frac{1}{\rho r^2}\frac{\partial}{\partial r} r^2 \left[\rho u_r^2 + \frac{1}{8\pi}\left(B_\theta^2 + B_\phi^2 - B_r^2\right)\right] - \frac{1}{\rho r \sin\theta}\frac{\partial}{\partial \theta}\sin\theta\left[\rho u_r u_\theta - \frac{B_r B_\theta}{4\pi}\right] \\ &- \frac{1}{\rho r \sin\theta}\frac{\partial}{\partial \phi}\left[\rho u_r u_\phi - \frac{B_r B_\phi}{4\pi}\right] - g + r\sin^2\theta\Omega_0^2 + 2\Omega_0 \sin\theta u_\phi + \hat{\mathbf{r}}\cdot\mathbf{D}_\mathbf{u}. \end{aligned} \tag{11.24}$$

The remaining terms are

$$\left.\frac{\partial u_r}{\partial t}\right|_{r_1,r_2} = 0 = \left.\delta u_r\right|_{r_1,r_2} - \left.\frac{1}{\rho}\frac{\partial P}{\partial r}\right|_{r_1,r_2}. \tag{11.25}$$

Thus to ensure the consistency of the velocity evolution equations, the radial gradient of the pressure is set at the upper and lower radial boundaries as

$$\left.\frac{\partial P}{\partial r}\right|_{r_1,r_2} = \left.\rho\delta u_r\right|_{r_1,r_2}. \tag{11.26}$$

The magnetic boundary conditions also have two orthogonal options. They can be perfectly conducting or normal-field. The perfectly conducting boundary implies a surface current such that the normal field vanishes at the boundary. While there are many choices due to the gauge freedom of the vector potential, only the simplest is implemented wherein

$$\begin{cases} \left.A_\theta\right|_{r_1,r_2} = 0 \\ \left.A_\phi\right|_{r_1,r_2} = 0 \end{cases} \qquad \text{Perfect Conductor} \tag{11.27}$$

while A_r is left free on the boundaries. This satisfies the constraint that $\left.B_r\right|_{r_1,r_2} = 0$, and that the horizontal field is nearly unconstrained, yet remains divergence free. On the other hand, for the normal-field condition, the horizontal fields must vanish implying that

$$\begin{cases} \left.A_r\right|_{r_1,r_2} = 0 \\ \left.\dfrac{\partial A_\theta}{\partial r}\right|_{r_1,r_2} = -\left.\dfrac{A_\theta}{r}\right|_{r_1,r_2} \\ \left.\dfrac{\partial A_\phi}{\partial r}\right|_{r_1,r_2} = -\left.\dfrac{A_\phi}{r}\right|_{r_1,r_2} \end{cases} \qquad \text{Radial Field} \tag{11.28}$$

11.2.2 Latitudinal Boundaries

The latitudinal boundaries are set such that the system is thermally insulated, namely that

$$\left.\frac{\partial S}{\partial \theta}\right|_{\theta_1,\theta_2} = 0. \tag{11.29}$$

As with the radial velocity boundary condition, the latitudinal conditions may be stress-free or no-slip, with each directional component treated individually. The boundary is currently only impenetrable with $u_\theta|_{\theta_1,\theta_2} = 0$. The radial and longitudinal velocity boundary conditions are

$$\begin{cases} u_r|_{\theta_1,\theta_2} & = 0 & \text{No-Slip} \\ u_\phi|_{\theta_1,\theta_2} & = 0 & \\ \left.\dfrac{\partial u_r}{\partial\theta}\right|_{\theta_1,\theta_2} & = 0 & \text{Stress-Free} \\ \left.\dfrac{\partial u_\phi}{\partial\theta}\right|_{\theta_1,\theta_2} & = \cot\theta u_\phi & \end{cases} \tag{11.30}$$

Again to maintain the numerical consistency of the pressure derivatives at the latitudinal boundaries, all terms of the latitudinal component of the momentum equation are computed less the pressure derivative as

$$\begin{aligned}\delta u_\theta = &-\frac{u_\theta}{\rho}\frac{\partial\rho}{\partial t} - \frac{1}{\rho r^2}\frac{\partial}{\partial r}r^2\left[\rho u_\theta u_r - \frac{B_\theta B_r}{4\pi}\right] - \frac{1}{\rho r\sin\theta}\frac{\partial}{\partial\theta}\sin\theta\left[\rho u_\theta^2 + \frac{1}{8\pi}\left(B_r^2 + B_\phi^2 - B_\theta^2\right)\right] \\ &- \frac{1}{\rho r\sin\theta}\frac{\partial}{\partial\phi}\left[\rho u_\theta u_\phi - \frac{B_\theta B_\phi}{4\pi}\right] + r\sin\theta\cos\theta\Omega_0^2 + 2\Omega_0\cos\theta u_\phi + \hat{\boldsymbol{\theta}}\cdot\mathbf{D}_\mathbf{u},\end{aligned} \tag{11.31}$$

then, with impenetrable boundaries, the remaining terms are

$$\left.\frac{\partial u_\theta}{\partial t}\right|_{\theta_1,\theta_2} = 0 = \delta u_\theta|_{\theta_1,\theta_2} - \left.\frac{1}{\rho r}\frac{\partial P}{\partial\theta}\right|_{\theta_1,\theta_2}. \tag{11.32}$$

Thus, the radial gradient of the pressure is set at the upper and lower radial boundaries as

$$\left.\frac{\partial P}{\partial\theta}\right|_{\theta_1,\theta_2} = r\rho\delta u_\theta|_{\theta_1,\theta_2}. \tag{11.33}$$

The magnetic conditions are again either normal field or perfectly conducting.

$$\begin{cases} A_r|_{\theta_1,\theta_2} & = 0 \\ A_\phi|_{\theta_1,\theta_2} & = 0 \end{cases} \quad \text{Perfect Conductor} \tag{11.34}$$

while A_θ is left free on the boundaries. This satisfies the constraint that $B_\theta|_{\theta_1,\theta_2} = 0$, and that the horizontal field is nearly unconstrained, yet remains divergence free. On the other hand, for the normal field condition, the horizontal fields must vanish implying that

$$\begin{cases} A_\theta|_{\theta_1,\theta_2} & = 0 \\ \left.\dfrac{\partial A_\phi}{\partial\theta}\right|_{\theta_1,\theta_2} & = -\cot\theta A_\phi|_{\theta_1,\theta_2} \\ \left.\dfrac{\partial A_r}{\partial\theta}\right|_{\theta_1,\theta_2} & = 0 \end{cases} \quad \text{Normal Field} \tag{11.35}$$

11.2.3 Open Boundary Conditions

The general framework for the open boundary conditions is largely in place, as described in the previous subsection. There need only be a subtle shift in perspective between the impenetrable and open boundary conditions. The impenetrable boundary requires that the time derivative of the radial velocity vanish, and so constrains the pressure gradient there. A numerically sensible open boundary for a convection simulation is one that conserves mass and momentum within the domain. This is accomplished by requiring that the horizontally-averaged flow be hydrostatic at the boundary. In the current state of CSS, there is no implementation of an open boundary for the magnetic fields nor are there open conditions on the latitudinal boundaries.

When considering a purely open boundary, one with no information provided from outside the domain, there is only a small change in how the horizontal velocities are evolved at the boundary. However, if the boundary condition is no-slip, they are directly specified to be zero. A new term is added to the evolution equations of the horizontal velocities that compensates for any outgoing momentum through the addition of a uniform momentum into the inflows.

$$\left.\frac{\partial u_\theta}{\partial t}\right|'_{r_1,r_2} = \left.\frac{\partial u_\theta}{\partial t}\right|_{r_1,r_2} + f\left(\theta,\phi\right)\frac{\langle p_\theta^{r_1,r_2}\rangle}{\langle m^{\text{in}}_{r_1,r_2}\rangle \tau_{r_1,r_2}}, \tag{11.36}$$

$$\left.\frac{\partial u_\phi}{\partial t}\right|'_{r_1,r_2} = \left.\frac{\partial u_\phi}{\partial t}\right|_{r_1,r_2} + f\left(\theta,\phi\right)\frac{\langle p_\phi^{r_1,r_2}\rangle}{\langle m^{\text{in}}_{r_1,r_2}\rangle \tau_{r_1,r_2}}. \tag{11.37}$$

Here f is a position dependent mask selecting points that are incoming or outgoing depending upon the sign of the velocity normal to the boundary plane, $p_{\theta,\phi}$ are the horizontally-averaged values of the horizontal momenta within the outflows, $m^{\text{in}}_{r_1,r_2}$ is the mass of the inflows at the boundary, and τ_{r_1,r_2} is the drag time scale, so

$$f(\theta,\phi) = \begin{cases} 1 & \text{If incoming} \\ 0 & \text{If outgoing} \end{cases}, \tag{11.38}$$

$$\langle m^{\text{in}} \rangle_r = \frac{\int_{\partial V} f(\theta,\phi)\, \rho r^2 \sin\theta d\theta d\phi}{\int_{\partial V} f(\theta,\phi)\, r^2 \sin\theta d\theta d\phi}, \tag{11.39}$$

$$\langle p_\theta \rangle = \frac{\int_{\partial V} (1 - f(\theta,\phi))\, \rho u_\theta r^2 \sin\theta d\theta d\phi}{\int_{\partial V} (1 - f(\theta,\phi))\, r^2 \sin\theta d\theta d\phi}, \tag{11.40}$$

$$\langle p_\phi \rangle = \frac{\int_{\partial V} (1 - f(\theta,\phi))\, \rho u_\phi r^2 \sin\theta d\theta d\phi}{\int_{\partial V} (1 - f(\theta,\phi))\, r^2 \sin\theta d\theta d\phi}, \tag{11.41}$$

$$\tau_{r_1,r_2} = \frac{\Delta r}{\max\limits_{r_1,r_2} |u_r|}. \tag{11.42}$$

The equations for the radial velocity and the entropy are modified so that they are pulled toward the values of the nearest interior plane on the grid crossing time scale of the fastest flow directed out of the domain on this interior plane. This time scale is typically far less than the sound crossing time given the large sound speed near the bottom of the convective domains being simulated, so the excitation of sound waves by the boundary is minimized. Furthermore, the pressure gradient is set to be hydrostatic, in a fashion similar to that for the impenetrable boundaries.

The radial velocity at the boundary must also take into account the density stratification of the domain, so the values of the radial velocity at the boundary plane are pulled toward the values of the interior plane multiplied by the ratio of the mean density of the two planes. Similarly, the entropy is dragged towards the interior value, but with a mean entropy gradient enforced by dragging the mean value at the boundary toward the desired value at the same rate as the pointwise values. To make this more concrete,

$$\left.\frac{\partial u_r}{\partial t}\right|_{r_1} = \frac{1}{\tau_{r_1}}\left(\frac{\overline{\rho}_{r_1+\Delta r}}{\overline{\rho}_{r_1}}\, u_r|_{r_1+\Delta r} - u_r|_{r_1}\right) - \frac{\langle p_r^{r_1}\rangle}{\langle m_{r_1}\rangle \Delta t}, \tag{11.43}$$

$$\left.\frac{\partial u_r}{\partial t}\right|_{r_2} = \frac{1}{\tau_{r_2}}\left(\frac{\overline{\rho}_{r_2-\Delta r}}{\overline{\rho}_{r_2}}\, u_r|_{r_2-\Delta r} - u_r|_{r_2}\right) - \frac{\langle p_r^{r_2}\rangle}{\langle m_{r_2}\rangle \Delta t}, \tag{11.44}$$

$$\left.\frac{\partial s}{\partial t}\right|_{r_1} = \frac{1}{\tau_{r_1}}\left(s|_{r_1+\Delta r} - s|_{r_1} - \langle s_{r_1}\rangle + \overline{s}_{r_1}\right), \tag{11.45}$$

$$\left.\frac{\partial s}{\partial t}\right|_{r_2} = \frac{1}{\tau_{r_2}}\left(s|_{r_2-\Delta r} - s|_{r_2} - \langle s_{r_2}\rangle + \overline{s}_{r_2}\right), \tag{11.46}$$

with

$$\langle m\rangle = \frac{1}{A}\int_{\partial V} \rho r^2 \sin\theta d\theta d\phi, \tag{11.47}$$

$$\langle p_r\rangle = \frac{1}{A}\int_{\partial V} \rho u_r r^2 \sin\theta d\theta d\phi, \tag{11.48}$$

$$\langle s\rangle = \frac{1}{A}\int_{\partial V} s r^2 \sin\theta d\theta d\phi, \tag{11.49}$$

and where $A = \int_{\partial V} r^2 \sin\theta d\theta d\phi$ the area of the boundary. The pressure gradient condition is thus modified to enforce the constraints placed on the radial velocities as

$$\left.\frac{\partial P}{\partial r}\right|_{r_1,r_2} = \rho \delta u_r|_{r_1,r_2} - \rho \left.\frac{\partial u_r}{\partial t}\right|_{r_1,r_2}. \tag{11.50}$$

with the time derivative evaluated as in Equations 11.43 and 11.44.

11.3 Diffusion Schemes

To begin, let us define the components of the momentum, induction, and energy equations that were omitted in §11.1. These are diffusive terms that, in the Navier-Stokes equations, are the first order approximations to the net effects of particle interactions at the micro-scale.

11.3.1 Newtonian Eddy Viscosity

The Newtonian eddy viscosity scheme is one in which a dynamic viscosity, magnetic diffusion, and a thermal conductivity are prescribed. The values of these diffusivities are typically many orders of magnitude higher than the expected molecular values. This has the effect of moving the dissipation scale from the molecular scale into the spectrally resolved domain. However, the magnitude of diffusion necessary to maintain numerical stability is often much higher than the minimum value required to displace the dissipation scale to the Nyquist wavenumber of the simulation. In any case, the diffusive terms omitted in §11.1 can thus be defined as

$$\mathrm{D}_\rho = 0, \tag{11.51}$$

$$\mathrm{D}_s = \boldsymbol{\nabla} \cdot [\kappa_T \boldsymbol{\nabla} T(\rho, s) + \kappa_S \boldsymbol{\nabla} s], \tag{11.52}$$

$$\mathbf{D_u} = \frac{1}{\rho} \boldsymbol{\nabla} \cdot \left[2\mu \left(\mathbf{e} - \frac{1}{3} \mathbf{I} \boldsymbol{\nabla} \cdot \mathbf{u} \right) \right], \tag{11.53}$$

$$\mathbf{D_A} = \eta \boldsymbol{\nabla} \times \mathbf{B}, \tag{11.54}$$

where the dynamic viscosity μ, magnetic diffusivity η, thermal diffusion κ_T, and entropy diffusion κ_s are functions of radius and where $\mathbf{e}$ is the stress tensor and $\mathbf{I}$ the unit tensor. Yet the entropy diffusion term must be used with caution as it can violate the second law of thermodynamics. Finally, the viscous and ohmic heating is thus

$$\Phi = 2\mu \left[\mathbf{e} : \mathbf{e} - \frac{1}{3} (\boldsymbol{\nabla} \cdot \mathbf{u})^2 \right] + \eta \mathbf{J}^2 \tag{11.55}$$

where the colon denotes a full tensor contraction on $\mathbf{e}$ and $\mathbf{J} = \boldsymbol{\nabla} \times \mathbf{B}$ is the electric current. From a computational standpoint, the downside to using the eddy diffusion model in CSS is that it requires extra storage, communication, and computation to handle the second derivatives and the cross-derivatives necessary for it.

11.3.2 Slope-Limited Diffusion

The slope-limited diffusion scheme, as discussed in Chapter 4, is implemented in CSS as well. The difference between the implementation in ASH and here is that the diffusion is not filtered at high latitudes and there is sometimes a need to use the density diffusion for numerical stability. The latter does not always have to be used, as the density usually remains smooth if the velocity field is well resolved and no shocks are present. On the other hand, it will be needed when the number of radial grid points is chosen to be low, which allows larger time steps, but can under-resolve the stratification leading to two-zone grid-scale oscillations. In this scheme then, let $\mathcal{S}$ be the discrete slope-limited diffusion operator defined in Equation 4.71. The diffusive terms then become

$$\mathrm{D}_\rho = \mathcal{S}\left[\rho\right], \tag{11.56}$$

$$\mathrm{D}_s = \mathcal{S}\left[s\right], \tag{11.57}$$

$$\mathbf{D}_\mathbf{u} = \mathcal{S}\left[u_r\right]\hat{\mathbf{r}} + \mathcal{S}\left[u_\theta\right]\hat{\boldsymbol{\theta}} + \mathcal{S}\left[u_\phi\right]\hat{\boldsymbol{\phi}}, \tag{11.58}$$

$$\mathbf{D}_\mathbf{A} = \mathcal{S}\left[A_r\right]\hat{\mathbf{r}} + \mathcal{S}\left[A_\theta\right]\hat{\boldsymbol{\theta}} + \mathcal{S}\left[A_\phi\right]\hat{\boldsymbol{\phi}}. \tag{11.59}$$

Since D_ρ is now non-zero, there is a term in the momentum equation arising from the time derivative of ρ that compensates for any change in the momentum due to mass diffusion. Recall from §4.4 that the cell-edge diffusion fluxes need to be interpolated to cell-center to compute the velocity and magnetic diffusion tensors, being $\boldsymbol{\tau}$ and $\boldsymbol{\mu}$ respectively. Note the latter tensor is not directly proportional to the diffusion of the vector potential. Rather it is proportional to its curl, so this heating is only accurate to within the precision of the numerical scheme. These tensors are almost always non-symmetric and so have anti-symmetric components that contribute to the heating. Such terms vanish for the eddy diffusion approximation as the diffusion tensor is symmetric. The viscous and ohmic heating arising from these diffusive processes are thus

$$\Phi = \boldsymbol{\tau}^{\mathrm{T}} : \boldsymbol{\nabla}\rho\mathbf{u} + \frac{1}{4\pi}\boldsymbol{\mu}^{\mathrm{T}} : \boldsymbol{\nabla}\mathbf{B} - 2\rho\mathbf{u}\cdot\boldsymbol{\nabla}\cdot\boldsymbol{\tau}^{\mathrm{a}} - \frac{1}{2\pi}\mathbf{B}\cdot\boldsymbol{\nabla}\cdot\boldsymbol{\mu}^{\mathrm{a}}. \tag{11.60}$$

with the superscript a denoting the anti-symmetric portion of the tensors and T being the transpose operator.

11.4 Implementation and Evolution of CSS

CSS has gone through many incarnations: from the original code to a hybrid OpenMP/MPI code to a vector optimized hybrid code and so on until it reached its current implementation. It is written in Fortran 90 for optimal speed relative to C++. The current version solves the MHD equations discretized on a nonuniform spatial grid in spherical coordinates using one of two time-stepping algorithms. A truncated compact finite difference scheme is employed for the spatial derivatives. The computational workload is evenly divided across all the requested message passing interface (MPI) communicators with a 3-D decomposition. The computations are parallelized using only the MPI 2.2 standard, as will be described below.

11.4.1 Program Design

The layout of the program is fairly straightforward. The primary program calls all the initialization routines of each module. First all processors read a namelist-formatted file containing all the parameters of the run, including domain size, relevant physical parameters, problem size and node configuration and so on. Given these parameters, the processors initialize MPI communications and define a Cartesian node layout that optimizes node placement for the highest bandwidth and minimum latency. Derivative coefficients and matrices are precomputed and memory is allocated on each MPI communicator based on the layout and problem size. The physical problem is then initialized either from a checkpoint of a previous run or by constructing the initial primitive variable values from the physical input parameters.

The fundamental computational loop of the program calls only three subroutines. The first conditionally computes the step size, which is infrequently called as the time step is con-

strained by the Currant-Friedrichs-Lewy (CFL) condition on the fast magneto-sonic modes and is most often very much greater than the flow speeds. The second calls the time stepping routine. The third conditionally checks whether or not the current time step number corresponds to the desired output cadence for a particular output type. So, as one would usually want, the vast majority of the computational effort resides in evolving the simulation. When I/O is desired, it handled with MPI I/O routines that maximize bandwidth to the disk, which is particularly important for checkpointing.

There are two optional features that include additional physics into the simulation. This can be inflows specified from ASH and flows specified at the upper boundary through statistical methods derived from photospheric simulations.

11.4.2 Time Evolution and Error Analysis

There are currently two time-stepping algorithms available within CSS. On a per time step basis, the fastest is a total variation diminishing (TVD) third-order Runge-Kutta scheme (Gottlieb & Shu, 1998). The second is the standard fourth-order Runge-Kutta scheme (Runge, 1895). The slope-limited diffusion is calculated only once per time step and added to the solution with a forward Euler scheme. It could be computed at each evaluation in the Runge-Kutta methods, but this has been found to be unnecessary and much more expensive.

The third-order Runge-Kutta (RK3) method has three stages that are given by

$$\mathbf{v}_1 = \mathbf{v}_n + \Delta t R\left(t_n, \mathbf{v}_n\right), \tag{11.61}$$

$$\mathbf{v}_2 = \frac{3}{4}\mathbf{v}_n + \frac{1}{4}\mathbf{v}_1 + \frac{1}{4}\Delta t R\left(t_n + \frac{1}{4}\Delta t, \mathbf{v}_1\right), \tag{11.62}$$

$$\mathbf{v}_{n+1} = \frac{1}{3}\mathbf{v}_n + \frac{2}{3}\mathbf{v}_2 + \frac{2}{3}\Delta t R\left(t_n + \frac{2}{3}\Delta t, \mathbf{v}_2\right). \tag{11.63}$$

where n denotes the N-th time step, $\Delta t \leq \Delta t_{CFL}$ is the physical time step in seconds, R is the call to the right-hand side of the discretized version of Equations 11.11-11.18, and $\mathbf{v}$ is the vector containing all primitive variables at all locations within the domain of the MPI communicator. Note that all coefficients are positive, which is ideal for a TVD method.

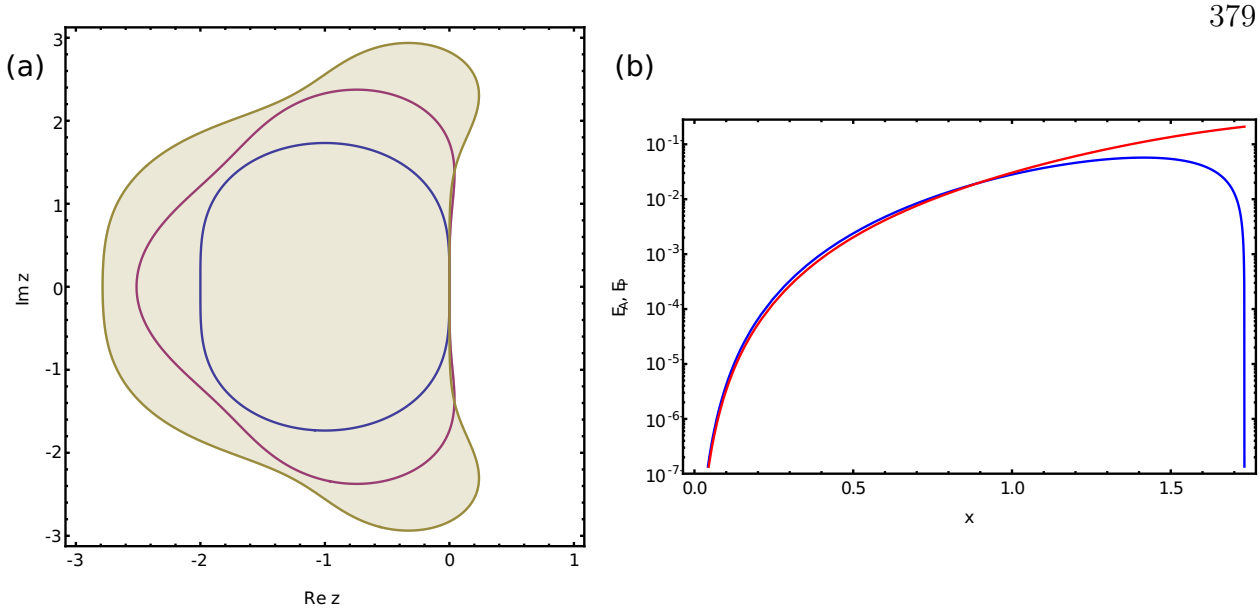

Figure 11.2: (a) Stability regions of three Runge-Kutta methods, with second-order in blue, third-order in magenta, and fourth-order in brass. The shaded region is the region of stability. (b) Phase (blue) and amplitude (red) errors as a function of step size for the third-order method.

Similarly, the fourth-order Runge-Kutta (RK4) method has four stages that are given by

$$\mathbf{k} = \Delta t R\left(t_n, \mathbf{v}_n\right), \tag{11.64}$$

$$\mathbf{v}_{n+1} = \mathbf{v}_n + \frac{1}{6}\mathbf{k}, \tag{11.65}$$

$$\mathbf{k} = \Delta t R\left(t_n + \frac{1}{2}\Delta t, \mathbf{v}_n + \frac{1}{2}\mathbf{k}\right), \tag{11.66}$$

$$\mathbf{v}_{n+1} = \mathbf{v}_{n+1} + \frac{1}{3}\mathbf{k}, \tag{11.67}$$

$$\mathbf{k} = \Delta t R\left(t_n + \frac{1}{2}\Delta t, \mathbf{v}_n + \frac{1}{2}\mathbf{k}\right), \tag{11.68}$$

$$\mathbf{v}_{n+1} = \mathbf{v}_{n+1} + \frac{1}{3}\mathbf{k}, \tag{11.69}$$

$$\mathbf{k} = \Delta t R\left(t_n + \Delta t, \mathbf{v}_n + \mathbf{k}\right), \tag{11.70}$$

$$\mathbf{v}_{n+1} = \mathbf{v}_{n+1} + \frac{1}{6}\mathbf{k}, \tag{11.71}$$

where $\mathbf{k}$ is the time derivative evaluated at stage i. There is clearly greater overhead and computational expense with the fourth-order method. It has a slightly larger region of

stability with respect to the linear problem $y' = \lambda y$ with λ being some complex number. This problem reduces to an iterative map $y_{n+1} = r(z)y_n$, with $r(z) = 1 + z + z^2/2 + z^3/6$ for the TVD RK3 method and $r(z) = 1 + z + z^2/2 + z^3/6 + z^4/24$ for the RK4 method. These regions of stability are shown in Figure 11.2a.

The time stepping routine calls at most six procedures depending on if there are open boundaries with specified flows or not. If flows are specified by ASH at the lower boundary, the first call is to read and interpolate an ASH inflow. The second call is to the slope-limited diffusion routine. Then three or four calls are made to the "right-hand-side" routine R that computes time derivatives at all points within the domain of the MPI communicator. A routine that sets boundary values is called. If the boundaries are open and specified, three more routines are called.

The time stepping routine uses at most six storage arrays, two for the slope-limited diffusion, two storage arrays for temporary values between evaluations of R, one for storing the values of the fields for use in the next time step. One additional storage array is needed if eddy diffusion is used.

11.4.3 Modified Compact Finite Differences

Compact finite differences are a particular numerical derivative scheme that can attain nearly spectral resolution (Lele, 1992). They are finite differences in the sense that they have a fixed stencil width. What sets them apart from the Padé scheme and from simple finite differences is that they result from a double expansion of the derivative value of some function f at a grid point x_k as

$$\sum_{i=-M}^{i=M} \alpha_i f'\left(x_{k+i}\right) = \sum_{j=-N}^{j=N} a_j f\left(x_{k+j}\right). \tag{11.72}$$

where $2M$ is the bandwidth of the matrix with coefficients α_i that is required to solve for the now implicitly defined derivative f'. The finite difference stencil of the right-hand side has coefficients a_j and a stencil size $2N$. It is the implicit definition of the derivative that enhances

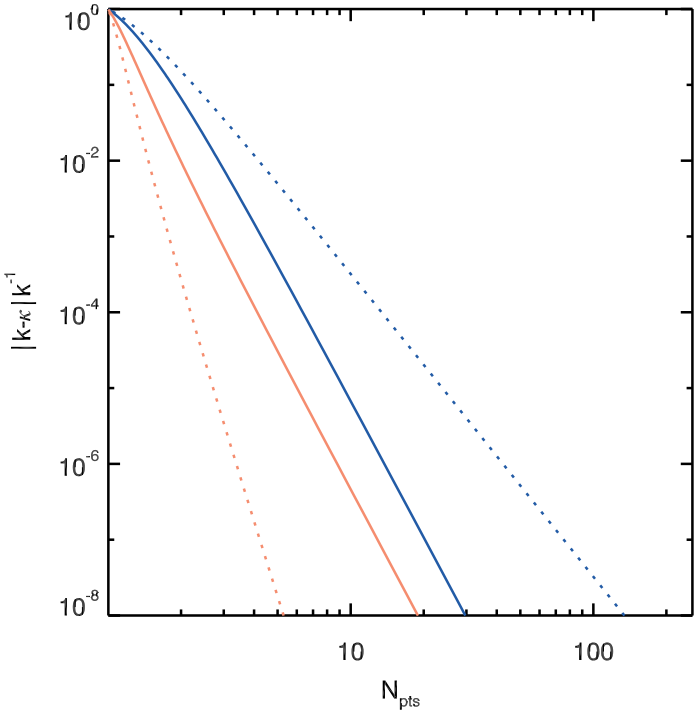

Figure 11.3: Dispersion errors $|k - \kappa(k)|k^{-1}$ for a single Fourier mode as the number of points N_{pts} resolving it is increased in four different compact finite difference (CFD, red) and standard finite difference (FD, blue) schemes. The dotted blue line is a fourth-order FD, solid blue is sixth-order FD, solid red is sixth-order CFD, and dotted red is tenth-order CFD.

their resolution, or more appropriately it is what reduces their dispersive numerical errors. This effectively links the derivative values of all the grid points together. Thus the compact finite difference method approximates a spectral method, which would have $M = N = K/2$, with K the total number of grid points. The version used in CSS is

$$\beta f'_{i-2} + \alpha f'_{i-1} + f'_i + \alpha f'_{i+1} + \beta f'_{i+2} = c\frac{f_{i+3} - f_{i-3}}{6\Delta x} + b\frac{f_{i+2} - f_{i-2}}{4\Delta x} + a\frac{f_{i+1} - f_{i-1}}{2\Delta x}. \quad (11.73)$$

This could be generalized for a nonuniform grid and is a planned change in CSS, where the nonuniform grid is currently accomplished through a Jacobian transformation. The simple sixth-order scheme has $\beta = c = 0$, $\alpha = 1/3$, $a = 14/9$, and $b = 1/9$, which yields a truncation error of $4/7!\Delta x^6 f^{(7)}$. The coefficients are found through matching terms in Taylor expansions about f'_i and f_i that provide a set of equations for the coefficients, with one free parameter α.

With the choice of $\alpha = 1/3$, the scheme becomes sixth order. The implicit definition of the derivative now requires a tridiagonal solve in addition to the finite difference. Thus the total operation count including both the necessary tridiagonal solve and finite difference is $7K-2$ multiplications and $6K-2$ additions, which should be compared to the $6K$ multiplications and $6K$ additions for a simple centered finite difference scheme of the same order. The dispersion modified wavenumber κ of the derivative scheme is

$$\kappa(k) = \frac{a \sin k + b/2 \sin 2k + c/3 \sin 3k}{1 + 2\alpha \cos k + 2\beta \cos 2k}, \tag{11.74}$$

which is found by admitting a Fourier mode with $f(x) = \exp(iks)$. Here the scaled wavenumber $k \in [0, 1]$ is $k = 2w\Delta x/L$ and the scaled coordinate is $s = x/\Delta x$, with w the physical wavenumber. Thus the exact derivative with respect to s is $f'(s) = ikf(s)$, or the spectral derivative should have no modified wave number with $\kappa(k) = k$. The dispersive error relative to a spectral scheme is shown in Figure 11.3. The relative error indicates how many points across a peak or a trough of a given Fourier mode are necessary for a particular derivative scheme to resolve the mode to certain level of accuracy. That is it measures the resolving power of a given derivative scheme. The fourth-order standard finite difference scheme clearly does not perform well, requiring about four times as many points to reach floating point machine precision when compared to the sixth-order standard finite difference. Likewise, the sixth-order compact finite difference needs only 50% of the points as the sixth-order standard finite difference does to resolve the same features. The tenth-order compact scheme is about a factor of two better than the sixth-order scheme, for a modest increase in computational effort.

For the second-order derivatives f'', a similar brew of coefficients yields a compact finite difference, where

$$\beta f''_{i-2} + \alpha f''_{i-1} + f''_i + \alpha f''_{i+1} + \beta f''_{i+2} = c\frac{f_{i+3} - 2f_i + f_{i-3}}{9\Delta x^2} + b\frac{f_{i+2} - 2f_i + f_{i-2}}{4\Delta x^2} + a\frac{f_{i+1} - 2f_i + f_{i-1}}{\Delta x^2}. \tag{11.75}$$

A scheme with a sixth-order truncation error $-(23/11)/7!\Delta x^6 f^{(8)}$ has coefficients $\beta = c = 0$, $\alpha = 2/11$, $a = 12/11$, $b = 3/11$, which are again found through collecting terms in the Taylor expansion by their order in Δx. So far, this has only dealt with interior points. The derivative values at the physical boundaries of the domain can be found in the same fashion as one need only relax the assumption of using centered differences. However, another method uses the properties of the numerical derivative for the interior points to choose the proper values in ghost cells outside the boundary so as to satisfy a given boundary condition. This is usually more efficient than computing the value at the boundary itself as that requires more conditional statements and asymmetrical workloads between boundary points and interior points. This is used in CSS as it is most compatible with how the derivatives are handled at internal boundaries between computational sub-domains that result from the domain decomposition. At such internal boundaries, a sixth-order standard finite difference is used to precondition the tridiagonal solve. This results in some loss of the global dispersion properties of the compact finite difference, but the gains in computational efficiency and parallelizability outweigh the losses. This approach gives the following implicit solve for the derivatives within a sample sub-domain

$$\begin{bmatrix} 1 & \alpha & 0 & 0 & 0 & \cdots & 0 \\ \alpha & 1 & \alpha & 0 & 0 & \cdots & 0 \\ 0 & \alpha & 1 & \alpha & 0 & \cdots & 0 \\ \vdots & & \ddots & \ddots & \ddots & & \vdots \\ 0 & \cdots & 0 & \alpha & 1 & \alpha & 0 \\ 0 & \cdots & 0 & 0 & \alpha & 1 & \alpha \\ 0 & \cdots & 0 & 0 & 0 & \alpha & 1 \end{bmatrix} \begin{bmatrix} f'_{-1} \\ f'_0 \\ f'_1 \\ \vdots \\ f'_{n-1} \\ f'_n \\ f'_{n+1} \end{bmatrix} = \begin{bmatrix} f'_{-1,FD} \\ r_0 \\ r_1 \\ \vdots \\ r_{n-1} \\ r_n \\ f'_{n+1,FD} \end{bmatrix} \tag{11.76}$$

where f'_{-1} and f'_{n+1} are ghost cell values one grid points outside the sub-domain. The values r are the right-hand side computations of the compact finite difference as above. In contrast, the boundary values are computed using a sixth-order centered standard finite difference constructed from values passed using MPI from the nearest neighbor sub-domains.

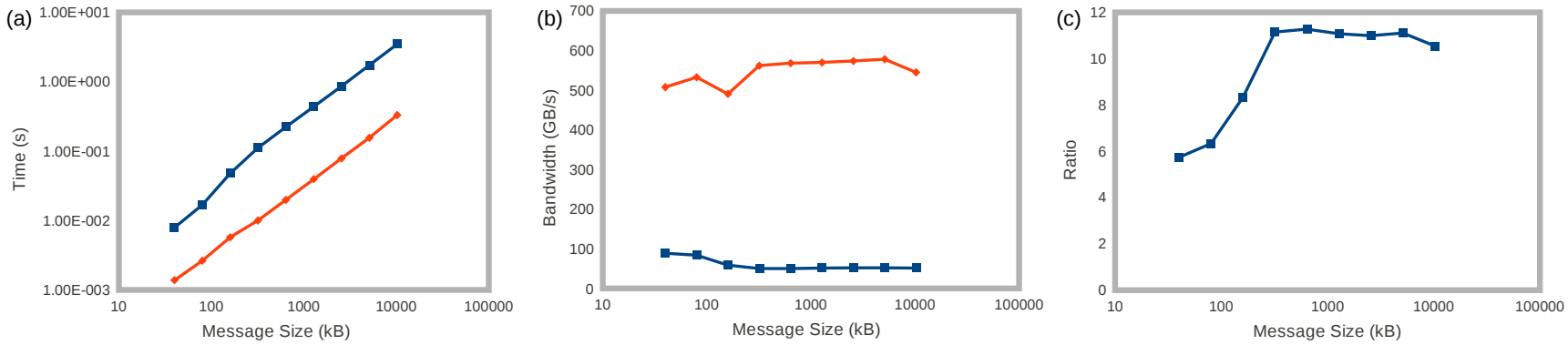

Figure 11.4: Bandwidth increases using an optimized MPI process layout versus message size in kilobytes (kB) in a 3D domain decomposition using round-robin process assignment (blue) and an optimized nearest-neighbor assignment (red). (a) Total time spent exchanging boundary information for 1536 Westmere cores on Pleiades at NASA Ames per time step. (b) Bisection bandwidth in gigabytes per second (GB/s). (c) The ratio of the bisection bandwidth using the two process assignment methods.

11.4.4 Parallelization

The parallelization of the code is accomplished through MPI. After initialization, when all processes have an identifier and can talk to each other, the MPI_CART_CREATE command is used to reorder nodes to conform to the domain decomposition. This accounts for the periodicity in longitude and optimally places processes with considerations for hardware structure and communication paths to assure that nearest-neighbor domains are physically nearby. This increases bandwidth by over a factor of ten, yielding an order of magnitude decrease in the clock cycles spent waiting on messages as can be seen in Figure 11.4. Furthermore, the communication is overlapped as much as possible with computation using non-blocking send and receives. This is accomplished binarily: first through splitting the communications by direction, where each node separately communicates with its two neighbors in radius, latitude, and longitude; and then each direction is split into two stages. Such an organization of the communication accommodates the layout of the computation of the time derivatives, which is broken out by direction to optimize memory usage and instruction reuse.

For each communication direction, the first stage initiates the message exchange prior to some heavy computational workload, where the message is packed into 1D buffer array. The odd numbered processors post a send first, whereas the even numbered processors first post a receive. After the workload is completed, the second stage finalizes the exchange through a wait all statement and unpacks the 1D buffer into the boundary value array. This way each MPI processes has to wait for at most two other MPI processes to finish their task, which is highly likely given the computational load between the two calls. All of these facets of CSS have permitted it to be highly scalable, reaching up to 50,000 cores as can be seen in Figure 11.5. The scaling there was still linear, so the wide availability of machines with millions of cores is eagerly being awaited.

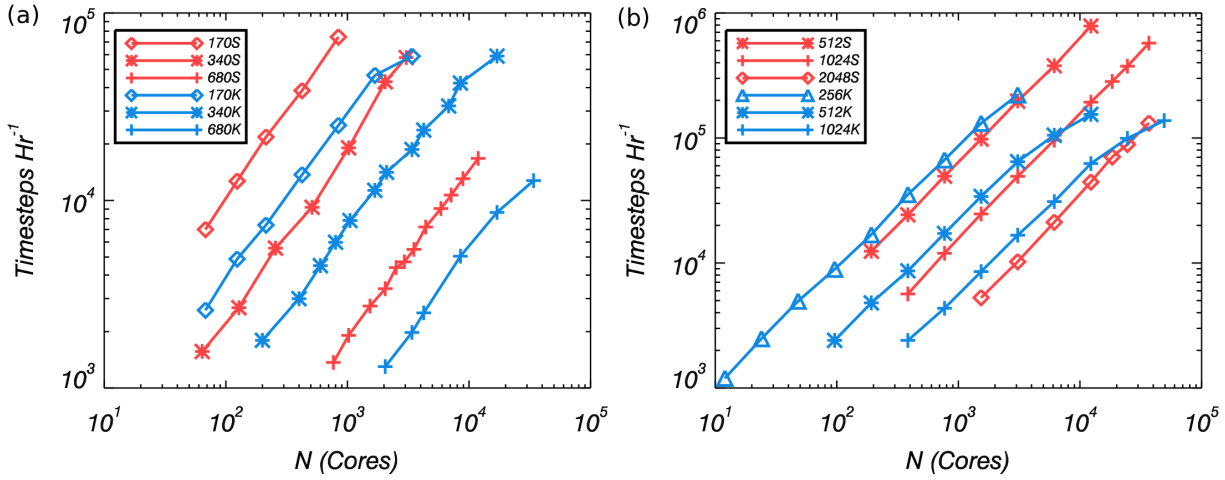

Figure 11.5: Strong scaling, fixed problem size and increasing core counts, for ASH-FD and CSS are shown on Kraken and Pleiades. (a) Time steps per wall-hour achieved in ASH simulations with 400 radial mesh points and horizontal resolution of spherical harmonic degree $\ell = 680$ on Kraken (blue, 680K), and on Sandy Bridge cores on Pleiades (red, 680S), and likewise for $\ell = 340$ and 170. (b) Time steps per wall-hour achieved in CSS simulations varied between 256^2 and 1024^2 horizontal grid points and 192 radial points for Kraken (blue, labeled 256K to 1024K). With larger memory nodes, CSS simulations with 576 radial grid points and up to 2048^2 horizontal grid points were run using Pleiades (red, labeled 512S to 2048S). CSS modeling shows strong linear scaling between 100 and 50,000 cores, reaching nearly 1 million time steps per wall clock hour (equivalently a month of evolution of a high-resolution solar convection simulation).

11.5 Euler Equation in 1D with SLD

A first and simple test of the numerical scheme employed in CSS is to apply it to the Sod shock tube problem, which is a standard test of the ability of a code to capture shocks as it has an analytical solution. This requires the solution of the Euler equations, so slope-limited diffusion is applied to achieve numerical stability. Quickly, the equations being evolved use are the 1-D Euler equations with a sixth-order compact finite differences for the derivatives and the TVD RK3 time stepping algorithm. These equations are

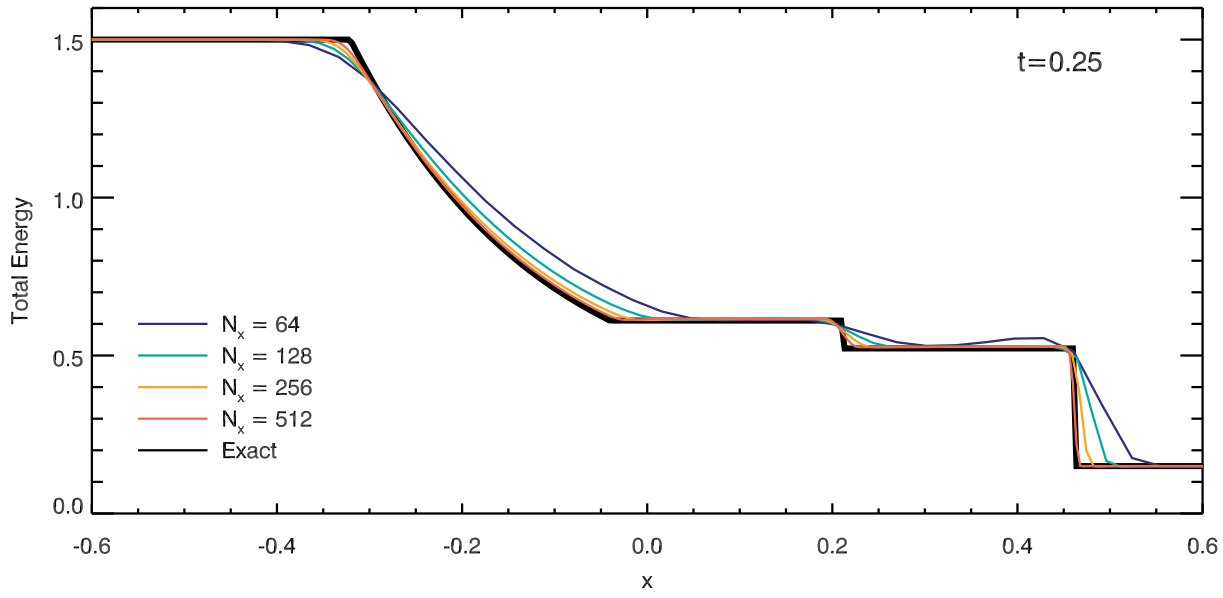

Figure 11.6: Sod shock tube problem solved using CSS numerical algorithms, showing the convergence to the exact solution with increasing resolution.

$$\frac{\partial \rho}{\partial t} = -u\frac{\partial \rho}{\partial x} - \rho\frac{\partial u}{\partial x} + \mathrm{D}_\rho, \tag{11.77}$$

$$\frac{\partial u}{\partial t} = -\frac{1}{\rho}\frac{\partial p}{\partial x} - u\frac{\partial u}{\partial x} - \frac{u}{\rho}\mathrm{D}_\rho + \mathrm{D}_u, \tag{11.78}$$

$$\frac{\partial e}{\partial t} = -u\frac{\partial h}{\partial x} - h\frac{\partial u}{\partial x} + \mathrm{D}_e, \tag{11.79}$$

$$p = (\gamma - 1)\left[e - \frac{1}{2}\rho u^2\right], \tag{11.80}$$

$$h = e + p, \tag{11.81}$$

$$e = \rho\epsilon + \frac{1}{2}\rho u^2, \tag{11.82}$$

where γ is the adiabatic exponent for this perfect gas, p is the pressure, h is the enthalpy, and e the total energy. The slope-limited diffusion operator is D. The classical Sod shock tube problem is defined over the interval $x \in [-1, 1]$ and has the initial conditions

$$\rho(x) = \begin{cases} 1 & x \leq 0 \\ 1/8 & x > 0 \end{cases}, \tag{11.83}$$

$$p(x) = \begin{cases} 1 & x \leq 0 \\ 1/10 & x > 0 \end{cases}, \tag{11.84}$$

$$u(x) = 0, \tag{11.85}$$

$$e(x) = \frac{p}{\gamma - 1}, \tag{11.86}$$

$$\gamma = \frac{5}{3}. \tag{11.87}$$

The solution of this problem is shown in Figure 11.6. The conservation of mass and energy is very good, even at low resolution. For the case with $N_x = 64$, the relative difference between the volume integrated mass at $t_1 = 0.25$ and $t_0 = 0.0$ is $\delta m = |m_{t_1} - m_{t_0}|/m_{t_0} = 6 \times 10^{-10}$ and for the volume integrated energy it is $\delta e = |e_{t_1} - e_{t_0}|/e_{t_0} = 8 \times 10^{-10}$. The other cases converge rapidly to the machine epsilon for double precision: with $\delta m = 1.0 \times 10^{-14}$ and $\delta e = 1.4 \times 10^{-14}$ for $N_x = 128$; $\delta m = 7.5 \times 10^{-15}$ and $\delta e = 9.9 \times 10^{-15}$ for $N_x = 256$; $\delta m = 9.8 \times 10^{-15}$ and $\delta e = 2.8 \times 10^{-15}$ for $N_x = 512$. The solution is very close to monotone, but at low resolution is not perfectly monotone. Indeed, this shows that the SLD operator does not guarantee this property for non-conservative schemes, rather it attempts to maintain a solution is close to monotone. On the other hand, it is very good at conserving mass and energy even if the phase and amplitude of the solution have modest errors, which is apparent in the $N_x = 64$ solution. If the resolution is only twice that, these errors quickly disappear given the excellent resolution properties of the compact finite differences and due to the TVD RK3 algorithm. It is quite remarkable that one can capture such shocks so well with a fairly simple high-order finite difference scheme such as CSS.

11.6 Numerical Tests Through Linear Waves

The following subsections rely upon the linearized Euler and Euler-Maxwell equations. The linearization of these equations give rise to the hydrodynamic and MHD wave equations, which in turn can be solved analytically under many circumstances. It should be noted that if the fields (pressure, density, entropy, velocity, and magnetic fields) of these equations are separated into the mean field and the fluctuating fields, then to first order in the fluctuating fields the equations are linear. To make this precise, first take the expansion about the mean fields as $P = P_0 + P'$, $\rho = \rho_0 + \rho'$, $S = S_0 + S'$, $\mathbf{v} = \mathbf{v}_0 + \mathbf{v}$, and $\mathbf{B} = \mathbf{B}_0 + \mathbf{B}'$. An archetypal field F_0 is independent of time and longitude, but can depend upon the two other spatial dimensions; in contrast, the fluctuations F' depend upon three spatial dimensions and time. Under such an expansion, the equations of 11.1 become

$$\frac{\partial \rho'}{\partial t} = -\boldsymbol{\nabla} \cdot \rho_0 \mathbf{v} - \boldsymbol{\nabla} \cdot \rho' \mathbf{v}_0, \tag{11.88}$$

$$\frac{\partial \mathbf{v}'}{\partial t} = -\mathbf{v}_0 \cdot \boldsymbol{\nabla}\mathbf{v} - \mathbf{v} \cdot \boldsymbol{\nabla}\mathbf{v}_0 - \frac{1}{\rho_0}\boldsymbol{\nabla} P' + \frac{\rho'}{\rho_0}\left(\boldsymbol{\Omega}_0 \mathbf{R} + 2\mathbf{v}_0 \times \boldsymbol{\Omega}_0 - \frac{1}{4\pi}\left(\boldsymbol{\nabla} \times \mathbf{B}_0\right) \times \mathbf{B}_0 - g\hat{\mathbf{r}}\right)$$
$$+ 2\mathbf{v}' \times \boldsymbol{\Omega}_0 + \frac{1}{4\pi\rho_0}\left(\boldsymbol{\nabla} \times \mathbf{B}_0 \times \mathbf{B}' + \boldsymbol{\nabla} \times \mathbf{B}' \times \mathbf{B}_0\right) + \mathbf{D}_{\mathbf{u}}, \tag{11.89}$$

$$\frac{\partial \mathbf{B}'}{\partial t} = \boldsymbol{\nabla} \times \left(\mathbf{v}' \times \mathbf{B}_0\right) + \boldsymbol{\nabla} \times \left(\mathbf{v}_0 \times \mathbf{B}'\right) + \mathbf{D}_B, \tag{11.90}$$

$$\frac{\partial s'}{\partial t} = -\mathbf{v}' \cdot \boldsymbol{\nabla} s_0 - \mathbf{v}_0 \cdot \boldsymbol{\nabla} s' - \frac{1}{\rho_0 T_0}\boldsymbol{\nabla} \cdot \mathbf{q}_0 + \mathbf{q}' + \Phi \tag{11.91}$$

11.6.1 Sound Waves

The first and most simple test of the numerical schemes employed in CSS is to assess their treatment of a monochromatic sound wave propagating in the periodic dimension of ϕ. To this end, the equations of §11.1 are solved under the constraint that there is no stratification (e.g. no gravity, which implies that ρ_0 is constant), rotation, mean flows, transverse flows, magnetic fields, entropy variations, or diffusion ($g = \Omega_0 = \mathbf{v}_0 = \mathrm{v}'_r = \mathrm{v}'_\theta = \mathbf{B} = s = \mathbf{D} = 0$). With such restrictions, the above linearized equations become

$$\frac{\partial \rho'}{\partial t} = -\frac{\rho_0}{r \sin\theta} \frac{\partial u'_\phi}{\partial \phi}, \tag{11.92}$$

$$\frac{\partial u'_\phi}{\partial t} = -\frac{1}{\rho_0 r \sin\theta} \frac{\partial P'}{\partial \phi}. \tag{11.93}$$

This is of course contingent upon the equation of state. So, assume an isothermal state, which requires that the speed of sound is constant with $P' = c_s^2 \rho'$ and c_s^2 is constant. The subsequent step is to take the second temporal derivative of equation 11.92. Upon the substitution of equation 11.93, this yields

$$\frac{\partial^2 \rho'}{\partial^2 t} = \frac{c_s^2}{r^2 \sin^2\theta} \frac{\partial^2 \rho'}{\partial \phi^2}. \tag{11.94}$$

Thus, the solution is simply

$$\rho' = \rho_1 \exp i\,(\omega t - k\phi), \tag{11.95}$$

where $\rho_1 = \rho_1(r, \theta)$ is the spatially dependent perturbation amplitude. This solution implies that the dispersion relationship is

$$\omega^2 = \frac{c_s^2 k^2}{r^2 \sin^2\theta}. \tag{11.96}$$

Since CSS is not a spectral code, the real part of equation 11.95 must be taken to give

$$\rho' = \rho_1 \cos\left[k\left(\frac{c_s t}{r \sin\theta} - \phi\right)\right]. \tag{11.97}$$

The azimuthal velocity that corresponds to this compressive density wave is found by inserting the previous expression for ρ' into equation 11.93, which yields

$$u'_\phi = c_s \frac{\rho_1}{\rho_0} \cos\left[k\left(\frac{c_s t}{r \sin\theta} - \phi\right)\right]. \tag{11.98}$$

Equations 11.97 and 11.98 provide analytical comparisons for the numerical solutions, so that any phasing and amplitude errors introduced by the various numerical schemes in CSS can be determined. They also provide the initial conditions for the code, wherein t is set to zero in equations 11.97 and 11.98. The propagation of this sound wave under various conditions is assessed below, with the three time-stepping schemes implemented in CSS, a non-uniform radial grid, and varying the longitudinal resolution.

11.6.2 Alfvén Waves

Unlike the compressive, traveling sound waves assessed in the previous subsection, finding an Alfvén wave solution in a sphere is much more difficult. The most simple assumptions that can be made are that the guiding magnetic field is force-free ($\boldsymbol{\nabla} \times \mathbf{B}_0 = 0$), and obviously divergence-less. Simultaneously, the velocity field must also be solenoidal so that the slow and fast magneto-acoustic waves are filtered out, this is accomplished by setting $\rho' = 0$ and by taking an isothermal equation of state for the background. Thus, the linearized Euler-MHD equations are solved under the constraint that there is no stratification, rotation, mean flows, entropy variations, diffusion, or resistivity ($g = \Omega_0 = \mathbf{v}_0 = S = \mathcal{D}_V = \mathcal{D}_B = 0$). With such restrictions, the linearized equations become

$$\frac{\partial \mathbf{v}'}{\partial t} = \frac{1}{4\pi\rho_0}\boldsymbol{\nabla} \times \mathbf{B}' \times \mathbf{B}_0, \tag{11.99}$$

$$\frac{\partial \mathbf{B}'}{\partial t} = \boldsymbol{\nabla} \times (\mathbf{v}' \times \mathbf{B}_0)\,. \tag{11.100}$$

Nominally, to find a traveling Alfvén wave the guide field $\mathbf{B}_0$ would be directed in the periodic dimension ϕ to accommodate the phase and group velocities that are directed along the guide field. However, no simple, mono-directional magnetic field that is curl-free and divergence-less exists. The work around is to solve for a standing radial Alfvén wave. This wave is directed along a radial guide field that is curl and divergence-free, namely $\mathbf{B}_0 = Br_2^2/r^2\hat{\mathbf{r}}$, where r_2 is the radius of the outer boundary. Since Alfvén waves are transverse, only the azimuthal quantities are allowed to vary such that $\mathrm{v}'_\phi = \mathrm{v}'_\phi(r,\theta,t)$ and $\mathrm{B}'_\phi = \mathrm{B}'_\phi(r,\theta,t)$. This assumption requires that $\mathrm{v}'_r = \mathrm{v}'_\theta = \mathrm{B}'_r = \mathrm{B}'_\theta = 0$ and implies that the velocity and fluctuating magnetic field are both automatically divergence-less. Therefore, the reduced equations are

$$\frac{\partial \mathrm{v}'_\phi}{\partial t} = \frac{1}{4\pi\rho_0}\hat{\boldsymbol{\phi}} \cdot [\boldsymbol{\nabla} \times \mathbf{B}' \times \mathbf{B}_0]\,, \tag{11.101}$$

$$\frac{\partial \mathrm{B}'_\phi}{\partial t} = \hat{\boldsymbol{\phi}} \cdot [\boldsymbol{\nabla} \times (\mathbf{v}' \times \mathbf{B}_0)]\,, \tag{11.102}$$

First, let the vector potential be $\mathbf{A} = \mathrm{v}'_\phi B_0 \hat{\boldsymbol{\theta}}$ with the Coulomb gauge ($\boldsymbol{\nabla} \cdot \mathbf{A} = 0$), which requires that the solution have the form $\mathrm{v}'_\phi = f(r,t)/\sin\theta$. If a second time derivative of equation 11.102 is taken, it reduces this system to the following single equation

$$\begin{aligned}
\frac{\partial^2 \mathrm{v}'_\phi}{\partial t^2} &= \frac{B_0}{4\pi\rho_0} \hat{\boldsymbol{\phi}} \cdot \left[(\boldsymbol{\nabla} \times \boldsymbol{\nabla} \times \mathbf{A}) \times \hat{\mathbf{r}} \right], \\
&= \frac{B_0}{4\pi\rho_0} \hat{\boldsymbol{\phi}} \cdot \left[\left(\boldsymbol{\nabla}\boldsymbol{\nabla} \cdot \mathbf{A} - \nabla^2 \mathbf{A} \right) \times \hat{\mathbf{r}} \right], \\
&= -\frac{B_0}{4\pi\rho_0} \hat{\boldsymbol{\phi}} \cdot \left[\left(\nabla^2 \mathbf{A} \right) \times \hat{\mathbf{r}} \right], \\
&= \frac{B_0}{4\pi\rho_0} \left[\nabla^2 - \frac{1}{r^2 \sin^2\theta} \right] A_\theta. \qquad (11.103)
\end{aligned}$$

Now substituting $\mathbf{A}$ back in and expanding the derivatives in equation 11.103, it is found that

$$\begin{aligned}
\frac{\partial^2 f}{\partial t^2} &= \frac{B_0 \sin\theta}{4\pi\rho_0} \left[\nabla^2 - \frac{1}{r^2 \sin^2\theta} \right] \frac{f B_0}{\sin\theta} \qquad (11.104) \\
&= \frac{B_0^2}{4\pi\rho_0} \left[\frac{\partial^2}{\partial r^2} - \frac{2}{r}\frac{\partial}{\partial r} + \frac{2}{r^2} \right] f, \qquad (11.105)
\end{aligned}$$

where the θ derivatives give rise to a term that cancels the last term in equation 11.103 and thus vanish. The guide field magnitude B_0 is pulled through the radial derivatives and is now on the left side of the brackets, which serves to modify some of the coefficients of the radial derivatives. Since a standing wave solution is sought, f must be of the form $f = \exp(i\omega t)u(r)$, where ω is the angular frequency of the wave. Therefore the previous equation becomes

$$\left[\frac{\partial^2}{\partial r^2} - \frac{2}{r}\frac{\partial}{\partial r} + \left(\frac{2}{r^2} + \frac{\omega^2}{v_A^2} \right) \right] u = 0, \qquad (11.106)$$

where $v_A = v_A(r) = B_0/\sqrt{4\pi\rho_0}$ is the radially dependent Alfvén speed. When the functional form of v_A is then inserted into this equation, this yields

$$\left[\frac{\partial^2}{\partial r^2} - \frac{2}{r}\frac{\partial}{\partial r} + \left(\frac{2}{r^2} + a^2 r^4 \right) \right] u = 0, \qquad (11.107)$$

where $a^2 = 4\pi\rho_0\omega^2/B^2 r_2^4$. This equation is simply a modified Bessel equation and has the general solution

$$u(x) = x^{\frac{3}{2}} \left[c_1 J_{-\frac{1}{6}}\left(x^3\right) + c_2 J_{\frac{1}{6}}\left(x^3\right) \right], \tag{11.108}$$

where $x = 3^{-1/3} a^{1/3} r$ and where c_1 and c_2 are arbitrary constants. To make use of this within CSS, the function u requires two boundary conditions: one on r_1 and another at r_2. For simplicity, let the solution have no-slip conditions on the radial boundaries. Therefore, the full solution is

$$\mathrm{v}'_\phi(x,\theta,t) = v_0 \csc\theta \cos(\omega t)\, x^{\frac{3}{2}} \left[J_{\frac{1}{6}}\left(x_1^3\right) J_{-\frac{1}{6}}\left(x^3\right) - J_{-\frac{1}{6}}\left(x_1^3\right) J_{\frac{1}{6}}\left(x^3\right) \right], \tag{11.109}$$

where v_0 is a constant velocity that is chosen such that $v_0 \ll v_A$ and where $x_1 = 3^{-1/3} a^{1/3} r_1$. The choice to fix $\mathrm{v}'_\phi = 0$ on r_1 provides one no-slip condition and gives rise to the above equation. The no-slip condition on r_2 requires that r_2 be chosen so that it lies at a zero of the function $u(r)$. This also determines the dispersion relationship of the wave, which can be seen if k is set to $k = 2\pi/r_2$ then

$$\sqrt{\frac{\beta\omega}{k}} \left[J_{\frac{1}{6}}\left(\alpha\omega k^2\right) J_{-\frac{1}{6}}\left(\beta\frac{\omega}{k}\right) - J_{-\frac{1}{6}}\left(\alpha\omega k^2\right) J_{\frac{1}{6}}\left(\beta\frac{\omega}{k}\right) \right] = 0, \tag{11.110}$$

where $\alpha = r_1^3/12\pi^2 v_A^0$, $\beta = 2\pi/3v_A^0$, and $v_A^0 = B/\sqrt{4\pi\rho_0}$. To be implementable in CSS, a vector potential is required that corresponds to both the guide field and fluctuating magnetic field. For the guide field, the following is a viable choice

$$A_\phi^0 = -\frac{B r_2^2}{r} \cot\theta, \tag{11.111}$$

The fluctuating vector potential can be found by appealing to the induction equation, with

$$\frac{\partial \mathrm{A}'_\theta}{\partial t} = \mathrm{v}'_\phi B_0. \tag{11.112}$$

Integrating this equation in time gives

$$\mathrm{A}'_\theta(x,\theta,t) = A_0 + \frac{B_0 v_0}{\omega} \csc\theta \sin(\omega t)\, x^{\frac{3}{2}} \left[J_{\frac{1}{6}}\left(x_1^3\right) J_{-\frac{1}{6}}\left(x^3\right) - J_{-\frac{1}{6}}\left(x_1^3\right) J_{\frac{1}{6}}\left(x^3\right) \right], \tag{11.113}$$

or $\mathrm{A}'_\theta = A_0 + \mathrm{v}'_\phi B_0 \tan \omega t/\omega$, where A_0 is an integration constant. Finally, choose $A_0 = 0$ so that A'_θ satisfies the normal perfect conductor boundary conditions shown above. Thus, when $t = 0$ the initial conditions are found for the standing Alfvén problem, which can provide a stringent test of the numerics in the MHD version of CSS or other spherical segment MHD codes.

11.7 Effects of Diffusion Schemes

It is currently infeasible to try to simulate the entire range of spatial and temporal scales on the Sun. It is even fairly difficult to simultaneously model a few tens of supergranules as well as capture the granulation, or capture supergranules and the deeper flows of the solar interior. However, it may still be possible to characterize the influence of granulation and deep global flows on the near-surface shear layer (NSSL) by coupling CSS with global convection models from below such as those from (Miesch et al., 2008) and with surface convection simulations from above (e.g. Rempel et al., 2009; Nordlund et al., 2009; Rempel & Schlichenmaier, 2011). Such a coupling, whether it is statistical or direct, requires a careful treatment of diffusion and boundary conditions (see §11.2 or §11.8). For instance, low diffusion is necessary to preserve the spatial structure and advective timescales of the downdrafts flowing into the CSS domain from the surface convection above. Given that the grid used here is five times coarser than that of typical surface convection simulations, this is no easy task.

11.7.1 Formulating the Problem

Consider two CSS numerical simulations in a 20° square patch centered on the equator that encompass most of the NSSL and some of the deep interior, rotating at the solar rate. Thus the spherical segment domains used in these simulations involve large portions of the Sun's inherent spherical geometry, which is necessary to properly capture the effects of rotation on supergranular scales. To simulate the larger scales of motion that are likely

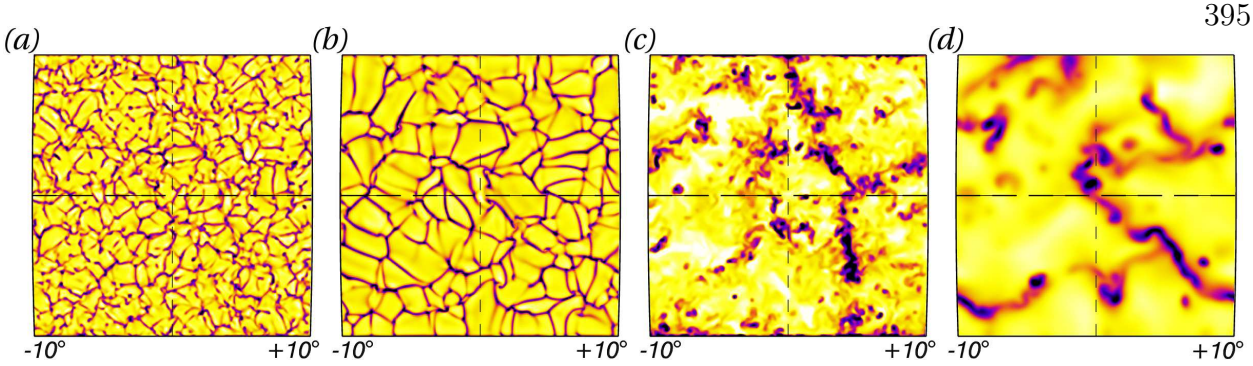

Figure 11.7: Radial velocities (u_r) at 0.99 $R_\odot$ in (a) the slope-limited diffusion *Case B*, and (b) the Newtonian-eddy diffusion *Case A*, and at 0.95 $R_\odot$ in (c) *Case B* and (d) *Case A*. Dark tones denote downflows and light tones denote upflows. Scaling values are $-1.34\,\mathrm{km\,s^{-1}}$, $0.59\,\mathrm{km\,s^{-1}}$ for (a) and (b) and $-0.73\,\mathrm{km\,s^{-1}}$, $0.24\,\mathrm{km\,s^{-1}}$ for (c) and (d), where positive u_r points outward.

to occur in the solar convection zone, a large-eddy simulation (LES) model is employed. In the Newtonian eddy diffusion scheme (*Case A*), the scales that are not explicitly computed in these simulations are parameterized and included in a sub-grid scale model of turbulent transport and diffusion. In the slope-limited diffusion (*Case B*), the primary goal is numerical stability of the code. Though, as was seen in §4.4, SLD can act as a filtered eddy diffusion that removes diffusion above the filtered scale. This could be considered an eddy diffusion model that limits the impact to only the largest wavenumbers. These simulations explore the effects of Newtonian-eddy and slope-limited diffusion schemes with an open lower radial boundary and closed upper boundary, as such they are identical except for the diffusion scheme.

In the Newtonian eddy diffusion (NED) scheme, the momentum and entropy diffusivities (μ and κ_S) are calculated based upon the desired Rayleigh number at the upper boundary with the constraint that the Prandtl number and the kinematic viscosity be constant throughout the domain. There are no directly comparable diffusive parameters in the SLD scheme as the eddy diffusion terms have been dropped. One may still control the level of diffusion, however, with specific choices of which slope-limiter is employed and what char-

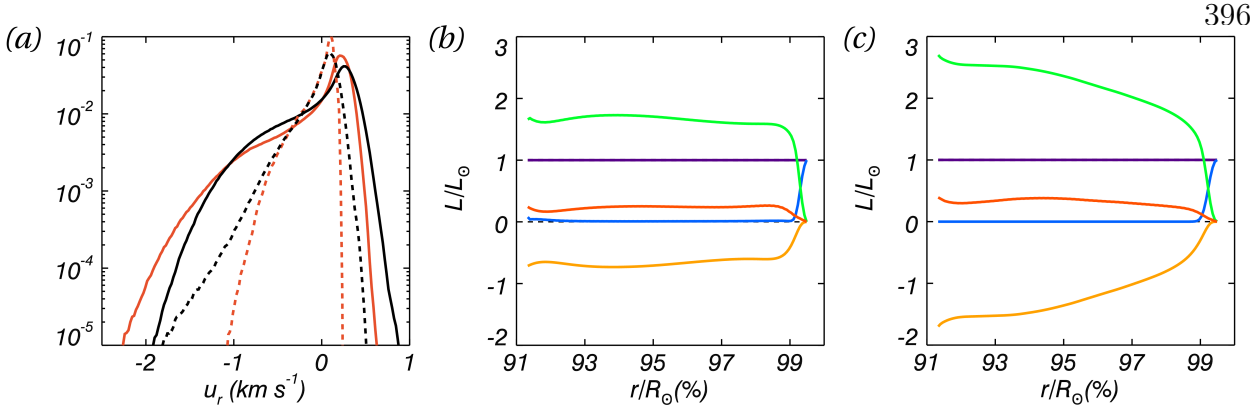

Figure 11.8: (a) PDFs of radial velocities at 0.99 $R_\odot$ (solid line) and 0.95 $R_\odot$ (dashed), for *Case B* (black) and *Case A* (red). Time-averaged radial energy flux balances for *Case A* (b) and *Case B* (c), with total flux in purple, radiative flux (blue), enthalpy flux (green), kinetic energy flux (orange), and acoustic flux (red).

acteristic velocity is used at cell interfaces. Figure 11.7 depicts snapshots of typical flows at two radii from the two diffusion schemes.

11.7.2 Comparing Two Diffusion Schemes

The simulations encompassing a $20° \times 20°$ domain are relatively low resolution with 128 radial mesh points and 256 points in latitude and longitude. The MESA stellar evolution code is used to establish a realistic initial stratification for the simulations. Since a perfect gas is assumed, the He and H ionization zones were not simulated. The impenetrable upper boundary is taken to be at 0.995 $R_\odot$ in order to exclude most of the radial extent of these zones. The permeable lower boundary is placed at 0.915 $R_\odot$, yielding a density contrast across the domain of 400. Each case has the lowest diffusivities that allow numerical stability in the NED (*Case A*) and SLD (*Case B*) regimes. Using a constant ν with depth in the NED case is rather restrictive in that the diffusion is larger than necessary away from the upper boundary, but for this analysis it is sufficient to characterize the differences between the two schemes.

Turning to the radial velocity patterns sampled in Figure 11.7, there is a striking shift

toward smaller spatial scales in *Case B* with considerably less power at large scales. At $0.99\,\mathrm{R}_\odot$ the peak of the spatial power spectrum in *Case A* is around 40 Mm. In *Case B*, however, there is a broad peak at scales around 20 Mm, more closely matching the supergranular scales of the Sun. As one descends deeper into the simulations (Figures 11.7c,d), the flows appear significantly more turbulent in *Case B* than in *Case A*.

Indeed, the downflowing structures of *Case B* become much narrower at depth with many more isolated plumes. The greater turbulence also manifests itself in larger extrema of each of the physical variables. For example, the radial velocities at $0.95\,\mathrm{R}_\odot$ in *Case B* have extrema that are twice that of *Case A* (Figure 11.8a). In *Case A*, a precipitous drop in the upflowing radial velocity probability density distribution (PDF) outside of about 0.1 $\mathrm{km\,s^{-1}}$ is indicative of just how uniform the upflows are. In stark contrast, the radial velocity PDF of *Case B* has twice the dynamic range, emphasizing that the upflows are indeed much more structured than those of *Case A*. While the radial mass flux PDF has higher velocity wings that contribute only one percent to the overall distribution, the bimodal nature of the temperature perturbation PDF has the effect of significantly amplifying the importance of these outlying values. Thus, the net effect of the larger wings in these PDFs is to shift the mean of the enthalpy flux in *Case B* to a higher value. The additional velocity in both the horizontal and radial flows greatly alter the kinetic energy distribution, as in *Case B* where the mean kinetic energy has nearly doubled and correspondingly decreased the kinetic energy flux (Figure 11.8c). A tentative next step is to have both diffusion schemes active at the same time. This will allow a systematic study on the convergence of solutions as the magnitude of the NED coefficients is lowered and SLD takes over as the primary diffusion.

11.8 Entropy Rain

Precisely how small-scale granulation formed at the photosphere helps to drive supergranulation and even larger scales of convection is still a bit of mystery. No single simulation can yet follow the coalescing networks of downflows as the descend from the photosphere

into the deep interior. One possibility is to model the action of the granulation as localized cooling events in a large-scale simulation. The idea is to mimic the local cooling associated with mixing at the edge of the cool downflows associated with the hierarchy of downflows descending from the surface. To this end, local sites with a decreased entropy sufficient to extract a solar energy flux are introduced at the upper boundary of a 3-D simulation of compressible convection in a rotating spherical shell segment.

As before, in order to investigate the dynamics of the 100-1000s of supergranules necessary for adequate statistics, the small scales that are not captured must be modeled. In this section, two methods of carrying the required solar energy flux through the top of the domain are considered, one using a spherically symmetric (uniform) cooling function while the other is a granular-scale stochastic cooling model. The dynamics and differential rotation profiles achieved in these simulations are subsequently assessed. It is found that with a sufficient number of stochastic cooling events compared to uniform cooling, supergranular scales begin to be realized in addition to a differential rotation that becomes increasingly like the NSSL.

11.8.1 Formulating the Problem

To begin to understand the dynamics of the near-surface shear layer, numerical simulations in spherical shell segments have been constructed that encompass most of the near-surface shear layer and some of the deep interior. The impenetrable upper boundary (r_2) is taken to be $0.995\,\mathrm{R}_\odot$ in order to exclude these zones. The lower radial boundary (r_1) is at $0.915\,\mathrm{R}_\odot$, which corresponds to a density contrast ($\Delta\rho = \rho_1/\rho_2 = 400$, where $\rho_1 = \rho(r_1)$ and $\rho_2 = \rho(r_2)$). The momentum and entropy diffusivities (μ and κ_s) are calculated based upon the desired Rayleigh number (Ra) at r_2 and so that the Prandtl number (Pr) is unity throughout the domain, and so these subgrid-scale diffusivities are functions of radius.

Table 11.1: Properties of the Computational Domain

	Case 1	*Case 2*	*Case 3*	*Case 4*
$\langle N \rangle$	0	250	500	1000
$\langle Ra \rangle$	5.98×10^6	7.63×10^6	7.90×10^6	7.94×10^6
$\langle Re \rangle$	133	152	151	150
$\langle Ro \rangle$	13.3	17.7	16.9	16.6
σ_-	228	248	249	250
σ_+	124	132	135	137

Table 11.1: For each case, the depth of the convection zone as modeled is 60 Mm, $\Delta\rho$ is 400, the angular size is $20^\circ \times 20^\circ$, with a resolution of $128 \times 256 \times 256$. $\langle N \rangle$ is the mean number of cooling sites. All cases were run with the same diffusivities and initial background. $\langle Ra \rangle$, $\langle Re \rangle$, and $\langle Ro \rangle$, are the average Rayleigh, Reynolds, and Rossby numbers in the domain. σ_+ and σ_- are the standard deviations of the positive and negative radial velocity probability distribution function in $\mathrm{m\,s^{-1}}$, respectively.

11.9 Modeling Granular Convection

The strong downflows that occur at edges of a granule drag more dense, lower entropy fluid into the interior. Hence, in this simple model it is assumed that the net mass flux is zero and the net entropy flux is negative when integrated over the volume of a granule. It is also assumed that the collective action of all the granular-scale dynamics contained within the simulated domain transports the required energy flux through the upper boundary. Therefore, the granules are modeled as cooling events that are advected with the flow, last for an average of 10 minutes, and have as small a spatial scale as the grid and diffusion will allow. The spatial structure of a cooling event is evident in Equation 11.114. The amplitudes of the cooling events are chosen at random from an exponential distribution with a mean determined by Equation 11.115. The horizontal extent of the cooling events is normally distributed with a mean angular size of $2\Delta\phi$ ($\langle\sigma\rangle$) in θ and ϕ. The spread of the radial exponential is fixed to $\sigma_r = 2\Delta r$ to speed computation. The cooling function is thus

$$\epsilon = -\boldsymbol{\nabla} \cdot (q_R \hat{\mathbf{r}}) = \left[\frac{2}{r} + \frac{1}{\sigma_r}\right] e^{-(r_2 - r)/\sigma_r} \sum_{n=1}^{N(t)} Q_n(t) e^{-\left[(\theta - \theta_n(t))^2 + (\phi - \phi_n(t))^2\right]/2\sigma_n^2}, \qquad (11.114)$$

where $Q_n(t)$ is the amplitude of the cooling event at time t, and the cooling events are also horizontally advected with the flow: $\theta_n(t) = \theta_n^0 + \frac{\Delta t u_\theta}{r_2}$, and $\phi_n(t) = \phi_n^0 + \frac{\Delta t u_\phi}{r_2}$. The average

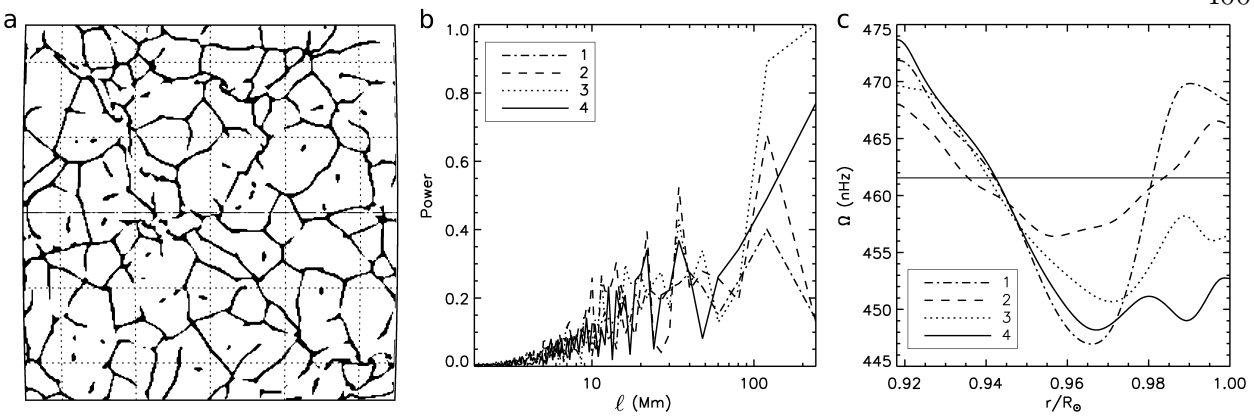

Figure 11.9: (a) A $20° \times 20°$ snapshot of radial velocities (u_r) taken at $0.99\,\mathrm{R}_\odot$ in case 2: downflows are black, upflows are white. (b) Horizontal scale ℓ in u_r power spectra averaged in time and latitude from cases 1 (solid), 2 (dotted), 3 (dashed), and 4 (dash-dotted). (c) Horizontally averaged rotation rate $\Omega(r)$, lines as above.

number of cooling events ($\langle N \rangle$), with ($\langle \sigma \rangle$), determines the mean strength

$$\langle Q \rangle = \frac{(\phi_2 - \phi_1)\,(\cos\theta_1 - \cos\theta_2)}{2\pi \langle N \rangle \langle \sigma \rangle^2} \left[\frac{L}{4\pi r^2} + \kappa_S \frac{\partial S}{\partial r} + \kappa_r \frac{\partial T}{\partial r} \right]_{r_2} . \tag{11.115}$$

Cooling events have a mean lifetime of 10 minutes, but can deviate significantly from this as the lifetimes are normally distributed as well. When a cooling event has reached the end of its lifetime, it is deleted and at least one new cooling event is generated. An exponential distribution is used to determine how many new events are generated, with the mean being unity. Similarly, at each time step there is also a chance to add new events.

11.9.1 Nature of the Convection

In a typical simulation, the convective cells are broad upflows bordered by strong, narrow downflows as seen in Figure 11.9a. The upflows are warm and the downflows are cool relative to the mean temperature. The typical radial velocities in Figure 11.9a are between $-1400\,\mathrm{m\,s^{-1}}$ for downflows and $400\,\mathrm{m\,s^{-1}}$ for upflows. Some basic parameters of the flows developed in these simulations can be seen in Table 11.1. The spatial scales present in the four cases can be seen in power spectra (Figure 11.9b). The supergranule-like scales in

Case 1 are about 40 Mm, just outside the accepted range for supergranules. A spherically symmetric cooling is used in *Case 1* which leads to horizontal scales near the surface that are primarily selected by the geometry of the domain. In cases with granular-scale cooling, the size scales seen in the simulation decrease due to the granular-scale forcing as evidenced by the leftward shift in the power of the peaks below 40 Mm in Figure 11.9b. In *Cases 2-4*, supergranular scales become much more prevalent with power increasing by 50-100% in the band between 10 Mm and 35 Mm. In *Case 2*, a prominent peak occurs around 10 Mm due to the relative paucity of cooling sites. Since there are only 250 cooling sites on average, each site necessarily induces a strong downflow, which ensures that the enthalpy flux is sufficient to carry out the solar flux. Furthermore, there are typically 15 sites at a single longitude or latitude so that the average distance between them is 10-15 Mm. Thus, since each cooling site is likely to be a strong downflow, power is present on the 10 Mm scale. Such a peak does not occur to the same extent in *Case 3* or *Case 4* because the probability of inducing a strong downflow at a cooling site decreases by factor between 2 to 4. However, a larger $\langle N \rangle$ reduces the average distance between cooling sites and thus allows for more interaction of the flows generated at the granular scales due to the advection and coalescence of the cooling sites.

As $\langle N \rangle$ is increased, the granular scale cooling disrupts the mean horizontal flows in the upper 20% of the domain which reduces the mean rotation rate as seen in Figure 11.9c. The reason the mean flows are affected is that when a cooling site forms in an upflow, it begins cooling nearby gas causing contracting horizontal flows and a downflow. So, the net effect of this cooling site is to reduce the horizontal flows within the upflow as well as slow the upflow's ascent as it has been cooled. Hence, as $\langle N \rangle$ increases the average number of cooling sites per upflow increases thus decreasing the mean horizontal flows as in Figure 11.9c. The radial boundaries used for these studies were impenetrable and stress-free leading to overturning of upflows at the top and downflows at the bottom of the domain. This is the primary reason the rotation rate at the bottom does not flatten out and why there is an

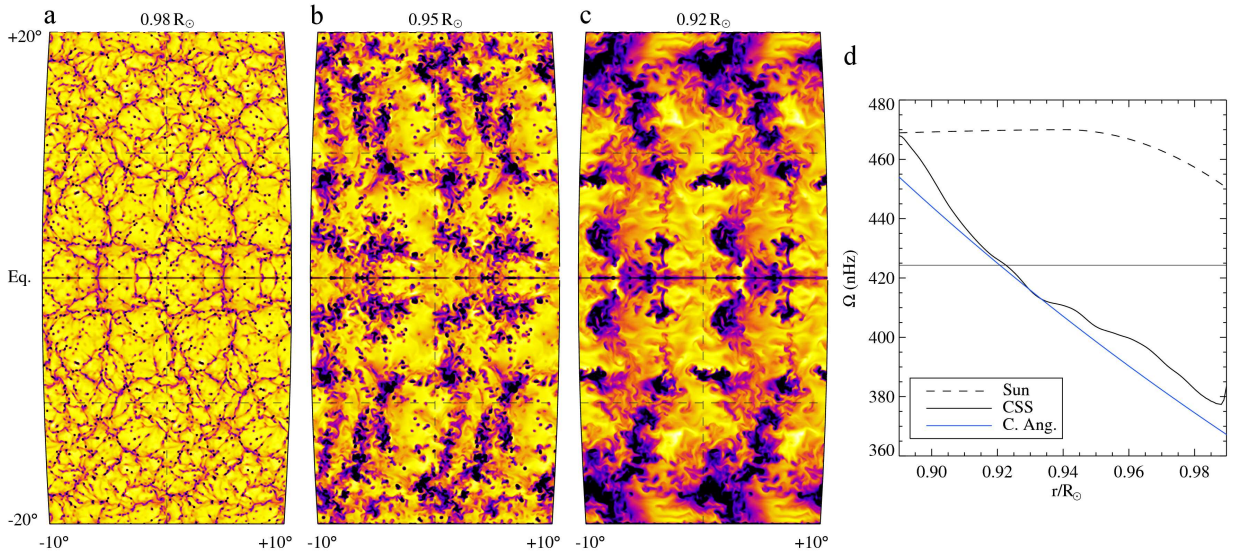

Figure 11.10: Evidence of merging plumes arising in a CSS simulation carried out with 'entropy rain' and open boundaries. The base simulation (20° in latitude and 10° in longitude) has been replicated once in longitude, and reflected across the equator to emphasize the largest scales. Horizontal planes of radial velocities (u_r) cut through the simulation domain at (a) 0.985 $R_\odot$ just below the open upper boundary, (b) 0.950 $R_\odot$ near the middle of the domain, and (c) 0.895 $R_\odot$ just above the open lower boundary. Downflows are dark tones. (d) Horizontally-averaged rotation rate $\Omega(r)$ with radius shown for this simulation (solid black) with the solid blue curve corresponding to the conservation of angular momentum per unit mass. Helioseismically determined Ω at the equator (dashed curve), while the frame rate is the horizontal solid line.

unrealistic shear layer near the upper boundary.

Building upon this early work, more recent simulations have utilized open radial boundaries that have somewhat eliminated the ill-effects of impenetrable boundaries. Such simulations also incorporate a more advanced plume model that employs flow statistics from a photospheric simulation, which will be described in greater detail in the next section. These plumes have both an entropy deficit and a momentum associated with them as they enter the simulation at the upper boundary. Figures 11.10(a-c) show that flows with large-scale structures can form even in the presence of open boundaries and small-scale plume driving. The large-scale flows deeper in the domain have some similarity to the banana cells, which are the most unstable modes of global-scale rotating convection and often seen in the global-

scale ASH simulations. However, despite admitting more physical boundary treatments, this approach does not yet produce a reasonable approximation to the NSSL. Instead, a new issue arises where too much momentum is carried deep into the domain as is visible in Figure 11.10d yielding a radial profile of differential rotation that is consistent with angular momentum conservation per unit mass. The method that currently seems to have the greater potential is having an open upper boundary and an informed lower boundary, where flows from deep within an ASH simulation are imposed.

11.10 Incorporating External Flows into CSS

Simulations (De Rosa et al., 2002) with ASH of supergranular and larger scales of convection in thin shells (extending from 0.90 to 0.98 $R_\odot$) revealed that a rotational shear layer can be achieved through partial conservation of angular momentum (cf. Gilman & Foukal, 1979) by scales of convection comparable to supergranulation. These sense the Coriolis forces only weakly, thereby yielding spin down as fluid is carried radially outward and away from the rotation axis at low latitudes. Although encouraging, such modeling was not capable of either capturing the giant cells very well, which requires much deeper shells, nor in describing the near-surface physics of supergranulation adequately. The outstanding issues concern how is the NSSL formed and maintained, and what determines its thickness, which may vary with latitude.

Giant cells of convection seen in ASH simulations (see Chapters 3, 5–9) have horizontal scales roughly comparable to the depth of the solar convection zone (200 Mm) (Miesch et al., 2008). However, giant cells have been observationally elusive, despite many to directly identify their signatures at the solar surface (Beck et al., 1998; Lisle et al., 2004), though perhaps recently they have been detected (Hathaway et al., 2013). To begin to resolve such fundamental issues, a few preliminary CSS simulations have sought to clarify how the giant cells of convection, so evident in global convection models, might be disrupted as those scales interact with the smaller scales dominant near the solar surface. These simulations

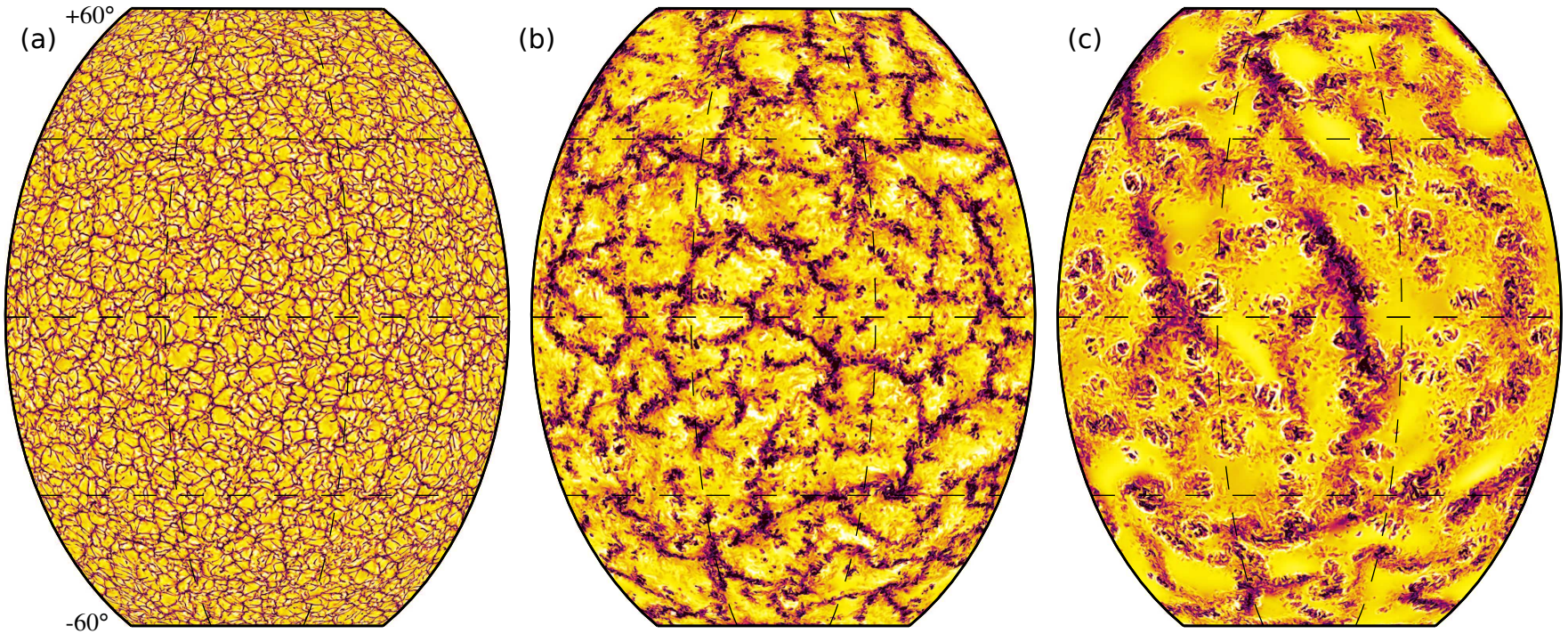

Figure 11.11: Near-surface convection and colliding flows studied in a CSS simulation, with large-scale ASH flows imposed from below and statistically defined plumes from above. Shown are orthographic projections at (a) $0.985\,\mathrm{R}_\odot$ below the open upper boundary, (b) $0.950\,\mathrm{R}_\odot$ near the middle of the domain, and at (c) $0.900\,\mathrm{R}_\odot$ just above the imposed flows at the lower boundary. Downflows are dark lanes in (a), which become shear unstable and merge into larger structures as in (b). The interaction between merging downflows structures from above and imposed large-scale flows from an ASH simulation becomes visible in (c). The full domains are fairly large, spanning 120° in latitude and 90° in longitude and $2240 \times 1680 \times 256$ in resolution.

were informed at their upper boundaries with a statistically determined flow and informed at their lower boundaries by an ASH simulation. The $\ell_{\max} = 170$ ASH simulation used at the lower boundary of CSS was four-fold periodic to match the longitudinal size of the CSS domain and extended from the base of the convection zone to $0.96\,\mathrm{R}_\odot$. The full domains for the CSS simulations were fairly large, spanning 120° in latitude and 90° in longitude and were between $n_\theta \times n_\phi \times n_r = 1024 \times 768 \times 256$ and $2240 \times 1680 \times 256$ in resolution. They also encompassed the upper 80 Mm of the convection zone. The boundary conditions defined in §11.2 are only slight modified to incorporate the entropy and the flows from ASH. The flows from ASH are first interpolated in time and space to match the grid size, the meridional flows are truncated at the latitudinal boundaries over a thin layer. Instead of pulling the values of the boundary plane to those of an interior plane of the simulation, the time evolving values from the prior ASH simulation are substituted for the interior values as

$$\left.\frac{\partial \mathbf{u}}{\partial t}\right|_{r_1} = \frac{1}{\tau_{r_1}} \left(\mathbf{u}|_{\mathrm{ASH}} - \mathbf{u}|_{r_1} \right), \tag{11.116}$$

$$\left.\frac{\partial s}{\partial t}\right|_{r_1} = \frac{1}{\tau_{r_1}} \left(s|_{\mathrm{ASH}} - s|_{r_1} - \langle s_{r_1} \rangle + \overline{s}_{r_1} \right), \tag{11.117}$$

where the averaged terms are defined as in §11.2 and the pressure gradient is computed in the same fashion.

The CSS simulations were informed by evolving downflow structures at the upper boundary whose statistics are consistent with those realized in the surface convection simulations with MSC, as described in Trampedach (2010). Unlike the cooling-site entropy rain model used in the simulations of the previous section, these flows consisted of fast, entropy deficient downflow plumes that enter the CSS domain through its upper radial boundary. The plumes were randomly placed on the upper boundary and were assumed to have a Gaussian spatial structure. The widths of these Gaussian plumes are determined by the statistical distribution of the widths of downflows in the MSC surface convection simulations. Similarly, their duration, entropy deficiency, and radial velocity are all chosen from statistical distributions and correlations of downflows derived from the MSC simulations at the

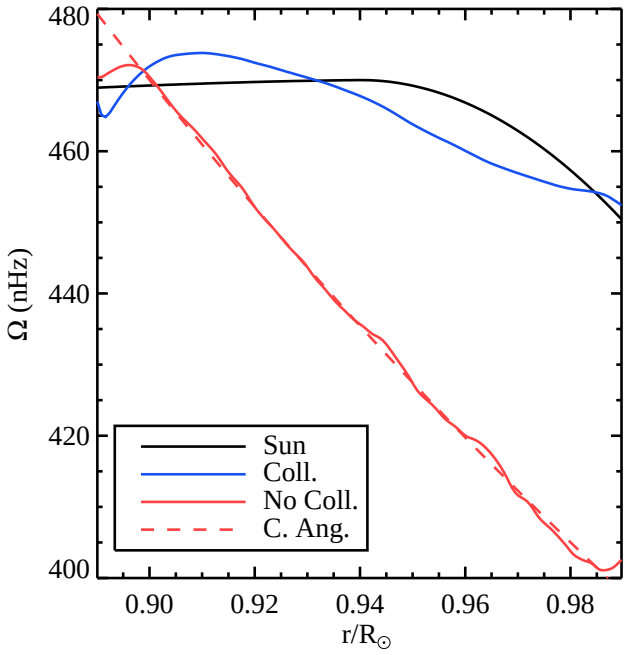

Figure 11.12: Horizontally-averaged rotation rate $\Omega(r)$ attained in two CSS simulations involving open upper boundary conditions and "low entropy rain" statistics informed by MSC modeling (red), and alternatively with those descending flows colliding with large-scale convective flows entering from the lower boundary (blue). Simple conservation of angular momentum is shown (dashed red), along with helioseismic profile (black).

depths corresponding to the CSS upper boundary. The correlations between these quantities have important implications for the dynamics of the shear layer, and thus cannot be chosen independently nor randomly.

The angular momentum transport across the upper and lower radial boundaries of CSS has a direct bearing on the maintenance of the NSSL. The upper boundary here was required to have zero net angular momentum flux, but the transport at the lower boundary was specified by the flows from ASH. The upper boundary conditions for the entropy rain are very similar to the ASH inflows. The entropy rain is simply treated as an exterior simulation that evolves on the boundary, so

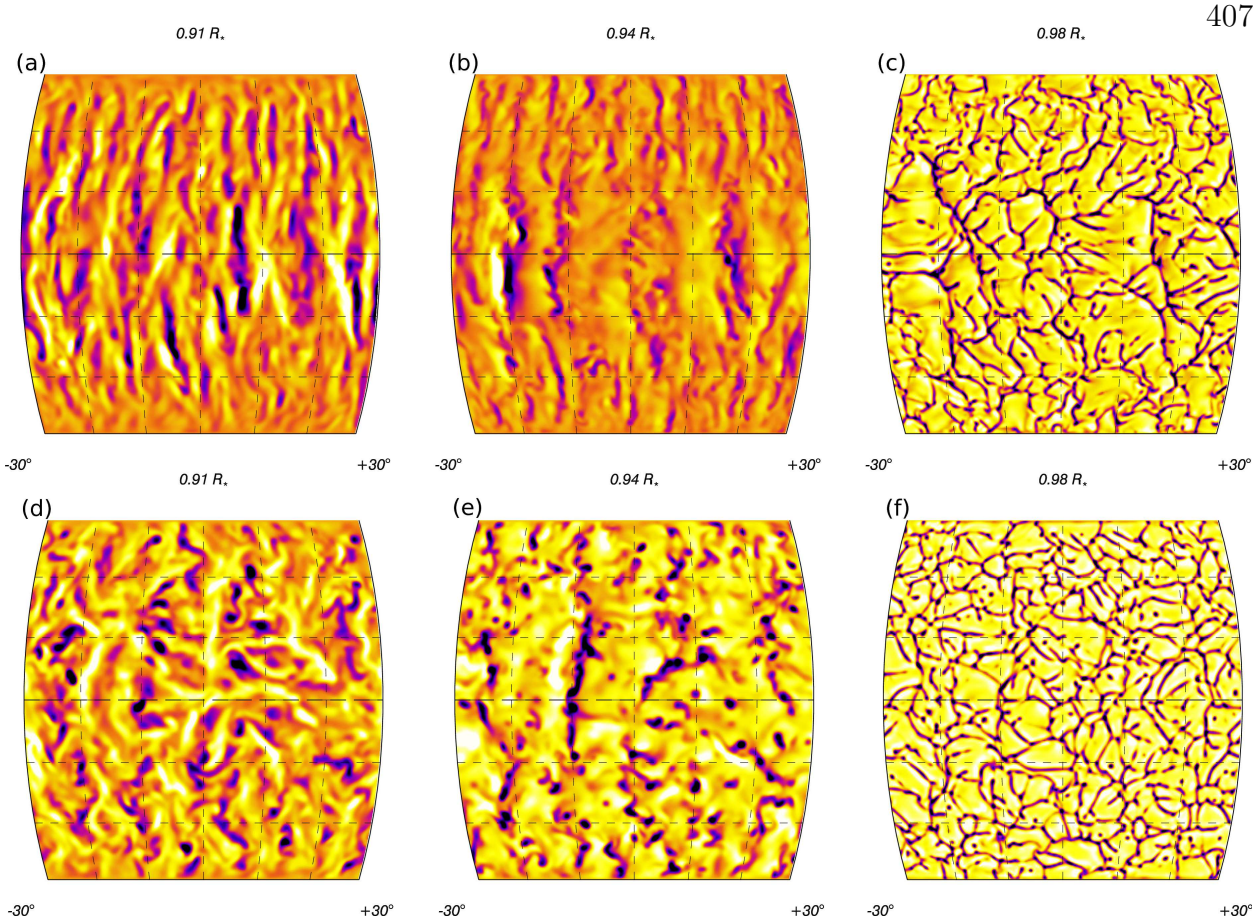

Figure 11.13: Rotationally constrained convection in CSS. (a-c) A Sun-like star rotating at $10\,\Omega_\odot$ at three depths, as labeled above each panel. (e-f) A Sun-like star rotating at $3\,\Omega_\odot$ at three depths, showing less rotational influence.

$$\left.\frac{\partial \mathbf{u}}{\partial t}\right|_{r_2} = \frac{1}{\tau_{r_2}}\left(\mathbf{u}|_{\rm rain} - \mathbf{u}|_{r_2}\right) - \frac{\langle \mathbf{p}_{r_2}\rangle}{\langle m_{r_2}\rangle \Delta t}, \tag{11.118}$$

$$\left.\frac{\partial s}{\partial t}\right|_{r_2} = \frac{1}{\tau_{r_2}}\left(s|_{\rm rain} - s|_{r_2} - \langle s_{r_2}\rangle + \overline{s}_{r_2}\right), \tag{11.119}$$

These simulations have explicitly specified the evolving flows at the lower boundary of CSS with velocities and thermodynamic perturbations from a fairly low resolution ASH simulation. Indeed, they have begun to enable the study of the challenging near-surface region in some detail where the intense downdrafts of the surface convection interact and merge with the large-scale upwelling and horizontally-sweeping flows of giant cells. The

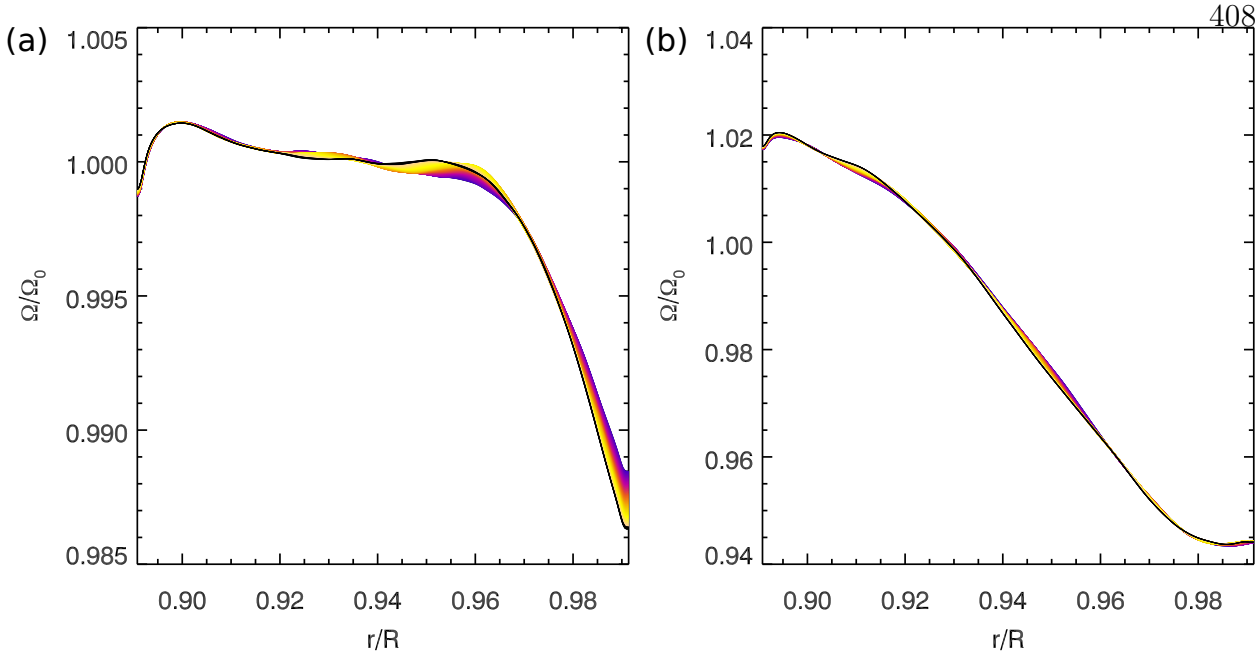

Figure 11.14: Shell-averaged angular velocity profiles with shear layers realized in CSS simulations. (a) A Sun-like star rotating at $10\,\Omega_\odot$, the color denotes the time evolution of the angular velocity with several hundred days represented, showing the presence of a near surface shear layer. (b) A Sun-like star rotating at $3\,\Omega_\odot$, lacking a shear layer due to the larger Rossby number throughout the domain.

simulation whose radial velocities at several depths are shown in Figure 11.11 has yielded a radial differential rotation that possesses a region of near-surface shear that becomes more uniform with greater depth as depicted in Figure 11.12. The transition to uniformity partly arises through the angular momentum flux into the domain from the ASH simulation and also through the transition to more rotationally constrained flows with the Rossby number falling below unity. The near-surface shear appears to be a consequence of the fast, angular momentum conserving flows falling from the upper boundary and continuously mixing with the broad upflows as the descend through the domain. This mixes flows with locally low Rossby number and those with locally larger Rossby numbers leading to the gradual loss of the angular momentum conserving properties of the downflows and to the change in the profile of the radial differential rotation.

Other recent CSS simulations have shed some light on this as well. These closed

domain simulations mimic the solar interior but are rotated more rapidly to attain a lower Rossby number in the domain. With a rapid enough rotation, a clear transition between surface convection cells and deeper rotationally constrained flows becomes evident as shown in Figures 11.13 and 11.14. Thus, the suspicion that the base of the NSSL reflects a shift in the nature of the meridional force balance, from baroclinic forcing in the deep convection zone to Reynolds and Maxwell stresses in the NSSL, may indeed occur and be due to the effective Rossby number of the local flows. Hence, future CSS modeling may focus on the character of the resulting meridional circulation which responds to zonal stresses in both the upper and lower convection zone through the mechanism of gyroscopic pumping (Miesch & Hindman, 2011).

11.11 Conclusions

Many aspects of the code need to be finalized and its capabilities truly put to the test. A thorough testing and understanding of all the options within the code, particularly those related to coupling codes together, needs to be undertaken. However, there is also much to be exploited in its already existing form. Indeed, the preliminary results using CSS are very encouraging, with properties of the solar near-surface shear layer beginning to emerge through two separate lines of investigation. One method presented here involves coupling the dynamics of the deep interior obtained in ASH simulations and a statistical description of the unresolved flows arising near the photosphere. The flows established in the first simulations utilizing these informed boundaries have the properties necessary to produce a region of near-surface shear and to transition to the more uniform rotation of the deep solar interior. Similarly, a second approach that decreases the bulk Rossby number of the flows in simulations of the full convection zone of F-type stars also yields a near-surface shear layer. The latter simulations are fully self-contained and self-consistent, suggesting that the method to self-consistently achieve a region of near-surface shear is to decrease the Rossby number of the flows. The only viable way to do this in a solar simulation is to decrease the

convective driving on the large scales, effectively controlling the resolved heat flux that is carried through the domain.

Chapter 12

Perspectives and Ponderings

Humanity's long road to understanding the nature of the Sun and the curiosity of the stars continues to be traveled. This thesis has only brushed the surface of the many intertwined phenomena at work within stars, beginning with their observed characteristics and then delving into the theories that are currently thought to describe their inner workings. With some of the latest computational tools, aspects of stellar magnetism have been explored that may be making significant contact with the observed character of solar and stellar magnetic activity. The hydrodynamics of stars slightly more massive than the Sun, the F-type stars, has been examined with an eye on how properties intrinsic to stellar dynamos scale with mass and rotation rate and how those properties change in the presence of a stable region below their convective regions. Subsequently, how dynamos may operate within the F-type stars has been explored, with the stable region playing a crucial role in the dynamo. The convective and magnetic properties of the cores of very massive stars has begun to be probed, with MG fields forming within the core. This bodes well for building a better understanding of the properties of highly magnetized stellar remnants. Finally, a new MHD code has been developed that with the results in hand holds good promise for untangling some of the dynamics of the solar near-surface shear layer as well as the properties of convection zones for which compressibility may play a role.

With those paths pursued, where do they now fork and diverge? There are many threads that have been sprinkled throughout this thesis that may provide intriguing routes

to understanding the deeper mathematical and physical properties of turbulence in general, which of course also as applicable to stellar dynamo theories. For the primary work presented here, the most immediately promising is the application of mixed subgrid-scale methods for building stellar dynamos. Indeed, the simulation presented in Chapter 5 may provide the launching point for understanding some of the observed global-scale properties of the solar dynamo, such as what might be setting the cycle period and what processes lead to grand minima. Subsequent analysis of simulations utilizing some of these techniques may help to pin down those processes leading to the global-scale magnetic field reversals. This path is one that is straight and narrow, with well defined parameters that can be varied. Assessing the impacts of the slope-limited diffusion operator is paramount to ensure that it is not impacting the solution in adverse ways. If it is not, one may embark on a parameter study of rotation, convective driving, magnetic Reynolds number, as well as effective thermal and magnetic Prandtl numbers through the variation of the resolution of the simulations. This still skirts the issue of what happens as a larger number of density scale heights are admitted in the system. Fortuitously, slope-limited diffusion permits simulations with it to admit larger density stratifications and yet remain numerically stable.

Exploring dynamo action in other low mass stars like the Sun may too yield broader insight into the fundamental mechanisms leading to stellar magnetic activity. For instance the role of a tachocline may be particularly evident for low mass stars with some possessing one and others slightly less massive that are fully convective. It may also be intriguing to look at the higher mass F-type stars with CSS that may also harbor a tachocline below their thin convection zones, which have fairly high Mach number flows throughout them and fast thermal relaxation times. Additionally, such stars rotate more rapidly than the Sun on average, and those that have observed activity cycles tend to have fairly short cycle periods. This permits greater contact and potential for refinement between observation and theory.

The short-lived massive stars also present intriguing prospects for developing a better understanding of how magnetism, rotation, and convection might impact their evolution and

their remnants. Several opportunities seem to arise with the preliminary results presented in Chapter 10. The most obvious is to include primordial fields to assess how superequipartition the magnetic field configuration might become, given that it is already four times greater than the kinetic energy. Utilizing more accurate subgrid-scale models in the radiative exterior may permit the entire gravity wave cavity to be simulated within ASH. Previous attempts at this had been made, but failed due to large mode amplitudes near the upper boundary. The amplification of the waves is in part due to their propagation down the density gradient, which naturally leads to amplification. Once the full-sphere implementation in ASH has been thoroughly vetted, it would be quite useful to retain the center-most portion of the core, rather than omitting it as has been done here. Then one could assess what impacts if any the core cutout has on the connectivity of the flow and magnetic structures. It would also be useful to implement the generalized pseudo-incompressible equations into the ASH framework in order to simulate the more extreme environments of both evolved massive stars and of the more massive main-sequence stars for whom radiation pressure plays an important if not dominant role.

Finally, there are many prospective directions to take with CSS. The current lines of investigation can be extended with recent modifications to the code that increase its speed by a factor of two more than what was seen in the strong-scaling plots of Chapter 11. Furthermore, extending beyond the solar realm to regimes that are similar but less restrictive may provide useful insight into processes such as magnetic buoyancy and the influence of a tachocline. In the longer term, it will be possible to build a generalized pseudo-incompressible framework that admits higher-order terms in the kinematic pressure allowing for sound waves. This will allow a mathematically-sound scale separation problem to be solved that retains acoustic modes where necessary and omits them where they are not. Such a code would be the next generation pseudo-spectral stellar convection code, being able to accurately and self-consistently evolve scales from the photosphere to the deep interior.

Bibliography

Abdussamatov, H. I. 1993, *The fine structure of solar granulation and its relationship to large-scale photospheric structures*, A&A, 272, 580

—. 2000, *Mesostructure of the solar granulation*, Astronomy Letters, 26, 192

Abdussamatov, H. I., & Zlatopolo'Skii, A. G. 1997, *Variation of fine-structure properties of solar granulation on a mesogranular scale*, Astronomy Letters, 23, 752

Abney, W. D. W. 1877a, *Effect of a star's rotation on its spectrum*, MNRAS, 37, 278

—. 1877b, *Photographic spectra showing the sun's rotation*, The Observatory, 1, 134

Abreu, J. A., Beer, J., Ferriz-Mas, A., McCracken, K. G., & Steinhilber, F. 2012, *Is there a planetary influence on solar activity?*, A&A, 548, A88

Abt, H. A., & Hunter, Jr., J. H. 1962, *Stellar Rotation in Galactic Clusters.*, ApJ, 136, 381

Abt, H. A., Levato, H., & Grosso, M. 2002, *Rotational Velocities of B Stars*, ApJ, 573, 359

Adzhemyan, L., Antonov, N., & Vasiliev, A. 1999, Field Theoretic Renormalization Group in Fully Developed Turbulence (Taylor & Francis)

Aerts, C., Briquet, M., Degroote, P., Thoul, A., & van Hoolst, T. 2011, *Seismic modelling of the β Cephei star HD 180642 (V1449 Aquilae)*, A&A, 534, A98

Aerts, C., Thoul, A., Daszyńska, J., et al. 2003, *Asteroseismology of HD 129929: Core Overshooting and Nonrigid Rotation*, Science, 300, 1926

Ammler-von Eiff, M., & Reiners, A. 2012, *New measurements of rotation and differential rotation in A-F stars: are there two populations of differentially rotating stars?*, A&A, 542, A116

Anderson, R. Y. 1982, *A long geoclimatic record from the Permian*, J. Geophys. Res., 87, 7285

Anderson, R. Y., & Dean, W. E. 1995, *Filling the Delaware Basin: Hydrologic and Climatic Controls on the Upper Permian Castile Formation Varved Evaporite*, in The Permian of Northern Pangea, ed. P. Scholle, T. Peryt, & D. Ulmer-Scholle (Springer Berlin Heidelberg), 61–78

Anderson, R. Y., & Kirkland, D. W. 1966, *Intrabasin Varve Correlation*, Geological Society of America Bulletin, 77, 241

Andersson, N., & Comer, G. L. 2013, *A covariant action principle for dissipative fluid dynamics: From formalism to fundamental physics*, ArXiv e-prints

Angenheister, G., Bartels, J., & Benndorf, H. 1928, Handbuch der Experimentalphysik, Vol. 25, Geophysik (Akadem. Verlagsges.)

Antokhin, I. I., Rauw, G., Vreux, J.-M., van der Hucht, K. A., & Brown, J. C. 2008, *XMM-Newton X-ray study of early type stars in the Carina OB1 association*, A&A, 477, 593

Arkani-Hamed, N., Bourjaily, J. L., Cachazo, F., et al. 2012, *Scattering Amplitudes and the Positive Grassmannian*, ArXiv e-prints

Arlt, R. 2009, *The Butterfly Diagram in the Eighteenth Century*, Sol. Phys., 255, 143

Arlt, R., Leussu, R., Giese, N., Mursula, K., & Usoskin, I. G. 2013, *Sunspot positions and sizes for 1825-1867 from the observations by Samuel Heinrich Schwabe*, MNRAS

Augustson, K. C., Brown, B. P., Brun, A. S., Miesch, M. S., & Toomre, J. 2012, *Convection and Differential Rotation in F-type Stars*, ApJ, 756, 169

Augustson, K. C., Brun, A. S., Miesch, M. S., & Toomre, J. 2013a, *Cycling Dynamo in a Young Sun: Grand Minima and Equatorward Propagation*, ApJ, 781, 169

Augustson, K. C., Brun, A. S., & Toomre, J. 2011, *Convection and dynamo action in B stars*, in IAU Symposium, Vol. 271, IAU Symposium, ed. N. H. Brummell, A. S. Brun, M. S. Miesch, & Y. Ponty, 361–362

Augustson, K. C., Brun, A. S., & Toomre, J. 2013b, *Dynamo Action and Magnetic Cycles in F-type Stars*, ApJ, 777, 153

Babcock, H. D. 1959, *The Sun's Polar Magnetic Field.*, ApJ, 130, 364

Babcock, H. W. 1947, *Zeeman Effect in Stellar Spectra.*, ApJ, 105, 105

—. 1961, *The Topology of the Sun's Magnetic Field and the 22-YEAR Cycle.*, ApJ, 133, 572

Babel, J., & Montmerle, T. 1997, *X-ray emission from Ap-Bp stars: a magnetically confined wind-shock model for IQ Aur.*, A&A, 323, 121

Backus, G. 1958, *A class of self-sustaining dissipative spherical dynamos*, Annals of Physics, 4, 372

Bai, T. 2003, *Periodicities in Solar Flare Occurrence: Analysis of Cycles 19-23*, ApJ, 591, 406

Baier, R., Romatschke, P., Thanh Son, D., Starinets, A. O., & Stephanov, M. A. 2008, *Relativistic viscous hydrodynamics, conformal invariance, and holography*, Journal of High Energy Physics, 4, 100

Balbus, S. A. 2009, *A simple model for solar isorotational contours*, MNRAS, 395, 2056

Balbus, S. A., Bonart, J., Latter, H. N., & Weiss, N. O. 2009, *Differential rotation and convection in the Sun*, MNRAS, 400, 176

Balbus, S. A., Latter, H., & Weiss, N. 2012, *Global model of differential rotation in the Sun*, MNRAS, 420, 2457

Balbus, S. A., & Latter, H. N. 2010, *The tachocline and differential rotation in the Sun*, MNRAS, 407, 2565

Balbus, S. A., & Schaan, E. 2012, *The stability of stratified, rotating systems and the generation of vorticity in the Sun*, MNRAS, 426, 1546

Baliunas, S. L., Nesme-Ribes, E., Sokoloff, D., & Soon, W. H. 1996, *A Dynamo Interpretation of Stellar Activity Cycles*, ApJ, 460, 848

Baliunas, S. L., Hartmann, L., Noyes, R. W., et al. 1983, *Stellar rotation in lower main-sequence stars measured from time variations in H and K emission-line fluxes. II - Detailed analysis of the 1980 observing season data*, ApJ, 275, 752

Baliunas, S. L., Horne, J. H., Porter, A., et al. 1985, *Time-series measurements of chromospheric CA II H and K emission in cool stars and the search for differential rotation*, ApJ, 294, 310

Baliunas, S. L., Donahue, R. A., Soon, W. H., et al. 1995, *Chromospheric variations in main-sequence stars*, ApJ, 438, 269

Ballot, J., Brun, A. S., & Turck-Chièze, S. 2007, *Simulations of Turbulent Convection in Rotating Young Solarlike Stars: Differential Rotation and Meridional Circulation*, ApJ, 669, 1190

Barnes, J. R., Cameron, A. C., Donati, J.-F., et al. 2005, *The dependence of differential rotation on temperature and rotation*, MNRAS, 357, L1

Barnes, S. A. 2007, *Ages for Illustrative Field Stars Using Gyrochronology: Viability, Limitations, and Errors*, ApJ, 669, 1167

Batchelor, G. K. 1953, *The conditions for dynamical similarity of motions of a frictionless perfect-gas atmosphere*, Quarterly Journal of the Royal Meteorological Society, 79, 224

Beck, J. G., Duvall, T. L., & Scherrer, P. H. 1998, *Long-lived giant cells detected at the surface of the Sun*, Nature, 394, 653

Berdyugina, S. V. 2005, *Starspots: A Key to the Stellar Dynamo*, Living Reviews in Solar Physics, 2, 8

Berghöfer, T. W., Schmitt, J. H. M. M., Danner, R., & Cassinelli, J. P. 1997, *X-ray properties of bright OB-type stars detected in the ROSAT all-sky survey.*, A&A, 322, 167

Berkeley, J., & Berman, D. S. 2013, *The Navier-Stokes equation and solution generating symmetries from holography*, Journal of High Energy Physics, 4, 92

Bessolaz, N., & Brun, A. S. 2011, *Towards a 3D dynamo model of the PMS star BP Tau*, Astron. Nachr., 332, 1045

Bessolaz, N., Zanni, C., Ferreira, J., Keppens, R., & Bouvier, J. 2008, *Accretion funnels onto weakly magnetized young stars*, A&A, 478, 155

Bhattacharyya, S., Minwalla, S., Hubeny, V. E., & Rangamani, M. 2008, *Nonlinear fluid dynamics from gravity*, Journal of High Energy Physics, 2, 45

Bidelman, W. P. 1954, *Catalogue and Bibliography of Emission-Line Stars of Types Later than B.*, ApJS, 1, 175

Bieber, J. W., & Rust, D. M. 1995, *The Escape of Magnetic Flux from the Sun*, ApJ, 453, 911

Bishop, R. L. 1968, Tensor analysis on manifolds (Courier Dover Publications)

Blackman, E. G., & Brandenburg, A. 2003, *Doubly Helical Coronal Ejections from Dynamos and Their Role in Sustaining the Solar Cycle*, ApJ, 584, L99

Böhm, K.-H. 1952, *Die Rotationsgeschwindigkeiten der Sterne. Mit 4 Textabbildungen*, ZAp, 30, 117

Böhm-Vitense, E., Robinson, R., Carpenter, K., & Mena-Werth, J. 2002a, *What Is Happening at Spectral Type F5 in Hyades F Stars?*, ApJ, 569, 941

—. 2002b, *What Is Happening at Spectral Type F5 in Hyades F Stars?*, ApJ, 569, 941

Borges, R., Carmona, M., Costa, B., & Don, W. S. 2008, *An improved weighted essentially non-oscillatory scheme for hyperbolic conservation laws*, Journal of Computational Physics, 227, 3191

Boussinesq, J. 1903, Théorie Analytique de la Chaleur, Vol. Tome II. (Paris Gauthier-Villars), 157–176

Bouvier, J., Forestini, M., & Allain, S. 1997, *The angular momentum evolution of low-mass stars.*, A&A, 326, 1023

Bracewell, R. N. 1988, *Spectral analysis of the Elatina series*, Sol. Phys., 116, 179

Braginskii, S. I. 1965, *Transport Processes in a Plasma*, Reviews of Plasma Physics, 1, 205

Braginsky, S. I., & Roberts, P. H. 1995, *Equations governing convection in earth's core and the geodynamo*, GApFD, 79, 1

Braithwaite, J., & Nordlund, Å. 2006, *Stable magnetic fields in stellar interiors*, A&A, 450, 1077

Brandenburg, A. 2007, *Near-surface shear layer dynamics*, in IAU Symposium, Vol. 239, IAU Symposium, ed. F. Kupka, I. Roxburgh, & K. L. Chan, 457–466

Brandenburg, A. 2009, *Large-scale Dynamos at Low Magnetic Prandtl Numbers*, ApJ, 697, 1206

Brandenburg, A., Käpylä, P. J., & Mohammed, A. 2004, *Non-Fickian diffusion and tau approximation from numerical turbulence*, Physics of Fluids, 16, 1020

Brandenburg, A., Moss, D., & Soward, A. M. 1998, *New results for the Herzenberg dynamo: steady and oscillatory solutions*, Royal Society of London Proceedings Series A, 454, 1283

Brandenburg, A., Sokoloff, D., & Subramanian, K. 2012, *Current Status of Turbulent Dynamo Theory. From Large-Scale to Small-Scale Dynamos*, Space Sci. Rev., 169, 123

Brandenburg, A., & Spiegel, E. A. 2008, *Modeling a Maunder minimum*, Astronomische Nachrichten, 329, 351

Brandenburg, A., & Subramanian, K. 2005, *Astrophysical magnetic fields and nonlinear dynamo theory*, Phys. Rep., 417, 1

Brandt, P. N., Ferguson, S., Shine, R. A., Tarbell, T. D., & Scharmer, G. B. 1991, *Variation of granulation properties on a mesogranular scale*, A&A, 241, 219

Bredberg, I., Keeler, C., Lysov, V., & Strominger, A. 2011, *Wilsonian approach to fluid/gravity duality*, Journal of High Energy Physics, 3, 141

Briquet, M., Aerts, C., Baglin, A., et al. 2011, *An asteroseismic study of the O9V star HD 46202 from CoRoT space-based photometry*, A&A, 527, A112

Brott, I., de Mink, S. E., Cantiello, M., et al. 2011, *Rotating massive main-sequence stars. I. Grids of evolutionary models and isochrones*, A&A, 530, A115

Brown, B. P. 2009, PhD thesis, University of Colorado at Boulder

Brown, B. P., Browning, M. K., Brun, A. S., Miesch, M. S., & Toomre, J. 2008, *Rapidly Rotating Suns and Active Nests of Convection*, ApJ, 689, 1354

—. 2010, *Persistent Magnetic Wreaths in a Rapidly Rotating Sun*, ApJ, 711, 424

Brown, B. P., Browning, M. K., Brun, A. S., Miesch, M. S., & Toomre, J. 2011a, *Global-scale Magnetism (and Cycles) in Dynamo Simulations of Stellar Convection Zones*, in Astronomical Society of the Pacific Conference Series, Vol. 448, 16th Cambridge Workshop on Cool Stars, Stellar Systems, and the Sun, ed. C. Johns-Krull, M. K. Browning, & A. A. West, 277

Brown, B. P., Miesch, M. S., Browning, M. K., Brun, A. S., & Toomre, J. 2011b, *Magnetic Cycles in a Convective Dynamo Simulation of a Young Solar-type Star*, ApJ, 731, 69

Brown, B. P., Vasil, G. M., & Zweibel, E. G. 2012, *Energy Conservation and Gravity Waves in Sound-proof Treatments of Stellar Interiors. Part I. Anelastic Approximations*, ApJ, 756, 109

Brown, T. M., Christensen-Dalsgaard, J., Dziembowski, W. A., et al. 1989, *Inferring the sun's internal angular velocity from observed p-mode frequency splittings*, ApJ, 343, 526

Browning, M. K. 2008, *Simulations of Dynamo Action in Fully Convective Stars*, ApJ, 676, 1262

Browning, M. K., Basri, G., Marcy, G. W., West, A. A., & Zhang, J. 2010, *Rotation and Magnetic Activity in a Sample of M-Dwarfs*, AJ, 139, 504

Browning, M. K., Brun, A. S., & Toomre, J. 2004, *Simulations of Core Convection in Rotating A-Type Stars: Differential Rotation and Overshooting*, ApJ, 601, 512

Browning, M. K., Miesch, M. S., Brun, A. S., & Toomre, J. 2006, *Dynamo Action in the Solar Convection Zone and Tachocline: Pumping and Organization of Toroidal Fields*, ApJ, 648, L157

Brummell, N., Tobias, S., & Cattaneo, F. 2010, *Dynamo efficiency in compressible convective dynamos with and without penetration*, Geophysical and Astrophysical Fluid Dynamics, 104, 565

Brummell, N. H., Clune, T. L., & Toomre, J. 2002, *Penetration and Overshooting in Turbulent Compressible Convection*, ApJ, 570, 825

Brun, A. S., Browning, M. K., & Toomre, J. 2005, *Simulations of Core Convection in Rotating A-Type Stars: Magnetic Dynamo Action*, ApJ, 629, 461

Brun, A. S., Miesch, M. S., & Toomre, J. 2004, *Global-Scale Turbulent Convection and Magnetic Dynamo Action in the Solar Envelope*, ApJ, 614, 1073

—. 2011, *Modeling the Dynamical Coupling of Solar Convection with the Radiative Interior*, ApJ, 742, 79

Brun, A. S., & Palacios, A. 2009, *Numerical Simulations of a Rotating Red Giant Star. I. Three-dimensional Models of Turbulent Convection and Associated Mean Flows*, ApJ, 702, 1078

Brun, A. S., & Toomre, J. 2002, *Turbulent Convection under the Influence of Rotation: Sustaining a Strong Differential Rotation*, ApJ, 570, 865

Brun, A. S., & Zahn, J.-P. 2006, *Magnetic confinement of the solar tachocline*, A&A, 457, 665

Budaev, V. P., Savin, S. P., & Zelenyi, L. M. 2011, *Investigation of intermittency and generalized self-similarity of turbulent boundary layers in laboratory and magnetospheric plasmas: towards a quantitative definition of plasma transport features*, Physics Uspekhi, 54, 875

Bullard, E., & Gellman, H. 1954, *Homogeneous Dynamos and Terrestrial Magnetism*, Royal Society of London Philosophical Transactions Series A, 247, 213

Busse, F. H. 2002, *Convective flows in rapidly rotating spheres and their dynamo action*, Phys. Fluids, 14, 1301

Busse, F. H., & Hood, L. L. 1982, *Differential rotation driven by convection in a rapidly rotating annulus*, Geophysical and Astrophysical Fluid Dynamics, 21, 59

Cane, H. V., Richardson, I. G., & von Rosenvinge, T. T. 1998, *Interplanetary magnetic field periodicity of ∼153 days*, Geophys. Res. Lett., 25, 4437

Cantiello, M., & Braithwaite, J. 2011, *Magnetic spots on hot massive stars*, A&A, 534, A140

Cantiello, M., Langer, N., Brott, I., et al. 2009, *Sub-surface convection zones in hot massive stars and their observable consequences*, A&A, 499, 279

Carrington, R. C. 1863, Observations of the spots on the sun from November 9 1853, to March 24, 1861, made at Redhill (Williams and Norgate)

Carroll, J. A. 1928, *The form of an absorption line in the spectrum of a rotating or expanding star*, MNRAS, 88, 548

Catala, C., Donati, J.-F., Shkolnik, E., Bohlender, D., & Alecian, E. 2007, *The magnetic field of the planet-hosting star τ Boötis*, MNRAS, 374, L42

Chabrier, G., & Baraffe, I. 1997, *Structure and evolution of low-mass stars*, A&A, 327, 1039

Chandrasekhar, S. 1961, Hydrodynamic and hydromagnetic stability (Oxford University Press)

Chaplin, W. J., & Miglio, A. 2013, *Asteroseismology of Solar-Type and Red-Giant Stars*, ArXiv e-prints

Charbonneau, P. 2010, *Dynamo Models of the Solar Cycle*, Living Reviews in Solar Physics, 7, 3

—. 2013, *Solar physics: The planetary hypothesis revived*, Nature, 493, 613

Charbonneau, P., & MacGregor, K. B. 2001, *Magnetic Fields in Massive Stars. I. Dynamo Models*, ApJ, 559, 1094

Charbonneau, P., St-Jean, C., & Zacharias, P. 2005, *Fluctuations in Babcock-Leighton Dynamos. I. Period Doubling and Transition to Chaos*, ApJ, 619, 613

Christensen-Dalsgaard, J. 2002, *Helioseismology*, Reviews of Modern Physics, 74, 1073

Cincunegui, C., Díaz, R. F., & Mauas, P. J. D. 2007, *Hα and the Ca II H and K lines as activity proxies for late-type stars*, A&A, 469, 309

Claret, A. 2007, *Does convective core overshooting depend on stellar mass?. Tests using double-lined eclipsing binaries*, A&A, 475, 1019

Clark, R. E. H., Magee, Jr., N. H., Mann, J. B., & Merts, A. L. 1982, *Collisional excitation rates of complex atomic ions by electron impact*, ApJ, 254, 412

Clune, T. L., Elliott, J. R., Miesch, M. S., Toomre, J., & Glatzmaier, G. A. 1999, *Computational aspects of a code to study rotating turbulent convection in spherical shells*, Para. Comp., 25, 361

Collier Cameron, A. 2007, *Differential rotation on rapidly rotating stars*, Astronomische Nachrichten, 328, 1030

Collier Cameron, A., Donati, J., & Semel, M. 2002, *Stellar differential rotation from direct star-spot tracking*, MNRAS, 330, 699

Corbard, T., & Thompson, M. J. 2002, *The subsurface radial gradient of solar angular velocity from MDI f-mode observations*, Sol. Phys., 205, 211

Cowling, T. G. 1933, *The magnetic field of sunspots*, MNRAS, 94, 39

Cruzan, O. R. 1962, *Translational addition theorem for spherical vector wave functions*, Quart. Appl. Math., 20, 33

Cunha, M. S., Aerts, C., Christensen-Dalsgaard, J., et al. 2007, *Asteroseismology and interferometry*, A&A Rev., 14, 217

de la Cruz Rodríguez, J., Socas-Navarro, H., Carlsson, M., & Leenaarts, J. 2012, *Non-local thermodynamic equilibrium inversions from a 3D magnetohydrodynamic chromospheric model*, A&A, 543, A34

De Rosa, M. L., Gilman, P. A., & Toomre, J. 2002, *Solar Multiscale Convection and Rotation Gradients Studied in Shallow Spherical Shells*, ApJ, 581, 1356

Decressin, T., Mathis, S., Palacios, A., et al. 2009, *Diagnoses to unravel secular hydrodynamical processes in rotating main sequence stars*, A&A, 495, 271

Degroote, P., Aerts, C., Samadi, R., et al. 2010a, *Asteroseismology of OB stars with CoRoT*, Astronomische Nachrichten, 331, 1065

Degroote, P., Aerts, C., Baglin, A., et al. 2010b, *Deviations from a uniform period spacing of gravity modes in a massive star*, Nature, 464, 259

DeRosa, M. L., Brun, A. S., & Hoeksema, J. T. 2012, *Solar Magnetic Field Reversals and the Role of Dynamo Families*, ApJ, 757, 96

Deubner, F.-L., & Gough, D. 1984, *Helioseismology: Oscillations as a Daignostic of the Solar Interior*, ARA&A, 22, 593

Deubner, F.-L., Ulrich, R. K., & Rhodes, Jr., E. J. 1979, *Solar p-mode oscillations as a tracer of radial differential rotation*, A&A, 72, 177

Dialetis, D., Macris, C., Prokakis, T., & Muller, R. 1988, *A possible relation between lifetime and location of solar granules*, A&A, 204, 275

Dikpati, M., & Charbonneau, P. 1999, *A Babcock-Leighton Flux Transport Dynamo with Solar-like Differential Rotation*, ApJ, 518, 508

Dikpati, M., & Gilman, P. A. 2001, *Flux-Transport Dynamos with α-Effect from Global Instability of Tachocline Differential Rotation: A Solution for Magnetic Parity Selection in the Sun*, ApJ, 559, 428

Donati, J.-F., Collier Cameron, A., & Petit, P. 2003, *Temporal fluctuations in the differential rotation of cool active stars*, MNRAS, 345, 1187

Donati, J.-F., Forveille, T., Collier Cameron, A., et al. 2006a, *The Large-Scale Axisymmetric Magnetic Topology of a Very-Low-Mass Fully Convective Star*, Science, 311, 633

Donati, J.-F., & Landstreet, J. D. 2009, *Magnetic Fields of Nondegenerate Stars*, ARA&A, 47, 333

Donati, J.-F., Semel, M., Carter, B. D., Rees, D. E., & Collier Cameron, A. 1997, *Spectropolarimetric observations of active stars*, MNRAS, 291, 658

Donati, J.-F., Howarth, I. D., Jardine, M. M., et al. 2006b, *The surprising magnetic topology of τ Sco: fossil remnant or dynamo output?*, MNRAS, 370, 629

Donati, J.-F., Morin, J., Petit, P., et al. 2008a, *Large-scale magnetic topologies of early M dwarfs*, MNRAS, 390, 545

Donati, J.-F., Moutou, C., Farès, R., et al. 2008b, *Magnetic cycles of the planet-hosting star τ Bootis*, MNRAS, 385, 1179

Dopita, M. A., & Sutherland, R. S. 2003, Astrophysics of the diffuse universe (Astrophysics of the diffuse universe, Berlin, New York: Springer, 2003. Astronomy and astrophysics library, ISBN 3540433627), 46

Dormy, E., Soward, A. M., Jones, C. A., Jault, D., & Cardin, P. 2004, *The onset of thermal convection in rotating spherical shells*, J. Fluid Mech., 501, 43

Dravins, D., Lindegren, L., & Torkelsson, U. 1990, *The rotationally broadened line profiles of Sirius*, A&A, 237, 137

Dufton, P. L., Langer, N., Dunstall, P. R., et al. 2013, *The VLT-FLAMES Tarantula Survey. X. Evidence for a bimodal distribution of rotational velocities for the single early B-type stars*, A&A, 550, A109

Durney, B. R., De Young, D. S., & Roxburgh, I. W. 1993, *On the generation of the large-scale and turbulent magnetic fields in solar-type stars*, Sol. Phys., 145, 207

Dyson, F. J. 1949, *The S Matrix in Quantum Electrodynamics*, Phys. Rev., 75, 1736

Eberhard, G., & Schwarzschild, K. 1913, *On the reversal of the calcium lines H and K in stellar spectra.*, ApJ, 38, 292

Eddy, J. A. 1976, *The Maunder Minimum*, Science, 192, 1189

Eddy, J. A., Gilman, P. A., & Trotter, D. E. 1976, *Solar rotation during the Maunder Minimum*, Sol. Phys., 46, 3

Edelen, D. G. B. 1984, *A theorem of Bäcklun revisited*, Quaestiones Mathematicae, 7, 263

Elliott, J. R. 1997, *Aspects of the solar tachocline*, A&A, 327, 1222

Elliott, J. R., Miesch, M. S., & Toomre, J. 2000, *Turbulent Solar Convection and Its Coupling with Rotation: The Effect of Prandtl Number and Thermal Boundary Conditions on the Resulting Differential Rotation*, ApJ, 533, 546

Elsasser, W. M. 1939, *On the Origin of the Earth's Magnetic Field*, Physical Review, 55, 489

—. 1946, *Induction Effects in Terrestrial Magnetism Part I. Theory*, Physical Review, 69, 106

—. 1947, *Induction Effects in Terrestrial Magnetism. Part III. Electric Modes*, Physical Review, 72, 821

—. 1955, *Hydromagnetism. I. A Review*, American Journal of Physics, 23, 590

Fan, Y. 2009, *Magnetic Fields in the Solar Convection Zone*, Living Reviews in Solar Physics, 6

Fan, Y., Featherstone, N., & Fang, F. 2013, *Three-Dimensional MHD Simulations of Emerging Active Region Flux in a Turbulent Rotating Solar Convective Envelope: the Numerical Model and Initial Results*, ArXiv e-prints

Fares, R., Moutou, C., Donati, J.-F., et al. 2013, *A small survey of the magnetic fields of planet-host stars*, MNRAS, 435, 1451

Fares, R., Donati, J.-F., Moutou, C., et al. 2009, *Magnetic cycles of the planet-hosting star τ Bootis - II. A second magnetic polarity reversal*, MNRAS, 398, 1383

Favata, F., Micela, G., Orlando, S., et al. 2008, *The X-ray cycle in the solar-type star HD 81809. XMM-Newton observations and implications for the coronal structure*, A&A, 490, 1121

Featherstone, N. A., Browning, M. K., Brun, A. S., & Toomre, J. 2007, *Dynamo action in the presence of an imposed magnetic field*, Astron. Nachr., 328, 1126

—. 2009, *Effects of Fossil Magnetic Fields on Convective Core Dynamos in A-type Stars*, ApJ, 705, 1000

Feigelson, E. D., Hornschemeier, A. E., Micela, G., et al. 2004, *The Chandra Deep Field-North Survey. XVII. Evolution of Magnetic Activity in Old Late-Type Stars*, ApJ, 611, 1107

Ferriz-Mas, A., & Schüssler, M. 1993, *Instabilities of magnetic flux tubes in a stellar convection zone I. Equatorial flux rings in differentially rotating stars*, Geophysical and Astrophysical Fluid Dynamics, 72, 209

Flanders, H. 1963, Differential forms with applications to the physical sciences (New York: Academic Press, 1963)

Fontenla, J. M., Avrett, E., Thuillier, G., & Harder, J. 2006, *Semiempirical Models of the Solar Atmosphere. I. The Quiet- and Active Sun Photosphere at Moderate Resolution*, ApJ, 639, 441

Fraunhofer, J. 1817, *Bestimmung des Brechungs-und des Farbenzerstreungs-Vermögens verschiedener Glasarten, in Bezug auf die Vervollkommnung achromatischer Fernröhre*, Annalen der Physik, 56, 264

Freytag, B., Steffen, M., Ludwig, H.-G., et al. 2012, *Simulations of stellar convection with CO5BOLD*, Journal of Computational Physics, 231, 919

Fröhlich, C. 2013, *Total Solar Irradiance: What Have We Learned from the Last Three Cycles and the Recent Minimum?*, Space Sci. Rev., 176, 237

Gailitis, A. 1973, *On the theory of Herzenberg's dynamo.*, Magnitnaia Gidrodinamika, 4, 12

Gallet, B., & Pétrélis, F. 2009, *From reversing to hemispherical dynamos*, Phys. Rev. E, 80, 035302

Galley, C. R. 2013, *Classical Mechanics of Nonconservative Systems*, Physical Review Letters, 110, 174301

Garaud, P., & Garaud, J.-D. 2008, *Dynamics of the solar tachocline - II. The stratified case*, MNRAS, 391, 1239

Gastine, T., Duarte, L., & Wicht, J. 2012, *Dipolar versus multipolar dynamos: the influence of the background density stratification*, A&A, 546, A19

Gaunt, J. A. 1929, *The Triplets of Helium*, Royal Society of London Philosophical Transactions Series A, 228, 151

Gauss, C. F. 1838, *Allgemeine Theorie des Erdmagnetismus: Resultate aus den Beobachten des magnetischen Vereins im Jahre 1838*, Leipzig. Reprinted in: Gauss, C. F. (1877). Werke Vol. 5, 5, 119

Gell-Mann, M., & Low, F. E. 1954, *Quantum Electrodynamics at Small Distances*, Phys. Rev., 95, 1300

Germano, M., Piomelli, U., Moin, P., & Cabot, W. H. 1991, *A dynamic subgrid-scale eddy viscosity model*, Physics of Fluids, 3, 1760

Ghizaru, M., Charbonneau, P., & Smolarkiewicz, P. K. 2010, *Magnetic Cycles in Global Large-eddy Simulations of Solar Convection*, ApJ, 715, L133

Ghoussoub, N. 2008, *A variational theory for monotone vector fields*, ArXiv e-prints

Ghoussoub, N., & Moameni, A. 2005, *On the existence of Hamiltonian paths connecting Lagrangian submanifolds*, ArXiv Mathematics e-prints

—. 2009, *Anti-symmetric Hamiltonians (II): Variational resolutions for Navier-Stokes and other nonlinear evolutions*, Annales de L'Institut Henri Poincare Section Physique Theorique, 26, 223

Gilman, P. A. 1977, *Nonlinear Dynamics of Boussinesq Convection in a Deep Rotating Spherical Shell. I.*, Geophys. Astrophys. Fluid Dyn., 8, 93

—. 1983, *Dynamically consistent nonlinear dynamos driven by convection in a rotating spherical shell. II - Dynamos with cycles and strong feedbacks*, ApJS, 53, 243

Gilman, P. A., & Foukal, P. V. 1979, *Angular velocity gradients in the solar convection zone*, ApJ, 229, 1179

Gilman, P. A., & Fox, P. A. 1997, *Joint Instability of Latitudinal Differential Rotation and Toroidal Magnetic Fields below the Solar Convection Zone*, ApJ, 484, 439

Gilman, P. A., & Glatzmaier, G. A. 1981, *Compressible convection in a rotating spherical shell. I - Anelastic equations. II - A linear anelastic model. III - Analytic model for compressible vorticity waves*, ApJS, 45, 335

Gizon, L., Duvall, T. L., & Schou, J. 2003, *Wave-like properties of solar supergranulation*, Nature, 421, 43

Gizon, L., & Solanki, S. K. 2004, *Measuring Stellar Differential rotation with asteroseismology*, Sol. Phys., 220, 169

Glansdorff, P., & Prigogine, I. 1954, *Sur Les Propriétés Différentielles De La Production d'Entropie*, Physica, 20, 773

Glatzmaier, G. A. 1984, *Numerical simulations of stellar convective dynamos. I - The model and method*, J. Comp. Phys., 55, 461

—. 1985, *Numerical simulations of stellar convective dynamos. II - Field propagation in the convection zone*, ApJ, 291, 300

Glatzmaier, G. A., & Gilman, P. A. 1981, *Compressible Convection in a Rotating Spherical Shell - Part Two - a Linear Anelastic Model*, ApJS, 45, 351

—. 1982, *Compressible convection in a rotating spherical shell. V - Induced differential rotation and meridional circulation*, ApJ, 256, 316

Gleissberg, W. 1939, *A long-periodic fluctuation of the sun-spot numbers*, The Observatory, 62, 158

Godunov, S. K. 1954, PhD thesis, Moscow State University.

—. 1959, *A difference scheme for numerical solution of discontinuous solution of hydrodynamic equations*, Math. Sbornik, 47, 271

Gottlieb, S., & Shu, C. W. 1998, *Total variation diminishing Runge-Kutta schemes*, Mathematics of Computation, 67, 73

Gough, D., & Toomre, J. 1991, *Seismic observations of the solar interior*, ARA&A, 29, 627

Gough, D. O. 1969, *The Anelastic Approximation for Thermal Convection*, JAS, 26, 448

Gough, D. O., & McIntyre, M. E. 1998, *Inevitability of a magnetic field in the Sun's radiative interior*, Nature, 394, 755

Grasso, D., & Rubinstein, H. R. 2001, *Magnetic fields in the early Universe*, Phys. Rep., 348, 163

Gray, D. F. 1977, *A quest for differential stellar rotation in A stars*, ApJ, 211, 198

—. 2005, The Observation and Analysis of Stellar Photospheres (Cambridge University Press)

Gray, R. O., Corbally, C. J., Garrison, R. F., McFadden, M. T., & Robinson, P. E. 2003, *Contributions to the Nearby Stars (NStars) Project: Spectroscopy of Stars Earlier than M0 within 40 Parsecs: The Northern Sample. I.*, AJ, 126, 2048

Grunhut, J. H., Wade, G. A., Leutenegger, M., et al. 2013, *Discovery of a magnetic field in the rapidly rotating O-type secondary of the colliding-wind binary HD 47129 (Plaskett's star)*, MNRAS, 428, 1686

Güdel, M., Guinan, E. F., & Skinner, S. L. 1997, *The X-Ray Sun in Time: A Study of the Long-Term Evolution of Coronae of Solar-Type Stars*, ApJ, 483, 947

Güdel, M., & Nazé, Y. 2009, *X-ray spectroscopy of stars*, A&A Rev., 17, 309

Guerrero, G., & de Gouveia Dal Pino, E. M. 2008, *Turbulent magnetic pumping in a Babcock-Leighton solar dynamo model*, A&A, 485, 267

Guerrero, G., Smolarkiewicz, P. K., Kosovichev, A., & Mansour, N. 2013, *Solar differential rotation: hints to reproduce a near-surface shear layer in global simulations*, in IAU Symposium, Vol. 294, IAU Symposium, ed. A. G. Kosovichev, E. de Gouveia Dal Pino, & Y. Yan, 417–425

Habets, G. M. H. J., & Heintze, J. R. W. 1981, *Empirical bolometric corrections for the main-sequence*, A&AS, 46, 193

Hale, G. E. 1908, *On the Probable Existence of a Magnetic Field in Sun-Spots*, ApJ, 28, 315

—. 1915, *The Direction of Rotation of Sun-Spot Vortices*, Proceedings of the National Academy of Science, 1, 382

Hale, G. E., Ellerman, F., Nicholson, S. B., & Joy, A. H. 1919, *The Magnetic Polarity of Sun-Spots*, ApJ, 49, 153

Hall, J. C. 2008, *Stellar Chromospheric Activity*, Living Reviews in Solar Physics, 5, 2

Hall, J. C., Lockwood, G. W., & Skiff, B. A. 2007, *The Activity and Variability of the Sun and Sun-like Stars. I. Synoptic Ca II H and K Observations*, AJ, 133, 862

Hanasoge, S. M., Duvall, T. L., & Sreenivasan, K. R. 2012, *Anomalously weak solar convection*, Proceedings of the National Academy of Science, 109, 11928

Hanasoge, S. M., Duvall, Jr., T. L., & DeRosa, M. L. 2010, *Seismic Constraints on Interior Solar Convection*, ApJ, 712, L98

Handler, G., Shobbrook, R. R., Vuthela, F. F., et al. 2003, *Asteroseismological studies of three β Cephei stars: IL Vel, V433 Car and KZ Mus*, MNRAS, 341, 1005

Hansen, C. J., Kawaler, S. D., & Trimble, V. 2004, Stellar interiors : physical principles, structure, and evolution (Stellar interiors : physical principles, structure, and evolution, 2nd ed., by C.J. Hansen, S.D. Kawaler, and V. Trimble. New York: Springer-Verlag, 2004.), 293

Harnden, Jr., F. R., Branduardi, G., Gorenstein, P., et al. 1979, *Discovery of an X-ray star association in VI Cygni /Cyg OB2/*, ApJ, 234, L51

Hathaway, D. H. 2010, *The Solar Cycle*, Living Reviews in Solar Physics, 7, 1

Hathaway, D. H., Upton, L., & Colegrove, O. 2013, *Giant Convection Cells Found on the Sun*, Science, 343, 4

Haurwitz, B. 1940, *The motion of atmospheric disturbances on the spherical earth*, J. Mar. Res., 3, 254

Hawley, S., Reid, I. N., & Gizis, J. 2000, *Magnetic Activity in Low Mass Stars and Brown Dwarfs*, in Astronomical Society of the Pacific Conference Series, Vol. 212, From Giant Planets to Cool Stars, ed. C. A. Griffith & M. S. Marley, 252

Hempelmann, A., Schmitt, J. H. M. M., & Stępień, K. 1996, *Coronal X-ray emission of cool stars in relation to chromospheric activity and magnetic cycles.*, A&A, 305, 284

Henry, G. W., Eaton, J. A., Hamer, J., & Hall, D. S. 1995, *Starspot evolution, differential rotation, and magnetic cycles in the chromospherically active binaries lambda andromedae, sigma Geminorum, II Pegasi, and V711 Tauri*, ApJS, 97, 513

Herschel, W. 1795, *On the Nature and Construction of the Sun and Fixed Stars. by William Herschel, LL.D. F. R. S.*, Royal Society of London Philosophical Transactions Series I, 85, 46

—. 1796, *On the Periodical Star α Herculis; With Remarks Tending to Establish the Rotatory Motion of the Stars on Their Axes. to Which is Added a Second Catalogue of the Comparative Brightness of the Stars. by William Herschel, LL.D. F. R. S.*, Royal Society of London Philosophical Transactions Series I, 86, 452

—. 1801, *Untersuchungen über die wärmende und die erleuchtende Kraft der farbigen Sonnenstrahlen; Versuch über die nicht - sichtbaren Strahlen der Sonne und deren Brechbarkeit; und Einrichtung grosser Teleskope zu Sonnenbeobachtungen*, Annalen der Physik, 7, 137

Herzenberg, A. 1958, *Geomagnetic Dynamos*, Royal Society of London Philosophical Transactions Series A, 250, 543

Hoekzema, N. M., & Brandt, P. N. 2000, *Small-scale topology of solar atmosphere dynamics. IV. On the relation of photospheric oscillations to meso-scale flows*, A&A, 353, 389

Howe, R. 2009, *Solar Interior Rotation and its Variation*, Living Reviews in Solar Physics, 6

Howe, R., Christensen-Dalsgaard, J., Hill, F., et al. 2000, *Dynamic Variations at the Base of the Solar Convection Zone*, Sci., 287, 2456

Howe, R., Komm, R., Hill, F., et al. 2006, *Large-Scale Zonal Flows Near the Solar Surface*, Sol. Phys., 235, 1

Hoyt, D. V., & Schatten, K. H. 1998, *Group Sunspot Numbers: A New Solar Activity Reconstruction*, Sol. Phys., 181, 491

Huang, S.-S. 1953, *A Statistical Study of the Rotation of the Stars.*, ApJ, 118, 285

Hubeny, I. 1988, *A computer program for calculating non-LTE model stellar atmospheres*, Computer Physics Communications, 52, 103

Hubeny, I., & Lanz, T. 1995, *Non-LTE line-blanketed model atmospheres of hot stars. 1: Hybrid complete linearization/accelerated lambda iteration method*, ApJ, 439, 875

Humboldt, A. v., & Bromme, T. 1850, Kosmos, Vol. 3 (Stuttgart Cotta), 656

Hunter, I., Lennon, D. J., Dufton, P. L., et al. 2008, *The VLT-FLAMES survey of massive stars: atmospheric parameters and rotational velocity distributions for B-type stars in the Magellanic Clouds*, A&A, 479, 541

Hurlburt, N., & De Rosa, M. 2008, *On the Stability of Active Regions and Sunspots*, ApJ, 684, L123

Hurlburt, N. E., DeRosa, M. L., Augustson, K. C., & Toomre, J. 2012, *Effects of Granulation upon Larger-Scale Convection*, in Astronomical Society of the Pacific Conference Series, Vol. 454, Hinode-3: The 3rd Hinode Science Meeting, ed. T. Sekii, T. Watanabe, & T. Sakurai, 13

Hurlburt, N. E., & Rucklidge, A. M. 2000, *Development of structure in pores and sunspots: flows around axisymmetric magnetic flux tubes*, MNRAS, 314, 793

Hurlburt, N. E., Toomre, J., & Massaguer, J. M. 1986, *Nonlinear compressible convection penetrating into stable layers and producing internal gravity waves*, ApJ, 311, 563

Iglesias, C. A., Rogers, F. J., & Wilson, B. G. 1992, *Spin-orbit interaction effects on the Rosseland mean opacity*, ApJ, 397, 717

Israel, W., & Stewart, J. M. 1979, *Transient relativistic thermodynamics and kinetic theory*, Annals of Physics, 118, 341

Jardine, M., & Unruh, Y. C. 1999, *Coronal emission and dynamo saturation*, A&A, 346, 883

Jeffreys, H. 1926, *The Rigidity of the Earth's Central Core.*, Geophysical Journal International, 1, 371

Jiang, G. 1996, *Efficient Implementation of Weighted ENO Schemes*, Journal of Computational Physics, 126, 202

Jones, C. A., Boronski, P., Brun, A. S., et al. 2011, *Anelastic convection-driven dynamo benchmarks*, Icarus, 216, 120

Jones, C. A., Kuzanyan, K. M., & Mitchell, R. H. 2009, *Linear theory of compressible convection in rapidly rotating spherical shells, using the anelastic approximation*, Journal of Fluid Mechanics, 634, 291

Jouve, L., Brown, B. P., & Brun, A. S. 2010, *Exploring the P_{cyc} vs. P_{rot} relation with flux transport dynamo models of solar-like stars*, A&A, 509, A32

Jouve, L., & Brun, A. S. 2007, *On the role of meridional flows in flux transport dynamo models*, A&A, 474, 239

Joy, A. H., & Wilson, R. E. 1949, *Stars whose Spectra have Bright H and K Lines of Calcium.*, ApJ, 109, 231

Jurčišinová, E., Jurčišin, M., & Remecký, R. 2013, *Turbulent Prandtl number in a model of passively advected vector field: Two-loop renormalization group result*, Phys. Rev. E, 88, 011002

Kahn, F. D. 1961, *Sound Waves Trapped in the Solar Atmosphere.*, ApJ, 134, 343

Kahn, S. M., Leutenegger, M. A., Cottam, J., et al. 2001, *High resolution X-ray spectroscopy of zeta Puppis with the XMM-Newton reflection grating spectrometer*, A&A, 365, L312

Käpylä, P. J., Korpi, M. J., & Tuominen, I. 2004, *Local models of stellar convection:. Reynolds stresses and turbulent heat transport*, A&A, 422, 793

Käpylä, P. J., Mantere, M. J., & Brandenburg, A. 2012, *Cyclic Magnetic Activity due to Turbulent Convection in Spherical Wedge Geometry*, ApJ, 755, L22

Käpylä, P. J., Mantere, M. J., Cole, E., Warnecke, J., & Brandenburg, A. 2013, *Effects of strong stratification on equatorward dynamo wave propagation*, ArXiv e-prints

Käpylä, P. J., Mantere, M. J., Guerrero, G., Brandenburg, A., & Chatterjee, P. 2011, *Reynolds stress and heat flux in spherical shell convection*, A&A, 531, A162

Kazantsev, A. P. 1968, *Enhancement of a Magnetic Field by a Conducting Fluid*, Soviet Journal of Experimental and Theoretical Physics, 26, 1031

Kazantsev, A. P., Ruzmaikin, A. A., & Sokolov, D. D. 1985, *Magnetic field transport by an acoustic turbulence-type flow*, Zhurnal Eksperimentalnoi i Teoreticheskoi Fiziki, 88, 487

Kazantsev, E., Sommeria, J., & Verron, J. 1998, *Subgrid-Scale Eddy Parameterization by Statistical Mechanics in a Barotropic Ocean Model*, Journal of Physical Oceanography, 28, 1017

Keller, S. C. 2004, *Rotation of Early B-type Stars in the Large Magellanic Cloud: The Role of Evolution and Metallicity*, Pub. Astro. Soc. Australia, 21, 310

Kemp, J. C., Swedlund, J. B., Landstreet, J. D., & Angel, J. R. P. 1970, *Discovery of Circularly Polarized Light from a White Dwarf*, ApJ, 161, L77

Kippenhahn, R. 1963, *Differential Rotation in Stars with Convective Envelopes.*, ApJ, 137, 664

Kiraga, M., & Stepien, K. 2007, *Age-Rotation-Activity Relations for M Dwarf Stars*, Acta Astronomica, 57, 149

Kirchhoff, G. 1860, *Ueber die Fraunhofer'schen Linien*, Annalen der Physik, 185, 148

Kirchhoff, G., & Bunsen, R. 1860, *Chemische analyse durch spectralbeobachtungen*, Annalen der Physik, 186, 161

Kirkland, D. W. 2003, *An explanation for the varves of the Castile evaporites (Upper Permian), Texas and New Mexico, USA*, Sedimentology, 50, 899

Kitchatinov, L. L. 2010, *Stability of the differential rotation of stars*, Astron. Rep., 54, 1

Kleeorin, N., & Rogachevskii, I. 1999, *Magnetic helicity tensor for an anisotropic turbulence*, Phys. Rev. E, 59, 6724

Kleeorin, N., Rogachevskii, I., & Sokoloff, D. 2002, *Magnetic fluctuations with a zero mean field in a random fluid flow with a finite correlation time and a small magnetic diffusion*, Phys. Rev. E, 65, 036303

Kolmogorov, A. 1941, *The Local Structure of Turbulence in Incompressible Viscous Fluid for Very Large Reynolds' Numbers*, Akademiia Nauk SSSR Doklady, 30, 301

Kraft, R. P. 1967, *Studies of Stellar Rotation. V. The Dependence of Rotation on Age among Solar-Type Stars*, ApJ, 150, 551

Kraichnan, R. H. 1972, *Test-field model for inhomogeneous turbulence*, Journal of Fluid Mechanics, 56, 287

Krause, F., & Raedler, K.-H. 1980, Mean-field magnetohydrodynamics and dynamo theory

Küker, M., & Rüdiger, G. 2005, *Differential rotation of main sequence F stars*, A&A, 433, 1023

—. 2007, *Modelling the differential rotation of F stars*, Astron. Nachr., 328, 1050

Langer, N. 2012, *Presupernova Evolution of Massive Single and Binary Stars*, ARA&A, 50, 107

Lantz, S. R. 1992, PhD thesis, CORNELL UNIVERSITY.

Lanza, A. F., Bonomo, A. S., & Rodonò, M. 2007, *Comparing different approaches to model the rotational modulation of the Sun as a star*, A&A, 464, 741

Lanza, A. F., Rodono, M., & Zappala, R. A. 1993, *Fourier analysis of spotted star light curves as a tool to detect stellar differential rotation*, A&A, 269, 351

Lanza, A. F., Pagano, I., Leto, G., et al. 2009, *Magnetic activity in the photosphere of CoRoT-Exo-2a. Active longitudes and short-term spot cycle in a young Sun-like star*, A&A, 493, 193

Larmor, J. 1919, *How could a rotating body such as the Sun become a magnet?*, Rep. Brit. Assoc., 87, 159

Latour, J., Spiegel, E. A., Toomre, J., & Zahn, J.-P. 1976, *Stellar convection theory. I - The anelastic modal equations*, ApJ, 207, 233

Lax, P. 1973, Hyperbolic Systems of Conservation Laws and the Mathematical Theory of Shock Waves, CBMS-NSF Regional Conference Series in Applied Mathematics No. nos. 11-16 (Society for Industrial and Applied Mathematics)

Lean, J. L., & Brueckner, G. E. 1989, *Intermediate-term solar periodicities - 100-500 days*, ApJ, 337, 568

Leenaarts, J., Pereira, T. M. D., Carlsson, M., Uitenbroek, H., & De Pontieu, B. 2013, *The Formation of IRIS Diagnostics. II. The Formation of the Mg II h & k Lines in the Solar Atmosphere*, ApJ, 772, 90

Leighton, R. B. 1969, *A Magneto-Kinematic Model of the Solar Cycle*, ApJ, 156, 1

Leighton, R. B., Noyes, R. W., & Simon, G. W. 1962, *Velocity Fields in the Solar Atmosphere. I. Preliminary Report.*, ApJ, 135, 474

Lele, S. K. 1992, *Compact Finite Difference Schemes with Spectral-like Resolution*, Journal of Computational Physics, 103, 16

Lerche, I. 1974, *Concerning a criterion for the validity of the first order smoothing approximation.*, Journal of Mathematical Physics, 15, 1967

Liseau, R., Montesinos, B., Olofsson, G., et al. 2013, *α Centauri A in the far infrared. First measurement of the temperature minimum of a star other than the Sun*, A&A, 549, L7

Lisle, J. P., Rast, M. P., & Toomre, J. 2004, *Persistent North-South Alignment of the Solar Supergranulation*, ApJ, 608, 1167

Livingston, W., Wallace, L., White, O. R., & Giampapa, M. S. 2007, *Sun-as-a-Star Spectrum Variations 1974-2006*, ApJ, 657, 1137

Lockwood, G. W., Skiff, B. A., Henry, G. W., et al. 2007, *Patterns of Photometric and Chromospheric Variation among Sun-like Stars: A 20 Year Perspective*, ApJS, 171, 260

Longuet-Higgins, M. S. 1964, *Planetary Waves on a Rotating Sphere*, Proc. Roy. Soc. A, 279, 446

Lou, Y.-Q. 2000, *Rossby-Type Wave-Induced Periodicities in Flare Activities and Sunspot Areas or Groups during Solar Maxima*, ApJ, 540, 1102

Lucy, L. B., & White, R. L. 1980, *X-ray emission from the winds of hot stars*, ApJ, 241, 300

MacDonald, J., & Mullan, D. J. 2004, *Magnetic fields in massive stars: dynamics and origin*, MNRAS, 348, 702

Maeder, A. 1975, *Stellar evolution. III - The overshooting from convective cores*, A&A, 40, 303

Maeder, A., & Meynet, G. 2012, *Rotating massive stars: From first stars to gamma ray bursts*, Rev. Mod. Phys., 84, 25

Malkus, W. V. R., & Proctor, M. R. E. 1975, *The macrodynamics of alpha-effect dynamos in rotating fluids*, Journal of Fluid Mechanics, 67, 417

Malyshkin, L. M., & Boldyrev, S. 2010, *Magnetic Dynamo action at Low Magnetic Prandtl Numbers*, Physical Review Letters, 105, 215002

Marsden, S. C., Mengel, M. W., Donati, F., et al. 2006, *The Magnetic Activity of Young Suns: Magnetic Topologies and Differential Rotation of F- and G-Dwarfs*, in Astronomical Society of the Pacific Conference Series, Vol. 358, Astronomical Society of the Pacific Conference Series, ed. R. Casini & B. W. Lites, 401–+

Marsden, S. C., Waite, I. A., Carter, B. D., & Donati, J.-F. 2005, *Doppler imaging and surface differential rotation of young open cluster stars - I. HD 307938 (R58) in IC 2602*, MNRAS, 359, 711

Mathur, S., García, R. A., Morgenthaler, A., et al. 2013, *Constraining magnetic-activity modulations in three solar-like stars observed by CoRoT and NARVAL*, A&A, 550, A32

Mathur, S., García, R. A., Régulo, C., et al. 2010, *Determining global parameters of the oscillations of solar-like stars*, A&A, 511, A46

Matt, S., & Pudritz, R. E. 2008, *Accretion-powered Stellar Winds. II. Numerical Solutions for Stellar Wind Torques*, ApJ, 678, 1109

Matt, S. P., Do Cao, O., Brown, B. P., & Brun, A. S. 2011, *Convection and differential rotation properties of G and K stars computed with the ASH code*, Astronomische Nachrichten, 332, 897

Maunder, E. W. 1903, *Spoerer's law of zones*, The Observatory, 26, 329

—. 1904, *Note on the distribution of sun-spots in heliographic latitude, 1874-1902*, MNRAS, 64, 747

McComas, D. J., Dayeh, M. A., Funsten, H. O., Livadiotis, G., & Schwadron, N. A. 2013, *The Heliotail Revealed by the Interstellar Boundary Explorer*, ApJ, 771, 77

McIntyre, M. E. 1998, *Breaking Waves and Global-Scale Chemical Transport in theEarth's Atmosphere, with Spinoffs for the Sun's Interior*, Prog. Theor. Phys. Supp., 130, 137

Meneveau, C., & Katz, J. 2000, *Scale-Invariance and Turbulence Models for Large-Eddy Simulation*, Annual Review of Fluid Mechanics, 32, 1

Metcalfe, T. S., Basu, S., Henry, T. J., et al. 2010, *Discovery of a 1.6 Year Magnetic Activity Cycle in the Exoplanet Host Star ι Horologii*, ApJ, 723, L213

Micela, G., Sciortino, S., Serio, S., et al. 1985, *Einstein X-ray survey of the Pleiades - The dependence of X-ray emission on stellar age*, ApJ, 292, 172

Middelkoop, F. 1982, *Magnetic structure in cool stars. IV - Rotation and CA II H and K emission of main-sequence stars*, A&A, 107, 31

Miesch, M. S. 1998, PhD thesis, AA(UNIVERSITY OF COLORADO AT BOULDER)

—. 2005, *Large-Scale Dynamics of the Convection Zone and Tachocline*, Liv. Rev. Solar Phys., 2, 1

Miesch, M. S., & Brown, B. P. 2012, *Convective Babcock-Leighton Dynamo Models*, ApJ, 746, L26

Miesch, M. S., Brun, A. S., DeRosa, M. L., & Toomre, J. 2008, *Structure and Evolution of Giant Cells in Global Models of Solar Convection*, ApJ, 673, 557

Miesch, M. S., Brun, A. S., & Toomre, J. 2006, *Solar Differential Rotation Influenced by Latitudinal Entropy Variations in the Tachocline*, ApJ, 641, 618

Miesch, M. S., Elliott, J. R., Toomre, J., et al. 2000, *Three-dimensional Spherical Simulations of Solar Convection. I. Differential Rotation and Pattern Evolution Achieved with Laminar and Turbulent States*, ApJ, 532, 593

Miesch, M. S., Featherstone, N. A., Rempel, M., & Trampedach, R. 2012, *On the Amplitude of Convective Velocities in the Deep Solar Interior*, ApJ, 757, 128

Miesch, M. S., & Hindman, B. W. 2011, *Gyroscopic Pumping in the Solar Near-surface Shear Layer*, ApJ, 743, 79

Miesch, M. S., & Toomre, J. 2009, *Turbulence, Magnetism, and Shear in Stellar Interiors*, Annual Review of Fluid Mechanics, 41, 317

Mignone, A., Tzeferacos, P., & Bodo, G. 2010, *High-order conservative finite difference GLM-MHD schemes for cell-centered MHD*, Journal of Computational Physics, 229, 5896

Mittag, M., Schmitt, J. H. M. M., & Schröder, K.-P. 2013, *Ca II H+K fluxes from S-indices of large samples: a reliable and consistent conversion based on PHOENIX model atmospheres*, A&A, 549, A117

Mobbs, S. D. 1982, *Variational principles for perfect and dissipative fluid flows*, Royal Society of London Proceedings Series A, 381, 457

Moffatt, H. K. 1970, *Turbulent dynamo action at low magnetic Reynolds number*, Journal of Fluid Mechanics, 41, 435

—. 1978, Magnetic field generation in electrically conducting fluids (Cambridge, England, Cambridge University Press. 353 p.)

—. 1983, *Transport effects associated with turbulence with particular attention to the influence of helicity*, Reports on Progress in Physics, 46, 621

Moffatt, H. K., & Proctor, M. R. E. 1982, *The role of the helicity spectrum function in turbulent dynamo theory*, Geophysical and Astrophysical Fluid Dynamics, 21, 265

Morel, P. 1997, *CESAM: A code for stellar evolution calculations*, A&AS, 124, 597

Moreno-Insertis, F., Schuessler, M., & Ferriz-Mas, A. 1992, *Storage of magnetic flux tubes in a convective overshoot region*, A&A, 264, 686

Morgenthaler, A., Petit, P., Morin, J., et al. 2011, *Direct observation of magnetic cycles in Sun-like stars*, Astronomische Nachrichten, 332, 866

Morin, J., Donati, J.-F., Petit, P., et al. 2010, *Large-scale magnetic topologies of late M dwarfs*, MNRAS, 407, 2269

—. 2008, *Large-scale magnetic topologies of mid M dwarfs*, MNRAS, 390, 567

Mullan, D. J., & MacDonald, J. 2005, *Dynamo-generated magnetic fields at the surface of a massive star*, MNRAS, 356, 1139

Müller, D. A. N., Steiner, O., Schlichenmaier, R., & Brandt, P. N. 2001, *Time-slice diagrams of solar granulation*, Sol. Phys., 203, 211

Müller, W.-C., & Malapaka, S. K. 2013, *Role of helicities for the dynamics of turbulent magnetic fields*, Geophysical and Astrophysical Fluid Dynamics, 107, 93

Nazé, Y., Broos, P. S., Oskinova, L., et al. 2011, *Global X-ray Properties of the O and B Stars in Carina*, ApJS, 194, 7

Nelson, N. J., Brown, B. P., Brun, A. S., Miesch, M. S., & Toomre, J. 2011, *Buoyant Magnetic Loops in a Global Dynamo Simulation of a Young Sun*, ApJ, 739, L38

—. 2013a, *Magnetic Wreaths and Cycles in Convective Dynamos*, ApJ, 762, 73

Nelson, N. J., Brown, B. P., Sacha Brun, A., Miesch, M. S., & Toomre, J. 2013b, *Buoyant Magnetic Loops Generated by Global Convective Dynamo Action*, Sol. Phys., 20

Nordlund, Å., Stein, R. F., & Asplund, M. 2009, *Solar Surface Convection*, Living Reviews in Solar Physics, 6, 2

November, L. J., Toomre, J., Gebbie, K. B., & Simon, G. W. 1981, *The detection of meso-granulation on the sun*, ApJ, 245, L123

Noyes, R. W., Hartmann, L. W., Baliunas, S. L., Duncan, D. K., & Vaughan, A. H. 1984, *Rotation, convection, and magnetic activity in lower main-sequence stars*, ApJ, 279, 763

Noyes, R. W., & Leighton, R. B. 1963, *Velocity Fields in the Solar Atmosphere. II. The Oscillatory Field.*, ApJ, 138, 631

Oda, N. 1984, *Morphological study of the solar granulation. III - The mesogranulation*, Sol. Phys., 93, 243

Ogura, Y., & Charney, J. G. 1962, *A Numerical Model of Thermal Convection in the Atmosphere*, Proc. Int. Symp. Num. Wea. Prediction, 10, 431

Ogura, Y., & Phillips, N. A. 1962, *Scale Analysis of Deep and Shallow Convection in the Atmosphere*, JAS, 19, 173

Oláh, K., Strassmeier, K. G., Kovári, Z., & Guinan, E. F. 2001, *Time-series photometric spot modeling. IV. The multi-periodic K5Ve binary V833 Tauri*, A&A, 372, 119

Oldham, R. D. 1906, *Earthquake Origins*, Nature, 73, 620

Olver, P. J. 1993, *Internal, external and generalized symmetries*, Adv. in Math., 53, 53

Onsager, L. 1931, *Reciprocal Relations in Irreversible Processes. I.*, Physical Review, 37, 405

Opher, M., Bibi, F. A., Toth, G., et al. 2009, *A strong, highly-tilted interstellar magnetic field near the Solar System*, Nature, 462, 1036

Orszag, S. A. 1970, *Analytical theories of turbulence*, Journal of Fluid Mechanics, 41, 363

Oskinova, L. M., Hamann, W.-R., Cassinelli, J. P., Brown, J. C., & Todt, H. 2011, *X-ray emission from massive stars with magnetic fields*, Astronomische Nachrichten, 332, 988

Owocki, S. P., & Cohen, D. H. 1999, *A Simple Scaling Analysis of X-Ray Emission and Absorption in Hot-Star Winds*, ApJ, 520, 833

Pallavicini, R., Golub, L., Rosner, R., et al. 1981, *Relations among stellar X-ray emission observed from Einstein, stellar rotation and bolometric luminosity*, ApJ, 248, 279

Parker, E. N. 1955, *Hydromagnetic Dynamo Models.*, ApJ, 122, 293

—. 1958, *Dynamics of the Interplanetary Gas and Magnetic Fields.*, ApJ, 128, 664

—. 1977, *The origin of solar activity*, ARA&A, 15, 45

—. 1987, *The dynamical oscillation and propulsion of magnetic fields in the convective zone of a star. I - General considerations*, ApJ, 312, 868

—. 1993, *A solar dynamo surface wave at the interface between convection and nonuniform rotation*, ApJ, 408, 707

Patten, B. M., & Simon, T. 1996, *The Evolution of Rotation and Activity in Young Open Clusters: IC 2391*, ApJS, 106, 489

Paxton, B., Bildsten, L., Dotter, A., et al. 2011, *Modules for Experiments in Stellar Astrophysics (MESA)*, ApJS, 192, 3

Pedlosky, J. 1982, Geophysical fluid dynamics, ed. Pedlosky, J.

Peres, G., Orlando, S., Reale, F., Rosner, R., & Hudson, H. 2000, *The Sun as an X-Ray Star. II. Using theYohkoh/Soft X-Ray Telescope-derived Solar Emission Measure versus Temperature to Interpret Stellar X-Ray Observations*, ApJ, 528, 537

Petit, V., Owocki, S. P., Wade, G. A., et al. 2013, *A magnetic confinement versus rotation classification of massive-star magnetospheres*, MNRAS, 429, 398

Petrovay, K. 2000, *What Makes the Sun Tick? The Origin of the Solar Cycle*, in ESA Special Publication, Vol. 463, The Solar Cycle and Terrestrial Climate, Solar and Space weather, ed. A. Wilson, 3

Petrovay, K. 2003, *A Consistent one-Dimensional Model for the Turbulent Tachocline*, Sol. Phys., 215, 17

Phan-Bao, N., Lim, J., Donati, J.-F., Johns-Krull, C. M., & Martín, E. L. 2009, *Magnetic Field Topology in Low-Mass Stars: Spectropolarimetric Observations of M Dwarfs*, ApJ, 704, 1721

Pipin, V. V., & Kosovichev, A. G. 2013, *The Mean-field Solar Dynamo with a Double Cell Meridional Circulation Pattern*, ApJ, 776, 36

Pizzolato, N., Maggio, A., Micela, G., Sciortino, S., & Ventura, P. 2003, *The stellar activity-rotation relationship revisited: Dependence of saturated and non-saturated X-ray emission regimes on stellar mass for late-type dwarfs*, A&A, 397, 147

Ponty, Y., Mininni, P. D., Montgomery, D. C., et al. 2005, *Numerical Study of Dynamo Action at Low Magnetic Prandtl Numbers*, Physical Review Letters, 94, 164502

Potter, A. T., Tout, C. A., & Eldridge, J. J. 2012, *Towards a unified model of stellar rotation*, MNRAS, 419, 748

Pouquet, A., Frisch, U., & Leorat, J. 1976, *Strong MHD helical turbulence and the nonlinear dynamo effect*, Journal of Fluid Mechanics, 77, 321

Pratt, S. 2008, *Formulating viscous hydrodynamics for large velocity gradients*, Phys. Rev. C, 77, 024910

Racine, É., Charbonneau, P., Ghizaru, M., Bouchat, A., & Smolarkiewicz, P. K. 2011, *On the Mode of Dynamo Action in a Global Large-eddy Simulation of Solar Convection*, ApJ, 735, 46

Radick, R. R., Lockwood, G. W., Skiff, B. A., & Baliunas, S. L. 1998, *Patterns of Variation among Sun-like Stars*, ApJS, 118, 239

Rädler, K. H. 1968, *On the Electrodynamics of Conducting Fluids in Turbulent Motion. I. The Principles of Mean Field Electrodynamics*, Zeitschrift Naturforschung Teil A, 23, 1841

Rädler, K.-H., Kleeorin, N., & Rogachevskii, I. 2003, *The Mean Electromotive Force for MHD Turbulence: The Case of a Weak Mean Magnetic Field and Slow Rotation*, Geophysical and Astrophysical Fluid Dynamics, 97, 249

Rast, M. P. 1995, *On the nature of 'exploding' granules and granule fragmentation*, ApJ, 443, 863

—. 2003, *The Scales of Granulation, Mesogranulation, and Supergranulation*, ApJ, 597, 1200

Rast, M. P., Ortiz, A., & Meisner, R. W. 2008, *Latitudinal Variation of the Solar Photospheric Intensity*, ApJ, 673, 1209

Rast, M. P., & Toomre, J. 1993, *Compressible Convection with Ionization. II. Thermal Boundary-Layer Instability*, ApJ, 419, 240

Reiners, A. 2006, *Rotation- and temperature-dependence of stellar latitudinal differential rotation*, A&A, 446, 267

—. 2007, *Differential rotation in F stars*, Astron. Nachr., 328, 1034

—. 2012, *Observations of Cool-Star Magnetic Fields*, Living Reviews in Solar Physics, 9, 1

Reiners, A., & Schmitt, J. H. M. M. 2002a, *Can star spots mimic differential rotation?*, A&A, 388, 1120

—. 2002b, *Evidence for strong differential rotation in Li-depleted fast rotating F-stars*, A&A, 393, L77

—. 2002c, *On the feasibility of the detection of differential rotation in stellar absorption profiles*, A&A, 384, 155

—. 2003a, *Differential rotation in rapidly rotating F-stars*, A&A, 412, 813

—. 2003b, *Rotation and differential rotation in field F- and G-type stars*, A&A, 398, 647

Reinhold, T., Reiners, A., & Basri, G. 2013, *Rotation and differential rotation of active Kepler stars*, ArXiv e-prints

Rempel, M. 2004, *Overshoot at the Base of the Solar Convection Zone: A Semianalytical Approach*, ApJ, 607, 1046

—. 2005, *Solar Differential Rotation and Meridional Flow: The Role of a Subadiabatic Tachocline for the Taylor-Proudman Balance*, ApJ, 622, 1320

—. 2006a, *Flux-Transport Dynamos with Lorentz Force Feedback on Differential Rotation and Meridional Flow: Saturation Mechanism and Torsional Oscillations*, ApJ, 647, 662

—. 2006b, *Transport of Toroidal Magnetic Field by the Meridional Flow at the Base of the Solar Convection Zone*, ApJ, 637, 1135

Rempel, M., & Schlichenmaier, R. 2011, *Sunspot Modeling: From Simplified Models to Radiative MHD Simulations*, Living Reviews in Solar Physics, 8, 3

Rempel, M., Schüssler, M., & Knölker, M. 2009, *Radiative Magnetohydrodynamic Simulation of Sunspot Structure*, ApJ, 691, 640

Ribes, J. C., & Nesme-Ribes, E. 1993, *The solar sunspot cycle in the Maunder minimum AD1645 to AD1715*, A&A, 276, 549

Rieger, E., Kanbach, G., Reppin, C., et al. 1984, *A 154-day periodicity in the occurrence of hard solar flares?*, Nature, 312, 623

Rieutord, M., & Rincon, F. 2010, *The Sun's Supergranulation*, Living Reviews in Solar Physics, 7, 2

Rieutord, M., Roudier, T., Malherbe, J. M., & Rincon, F. 2000, *On mesogranulation, network formation and supergranulation*, A&A, 357, 1063

Roberts, G. O. 1970, *Spatially Periodic Dynamos*, Royal Society of London Philosophical Transactions Series A, 266, 535

Roberts, P. H., & Soward, A. M. 1975, *A unified approach to mean field electrodynamics*, Astronomische Nachrichten, 296, 49

Robinson, R. D. 1979, *Stellar Magnetic Field Measurements: A New Method*, in Bulletin of the American Astronomical Society, Vol. 11, Bulletin of the American Astronomical Society, 633

Robinson, R. D., Worden, S. P., & Harvey, J. W. 1980, *Observations of magnetic fields on two late-type dwarf stars*, ApJ, 236, L155

Rogers, T. M., & Glatzmaier, G. A. 2006, *Angular Momentum Transport by Gravity Waves in the Solar Interior*, ApJ, 653, 756

Rüdiger, G. 1989, Differential rotation and stellar convection. Sun and the solar stars, ed. Rüdiger, G.

Rüdiger, G., & Arlt, R. 2003, Physics of the solar cycle, 147

Rüdiger, G., & Kitchatinov, L. L. 1997, *The slender solar tachocline: a magnetic model*, Astronomische Nachrichten, 318, 273

Ruediger, G., & Brandenburg, A. 1995, *A solar dynamo in the overshoot layer: cycle period and butterfly diagram.*, A&A, 296, 557

Runge, C. 1895, *Über die numerische Auflösung von Differentialgleichungen.*, Math. Ann., 46, 167

Saar, S., & Brandenburg, A. 2001, *Further Analysis of Stellar Magnetic Cycle Periods*, in Astronomical Society of the Pacific Conference Series, Vol. 248, Magnetic Fields Across the Hertzsprung-Russell Diagram, ed. G. Mathys, S. K. Solanki, & D. T. Wickramasinghe, 231

Saar, S. H. 2009, *The Activity Cycles and Surface Differential Rotation of Single Dwarfs*, in Astronomical Society of the Pacific Conference Series, Vol. 416, Solar-Stellar Dynamos as Revealed by Helio- and Asteroseismology: GONG 2008/SOHO 21, ed. M. Dikpati, T. Arentoft, I. González Hernández, C. Lindsey, & F. Hill, 375

Saar, S. H., & Brandenburg, A. 1999, *Time Evolution of the Magnetic Activity Cycle Period. II. Results for an Expanded Stellar Sample*, ApJ, 524, 295

Sabine, E. 1852, *On Periodical Laws Discoverable in the Mean Effects of the Larger Magnetic Disturbances. No. II*, Royal Society of London Philosophical Transactions Series I, 142, 103

Sana, H., Rauw, G., Nazé, Y., Gosset, E., & Vreux, J.-M. 2006, *An XMM-Newton view of the young open cluster NGC 6231 - II. The OB star population*, MNRAS, 372, 661

Saslaw, W. C., & Schwarzschild, M. 1965, *Overshooting from Stellar Convective Cores.*, ApJ, 142, 1468

Schatten, K. H., Wilcox, J. M., & Ness, N. F. 1969, *A model of interplanetary and coronal magnetic fields*, Sol. Phys., 6, 442

Schekochihin, A. A., Cowley, S. C., Taylor, S. F., Maron, J. L., & McWilliams, J. C. 2004, *Simulations of the Small-Scale Turbulent Dynamo*, ApJ, 612, 276

Schekochihin, A. A., Iskakov, A. B., Cowley, S. C., et al. 2007, *Fluctuation dynamo and turbulent induction at low magnetic Prandtl numbers*, New Journal of Physics, 9, 300

Schmitt, J. H. M. M., Golub, L., Harnden, Jr., F. R., et al. 1985, *An Einstein Observatory X-ray survey of main-sequence stars with shallow convection zones*, ApJ, 290, 307

Schmitt, J. H. M. M., & Liefke, C. 2004, *NEXXUS: A comprehensive ROSAT survey of coronal X-ray emission among nearby solar-like stars*, A&A, 417, 651

Schou, J., Antia, H. M., Basu, S., et al. 1998, *Helioseismic Studies of Differential Rotation in the Solar Envelope by the Solar Oscillations Investigation Using the Michelson Doppler Imager*, ApJ, 505, 390

Schrijver, C. J., & Zwaan, C. 2000, Solar and Stellar Magnetic Activity

Schrinner, M., Rädler, K.-H., Schmitt, D., Rheinhardt, M., & Christensen, U. R. 2007, *Mean-field concept and direct numerical simulations of rotating magnetoconvection and the geodynamo*, Geophysical and Astrophysical Fluid Dynamics, 101, 81

Schulz, N. S., Canizares, C. R., Huenemoerder, D., & Lee, J. C. 2000, *X-Ray Line Emission from the Hot Stellar Wind of θ^1 Orionis C*, ApJ, 545, L135

Schüssler, M., Caligari, P., Ferriz-Mas, A., & Moreno-Insertis, F. 1994, *Instability and eruption of magnetic flux tubes in the solar convection zone*, A&A, 281, L69

Schuster, A. 1911, *A Critical Examination of the Possible Causes of Terrestrial Magnetism*, Proceedings of the Physical Society of London, 24, 121

Schwabe, M. 1844, *Sonnenbeobachtungen im Jahre 1843. Von Herrn Hofrath Schwabe in Dessau*, Astronomische Nachrichten, 21, 233

Schwadron, N. A., Allegrini, F., Bzowski, M., et al. 2011, *Separation of the Interstellar Boundary Explorer Ribbon from Globally Distributed Energetic Neutral Atom Flux*, ApJ, 731, 56

Shajn, G., & Struve, O. 1929, *On the rotation of the stars*, MNRAS, 89, 222

Silva-Valio, A., & Lanza, A. F. 2011, *Time evolution and rotation of starspots on CoRoT-2 from the modelling of transit photometry*, A&A, 529, A36+

Simard, C., Charbonneau, P., & Bouchat, A. 2013, *Magnetohydrodynamic Simulation-driven Kinematic Mean Field Model of the Solar Cycle*, ApJ, 768, 16

Simon, G. W., & Leighton, R. B. 1964, *Velocity Fields in the Solar Atmosphere. III. Large-Scale Motions, the Chromospheric Network, and Magnetic Fields.*, ApJ, 140, 1120

Skumanich, A. 1972, *Time Scales for CA II Emission Decay, Rotational Braking, and Lithium Depletion*, ApJ, 171, 565

Smith, M. A., & Gray, D. F. 1976, *Fourier analysis of spectral line profiles - A new tool for an old art*, PASP, 88, 809

Soderblom, D. R., Stauffer, J. R., Hudon, J. D., & Jones, B. F. 1993a, *Rotation and chromospheric emission among F, G, and K dwarfs of the Pleiades*, ApJS, 85, 315

Soderblom, D. R., Stauffer, J. R., MacGregor, K. B., & Jones, B. F. 1993b, *The evolution of angular momentum among zero-age main-sequence solar-type stars*, ApJ, 409, 624

Spiegel, E. A. 1972, *A History of Solar Rotation*, NASA Special Publication, 300, 61

Spiegel, E. A., & Weiss, N. O. 1980, *Magnetic activity and variations in solar luminosity*, Nature, 287, 616

Spiegel, E. A., & Zahn, J.-P. 1992, *The solar tachocline*, A&A, 265, 106

Spörer, F. W. G. 1890, *Prof. Spoerer's researches on Sun-spots*, MNRAS, 50, 251

Spörer, G. 1889, *Sur les taches du Soleil.*, Comptes Rendus, 108, 485

Spruit, H. 1997, *Convection in stellar envelopes: a changing paradigm*, Mem. Soc. Astron. Italiana, 68, 397

Spruit, H. C., & van Ballegooijen, A. A. 1982a, *Erratum - Stability of Toroidal Flux Tubes in Stars*, A&A, 113, 350

—. 1982b, *Stability of toroidal flux tubes in stars*, A&A, 106, 58

Stassun, K. G., Hebb, L., Covey, K., et al. 2011, *The M4 Transition: Toward a Comprehensive Understanding of the Transition into the Fully Convective Regime*, in Astronomical Society of the Pacific Conference Series, Vol. 448, 16th Cambridge Workshop on Cool Stars, Stellar Systems, and the Sun, ed. C. Johns-Krull, M. K. Browning, & A. A. West, 505

Steenbeck, M., & Krause, F. 1969, *Zur Dynamotheorie stellarer und planetarer Magnetfelder I. Berechnung sonnenähnlicher Wechselfeldgeneratoren*, Astronomische Nachrichten, 291, 49

Steenbeck, M., Krause, F., & Rädler, K.-H. 1966, *Berechnung der mittleren Lorentz-Feldstärke für ein elektrisch leitendes Medium in turbulenter, durch Corliolis-Kräfte beeinflußter Bewegung*, Zeitschrift Naturforschung Teil A, 21, 369

Stein, R. F. 2012, *Solar Surface Magneto-Convection*, Living Reviews in Solar Physics, 9, 4

Stenflo, J. O., & Kosovichev, A. G. 2012, *Bipolar Magnetic Regions on the Sun: Global Analysis of the SOHO/MDI Data Set*, ApJ, 745, 129

Stone, E. C., Cummings, A. C., McDonald, F. B., et al. 2005, *Voyager 1 Explores the Termination Shock Region and the Heliosheath Beyond*, Science, 309, 2017

—. 2008, *An asymmetric solar wind termination shock*, Nature, 454, 71

Stothers, R. B., & Chin, C.-W. 1993, *Iron and molecular opacities and the evolution of Population I stars*, ApJ, 412, 294

Strassmeier, K. G. 2005, *Stellar activity cycles: observing the dynamo?*, Astronomische Nachrichten, 326, 269

—. 2009, *Starspots*, A&A Rev., 17, 251

Strugarek , A., Brun, A. S., & Zahn, J.-P. 2011, *Magnetic confinement of the solar tachocline: The oblique dipole*, Astronomische Nachrichten, 332, 891

Strugarek, A., Brun, A. S., & Zahn, J.-P. 2011, *Magnetic confinement of the solar tachocline: II. Coupling to a convection zone*, A&A, 532, A34

Struve, O. 1930, *On the axial rotation of stars.*, ApJ, 72, 1

Stuke, H. 2011, PhD thesis, Free University Berlin.

Sturrock, P. A., Bertello, L., Fischbach, E., et al. 2013, *An analysis of apparent r-mode oscillations in solar activity, the solar diameter, the solar neutrino flux, and nuclear decay rates, with implications concerning the Sun's internal structure and rotation, and neutrino processes*, Astroparticle Physics, 42, 62

Suess, H. E. 1980, *The Radiocarbon Record in Tree Rings of the Last 8000 Years*, Radiocarbon, 22, 200

Suresh, A., & Huynh, H. T. 1997, *Accurate Monotonicity-Preserving Schemes with Runge Kutta Time Stepping*, Journal of Computational Physics, 136, 83

Sweby, P. K. 1984, *High Resolution Schemes Using Flux Limiters for Hyperbolic Conservation Laws*, SIAM Journal on Numerical Analysis, 21, 995

Swisdak, M., Drake, J. F., & Opher, M. 2013, *A Porous, Layered Heliopause*, ApJ, 774, L8

Telleschi, A., Güdel, M., Briggs, K. R., Audard, M., & Palla, F. 2007, *X-ray emission from T Tauri stars and the role of accretion: inferences from the XMM-Newton extended survey of the Taurus molecular cloud*, A&A, 468, 425

Thompson, M. J., Christensen-Dalsgaard, J., Miesch, M. S., & Toomre, J. 2003, *The Internal Rotation of the Sun*, ARA&A, 41, 599

Thompson, M. J., Toomre, J., Anderson, E. R., et al. 1996, *Differential Rotation and Dynamics of the Solar Interior*, Sci., 272, 1300

Thoul, A., Degroote, P., Catala, C., et al. 2013, *High-precision CoRoT space photometry and fundamental parameter determination of the B2.5V star HD 48977*, A&A, 551, A12

Title, A. M., Tarbell, T. D., Topka, K. P., et al. 1989, *Statistical properties of solar granulation derived from the SOUP instrument on Spacelab 2*, ApJ, 336, 475

Tobias, S. M. 1997, *The solar cycle: parity interactions and amplitude modulation.*, A&A, 322, 1007

Toomre, J., Zahn, J.-P., Latour, J., & Spiegel, E. A. 1976, *Stellar convection theory. II - Single-mode study of the second convection zone in an A-type star*, ApJ, 207, 545

Townsend, R. H. D. 1997, *Spectroscopic modelling of non-radial pulsation in rotating early-type stars*, MNRAS, 284, 839

Trampedach, R. 2007, *A New Stellar Atmosphere Grid-in 3D*, in American Institute of Physics Conference Series, Vol. 948, Unsolved Problems in Stellar Physics: A Conference in Honor of Douglas Gough, ed. R. J. Stancliffe, G. Houdek, R. G. Martin, & C. A. Tout, 141–148

Trampedach, R. 2010, *Convection in stellar models*, Ap&SS, 328, 213

Trampedach, R., & Stein, R. F. 2011, *The Mass Mixing Length in Convective Stellar Envelopes*, ApJ, 731, 78

Trümper, J., Pietsch, W., Reppin, C., et al. 1977, *Evidence for strong cyclotron emission in the hard x-ray spectrum of Her X-1*, Annals of the New York Academy of Sciences, 302, 538

Underhill, A. B. 1968, *Numerical experiments concerning the rotational broadening of spectral lines*, Bull. Astron. Inst. Netherlands, 19, 526

Usoskin, I. G. 2008, *A History of Solar Activity over Millennia*, Living Reviews in Solar Physics, 5, 3

—. 2013, *A History of Solar Activity over Millennia*, Living Reviews in Solar Physics, 10, 1

Usoskin, I. G., Mursula, K., Arlt, R., & Kovaltsov, G. A. 2009, *A Solar Cycle Lost in 1793-1800: Early Sunspot Observations Resolve the Old Mystery*, ApJ, 700, L154

Usoskin, I. G., Solanki, S. K., & Kovaltsov, G. A. 2007, *Grand minima and maxima of solar activity: new observational constraints*, A&A, 471, 301

Čada, M., & Torrilhon, M. 2009, *Compact third-order limiter functions for finite volume methods*, Journal of Computational Physics, 228, 4118

Vaiana, G. S., Cassinelli, J. P., Fabbiano, G., et al. 1981, *Results from an extensive Einstein stellar survey*, ApJ, 245, 163

van Leer, B. 1973, *Towards the ultimate conservative difference scheme I. The quest of monotonicity*, in Lecture Notes in Physics, Berlin Springer Verlag, Vol. 18, Lecture Notes in Physics, Berlin Springer Verlag, 163–168

van Leer, B. 1979, *Towards the ultimate conservative difference scheme. V - A second-order sequel to Godunov's method*, Journal of Computational Physics, 32, 101

Vandakurov, Y. V. 1967, *The Frequency Distribution of Stellar Oscillations.*, AZh, 44, 786

Vasil, G. M., Lecoanet, D., Brown, B. P., Wood, T. S., & Zweibel, E. G. 2013, *Energy Conservation and Gravity Waves in Sound-proof Treatments of Stellar Interiors. II. Lagrangian Constrained Analysis*, ApJ, 773, 169

Vasil'ev, A. 2004, The Field Theoretic Renormalization Group in Critical Behavior Theory and Stochastic Dynamics (Taylor & Francis)

Vaughan, A. H., & Preston, G. W. 1980, *A survey of chromospheric CA II H and K emission in field stars of the solar neighborhood*, PASP, 92, 385

Vaughan, A. H., Preston, G. W., Baliunas, S. L., et al. 1981, *Stellar rotation in lower main-sequence stars measured from time variations in H and K emission-line fluxes. I - Initial results*, ApJ, 250, 276

Vaughan, A. H., Preston, G. W., & Wilson, O. C. 1978, *Flux measurements of CA II H and K emission*, PASP, 90, 267

Vernazza, J. E., Avrett, E. H., & Loeser, R. 1981, *Structure of the solar chromosphere. III - Models of the EUV brightness components of the quiet-sun*, ApJS, 45, 635

Verner, G. A., Elsworth, Y., Chaplin, W. J., et al. 2011, *Global asteroseismic properties of solar-like oscillations observed by Kepler: a comparison of complementary analysis methods*, MNRAS, 415, 3539

Vidotto, A. A., Fares, R., Jardine, M., et al. 2012, *The stellar wind cycles and planetary radio emission of the τ Boo system*, MNRAS, 423, 3285

Vilhu, O. 1984, *The nature of magnetic activity in lower main sequence stars*, A&A, 133, 117

Vilhu, O., & Walter, F. M. 1987, *Chromospheric-coronal activity at saturated levels*, ApJ, 321, 958

Vishik, M. M. 1989, *Magnetic field generation by the motion of a highly conducting fluid*, Geophysical and Astrophysical Fluid Dynamics, 48, 151

Vögler, A., & Schüssler, M. 2007, *A solar surface dynamo*, A&A, 465, L43

Waldron, W. L., & Cassinelli, J. P. 2001, *Chandra Discovers a Very High Density X-Ray Plasma on the O Star ζ Orionis*, ApJ, 548, L45

Wang, Y.-M., & Sheeley, Jr., N. R. 1991, *Magnetic flux transport and the sun's dipole moment - New twists to the Babcock-Leighton model*, ApJ, 375, 761

Warnecke, J. 2013, PhD thesis, University of Stockholm

Warnecke, J., Käpylä, P. J., Mantere, M. J., & Brandenburg, A. 2012, *Ejections of Magnetic Structures Above a Spherical Wedge Driven by a Convective Dynamo with Differential Rotation*, Sol. Phys., 280, 299

—. 2013a, *Spoke-like differential rotation in a convective dynamo with a coronal envelope*, ArXiv e-prints

Warnecke, J., Losada, I. R., Brandenburg, A., Kleeorin, N., & Rogachevskii, I. 2013b, *Bipolar magnetic structures driven by stratified turbulence with a coronal envelope*, ArXiv e-prints

Wasiutynski, J. 1946, *Studies in Hydrodynamics and Structure of Stars and Planets*, Astrophysica Norvegica, 4, 1

Watson, M. 1981, *Shear instability of differential rotation in stars*, Geophys. Astrophys. Fluid Dyn., 16, 285

Watts, A. L., Andersson, N., Beyer, H., & Schutz, B. F. 2003, *The oscillation and stability of differentially rotating spherical shells: the normal-mode problem*, MNRAS, 342, 1156

Wedemeyer-Böhm, S., Lagg, A., & Nordlund, Å. 2009, *Coupling from the Photosphere to the Chromosphere and the Corona*, Space Sci. Rev., 144, 317

Weiss, N. O. 1964, *Convection in the Presence of Restraints*, Royal Society of London Philosophical Transactions Series A, 256, 99

Weiss, N. O., Cattaneo, F., & Jones, C. A. 1984, *Periodic and aperiodic dynamo waves*, Geophysical and Astrophysical Fluid Dynamics, 30, 305

Weiss, N. O., & Tobias, S. M. 2000, *Physical Causes of Solar Activity*, Space Sci. Rev., 94, 99

West, A. A., Hawley, S. L., Bochanski, J. J., et al. 2008, *Constraining the Age-Activity Relation for Cool Stars: The Sloan Digital Sky Survey Data Release 5 Low-Mass Star Spectroscopic Sample*, AJ, 135, 785

Williams, G. E., & Sonett, C. P. 1985, *Solar signature in sedimentary cycles from the late Precambrian Elatina Formation, Australia*, Nature, 318, 523

Wilson, K. G., & Kogut, J. 1974, *The renormalization group and the expansion*, Physics Reports, 12, 75

Wilson, O. C. 1963, *A Probable Correlation Between Chromospheric Activity and Age in Main-Sequence Stars.*, ApJ, 138, 832

—. 1966, *Stellar Convection Zones, Chromospheres, and Rotation*, ApJ, 144, 695

—. 1978, *Chromospheric variations in main-sequence stars*, ApJ, 226, 379

Wittmann, A. D., & Xu, Z. T. 1987, *A catalogue of sunspot observations from 165 BC to AD 1684*, A&AS, 70, 83

Wolf, R. 1850, *Mittheilungen über die Sonnenflecken I*, Astronomische Mitteilungen der Eidgenössischen Sternwarte Zurich, 1, 3

—. 1861, *Mittheilungen über die Sonnenflecken XIII*, Astronomische Mitteilungen der Eidgenössischen Sternwarte Zurich, 2, 83

—. 1866, *Mittheilungen über die Sonnenflecken XX*, Astronomische Mitteilungen der Eidgenössischen Sternwarte Zurich, 2, 311

Wollaston, W. 1802, *A Method of Examining Refractive and Dispersive Powers, by Prismatic Reflection*, Phil. Trans. London, 92, 365

Wood, T. S., McCaslin, J. O., & Garaud, P. 2011, *The Sun's Meridional Circulation and Interior Magnetic Field*, ApJ, 738, 47

Wood, T. S., & McIntyre, M. E. 2007, *Confinement of the Sun's Interior Magnetic Field: Some Exact Boundary-layer Solutions*, in AIP Conf. Ser., Vol. 948, Unsolved Problems in Stellar Physics: A Conference in Honor of Douglas Gough, 303–308

Wright, J. T., Marcy, G. W., Butler, R. P., & Vogt, S. S. 2004, *Chromospheric Ca II Emission in Nearby F, G, K, and M Stars*, ApJS, 152, 261

Wright, N. J., Drake, J. J., & Civano, F. 2010, *Stellar X-ray Sources in the Chandra COSMOS Survey*, ApJ, 725, 480

Wright, N. J., Drake, J. J., Mamajek, E. E., & Henry, G. W. 2011, *The Stellar-activity-Rotation Relationship and the Evolution of Stellar Dynamos*, ApJ, 743, 48

Yadav, R. K., Gastine, T., Christensen, U. R., & Duarte, L. D. V. 2013, *Consistent Scaling Laws in Anelastic Spherical Shell Dynamos*, ApJ, 774, 6

Yoshimura, H. 1975, *Solar-cycle dynamo wave propagation*, ApJ, 201, 740

Zahn, J.-P. 1991, *Convective penetration in stellar interiors*, A&A, 252, 179

—. 1992, *Circulation and turbulence in rotating stars*, A&A, 265, 115

Zahn, J.-P. 1999, *Beyond the Mixing-Length Treatment: Why and How?*, in Astronomical Society of the Pacific Conference Series, Vol. 173, Stellar Structure: Theory and Test of Connective Energy Transport, ed. A. Gimenez, E. F. Guinan, & B. Montesinos, 121

Zahn, J.-P., Brun, A. S., & Mathis, S. 2007, *On magnetic instabilities and dynamo action in stellar radiation zones*, A&A, 474, 145

Zaqarashvili, T. V., Carbonell, M., Oliver, R., & Ballester, J. L. 2010, *Magnetic Rossby Waves in the Solar Tachocline and Rieger-Type Periodicities*, ApJ, 709, 749

Zhang, C.-Y., Ling, Y., Niu, C., Tian, Y., & Wu, X.-N. 2012, *Magnetohydrodynamics from gravity*, Phys. Rev. D, 86, 084043

Zhang, K. 1992, *Spiralling columnar convection in rapidly rotating spherical fluid shells*, Journal of Fluid Mechanics, 236, 535

Zhao, J., Bogart, R. S., Kosovichev, A. G., Duvall, Jr., T. L., & Hartlep, T. 2013, *Detection of Equatorward Meridional Flow and Evidence of Double-cell Meridional Circulation inside the Sun*, ApJ, 774, L29

Appendix A

Derivation of the Multi-Fluid Electrodynamically-Coupled Field Equations

A set of equations is needed from which a Lagrangian can then be constructed. There are many places one can start from, for instance a fairly general starting point could be the classical mechanics Hamiltonian of the universe $H_U = \sum_{n=1}^{N} H_n = \sum_n \mathbf{p}_n^2/2m_n + \Phi_n(t, \mathbf{q}_1, \cdots, \mathbf{q_n}, \cdots \mathbf{q}_N)$, where Φ_n embodies the interaction of particle n with all other particles in the universe through gravity and electromagnetic forces. This, while somewhat flippant, underscores one of the fundamental problems in dealing with systems that involve more than a single particle: the coupling between greater numbers of particles quickly leads to an unsolvable system. One can instead parameterize the problem, utilizing statistical ensembles of large numbers of such particles. Under this assumption the 6-N_p dimensional phase space tracks of all the individual particles become indistinguishable, forming a 6-S dimensional Riemannian manifold, where S is the total number of particle species in the plasma. The evolution of an infinitessimal volume of this manifold is governed by Liouville's theorem which states that, given the phase space density $f_s(\mathbf{x}, \mathbf{v}, t)$ of species s, this density is constant along any trajectory in phase space. Since the manifold is Riemannian this evolution can be written as

$$\frac{\partial f_s}{\partial t} + \mathbf{v} \cdot \boldsymbol{\nabla}_{\mathbf{x}} f_s + \frac{\mathbf{F}_s}{m_s} \cdot \boldsymbol{\nabla}_{\mathbf{v}} f_s = \left.\frac{\partial f_s}{\partial t}\right|_{col}, \tag{A.1}$$

where $\mathbf{F}$ is the total force on species s, the collisional forces are included in the term on the right hand side, relativity has been neglected, and by definition the number density of species

s is $n_s = \int d\mathbf{v} f_s$. Further, we have assumed that the radiation field acts instantaneously to equilibrate a given species and have not accounted for its interaction with the plasma. The goal is to integrate out the velocity dependence by integrating over moments in velocity space and supplementing the resulting equations with a closure. Let $\chi_s(\mathbf{v})$ be the generator of the velocity moments. After integrating by parts and using the fact that χ_s is only a function of the velocity, one can find the generalized transport equation for the ensemble averaged value of $\overline{\chi} = 1/n_s \int d\mathbf{v} \chi f_s$

$$\frac{\partial n_s \overline{\chi}}{\partial t} + \boldsymbol{\nabla} \cdot n_s \overline{\chi \mathbf{v}} - n_s \overline{\frac{\mathbf{F}_s}{m_s} \cdot \boldsymbol{\nabla}_{\mathbf{v}} \chi} = \left. \frac{\partial n_s \overline{\chi}}{\partial t} \right|_{col}, \tag{A.2}$$

The zeroth moment is that of the mass density with $\chi = m_s$ and species mass m_s, which yields

$$\frac{\partial m_s n_s}{\partial t} + \boldsymbol{\nabla} \cdot m_s n_s \int d\mathbf{v} f_s \mathbf{v} = m_s \int d\mathbf{v} \left. \frac{\partial f_s}{\partial t} \right|_{col} = \dot{M}_s. \tag{A.3}$$

The collisional term subsumes all interactions that lead to the change of one species into another, such as chemical reactions, nuclear fusion or fission, or ionization for example, and as such acts as a source or sink of mass ($\dot{M}_s$). Let the total velocity be $\mathbf{v} = \mathbf{u}_s + \mathbf{v}'$, with $\mathbf{u}_s$ the bulk velocity and $\mathbf{v}'$ fluctuations such that $1/n_s \int d\mathbf{v} f_s \mathbf{v} = \mathbf{u}_s$ (so $\overline{\mathbf{v}'} = 0$) and let $\rho_s = m_s n_s$ be the mass density. Then the equation for the conservation of mass is

$$\frac{\partial \rho_s}{\partial t} + \boldsymbol{\nabla} \cdot \rho_s \mathbf{u}_s = \dot{M}_s. \tag{A.4}$$

The first moment gives rise to the momentum equations, wherein $\chi = m_s \mathbf{v}$. Thus Equation A.2 becomes

$$\frac{\partial \rho_s \mathbf{u}_s}{\partial t} + \boldsymbol{\nabla} \cdot \left[\rho_s \int d\mathbf{v} f_s \mathbf{v} \otimes \mathbf{v} \right] - n_s \overline{\mathbf{F}}_s = \int d\mathbf{v} \left. \frac{\partial \rho_s f_s \mathbf{v}}{\partial t} \right|_{col} = \dot{\mathbf{Q}}_s, \tag{A.5}$$

The dyadic form $\rho_s \mathbf{v} \otimes \mathbf{v}$ produces the bulk velocity dyadic but also the correlations of fluctuating velocities as $\rho_s \overline{\mathbf{v} \otimes \mathbf{v}} = m_s \int d\mathbf{v} f_s \mathbf{u}_s \otimes \mathbf{u}_s + 2\mathbf{u}_s \otimes \mathbf{v}'_s + \mathbf{v}'_s \otimes \mathbf{v}'_s = \rho_s \mathbf{u}_s \otimes \mathbf{u}_s + \rho_s \overline{\mathbf{v}'_s \otimes \mathbf{v}'_s}$. The fluctuating velocity dyadic $\rho_s \overline{\mathbf{v}'_s \otimes \mathbf{v}'_s}$ may be interpreted as the partial pressure tensor $\mathbf{P}_s$. The collisional term $\dot{\mathbf{Q}}_s$ describes the sources and sinks of momentum. Thus the momentum conservation equation is

$$\frac{\partial \rho_s \mathbf{u}_s}{\partial t} + \boldsymbol{\nabla} \cdot [\rho_s \mathbf{u}_s \otimes \mathbf{u}_s + \mathbf{P}_s] = \dot{\mathbf{Q}}_s + n_s \overline{\mathbf{F}}_s. \tag{A.6}$$

The final equation, before introducing a closure, is the conservation of energy where $\chi = 1/2 m_s \mathbf{v}^2$. Again appealing to Equation A.2, we have

$$\frac{1}{2}\frac{\partial \rho_s \overline{\mathbf{v}^2}}{\partial t} + \frac{1}{2}\boldsymbol{\nabla} \cdot \rho_s \overline{\mathbf{v}^3} - n_s \overline{\mathbf{F}_s \cdot \mathbf{v}} = \frac{1}{2}\int d\mathbf{v} \frac{\partial \rho_s f_s \mathbf{v}^2}{\partial t}\bigg|_{col} = \dot{K}_s. \tag{A.7}$$

The first term on the left hand side is

$$\frac{1}{2}\frac{\partial \rho_s \overline{\mathbf{v}^2}}{\partial t} = \frac{\partial}{\partial t}\int d\mathbf{v} \frac{1}{2}\rho_s \left(\mathbf{u}_s^2 + 2\mathbf{u}_s \cdot \mathbf{v}'_s + \mathbf{v}'^2_s\right) = \frac{\partial}{\partial t}\frac{1}{2}\rho_s \left(\mathbf{u}_s^2 + \overline{\mathbf{v}'^2_s}\right) = \frac{\partial E_s}{\partial t}, \tag{A.8}$$

where the energy density is $E_s = 1/2\rho_s \left(\mathbf{u}_s^2 + \overline{\mathbf{v}'^2_s}\right)$. The energy flux divergence in Equation A.7 is

$$\begin{aligned}
\frac{1}{2}\boldsymbol{\nabla} \cdot \rho_s \overline{\mathbf{v}^3} &= \boldsymbol{\nabla} \cdot \int d\mathbf{v} \frac{1}{2}\rho_s \mathbf{v}^3 \\
&= \boldsymbol{\nabla} \cdot \int d\mathbf{v} \frac{1}{2}\rho_s \left(\mathbf{u}_s^2 + 2\mathbf{u}_s \cdot \mathbf{v}'_s + \mathbf{v}'^2_s\right)(\mathbf{u}_s + \mathbf{v}'_s) \\
&= \boldsymbol{\nabla} \cdot \int d\mathbf{v} \frac{1}{2}\rho_s \left(\mathbf{u}_s^3 + \mathbf{u}_s^2 \mathbf{v}'_s + 2\mathbf{v}'_s \cdot \mathbf{u}_s \otimes \mathbf{u}_s + 2\mathbf{u}_s \cdot \mathbf{v}'_s \otimes \mathbf{v}'_s + \mathbf{u}_s \mathbf{v}'^2_s + \mathbf{v}'^3_s\right) \\
&= \boldsymbol{\nabla} \cdot \left[\frac{1}{2}\rho_s \left(\mathbf{u}_s^3 + 2\mathbf{u}_s \cdot \overline{\mathbf{v}'_s \otimes \mathbf{v}'_s} + \mathbf{u}_s \overline{\mathbf{v}'^2_s} + \overline{\mathbf{v}'^3_s}\right)\right] \\
&= \boldsymbol{\nabla} \cdot \left[E_s \mathbf{u}_s + \mathbf{u}_s \cdot \mathbf{P}_s + \frac{1}{2}\rho_s \overline{\mathbf{v}'^3_s}\right]
\end{aligned} \tag{A.9}$$

The last term in the energy flux divergence is an internal heat flux ($\mathbf{q}_s = 1/2\rho_s \overline{\mathbf{v}'^3_s}$), arising from the triple product correlation of the fluctuating microscopic velocity field that describes the internal redistribution of kinetic energy. The work done by forces acting on the species is $\overline{\mathbf{F}_s \cdot \mathbf{v}}$, which reduces to $\overline{\mathbf{F}}_s \cdot \mathbf{u}_s + \overline{\mathbf{F}_s \cdot \mathbf{v}'_s}$. The fluctuating portion of the work will be zero if there are no velocity dependent forces. Hence the species specific energy conservation equation is

$$\frac{\partial E_s}{\partial t} + \boldsymbol{\nabla} \cdot [E_s \mathbf{u}_s + \mathbf{u}_s \cdot \mathbf{P}_s + \mathbf{q}_s] = \dot{K}_s + n_s \overline{\mathbf{F}_s \cdot \mathbf{v}}. \tag{A.10}$$

At this point, since the goal is to derive the single fluid MHD equations relevant to this thesis, the force can be directly expressed as $\mathbf{F}_s = q_s(\mathbf{E}+\mathbf{v}/c\times\mathbf{B})+m_s\boldsymbol{\nabla}\Phi$, with q_s the charge of species s, the electric field $\mathbf{E}$, magnetic field $\mathbf{B}$, and Φ the external gravitational field under the assumption of minimal self-gravity. Thus the force term in the momentum equation is $n_s\overline{\mathbf{F}}_s = \varrho_s\overline{\mathbf{E}} + \varrho_s\mathbf{u}_s/c\times\overline{\mathbf{B}} + \rho_s\boldsymbol{\nabla}\Phi$ and the work that these forces do is

$$\begin{aligned} n_s\overline{F_s\cdot\mathbf{v}} &= \int d\mathbf{v} q_s f_s(\mathbf{E}+\frac{\mathbf{v}}{c}\times\mathbf{B})\cdot\mathbf{v} + f_s m_s\mathbf{v}\cdot\boldsymbol{\nabla}\Phi \\ &= \varrho_s\mathbf{u}_s\cdot\overline{E} + \rho_s\mathbf{u}_s\cdot\boldsymbol{\nabla}\Phi \end{aligned} \tag{A.11}$$

where the charge density is $\varrho_s = q_s n_s$. Therefore the full system of equations for each species is

$$\frac{\partial\rho_s}{\partial t} + \boldsymbol{\nabla}\cdot\rho_s\mathbf{u}_s = \dot{M}_s, \tag{A.12}$$

$$\frac{\partial\rho_s\mathbf{u}_s}{\partial t} + \boldsymbol{\nabla}\cdot[\rho_s\mathbf{u}_s\otimes\mathbf{u}_s + \mathbf{P}_s] = \dot{\mathbf{Q}}_s + \varrho_s\overline{\mathbf{E}} + \varrho_s\frac{\mathbf{u}_s}{c}\times\overline{\mathbf{B}} + \rho_s\boldsymbol{\nabla}\Phi, \tag{A.13}$$

$$\frac{\partial E_s}{\partial t} + \boldsymbol{\nabla}\cdot[E_s\mathbf{u}_s + \mathbf{u}_s\cdot\mathbf{P}_s + \mathbf{q}_s] = \dot{K}_s + \varrho_s\mathbf{u}_s\cdot\overline{\mathbf{E}} + \rho_s\mathbf{u}_s\cdot\boldsymbol{\nabla}\Phi. \tag{A.14}$$

The next step is to sum over all species, where $\rho = \sum_s \rho_s$, $\rho\mathbf{u} = \sum_s \rho_s\mathbf{u}_s$, $\varrho = \sum_s \varrho_s$, and $\mathbf{J} = \sum_s \varrho_s\mathbf{u}_s/c$. If there is no net mass, momentum, or energy loss or gain in the system arising from collisions, so $\sum_s \dot{M}_s = \sum_s \dot{\mathbf{Q}}_s = \sum_s \dot{K}_s = 0$. Thus the continuity equation is

$$\sum_s \frac{\partial\rho_s}{\partial t} + \boldsymbol{\nabla}\cdot\rho_s\mathbf{u}_s = \frac{\partial\rho}{\partial t} + \boldsymbol{\nabla}\cdot\rho\mathbf{u} = 0. \tag{A.15}$$

It is also useful to transform the individual species bulk velocities to the frame of the bulk motion. The differences in the bulk motion of each species provides an additional, but constant, internal energy and partial pressure. The velocity difference $\mathbf{w}_s = \mathbf{u}_s - \mathbf{u}$ is a constant for each species and so has no correlation with the fluctuating motions, with $\sum_s \mathbf{w}_s = 0$. Thus the pressure becomes $\mathbf{P} = \sum_s \rho_s\overline{(\mathbf{v}_s-\mathbf{u})\otimes(\mathbf{v}_s-\mathbf{u})} = \sum_s \mathbf{P}_s + \rho_s\mathbf{w}_s\otimes\mathbf{w}_s$, similarly the momentum dyadic is $\sum_s \rho_s\mathbf{u}_s\otimes\mathbf{u}_s = \rho\mathbf{u}\otimes\mathbf{u} + \sum_s \rho_s\mathbf{w}_s\otimes\mathbf{w}_s$. Hence the momentum equation is

$$\sum_s \frac{\partial \rho_s \mathbf{u}_s}{\partial t} + \boldsymbol{\nabla} \cdot [\rho_s \mathbf{u}_s \otimes \mathbf{u}_s + \mathbf{P}_s] - \dot{\mathbf{Q}}_s - \varrho_s \overline{\mathbf{E}} - \varrho_s \frac{\mathbf{u}_s}{c} \times \overline{\mathbf{B}} - \rho_s \boldsymbol{\nabla} \Phi = 0,$$
$$\frac{\partial \rho \mathbf{u}}{\partial t} + \boldsymbol{\nabla} \cdot [\rho \mathbf{u} \otimes \mathbf{u} + \mathbf{P}] - \varrho \mathbf{E} - \mathbf{J} \times \mathbf{B} - \rho \boldsymbol{\nabla} \Phi = 0. \tag{A.16}$$

The total energy density is $E = \sum_s 1/2 \rho_s (\mathbf{u}^2 + \mathbf{w}_s^2 + \overline{\mathbf{v}'^2_s}) = \sum_s E_s + \sum_s 1/2 \rho_s \mathbf{w}_s^2 = 1/2 \rho \mathbf{u}^2 + \epsilon$, where ϵ is the internal energy. The heat flux becomes

$$\begin{aligned} \mathbf{q} &= \sum_s \frac{1}{2} \rho_s \overline{(\mathbf{v}_s - \mathbf{u})^3}, \\ &= \sum_s \mathbf{q}_s + \frac{1}{2} \rho_s \overline{\mathbf{v}'^2_s} \mathbf{w}_s + \mathbf{w}_s \cdot \mathbf{P}_s + \frac{1}{2} \rho_s \mathbf{w}_s^3. \end{aligned} \tag{A.17}$$

The energy fluxes within the divergence operator in the energy conservation equation are

$$\begin{aligned} \text{Flux} &= \sum_s E_s (\mathbf{u} + \mathbf{w}_s) + (\mathbf{u} + \mathbf{w}_s) \cdot \mathbf{P}_s + \mathbf{q}_s \\ &= \mathbf{u} \sum_s E_s + \sum_s \mathbf{w}_s E_s + \mathbf{u} \cdot \sum_s \mathbf{P}_s + \sum_s \mathbf{w}_s \cdot \mathbf{P}_s + \mathbf{q} - \sum_s \left[\frac{1}{2} \rho_s \overline{\mathbf{v}'^2_s} \mathbf{w}_s + \mathbf{w}_s \cdot \mathbf{P}_s + \frac{1}{2} \rho_s \mathbf{w}_s^3 \right] \\ &= \mathbf{u} E + \sum_s \frac{1}{2} \rho_s \mathbf{w}_s \left(\mathbf{u}^2 + 2 \mathbf{u} \cdot \mathbf{w}_s + \mathbf{w}_s^2 + \overline{\mathbf{v}'^2_s} \right) + \mathbf{u} \cdot \left(\mathbf{P} - \sum_s \rho_s \mathbf{w}_s \otimes \mathbf{w}_s \right) \\ &\quad + \mathbf{q} - \sum_s \left[\frac{1}{2} \rho_s \overline{\mathbf{v}'^2_s} \mathbf{w}_s + \frac{1}{2} \rho_s \mathbf{w}_s^3 \right] \\ &= \mathbf{u} E + \mathbf{u} \cdot \mathbf{P} + \mathbf{q} \end{aligned} \tag{A.18}$$

Thus the full set of fluid equations for the plasma are

$$\frac{\partial \rho}{\partial t} + \boldsymbol{\nabla} \cdot \rho \mathbf{u} = 0, \tag{A.19}$$
$$\frac{\partial \rho \mathbf{u}}{\partial t} + \boldsymbol{\nabla} \cdot [\rho \mathbf{u} \otimes \mathbf{u} + \mathbf{P}] = \varrho \mathbf{E} + \mathbf{J} \times \mathbf{B} + \rho \boldsymbol{\nabla} \Phi, \tag{A.20}$$
$$\frac{\partial E}{\partial t} + \boldsymbol{\nabla} \cdot [\mathbf{u} E + \mathbf{u} \cdot \mathbf{P} + \mathbf{q}] = \mathbf{J} \cdot \mathbf{E} + \rho \mathbf{u} \cdot \boldsymbol{\nabla} \Phi, \tag{A.21}$$
$$E = \frac{1}{2} \rho \mathbf{u}^2 + \epsilon. \tag{A.22}$$

It is worth noting that the pressure tensor, as it currently stands, has two primary components the standard isotropic pressure $\mathcal{P} = Tr(\mathbf{P})$ and an anistropic part that is related to viscous diffusion tensor D_{ij}, so that $P_{ij} = \mathcal{P}\delta_{ij} + D_{ij}$ where δ_{ij} is the identity tensor. So far, the evolution of the plasma has been described without the coevolution of the electromagetic field, though without a direct coupling to the radiation field. To this end, we will need Maxwell's equations.

$$\boldsymbol{\nabla} \cdot \mathbf{E} = 4\pi\varrho \tag{A.23}$$

$$\boldsymbol{\nabla} \cdot \mathbf{B} = 0 \tag{A.24}$$

$$\boldsymbol{\nabla} \times \mathbf{E} = -\frac{1}{c}\frac{\partial \mathbf{B}}{\partial t} \tag{A.25}$$

$$\boldsymbol{\nabla} \times \mathbf{B} = 4\pi\mathbf{J} + \frac{1}{c}\frac{\partial \mathbf{E}}{\partial t} \tag{A.26}$$

If Equation A.13 is multiplied by q_s/cm_s, the resulting equation for $\mathbf{J}$ is

$$\frac{\partial}{\partial t}\sum_s \varrho_s \frac{\mathbf{u}_s}{c} + \boldsymbol{\nabla} \cdot \left[\sum_s \varrho_s \frac{\mathbf{u}_s}{c} \otimes \mathbf{u}_s + \frac{q_s}{cm_s}\mathbf{P}_s\right] = \sum_s \left[\varrho_s \frac{\overline{\mathbf{F}}}{cm_s} + \frac{q_s}{cm_s}\dot{\mathbf{Q}}_s\right] \tag{A.27}$$

Applying the conventions and definitions from above this becomes

$$\frac{\partial \mathbf{J}}{\partial t} + \boldsymbol{\nabla} \cdot [\mathbf{J} \otimes \mathbf{u} + \mathbf{u} \otimes (\mathbf{J} - \varrho\mathbf{u}) + \boldsymbol{\Pi}] = \sum_s \left[\frac{\varrho_s q_s}{cm_s}\left(\mathbf{E} + \frac{\mathbf{u}_s}{c} \times \mathbf{B}\right) + \frac{\varrho_s}{c}\boldsymbol{\nabla}\Phi + \frac{q_s}{cm_s}\dot{\mathbf{Q}}_s\right], \tag{A.28}$$

where we have used the relationship

$$\begin{aligned}
\sum_s \varrho_s \frac{\mathbf{u}_s}{c} \otimes \mathbf{u}_s &= \varrho\frac{\mathbf{u}}{c} \otimes \mathbf{u} + \mathbf{u} \otimes \mathbf{J}_w + \mathbf{J}_w \otimes \mathbf{u} + \sum_s \left[\varrho_s \frac{\mathbf{w}_s}{c} \otimes \mathbf{w}_s + \frac{1}{c}\overline{\mathbf{v}'_s \otimes \mathbf{v}'_s}\right], \\
&= \mathbf{J} \otimes \mathbf{u} + \mathbf{u} \otimes \left(\mathbf{J} - \varrho\frac{\mathbf{u}}{c}\right) + \Pi, \\
\boldsymbol{\Pi} &= \sum_s \left[\varrho_s \frac{\mathbf{w}_s}{c} \otimes \mathbf{w}_s + \frac{1}{c}\overline{\mathbf{v}'_s \otimes \mathbf{v}'_s}\right], \\
\mathbf{J}_w &= \sum_s \varrho_s \frac{\mathbf{w}_s}{c},
\end{aligned} \tag{A.29}$$

and where $\mathbf{J}_w$ is the current arising from differences between the bulk velocity and the mean velocity of a given species. This is a fairly general Ohm's law. Thus the evolution of the electromagnetic field and charged currents remain tightly coupled to the properties of the constituents of the plasma, whereas the fluid equations are greatly simplified for the plasma as a whole. In summary, the electrohydrodynamic equations for a single species are

Fluid Equations

$$\frac{\partial \rho_s}{\partial t} + \boldsymbol{\nabla} \cdot \rho_s \mathbf{u}_s = \dot{M}_s, \tag{A.30}$$

$$\frac{\partial \rho_s \mathbf{u}_s}{\partial t} + \boldsymbol{\nabla} \cdot [\rho_s \mathbf{u}_s \otimes \mathbf{u}_s + \mathbf{P}_s] = \dot{\mathbf{Q}}_s + \varrho_s \mathbf{E} + \mathbf{J}_s \times \mathbf{B} + \rho_s \boldsymbol{\nabla} \Phi, \tag{A.31}$$

$$\frac{\partial E_s}{\partial t} + \boldsymbol{\nabla} \cdot [E_s \mathbf{u}_s + \mathbf{u}_s \cdot \mathbf{P}_s + \mathbf{q}_s] = \dot{K}_s + \mathbf{J}_s \cdot \mathbf{E} + \rho_s \mathbf{u}_s \cdot \boldsymbol{\nabla} \Phi, \tag{A.32}$$

$$E_s = \frac{1}{2} \rho_s \left(\mathbf{u}_s^2 + \overline{\mathbf{v}'^2_s} \right), \tag{A.33}$$

Maxwell′s Equations

$$\boldsymbol{\nabla} \cdot \mathbf{E} = 4\pi \varrho, \qquad \boldsymbol{\nabla} \cdot \mathbf{B} = 0, \tag{A.34}$$

$$\boldsymbol{\nabla} \times \mathbf{E} = -\frac{1}{c} \frac{\partial \mathbf{B}}{\partial t}, \qquad \boldsymbol{\nabla} \times \mathbf{B} = 4\pi \mathbf{J} + \frac{1}{c} \frac{\partial \mathbf{E}}{\partial t}, \tag{A.35}$$

Ohm′s Law

$$\frac{\partial \mathbf{J}_s}{\partial t} + \boldsymbol{\nabla} \cdot [\mathbf{J}_s \otimes \mathbf{u}_s] = \frac{\varrho_s q_s}{c m_s} \left(\mathbf{E} + \frac{\mathbf{u}_s}{c} \times \mathbf{B} \right) + \frac{\varrho_s}{c} \boldsymbol{\nabla} \Phi + \frac{q_s}{c m_s} \dot{\mathbf{Q}}_s. \tag{A.36}$$

Similarly, for the entire fluid and summed over species and noting Maxwell's equations above, the plasma electrohydrodynamic equations are

Fluid Equations

$$\frac{\partial \rho}{\partial t} + \boldsymbol{\nabla} \cdot \rho \mathbf{u} = 0, \tag{A.37}$$

$$\frac{\partial \rho \mathbf{u}}{\partial t} + \boldsymbol{\nabla} \cdot [\rho \mathbf{u} \otimes \mathbf{u} + \mathbf{P}] = \varrho \mathbf{E} + \mathbf{J} \times \mathbf{B} + \rho \boldsymbol{\nabla} \Phi, \tag{A.38}$$

$$\frac{\partial E}{\partial t} + \boldsymbol{\nabla} \cdot [\mathbf{u} E + \mathbf{u} \cdot \mathbf{P} + \mathbf{q}] = \mathbf{J} \cdot \mathbf{E} + \rho \mathbf{u} \cdot \boldsymbol{\nabla} \Phi, \tag{A.39}$$

$$E = \frac{1}{2} \rho \mathbf{u}^2 + \epsilon, \tag{A.40}$$

Ohm′s Law

$$\frac{\partial \mathbf{J}}{\partial t} + \boldsymbol{\nabla} \cdot \left[\mathbf{J} \otimes \mathbf{u} + \mathbf{u} \otimes \left(\mathbf{J} - \varrho \frac{\mathbf{u}}{c} \right) + \boldsymbol{\Pi} \right] = \sum_s \left[\frac{\varrho_s q_s}{c m_s} \left(\mathbf{E} + \frac{\mathbf{u}_s}{c} \times \mathbf{B} \right) + \frac{\varrho_s}{c} \boldsymbol{\nabla} \Phi + \frac{q_s}{c m_s} \dot{\mathbf{Q}}_s \right]. \tag{A.41}$$

Appendix B

An Exposition on Meridional Flows and Gyroscopic Pumping

B.1 Navier-Stokes Momentum Equation

We begin with the equation that expresses the conservation of momentum in a magnetized, compressible fluid within an inertial frame.

$$\rho\frac{\partial \mathbf{v}}{\partial t} + \rho\mathbf{v}\cdot\nabla\mathbf{v} = -\nabla P + \rho\mathbf{g} + \boldsymbol{\nabla}\cdot\mathcal{D} + \frac{1}{4\pi}\left(\nabla\times\mathbf{B}\right)\times\mathbf{B} \tag{B.1}$$

A standard notation is used: $\mathbf{v}$ is the bulk velocity of the fluid, $\mathbf{B}$ the magnetic field, ρ is the density, P is the pressure, $\mathbf{g}$ is the acceleration due to gravity, and $\mathcal{D}$ is the viscous stress tensor, with elements

$$\mathcal{D}_{ij} = 2\rho\nu\left[e_{ij} - \frac{1}{3}\left(\boldsymbol{\nabla}\cdot\mathbf{v}\right)\delta_{ij}\right] \tag{B.2}$$

where ν is the kinematic viscosity. We use spherical polar coordinates (r,θ,ϕ) in this derivation. In a rotating coordinate system, equation B.1 becomes

$$\rho\frac{\partial \mathbf{u}}{\partial t} + \rho\mathbf{u}\cdot\nabla\mathbf{u} = -\nabla P + \rho\mathbf{g}_{eff} - 2\rho\Omega_0\times\mathbf{u} - \boldsymbol{\nabla}\cdot\mathcal{D} + \frac{1}{4\pi}\left(\nabla\times\mathbf{B}\right)\times\mathbf{B} \tag{B.3}$$

where $\boldsymbol{\Omega_0} = \Omega_0\hat{z}$, $\mathbf{g}_{eff} = \nabla\left[\Psi_g + \frac{1}{2}\lambda^2\Omega_0^2\right]$, Ψ_g is the gravitational potential. Multiplying the zonal component of equation B.3 by $\lambda = r\sin\theta$ yields

$$\rho\frac{\partial \lambda u_\phi}{\partial t} = -\rho\lambda\mathbf{u}\cdot\nabla u_\phi - \left(2\Omega_0\lambda + u_\phi\right)\rho u_\lambda - \frac{\partial P}{\partial\phi} + \rho\frac{\partial\Psi_g}{\partial\phi} - \lambda\hat{\boldsymbol{\phi}}\cdot\boldsymbol{\nabla}\cdot\mathcal{D} + \frac{\lambda}{4\pi}\left(\nabla\times\mathbf{B}\right)\times\mathbf{B} \tag{B.4}$$

The first two terms on the right hand side can be combined and the left hand side reduced using the continuity equation ($\frac{\partial\rho}{\partial t} = -\boldsymbol{\nabla}\cdot\rho\mathbf{u}$) to give

$$\frac{\partial \rho L}{\partial t} = -\boldsymbol{\nabla} \cdot \left[\rho \mathbf{u} L - \frac{\lambda}{4\pi} \mathcal{M} \hat{\boldsymbol{\phi}} \right] - \frac{\partial P_{tot}}{\partial \phi} + \rho \frac{\partial \Psi_g}{\partial \phi} - \lambda \hat{\boldsymbol{\phi}} \cdot \boldsymbol{\nabla} \cdot \mathcal{D} \tag{B.5}$$

where $P_{tot} = P_{gas} + \frac{B^2}{8\pi}$ is the total pressure and $\mathcal{M}$ is the Maxwell stress tensor. The last term can be written as the divergence of a diffusive flux, if we note that

$$\begin{aligned} \boldsymbol{\nabla} \cdot \lambda \mathbf{D} &= \hat{\boldsymbol{\phi}} \cdot [\boldsymbol{\nabla} \cdot \lambda \mathcal{D}] \\ &= \left[\frac{1}{\mathcal{D}_{r\phi} r^2} \frac{\partial}{\partial r} r^2 [\lambda] + \frac{1}{\mathcal{D}_{\theta\phi} r \sin\theta} \frac{\partial}{\partial \theta} \sin\theta [\lambda] + \frac{\partial \mathcal{D}_{\phi\phi}}{\partial \phi} \right] + 2 \sin\theta \mathcal{D}_{r\phi} + 2 \cos\theta \mathcal{D}_{\theta\phi} \\ &= \lambda \left[\boldsymbol{\nabla} \cdot \left(\mathcal{D} \hat{\boldsymbol{\phi}} \right) \right] + \left(\mathcal{D} \hat{\boldsymbol{\phi}} \right) \cdot \hat{\lambda} \end{aligned} \tag{B.6}$$

where $\mathbf{D} = \mathcal{D}\hat{\boldsymbol{\phi}} = \mathcal{D}_{r\phi}\hat{\mathbf{r}} + \mathcal{D}_{\theta\phi}\hat{\boldsymbol{\theta}} + \mathcal{D}_{\phi\phi}\hat{\boldsymbol{\phi}}$ and $\mathbf{M} = \mathcal{M}\hat{\boldsymbol{\phi}} = \mathcal{M}_{r\phi}\hat{\mathbf{r}} + \mathcal{M}_{\theta\phi}\hat{\boldsymbol{\theta}} + \mathcal{M}_{\phi\phi}\hat{\boldsymbol{\phi}}$. Thus, equation B.5 becomes

$$\frac{\partial \rho L}{\partial t} = -\boldsymbol{\nabla} \cdot \left[\rho \mathbf{u} L + \lambda \mathbf{D} - \frac{\lambda}{4\pi} \mathbf{M} \right] - \frac{\partial P_{tot}}{\partial \phi} + \rho \frac{\partial \Psi_g}{\partial \phi} \tag{B.7}$$

If we now take a temporal and azimuthal average of this equation we arrive at

$$\langle \frac{\partial \rho L}{\partial t} \rangle_{t,\phi} = -\langle \boldsymbol{\nabla} \cdot \left[\rho \mathbf{u} L + \lambda \mathbf{D} - \frac{\lambda}{4\pi} \mathbf{M} \right] \rangle_{t,\phi} - \langle \frac{\partial P_{tot}}{\partial \phi} + \rho \frac{\partial \Psi_g}{\partial \phi} \rangle_{t,\phi} \tag{B.8}$$

Now introduce mean fields that depend only on r and θ and time dependent fluctuating fields with zero mean such that

$$\begin{aligned} P &= \overline{P} + P' \\ \rho &= \overline{\rho} + \rho' \\ L &= \overline{L} + L' = \left(\lambda^2 \Omega_0 + \lambda \overline{u}_\phi \right) + \lambda u'_\phi \\ \mathbf{u} &= \overline{\mathbf{u}} + \mathbf{u}' \\ \mathbf{B} &= \overline{\mathbf{B}} + \mathbf{B}' \end{aligned} \tag{B.9}$$

With such a substitution, the ϕ derivatives here drop out leaving

$$\langle \frac{\partial \rho L}{\partial t} \rangle = -\langle \boldsymbol{\nabla} \cdot \left[\rho \mathbf{u} L + \lambda \mathbf{D} - \frac{\lambda}{4\pi} \mathbf{M} \right] \rangle \tag{B.10}$$

Since $\mathcal{D}$ is a linear operator on $\mathbf{v}$, and after applying the average to the expansion of these fields, we find

$$\boldsymbol{\nabla}\cdot\left[\overline{\rho}\overline{\mathbf{u}}\overline{L}+\overline{\rho'\mathbf{u}'L}+\overline{\mathbf{u}}\overline{\rho'L'}+\overline{\rho}\overline{\mathbf{u}'L'}+\overline{\rho'\mathbf{u}'L'}+\lambda\overline{\mathbf{D}}+\lambda\mathbf{D}'-\frac{\lambda}{4\pi}\left(\overline{\mathbf{B}}_{\mathbf{P}}\overline{B_\phi}+\overline{\mathbf{B}'_{\mathbf{P}}B'_\phi}\right)\right]\approx 0 \tag{B.11}$$

where the mean diffusive flux is $\overline{\mathbf{D}}=2\overline{\rho}\nu\mathcal{D}\left[\overline{\mathbf{u}}\right]\hat{\boldsymbol{\phi}}$, the fluctuating mean is $\mathbf{D}'=2\nu\overline{\rho'\mathcal{D}\left[\mathbf{u}'\right]}\hat{\boldsymbol{\phi}}$, and $\mathbf{B}_P$ is the poloidal field. In the anelastic approximation $\boldsymbol{\nabla}\cdot\overline{\rho}\overline{\mathbf{u}}=0$, which implies that $\rho'=0$. Therefore, the averaged compressible equation above is reduced to

$$\boldsymbol{\nabla}\cdot\left[\overline{\rho}\overline{\mathbf{u}}\overline{L}+\overline{\rho}\overline{\mathbf{u}'L'}+\lambda\overline{\mathbf{D}}-\frac{\lambda}{4\pi}\left(\overline{\mathbf{B}}_{\mathbf{P}}\overline{B_\phi}+\overline{\mathbf{B}'_{\mathbf{P}}B'_\phi}\right)\right]\approx 0 \tag{B.12}$$

B.2 Meridional Flows and Zonal Torques

The anelastic averaged zonal momentum equation B.12, can then be considered to have two parts where the divergence of the mean meridional mass flux falls out because it is defined to be zero. Hence,

$$\overline{\rho}\overline{\mathbf{u}}\cdot\nabla\overline{L}\approx-\boldsymbol{\nabla}\cdot\left[\overline{\rho}\overline{\mathbf{u}'L'}+\lambda\overline{\mathbf{D}}-\frac{\lambda}{4\pi}\left(\overline{\mathbf{B}}_{\mathbf{P}}\overline{B_\phi}+\overline{\mathbf{B}'_{\mathbf{P}}B'_\phi}\right)\right]=-\boldsymbol{\nabla}\cdot\left[\lambda\overline{\rho}\overline{\mathbf{u}'u'_\phi}+\lambda\overline{\mathbf{D}}-\frac{\lambda}{4\pi}\left(\overline{\mathbf{B}}_{\mathbf{P}}\overline{B_\phi}+\overline{\mathbf{B}'_{\mathbf{P}}B'_\phi}\right)\right]$$

Further, the mean diffusive flux can be simplified to $\lambda\overline{\mathbf{D}}=\overline{\rho}\lambda\nu\nabla\Omega$, where $\Omega=\Omega_0+\overline{u}_\phi/\lambda$. So, equation B.12 becomes

$$\overline{\rho}\overline{\mathbf{u}}\cdot\nabla\overline{L}\approx-\boldsymbol{\nabla}\cdot\left[\lambda\overline{\rho}\overline{\mathbf{u}'u'_\phi}+\overline{\rho}\lambda^2\nu\nabla\Omega-\frac{\lambda}{4\pi}\left(\overline{\mathbf{B}}_{\mathbf{P}}\overline{B_\phi}+\overline{\mathbf{B}'_{\mathbf{P}}B'_\phi}\right)\right] \tag{B.13}$$

The right hand side is defined to be the zonal torque, so that $\overline{\rho}\overline{\mathbf{u}}\cdot\nabla\overline{L}=\mathcal{F}$. Since the mass flux is divergence-less, it can be represented as a stream function ψ such that $\overline{\rho}\overline{\mathbf{u}}=\boldsymbol{\nabla}\times\psi\hat{\boldsymbol{\phi}}$. This can be done because the ϕ components drop out by definition. Define a unit vector normal to contours of angular momentum per unit mass ($\overline{L}$), which is $\hat{n}=\frac{g_r}{|\mathbf{g}|}\hat{\mathbf{r}}+\frac{g_\theta}{|\mathbf{g}|}\hat{\boldsymbol{\theta}}$ where $\mathbf{g}=\nabla\overline{L}$. Then equation B.13 can be simplified so that

$$\begin{aligned}
&\boldsymbol{\nabla}\times\left[\psi\hat{\boldsymbol{\phi}}\right]\cdot\nabla\overline{L}=\mathcal{F}\\
&\boldsymbol{\nabla}\times\left[\psi\hat{\boldsymbol{\phi}}\right]\cdot\hat{n}=\frac{\mathcal{F}}{\left|\nabla\overline{L}\right|}\\
&\frac{1}{r\sin\theta}\frac{\partial}{\partial\theta}\left(\sin\theta\psi\right)n_r-\frac{1}{r}\frac{\partial}{\partial r}\left(r\psi\right)n_\theta=\frac{\mathcal{F}}{|\nabla\overline{L}|}
\end{aligned}$$

If this last equation is multiplied by λ, then

$$\frac{1}{r}\frac{\partial \lambda\psi}{\partial \theta}n_r - \frac{\partial \lambda\psi}{\partial r}n_\theta = \frac{\lambda\mathcal{F}}{|\nabla \overline{L}|} \tag{B.14}$$

We now define a vector $\hat{t}$ that is tangent to contours of $\overline{L}$. This requires $\hat{n}\cdot\hat{t} = 0$ and a choice in its orientation. Here we choose its orientation to be clockwise such that $\hat{t} = -n_\theta\hat{\mathbf{r}} + n_r\hat{\boldsymbol{\theta}}$, where n_r and n_θ are the components of $\hat{n}$. Then, equation B.14 can be reformed so that

$$\nabla(\lambda\psi)\cdot\hat{t} = \frac{\lambda\mathcal{F}}{|\nabla \overline{L}|} \tag{B.15}$$

Integrate equation B.15 along portions of the contours of $\overline{L}$ that are defined by a parameterized curve $\mathbf{r} = r(s)\hat{\mathbf{r}} + \theta(s)\hat{\boldsymbol{\theta}}$ such that $\overline{L}(\mathbf{r}) = \overline{L}_0$ where $\overline{L}_0 \in \left[\min \overline{L}, \max \overline{L}\right]$. The endpoints of this curve are $\mathbf{a}$ at the lower boundary and $\mathbf{b}$ at the upper end point. Let s be the arclength along this contour, then the integral is

$$\int_C \nabla(\lambda\psi)\cdot\hat{t}ds = \int_C \frac{\lambda\mathcal{F}}{|\nabla \overline{L}|}ds \tag{B.16}$$

However, $\nabla(\lambda\psi)\cdot\hat{t}$ is simply the derivative of $\lambda\psi$ along the contours of $\overline{L}$. Therefore, the left hand side of equation B.16 is simply $\int_C \frac{\partial\lambda\psi}{\partial s}ds = \lambda\psi|_{\mathbf{a}}^{\mathbf{b}}$. Let us for the moment make a few assumptions, first the boundary conditions on the flow field are stress-free and impenetrable at the upper and lower radial boundaries. This means that the contours of $\overline{L}$ are all open and have end points on these boundaries. Since the boundaries are impenetrable, we enforce the boundary condition that $\psi = 0$ on the radial boundaries. The integral in equation B.16 then proceeds clockwise from the lower boundary in the southern hemisphere to an arbitrary point along the contour which yields

$$\psi = \frac{1}{\lambda}\int_C \frac{\lambda\mathcal{F}}{|\nabla \overline{L}|}ds \tag{B.17}$$

B.3 Meridional Flows Due to Zonal Torques in ASH

To numerically compute the integral in equation B.17, we use IDL's routine contour which generates the paths in polar coordinates. These paths are then used to identify which points of the right hand side of the same equation are on the path. The arclength along the path is computed and the right hand side as defined previously is integrated along it. This procedure has been applied to the torques found in the F-star simulations analyzed in this thesis. The following plots show this for six cases.

B.4 Thermal Wind, Geostrophy, and Gyroscopic Pumping

We begin with equation B.3, where a time and azimuthal average are taken yielding

$$\nabla\langle\overline{P}_{tot}+P'_{tot}\rangle=-\langle(\overline{\rho}+\rho')\,\mathbf{u}\cdot\nabla\mathbf{u}\rangle+\langle\rho\rangle\mathbf{g}_{eff}-2\langle\rho\Omega_0\times\mathbf{u}\rangle-\langle\boldsymbol{\nabla}\cdot\mathcal{D}\rangle-\frac{1}{4\pi}\langle\boldsymbol{\nabla}\cdot\mathcal{M}\rangle$$

Further, if we assume that the flows are anelastic, in hydrostatic balance, and also take the fluctuating fields from equation B.9 with the exception that $\mathbf{u}=\mathbf{u}_m+\overline{u}_\phi\hat{\boldsymbol{\phi}}+\mathbf{u}'$, then the averaged advection term is

$$\langle\mathbf{u}\cdot\nabla\mathbf{u}\rangle=\frac{1}{2}\nabla\langle\mathbf{u}'\cdot\mathbf{u}'\rangle+\mathbf{u}_m\cdot\nabla\mathbf{u}_m+\frac{1}{\lambda}\mathbf{u}_m\cdot\nabla\left(\lambda\overline{u}_\phi\right)\hat{\boldsymbol{\phi}}-\frac{\overline{u}_\phi^2}{2\lambda}\hat{\lambda}+\langle\vec{\omega}'\times\mathbf{u}'\rangle \tag{B.18}$$

When the Coriolis terms are expanded as well, it is seen that

$$\nabla P'_{tot}=-\overline{\rho}\langle\mathbf{u}\cdot\nabla\mathbf{u}\rangle+\langle\rho'\rangle\mathbf{g}_{eff}+2\Omega_0\overline{\rho}\left(\overline{u}_\phi\hat{\lambda}-\overline{u}_\lambda\hat{\boldsymbol{\phi}}\right)-\langle\boldsymbol{\nabla}\cdot\mathcal{D}\rangle-\frac{1}{4\pi}\langle\boldsymbol{\nabla}\cdot\mathcal{M}\rangle \tag{B.19}$$

For the moment we will neglect the largest term in the advection equation ($\frac{\overline{u}_\phi^2}{2\lambda}$), and from dimensional analysis we can neglect all other terms except the Coriolis term if the system is rotating sufficiently rapidly. For the cases mentioned above, this is largely the case. Thus, equation B.19 becomes

$$\nabla P'_{tot}=2\Omega_0\overline{\rho u}_\phi\hat{\lambda} \tag{B.20}$$

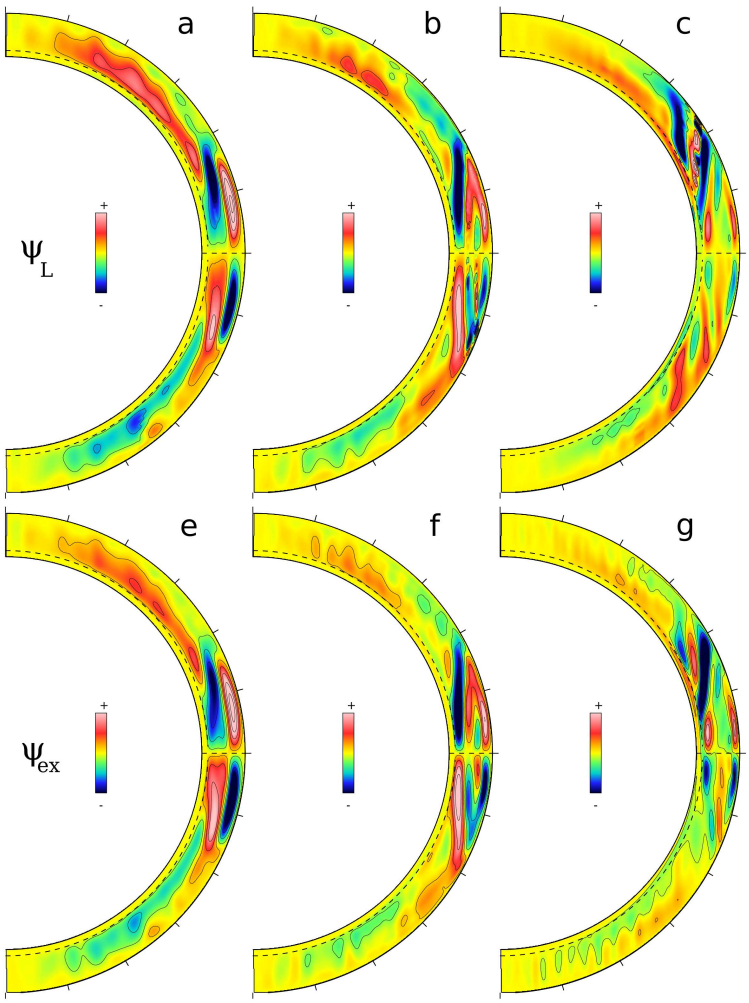

Figure B.1: The meridional flow stream function ψ_L as defined in equation B.17 for the $1.2\,M_\odot$ F star ASH simulations at (a) $5\,\Omega_\odot$, (b) $10\,\Omega_\odot$, and (c) $20\,\Omega_\odot$. The second row of figures is the stream function as derived directly from the meridional mass flux for the same cases in panels (e-g).

Therefore, the primarily pressure balance is in cylindrical radius, namely the cylindrical derivative of P' is small relative to the derivative in cylindrical radius (λ). Next we take the curl of equation B.3, that has been divided by the density and expanded into fluctuating and mean components, and examine its azimuthal component.

$$\begin{aligned}\frac{\partial \omega_\phi}{\partial t} &= \hat{\boldsymbol{\phi}} \cdot \left[-\nabla \times (\mathbf{u} \cdot \nabla \mathbf{u}) - \nabla \times \left(\frac{1}{\overline{\rho}} \nabla P'_{tot} \right) + \nabla \times \left(\frac{\rho'}{\overline{\rho}} \mathbf{g}_{eff} \right) - 2\Omega_0 \nabla \times (\hat{z} \times \mathbf{u}) \right. \\ &- \left. \nabla \times \left(\frac{1}{\overline{\rho}} \boldsymbol{\nabla} \cdot \mathcal{D} \right) + \nabla \times \left(\frac{1}{4\pi\overline{\rho}} \boldsymbol{\nabla} \cdot \mathcal{M} \right) \right] \end{aligned} \tag{B.21}$$

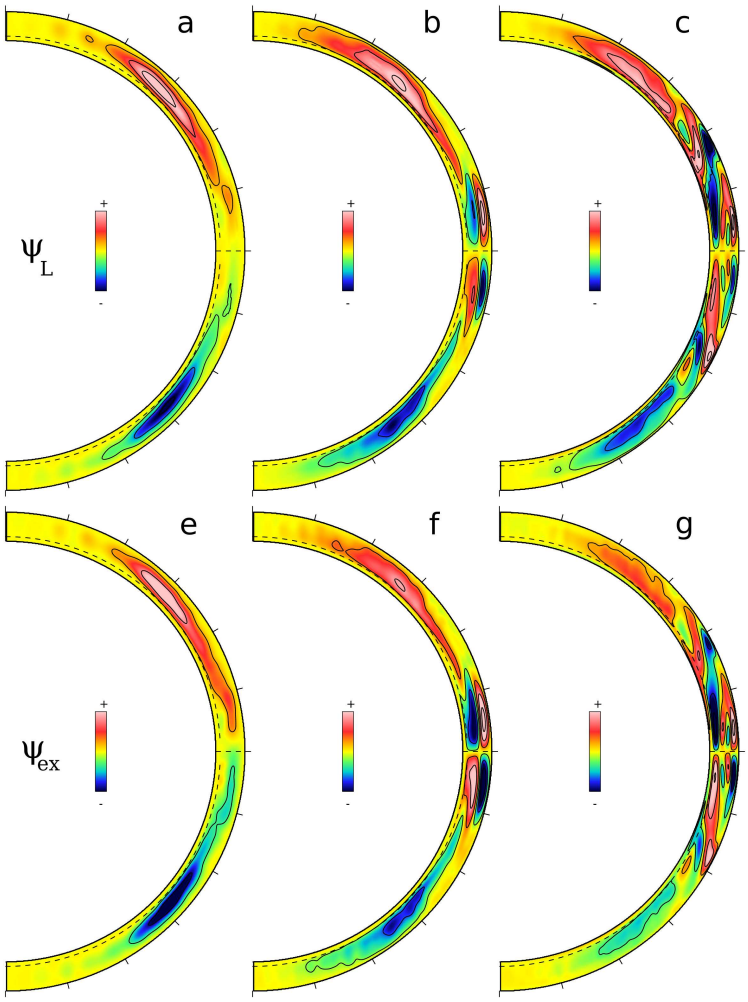

Figure B.2: The meridional flow stream function ψ_L as defined in equation B.17 for the $1.3\,M_\odot$ F star ASH simulations at (a) $5\,\Omega_\odot$, (b) $10\,\Omega_\odot$, and (c) $20\,\Omega_\odot$. The second row of figures is the stream function as derived directly from the meridional mass flux for the same cases in panels (e-g).

where $\vec{\omega}$ is the vorticity vector. Using some simple vector derivative identities, it is seen that

$$\nabla \times (\mathbf{u} \cdot \nabla \mathbf{u}) = \nabla \times \left[\tfrac{1}{2}\nabla (\mathbf{u} \cdot \mathbf{u}) + \vec{\omega} \times \mathbf{u}\right] = \mathbf{u} \cdot \nabla \vec{\omega} - \vec{\omega} \cdot \nabla \mathbf{u} + \vec{\omega} \nabla \cdot \mathbf{u}.$$

$$\begin{aligned} \frac{\partial \omega_\phi}{\partial t} &= \vec{\omega} \cdot \nabla u_\phi - \mathbf{u} \cdot \nabla \omega_\phi + \frac{u_\lambda \omega_\phi - u_\phi \omega_\lambda}{\lambda} + \omega_\phi u_r \frac{\partial \ln \overline{\rho}}{\partial r} + 2\Omega_0 \frac{\partial \overline{u}_\phi}{\partial z} + \hat{\boldsymbol{\phi}} \cdot \nabla \times \left(\frac{1}{\overline{\rho}} \mathbf{J} \times \mathbf{B}\right) \\ &+ \hat{\boldsymbol{\phi}} \cdot \nabla \times \left(\frac{\rho'}{\overline{\rho}} \mathbf{g}_{eff}\right) - \hat{\boldsymbol{\phi}} \cdot \nabla \times \left(\frac{1}{\overline{\rho}} \nabla P'\right) - \hat{\boldsymbol{\phi}} \cdot \nabla \times \left(\frac{1}{\overline{\rho}} \boldsymbol{\nabla} \cdot \mathcal{D}\right) - \hat{\boldsymbol{\phi}} \cdot \nabla \times \left(\frac{1}{\overline{\rho}} \boldsymbol{\nabla} \cdot \mathcal{D}\right) \end{aligned}$$

where $\mathbf{J} = \frac{1}{4\pi} \nabla \times \mathbf{B}$ is the current density. Simplifying the thermodynamic terms, expanding diffusive terms, and taking a azimuthal and temporal average, we arrive at

$$\begin{aligned}
\frac{\partial\langle\omega_\phi\rangle}{\partial t} &= 2\Omega_0\frac{\partial\overline{u}_\phi}{\partial z} - \frac{g}{rC_P}\frac{\partial S'}{\partial\theta} - \frac{1}{r\overline{\rho}C_P}\frac{\partial\overline{S}}{\partial r}\frac{\partial P'}{\partial\theta} \\
&+ \left\langle\vec{\omega}\cdot\nabla u_\phi - \mathbf{u}\cdot\nabla\omega_\phi + \frac{u_\lambda\omega_\phi - u_\phi\omega_\lambda}{\lambda} - \omega_\phi u_r\frac{\partial\ln\overline{\rho}}{\partial r}\right\rangle \\
&+ \frac{1}{\overline{\rho}r}\left\langle\frac{\partial}{\partial\theta}\left(\boldsymbol{\nabla}\cdot\mathcal{D}\right)\cdot\hat{\mathbf{r}}\right\rangle - \frac{1}{\overline{\rho}}\left\langle\left(\frac{1}{r} - \frac{\partial\ln\overline{\rho}}{\partial r} + \frac{\partial}{\partial r}\right)\left(\boldsymbol{\nabla}\cdot\mathcal{D}\right)\cdot\hat{\boldsymbol{\theta}}\right\rangle \\
&+ \frac{1}{\overline{\rho}}\Big\langle\mathbf{B}\cdot\nabla J_\phi - \mathbf{J}\cdot\nabla B_\phi + \frac{B_\phi J_\lambda - B_\lambda J_\phi}{\lambda} + \frac{\partial\ln\overline{\rho}}{\partial r}\left(J_r B_\phi - J_\phi B_r\right)\Big\rangle. \quad \text{(B.22)}
\end{aligned}$$

If the time average taken is long enough then the l.h.s. should vanish leaving

$$\begin{aligned}
2\Omega_0\frac{\partial\overline{u}_\phi}{\partial z} &\approx \frac{g}{rC_P}\frac{\partial S'}{\partial\theta} + \frac{1}{r\overline{\rho}C_P}\frac{\partial\overline{S}}{\partial r}\frac{\partial P'}{\partial\theta} \\
&+ \left\langle\mathbf{u}\cdot\nabla\omega_\phi - \vec{\omega}\cdot\nabla u_\phi + \frac{u_\phi\omega_\lambda - u_\lambda\omega_\phi}{\lambda} + \omega_\phi u_r\frac{\partial\ln\overline{\rho}}{\partial r}\right\rangle \\
&- \frac{1}{\overline{\rho}r}\left\langle\frac{\partial}{\partial\theta}\left(\boldsymbol{\nabla}\cdot\mathcal{D}\right)\cdot\hat{\mathbf{r}}\right\rangle + \frac{1}{\overline{\rho}}\left\langle\left(\frac{1}{r} - \frac{\partial\ln\overline{\rho}}{\partial r} + \frac{\partial}{\partial r}\right)\left(\boldsymbol{\nabla}\cdot\mathcal{D}\right)\cdot\hat{\boldsymbol{\theta}}\right\rangle \\
&+ \frac{1}{\overline{\rho}}\Big\langle\mathbf{J}\cdot\nabla B_\phi - \mathbf{B}\cdot\nabla J_\phi + \frac{B_\lambda J_\phi - B_\phi J_\lambda}{\lambda} + \frac{\partial\ln\overline{\rho}}{\partial r}\left(J_\phi B_r - J_r B_\phi\right)\Big\rangle. \quad \text{(B.23)}
\end{aligned}$$

Within the convection zone of ASH simulations the pressure contribution to the baroclinic terms is small. The Reynolds stresses (line two of equation B.22) and diffusive terms (line three of the same equation) are important only near the boundaries. Summarizing the results for geostrophy (equation B.20) and a thermal wind, we have

$$\begin{aligned}
\frac{\partial P'}{\partial\lambda} &= 2\Omega_0\overline{\rho u}_\phi \\
\frac{\partial S'}{\partial\theta} &= \frac{2\Omega_0 C_P r}{g}\frac{\partial\overline{u}_\phi}{\partial z}
\end{aligned}$$

This provides a integrable form for $\overline{u}_\phi$ that depends only upon the background and thermodynamic state of an anelastic system. Therefore, we can compute the dependence of the denominator in equation B.17 upon the thermodynamic state of this system, where

$$\begin{aligned}
|\nabla L| &= \left[\left(2\Omega_0\lambda + \overline{u}_\phi + \lambda\frac{\partial\overline{u}_\phi}{\partial\lambda}\right)^2 + \left(\lambda\frac{\partial\overline{u}_\phi}{\partial z}\right)^2\right]^{\frac{1}{2}} \\
&= (2\Omega_0\lambda)\left[\left(1 + \frac{1}{4\Omega_0^2\lambda}\frac{\partial}{\partial\lambda}\left(\frac{\lambda}{\overline{\rho}}\frac{\partial P'}{\partial\lambda}\right)\right)^2 + \left(\frac{g}{4\Omega_0^2 C_P r}\frac{\partial S'}{\partial\theta}\right)^2\right]^{\frac{1}{2}} \quad \text{(B.24)}
\end{aligned}$$

Therefore, equation B.17 becomes

$$\psi = \frac{1}{2\Omega_0 \lambda} \int_C \mathcal{F} \left[\left(1 + \frac{1}{4\Omega_0^2 \lambda} \frac{\partial}{\partial \lambda} \left(\frac{\lambda}{\overline{\rho}} \frac{\partial P'}{\partial \lambda} \right) \right)^2 + \left(\frac{g}{4\Omega_0^2 C_P r} \frac{\partial S'}{\partial \theta} \right)^2 \right]^{-\frac{1}{2}} ds \tag{B.25}$$

However, we have found in the F star simulations that the buoyancy terms are of nearly equal importance when compared to the Coriolis terms. This means that the azimuthally averaged density perturbations are large enough to make this term important, thus we have the relations

$$\begin{aligned} \nabla P' &= 2\Omega_0 \overline{\rho u}_\phi \hat{\lambda} - \rho' g \hat{\mathbf{r}} \\ \frac{\partial S'}{\partial \theta} &= \frac{2\Omega_0 C_P r}{g} \frac{\partial \overline{u}_\phi}{\partial z} \end{aligned}$$

If we consider the energy equation, an equation for the entropy that depends only upon the meridional flow and background state can be found. Also taking the divergence of the pressure equation in the line above, leads to a system of equations for the entropy, pressure, and meridional flow (Too be expanded upon)...

$$\nabla^2 S' = \frac{\partial \ln \hat{\rho} \hat{T} \kappa_S}{\partial r} \frac{\partial S'}{\partial r} - \frac{\nabla \times \psi \hat{\boldsymbol{\phi}}}{\hat{\rho} \kappa_S} \cdot \nabla S' + \epsilon \tag{B.26}$$

$$\nabla^2 P' = \frac{2\Omega_0}{\lambda} \frac{\partial}{\partial \lambda} \left(\hat{\rho} \lambda \overline{u}_\phi \right) - \frac{1}{r^2} \frac{\partial}{\partial r} \left(r^2 \rho' g \right) \tag{B.27}$$

$$\psi = \frac{1}{\lambda} \int_C \frac{\lambda \mathcal{F}}{|\nabla L|} ds \tag{B.28}$$

The thermal wind relationship between the entropy and the mean azimuthal velocity allows us to eliminate one or the other from the above set of equations. Whether attempting to determine the thermal structure of the star from the differential rotation or vice versa, this set of equations can be used in conjunction either with a measured or modeled Reynolds stress to predict the meridional flows that are established in a particular system. Also, if we consider Miesch & Hindman (2011), this set of equations will allow us to estimate the extent to which the large latitudinal temperature contrasts seen in our global scale models extend into the near surface region.

In the near surface regions it is likely that rather than a thermal wind balance, a Reynolds stress balance is achieved. This means that the denominator in the integral for the meridional flow streamfunction will be modified as the differential rotation near the surface likely has a different character from that of the interior. However, if we can model the angular momentum fluxes in these layers, we can predict how the meridional flows will respond to the changing differential rotation near the surface. Then, using the energy and pressure equations, we may ascertain how the turbulent surface layers respond to a latitudinal gradient of temperature. Namely, we can estimate the latitudinal thermal contrast at the surface given the thermal structure established at depth.

Appendix C

Derivation of the Shear Instability Equations

C.1 Euler Equations

We begin with the equations that expressing the conservation of mass, momentum, and entropy, assuming adiabatic motions, in a compressible fluid within an inertial frame.

$$\frac{\partial \rho}{\partial t} + \boldsymbol{\nabla} \cdot \rho \mathbf{v} = 0, \tag{C.1}$$

$$\frac{\partial \rho \mathbf{v}}{\partial t} + \mathbf{v} \cdot \boldsymbol{\nabla} \rho \mathbf{v} = -\nabla P + \rho \mathbf{g}, \tag{C.2}$$

$$\frac{\partial S}{\partial t} + \mathbf{v} \cdot \boldsymbol{\nabla} S = 0. \tag{C.3}$$

A standard notation is used: $\mathbf{v}$ is the bulk velocity of the fluid, ρ is the density, P is the pressure, $\mathbf{g}$ is the acceleration due to gravity. We use spherical polar coordinates (r, θ, ϕ) in this derivation. We make the assumption that there is a bulk azimuthal flow $\mathbf{v}_0 = v_0 \hat{\boldsymbol{\phi}}$, where $v_0 = v_0(r, \theta)$. There is also a background state with $P_0 = P_0(r, \theta)$, $\rho_0 = \rho_0(r, \theta)$, and $S_0 = S_0(r, \theta)$. If we expand the above Euler equations about the background state, letting the perturbation quantities be $\mathbf{v}'$, ρ', S', and P', we arrive at

$$\frac{\partial \rho'}{\partial t} + \boldsymbol{\nabla} \cdot \rho_0 \mathbf{v}_0 + \boldsymbol{\nabla} \cdot \rho_0 \mathbf{v}' + \boldsymbol{\nabla} \cdot \rho' \mathbf{v}_0 = 0, \tag{C.4}$$

$$\rho_0 \frac{\partial \mathbf{v}'}{\partial t} + \mathbf{v}_0 \frac{\partial \rho'}{\partial t} + \mathbf{v} \cdot \boldsymbol{\nabla} \rho \mathbf{v} = -\boldsymbol{\nabla} P_0 - \boldsymbol{\nabla} P' + \rho_0 \mathbf{g} + \rho' \mathbf{g}, \tag{C.5}$$

$$\frac{\partial S'}{\partial t} + \mathbf{v}_0 \cdot \boldsymbol{\nabla} S_0 + \mathbf{v}_0 \cdot \boldsymbol{\nabla} S' + \mathbf{v}' \cdot \boldsymbol{\nabla} S_0 = 0, \tag{C.6}$$

where the time derivatives of the background state quantities have been omitted as they are zero by definition. It is helpful to separately expand the advection operator due to its length and direction dependence as shown in the following

$$\hat{\mathbf{r}}\cdot[\mathbf{v}\cdot\boldsymbol{\nabla}\rho\mathbf{v}] = \mathrm{v_r}'\frac{\partial}{\partial r}\left[(\rho_0+\rho')\,\mathrm{v_r}'\right] + \frac{\mathrm{v}'_\theta}{r}\frac{\partial}{\partial\theta}\left[(\rho_0+\rho')\,\mathrm{v_r}'\right] + \frac{v_0+\mathrm{v}'_\phi}{r\sin\theta}\frac{\partial}{\partial\phi}\left[(\rho_0+\rho')\,\mathrm{v_r}'\right] - \frac{1}{r}(\rho_0+\rho')\left[\mathrm{v}'^2_\theta + \left(v_0+\mathrm{v}'_\phi\right)^2\right], \tag{C.7}$$

$$\hat{\boldsymbol{\theta}}\cdot[\mathbf{v}\cdot\boldsymbol{\nabla}\rho\mathbf{v}] = \mathrm{v_r}'\frac{\partial}{\partial r}\left[(\rho_0+\rho')\,\mathrm{v}'_\theta\right] + \frac{\mathrm{v}'_\theta}{r}\frac{\partial}{\partial\theta}\left[(\rho_0+\rho')\,\mathrm{v}'_\theta\right] + \frac{v_0+\mathrm{v}'_\phi}{r\sin\theta}\frac{\partial}{\partial\phi}\left[(\rho_0+\rho')\,\mathrm{v}'_\theta\right] + \frac{1}{r}(\rho_0+\rho')\left[\mathrm{v_r}'\mathrm{v}'_\theta - \cot\theta\left(v_0+\mathrm{v}'_\phi\right)^2\right], \tag{C.8}$$

$$\hat{\boldsymbol{\phi}}\cdot[\mathbf{v}\cdot\boldsymbol{\nabla}\rho\mathbf{v}] = \mathrm{v_r}'\frac{\partial}{\partial r}\left[(\rho_0+\rho')\left(v_0+\mathrm{v}'_\phi\right)\right] + \frac{\mathrm{v}'_\theta}{r}\frac{\partial}{\partial\theta}\left[(\rho_0+\rho')\left(v_0+\mathrm{v}'_\phi\right)\right] + \frac{v_0+\mathrm{v}'_\phi}{r\sin\theta}\frac{\partial}{\partial\phi}\left[(\rho_0+\rho')\left(v_0+\mathrm{v}'_\phi\right)\right] + \frac{1}{r}(\rho_0+\rho')\left(v_0+\mathrm{v}'_\phi\right)\left[\mathrm{v_r}' + \cot\theta\mathrm{v}'_\theta\right], \tag{C.9}$$

C.2 Linearization

Examining the zeroth order terms of all equations, we find that

$$\boldsymbol{\nabla}\cdot\rho_0\mathbf{v}_0 = 0, \tag{C.10}$$

$$\mathbf{v}_0\cdot\boldsymbol{\nabla}S_0 = 0, \tag{C.11}$$

$$\nabla P_0 + \rho_0 g\hat{\mathbf{r}} + [\mathbf{v}\cdot\boldsymbol{\nabla}\rho\mathbf{v}]_0 = \nabla P_0 + \rho_0 g\hat{\mathbf{r}} - \frac{\rho_0 v_0^2}{r}\hat{\mathbf{r}} - \frac{\cot\theta\rho_0 v_0^2}{r}\hat{\boldsymbol{\theta}} = 0, \tag{C.12}$$

this indicates that the star is indeed in hydrostatic balance with a geostrophic balance of the centripetal acceleration, which is in turn due to the bulk rotation of the star. Next, we look at the linear terms of the advection operator before turning to the fully linearized equations

$$\hat{\mathbf{r}}\cdot[\mathbf{v}\cdot\boldsymbol{\nabla}\rho\mathbf{v}]_1 = \frac{\rho_0 v_0}{r\sin\theta}\frac{\partial\mathrm{v_r}'}{\partial\phi} - \frac{2\rho_0 v_0\mathrm{v}'_\phi}{r} - \frac{\rho' v_0^2}{r}, \tag{C.13}$$

$$\hat{\boldsymbol{\theta}}\cdot[\mathbf{v}\cdot\boldsymbol{\nabla}\rho\mathbf{v}]_1 = \frac{\rho_0 v_0}{r\sin\theta}\frac{\partial\mathrm{v}'_\theta}{\partial\phi} - \frac{2\cot\theta\rho_0 v_0\mathrm{v}'_\phi}{r} - \frac{\cot\theta\rho' v_0^2}{r}, \tag{C.14}$$

$$\hat{\boldsymbol{\phi}}\cdot[\mathbf{v}\cdot\boldsymbol{\nabla}\rho\mathbf{v}]_1 = \mathrm{v_r}'\frac{\partial\rho_0 v_0}{\partial r} + \frac{\mathrm{v}'_\theta}{r}\frac{\partial\rho_0 v_0}{\partial\theta} + \frac{\rho_0 v_0}{r\sin\theta}\frac{\partial\mathrm{v}'_\phi}{\partial\phi} + \frac{v_0^2}{r\sin\theta}\frac{\partial\rho'}{\partial\phi} + \frac{\rho_0 v_0}{r}\left(\mathrm{v_r}' + \cot\theta\mathrm{v}'_\theta\right). \tag{C.15}$$

The linearized Euler equations are then

$$\frac{\partial \rho'}{\partial t} + \boldsymbol{\nabla} \cdot \rho_0 \mathbf{v}' + \frac{v_0}{r \sin\theta} \frac{\partial \rho'}{\partial \phi} = 0, \tag{C.16}$$

$$\rho_0 \frac{\partial \mathrm{v_r}'}{\partial t} + \frac{\rho_0 v_0}{r \sin\theta} \frac{\partial \mathrm{v_r}'}{\partial \phi} - \frac{2\rho_0 v_0 \mathrm{v}'_\phi}{r} - \frac{\rho' v_0^2}{r} + \frac{\partial P'}{\partial r} + \rho' g = 0, \tag{C.17}$$

$$\rho_0 \frac{\partial \mathrm{v}'_\theta}{\partial t} + \frac{\rho_0 v_0}{r \sin\theta} \frac{\partial \mathrm{v}'_\theta}{\partial \phi} - \frac{2\cot\theta \rho_0 v_0 \mathrm{v}'_\phi}{r} - \frac{\cot\theta \rho' v_0^2}{r} + \frac{1}{r} \frac{\partial P'}{\partial \theta} = 0, \tag{C.18}$$

$$\begin{aligned} &\rho_0 \frac{\partial \mathrm{v}'_\phi}{\partial t} + v_0 \frac{\partial \rho'}{\partial t} + \mathrm{v_r}' \frac{\partial \rho_0 v_0}{\partial r} + \frac{\mathrm{v}'_\theta}{r} \frac{\partial \rho_0 v_0}{\partial \theta} + \frac{\rho_0 v_0}{r \sin\theta} \frac{\partial \mathrm{v}'_\phi}{\partial \phi} + \frac{v_0^2}{r \sin\theta} \frac{\partial \rho'}{\partial \phi} \\ &\quad + \frac{\rho_0 v_0}{r} \left(\mathrm{v_r}' + \cot\theta \mathrm{v}'_\theta\right) + \frac{1}{r \sin\theta} \frac{\partial P'}{\partial \phi} = 0, \end{aligned} \tag{C.19}$$

$$\frac{\partial S'}{\partial t} + \frac{v_0}{r \sin\theta} \frac{\partial S'}{\partial \phi} + \mathrm{v_r}' \frac{\partial S_0}{\partial r} + \frac{\mathrm{v}'_\theta}{r} \frac{\partial S_0}{\partial \theta} = 0, \tag{C.20}$$

C.3 Assumptions and Simplifications

By employing the Euler equations from the start, we have implicitly assumed that diffusion is not present. This is not the case in our models, nor in a real star where a small but non-zero diffusion is indeed present, where it will act couple radial and horizontal motions. This complicates the issue and renders some of the assumptions made below invalid, and is currently ignored because the diffusive timescales in both our models and in stars is much longer than than the rotational timescale. Moving forward with the Euler equations, we further suppose that there are no compositional gradients are present in the region of interest, and therefore define the Brunt-Väisälä frequency as $N^2 = \frac{g}{c_P} \frac{\partial S_0}{\partial r}$ and also note that $\Omega = \frac{v_0}{r \sin\theta}$. Since we are considering motions deep within a star, inside the radiative zone, the speed of sound is large and the sound crossing time is much shorter than the rotational time scale which is of interest in this problem. Thus, acoustic waves are eliminated from the solutions by setting the time derivative of the density perturbations to zero. We also assume that the isochoric surfaces are spherical. With these assumptions equations C.16-C.20 become

$$\boldsymbol{\nabla}\cdot\rho_0\mathbf{v}' + \Omega\frac{\partial\rho'}{\partial\phi} = 0, \tag{C.21}$$

$$\rho_0\frac{\partial \mathrm{v_r}'}{\partial t} + \rho_0\Omega\frac{\partial \mathrm{v_r}'}{\partial\phi} - 2\sin\theta\rho_0\Omega\mathrm{v}'_\phi - \rho' r\sin^2\theta\Omega^2 + \frac{\partial P'}{\partial r} + \rho' g = 0, \tag{C.22}$$

$$\rho_0\frac{\partial \mathrm{v}'_\theta}{\partial t} + \rho_0\Omega\frac{\partial \mathrm{v}'_\theta}{\partial\phi} - 2\cos\theta\rho_0\Omega\mathrm{v}'_\phi - \rho' r\sin\theta\cos\theta\Omega^2 + \frac{1}{r}\frac{\partial P'}{\partial\theta} = 0, \tag{C.23}$$

$$\begin{aligned}\rho_0\frac{\partial \mathrm{v}'_\phi}{\partial t} + \mathrm{v_r}'\frac{\partial\rho_0 v_0}{\partial r} + \rho_0\mathrm{v}'_\theta\frac{\partial\sin\theta\Omega}{\partial\theta} + \rho_0\Omega\frac{\partial \mathrm{v}'_\phi}{\partial\phi} + r\sin\theta\Omega^2\frac{\partial\rho'}{\partial\phi}\\ + \rho_0\Omega\left(\sin\theta\mathrm{v_r}' + \cos\theta\mathrm{v}'_\theta\right) + \frac{1}{r\sin\theta}\frac{\partial P'}{\partial\phi} = 0,\end{aligned} \tag{C.24}$$

$$\frac{\partial S'}{\partial t} + \Omega\frac{\partial S'}{\partial\phi} + \frac{c_P N^2 \mathrm{v_r}'}{g} + \frac{\mathrm{v}'_\theta}{r}\frac{\partial S_0}{\partial\theta} = 0, \tag{C.25}$$

For the F-type stars N is typically much larger than Ω, with N being a few mHz and Ω a few μHz. Let us now expand the energy equation in terms of the ratio of the rotational frequency to the buoyancy frequency, namely

$$\frac{1}{N^2}\left[\frac{\partial S'}{\partial t} + \Omega\frac{\partial S'}{\partial\phi}\right] + \frac{c_P \mathrm{v_r}'}{g} + \frac{\mathrm{v}'_\theta}{rN^2}\frac{\partial S_0}{\partial\theta} = 0. \tag{C.26}$$

Now, if we consider the star to be in thermal wind balance $\frac{1}{r}\frac{\partial S_0}{\partial\theta} \approx \frac{c_P\lambda}{g}\frac{\partial\Omega^2}{\partial z}$ where λ and z are the cylindrical radius and height respectively, then

$$\frac{\mathrm{v_r}'}{\mathrm{v}'_\theta} + \frac{g}{c_P N^2 \mathrm{v}'_\theta}\left[\frac{\partial S'}{\partial t} + \Omega\frac{\partial S'}{\partial\phi}\right] + \frac{\Omega^2}{N^2}\left(\lambda\frac{\partial\ln\Omega^2}{\partial z}\right) = 0. \tag{C.27}$$

Further, since we are interested in the shear instability due to the differential rotation, the time scale of consideration is the rotation period. Thus, consider $\partial_t \to \Omega$, so that the above equation becomes

$$\frac{\mathrm{v_r}'}{\mathrm{v}'_\theta} + \frac{\Omega^2}{N^2}\left[\frac{g}{\Omega\mathrm{v}'_\theta}\frac{S'}{c_P} + \lambda\frac{\partial\ln\Omega^2}{\partial z}\right] = 0. \tag{C.28}$$

For the problem we are considering, both of the terms inside of the square brackets are of order one. Thus, for the stiffly stratified medium within the stable region of the F-type stars, we have $\Omega^2/N^2 \ll 1$ which implies that $\mathrm{v_r}'/\mathrm{v}'_\theta \ll 1$. Therefore, the motions we

expect are primarily horizontal with a very small radial component due to gravity waves. We now consider the radial component of the momentum equation, where it has been non-dimensionalized by assuming that $\mathrm{v_r}' = RNu_r'$, $\tilde{t} = Nt$, $\mathrm{v}_\phi' = R\Omega_0 u_\phi'$, $P' = \rho_1 R^2 \Omega_0^2 \tilde{P}'$, $\rho' = \rho_1 \tilde{\rho}'$ (where ρ_1 is a reference density), $\Omega = \Omega_0 \tilde{\Omega}$, and $r = R\tilde{r}$

$$\frac{\partial u_r'}{\partial \tilde{t}} + \frac{\Omega_0}{N}\tilde{\Omega}\frac{\partial u_r'}{\partial \phi} - 2\sin\theta\tilde{\Omega}u_\phi'\frac{\Omega_0^2}{N^2} - \tilde{\rho}'\tilde{r}\sin^2\theta\tilde{\Omega}^2\frac{\Omega_0^2}{N^2} + \frac{\rho_1}{\rho_0}\frac{\Omega_0^2}{N^2}\frac{\partial \tilde{P}'}{\partial r} + \frac{\rho_1 c_P \tilde{\rho}'}{\rho_0 R}\left[\frac{\partial S_0}{\partial r}\right]^{-1} = 0. \tag{C.29}$$

$$\frac{\partial u_r'}{\partial \tilde{t}} + \frac{\rho_1 c_P \tilde{\rho}'}{\rho_0 R}\left[\frac{\partial S_0}{\partial r}\right]^{-1} = 0. \tag{C.30}$$

here Ω_0 is an appropriate reference rotation rate. If only the terms of zeroth order in Ω_0/N are kept as in C.29, we find equation C.30. Taking the result from above that $\mathrm{v_r}' \approx 0$ to second order in Ω_0/N, it is clear that equation C.30 implies that $\rho' = 0$. With both sound and gravity waves eliminated from the system the equations to be solved reduce to

$$\boldsymbol{\nabla} \cdot \rho_0 \mathbf{v}' = 0, \tag{C.31}$$

$$\frac{\partial m_\theta'}{\partial t} + \Omega\frac{\partial m_\theta'}{\partial \phi} - 2\cos\theta\Omega m_\phi' + \frac{1}{r}\frac{\partial P'}{\partial \theta} = 0, \tag{C.32}$$

$$\frac{\partial m_\phi'}{\partial t} + m_\theta'\frac{\partial \sin\theta\Omega}{\partial \theta} + \Omega\frac{\partial m_\phi'}{\partial \phi} + \cos\theta\Omega m_\theta' + \frac{1}{r\sin\theta}\frac{\partial P'}{\partial \phi} = 0, \tag{C.33}$$

$$\frac{\partial S'}{\partial t} + \Omega\frac{\partial S'}{\partial \phi} + \frac{m_\theta'}{r\rho_0}\frac{\partial S_0}{\partial \theta} = 0, \tag{C.34}$$

where $\mathbf{m}' = \rho_0 \mathbf{v}$ is the momentum density.

C.4 Streamfunction Formulation

Since the flow is anelastic, with no radial flow to $\mathcal{O}\left(\Omega_0^2/N^2\right)$, as shown in equation C.31, the system of equations may be reduced to a single equation for the streamfunction Ψ, which is defined such that $\mathbf{m}' = \boldsymbol{\nabla} \times (\Psi \hat{\mathbf{r}})$. This means that $m_\theta' = \frac{1}{\sin\theta}\frac{\partial \Psi}{\partial \phi}$ and $m_\phi' = -\frac{\partial \Psi}{\partial \theta}$. We have omitted the radius r in the spherical curl operator has been omitted as there is no longer radial dependence at any given spherical shell within the region of the star where $\Omega_0/N \ll 1$ is a valid assumption. This generally occurs within the radiative zone of the F-type stars.

The pressure perturbations are eliminated by taking the curl of the momentum equations, which yields a single equation for Ψ as below

$$\frac{1}{\sin\theta}\frac{\partial}{\partial\theta}\left[-\sin\theta\frac{\partial^2\Psi}{\partial t\partial\theta}+\frac{\partial\sin\theta\Omega}{\partial\theta}\frac{\partial\Psi}{\partial\phi}-\sin\theta\Omega\frac{\partial^2\Psi}{\partial\theta\partial\phi}+\cos\theta\Omega\frac{\partial\Psi}{\partial\phi}+\frac{\partial P'}{\partial\phi}\right] - \frac{1}{\sin\theta}\frac{\partial}{\partial\phi}\left[\frac{1}{\sin\theta}\frac{\partial^2\Psi}{\partial t\partial\phi}+\frac{\Omega}{\sin\theta}\frac{\partial^2\Psi}{\partial\phi^2}+2\cos\theta\Omega\frac{\partial\Psi}{\partial\theta}+\frac{\partial P'}{\partial\theta}\right]=0, \tag{C.35}$$

which reduces to

$$-\nabla^2\frac{\partial\Psi}{\partial t}-\frac{\Omega}{\sin^2\theta}\frac{\partial^3\Psi}{\partial\phi^3}-2\cot\theta\Omega\frac{\partial^2\Psi}{\partial\theta\partial\phi}-\frac{1}{\sin\theta}\frac{\partial}{\partial\theta}\left[\sin\theta\Omega\frac{\partial^2\Psi}{\partial\theta\partial\phi}\right] + \frac{1}{\sin\theta}\frac{\partial}{\partial\theta}\left[\frac{\partial}{\partial\theta}\left(\sin\theta\Omega\right)\frac{\partial\Psi}{\partial\phi}\right]+\frac{1}{\sin\theta}\frac{\partial}{\partial\theta}\left[\cos\theta\Omega\frac{\partial\Psi}{\partial\phi}\right]=0. \tag{C.36}$$

Expanding the θ derivatives we arrive at

$$-\nabla^2\frac{\partial\Psi}{\partial t}-\frac{\Omega}{\sin^2\theta}\frac{\partial^3\Psi}{\partial\phi^3}-\Omega\frac{\partial^3\Psi}{\partial\theta^2\partial\phi}-3\cot\theta\Omega\frac{\partial^2\Psi}{\partial\theta\partial\phi} + \frac{1}{\sin\theta}\frac{\partial^2}{\partial\theta^2}\left(\sin\theta\Omega\right)\frac{\partial\Psi}{\partial\phi}+\frac{1}{\sin\theta}\frac{\partial}{\partial\theta}\left(\cos\theta\Omega\right)\frac{\partial\Psi}{\partial\phi}=0. \tag{C.37}$$

Further simplifying this by combining terms into the spherical Laplacian operator and reducing the remaining terms the previous equation becomes

$$\left[\frac{\partial}{\partial t}+\Omega\frac{\partial}{\partial\phi}\right]\nabla^2\Psi-\left[\frac{\partial^2\Omega}{\partial\theta^2}+3\cot\theta\frac{\partial\Omega}{\partial\theta}-2\Omega\right]\frac{\partial\Psi}{\partial\phi}=0. \tag{C.38}$$

Now define $\mu=\cos\theta$, which implies $\frac{\partial}{\partial\mu}=\frac{1}{\sin\theta}\frac{\partial}{\partial\theta}$, and recast the second term as follows

$$\left[\frac{\partial}{\partial t}+\Omega\frac{\partial}{\partial\phi}\right]\nabla^2\Psi-\frac{\partial^2}{\partial\mu^2}\left[\left(1-\mu^2\right)\Omega\right]\frac{\partial\Psi}{\partial\phi}=0. \tag{C.39}$$

C.5 Solutions

Let $\Psi=\sum_{n=m}^{\infty}a_nY_n^m\left(\mu,\phi\right)e^{-im\omega_mt}$, where n and m are integer spherical harmonic orders and ω_m is the frequency of the fixed m mode, and where $V=\frac{\partial^2}{\partial\mu^2}\left[\left(1-\mu^2\right)\Omega\right]$, then equation C.39 becomes

$$\sum_{n=m}^{\infty}\left\{\left[\left(\Omega-\omega_m\right)n\left(n+1\right)\right]+V\right\}a_nY_n^m=0. \tag{C.40}$$

Note the multiplication by $e^{im\omega_m t}$ and division by the im that resulted from the ϕ and t derivatives. To extend the work of Watson (1981) and Gilman & Fox (1997), among others, expand the rotation profile Ω and the function V in Legendre polynomials as $\Omega = \sum_{\ell=0}^{\infty} b_\ell Y_\ell^0$ and $V = \sum_{\ell=0}^{\infty} c_\ell Y_\ell^0$ where we have assumed that Ω and V are symmetric about the equator. This produces the following

$$\sum_{n=m}^{\infty} \left[\omega_m n\left(n+1\right) a_n Y_n^m\right] - \sum_{n=m}^{\infty}\sum_{\ell=0}^{\infty} \left\{\left[n\left(n+1\right) b_\ell + c_\ell\right] a_n Y_\ell^0 Y_n^m\right\} = 0. \tag{C.41}$$

The coefficients of Ψ are then extracted by integrating over the spherical shell against a third conjugate spherical harmonic $\overline{Y}_q^m$, which gives

$$\begin{aligned}\sum_{n=m}^{\infty} a_n \Bigg\{ & \omega_m n\left(n+1\right) \int_{-1}^{1}\int_{0}^{2\pi} \overline{Y}_q^m Y_n^m \left(1-\mu^2\right)^{1/2} d\phi d\mu \\ & - \sum_{\ell=0}^{\infty} \left[n\left(n+1\right) b_\ell + c_\ell\right] \int_{-1}^{1}\int_{0}^{2\pi} \overline{Y}_q^m Y_n^m Y_\ell^0 \left(1-\mu^2\right)^{1/2} d\phi d\mu \Bigg\} = 0.\end{aligned} \tag{C.42}$$

Next we use the orthogonality relation for the spherical harmonics to give a final form to the most general solution. Since $m > 0$ and $n \geq m$ no factorials are less than zero, and n is nonzero so we may divide the solution through by $n\left(n+1\right)$ in equation C.42 and redefining the arbitrary coefficient a_n. This leads to the following eigenvalue problem

$$\sum_{n=m}^{\infty} a_n \left\{ -(-1)^m \omega_m \delta_{q,n} + \sum_{\ell=0}^{\infty} G_{q,n,\ell}^m \left[n\left(n+1\right) b_\ell + c_\ell\right] \right\}, \tag{C.43}$$

$$\tag{C.44}$$

Following Cruzan (1962), the Gaunt integral coefficients ($G_{q,n,\ell}^m$, Gaunt (1929)) are

$$G_{q,n,\ell}^m = \frac{\left[\left(2q+1\right)\left(2n+1\right)\left(2\ell+1\right)\right]^{1/2}}{\sqrt{4\pi} n\left(n+1\right)} \begin{pmatrix} q & n & \ell \\ 0 & 0 & 0 \end{pmatrix} \begin{pmatrix} q & n & \ell \\ -m & m & 0 \end{pmatrix} \tag{C.45}$$

where the Wigner-3j symbols $\begin{pmatrix} j_1 & j_2 & j_3 \\ m_1 & m_2 & m_3 \end{pmatrix}$ have been used. We omit the general form of the second Wigner-3j symbol for simplicity. However, the first Wigner-3j symbol in equation C.45 is a special case of these symbols, where

$$\begin{pmatrix} q & n & \ell \\ 0 & 0 & 0 \end{pmatrix} = \begin{cases} (-1)^{J/2} \left[\frac{(J-2q)!(J-2n)!(J-2\ell)!}{(J+1)!}\right]^{1/2} \frac{(J/2-q)!(J/2)!}{(J/2-n)!(J/2-\ell)!} & \text{if } J \text{ is even} \\ 0 & \text{if } J \text{ is odd} \end{cases}, \quad \text{(C.46)}$$

here $J = q + n + \ell$. It is clear from this last relation that there is a decoupling of even and odd spherical harmonic degrees n. In particular for a given n, only terms that are integer multiples of two distant from n are included in the computation of the coefficients a_n. This is a consequence of the choice to expand the angular velocity Ω and V in only even order spherical harmonics, reflecting the assumption that they are symmetric about the equator.

C.6 Eigenvalues

To find the eigenvalues, namely the frequency ω_m, one in principal would compute the determinant of the matrix $\mathcal{A}$ that arises from equation C.43, as they are determined from the condition that there be an non-trivial solution for Ψ. This matrix will be band diagonal with the width of the band determined by the maximum degree ℓ to which the angular velocity and V are expanded, namely it will be $2\ell + 1$. Unlike Watson (1981), there is a unique matrix for each m. Omitting the eigenvalue identity matrix, the matrix $\mathcal{A}$ has the following structure

$$\mathcal{A}^m_{n,q} = \begin{cases} \sum_{\ell=|q-n|}^{(q+n)} G^m_{q,n,\ell} \left[n\left(n+1\right) b_\ell + c_\ell\right] & \text{for } |n-\ell| \leq q \leq n+\ell \\ 0 & \text{otherwise} \end{cases} \quad \text{(C.47)}$$

where the sum over ℓ has been truncated by the use of the triangle condition on ℓ with respect to q and n. There is also of course a triangle condition on the degree q, wherein $|n-\ell| \leq q \leq n+\ell$. This limits the band to $2\ell+1$. To solve this system, it must be truncated. The minimum rank of the matrix is at least $4\ell + 2$, but typically must be much larger to accurately capture the eigenfrequency ω_m. This in turn depends upon the accuracy of the truncation of the expansion of Ω and V, which at maximum for ASH simulations can be $\ell_{\max} \approx 1000$. Usually, however, the expansion is very good for $\ell_{\max} \approx 24$.

Appendix D

Entropy Diffusion

In a simple fluid system with no mass flux across boundaries, the total rate of entropy change of the system is

$$\dot{S} = \int_V \frac{dV}{T}\frac{dQ}{dt} + \int_{\partial V} \frac{\mathbf{F}_e \cdot d\mathbf{A}}{T}, \tag{D.1}$$

where the rate of change in internal energy is integrated over the relevant volume; the external heat fluxes into the system are accounted for in the second term. Through the first law of thermodynamics, the rate of change in internal energy in the presence of diffusive processes can be written in coordinate space as

$$\frac{dQ}{dt} = -\boldsymbol{\nabla} \cdot \mathbf{F} + \Phi. \tag{D.2}$$

Using $\boldsymbol{\nabla} \cdot (\mathbf{F}/T) = (\boldsymbol{\nabla} \cdot \mathbf{F})\, T + \mathbf{F} \cdot \nabla\,(1/T)$ and Gauss's law, Equation 1 becomes

$$\dot{S} = \int_V \frac{\Phi}{T} - \frac{\mathbf{F}}{T} \cdot \boldsymbol{\nabla} \ln T dV + \int_{\partial V} \frac{1}{T}\,(\mathbf{F}_e - \mathbf{F}) \cdot d\mathbf{A}. \tag{D.3}$$

Assume flux boundary conditions such that the boundary integral vanishes. Then, for entropy diffusion

$$\dot{S} = \int_V \frac{\Phi}{T} + \kappa_S \boldsymbol{\nabla} S \cdot \boldsymbol{\nabla} \ln T dV. \tag{D.4}$$

This looks innocuous, yet it hides some pernicious behavior. In a sub-adiabatic region, where $\boldsymbol{\nabla} T$ is negative and $\boldsymbol{\nabla} S$ is positive, this clearly can violate the second law unless the viscous heating is much larger than the entropy diffusion. If instead the viscosity is negligible, trouble rears its head and $\dot{S} \leq 0$ in a sub-adiabatic region. It could be that the convection

zone is safe from this issue, but there can also be local sub-adiabaticity in the convection zone. While such fluctuations about adiabaticity are weak and temporary, it is nonetheless unphysical. However, if there is a fixed flux through the system, the boundary integral does not vanish indicating that there is an inbalance in the net flux entering and exiting the system. In this case, the second law would remain safe. For a thermal conductivity, the positive definite form for the entropy evolution is

$$\dot{S} = \int_V \frac{\Phi}{T} + \kappa_T \left(\nabla \ln T\right)^2 dV. \tag{D.5}$$

The entropy diffusion can be recast into a usable form. For a perfect gas,

$$\dot{S} = \int_V \frac{\Phi}{T} + \kappa_S \left(\left(\nabla \ln T\right)^2 - \left(\gamma - 1\right) \nabla \ln \rho \cdot \nabla \ln T\right) dV, \tag{D.6}$$

In these terms entropy diffusion amounts to a thermal diffusion as well as a mass diffusion for a perfect gas (it could also be a pressure diffusion). If instead only a thermal conductivity is admitted, it couples the energy equation and the momentum equations through the pressure. Thus a thermal conduction can be regarded as modifying the pressure rails that guide the system. Effectively, in the context of Chapter 4, there should be a modified Lagrangian and a set of modified LBR equations due to diffusion. The entropy equation with thermal conduction is,

$$\frac{dS}{dt} = \frac{1}{\rho T} \left\{ \boldsymbol{\nabla} \cdot \left[\kappa_T \left(\left. \frac{\partial \ln T}{\partial P} \right|_S \nabla P + \left. \frac{\partial \ln T}{\partial S} \right|_P \nabla S \right) \right] + \Phi \right\} \tag{D.7}$$

So, another way to think about the thermal conductivity in regards to entropy production is that it is simultaneously a sub-grid-scale model for entropy mixing through the ∇S term and for the entropy production by unresolved motions that are wrapped into the pressure, effectively being an additional subgrid-scale viscous heating.

Next consider the effect of entropy diffusion on entropy production in gravity waves. For wavelengths much shorter than gradient length scales in the system, the rate of entropy production is

$$\dot{S}_{\text{waves}} = \frac{\kappa_0 \rho_0}{T_0} \boldsymbol{\nabla} S' \cdot \boldsymbol{\nabla} T'. \tag{D.8}$$

For an ideal gas,

$$\frac{S}{c_P} = \ln \frac{P^{1/\gamma}}{\rho}. \tag{D.9}$$

Linearizing this equation gives

$$\frac{T'}{T_0} = \frac{S'}{c_P} + \frac{\gamma - 1}{\gamma}\frac{P'}{P_0}. \tag{D.10}$$

with primes denoting perturbations. Let the dissipation be weak and assume gravity waves under the Lantz-Braginsky-Roberts equations, which has the kinematic pressure ϖ (see Chapter 4). Thus the linearized momentum equation is

$$-\omega^2 \boldsymbol{\xi} = -\boldsymbol{\nabla}\varpi - S'\boldsymbol{\nabla}T_0. \tag{D.11}$$

The horizontal divergence of this equation, under the anelastic condition of $\boldsymbol{\nabla} \cdot \rho_0 \mathbf{u}$, leaves

$$\nabla_h^2 \varpi = -\omega^2 \left(\frac{d\xi_z}{dz} + \xi_z \frac{d \ln \rho_0}{dz} \right) = -k_h^2 \varpi, \tag{D.12}$$

where the last step is valid for plane waves. The wave equation for the vertical displacement ξ_z is then

$$\omega^2 \xi_z - \frac{\omega^2}{k_h^2}\frac{d}{dz}\left(\frac{d\xi_z}{dz} + \xi_z \frac{d \ln \rho_0}{dz} \right) = -\frac{gS'}{c_P}. \tag{D.13}$$

Under the WKB approximation (e.g., large wavenumber local modes), the solution is simply

$$\xi_z = \frac{\xi_0}{\sqrt{\rho_0 k_z}} \exp\left[i \int k_z dz \right]. \tag{D.14}$$

Substituting it back into the wave equation gives the expanded result

$$\omega^2 \xi_z \left\{ 1 + \frac{1}{k_h^2}\left[k_z^2 + i\frac{dk_z}{dz} - \frac{1}{2}\frac{d^2 \ln \rho_0}{dz^2} + \frac{1}{4}\left(\frac{d \ln \rho_0}{dz} \right)^2 + \frac{1}{2}\frac{d^2 \ln k_z}{dz^2} - \frac{1}{4}\left(\frac{d \ln \rho_0}{dz} \right)^2 \right] \right\} = -\frac{gS'}{c_P}. \tag{D.15}$$

If the changes in the background potential are indeed slow, then the derivative terms may be omitted. Thus, the wave equation for ξ_z becomes the simple form

$$\omega^2 \xi_z \left(1 + \frac{k_z^2}{k_h^2} \right) = -\frac{gS'}{c_P}. \tag{D.16}$$

From Chapter 4, it is known that the Eulerian perturbations for the entropy are $S' = -\boldsymbol{\xi} \cdot \nabla S_0$. For the situation considered here S_0 has only vertical derivatives so

$$S' = -\xi_z \frac{dS_0}{dz}. \tag{D.17}$$

Note that the Brunt-Väisälä frequency is

$$N^2 = \frac{g}{c_P}\frac{dS_0}{dz}, \tag{D.18}$$

and the vertical displacement can be written

$$\xi_z = -\frac{gS'}{N^2 c_P}. \tag{D.19}$$

With these equations in hand, the dispersion relationship can be found by substituting them into Equation D.16 yielding

$$k_z^2 = k_h^2 \left(\frac{N^2}{\omega^2} - 1\right), \tag{D.20}$$

which is the large-wavenumber limit of the gravity wave dispersion relation.

With these relationships in hand, the growth rate of waves may be assessed by using the estimated wave damping rate argument of (Braginskii, 1965), but taking into account the presence of entropy diffusion in a stable stratification. First use the linearized equation of state with the substitution of the kinematic pressure ϖ for P', which yields

$$\frac{T'}{T_0} = \frac{S'}{c_P} + \frac{\gamma - 1}{\gamma}\frac{\rho_0 \varpi}{P_0}. \tag{D.21}$$

Then use Equation D.12 to eliminate the kinematic pressure to find

$$\frac{T'}{T_0} = \frac{S'}{c_P} + \frac{\gamma - 1}{\gamma}\frac{\rho_0}{P_0}\frac{\omega^2}{k_h^2}\left(\frac{d\xi_z}{dz} + \xi_z \frac{d\ln\rho_0}{dz}\right). \tag{D.22}$$

Recalling the WKB approximation, this becomes

$$\frac{T'}{T_0} = \frac{S'}{c_P} + \frac{\gamma - 1}{\gamma}\frac{\rho_0}{P_0}\frac{\omega^2}{k_h^2}\left[ik_z + \frac{1}{2}\left(\frac{d\ln\rho_0}{dz} - \frac{d\ln k_z}{dz}\right)\right]\xi_z. \tag{D.23}$$

Luckily, Equation D.19 allows this to be simplified further to

$$\frac{T'}{T_0} = \frac{S'}{c_P}\left\{1 - \frac{\gamma - 1}{\gamma}\frac{\rho_0}{P_0}\frac{g\omega^2}{N^2 k_h^2}\left[ik_z + \frac{1}{2}\left(\frac{d\ln\rho_0}{dz} - \frac{d\ln k_z}{dz}\right)\right]\right\}, \tag{D.24}$$

Only the real-valued terms in the equation can contribute to entropy production, as imaginary terms produce only phase offsets. The derivative of the wavenumber k_z follows from the dispersion relationship, assuming that the horizontal wavenumber does not vary in z, as

$$\frac{d\ln k_z}{dz} = \frac{1}{2}\frac{dN^2}{dz}\left(N^2-\omega^2\right)^{-1}. \tag{D.25}$$

If the stratification remains so that $d\rho_0/dz < 0$, that term in the equation only contributes to positive entropy production. The question then remains what is the possible wave growth rate in the presence of entropy diffusion? If the wavenumber is assumed to vary much more rapidly than the density, the term involving its derivative will dominate that expression. Furthermore, if one makes k_h increasingly large relative to k_z, the expression for the temperature fluctuations simplifies to

$$\frac{T'}{T_0} \approx \frac{(\gamma-1)\,g\omega^2}{4k_h^2 c_{s,0}^2\left(N^2-\omega^2\right)}\frac{d\ln N^2}{dz}\frac{S'}{c_P} \tag{D.26}$$

Returning to the expression for entropy production or destruction through its diffusion $q = \kappa_S \boldsymbol{\nabla} S \cdot \boldsymbol{\nabla} T$, it is clear that if $\boldsymbol{\nabla} S > 0$ and $\boldsymbol{\nabla} T < 0$ then the second law is violated. What about for the waves, could they be growing unphysically as well? This depends upon the sign of dN^2/dz, so they too can be violating the second law. The remaining question is how fast might they be growing? Following (Braginskii, 1965), which gives an argument that connects the wave damping rate Γ with the rate of entropy production in the limit of weak damping ($|\Gamma/\omega| \ll 1$). Extending this argument to wave growth and utilizing the expression for the LBR wave energy density ($E = \rho S'^2 g^2/N^2 c_P^2$) from (Brown et al., 2012), it is found that

$$\Gamma_S = \frac{q}{2E} \approx \frac{\kappa_S k_B T_0 N^2}{8mg^2 H_P\left(N^2-\omega^2\right)} \tag{D.27}$$

If this growth rate Γ_S is greater than the diffusion damping time, the gravity waves can grow artificially. With the form of the denominator, this is particularly true for waves with frequencies close to the Brunt-Väisälä frequency. This growth rate is assessed for the radiative envelopes of the B-type stars in Chapter 10. Beyond the uncontrolled growth of linear waves, this result and the simple thermodynamic argument above point to problems with the concept of entropy diffusion despite its original physical motivation.

Appendix E

Reduced Sound Speed

This chapter outlines the reduced sound-speed equations as implementated in the Compressive Spherical Segment (CSS) code. The following set of Navier-Stokes equations are for a fully compressible, rotating fluid in a spherical domain with standard orthonormal coordinates and unit vectors. The rotation axis is chosen to align with the z-axis such that

$$\mathbf{\Omega} = \Omega\hat{\mathbf{z}} = \Omega\left[\cos\theta\hat{\mathbf{r}} - \sin\theta\hat{\boldsymbol{\theta}}\right]. \tag{E.1}$$

The centripetal acceleration ($\mathbf{a}_c = \mathbf{\Omega} \times \mathbf{r} \times \mathbf{r}$) due to the rotating frame depends upon the axial radius vector

$$\mathbf{R} = r\sin\theta\left[\sin\theta\hat{\mathbf{r}} + \cos\theta\hat{\boldsymbol{\theta}}\right]. \tag{E.2}$$

Thus, the equations of motion are mass continuity,

$$\frac{\partial\rho}{\partial t} = -(1-\alpha)\frac{\partial\rho u_j}{\partial x_j}, \tag{E.3}$$

conservation of momentum,

$$\frac{\partial\rho u_i}{\partial t} = -\frac{\partial}{\partial x_j}\left[\rho u_i u_j\right] - \frac{\partial P}{\partial x_i} + \rho f_i + \frac{\partial\mu D_{ij}}{\partial x_j} + 2\rho\left(\mathbf{u}\times\mathbf{\Omega}\right)_i + \rho\Omega^2 R_i, \tag{E.4}$$

and conservation of internal energy,

$$\frac{\partial}{\partial t}\left[\rho e + \frac{1}{2}\rho u_i^2\right] = -\frac{\partial}{\partial x_j}\left[\rho u_j\left(\frac{1}{2}u_i^2 + e + \frac{P}{\rho}\right)\right] - \frac{\partial q_j}{\partial x_j} + \rho\epsilon. \tag{E.5}$$

The viscous stress tensor $\mathcal{D}$ is defined as

$$\mathcal{D}_{ij} = 2\left[e_{ij} - \frac{1}{3}\nabla\cdot\mathbf{u}\delta_{ij}\right], \tag{E.6}$$

and the viscous heating term Φ is defined as

$$\Phi = \frac{1}{2}\mathcal{D} : \mathcal{D} = 2\left[\mathbf{e} : \mathbf{e} - \frac{1}{3}\left(\nabla \cdot \mathbf{u}\right)^2\right]. \tag{E.7}$$

In both equations E.6 and E.7 the tensor $\mathbf{e}$ is the strain rate tensor and is itself a function of $\mathbf{u}$. With these equations in hand, we can move forward to reduce the system to the primitive variables and recover the modified Navier-Stokes equations. First, the momentum equation will be dealt with and then the energy equation. The first step to simplifying the momentum equation is to use the continuity equation as so:

$$\begin{aligned}
\rho\frac{\partial u_i}{\partial t} + u_i\frac{\partial \rho}{\partial t} &= \rho\frac{\partial u_i}{\partial t} - (1-\alpha)u_i\frac{\partial \rho u_j}{\partial x_j}, \\
\rho\frac{\partial u_i}{\partial t} &= (1-\alpha)u_i\frac{\partial \rho u_j}{\partial x_j} - \frac{\partial \rho u_i u_j}{\partial x_j} + \cdots, \\
\rho\frac{\partial u_i}{\partial t} &= -\alpha u_i\frac{\partial \rho u_j}{\partial x_j} - \rho u_j\frac{\partial u_i}{\partial x_j} + \cdots, \\
\rho\frac{\partial u_i}{\partial t} &= -\alpha u_i\frac{\partial \rho u_j}{\partial x_j} - \rho u_j\frac{\partial u_i}{\partial x_j} - \frac{\partial P}{\partial x_i} + \rho f_i + \frac{\partial \mu D_{ij}}{\partial x_j} + 2\rho\left(\mathbf{u}\times\mathbf{\Omega}\right)_i + \rho\Omega^2 R_i.
\end{aligned}$$

Thus, the momentum equation remains essentially the same but with the addition of a term proportional to α that modifies the convective terms in the Navier-Stokes equations. The energy equation is slightly more complicated in that we must deal with the kinetic energy terms.

$$\begin{aligned}
\frac{\partial \frac{1}{2}\rho u_i^2}{\partial t} &= \frac{1}{2}u_i^2\frac{\partial \rho}{\partial t} + \rho u_i\frac{\partial u_i}{\partial t}, \\
&= -\frac{1}{2}\left(1-\alpha\right)u_i^2\frac{\partial \rho u_j}{\partial x_j} - \alpha u_i^2\frac{\partial \rho u_j}{\partial x_j} - \rho u_i u_j\frac{\partial u_i}{\partial x_j} - u_i\frac{\partial P}{\partial x_i} + \rho u_i f_i + u_i\frac{\partial \mu D_{ij}}{\partial x_j} + \rho\Omega^2 u_i R_i \\
&= -\frac{1}{2}\left(1+\alpha\right)u_i^2\frac{\partial \rho u_j}{\partial x_j} - \rho u_i u_j\frac{\partial u_i}{\partial x_j} - u_i\frac{\partial P}{\partial x_i} + \rho u_i f_i + u_i\frac{\partial \mu D_{ij}}{\partial x_j} + \rho\Omega^2 u_i R_i
\end{aligned}$$

Hence, the energy equation becomes

$$\begin{aligned}
\frac{\partial \rho e}{\partial t} &= \frac{1}{2}\left(1+\alpha\right)u_i^2\frac{\partial \rho u_j}{\partial x_j} + \rho u_i u_j\frac{\partial u_i}{\partial x_j} + u_i\frac{\partial P}{\partial x_i} - \rho u_i f_i - u_i\frac{\partial \mu D_{ij}}{\partial x_j} - \rho\Omega^2 u_i R_i \\
&\quad -\frac{\partial}{\partial x_j}\left[\rho u_j\left(\frac{1}{2}u_i^2 + e + \frac{P}{\rho}\right)\right] - \frac{\partial q_j}{\partial x_j} + \rho\epsilon, \\
\rho\frac{\partial e}{\partial t} - \left(1-\alpha\right)e\frac{\partial \rho u_j}{\partial x_j} &= \frac{1}{2}\left(1+\alpha\right)u_i^2\frac{\partial \rho u_j}{\partial x_j} + \rho u_i u_j\frac{\partial u_i}{\partial x_j} + u_i\frac{\partial P}{\partial x_i} - \rho u_i f_i - u_i\frac{\partial \mu D_{ij}}{\partial x_j} - \rho\Omega^2 u_i R_i \\
&\quad -\frac{\partial}{\partial x_j}\left[\rho u_j\left(\frac{1}{2}u_i^2 + e + \frac{P}{\rho}\right)\right] - \frac{\partial q_j}{\partial x_j} + \rho\epsilon,
\end{aligned}$$

now eliminate the kinetic energy u_i^2 terms and second simplify the convective derivatives of e

$$\rho\frac{\partial e}{\partial t} - (1-\alpha)\, e\frac{\partial \rho u_j}{\partial x_j} = \frac{\alpha}{2}u_i^2\frac{\partial \rho u_j}{\partial x_j} + u_i\frac{\partial P}{\partial x_i} - \rho u_i f_i - u_i\frac{\partial \mu D_{ij}}{\partial x_j} - \rho\Omega^2 u_i R_i$$
$$- \frac{\partial}{\partial x_j}\left[\rho u_j\left(e + \frac{P}{\rho}\right)\right] - \frac{\partial q_j}{\partial x_j} + \rho\epsilon, \tag{E.8}$$

$$\rho\left[\frac{\partial e}{\partial t} + u_j\frac{\partial e}{\partial x_j}\right] = \alpha\left(\frac{1}{2}u_i^2 - e\right)\frac{\partial \rho u_j}{\partial x_j} + u_i\frac{\partial P}{\partial x_i} - \rho u_i f_i - u_i\frac{\partial \mu D_{ij}}{\partial x_j} - \rho\Omega^2 u_i R_i$$
$$- \frac{\partial P u_j}{\partial x_j} - \frac{\partial q_j}{\partial x_j} + \rho\epsilon. \tag{E.9}$$

Lastly, simplify the terms involving the pressure

$$\rho\left[\frac{\partial e}{\partial t} + u_j\frac{\partial e}{\partial x_j}\right] = \alpha\left(\frac{1}{2}u_i^2 - e\right)\frac{\partial \rho u_j}{\partial x_j} + u_i\frac{\partial P}{\partial x_i} - \rho u_i f_i - u_i\frac{\partial \mu D_{ij}}{\partial x_j} - \rho\Omega^2 u_i R_i$$
$$- \frac{\partial P u_j}{\partial x_j} - \frac{\partial q_j}{\partial x_j} + \rho\epsilon, \tag{E.10}$$

$$\rho\left[\frac{\partial e}{\partial t} + u_j\frac{\partial e}{\partial x_j}\right] = \alpha\left(\frac{1}{2}u_i^2 - e\right)\frac{\partial \rho u_j}{\partial x_j} - \rho u_i f_i - u_i\frac{\partial \mu D_{ij}}{\partial x_j} - \rho\Omega^2 u_i R_i$$
$$- P\frac{\partial u_j}{\partial x_j} - \frac{\partial q_j}{\partial x_j} + \rho\epsilon. \tag{E.11}$$

E.1 Equations of State

While equations E.3-E.5 are to be solved for ρ, P, T, e, and the three components of $\mathbf{u}$, they comprise only five independent relations. Since only two of the four state variables are independent, the system is closed by first specifying an equation of state (typically relating the state variables ρ, P, and T) and then deriving an equation for e. If we assume a near-perfect gas, the equation of state is

$$P = \frac{\gamma - 1}{\gamma} C_P \rho T. \tag{E.12}$$

where γ is the adiabatic index and C_P is the constant pressure specific heat. Thus, the internal energy is

$$e = C_V T. \tag{E.13}$$

Another useful state variable is the specific entropy. For a perfect gas this is

$$s = C_P \left(\frac{1}{\gamma} \ln P - \ln \rho \right). \tag{E.14}$$

or

$$P = \rho^\gamma e^{\gamma s / C_P} \tag{E.15}$$

E.2 Additional Constraints

$$\mathbf{q} = -\left(\kappa_r + \kappa_{sc} T^3 \right) \nabla T - \kappa_s \nabla S. \tag{E.16}$$

Using the equation of state above and assuming that C_P is constant, an equation for the evolution of the specific entropy can be derived from the energy conservation equation. To do so, use the second law of thermodynamics

$$de = Tds - PdV = Tds + \frac{P}{\rho^2} d\rho, \tag{E.17}$$

$$\frac{de}{dt} = T\frac{ds}{dt} + \frac{P}{\rho^2}\frac{d\rho}{dt}. \tag{E.18}$$

The energy equation is

$$\begin{aligned}
\rho \frac{de}{dt} &= \alpha \left(\frac{1}{2} u_i^2 - e \right) \frac{\partial \rho u_j}{\partial x_j} - \rho u_i f_i - u_i \frac{\partial \mu D_{ij}}{\partial x_j} - \rho \Omega^2 u_i R_i - P \frac{\partial u_j}{\partial x_j} - \frac{\partial q_j}{\partial x_j} + \rho \epsilon, \\
\rho T \frac{ds}{dt} + \frac{P}{\rho}\frac{d\rho}{dt} &= \alpha \left(\frac{1}{2} u_i^2 - e \right) \frac{\partial \rho u_j}{\partial x_j} - \cdots, \\
\rho T \frac{ds}{dt} &= \alpha \left(\frac{1}{2} u_i^2 - e - \frac{P}{\rho} \right) \frac{\partial \rho u_j}{\partial x_j} - \rho u_i f_i - u_i \frac{\partial \mu D_{ij}}{\partial x_j} - \rho \Omega^2 u_i R_i - \frac{\partial q_j}{\partial x_j} + \rho \epsilon.
\end{aligned}$$

where the equation $d\rho/dt = \alpha \boldsymbol{\nabla} \cdot \rho \mathbf{u} - \rho \boldsymbol{\nabla} \cdot \mathbf{u}$ has been invoked. However, $e = C_P T - \frac{P}{\rho}$, so the α enhanced entropy equation becomes

$$\rho T \frac{ds}{dt} = \alpha \left(\frac{1}{2} u_i^2 - C_P T \right) \frac{\partial \rho u_j}{\partial x_j} - \rho u_i f_i - u_i \frac{\partial \mu D_{ij}}{\partial x_j} - \rho \Omega^2 u_i R_i - \frac{\partial q_j}{\partial x_j} + \rho \epsilon. \tag{E.19}$$

E.3 Modified Sound Wave Propagation

Under a simple linearization of the above equations in which we assume a local subdomain with the following properties

$$\begin{aligned}
\rho &= \rho_0 + \rho_1, \\
s &= s_0, \\
P &= P_0 \left(1 + \frac{\gamma \rho_1}{\rho_0}\right),
\end{aligned}$$

where $\rho_0 = s_0 = P_0 = const.$. Then to first order the above equations become

$$\begin{aligned}
\frac{\partial \rho_1}{\partial t} &= -\left(1-\alpha\right)\rho_0 \nabla \cdot \mathbf{u}, \\
\frac{\partial \mathbf{u}}{\partial t} &= -\frac{1}{\rho_0}\nabla P
\end{aligned}$$

If we assume wavelike solutions of the form

$$\begin{aligned}
\rho_1 &= \rho_2 e^{i(\mathbf{k}\cdot\mathbf{r}-\omega t)}, \\
\mathbf{u} &= \mathbf{u}_0 e^{i(\mathbf{k}\cdot\mathbf{r}-\omega t)}
\end{aligned}$$

then, we have

$$\begin{aligned}
\omega \rho_2 &= \left(1-\alpha\right)\rho_0 \mathbf{k}\cdot\mathbf{u}_0, \\
\omega \mathbf{u} &= \frac{\gamma \mathbf{k} P_0}{\rho_0}\frac{\rho_2}{\rho_0}
\end{aligned}$$

noting that $\frac{\gamma P_0}{\rho_0} = c_s^2$ this becomes

$$\begin{aligned}
\omega^2 \mathbf{u} &= \mathbf{k} c_s^2 \left(1-\alpha\right)\mathbf{k}\cdot\mathbf{u}_0, \\
\omega &= k c_s \sqrt{1-\alpha}.
\end{aligned}$$